Edited by
Gerhard Gompper, Michael Schick

WILEY-VCH

Soft Matter

Volume 2
Complex Colloidal Suspensions

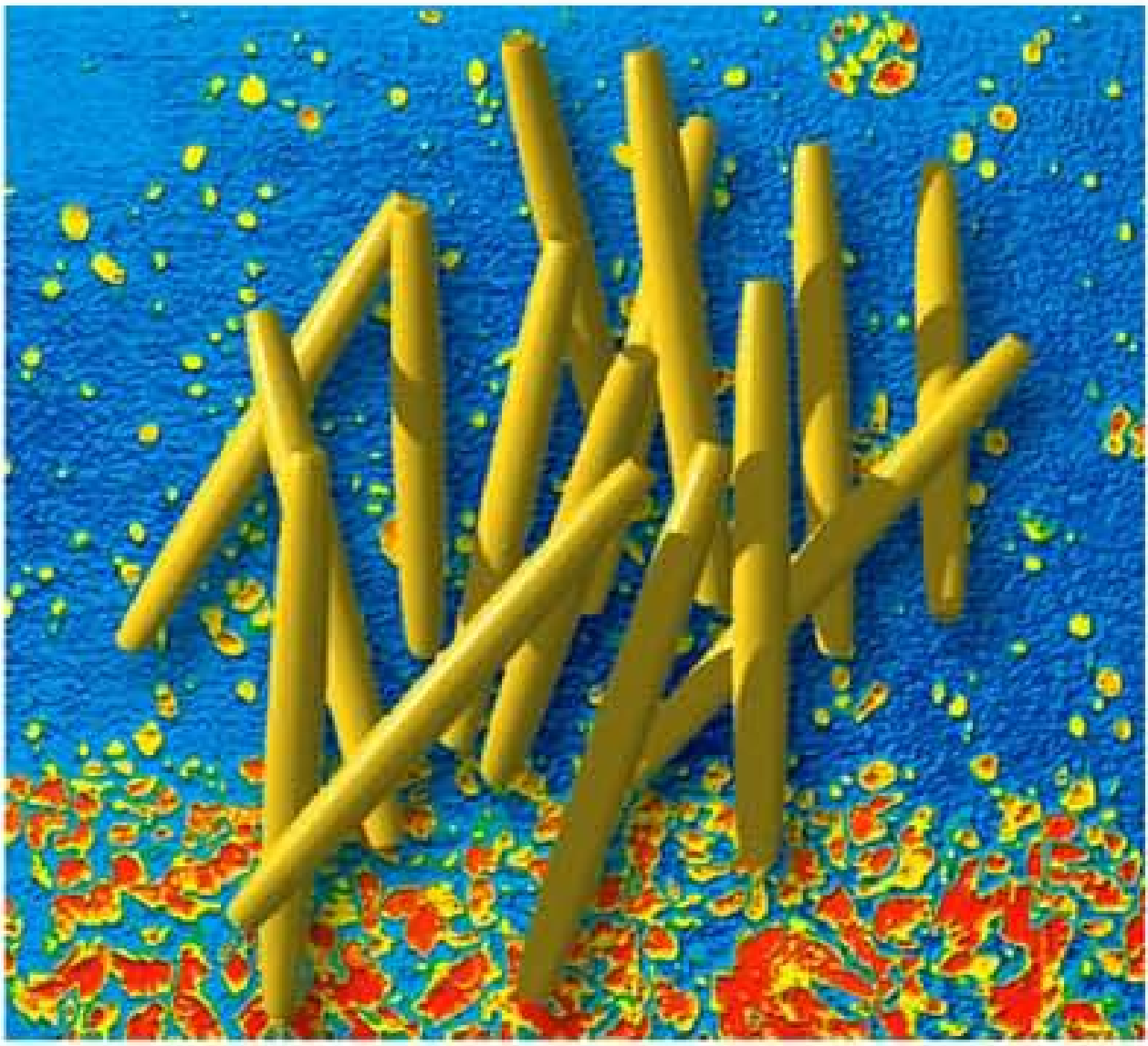

Soft Matter

Edited by
G. Gompper, M. Schick

Volumes Published in this Series

Volume 1: Polymer Melts and Mixtures

1 Polymer Dynamics in Melts
Andreas Wischnewski and Dieter Richter

2 Self-Consistent Field Theory and Its Applications
Mark W. Matsen

3 Comparison of Self-Consistent Field Theory and Monte Carlo Simulations
Marcus Müller

Volume 2: Complex Colloidal Suspensions

1 Phase Behavior of Rod-Like Viruses and Virus–Sphere Mixtures
Zvonimir Dogic and Seth Fraden

2 Field Theory of Polymer–Colloid Interactions
Erich Eisenriegler

3 Rod-Like Brownian Particles in Shear Flow
Jan K. G. Dhont and Wim J. Briels

Soft Matter

Volume 2: Complex Colloidal Suspensions

Edited by
Gerhard Gompper and Michael Schick

WILEY-VCH Verlag GmbH & Co. KGaA

Editors

Prof. Dr. Gerhard Gompper
Institute of Solid State Research
Research Centre Jülich
52525 Jülich
Germany

Prof. Dr. Michael Schick
Department of Physics
University of Washington
Seattle, WA 98195-1560
USA

Cover illustration
The picture shows a polarization light micrograph of colloidal boehmite rods during isotropic-nematic phase separation. Blue color indicates the isotropic, red color the nematic phase. The nematic droplets sink to the bottom because their density is slightly larger. The schematic picture in the front shows the orientational ordering of colloidal rods in the nematic phase. (Original pictures courtesy of J. Dhont and Z. Dogic).

Library of Congress Card No.: applied for

British Library Cataloguing-in-Publication Data:
A catalogue record for this book is available from the British Library.

Bibliographic information published by Die Deutsche Bibliothek
Die Deutsche Bibliothek lists this publication in the Deutsche Nationalbibliografie; detailed bibliographic data is available in the Internet at http://dnb.ddb.de

Printed in the Federal Republic of Germany
Printed on acid-free and chlorine-free paper

Cover Design: SCHULZ Grafik-Design, Fußgönheim
Composition: Steingraeber Satztechnik GmbH, Ladenburg
Printing: betz-druck GmbH, Darmstadt
Bookbinding: Litges & Dopf Buchbinderei GmbH, Heppenheim

ISBN-13: 978-3-527-31369-3
ISBN-10: 3-527-31369-9

Preface

The study of Soft Matter is concerned with understanding the properties of materials which have structural length scales in the range of a few nanometers to several micrometers, and which are strongly affected by thermal fluctations. Several interesting properties follow immediately from these seemingly simple conditions. For example, the long length scales imply that small external fields can lead to large perturbations, which is the origin of the name "Soft Matter". Similarly, long length scales and an energy scale on the order of the thermal energy $k_{\mathrm{B}}T$ imply large structural relaxation times. Therefore, phenomena far from thermal equilibrium play a very important role.

Most soft-matter components are macromolecules which exhibit polymeric, colloidal, or amphiphilic properties. Although these materials have been studied for a long time, it has been realized only in the last two decades that these systems share many properties, so that a large synergy arises from a unification of these subfields. In recent years, this unification has become more urgent due to the fact that many biological systems and biomaterials simultaneously contain several components with different polymeric, amphiphilic and colloidal character. One example, in which all these properties are united in a single macromolecule, is provided by membrane proteins. They consist of a linear chain of amino acids, and are therefore hetero-polymers, have hydrophobic and hydrophilic parts to favor localisation in a lipid bilayer membrane, and are therefore amphiphilic, and behave in some of their properties like a cylindrical barrel, and are therefore colloidal.

The first volume of this Soft Matter series focused on system in which the polymeric properties were dominant. In this second volume, our attention is turned to systems in which the colloidal character prevails. In Chapter 1, Zvonimir Dogic and Seth Fraden provide an excellent overview of the surprising variety of structures which self-assemble in the apparently simple system consisting of a mixture of colloidal spheres and rods. In addition, the system contains non-adsorbing polymers, which serve to induce an effective attractive interaction between the colliodal components. This "depletion in-

Soft Matter, Vol. 2: Complex Colloidal Suspensions. Edited by G. Gompper and M. Schick

ISBN: 3-527-31369-9

teraction" arises from the change of accessible conformations of a polymer in the vicinity of surfaces. The theoretical description of the colloid-polymer interaction is the topic of Chapter 2 of Erich Eisenriegler, who employs the very powerful tools developed for critical phenomena to extract the universal properties of these systems. Finally, in Chapter 3, Jan Dhont and Wim Briels authoritatively describe the behavior of rod-like colloids in shear flow. This chapter addresses some of the very interesting phenomena arising in systems far from thermal equilibrium. While such non-equilibrium dynamics play an important role in all soft matter systems, colloids provide a nice model system in which to study them because colloid suspensions are comparatively simple. Thus progress in studying and understanding the new phenomena is achieved most easily.

We anticipate that the high standards set by the authors of these initial two volumes will inspire a similar level in those participating in subsequent ones. For our part, we will strive to ensure that the contents of future volumes will be as stimulating as these initial ones.

November 2005 Gerhard Gompper and Michael Schick

Contents

Soft Matter, Vol. 2: Complex Colloidal Suspensions. Edited by G. Gompper and M. Schick

ISBN: 3-527-31369-9

List of Contributors

Dr. Wim J. Briels
Computational Dispersion Rheology
Department of Applied Physics
University of Twente
Postbus 217
7500 AE Enschede
The Netherlands

Prof. Jan Dhont
Institut für Festkörperforschung
Forschungszentrum Jülich
52425 Jülich
Germany

Dr. Zvonimir Dogic
Rowland Institute at
Harvard University
100 Edwin H. Land Boulevard
Cambridge, MA 02142
USA

Prof. Erich Eisenriegler
Institut für Festkörperforschung
Forschungszentrum Jülich
52425 Jülich
Germany

Prof. Seth Fraden
Complex Fluids Group
Department of Physics
Brandeis University
Waltham, MA 02454
USA

Soft Matter, Vol. 2: Complex Colloidal Suspensions. Edited by G. Gompper and M. Schick

ISBN: 3-527-31369-9

1
Phase Behavior of Rod-Like Viruses and Virus–Sphere Mixtures

Zvonimir Dogic and Seth Fraden

Abstract

An overview is given of the experimental work on the liquid crystalline phase behavior of semi-flexible viruses in an aqueous solution. We start by briefly summarizing the theoretical work of Onsager which describes the isotropic-nematic phase transitions of perfectly rigid rods. Extensions of the Onsager theory to the case of semi-flexible and charged rods are presented. In the first part of the review we focus on the phase behavior of a pure solution of semi-flexible virus *fd*. With increasing concentration *fd* form isotropic, cholesteric and smectic phase. In the limit of high ionic strength the agreement between the Onsager theory and experiments on the isotropic-nematic phase of *fd* virus is quantitative. The discrepancies at low ionic strength strongly hint at a need to rigorously incorporate electrostatic interactions into phase behavior of rigid rods. In the second part of the review we focus on the phase behavior of mixtures of rods with either hard spheres or flexible polymers. Amongst others we described a number of novel phases observed in these mixtures such as a lamellar phase, columnar phase, colloidal membranes and surface induced smectic phase. These structures are still very poorly understood and there is a clear need for the theoretical work explaining their stability.

1.1
Introduction

The reasons physicists give for studying colloids are varied. Our initial motivation was that colloids can serve as model experimental systems to study simple fluids because, with careful preparation, colloids approximate hard particles. Numerous studies have investigated the phase behavior, structure,

Soft Matter, Vol. 2: Complex Colloidal Suspensions. Edited by G. Gompper and M. Schick

ISBN: 3-527-31369-9

and macroscopic viscoelastic properties of suspensions of spherical colloids (Poon and Pusey 1995). Far less studied have been colloids of anisotropic shape, in spite of their long-recognized similarity to liquid crystals. Counterintuitively, hard-rod fluids are theoretically simpler systems to understand than hard spheres (Forsyth et al. 1978). This surprising fact was first recognized by Onsager (1949), who realized that the isotropic–nematic (I–N) transition in the rod-like colloid tobacco mosaic virus (TMV) occurred at such low concentrations that only two-body interactions were necessary in order to quantitatively explain the I–N phase transition. In fact, in the limit of long thin rods, Onsager's theory becomes exact. This is in contrast to the theory of phase transitions of hard spheres, for which no exact results exist (in three dimensions).

For some years, the Complex Fluids Group at Brandeis has studied the liquid-crystalline behavior of suspensions of TMV (Fraden et al. 1985; Hurd et al. 1985; Wen and Meyer 1987; Oldenbourg et al. 1988; Fraden et al. 1989; Meyer 1990; Fraden et al. 1993; Wang et al. 1994; Fraden 1995; Adams and Fraden 1998) and filamentous phage *fd* (Tang and Fraden 1993; Tang and Fraden 1995; Fraden 1995; Tang and Fraden 1996; Dogic and Fraden 1997; Adams et al. 1998; Dogic et al. 2000; Dogic and Fraden 2001; Grelet and Fraden 2003; Dogic 2003; Purdy et al. 2003; Purdy and Fraden 2004a; Purdy and Fraden 2004b; Purdy et al. 2005). TMV is a beautiful colloidal rod (Kreibig and Wetter 1980; Wetter 1985). It is completely rigid and forms isotropic, nematic, smectic and colloidal crystalline phases. However, TMV is difficult to work with. One must cultivate tobacco plants, infect them with virus, harvest the crop, extract the virus – which takes months – and, in addition, all this must be done with care to preserve the monodispersity of the virus. Physics graduate students rebel at the thought of producing enough virus for a PhD thesis! Without an abundant source of TMV, studies of its phase behavior are impracticable.

So our laboratory switched from TMV to the semi-flexible bacteriophage *fd*, which also forms several liquid-crystalline phases: isotropic, cholesteric, and smectic, but not colloidal crystals. Because *fd* infects bacteria, growing *fd* is relatively quick and easy. Furthermore, genetic engineering of *fd* is well established, and we have produced mutants of varying length and charge.

This chapter describes the phase behavior of *fd* virus suspensions. First, we present our results on *fd* alone. The results obtained up to 1995 are summarized in another review article (Fraden 1995). While theory and experiment are in agreement for the isotropic–cholesteric phase transition for suspensions with high salt concentrations used to screen long-range electrostatic repulsion, theoretical explanations of all other phases fail. We see a quantitative discrepancy between theory and experiment for the nematic phase at low ionic strength, and multiple quantitative and qualitative breakdowns of the

theory of the smectic phase. Also, we have not even a clue of why a cholesteric phase is observed in *fd*, but a nematic in a closely related species, *pf1*, which has a nearly identical atomic structure (Grelet and Fraden 2003). Second, we present results on mixtures of the viral rods with spherical colloids or spherical polymers. Some of the phase behavior, such as depletion-induced phase separation, was as anticipated. But an astounding array of unexpected results was also observed. A laundry list includes microphase separation of rods and spheres into columnar, cubic, and lamellar structure; isolated colloidal membranes consisting of a sheet of rods and stabilized via protrusion forces; and a quasi-two-dimensional smectic phase that exists on the isotropic–nematic interface that plays a key role in phase separation kinetics. While originally we were motivated to study virus suspensions because they are model systems of simple fluids, now we are motivated by a spirit of exploration driven by the expectation that more unexpected results will follow the ones described below.

1.2
Entropy-Driven Ordering Within the Second Virial Approximation

In the first part of this chapter we briefly review the theoretical work describing liquid-crystalline phase transitions in colloidal rods. This is not meant to be exhaustive. For more detailed theoretical accounts, the reader is referred to recent review articles (Stephen and Straley 1974; Odijk 1986; Vroege and Lekkerkerker 1992) and the original article by Onsager (1949).

The majority of studies of the ordering transitions in hard-particle fluids belong to a class of theories called density-functional theories (DFTs) (Hansen and McDonald 1986). The simplest version of DFT takes into account the interactions between particles at the level of second virial approximation. The free energy of a hard-particle fluid is then

$$\frac{F}{k_{\mathrm{B}}T} = \int_V \mathrm{d}\boldsymbol{r}\, \rho(\boldsymbol{r}) \ln[\rho(\boldsymbol{r})] - \tfrac{1}{2} \int_V \mathrm{d}\boldsymbol{r}_1 \int_V \mathrm{d}\boldsymbol{r}_2\, \rho(\boldsymbol{r}_1)\rho(\boldsymbol{r}_2)\beta(\boldsymbol{r}_1, \boldsymbol{r}_2) \qquad (1.1)$$

where k_{B} is the Boltzmann constant, T is the absolute temperature, $\rho(\boldsymbol{r})$ denotes the density of particles, $\boldsymbol{r}_1$ and $\boldsymbol{r}_2$ are vectors denoting the position and/or orientation of two particular particles, and $\beta(\boldsymbol{r}_1, \boldsymbol{r}_2)$ is the Meyer–Meyer overlap function. Its value equals -1 if there is any overlap between two hard particles located at $\boldsymbol{r}_1$ and $\boldsymbol{r}_2$; otherwise its value is equal to zero. This expression has been used for a variety of cases to study entropy-induced ordering in hard-particle fluids. Onsager (1949) was the first to show that Eq. (1.1) is essentially exact for isotropic spherocylinders when $L/D_{\mathrm{sc}} \to \infty$, where L is the length and D_{sc} is the diameter of the spherocylinder. As

the aspect ratio of spherocylinders is increased, the third and higher virial coefficients become negligible.

The second virial theory also predicts a stable smectic phase in a solution of perfectly aligned spherocylinders as well as for spherocylinders with both positional and orientational degrees of freedom (Hosino et al. 1979; Mulder 1987; van Roij et al. 1995; van der Schoot 1996). However, to describe the suspensions quantitatively at the densities of the nematic–smectic (N–S) phase transition, it is necessary to include higher virial coefficients in the free-energy expression. For perfectly aligned spherocylinders, inclusion of the third and fourth virial coefficients into the free energy results in theoretical predictions for the N–S transitions that are in quantitative agreement with simulation results. The calculations that consider ordering transitions using only second virial coefficients are uncontrolled approximations, unless it can be shown that higher virial coefficients are negligible, as is the case of the Onsager treatment of the I–N phase transition.

In any hard-particle fluid, due to the simplicity of the interaction potential, the energy of any allowed configuration is simply proportional to $nk_{\mathrm{B}}T$, with n being the number density of particles. Due to this simple fact, the minimum of the free energy of a hard-particle fluid $F = E - ST = T(\alpha - S)$ (α is a constant) is equivalent to the maximum of the entropy. Furthermore, the resulting phase diagram is temperature-independent (athermal) because both α and S are independent of temperature. Ordering transitions in hard-particle fluids are still possible because the expression for entropy, or equivalently free energy, splits into two parts. The first integral in Eq. (1.1) is the ideal part of the free energy and always attains a minimum value for the uniform probability distribution $\rho(\boldsymbol{r}) =$ constant. Therefore, this contribution to the total free energy always suppresses an ordering transition. The second integral in Eq. (1.1) represents the second virial approximation for the interaction free energy, which is proportional to the excluded volume, and under certain circumstances is lower for an ordered state. Therefore, the interaction part of the free energy drives the system toward ordering. The actual location of the ordering transition is determined from the competition between the ideal and interaction contributions to the total free energy. In this section, we briefly review the theoretical description of phase transitions that can be described using Eq. (1.1) for pure hard rods.

1.2.1
Isotropic–Nematic Phase Transition Within the Second Virial Approximation

The density functional of the sort shown in Eq. (1.1) was first used in a seminal paper by Onsager (1949). He was seeking to explain the formation of the nematic phase in solutions of rod-like tobacco mosaic virus (TMV), inorganic

needles of vanadium pentoxide, and discs of bentonite. These transitions were found to occur at very low volume fraction (Zocher 1925; Bawden et al. 1936).

In the Onsager theory, the system is assumed to be spatially uniform and therefore it is assumed that $\rho(\boldsymbol{r}, \Omega) = (N/V) f(\Omega)$, where Ω is the solid angle describing the orientation of the spherocylinder, N is the number of rods, and V is the volume of the system. Since $f(\Omega)$ indicates the probability that a rod is pointing at a solid angle Ω, it should be normalized as follows:

$$\int f(\Omega)\,\mathrm{d}\Omega = 1 \tag{1.2}$$

Using this information, it is possible to recast Eq. (1.1) into an Onsager free-energy functional for a solution of rod-like molecules:

$$F = \log\left(\frac{N}{V}\right) + \int f(\Omega)\log[4\pi f(\Omega)]\,\mathrm{d}\Omega$$
$$-\frac{1}{2}\frac{N}{V}\iint \beta(\Omega,\Omega') f(\Omega) f(\Omega')\,\mathrm{d}\Omega\,\mathrm{d}\Omega' \tag{1.3}$$

The function $\beta(\Omega, \Omega')$ is the excluded volume of the spherocylinder with orientation Ω' due to the presence of another spherocylinder with orientation Ω. For two spherocylinders it is given by

$$\beta(\Omega,\Omega') = \beta(\gamma) = -2L^2 D_{\mathrm{sc}} \sin\gamma - 2\pi D_{\mathrm{sc}}^2 L - \tfrac{4}{3}\pi D_{\mathrm{sc}}^3 \tag{1.4}$$

where γ is the relative angle between the two spherocylinders. For spherocylinders with a large aspect ratio, the first term in Eq. (1.4) dominates, and it can be shown that the contribution of the other terms is of the same order as the contribution of the third virial coefficient. Therefore, it is often assumed that $\beta(\gamma) = -2L^2 D_{\mathrm{sc}} \sin\gamma$.

By using this approximation and variational calculus to minimize Eq. (1.3) with respect to the distribution function $f(\Omega)$, one obtains the following integral equation:

$$\log[4\pi f(\theta)] = \lambda - \frac{8\rho}{\pi}\int \sin\theta\, f(\theta)\,\mathrm{d}\theta \tag{1.5}$$

where $\rho = \frac{1}{4}\pi L^2 D_{\mathrm{sc}} N/V$ and λ is a constant determined through normalization of the constraint in Eq. (1.2). This integral equation cannot be solved analytically. However, it has been solved using two different numerical procedures, which yield almost identical results (Herzfeld et al. 1984; Lekkerkerker et al. 1984). Once the probability distribution function is known, it is easy to

calculate the nematic order parameter (S_2) using the following relation:

$$S_2 = 2\pi \int_0^{\pi} [\tfrac{3}{2}\cos\theta - \tfrac{1}{2}] f(\theta) \sin\theta \, \mathrm{d}\theta \tag{1.6}$$

In this equation we assume that the orientational distribution function is uniaxial and therefore $f(\Omega) = f(\theta)$, where θ is the angle between the orientation of a specific rod and the nematic director. The value of the nematic order parameter varies between 0 and 1, with $S_2 = 0$ describing a perfectly isotropic solution and $S_2 = 1$ describing a perfectly aligned nematic phase. Although the numerical solution of Eq. (1.5) yields the most accurate results, it is also possible to proceed from Eq. (1.3) by assuming a form of the orientational distribution function, such as

$$f(\alpha, \cos\theta) = \frac{\alpha \cosh(\alpha \cos\theta)}{4\pi \sinh\alpha} \tag{1.7}$$

Using this ansatz, first introduced by Onsager, and evaluating the integrals for the case of hard rods, Onsager obtained an expression for the free energy as a function of dimensionless concentration ρ and orientation parameter α:

$$\begin{aligned} F(\alpha, \rho) &= \rho \log \rho + \sigma(\alpha)\rho + \xi(\alpha)\rho^2 \\ \sigma(\alpha) &= \log\left(\frac{\alpha \cosh\alpha}{4\pi \sinh\alpha}\right) - 1 + \frac{\arctan(\mathrm{e}^{\alpha}) - \arctan(\mathrm{e}^{-\alpha})}{\sinh\alpha} \\ \xi(\alpha) &= \frac{2I_2(\alpha)}{\sinh^2\alpha} \end{aligned} \tag{1.8}$$

The advantage of assuming the probability distribution (1.7) is the analytical expression for the free energy (1.8). The most convenient variable to formulate the Onsager theory is the dimensionless concentration

$$\rho = B_2^{\mathrm{iso}} \frac{N}{V} = \frac{\pi}{4} L^2 D_{\mathrm{sc}} \frac{N}{V} = \frac{L}{D_{\mathrm{sc}}} \phi \tag{1.9}$$

where ϕ is the volume fraction of rods and $B_2^{\mathrm{iso}} = (\pi/4) L^2 D_{\mathrm{sc}}$ is the second virial coefficient for a suspension of hard rods in an isotropic solution. By performing a stability analysis of the Onsager equation, Kayser and Raveche (1978) found that the isotropic phase becomes unstable toward orientational fluctuations when $\rho = 4$. It follows that, within the Onsager theory, the volume fraction of hard rods at the I–N transition scales as $\phi = 4D_{\mathrm{sc}}/L$. Therefore, for long thin rods, the volume fraction of the I–N transition is small and the virial theory, which is an expansion of the free energy in density, becomes

accurate at the level of the second virial coefficient. Numerical calculations of the second and third virial coefficients indicate that the Onsager theory is quantitatively correct for rods with $L/D_{\mathrm{sc}} > 100$ (Frenkel 1988).

However, the second-order transition predicted by the stability analysis is preempted by a first-order phase transition. Minimizing the Onsager free energy with respect to the orientational distribution function numerically and subsequently solving the coexistence equations yields the following concentration of the coexisting isotropic and nematic phases:

$$\rho_{\mathrm{iso}} = 3.289, \quad \rho_{\mathrm{nem}} = 4.192, \quad S_2 = 0.7922 \tag{1.10}$$

These results were obtained by Herzfeld et al. (1984), Lekkerkerker et al. (1984), and Chen (1993). The Onsager trial function (Eq. 1.7) yields the following coexistence concentrations:

$$\rho_{\mathrm{iso}} = 3.339, \quad \rho_{\mathrm{nem}} = 4.487, \quad S_2 = 0.848 \tag{1.11}$$

By comparing the accurate numerical result from Eq. (1.5) with the Onsager approximation (Eq. 1.8), we observe a difference in both the coexistence concentrations at the I–N phase transition and the nematic order parameter (S_2) of the nematic phase.

1.2.2 Extension of Onsager Theory to Charged Rods

The Onsager theory outlined in the previous section can be extended to the experimentally important case of charge-stabilized rods. The first treatment of the I–N phase transition of charged rods can be found in the original paper by Onsager (1949) and was elaborated by Stroobants et al. (1986). Besides the hard-core repulsive interaction, charged rods have a long-range repulsive interaction of the following form:

$$\frac{U_{\mathrm{el}}(x)}{k_{\mathrm{B}}T} = \frac{A' \, \mathrm{e}^{-\kappa(x - D_{\mathrm{sc}})}}{\sin\gamma} \tag{1.12}$$

where x is the closest distance between two charged rods, A' is the proportionality constant obtained by solving the Poisson–Boltzmann equation, κ^{-1} is the Debye screening length, and γ is the angle between two rods. In the case of charged rods, there are contributions to the second virial coefficient from both the hard-core excluded-volume interaction and the long-range electrostatic repulsion interaction. These two contributions can be calculated separately. Integrating the interaction potential over a uniform orientational

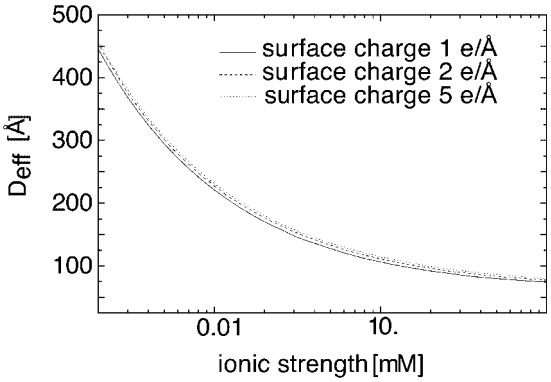

Fig. 1.1 The effective diameter for a charged rod calculated from Eq. (1.13) for a range of ionic strengths. The hard-rod diameter $D_{\rm bare} = 66$ Å is that of the *fd* virus. Due to the highly nonlinear nature of the Poisson–Boltzmann equation, the value of $D_{\rm eff}$ barely changes as the surface charge varies from $1\ {\rm e}^-/$Å to $10\ {\rm e}^-/$Å. Experiments indicate that the surface charge is about $2\ {\rm e}^-/$Å at pH 8.0 (Zimmermann et al. 1986). (Taken from Tang and Fraden, 1996).

distribution function that describes the isotropic phase, we obtain the following expression for the second virial coefficient of charged rods (see Fig. 1.1):

$$B_2^{\rm iso} = \tfrac{1}{4}\pi L^2 D_{\rm eff} = \tfrac{1}{4}\pi D L^2 + \tfrac{1}{4}\pi\kappa^{-1}L^2(\ln A' + C_E + \ln 2 - \tfrac{1}{2}) \quad (1.13)$$

where $D_{\rm eff} = (\ln A' + C_E + \ln 2 - \frac{1}{2})/\kappa$. It follows that the thermodynamics of charged rods in the isotropic suspension will be equivalent to the thermodynamics of thicker hard rods with effective diameter $D_{\rm eff}$.

However, if the interaction potential is integrated over an anisotropic distribution function, then the relationship given by Eq. (1.13) is no longer exact. The reason for this is that the electrostatic energy is lower for perpendicular rods than for parallel rods. Therefore, the charge effectively destabilizes the nematic phase by shifting the I–N transition to higher concentrations and reducing the order parameter of the nematic phase coexisting with the isotropic phase. However, most biopolymers (including *fd* virus) are highly charged, in which case it turns out that the electrostatic "twisting" effect is insignificant compared to the excluded-volume interactions (Stroobants et al. 1986; Tang and Fraden 1995). Therefore, from now on we approximate $D_{\rm eff}$ in the nematic phase by $D_{\rm eff}$ of the isotropic phase. This is reasonable for coexisting phases, but we expect this approximation to get progressively worse with increasing concentration.

1.2.3 Extension of Onsager Theory to Semi-Flexible Rods

Semi-flexible rods are characterized by their persistence length, which is the length along the contour of the chain after which the local tangents become uncorrelated. The effect of semi-flexibility on the isotropic–nematic phase transition was first considered by Khokhlov and Semenov (1982). For semi-flexible rods, besides orientational and translational entropy, it is also necessary to take into account the internal configurations of the semi-flexible chain. This modifies the orientational entropy term in Eq. (1.1), while the excluded-volume term between rod-like segments is still treated as in the Onsager theory for rigid rods. The resulting expression for the free energy has been solved analytically in the limit of almost rigid rods ($P \gg L$) and very flexible rods ($L \ll P$) (Khokhlov and Semenov 1981; Khokhlov and Semenov 1982). It is possible to interpolate empirically between these two solutions and obtain a numerical approximation for the configurational entropy of rods with arbitrary persistence length, as was done by Hentschke (1990), Odijk (1986), and DuPre and Yang (1991). This interpolated expression can be combined with the Onsager approximation for the orientational distribution to obtain analytical results for the I–N phase transition of semi-flexible rods. In Fig. 1.2 these results are compared to accurate numerical solutions of the Khokhlov–Semenov free energy due to Chen (1993).

From Fig. 1.2a we conclude that increasing flexibility destabilizes the nematic phase by displacing the I–N transition to higher volume fractions. Increasing the flexibility also drastically reduces the concentration difference between the coexisting isotropic and nematic phases (figure not shown) and the order parameter of the nematic phase (Fig. 1.2b). The Onsager approximation (Eq. 1.7) for the orientational distribution function (ODF) qualitatively agrees with the accurate numerical results due to Chen. It is important to note that the agreement between these approximations for the location of the phase transition (Fig. 1.2a) is much better than for the order parameter of the coexisting nematic phases (Fig. 1.2b). This indicates that measuring the order parameter is a more sensitive test of the theory for the I–N phase transition.

Chen compares his numerical solution to the analytical solution of Khokhlov and Semenov, who also use the Onsager approximation for the ODF. This comparison in Chen's paper seems much better than what is shown in Fig. 1.2. The reason for this is that Khokhlov and Semenov, besides using the Onsager approximation for the ODF, also approximate the excluded volume $\xi(\alpha)$ by expanding it in powers of α. These two approximations fortuitously cancel each other, and the final result seemingly agrees better with the numerical solution.

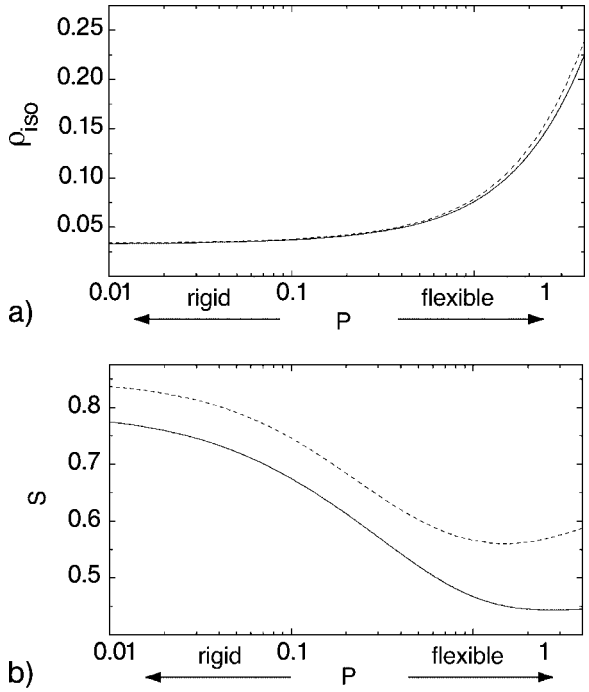

Fig. 1.2 (a) Concentration [$\rho_{\rm iso} = (4/\pi)L^2 D_{\rm sc}(N/V)$] and (b) order parameter (S_2) of the nematic phase coexisting with the isotropic phase as a function of the flexibility of the particle $P = L/l_{\rm p}$. The full lines are the exact numerical results within the second virial approximation due to Chen (1993), while the dashed lines are results obtained by using the Onsager approximation for the orientational distribution function (Eq. 1.7). In both parts the aspect ratio of the rods is fixed at 100 and the persistence length $l_{\rm p}$ varies from infinity to 25.

1.2.4
Extension of Onsager Theory to Rods With Finite Aspect Ratio Using Scaled Particle Theory

The scaled particle theory (SPT) of hard rods was developed by Cotter and Wacker (1978) and Cotter (1979). The main advantage of the scaled particle theory is that it takes into account third and all higher virial coefficients in an approximate way. Therefore, this theory should be more adequate at describing the data at higher concentration of rods or equivalently rods with lower $L/D_{\rm sc}$ ratios. We note that the expression for the free energy reduces to the Onsager second virial approximation for very long rods. For spherical particles, the SPT free energy reduces to the Percus–Yevick free energy for hard spheres.

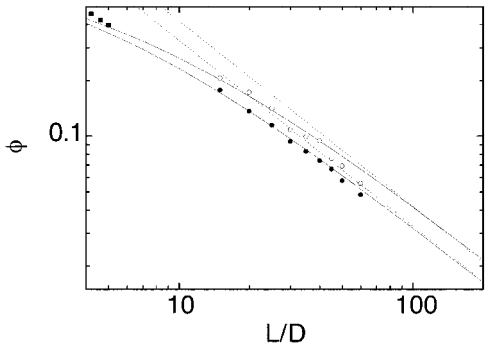

Fig. 1.3 The I–N coexistence concentrations as a function of the aspect ratio $(L/D_{\rm sc})$ as predicted by the scaled particle theory for rigid rods (full lines) and as predicted by a theory that only includes the second virial coefficient (dashed lines). The circles are the results of computer simulations (Bolhuis and Frenkel 1997). The filled squares at low $L/D_{\rm sc}$ represent results from the same work but the coexistence width was too narrow to be measured. The coexistence is plotted in terms of real volume fraction $\phi = \frac{1}{6}\pi D_{\rm sc}^3 + \frac{1}{4}LD_{\rm sc}^2\pi$, while the total aspect ratio including the hemispheres is $L/D_{\rm sc} + 1$.

The scaled particle expression accounts for higher virial coefficients in an approximate way. Comparing the SPT prediction for the I–N phase transition with the solution obtained through the second virial approximation provides a way to establish the range of $L/D_{\rm sc}$ ratios for which the second virial approximation is quantitatively valid. The results are shown in Fig. 1.3. At $L/D_{\rm sc} = 45$ the second virial approximation yields I–N coexistence concentrations that are 10% different from the scaled particle result. We conclude that for rods with $L/D_{\rm sc} > 75$ the second virial approximation quantitatively describes the I–N transitions in hard rods. Currently available computer simulation results agree very well with the scaled particle theory (Bolhuis and Frenkel 1997; Kramer and Herzfeld 1998).

1.2.5
Nematic–Smectic Phase Transition Within the Second Virial Approximation

Here we review the interplay between the ideal and interaction contributions to the free energy that are responsible for the formation of the smectic phase in parallel hard rods. From the second virial approximation (Eq. 1.1), we can easily find the free-energy difference between a weakly ordered smectic and a uniform nematic state (Mulder 1987):

$$\begin{aligned}\delta F &= F_{\rm layered} - F_{\rm uniform} \\ &= F(n + a\cos(kz)) - F(n) = n + 8n^2 j_0(k)\end{aligned} \tag{1.14}$$

A positive free-energy difference $\delta F(n,k) > 0$ implies that at volume fraction n and wavevector k the nematic phase has the lowest free energy and therefore is the equilibrium phase. On the other hand, at values of n_c and k_c that satisfy the equation $\delta F(n_c, k_c) = 0$ the system becomes unstable toward smectic fluctuations since they do not cost any energy to create. We identify n_c and k_c as the critical volume fraction and critical wavevector of the second-order nematic–smectic phase transition.

It is important to note that the first term in Eq. (1.14) originates from the ideal part of the free energy in Eq. (1.1), while the second term in Eq. (1.14) originates from the interaction part of the free energy in Eq. (1.1). We observe that the difference in the ideal part of the free energy between the layered and uniform phase is always positive and given by $\delta F \propto n$. Therefore, the ideal part of the free energy always suppresses the ordering transition as expected. On the other hand, the difference in the interaction part of the free energy between the uniform and layered phase is given by $\delta F \propto n^2 j_0(k)$. Since this part of the free-energy difference scales as n^2, for high enough volume fraction of rods and for specific values of wavevector k this term is negative and large enough to drive the system toward the smectic phase. Considering the highly approximate nature of the theory, the conditions $n_c = 0.575$ and $k_c = 2\pi/1.398L$ obtained for the nematic–smectic phase transition compare favorably to the results of the computer simulations of parallel rods $n_c = 0.43$ and $k_c = 2\pi/1.27L$ (Frenkel et al. 1988). Inclusion of the third virial coefficient brings the theoretical prediction for the N–S transition closer to what is observed in simulations (Mulder 1987).

The above simple model suggests a physical picture of the excluded-volume effects responsible for the formation of a smectic phase first introduced by Wen and Meyer (1987). A spatially uniform nematic phase results in a very inefficient packing of rods, as shown in Fig. 1.4a. In such a state the ideal

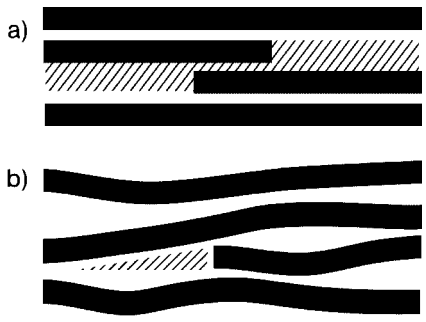

Fig. 1.4 A schematic illustration of the excluded-volume interaction in a dense suspension of aligned rods for the case of (a) rigid rods and (b) semi-flexible rods. (From Tkachenko, 1996).

part of the free energy attains its minimum value while the interaction part does not. The reason for this is that the nematic phase is under the constraint of uniform packing, and thus the excluded volume between any two rods is eight times the volume of a single rod, since rods are allowed to approach each other from any direction. One way to decrease the excluded volume is to impose a smectic-like periodic density modulation. Then the probability of two rods approaching each other along their axial direction will decrease, while the probability of sideways approach will increase. For example, in an extreme case where the probability distribution of the centers of rods consists of very sharp delta-like functions spaced at distances slightly longer than the rod length, rods are allowed to approach each other only sideways and overlap between the ends of the rods is completely forbidden. Consequently, the excluded volume between two rods will be half the value of the excluded volume for a uniform density distribution. For this simple reason, the value of the interaction part of the free energy decreases with increasing order in Eq. (1.14). The actual volume fraction of the ordering transition and the resulting density distribution $\rho(\boldsymbol{r})$ is therefore determined by the competition between the ideal and interaction parts of the free energy given in expression (1.1). The treatment of the nematic–smectic phase transition of the second virial approximation was also extended to the case of rods with orientational freedom (van Roij et al. 1995). In this case the calculation becomes much more involved.

It is easy to extend the above argument to consider the influence of flexibility on the nematic–smectic phase transition (Tkachenko 1996; van der Schoot 1996). Experimentally, it is found that flexibility acts to stabilize the nematic phase and destabilize the smectic phase (Dogic and Fraden 1997). As was first noticed by Tkachenko (1996), in the case of perfectly aligned rigid-rod nematics the only way to fill the space created by the end of a rod is to place another rod above it, as shown in Fig. 1.4a. In the case of a nematic solution of semi-flexible rods, it is possible for other molecules to occupy space around the end of a particular molecule by deflecting around its end, as shown in Fig. 1.4b. This results in more efficient packing of semi-flexible rods in the nematic state, which in turn leads to the suppression of the nematic–smectic phase transition. This picture of the effect of flexibility on the nematic–smectic phase transition has been confirmed using computer simulations (Polson 1997).

1.2.6
Phase Behavior of a Binary Mixture of Hard Particles

Recently the second virial approximation has also been extended to study ordering and demixing transitions in binary mixtures of hard rods (Koda and

Kimura 1994; Cui and Cheng 1994; van Roij 1994; Sear and Jackson 1995; Sear and Mulder 1996; van Roij 1996; van Roij and Mulder 1996; Dijkstra and van Roij 1997; van Roij et al. 1998). In many of these cases it is not obvious if terminating the free-energy expansions at a second virial level is sufficient to describe the phase diagram of a binary mixture. For example, it was recently shown that, although Onsager theory quantitatively describes the I–N phase transitions of rods, it fails to predict even the qualitative features of a binary mixture of rods with two different diameters (Purdy et al. 2005). In other cases, such as a mixture of perfectly aligned spherocylinders and hard spheres, the second virial theory predicts the right qualitative features, as has been verified by computer simulations for the lamellar phase, but fails to describe the columnar phase (Adams et al. 1998). Expressions for the stability matrix for a binary mixture of parallel spherocylinders and spheres are given in Koda et al. (1996) and Dogic et al. (2000).

1.3 Experimental Phase Diagram of an *fd* Virus Suspension

Theory and simulation indicate that, with increasing concentration, rod-like particles will form isotropic, nematic, and smectic phases (Hosino et al. 1979; Mulder 1987; Wen and Meyer 1987; Frenkel et al. 1988; Bolhuis and Frenkel 1997). The columnar phase turns out to be metastable with respect to the smectic phase for all aspect ratios and rod concentrations (Bolhuis and Frenkel 1997). So far, the only experimental systems whose phase behavior agrees with theoretical predictions are colloidal suspensions of the viruses *fd*, *pf1*, and TMV, and inorganic β-FeOOH rods (Maeda and Maeda 2003). This is due to the fact that Nature makes all viruses identical to each other. This results in a colloidal suspension of very high monodispersity, much higher than what can be achieved with current synthetic methods. Recently, using a combination of recombinant DNA technology and traditional chemical methods, it has been possible to prepare monodisperse poly(benzyl L-glutamate) (PBLG) polymers. Although these polymers are not available in large quantities, they were reported to form a smectic phase (Yu et al. 1997). This is a potentially powerful technique to create novel liquid crystals. While the present chapter focusses on the fundamental aspects of the phase behavior of rods and rod–sphere mixtures, individual viruses and virus assemblies might become technologically useful materials. In this respect, the recent work by Belcher's group seems promising (Lee et al. 2002).

In this chapter we focus on the phase behavior of the rod-like bacteriophage *fd* and its closely related M13. The phase behavior of another class of anisotropic colloids composed of minerals has recently been reviewed else-

where (Gabriel and Davidson 2003). The phase behavior of polymeric liquid crystals such as PBLG is reviewed in Sato and Teramoto (1994). Historically, the first observation of the nematic liquid-crystalline phase of *fd* was reported in the study by Lapointe and Marvin (1973). Shortly thereafter a smectic phase was also reported in a little noticed paper (Booy and Fowler 1985).

We note that *fd* forms a cholesteric instead of a nematic phase. Cholesteric and nematic phases are locally identical to each other. It often takes many days after sample preparation for the *fd* solution to form a fully twisted cholesteric phase. This indicates that the free-energy difference between these two structures is very small. Therefore, we expect that the Onsager theory equally well describes the isotropic–nematic and isotropic–cholesteric phase transitions. In this chapter we use the terms "nematic" and "cholesteric" interchangeably depending on the particular context. Often, when confined to small droplets, such as tactoids observed at the isotropic–cholesteric coexistence, the cholesteric phase is unable to develop and the sample remains nematic.

1.3.1
Properties and Preparation of Filamentous Bacteriophage

The structure of the bacteriophage *fd* is very simple, with a self-assembled hollow cylindrical shell composed of roughly 2800 copies of a single coat protein pVIII. A single circular strand of DNA is enclosed within this hollow shell. The length of the whole virus is determined by the length of the DNA. The ends of the assembly are covered with end-capping proteins, which are different from the major coat protein pVIII. In addition, the two ends are different from one another, which makes *fd* a polar colloid. This characteristic can be used to label each end selectively (Lee et al. 2002).

The physical characteristics of the *fd* virus are a contour length of 880 nm, bare diameter of 6.6 nm, and aspect ratio $L/D_{\mathrm{sc}} \approx 130$. The semi-flexibility of the virus is characterized by the persistence length, $l_{\mathrm{p}} = 2.2$ μm, which has been reported to change with temperature (Tang and Fraden 1996). The colloidal stability of the virus is preserved due to the fact that it has a very high negative surface charge at pH 8.0 (Zimmermann et al. 1986). For a more comprehensive list of most of the known physical constants of *fd*, the reader is referred to the review article by Fraden (1995).

There are well-established methods for growing bacteriophage *fd* and closely related M13 (Maniatis et al. 2000; Dogic and Fraden 2001). In brief, one first grows a large quantity of *Escherichia coli* host. Once the host strain reaches log phase, it is infected with viruses at a well-defined multiplicity of infection (MOI) and the culture is grown for an additional eight hours. The bacterium is separated from the culture by centrifugation at low speed, and the virus in the supernatant is concentrated by adding a neutral polymer, such

as poly(ethylene glycol) (PEG, molecular weight $M_w = 8000$), which acts as a depleting agent. In principle, it is possible to purify the virus further using a cumbersome CsCl gradient centrifugation step. In practice, we found that a two-step sequence of low-speed and high-speed centrifugation produces *fd* virus of sufficient purity for most of our experiments. Once grown, *fd* should be kept in a low-ionic-strength buffer at 4°C. Under these conditions, the solution should be stable for at least a year, although it is difficult to prevent microbial growth over such a long time period even in the presence of sodium azide. Therefore, before use of the virus, we dialyze it against fresh buffer and spin-down aggregates and bacterial debris using a low-speed centrifugation step. The usual yields are about 15–20 mg per liter of infected *E. coli* culture.

There is a tendency for all viruses to form a multimeric structure with a contour length that is an integer multiple of the length of wild-type *fd*. We have found that it is important to choose the appropriate *E. coli* host strain in order to reduce the number of multimers. Although recA$^+$ strains such as JM101 grow faster and produce higher yields of virus, we found that these hosts have a tendency to form dimer and multimer viruses. These can easily be identified once the viruses are labeled and visualized using fluorescence microscopy. Viruses purified from recA$^+$ host form smectic phase at different concentrations when compared to viruses purified form recA$^-$ strains such as Xl1-Blue. In addition, many other structures, such as the lamellar phase described in Section 1.6, are not observed in an *fd* virus grown in recA$^+$ strains. This is presumably due to increased polydispersity of the virus.

It is difficult to assess the polydispersity of the virus. It has a pronounced tendency to break or aggregate during preparation of grids for electron microscopy. It is possible to run agarose gel electrophoresis on whole viruses that are stained with Commassie Blue protein stain (Griess et al. 1990). However, sometimes longer *fd* does not easily enter the gels. It is also possible to strip the virus of its protein and run DNA gel electrophoresis, which is subsequently stained with ethidium bromide. Recently, we have prepared *fd* viruses labeled with the fluorescent dye Alexa 488 (Molecular Probes), which appear very bright when viewed via fluorescence microscopy. These could be used to quantify the polydispersity of the virus. When labeled at very high fraction with Alexa 488 (Molecular Probes) dye, we do not observe any aggregation over a period of a year. In contrast, if the viruses are labeled with larger and more hydrophobic dyes, such as tetramethyl rhodamine (TAMRA), they aggregate into bundles over a period of days. With the proper use of anti-bleaching solution, it is possible to observe Alexa 488-labeled viruses continuously for 5–10 min under full illumination with a 100 W mercury lamp. Figure 1.5 shows a fluorescent microscopy image of Alexa 488-labeled recA$^+$ *fd*. It is easy to observe a number of *fd* with a contour length much longer than that of wild-type *fd*.

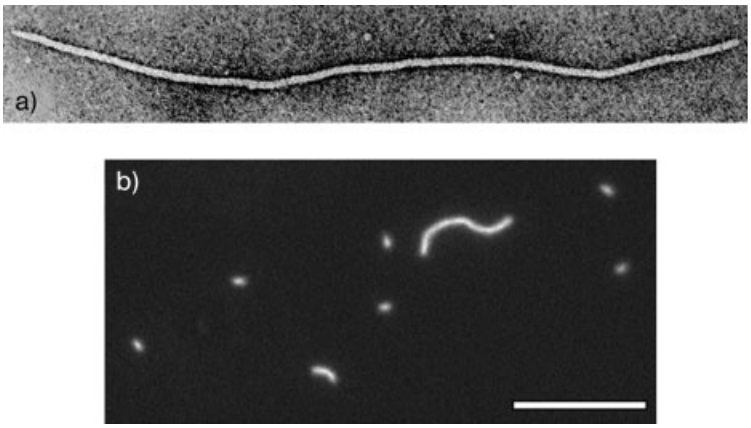

Fig. 1.5 (a) Electron microscope image of a bacteriophage *fd*. The contour length of the virus corresponds to 0.9 μm. (b) Image of a dilute isotropic solution of *fd* confined to a chamber of approximately 1 μm thickness. The presence of *fd* with much larger contour length than the wild type is easily seen. The *fd* was grown in recA$^+$ strain (JM101) and labeled with Alexa 488 (Molecular Probes). The image was taken with a fluorescent microscope equipped with a cooled charge-coupled device (CCD) camera (CoolSnap HQ, Roper Scientific). The scale bar indicates 10 μm. (From Model and Russel, 1988).

All the available data point to the fact that the contour length of *fd* is determined by the size of its DNA. Therefore, it is possible to alter the length of the *fd* by simply adding additional DNA into the *fd* genome using standard recombinant DNA techniques. A few decades ago *fd* with different contour lengths were genetically engineered and used to study the rotational diffusion of rod-like colloids with varying aspect ratio (Maguire et al. 1980). However, this potentially powerful method was not pursued any further. Using similar methods, mutants up to 5 μm long have been described in the biological literature (Herrmann et al. 1980). We have tried to reproduce this method, but have found that, during a large-scale preparation involving many generations of bacterial division, foreign DNA is easily expelled. The resulting culture quickly reverts back to wild-type *fd*. We have had more success in creating mutant *fd* using the phagemid methods, as described in detail in Sambrook et al. (1989). The resulting *fd* are sufficiently monodisperse to form a smectic phase, as shown in Fig. 1.16. For more details, the reader is referred to Dogic and Fraden (2001).

1.3.2
Isotropic–Cholesteric Phase Transition in *fd* Virus Suspensions

Due to the entropic nature of the *fd* suspension, the only variable that determines the phase behavior is the density of the constituent rods. Therefore, with increasing *fd* concentration, an isotropic suspension of *fd* undergoes a first-order phase transition to the nematic/cholesteric phase. It follows that the density of the cholesteric phase is higher than that of the isotropic phase in a coexisting sample. The denser cholesteric phase slowly sediments to the bottom of the sample container, resulting in a macroscopically phase-separated sample (Fig. 1.6).

Recently we compared the experimental results of the isotropic–cholesteric (I–Ch) transition quantitatively to the predictions of the Onsager theory (Tang and Fraden 1996; Purdy and Fraden 2004a). To accomplish this, it is necessary to take into account both the charge and the flexibility of an *fd* virus. It is possible to describe the thermodynamic behavior of a dilute suspension of charged rods using the concept of effective diameter, D_{eff}, as explained in Section 1.2.2, where D_{eff} for *fd* is plotted for three different surface charges (Fig. 1.1). Due to the nonlinear nature of the Poisson–Boltzmann equation, changing the surface charge by an order of magnitude has minimal effect

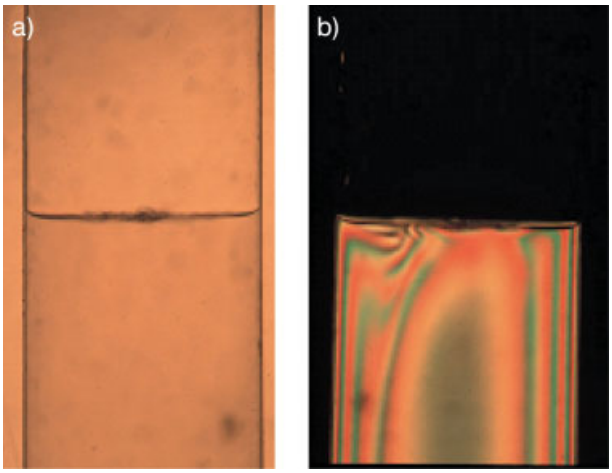

Fig. 1.6 The bulk phase separation between isotropic and nematic phases observed in a TMV suspension. The image on the left is taken with white light, while the image on the right is taken between crossed polarizers. Since the difference in density between the nematic and isotropic phases can be up to 30% over a period of days, the nematic phase sediments to the bottom. The phase diagram for TMV suspension is shown in Fraden et al. (1989). Identical bulk phase separation is observed in *fd* suspension. By measuring the concentration of the virus in coexisting phases, it is possible to determine a phase diagram such as the one shown in Fig. 1.7.

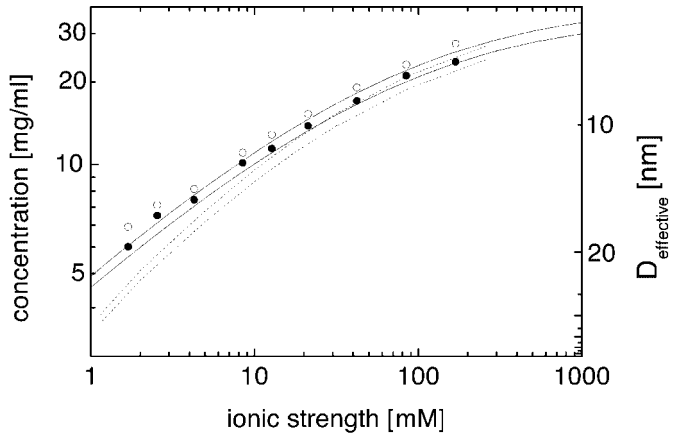

Fig. 1.7 The I–Ch coexistence concentrations measured in an aqueous suspension of *fd* virus as a function of the ionic strength (Tang and Fraden 1995). The full lines are the numerical solution of Chen (1993) for the I–Ch coexistence, which treats excluded-volume interactions at the second virial level while the orientational distribution function is calculated numerically. The dashed lines are the scaled particle theory solution for the I–Ch coexistence in which all virial coefficients are included in an approximate way and the orientational distribution function has an approximate form given by Eq. (1.7). The scale on the right-hand side indicates the effective diameter for a given ionic strength. (From Tang and Fraden, 1996).

on the resulting $D_{\rm eff}$. The flexibility is included according to the prescription given by Khokhlov and Semenov, and discussed in more detail in Section 1.2.3.

Figure 1.7 shows that, with increasing ionic strength, the location of the I–Ch phase transition shifts to higher concentrations. However, increasing ionic strength increases $L/D_{\rm eff}$, which in Onsager theory should decrease the volume fraction of the rods at the I–N transition. The discrepancy can easily be understood if one looks at the condition for instability of the isotropic phase: $(4/\pi)L^2 D_{\rm eff}(N/V) = 4$. The concentration in Fig. 1.7 is not proportional to the effective volume fraction, but to the number density of the virus. If $D_{\rm eff}$ is decreased with the length of the rod remaining constant, it follows that the number density of the virus at the transition has to increase so that the condition for the nematic/cholesteric instability is still satisfied. The experimental data points are compared to the numerical solution of Chen (1993), who approximates the excluded-volume interaction by the second virial coefficient and treats the ODF in an accurate numerical way. We have also plotted the result of a theory in which higher virial coefficients have been taken into account within the scaled particle theory while the orientational degrees of a semi-flexible polymer confined by the nematic field is approximated using the approximation described in Section 1.2.3.

At first sight the agreement between the theory due to Chen and the experiment as shown in Fig. 1.7 is quite good. However, there is reason to

believe that this agreement is fortuitous at low ionic strength. For example, at 1 mM ionic strength, $D_{\text{eff}} \approx 60$ nm, which results in the aspect ratio $L/D_{\text{eff}} \approx 15$. Figure 1.3 clearly shows that for these small aspect ratios third and higher virial coefficients cannot be ignored. Indeed, the results of the scaled particle theory, which include these higher coefficients, predict that the I–N(Ch) transition is located at significantly lower concentration than that found by the experiments and Chen's theory. The agreement between the scaled particle theory, experiments, and Chen's theory is much better at high ionic strength where the effective aspect ratio is large (at 100 mM ionic strength, $L/D_{\text{eff}} \approx 83$), and therefore the excluded-volume interactions are more accurately approximated by the second virial coefficient.

We note that the results from the scaled particle theory shown in Fig. 1.7 should also be treated with a degree of skepticism. To compare the scaled particle theory with experiments on charged rods, we use the effective diameter of the rod. However, the concept of D_{eff} introduced in Eq. (1.13) is only rigorously justified for conditions for which the second virial coefficient is quantitatively valid. There has been a recent theoretical attempt to extend the scaled particle theory to charged particles (Kramer and Herzfeld 1999; Kramer and Herzfeld 2000). Unfortunately, this theory does not extrapolate to Onsager theory for dilute rods, in contrast to the scaled particle theory for hard rods. We also note that the twisting factor ignored in our treatment of D_{eff} for *fd* is strongest at low ionic strength (Stroobants et al. 1986). This effect displaces the I–N(Ch) transition to higher densities.

The effect of the contour length of M13 virus on the I–Ch phase transitions has also been measured (Purdy and Fraden 2004a). Mutant viruses of various contour lengths have been prepared using molecular cloning as described in Section 1.3.1. Figure 1.8 shows the location of the I–Ch phase transition as a function of contour length in terms of the dimensionless concentration $b_{\text{eff}} c_i$. The Onsager theory predicts that the location of the I–Ch will occur when $b_{\text{eff}} c_i \approx 4$. In these units the location of the phase transition is independent of the aspect ratio of the rods, as indicated by the dashed line. Including finite flexibility significantly shifts the location of the I–Ch phase transition to higher concentration, as indicated by the full line. The I–Ch phase transition at high ionic strength, indicated by filled triangles, agrees well with these predictions. However, as the ionic strength decreases to 10 mM, there is a significant deviation between experiment and theory.

Another important parameter that characterizes the I–Ch phase transition is the order parameter of the nematic/cholesteric phase at coexistence. Figure 1.9 shows the behavior of the nematic order parameter as a function of both the contour length and the ionic strength. The order parameter can be extracted from birefringence measurements once the birefringence per particle is measure using X-ray scattering as described in Section 1.3.5 and Purdy

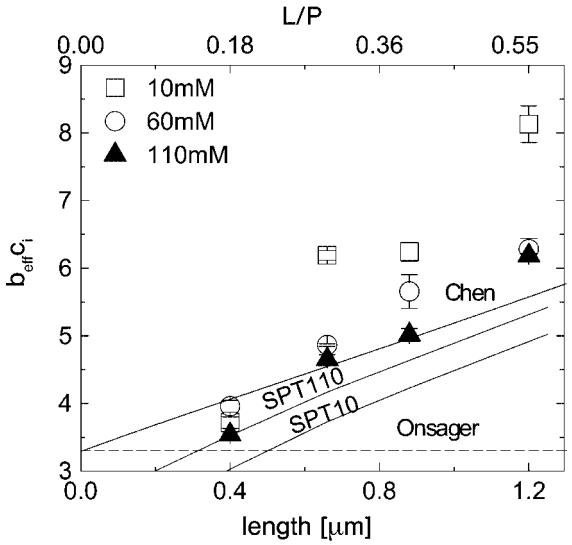

Fig. 1.8 Dimensionless concentration of the isotropic phase in coexistence with the nematic phase as a function of M13 contour length at pH 8.2. The dimensionless concentration $b_{\rm eff}c_i = (\pi/4)D_{\rm eff}L^2N_i/V$. For rigid rods, the Onsager theory predicts that the location of the I–N phase transition is independent of the theory (dashed line). The solid lines SPT110 and SPT10 are the results of the scaled particle theory for ionic strengths of 110 and 10 mM. SPT agrees with experiment at high ionic strengths, but fails for low ionic strength. (From Purdy and Fraden, 2004a).

et al. (2003). Onsager theory predicts that for rigid rods the order parameter of the coexisting nematic phase is approximately $S_2 = 0.8$. For finite flexibility, the order parameter significantly decreases, as indicated by the full line (solution due to Chen) and short-dashed lines (solutions with SPT). At high ionic strength, the measurements of the order parameter follow the theoretical predictions almost quantitatively. However, at the lowest ionic strength of 5 mM, the order parameter is almost independent of the ratio of contour length to persistence length and much higher than the theoretical predictions, which account for flexibility. Surprisingly, the low-ionic-strength data agree with the Onsager model for rigid rods. The theory of electrostatic stiffening of a charged polymer predicts that the persistence length of *fd* is independent of ionic strength because the bare persistence length of *fd* is very long (Purdy and Fraden 2004a).

From these data we conclude that the Onsager theory, extended to account for flexibility and charge, quantitatively describes the I–Ch phase transition of wild-type *fd* in the limit of high ionic strength. With decreasing ionic strength, there is a systematic disagreement between the experimental results and theoretical predictions. In this limit the location of the isotropic–nematic phase

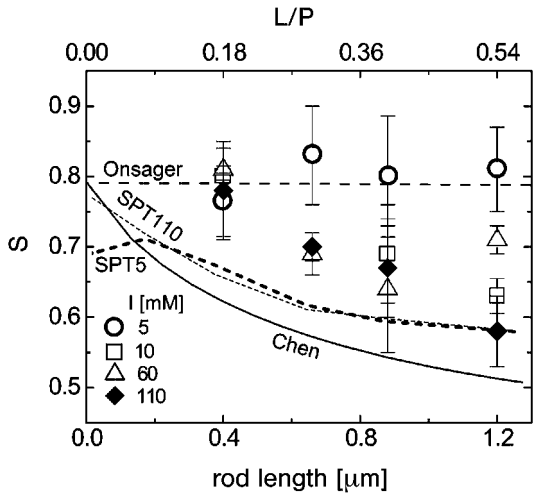

Fig. 1.9 Experiments and theory showing the dependence of the order parameter of coexisting nematic phase as a function of rod length for four different ionic strengths. The horizontal long-dashed line represents the prediction of the Onsager theory, the full line is the theoretical calculation by Chen, while the short-dashed lines are the predictions of the scaled particle theory for 5 mM (SPT5) and 110 mM (SPT110) ionic strength. The theoretical curves are calculated for rods with persistence length of 2.2 μm, while the contour length varies between 0.4 and 1.2 μm. (From Purdy and Fraden, 2004a).

transition is at higher rod concentration than theoretical predictions, and the nematic order parameter is also higher than predicted. This is probably due to the approximate incorporation of the electrostatic interaction into the theoretical free energy via D_{eff}.

1.3.3
Polymer-Coated *fd* Virus and Its Isotropic–Cholesteric Phase Transition

It is possible to eliminate electrostatic interactions between viruses by preparing sterically stabilized *fd* suspensions. This is achieved by covalently coupling poly(ethylene glycol) (PEG) to the amine groups that are present on the virus surface (Dogic and Fraden 2001). Water at room temperature is a good solvent for PEG, and therefore PEG-coated surfaces interact through purely repulsive interactions (Kuhl et al. 1994). By measuring the increase in the index of refraction of PEG-coated virus suspensions, the number of attached polymers per virus can be determined. These measurements indicate that the density of the deposited polymer is at the transition from isolated "mushrooms" to an extended brush-like coverage (Grelet and Fraden 2003). It is important to mention that polymer-stabilized rods still have a charged surface, and that the

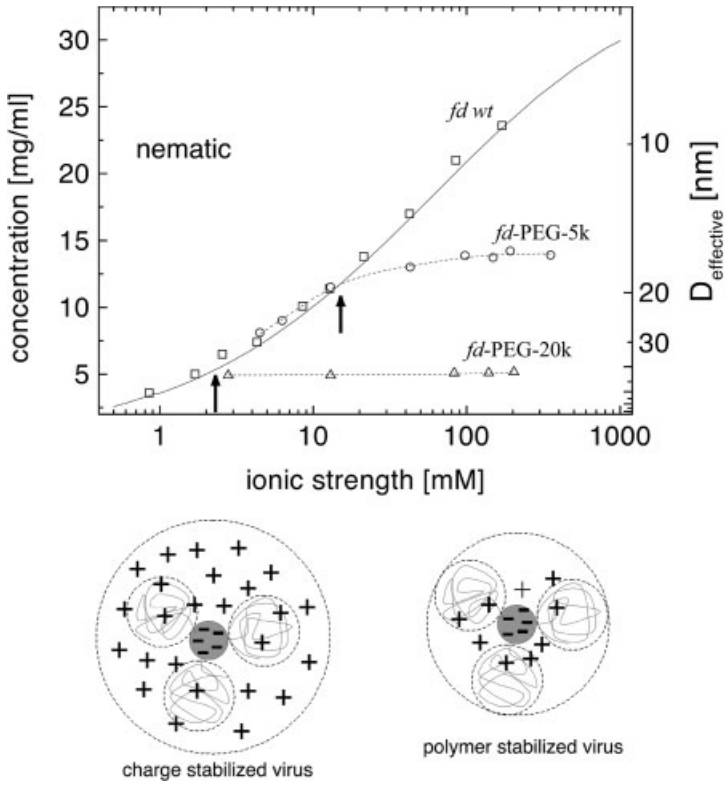

Fig. 1.10 The concentration of the isotropic phase that coexists with the nematic phase as a function of ionic strength. The data are shown for pure *fd* suspension (open squares), *fd* coated with PEG-5000 (open circles), and *fd* coated with PEG-20000 (open triangles). (The dotted lines are a guide to the eye.) The labels on the right-hand side indicate the effective diameter at which the location of the I–Ch transition occurs. The I–N transition of PEG-coated virus becomes independent of ionic strength (indicated by arrows) when the effective diameter of the virus is set by the polymer diameter and not by the range of the electrostatic repulsion. (After Dogic and Fraden, 2001).

effective interaction between two viruses will be a combination of electrostatic and steric repulsion.

Polymer-stabilized *fd* undergoes an isotropic to cholesteric phase transition. Figure 1.10 shows the concentration of the coexisting isotropic phase for a suspension of bare *fd* and *fd* coated with PEG-5000 and PEG-20000. For *fd*–PEG-20000, the location of the I–Ch phase transition is completely independent of the ionic strength. This indicates that steric repulsion has a longer range than electrostatic repulsion for the range of ionic strengths studied. However, for *fd*–PEG-5000, it is possible to observe a transition from the sterically stabilized region to the electrostatically stabilized region by measuring the ionic-strength dependence of the I–Ch transition. At high ionic

strength, the transition is independent of the ionic strength, indicating steric repulsion. With decreasing ionic strength, the concentration of the I–Ch transition decreases and agrees with the I–Ch transition of the bare virus. In this regime the virus is electrostatically stabilized. From Fig. 1.10 we can deduce that the steric size of the virus–polymer complex is $D_{\mathrm{eff}} = 45$ nm, which is approximately equal to $D_{\mathrm{bare}} + 4R_{\mathrm{g}} = 35$ nm. This indicates that the density of the grafted PEG is slightly in the "extended" brush regime. Although not the subject of this chapter, we note that by using polymer-stabilized viruses it is possible to study the phase behavior of a binary mixture of rods with different diameters (Purdy et al. 2005).

1.3.4
Cholesteric Phase of *fd* Virus

The cholesteric phase is locally identical to the nematic phase. However, in a cholesteric phase the nematic director twists into a helical structure. The *fd* virus forms a cholesteric phase as evidenced by the typical cholesteric fingerprint texture shown in Fig. 1.11. The distance that it takes for the director to rotate by 2π is called the "cholesteric pitch". Experimentally, it is easy to determine the value of the pitch by simply measuring the distance between either two dark or two bright lines in images such as Fig. 1.11. The cholesteric pitch will also diffract light, from which the magnitude of the pitch can be determined (Oldenbourg 1981).

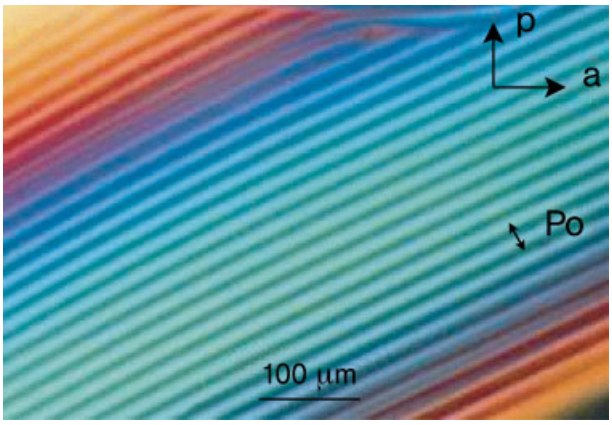

Fig. 1.11 An image of a cholesteric phase of *fd* taken with a polarization microscope. The locations of the polarizers and analyzer are indicated by arrows. The dark lines correspond to regions where rods point perpendicular to the image, while the bright regions correspond to regions where the rods lie in the plane. The best way to observe the cholesteric texture such as the one shown here is to fill a cylindrical X-ray capillary and focus on its midplane. (After Dogic and Fraden, 2000).

In thermotropic liquid crystals it is conventional wisdom that chiral molecules will form a cholesteric phase while achiral molecules will form a nematic phase. However, this does not seem to be true for colloidal rods, and the molecular origin of the cholesteric phase remains poorly understood. Some chiral polymers such as *fd*, PBLG, and DNA form a well-developed cholesteric phase (DuPre and Duke 1975; Van Winkle et al. 1990; Livolant 1991; Leforestier and Livolant 1993; Dogic and Fraden 2000). However, other viruses such as TMV and *pf1* form nematic structures under the same conditions in which the cholesteric twisting is observed in *fd* suspension. Surprisingly, the molecular structure of TMV and *pf1* is also chiral and quite similar to *fd*. The main challenge is to formulate a microscopic theory of chiral polymers and explain why some chiral molecules such as *fd* form a cholesteric phase while others like *pf1* and TMV form a nematic phase.

Following the initial work of Onsager (1949), Straley (1976) was the first to propose a microscopic theory of the cholesteric phase based on excluded volume. He considered a nematic solution of rod-like molecules that have additional chiral threads similar to chiral screws. Similar to Onsager, in the Straley model the formation of the cholesteric phase is driven by pure excluded-volume effects. The excluded volume between two screw-like rods is minimum not when they are parallel to each other, but when they approach each other at a specific angle at which the chiral grooves can interpenetrate. The initial work of Straley was extended to semi-flexible molecules (Odijk 1987; Pelcovits 1996). More recent work indicates that the mean-field approaches used by Straley fail to describe the cholesteric phase since rotations along the rods' long axis effectively average out the chiral structure of the molecules (Harris et al. 1997). These latter authors further argue that it is the biaxial correlations that are responsible for the formation of the cholesteric pitch. In addition to excluded-volume interactions, it has been proposed that other types of chiral interactions, such as van der Waals, can induce the formation of the cholesteric phase (Issaenko et al. 1999).

As already mentioned, the origin of the cholesteric phase in *fd* solution is not understood. Even when *fd* is coated with a thick layer of achiral PEG polymer, the resulting polymer-stabilized rods still form a cholesteric structure (Grelet and Fraden 2003). This would imply that it is not the microscopic chiral arrangement of coat proteins that is responsible for the cholesteric structure; rather it has been suggested that the virus twists into a mesoscopic helical structure. However, up to now there has been no concrete experimental evidence to support this hypothesis. Interestingly, the relative angle between two neighboring molecules is very small in a cholesteric phase. The typical size of the cholesteric pitch is roughly 20 μm, while the spatial separation between two rods in such a sample would be of the order of 20 nm. This would indicate that there are about 1000 molecules along the cholesteric pitch, which

results in the average angle between two rods being at most a fraction of a degree. This is much smaller than the average angle by which the rods locally fluctuate due to the width of the orientation distribution function, which is typically in the range of $0.6 < S_2 < 0.9$.

The cholesteric pitch has been measured as a function of virus concentration and ionic strength. At a high ionic strength of 100 mM, the cholesteric pitch decreases with increasing concentration according to the power law $P \propto c^{-\nu}$, where $\nu = 1.65$ (Dogic and Fraden 2000). As the *fd* concentration approaches the smectic phase, the cholesteric pitch deviates from the above power law and it slowly unwinds. This is presumably due to pre-smectic fluctuations, since similar behavior is observed in thermotropic liquid crystals (Pindak et al. 1974). Upon decreasing the ionic strength to 4 mM, the value of the power-law exponent ν systematically decreases to 1.1. Interestingly the exponent ν measured at high ionic strength agrees with the theoretical predictions of Odijk (1987). This result also agrees with previous measurements on PBLG (DuPre and Duke 1975). Measurements of the cholesteric pitch of DNA are inconsistent with each other (Jizuka and Yang 1978; Senechal et al. 1980). In conclusion, much still remains unanswered about the microscopic origin of the cholesteric pitch.

1.3.5
Nematic Order Parameter of *fd* Virus Suspensions

As discussed in the theory section (Section 1.2.3 and Fig. 1.2b), the effect of finite rod flexibility has a dramatic effect on the order parameter of the nematic phase. For example, the Khokhlov–Semenov (KS) theory predicts that the finite flexibility of *fd* reduces the nematic order parameter S_2 of the coexisting nematic phase from the rigid-rod limit of 0.8 down to 0.65. The fact that the I–Ch coexistence concentrations agree with the KS theory provides an indirect test of the KS theory. However, a more stringent test of this theory would be to measure the nematic order parameter.

It is possible to induce the cholesteric to nematic phase transition by placing the sample in a sufficiently strong magnetic field (Meyer 1968; Meyer 1969). This fact was used to prepare uniformly aligned monodomain nematics and subsequently to measure their nematic order parameter. The applied field is strong enough to align the sample but at the same time does not affect the orientational distribution function. The traditional techniques for determining the nematic order parameter are X-ray scattering and quantitative measurements of the birefringence. To determine the absolute value of the order parameter from the birefringence measurements, it is necessary to know the birefringence per particle, which has to be determined indepen-

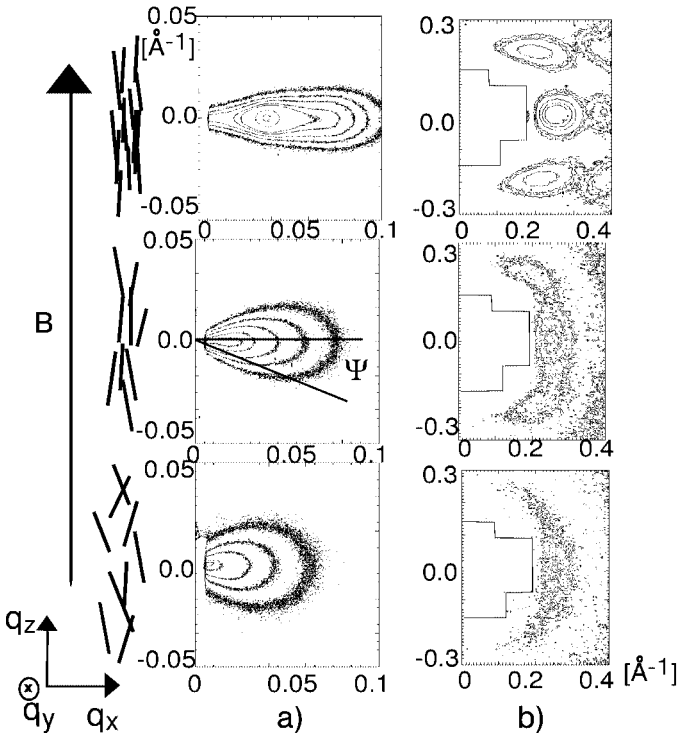

Fig. 1.12 Contour plots of X-ray diffraction of a magnetically aligned *fd* suspension at concentrations of 93, 33, and 15.5 mg ml^{-1}, respectively, in 10 mM ionic-strength buffer. In column (a) scattering at small reciprocal angles up to 0.1 Å^{-1} due to inter-particle interference is shown. In column (b) the intra-particle scattering at higher angles reveals the *fd* form factor, and the low-angle inter-particle interference is blocked by the beam-stop. The orientational distribution function can be determined from the angular spread in both the intra-particle and inter-particle peaks. (After Purdy et al., 2003).

dently. Both of these techniques were used to measure the nematic order parameter of an *fd* suspension (Purdy et al. 2003).

X-ray scattering patterns from colloidal nematic liquid crystals are shown in Fig. 1.12. The scattering at small angle shows a typical butterfly pattern, which is due to the interference between neighboring rods (Ao and Meyer 1991; Kamien et al. 1992; LeDoussal and Nelson 1991; Savenko and Dijkstra 2004). This pattern is usually observed in polymer liquid crystals without much internal structure, such as PBLG. The intensity along an arc of constant radius is usually assumed to be a function of the orientational distribution function. At low angles this is an assumption that needs to be tested. The reason for this is that, unlike spherical particles, the structure factor of a solution of rod-like particles does not necessarily decouple from the anisotropic form factor, and it is the decoupling assumption that needs to be tested. Here we compare the

order parameter obtained at low angles with that obtained at high angles to test the decoupling assumption.

In addition to inter-particle scattering at low angles, a nematic *fd* solution shows a clear scattering pattern at high angles due to the single-particle form factor (Fig. 1.12). At these high angles the structure function is unity, and inter-particle interference does not contribute to the scattering. Therefore, in this region the precise shape of the orientational distribution function can be rigorously determined from the scattering pattern. This method has previously been used to determine S for nematic TMV suspensions (Oldenbourg et al. 1988). But up to now the decoupling approximation has not been tested by comparing the ODF obtained from low-angle inter-particle scattering and high-angle intra-particle scattering.

Figure 1.12 shows the scattering patterns due to both inter-particle and intra-particle interference taken on magnetically aligned nematic monodomains of *fd*. With increasing rod concentration, the width of the patterns decreases, which indicates that the order parameter increases. The concentration dependence of the order parameter is shown in Fig. 1.13. As can be seen, the agreement between theory and experiment is very good at high ionic strength. We note that at a lower ionic strength of 10 mM there is a noticeable discrepancy between the theoretical curve and experimental data (data not shown) consistent with the discrepancies observed for the isotropic–cholesteric coexistence (Purdy et al. 2003).

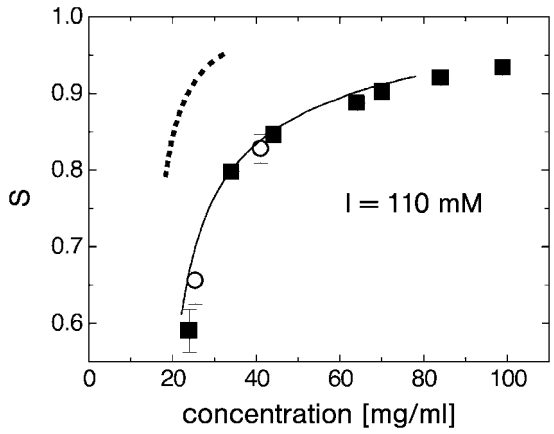

Fig. 1.13 Nematic order parameter of the *fd* phase obtained from an X-ray scattering pattern such as those shown in Fig. 1.12. The filled squares are the order-parameter values obtained from inter-particle scattering, while the open circles are obtained from intra-particle scattering. The solid line shows the prediction of the scaled particle theory extended to semi-flexible charged rods as described in the theory section (Section 1.2.4). The dotted line is the prediction of the Onsager theory for rigid charged rods. (After Purdy et al., 2003).

Equally important, we find that the order parameters obtained from inter-particle and intra-particle scattering are always almost identical. This supports the decoupling approximation and provides validation for measurements of the order parameter from low-angle inter-particle scattering patterns. In addition, it has been shown that the birefringence scales in the same way as the order parameter obtained from X-ray scattering. From this comparison the magnetic birefringence per single rod *fd* can be determined to be $\Delta n_{\mathrm{sat}}/c = 3.8 \times 10^{-5}$ ml mg^{-1}, where c is the concentration of rods. We believe that measurement of the concentration dependence of the order parameter represents the most stringent test for the validity of the KS theory to date. The breakdown of the theory at low ionic strength indicates the need to improve the treatment of electrostatic repulsion for strongly interacting particles.

Direct visualization of fluorescently labeled polymers dissolved in a nematic *fd* background is another novel method by which it is possible to measure the nematic order parameter. Figure 1.14 shows images of four different labeled polymers dissolved in the invisible background of unlabeled *fd* nematics. The conformation of the rods changes from coil-like to rod-like as the background fluid undergoes an isotropic–nematic phase transition. Interestingly, this is true for relatively rigid rods such as neurofilaments, worm-like micelles and actin, while relatively flexible DNA demixes from the background *fd* suspension. Using these images, it is possible to determine the order parameter of polymers dissolved in the background nematic. It is found that the order parameter significantly increases with increasing length of the dissolved polymer. For more information, the reader is referred to Dogic et al. (2004b).

It might be possible to determine the nematic order parameter of a nematic suspension by directly labeling *fd* rods. Present experiments indicate that the exposure times necessary to acquire sufficient signal are too long to determine the orientation of an individual *fd* virus accurately. During the necessary exposure time, individual rods undergo significant rotational diffusion, which blurs the signal. Using a laser as an illumination source, it might be possible to reduce the exposure time to levels where order-parameter measurements are possible.

1.3.6
Smectic Phase of *fd* Virus

At high concentration, *fd* forms a smectic A phase in which rods have long-range orientational order and one-dimensional positional order. The smectic phase in a suspension of *fd* was first reported in Booy and Fowler (1985). The smectic phase is easily recognized by the bright iridescence it exhibits when it is illuminated by white light, as shown in Fig. 1.15. Due to the large contour

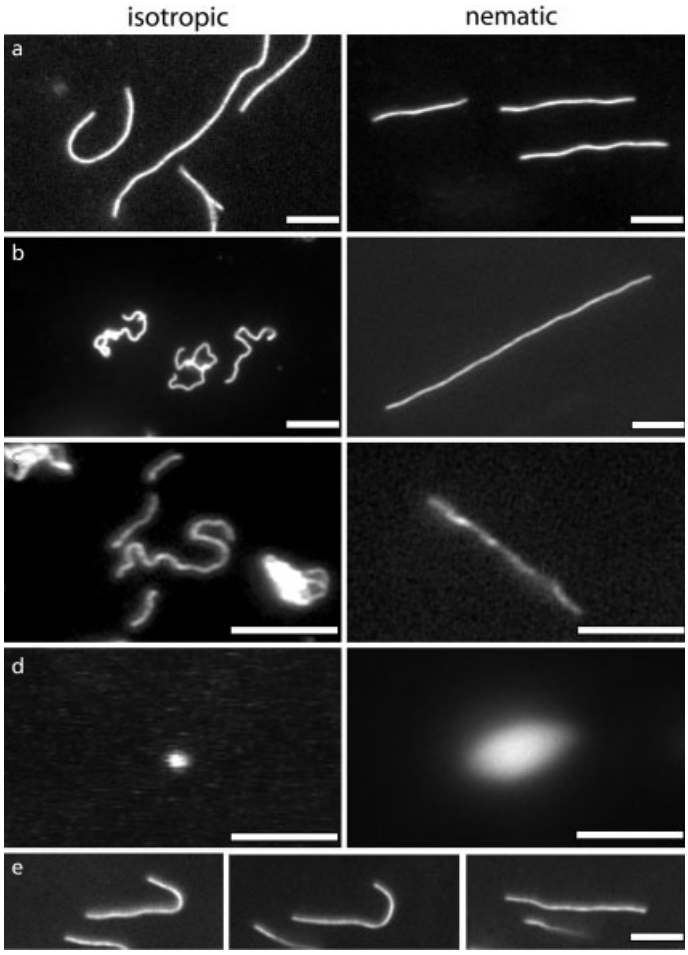

Fig. 1.14 Images of fluorescently labeled biopolymer in isotropic (left panels) and nematic (right panels) background suspensions composed of *fd* virus. (a)–(d) Images of actin ($l_{\mathrm{p}} = 16$ μm), worm-like micelles ($l_{\mathrm{p}} = 0.6$ μm), neurofilaments ($l_{\mathrm{p}} = 0.2$ μm), and DNA ($l_{\mathrm{p}} = 0.05$ μm), respectively. (e) A sequence of images illustrating the escape of an actin filament from a hairpin defect. Scale bar is 5 μm. (After Dogic et al., 2004b).

length of *fd*, it is also possible to observe the smectic density modulation directly using video-enhanced optical microscopy (Figs. 1.15 and 1.16). When 488 nm light is used to scatter light from a smectic phase, it is possible to observe up to five Bragg peaks. From the relative intensities and positions of the peaks, it is possible to deduce the detailed structure of the smectic phase (Dogic and Fraden 1997).

Computer simulations predict that the concentration of the nematic to smectic phase transition is roughly a volume fraction of 0.5. Furthermore,

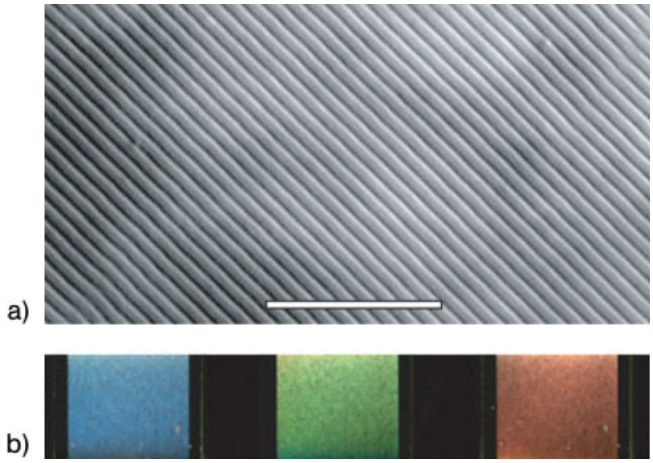

Fig. 1.15 (a) A differential interference contrast (DIC) image of the *fd* virus with varying contour length. The high-contrast lines are smectic gaps. Light scattering indicates that the smectic spacing is 920 nm while the half-width of the gap is 90 nm. Scale bar is 10 μm. (b) Light scattering of white light from a uniformly aligned one-dimensional density modulation of the smectic phase of *fd*. By changing the angle of the incident light, the Bragg condition $d = \lambda \sin\theta/2n$ changes and the sample appears with different colors.

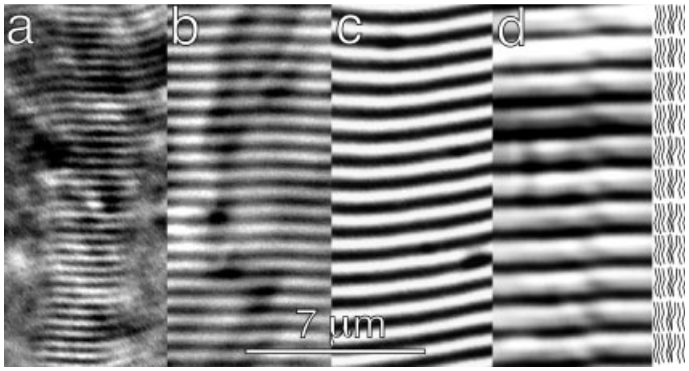

Fig. 1.16 Images of the smectic phase of four different mutants of the *fd* virus. The contour length varies from 0.4 to 1.2 μm. The mutant viruses are prepared according to standard methods of molecular cloning, as described in Section 1.3.1. (After Dogic and Fraden, 2001).

it is found that the location of this phase transition is independent of the aspect ratio of the rods (Bolhuis and Frenkel 1997). Initial studies (Dogic and Fraden 1997) carried out over a limited ionic-strength range indicated that the location of the nematic–smectic phase transition scales with D_{eff}^2.

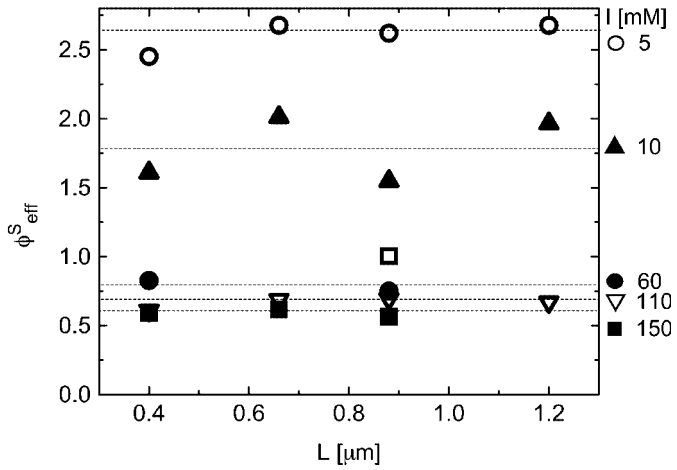

Fig. 1.17 Effective volume fraction of the nematic–smectic phase transition for multiple ionic strengths and contour lengths. The data are taken at pH 8.2. The actual volume fraction of the rods ϕ^s is rescaled using the effective diameter with the relationship $\phi^s_{\rm eff} = \phi^s(D^2_{\rm eff}/D^2)$, where D is the hard-core diameter. (After Purdy and Fraden, 2004b).

As discussed in Section 1.3.2, the concept of $D_{\rm eff}$ quantitatively describes the isotropic–nematic phase transition at high ionic strength. Recently, the nature of the cholesteric–smectic (Ch–S) phase transition in *fd* has been characterized in more detail (Purdy and Fraden 2004b). This new study leads to the conclusion that the electrostatics of highly concentrated charged rods cannot be accounted for with a simple concept such as $D_{\rm eff}$.

Figure 1.17 shows the dependences of the cholesteric–smectic phase transition on ionic strength and contour length. The data clearly show that varying the contour length of the rods has no effect on the location of the nematic–smectic phase transition. This is in agreement with theoretical and simulation predictions (Tkachenko 1996; Bolhuis and Frenkel 1997). However, the data below 60 mM ionic strength do not scale with $D^2_{\rm eff}$. Additionally, the effective volume fraction of the nematic–smectic phase transition at low ionic strength is much higher than the close packing of rods ($\phi = 0.92$), which leads to the conclusion that $D_{\rm eff}$ overestimates the electrostatic interactions.

The location of the nematic–smectic phase transition for suspensions of bacteriophages *fd* and M13 is shown in Fig. 1.18. The main difference between these two bacteriophages is the point mutation in the coat protein, which converts a negatively charged amino acid for the case of *fd* to a neutral one for the case of M13. This results in *fd* having higher charge than M13 by 30% for same conditions. The pH of the solution in Fig. 1.18 was adjusted so that the surface charge of *fd* and M13 suspensions are equivalent. With increasing ionic strength, the volume fraction ϕ^s of the nematic–smectic phase transi-

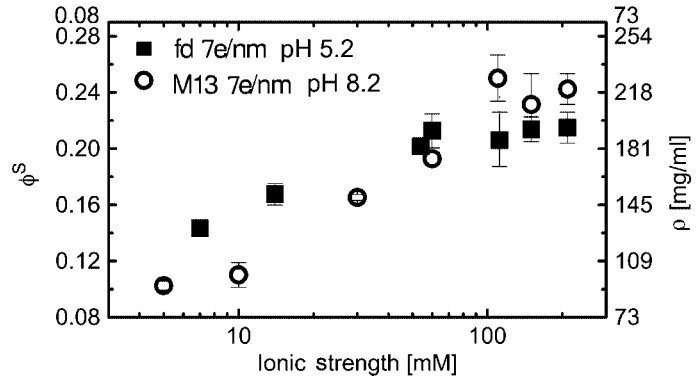

Fig. 1.18 The ionic-strength dependence of the nematic–smectic phase transition for suspensions of *fd* and M13. The pH of the suspension is adjusted so that the linear charge density is 7 e^- nm^{-1} for both rods. (After Purdy and Fraden, 2004b).

tion increases until it saturates at ionic strengths higher than 100 mM. There are two surprising conclusions that follow from the experiments described in Fig. 1.18. First, the concentration of the nematic–smectic phase transition saturates at ionic strengths higher than 100 mM. This leads to the conclusion that, in the limit where the Debye screening length becomes much smaller than the rod diameter, the phase behavior of charged rods approaches that of hard rods. Surprisingly, the nematic–smectic phase transition saturates at volume fraction 0.24, which is much lower than the theoretical prediction of 0.75 for semi-flexible rods (Tkachenko 1996; van der Schoot 1996; Polson 1997). Second, although the linear charge densities for *fd* and M13 are equal, the concentrations of the N–S phase transition in the limit of high ionic strength are not the same. This indicates that the electrostatic continuum model fails and that it is necessary to take into account the molecular arrangements of the charges on the virus.

Another colloidal system where the N–S phase transition has been carefully characterized is the suspension of rigid TMV rods (Wen et al. 1989). There are significant differences when the N–S phase transition in TMV is compared to the Ch–S of *fd*. The ratio of layer spacing to rod contour length is 1.3 for the case of TMV as compared to 1.03 for the case of semi-flexible *fd*. Significant pre-transitional smectic fluctuations are also observed in TMV suspensions, while no nematic–smectic pre-transitional fluctuations are observed in the case of semi-flexible *fd*. For a more detailed comparison of the nematic–smectic transition between these two systems, the reader is referred to Dogic and Fraden (1997). We also note that, in partially dried samples of *fd*, a smectic C phase is observed (Welsh et al. 1996; Lee et al. 2003).

We conclude this section on the phase behavior of hard rods by noting that the isotropic and nematic phases of *fd* suspension are well understood in the limit of high ionic strength. In this limit the rod charge can be quantitatively taken into account via the effective diameter. As the rod concentration increases to the smectic phase or the ionic strength decreases, the behavior of *fd* suspensions cannot be described by current theories. The experimental data indicate that there is a need to incorporate the electrostatic interaction at a more fundamental level in these cases. This remains an area where further theoretical and experimental work is needed.

1.4
Bulk Phase Behavior of Rod–Sphere and Rod–Polymer Mixtures

With the basic understanding of the phase behavior of a pure suspension of hard rods and hard spheres established, recent experiments have shifted toward exploring the phase behavior of more complex mixtures. As an introduction, we first briefly summarize the behavior of samples where hard spheres are mixed with depleting agents that are in an isotropic phase. These can be either a suspension of polymers, or small-diameter hard spheres, or an isotropic solution of rod-like molecules. After summarizing the behavior of these mixtures, we turn our attention to less explored systems where it is necessary to take into account orientational and/or positional ordering of rods.

In the rest of this chapter, we review the phase behavior of mixtures of rods with spherical polymers, such as dextran, poly(*N*-isopropylacrylamide) (NIPA), and poly(ethylene oxide) (PEO), and the behavior of rods with hard spheres, such as charge-stabilized polystyrene (PS) colloids. Many of the phenomena described are general to both rod–hard sphere mixtures and rod–polymer mixtures, while there are also important differences between these two cases. In general, we use "rod–sphere" mixture to refer to a generic mixture of rods with either hard spheres or polymers, while "rod–hard sphere" or "rod–polymer" refers to that specific mixture.

1.4.1
Depletion Interaction Between Hard Spheres

An important concept for understanding colloid–polymer mixtures is the depletion potential introduced by Asakura and Oosawa (AO) in the late 1950s (Asakura and Oosawa 1958). A few decades later the depletion interaction was rediscovered by Vrij (1976). In the non-additive AO model, spherical colloids with diameter D_{sp} interact with each other via the hard-core excluded-volume

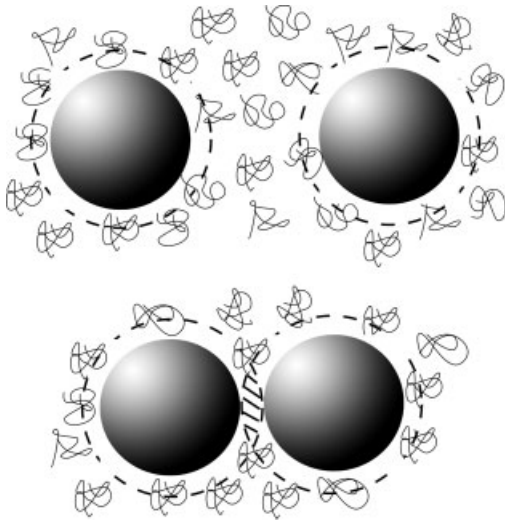

Fig. 1.19 A schematic illustration of the depletion attraction in the sphere–polymer mixture. Around each colloid of diameter D_{sp} there is a shell that is inaccessible to the center of mass of a polymer. As the two colloids approach each other, there is an overlap of the excluded-volume shells, which leads to the effective attractive potential.

interaction, polymers behave as an ideal gas with no interaction, while colloids interact with polymer through the excluded-volume interaction. Consequently, there is a volume shell, with radius equal to the polymer's radius of gyration R_{g}, around each colloid from which the center of mass of a polymer is excluded, as illustrated in Fig. 1.19. As two colloids approach each other, there is an overlap of the excluded-volume shells. The exclusion of the polymer between the colloids leads to an imbalance of the osmotic pressure, which in turns leads to an effective attractive force. The depletion force is proportional to $V_{\mathrm{excl}}\Pi_{\mathrm{polymer}}$, where V_{excl} is the excluded volume and Π_{polymer} is the osmotic pressure of the polymer solution. The range of the depletion attraction is proportional to the polymer radius of gyration (R_{g}), while the strength of the attraction is proportional to the polymer concentration.

An alternative explanation of the AO depletion can be gained by considering the total entropy of the sphere–polymer mixture. Bringing together two large colloids decreases the entropy of mixing of the system. However, the reduction of excluded volumes around large colloids results in an increase of the accessible volume to the more numerous smaller polymers, which in turn leads to an increase in the polymer component of the total entropy of the system. Since the entropy gain of the dispersed polymer is larger than the entropy loss of the clustered colloids, the net result is an effective attractive

potential with entropic origin. Therefore the depletion interaction is often paradoxically described as "attraction through repulsion".

The depletion interaction is a very general phenomenon that is always relevant to the phase behavior of mixtures. However, the quantitative AO theory breaks down for a number of experimentally relevant parameters. First, with increasing polymer size, it is easy for the polymer and the colloid to interpenetrate each other, which leads to a significant decrease in both the range and the strength of the depletion potential (Tuinier et al. 2000). Second, the AO model assumes that the polymer behaves as an ideal gas. While it is experimentally possible to achieve this condition by changing the solvent quality, frequently it is necessary to take into account the excluded-volume interaction between polymers (Hanke et al. 1999; Tuinier et al. 2003). The extreme limit of this case is two large colloids immersed in a suspension of colloids with much smaller size (Mao et al. 1995; Dijkstra et al. 1999). At a low density of the small colloids the interaction potential between the large colloids can be approximated using the AO interaction. However, with increasing concentration of the small colloids the effective intermolecular potential between the large colloids deviates significantly from the AO potential and exhibits significant oscillatory behavior, which is a consequence of the liquid-like structure of the small colloids. The oscillatory nature of the depletion potential in a binary mixture of hard colloids was measured using a scanning laser tweezer (Crocker et al. 1999). Third, the AO depletion is quantitatively valid when the polymer is in the dilute regime. In the semi-dilute region, the relevant length scale is determined by the polymer correlation range. Since this length scale is smaller than R_{g}, the range of the depletion attraction decreases with a crossover from the dilute to the semi-dilute regime. Such depletion attraction was directly measured with an optical tweezer using 1 μm silica spheres immersed in a DNA solution, which acts as a depleting agent (Verma et al. 2000). These experiments illustrate that, with a crossover from the dilute to the semi-dilute regime, the range of the depletion attraction rapidly decreases.

It is possible to induce a depletion attraction with other colloidal solutions besides polymers or spheres. For example, the depletion caused by a dilute isotropic suspension of rods has been studied in detail both theoretically and experimentally. The depletion interaction between flat plates immersed in a solution of rods has been calculated, and using the Derjaguin approximation the result was generalized to the interaction of spherical colloids (Mao et al. 1997). This depletion interaction was consequently obtained using the exact solution to first order in rod concentration by Marques and coworkers (Yaman et al. 1998). The exact calculation indicates that the Derjaguin approximation works well when the length of the rods is much smaller than the diameter of the spheres, but significantly overestimates the depletion potential when the rod length approaches the sphere diameter.

The depletion force between two spheres induced by the presence of a semi-dilute suspension of 0.9 μm long *fd* rods has recently been measured using a line tweezer (Lin et al. 2001). At short distances, there is a significant enhancement of the depletion interaction when compared to the "exact" theory developed for spheres immersed in a solution of rigid rods (Yaman et al. 1998). This is probably due to additional depletion associated with the bending degree of freedom of semi-flexible rods (Lau et al. 2003). Interestingly, by fitting the experimental data to their model, the authors were able to extract the persistence length of *fd* from their data. This turns out to be 1.1 μm, which differs significantly from previous measurements (Song et al. 1991). A systematic experimental study of how the depletion strength varies as a function of the ratio of sphere diameter D_{sp} to rod length (L) is so far lacking.

1.4.2 Phase Diagrams of Hard Spheres and Polymers or Isotropic Hard Rods

Once the depletion potential between two isolated spherical colloids has been "engineered" by choosing appropriate polymer size and concentration, it is of fundamental interest to understand how the chosen potential affects the phase behavior of spherical colloids. Theory, computer simulation, and experiments have shown that the parameter that most critically affects the phase behavior is the range of attractive interaction (Gast et al. 1983a; Gast et al. 1983b; Gast et al. 1986; Lekkerkerker et al. 1992; Hagen and Frenkel 1994). For potentials with very short-range attraction, there is a direct equilibrium phase transition from a dilute colloidal gas (G) to a concentrated colloidal crystal (C). There is an additional transition from the dilute colloidal gas to a dense disordered colloidal liquid (L), as illustrated in Fig. 1.20a. However, this transition is metastable with respect to the equilibrium gas–solid phase transition. Only when the range of attraction increases is a stable gas–liquid phase transition observed with associated critical and triple points. Experimentally, it is found that glassy states and/or gels often preempt the occurrence of the equilibrium phase transitions. The non-equilibrium nature of these states is poorly understood and is currently under intense study (Anderson and Lekkerkerker 2002). We note that, for spheres with very short-range attractive potentials, simulations predict the existence of a first-order phase transition between two solids with different densities (Bolhuis and Frenkel 1994a). So far this transition has not been observed in experiments.

The initial studies of Gast et al. (1983a), Gast et al. (1983b), and Gast et al. (1986) of the sphere–polymer mixture used thermodynamic perturbation theory to obtain the theoretical phase diagrams. Such theories treat the sphere–polymer mixture as a single-component system of spheres that have

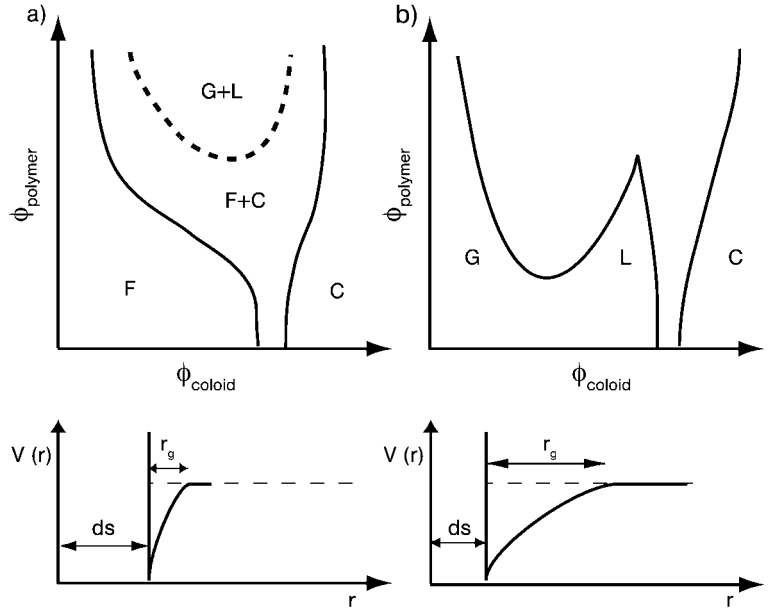

Fig. 1.20 The phase diagram of a colloid–polymer mixture is found to depend critically on the range of attraction, which in turn is determined by the polymer size (F = fluid, L = liquid, G = gas, and C = crystal). (a) For short-range attraction, only an equilibrium gas–solid phase transition is observed. We note that a gas–liquid phase transition is present but is metastable with the respect to the equilibrium gas–solid phase transition. (b) For colloids with long-range attraction, gas–liquid, liquid–solid, and direct gas–solid phase transitions are observed. The topology of this phase diagram closely resembles that of molecular liquids interacting with a van der Waals potential.

hard-core repulsive interactions to which the effect of attraction is considered as a perturbation. The underlying assumption is that depletion attraction is pairwise additive and that, in a sample where two phases coexist, the polymer concentration is the same in both phases. Non-additivity for sphere–polymer mixtures was treated via computer simulations and it was found that the depletion attraction is pairwise additive only if the ratio R_g/D_{sp} is sufficiently small (Meijer and Frenkel 1991; Meijer and Frenkel 1994). A more complete theory that takes into account the possibility of partitioning of the polymer across the phase boundary and accounts for the non-additive nature of the colloid–polymer mixture was subsequently developed by Lekkerkerker et al. (1992).

Studies of colloid–polymer mixtures show that the topology of the phase diagram depends critically on the range of attraction. This result is very general and is expected to hold for molecular liquids as well as for colloidal systems. The advantage of colloids is that the shape, range, and depth of the

intermolecular potential can be adjusted and experimentally measured. This makes colloids an ideal system to test the statistical-mechanical theories that predict the relationship between the macroscopic phase behavior of fluids and the microscopic intermolecular potential.

The phase behavior of a binary mixture of hard spheres is very different from that of a hard sphere–polymer mixture. On the theoretical side, the initial work by Lebowitz and Rowlison (1964) showed that, within the Percus–Yevick approximation, mixtures of hard spheres are miscible for all aspect ratios and concentrations. For a long time this was considered to be the general case. More recently, a more accurate liquid-state theory indicated that a binary mixture of spheres becomes unstable and demixes at high enough asymmetry (Biben and Hansen 1991). On the experimental side, liquid–liquid demixing has not been observed. It seems that this transition is preempted by the liquid-crystal phase transition where the solid composed of large spheres coexists with a liquid rich in spheres with smaller diameter (Dinsmore et al. 1995; Imhof and Dhont 1995; Dijkstra et al. 1998; Dijkstra 2001). In this way the phase behavior of binary hard spheres is reminiscent of a sphere–polymer mixture with large asymmetry (Fig. 1.20a). At even higher volume fraction, it is possible to obtain well-ordered binary alloys with complex crystalline structure (Bartlett et al. 1992).

As discussed previously (Section 1.4.1), isotropic rods are very effective depletion agents, especially when the length of the rod (L) is significantly smaller than the diameter of the hard sphere ($D_{\rm sp}$). However, there have been only limited studies on the phase behavior of a mixture of isotropic rods and colloidal spheres. In the initial work by Pecora and coworkers (Tracy et al. 1993), no demixing phase transition was observed in a mixture of rod-like PBLG and polystyrene spheres. Early simulations predicted a phase diagram reminiscent of those found in spheres with short-range attractions (Fig. 1.20a) when the ratio $D_{\rm sp}/L$ is smaller than 0.3 (Bolhuis and Frenkel 1994b). For larger ratios, both gas to liquid and liquid to crystal phase transitions are stable (Fig. 1.20b). These predictions have also been confirmed in theoretical work (Vliegenthart and Lekkerkerker 1999). Subsequently, the phase separation between crystals of silica spheres and an isotropic solution of boehmite (γ-AlOOH) rods coated with silica was observed (Koenderink et al. 1999). In these experiments, the ratio $D_{\rm sp}/L$ was kept constant at 0.3, exactly the parameter at which the gas–liquid phase transition becomes stable with respect to the gas–crystal phase transition. Interestingly, no gas–liquid phase coexistence was reported. In these studies the authors observe the formation of crystals via a two-step pathway (Vliegenthart et al. 1999). In a first step, the mixture forms a liquid-like aggregate that subsequently crystallizes. This point is discussed in greater detail in Section 1.9 on the kinetics of phase transitions. With increasing concentration of the rods, the suspension becomes

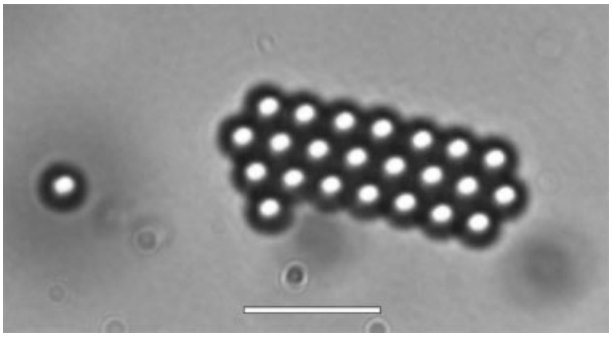

Fig. 1.21 A crystalline cluster of polystyrene spheres ($D_{\rm sp} = 2$ μm) grows on the walls when *fd* rods are added. The concentration of *fd* rods is roughly 2 mg ml^{-1}. Fluctuations of the crystalline cluster are clearly visible under the microscope. Scale bar indicates 10 μm.

highly viscous and the sample takes too long to equilibrate. In this case it is difficult to determine the final equilibrium phase.

We have also observed demixing in a mixture of 0.9 μm long *fd* viruses and large polystyrene spheres (Fig. 1.21). It is interesting that when rods at a fixed concentration (2 mg ml^{-1}) are mixed with small polystyrene spheres ($D_{\rm sp} = 1$ μm), no phase separation is observed. As the sphere size is increased ($D_{\rm sp} = 1.5$ μm), surface crystallization is observed, but not crystallization in the bulk. This is not surprising, since the overlap of excluded volume between a flat wall and a sphere is twice as large as that between two spheres. Surface crystallization has previously been observed for a binary mixture of hard spheres (Dinsmore et al. 1997). For spheres with $D_{\rm sp} = 2$ μm, we observe phase separation in the bulk, but the heavy particles quickly sediment to the bottom wall and spread out on the surface. The quantitative phase diagram for a mixture of spheres and isotropic rods as a function of rod and sphere concentrations and $D_{\rm sp}/L$ ratio is difficult to determine due to turbidity and sedimentation of the large spheres. A theoretical calculation explains why the phase separation in a sphere–rod mixture is so sensitive to the ratio of sphere diameter to rod length (Yaman et al. 1998). As the rod length approaches the sphere diameter, the strength of the depletion potential decreases significantly.

So far we have discussed the phase behavior of a mixture of spheres with depletants such as isotropic rods or polymer solutions. In the rest of this chapter we focus on a number of surprising phenomena that are observed in rod–polymer or rod–sphere mixtures at higher rod concentrations. In this case it is necessary to take into account either the orientational or the positional ordering of rods, or sometimes both.

1.5
Influence of Non-Adsorbing Polymer on the Isotropic–Nematic Phase Transition

The Onsager theory describes the entropy-driven isotropic–nematic phase transition in a suspension of rods that have purely repulsive hard-core interactions (Onsager 1949; Vroege and Lekkerkerker 1992). As a next step, it is important to examine how the presence of attractive interactions alters the nature of the I–N phase transitions. For low-molecular-weight liquid crystals, this issue has been reviewed extensively elsewhere (Gelbart and Barboy 1980). Experimentally, one feasible way to introduce attractions into hard rods is by adding a non-adsorbing polymer. In a similar way that the presence of polymers dramatically alters the phase behavior of hard spheres, it is reasonable to expect a significant influence of polymer on the phase behavior of hard rods. In this section we focus on the bulk I–N phase transition in rod–polymer mixtures, while in subsequent sections we consider the possibility of positionally ordered smectic phases. While it is tempting to connect the phase behavior of rod–polymer mixtures to that of a solution of rods with direct attractive interactions, there are also some important differences between these two systems. Most importantly, the depletion interaction in the rod–polymer mixture is an effective potential. Therefore, the strength of the interaction depends on the local concentration of polymer, which can vary considerably in the sample, especially if there are coexisting phases within the same sample.

In general, liquid-state theories that describe the behavior of rod-like particles are not as developed as theories for spherical particles. While the Onsager theory accurately describes the reference state of hard-rod fluids, introducing attractive interactions into such a theory is not as straightforward as for the case of hard spheres. The Onsager theory is based on a density expansion, and it is therefore valid only at low densities for solutions of rods that have a fair degree of orientational disorder. Rods with depletion-like attractive interactions attain the minimum of their intermolecular potential when they are parallel to each other and their centers of mass are at a minimum separation (Fig. 1.22). These are exactly the configurations that need to be avoided for the Onsager theory to converge at the level of the second virial coefficient (van der Schoot and Odijk 1992). To overcome this difficulty, Lekkerkerker and Stroobants (1994) have calculated the phase diagram of rod–polymer mixtures (Fig. 1.23) using the scaled particle free-energy expression of hard rods, which approximately takes into account higher virial coefficients and reduces to the Onsager theory in the appropriate limit (Lekkerkerker and Stroobants 1994; Bolhuis et al. 1997). Such an expression reproduces remarkably well the isotropic–nematic phase transitions for hard rods with finite size when compared to results of computer simulations (Kramer and Herzfeld 1998).

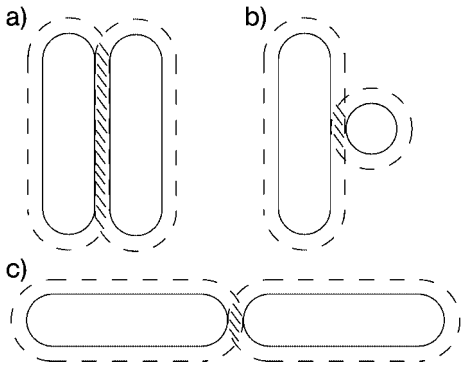

Fig. 1.22 The attractive interaction induced by adding polymer to a suspension of rod-like colloids. The strength of attraction is proportional to the overlap of the excluded volume, and it is strongest when the rods lie parallel to each other, as illustrated in case (a), as opposed to rods lying perpendicular to each other, as shown in case (b), or end-to-end, as in case (c).

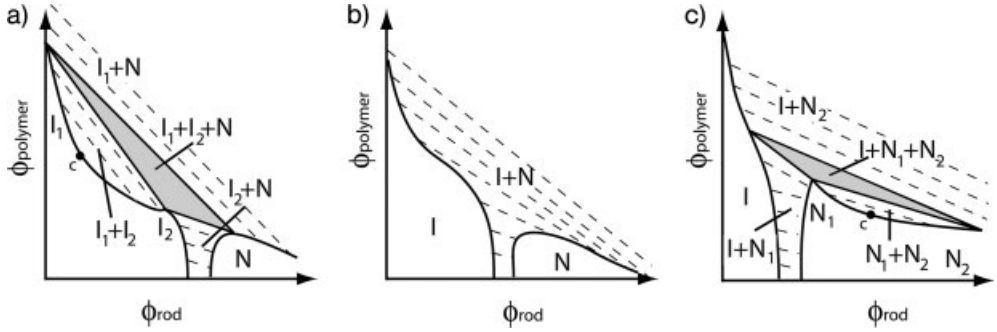

Fig. 1.23 The three possible phase diagrams of a rod–polymer mixture as predicted by Lekkerkerker and Stroobants (1994). For long-range attraction, in addition to I–N phase transition, a stable isotropic–isotropic phase transition is predicted. Dashed lines are tie-lines between coexisting phases. For very short-range attraction, the isotropic–isotropic coexistence disappears but a nematic–nematic phase appears. With both isotropic–isotropic and nematic–nematic coexistence, there is a triple point and an associated critical point. Because of the binary nature of the mixture, the triple point spans an entire solid triangle in the phase diagram.

The topology of the phase diagrams obtained using the scaled particle theory (SPT) bears a striking similarity to the phase diagrams of the hard sphere–polymer mixture previously described in Section 1.4.2. For rods with long-range attractions an isotropic–isotropic (I_1–I_2) phase transition is observed. As a consequence, there is a critical point associated with isotropic–isotropic demixing and a triple point in which two isotropic phases coexist with a nematic phase. Since the system contains two components, the triple point

spans an entire triangle in the phase diagram when plotted in the rod–polymer density–density plane. For a very short-range attraction, the system exhibits nematic–nematic phase transitions. A simpler calculation that directly extends the second virial Onsager free energy to include attractive interactions only predicts the widening of the isotropic–nematic coexistence and fails to predict either isotropic–isotropic or nematic–nematic coexistence (Warren 1994). In addition, Warren's theory abruptly breaks down and predicts coexistence between an infinitely dense nematic phase and dilute isotropic rods as soon as the second virial coefficient becomes negative. Because of this, Warren argues that the second virial theory extended to rod–polymer mixtures is only valid for very weak attractions, but it is not clear at which point this approximation breaks down.

There have been a few experiments that have studied the phase diagram of rod–sphere mixtures, most notably in cellulose–dextran and boehmite–polystyrene mixtures (Edgar and Gray 2002; Buitenhuis et al. 1995). In the latter work the authors observe a triple point in which two isotropic phases coexist with a nematic phase. In addition to these equilibrium phases, non-equilibrium gel-like phases are also reported at fairly low rod concentrations. In the former work on the cellulose–dextran mixture, only biphasic isotopic–nematic coexistence is observed, which widens with increasing polymer concentration.

Motivated by good agreement between the Onsager theory and experimental data for the I–Ch coexistence of filamentous *fd* rods, we have recently measured the I–Ch phase transition in the presence of a non-adsorbing polymer. Using fluorescein-labeled dextran, it is possible to obtain macroscopically phase-separated samples, measure the full phase diagram, and determine the tie-lines between coexisting isotropic and cholesteric phases (Dogic and Fraden 2001; Dogic et al. 2004a). An example of the typical phase diagram measured is shown in Fig. 1.24. In agreement with previous studies, it is found that adding polymer widens the coexistence between the isotropic and cholesteric phases. Using the *fd*–dextran mixture, it is also possible to observe preferential partitioning of the polymer into the isotropic phase, in qualitative agreement with the theoretical predictions. Unfortunately, with this system, we are not able to access the parameters for which I_1–I_2–N and I–N_1–N_2 phase coexistence is predicted in the work by Lekkerkerker and Stroobants (1994).

There are a number of reasons why quantitative comparison between the SPT theory and experiments is difficult (Dogic et al. 2004a). First, the theoretical work is valid for rods that interact through hard-core repulsive interaction, while the *fd* viruses used in the experiments are charge-stabilized. Because of the small diameter of *fd*, it is not possible to add enough salt to reduce the double-layer repulsive interaction to negligible levels and simultaneously

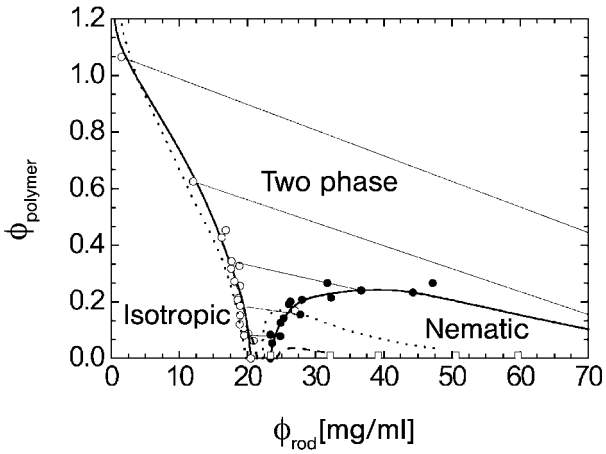

Fig. 1.24 Phase diagram of an *fd* virus and dextran ($R_g = 176$ Å) mixture at 100 mM ionic strength. The measured points indicate the rod and polymer concentrations of the coexisting isotropic and cholesteric phases. The full line indicates the phase boundary between the two-phase isotropic–cholesteric phase coexistence and stable single-phase isotropic and cholesteric phases. Tie-lines are indicated by thin full lines. (After Dogic et al., 2004a).

preserve the colloidal stability of the system. Therefore, repulsive double-layer interactions have to be incorporated into the theory. At the level of the second virial coefficient, it is possible to achieve this by replacing the hard-core diameter D_r with a larger effective diameter D_{eff} that is dependent on the ionic strength, as described in Section 1.2.2. This procedure is rigorously valid only for rod concentrations low enough that the Onsager second virial coefficient accurately describes the system. When comparing our data to theory, we have used D_{eff} as a hard-core diameter in the SPT theory, although in principle this is an approximation that is not well controlled. We note that there was a recent attempt by Herzfeld and coworkers to incorporate charge into scaled particle theory (Kramer and Herzfeld 1999; Kramer and Herzfeld 2000).

Second, the SPT theory is valid for perfectly rigid rods while *fd* is a semi-flexible rod with a persistence length of 2.2 μm. This flexibility is enough to significantly affect the nature of the isotropic–nematic phase transition, as explained in Section 1.2.3. The SPT theory has been modified to include flexibility in the same way that Khokhlov and Semenov extended Onsager theory to treat semi-flexible rods. The competition between attractive interaction and repulsive interaction can induce a bundling–unbundling transition (Kierfeld and Lipowsky 2003).

Third, the R_g of the polymers used in our experiments was equal to or even larger than the diameter of the rods. As mentioned in Section 1.4.1, for these

parameters the AO model of depletion attraction significantly overestimates both the range and the strength of the interaction. The reason for this is that the open polymer structure easily interpenetrates a slender rod. Since there is no analytical expression for the depletion potential in such a case, when comparing our experimental results to the SPT theory we have used results obtained from simulation.

In spite of these caveats, in the limit of high ionic strength the agreement between experiments and theory is quite good, as shown in Fig. 1.24. It remains to see if this is fortuitous. However, as the ionic strength decreases, the discrepancy between theory and experiment becomes significant. In conclusion, it is fair to say that an accurate liquid-state theory for rods that have an attractive attraction is still lacking. In Section 1.3.5 on the phase behavior of hard rods, we argued that the measurement of the order parameter is a more stringent test of the validity of the Onsager theory when compared to the measurements of the I–N phase coexistence. In the same spirit, we have attempted to measure the order parameter of the nematic phase at different polymer concentrations.

This is an important question when viewed in the context of the van der Waals theory of liquids, which for spherical particles states that the repulsive part of the intermolecular potential is mainly responsible for the liquid-like structure of fluids (Widom 1967). The attractive potential determines the density of the fluid by providing a cohesive energy that is largely independent of the exact configuration of the fluid. It remains to be seen if this van der Waals picture is also true for a liquid of attractive rods. If so, one would expect that the strength of the attraction only determines the density of the liquid of rods, while its structure, as characterized by the order parameter, would depend only on the constituent rod concentration. The nematic samples of the *fd*–polymer mixtures turn out to be quite viscous and it is difficult to reproducibly obtain monodomain samples, which results in noisy measurements of the order parameter. Although noisy, our results indicate that the van der Waals picture also holds for the rod–polymer mixtures. In other words, the nematic order parameter remains independent of the polymer concentration in a rod–polymer mixture. For more details, the reader is referred to Dogic et al. (2004a).

It is of interest to consider if the phase diagram for rod–polymer mixtures is generic to other rod-like systems in which it is possible to induce attractive interactions. For example, another well-studied and very effective agent for condensing charge-stabilized rods is multivalent counterions. Most biopolymers, such as *fd*, actin, DNA, and microtubules, are negatively charge-stabilized colloids under physiological pH conditions. Adding multivalent cations to such a solution induces the formation of tightly packed bundles (Tang et al. 1996; Tang et al. 1997; Bloomfield 1991). Bundle formation is usually observed at

a very low concentration of rods, and the effect of rod concentration has not been studied systematically. This corresponds to the upper left corner of the *fd*–dextran phase diagram shown in Fig. 1.24. Interestingly, when we prepare a mixture of a polymer at very high concentration and *fd*, we observe the formation of bundles that look remarkably similar to the bundles observed in the mixture of *fd* and multivalent counterions.

Recently, a study of a mixture of 50 nm long DNA fragments and trivalent or tetravalent spermidine and spermine condensing agent was published (Pelta et al. 1996; Sikorav et al. 1994). As opposed to other studies, the authors here use a finite concentration of DNA fragments and observe the formation of nematic (cholesteric) phase instead of bundles. In another recent study of actin filaments mixed with multivalent salts, the authors report the formation of a new phase in which actin is condensed into two-dimensional rafts, which subsequently stack on top of each other at 90° (Borukhov and Bruinsma 2001; Wong et al. 2003; Lee et al. 2004). Such a phase would have no analogy in rod–polymer mixtures. Clearly rod–counterion mixtures still remain poorly understood. In our view it would be of interest to compare such systems to the phase behavior of rod–polymer mixtures.

In this section we have only considered the influence of polymer on the bulk isotropic–nematic phase transition. When these studies are extended to account for the formation of the positionally ordered smectic phase, a whole range of new and unexpected phenomena are observed. These will be reviewed in the next few sections.

1.6
Entropically Driven Microphase Separation in Rod–Sphere Mixtures

The influence of polymers on the entropy-driven isotropic–nematic phase transition is qualitatively understood with a mixture being in either a single uniformly mixed phase or a macroscopically demixed phase. However, it has recently become apparent that there is a third possibility of a microphase-separated state for a wide range of polymer and/or hard-sphere sizes or concentrations. In microphase separation the system begins to phase-separate into regions that are rich in either rod or sphere component. Unlike bulk demixing, the phase-separating regions grow until they reach a critical size, at which point they organize into a well-ordered three-dimensional structure. The full complexity of the phase diagram of the *fd*–polystyrene (PS) sphere mixture for one sphere size is shown in Fig. 1.25. Other phases are observed for different sized spheres.

Usually microphase-separated states are found in amphiphilic molecules such as block copolymers, lipids or surfactants (Gelbart et al. 1994). The micro-

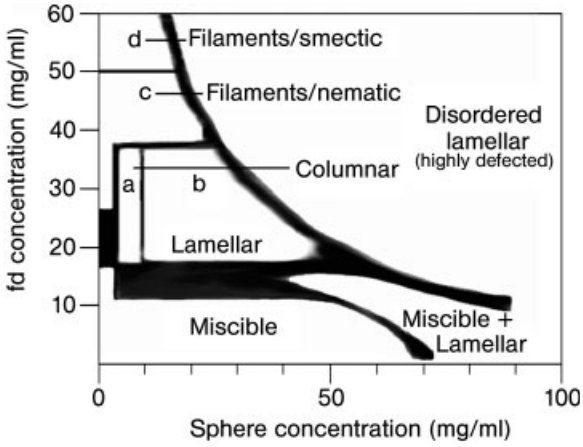

Fig. 1.25 Phase diagram of a mixture of *fd* virus and polystyrene spheres ($D_{\rm sp} = 100$ nm) in 10 mM Tris buffer. A suspension of pure *fd* forms isotropic, cholesteric (nematic), and smectic phases with increasing concentration, as described in Section 1.3. Increasing the volume fraction of spheres induces the formation of a number of microphase-separated states, most notably lamellar and columnar phases. Images of these structures are shown in Fig. 1.28. The isotropic–cholesteric phase transition for pure rods is at 18 mg ml^{-1} while the nematic–smectic phase transition is at 50 mg ml^{-1}. Filaments are layered structures discussed in more detail in Section 1.9.3. (After Adams et al., 1998).

phase-separated state formed in rod–polymer mixtures is different from the microphase-separated states formed by amphiphilic macromolecules in two fundamental respects. First, all amphiphilic molecules and block copolymers are characterized by a covalent bond between mutually immiscible blocks. Microphase-separated structures have enormous surface area and the resulting surface energy is very high. Consequently, in the absence of the bond between immiscible blocks, it is commonly assumed that such materials would bulk phase-separate into two immiscible macroscopic phases. In an *fd*–polystyrene mixture, the covalent bond between the immiscible components is absent, and the mixture is free to macroscopically phase-separate. Therefore, it is surprising that under certain conditions such a mixture forms a stable microphase-separated state instead of a macroscopically phase-separated sample. A microphase state in a mixture implies that the surface tension between the components of the mixture is very small. In amphiphilic and copolymeric systems, phase separation is largely driven by enthalpic contributions to the free energy. In rod–sphere mixtures the interactions that dominate the phase behavior of the system are hard-core excluded-volume interactions. All transitions in such a system are driven by a purely entropic contribution to the free energy, and it follows that microphase separation is a state with highest entropy, not lowest energy.

1.6.1 Lamellar Phase in Rod–Polymer and Rod–Sphere Mixtures

In this section we review the theoretical and experimental studies of the lamellar phase, which is the simplest microphase-separated state. The lamellar phase is characterized by one-dimensional long-range order in which liquid-like layers of rods are intercalated with layers of spheres. The existence of the lamellar phase was first predicted using a density-functional theory where the excluded-volume interactions are treated at the level of the second virial coefficient (Koda et al. 1996). Because of the highly approximate nature of the second virial approximation, the formation of the intercalated lamellar phase was also verified using Monte Carlo simulations in the same work. Both the theoretical model and the computer simulations made a number of simplifying assumptions, most importantly that the rods are perfectly aligned and that the diameters of the rods and spheres are equal. Therefore, in this model the rods do not exhibit an isotropic–nematic phase transition. The same model of a mixture of spheres and perfectly aligned spherocylinders was later generalized to include spheres of arbitrary size (Dogic et al. 2000).

The theoretical prediction for the stability diagram of a typical rod–sphere mixture is shown in Fig. 1.26. The theory predicts the stable entropy-driven formation of a lamellar phase when a low volume fraction of spheres is added to a nematic phase of perfectly aligned rods. At a high concentration of both rods and spheres, the model predicts complete bulk phase separation, while at low sphere/rod concentrations the mixture is miscible. More importantly, it is found that the rod–sphere mixture forms a layered lamellar phase at a lower volume fraction when compared to the formation of a layered smectic phase in a suspension of pure hard rods. Therefore, the spheres not only passively partition into the smectic gaps, but also actively shift the boundaries of the nematic–lamellar phase transition and significantly stabilize the lamellar phase. Recent simulations have considered rod–sphere mixtures in which the rods have full orientational degrees of freedom (Lago et al. 2004). The existence of a stable lamellar phase was confirmed in this more realistic model. It was also found that the spheres actively stabilize the lamellar phase with respect to the nematic phase, in agreement with theory and simulations on mixtures of spheres and perfectly aligned rods.

A simple intuitive picture for the formation and enhanced stability of the lamellar phase emerges from the consideration of the total excluded volume in a mixture. The entropy-driven transition to an ordered structure is always driven by a decrease in the total excluded volume of the system. Therefore, we would expect that the excluded volume of the lamellar phase is smaller than the excluded volume of the uniform rod–sphere mixture. It is useful to compare this quantity in two extreme cases: a spatially uniform mixture, and

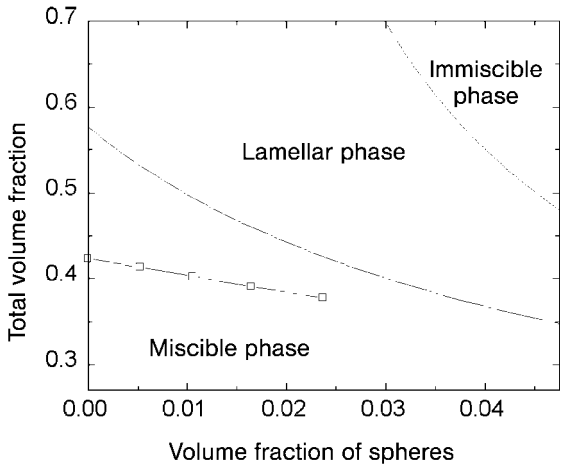

Fig. 1.26 Stability boundaries for a rod–sphere mixture calculated using the theory described in Section 1.2.6. For this particular phase diagram, the aspect ratio of the rods was $L/D_{\rm sc} = 20$ and the diameter of the spheres was equal to the diameter of the rods, $D_{\rm sc}/D_{\rm sp} = 1$. The full line indicates the theoretical prediction for the points in the phase diagram at which the system becomes unstable toward lamellar fluctuations. The dotted line indicates the instability toward complete demixing into two macroscopic phases. Squares indicate the nematic–lamellar phase transition obtained from Monte Carlo simulation. (After Dogic et al., 2000).

a perfectly ordered one-dimensional lamellar phase. Figure 1.27 illustrates the volume that is excluded to a spherocylinder due to the presence of either a sphere or another spherocylinder. For spherocylinders with large asymmetry, the excluded volume of a sphere is about half that of another spherocylinder. In a mixture in which the concentration of spherocylinders is spatially uniform, replacing a single spherocylinder with two spheres leaves the total excluded volume unchanged. However, this procedure significantly decreases the total volume fraction of the particles. Therefore, in a rod–sphere mixture we have

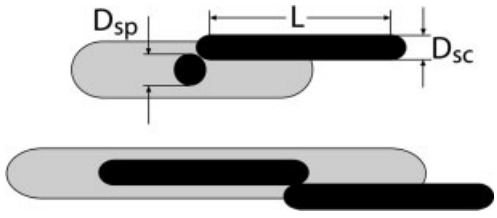

Fig. 1.27 The volume excluded to the center of mass of a spherocylinder due to the presence of a sphere or another spherocylinder is indicated by the lightly shaded region. The large excluded volume between a spherocylinder and a sphere is the reason for the enhanced formation of the lamellar phase. (After Dogic et al., 2000).

packing problems similar to those encountered in a suspension of pure spherocylinders, but at a lower total volume fraction. By forming a layered lamellar phase, the mixture can significantly reduce the total excluded volume because the periodic one-dimensional density order associated with lamellar order significantly reduces the probability of very unfavorable sphere–spherocylinder contacts. For quantitative details that emerge from the analysis of the second virial theory, the reader is referred to Dogic et al. (2000).

An alternative way to consider the enhanced stability of the lamellar phase in the rod–sphere mixture is to focus on the effect of spherocylinder ends. In Section 1.2.5, we discussed the formation of the smectic phase as a consequence of unfavorable packing that occurs around the ends of rod-like molecules. Adding spherical particles to the nematic phase of rods increases the effective concentration of the "ends" without significantly changing the total volume of the solution. The only way that the system can accommodate these extra "ends" is to undergo a transition to an entropy-stabilized microphase-separated state.

Subsequent to the prediction by Koda and coworkers, a layered lamellar phase was experimentally observed in a mixture of *fd* virus and polystyrene (PS) spheres (Koda et al. 1996; Adams et al. 1998). Under the experimental conditions, *fd* virus and PS spheres approximate the behavior of hard rods and spheres, respectively. An optical micrograph of a typical lamellar phase is shown in Fig. 1.28c. The layer periodicity of the lamellar phase is 1.1 μm while that of a smectic phase of pure *fd* suspension is 0.9 μm. Evidence from samples where the spheres are fluorescently labeled and from electron microscopy on freeze-fractured samples indicates that the structure of the lamellar phase is that of intercalated layers of spheres and rods. It is important to note that the experimental parameters were that the diameter of the sphere ($D_{\mathrm{sp}} = 0.1$ μm) is roughly 10 times smaller than the rod length ($L = 1$ μm) and 10 times larger than the rod diameter ($D_{\mathrm{sc}} \sim 10$ nm). These parameters are very different from the parameters used in the simulation by Koda and coworkers. The experimental results also show that spheres significantly stabilize the formation of the lamellar phase. As can be seen from the phase diagram shown in Fig. 1.25, the suspension of pure *fd* forms a layered smectic phase at 50 mg ml^{-1}. Adding spheres at a volume fraction of 2% induces the formation of the layered lamellar phase at 20 mg ml^{-1}. In addition to the above described case, the lamellar phase is consistently observed for a wide variety of PS sphere sizes ranging from 0.02 to 0.2 μm. After filling the sample chamber, we find that the layers will form within few minutes, and over the next few days the defects slowly anneal and the overall order improves. We have had samples that have remained layered for a period of a few years before drying up. This provides a strong indication that the lamellar phase is an equilibrium state and not a kinetically trapped structure.

Besides *fd*–PS mixtures, the lamellar phase has also been observed in mixtures of *fd* virus with a wide variety of polymers, such as poly(ethylene oxide) (PEO), dextran and poly(*N*-isopropylacrylamide) (NIPA). This is perhaps not too surprising since in the second virial theory the effect of the sphere–sphere excluded volume has negligible effects on the overall topology of the phase diagram. It is the polymer–spherocylinder excluded volume that drives the phase transition. The effect of the polymer size has not been systematically studied so far.

The second virial theory also indicates that it should be possible to obtain a lamellar phase in a binary mixture of rods with sufficiently different contour length (Koda and Kimura 1994). Due to a paucity of well-defined monodisperse hard-rod systems, to our knowledge the lamellar phase has only been observed in mixtures of *fd* and either colloidal spheres or polymer. As better-defined rod systems become available, we believe it will be shown that the lamellar phase is a generic structure found in all rod–sphere mixtures. We do note that lamellar-like structures have been observed in a study of polydisperse tobacco mosaic virus (TMV) and the spherical protein bovine serum albumin (BSA) (Adams and Fraden 1998).

While both lamellar and smectic phases have the same quasi-one-dimensional long-range order, the main difference between these phases is the spacing of the layers. Theory predicts that the lamellar layer spacing will swell with increasing volume fraction of spheres (Koda et al. 1996; Dogic and Fraden 2001). Therefore, it should be possible to go from the smectic to the lamellar phase without ever crossing a phase boundary. However, it is also possible to envision a first-order transition between coexisting smectic and lamellar phases. In such a sample there would be a coexistence between two layered phases with different layer spacings. On the experimental side, both the continuous swelling of the smectic phase and the coexistence between a smectic phase with periodicity of 0.9 μm and a lamellar phase with 1.1 μm periodicity have been observed. These are described in greater detail in Sections 1.9.3 and 1.9.4.

1.6.2
Columnar Phase and Chain-Like Structures in Mixtures of *fd* Virus and Hard Spheres

In addition to the lamellar phase, other more complex structures are observed in mixtures of *fd* rods and hard spheres. In particular, for a mixture of *fd* and 0.1 μm PS spheres a columnar structure is observed. The phase diagram (Fig. 1.25) shows that such a phase is formed when nematic rods are mixed with a low volume fraction of spheres. In the columnar phase, 0.1 μm spheres coalesce together until they reach a critical diameter of 0.3 μm. Subsequently

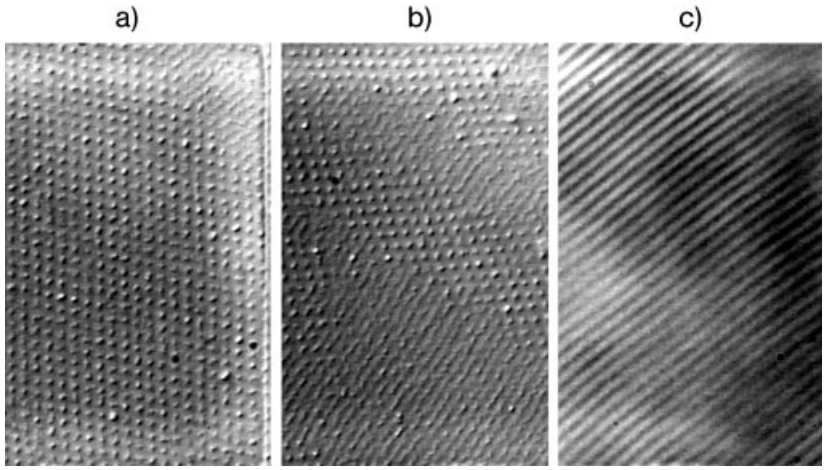

Fig. 1.28 DIC images of microphase-separated phases observed in a mixture of *fd* and polystyrene spheres ($D_{\mathrm{sp}} = 0.1$ μm). The phase diagram of this particular mixture is shown in Fig. 1.25. (a) At sphere concentrations below 1%, a stable columnar phase is observed (see Fig. 1.29). (b) At intermediate concentrations, the spaces between the columns gradually fill in and the sample continuously transforms into the lamellar phase. (c) At high sphere concentrations, a single-phase lamellar phase is formed with a layer spacing of 1.1 μm. Scale bar indicates 10 μm.

these clusters assemble into one-dimensional columnar structures, which are oriented perpendicular to the nematic director. Furthermore, these columns form a two-dimensional lattice (Figs. 1.28a and 1.29), which can have varying lattice parameters. Unlike the lamellar phase, which occurs for both PS–*fd* and polymer–*fd* mixtures, the columnar phase has so far only been observed in a PS–*fd* mixture.

With increasing sphere volume fraction, the columnar phase will continuously transform into the lamellar phase, as illustrated in Fig. 1.28b. A three-dimensional reconstruction of such a coexisting sample is shown in Fig. 1.29. In addition to 0.1 μm spheres, columnar phases have also been observed for sphere sizes ranging from 0.06 to 0.12 μm in diameter. A theoretical understanding of the stability of the columnar phase is currently lacking. In particular, it is not known what determines the spacing of the spherical columns in the direction perpendicular to the nematic director. Furthermore, it seems that 0.3 μm is a "magical" size of the column because mixtures of rods with spheres of diameters ranging from 0.06 to 0.12 μm assemble into the columnar phase where individual columns always have a final diameter of 0.3 μm. Individual spheres are observed to diffuse between columns, indicating that these are equilibrium and not kinetically trapped structures. The robustness of the diameter of the self-assembled columns suggests the examination of 0.3 μm spheres in a nematic background of *fd* rods.

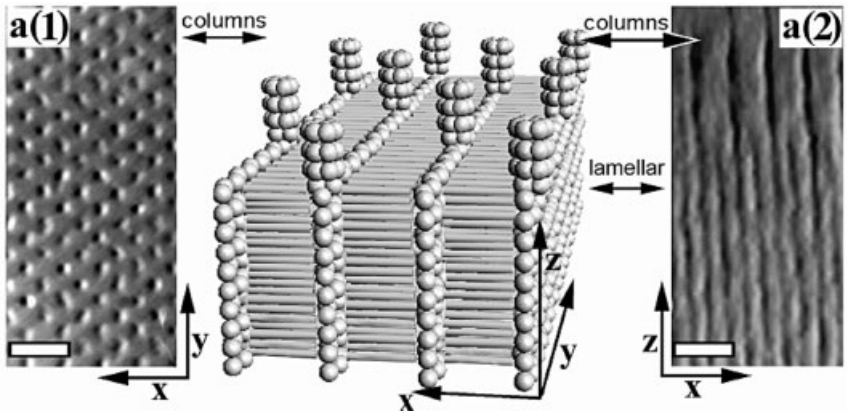

Fig. 1.29 A three-dimensional reconstruction using DIC optical microscopy of a sample in which the lamellar phase at the bottom coexists with the columnar phase at the top. The mixture is composed of 0.1 μm PS spheres and *fd* liquid crystals. The middle part is a schematic illustration of the arrangements of the rods and spheres in this particular sample. The rods in the top columnar phase are not drawn for clarity, but they form a nematic phase that fills the space between the columns. (a1) Image of the XY cross-section of the top columnar phase. (a2) Image of the ZX cross-section. The column spacing in the top columnar phase is twice the spacing of the bottom lamellar phase. Scale bars are 3 μm. (After Adams et al., 1998).

Unlike mixtures of *fd* and smaller spheres, large 0.3 μm spheres do not move easily through the nematic background and the sample is easily arrested in a metastable state. When a low volume fraction of 0.3 μm spheres are mixed with highly concentrated and well-aligned rods that are close to the nematic–smectic phase transition, chain-like structures form (Fig. 1.30b). These chains usually have an open structure, where the spacing between individual spheres can be several micrometers. However, this spacing is always a multiple of the *fd* contour length. The open-chain structure is highly metastable, and therefore we conclude that there is a large energetic barrier preventing spheres from hopping. Often it is possible to observe open chains even days after the original sample was prepared, although there is a slow tendency for spheres eventually to form closed chains where adjacent spheres are in contact. This indicates that closed-chain structures have lower free energy than open chains.

With decreasing concentration of the background *fd*, the nematic order decreases. When 0.3 μm spheres are suspended in such weakly aligned nematics, they arrange themselves into body-centered cubic (bcc) crystalline-like structures (Fig. 1.30d). At intermediate concentrations of background *fd*, we sometimes observe chains that have 90° turns (Fig. 1.30c). Curiously, when

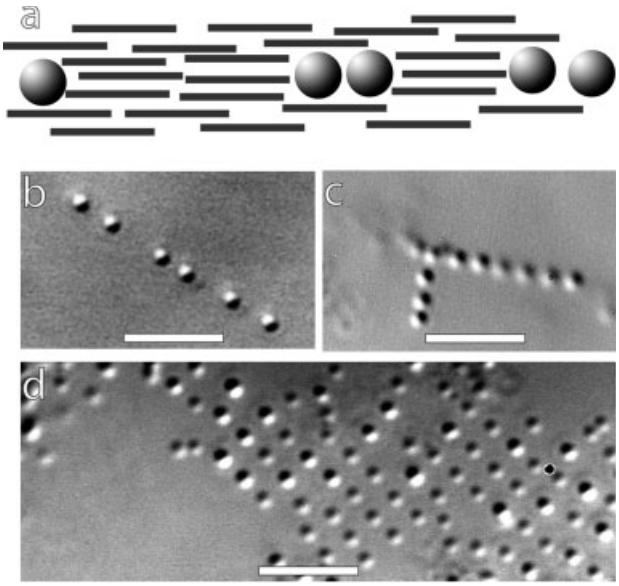

Fig. 1.30 (a) Arrangement of 0.3 and 0.4 μm polystyrene spheres dispersed in an *fd* nematic liquid crystal. (b) At high rod concentrations just below the nematic–smectic phase transition, 0.3 μm spheres form an elongated chain. The chain has an open structure in which spheres can be separated by a distance that is a multiple of the contour length of *fd*. (c) With decreasing concentration of the rods, we observe that the chains can assume configurations in which they come together at 90°. (d) At a concentration of *fd* just above the I–N phase transition, the spheres arrange themselves into cubic-like crystals. Scale bars indicate 5 μm.

we increase the size of the sphere to 0.4 μm, we no longer observe the formation of open chains, but only closed chains. Therefore, depletion stabilization is a maximum for 0.3 μm spheres.

The formation of open and closed one-dimensional chains can be qualitatively understood if we look at a schematic illustration of a suspension of spheres in a nematic background (Fig. 1.30a). The diameter of the spheres (300 nm) is much larger than the diameter of the *fd* rods (7 nm); therefore, a sphere acts as a wall that locally induces the formation of the smectic phase. A second sphere can easily be placed right next to an existing sphere or one rod length away along the nematic director because of the locally induced smectic correlations. This reasoning was used to theoretically explain the formation of the open-chain structures (van der Schoot 2000; van der Schoot 2002). For a sphere to hop between these two positions, there has to be a fluctuation where all the rods move away. This is energetically very unfavorable, and it is rarely observed in experiments. We suspect that as the sphere size increases beyond 0.3 μm it significantly distorts the local director. In this

case the elastic free energy of the nematic leads to long-range interactions that drive rearrangement of the spheres (Poulin et al. 1997). While the formation of chains is partially understood, the formation of bcc-like structures remains a mystery. One can only speculate that the chain-like structures are intimately connected to the formation of the lamellar phase, while bcc-like structures are related to the formation of the columnar phase observed in a mixture of *fd* and spheres with smaller diameter. It would be of great interest to explore the behavior of *fd*–sphere mixtures as a function of the contour length of *fd*. We are curious to learn if the columnar phase is observed for *fd* with other contour lengths. We encourage simulation and theoretical examination of the microphase-separated structures described in Figs. 1.29 and 1.30. The simulations will be challenging, as the dynamics are slow and a large number of particles are necessary. However, simulating a unit cell of the lamellar or columnar phase should be readily feasible.

1.7
Self-Assembled Colloidal Membranes and Twisted Ribbons

In the previous two subsections we described the formation of the lamellar and columnar phases that occur when a low volume fraction of spherical particles are added to a background nematic phase of *fd* virus. The behavior of rod–polymer mixtures at various conditions when a low volume fraction of rods is added to a high background concentration of isotropic polymers proves to be equally rich in surprising phenomena. The full phase diagram of an *fd*–dextran mixture is shown in the inset of Fig. 1.31. In Section 1.5 we focussed on the part of this phase diagram where bulk I–N phase separation is observed. Here we extend that work to take into account the positionally ordered smectic phase. At very high concentrations, the *fd*–polymer mixture becomes essentially immiscible and phase-separates into a polymer-rich isotropic phase and an essentially pure suspension of highly concentrated rods. According to the rules of thermodynamics, the osmotic pressures in these two coexisting phases will be equal. From previously published data, the relationship between dextran concentration and osmotic pressure is known, and thus the osmotic pressure of a suspension of rods can be deduced (Nordmeier 1993). In the *fd*–dextran mixture, the polymer osmotic pressure is analogous to temperature in molecular systems. With decreasing osmotic pressure (polymer concentration), the coexisting rods melt into the nematic phase; while with increasing polymer pressure, the rods freeze into the smectic phase. In the phase diagram shown in Fig. 1.31, there is the possibility of a triple point where the isotropic, nematic, and smectic phases coexist.

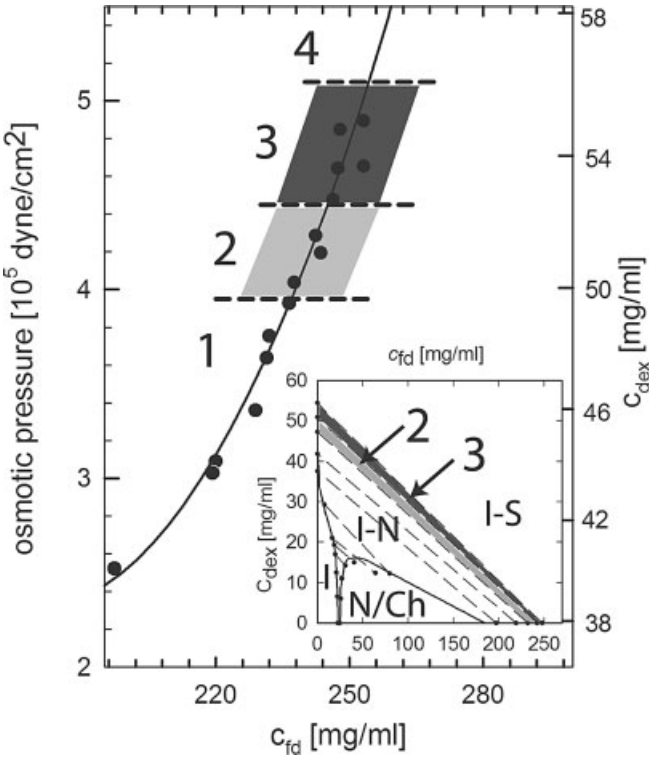

Fig. 1.31 The coexistence concentrations of a highly concentrated immiscible *fd*–dextran (M_w = 150 000) mixture. The dextran concentration and corresponding osmotic pressure are indicated on the vertical axis, while the *fd* concentration is plotted horizontally. Since the mixture is immiscible for these high concentrations, the osmotic pressure of the isotropic dextran solution is equal to the rod osmotic pressure. The complete phase diagram of a dextran–*fd* mixture is shown in the inset of the figure. Tie-lines along which the mixture phase-separates into coexisting phases are indicated with dashed lines. The *fd*–dextran mixture is dissolved in 190 mM NaCl and 10 mM Tris at pH 8.15. To obtain coexistence concentrations, the sample was centrifuged at 4000 g for 15 min. (After Dogic, 2003).

However, this point has not been determined due to the appearance of novel structures that will be described in the following sections.

In region 3 of the phase diagram, we observe condensation of rods into quasi-two-dimensional colloidal membranes. These membranes consist of a single layer of essentially parallel rods (Dogic and Fraden 2001; Dogic 2003). An image of a mature membrane that has been equilibrating for a few weeks is shown in Fig. 1.32. In Fig. 1.32a the rods point into the image plane and consequently the membrane is optically isotropic and shows no birefringence when observed with polarization microscopy. The interface between rods and background isotropic polymer solution shows significant fluctuations that are

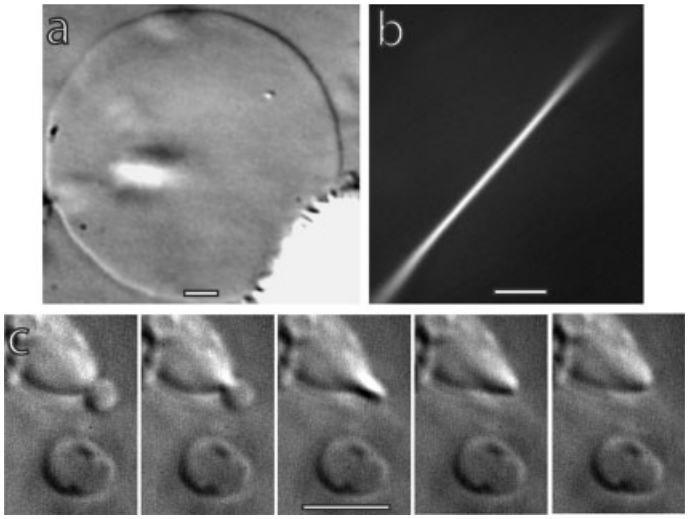

Fig. 1.32 Formation of colloidal membranes in mixtures of *fd* and dextran (M_w = 500 000) in 20 mM Tris and 100 mM NaCl buffer. (a) DIC image of a colloidal membrane viewed edge-on in which the *fd* rods lie perpendicular to the image plane. (b) Image of a membrane in which the *fd* rods lie in the image plane taken with polarization microscopy. (c) A sequence of images taken 1/30th of a second apart illustrating the lateral growth and coalescence of a membrane. The membranes coalesce only when they approach edge-on with the rods in each membrane oriented parallel to each other. Scale bars indicate 5 μm. (After Dogic, 2003; Dogic and Fraden, 2001).

associated with the membrane line tension. In Fig. 1.32b, the rods lie in the image plane and the thickness of the membrane is approximately equal to the contour length of an *fd* virus. In this view, the membrane exhibits visible fluctuations that are associated with its bending rigidity. In principle, both the bending rigidity and the line tension could be measured by analyzing the fluctuations of a sequence of images similar to those shown in Fig. 1.32. Because of their similarity to membranes formed by amphiphilic molecules such as lipids or block copolymers, we name these two-dimensional structures *colloidal membranes*.

Besides forming planar membranes, *fd*–polymer mixtures can also assemble into twisted ribbons (Fig. 1.33). In general we observe that ribbons form at lower polymer concentration, while with increasing polymer concentration flat membranes become more prevalent. The schematic illustration of the arrangement of rods in a twisted ribbon is shown in Fig. 1.33b. Images taken with a polarization microscope indicate alternating bright and dark regions along an individual ribbon. The bright birefringent regions correspond to areas where the rods lie in the plane of the image, and the dark regions indicate where the rods lie perpendicular to the image plane. It is possible for the

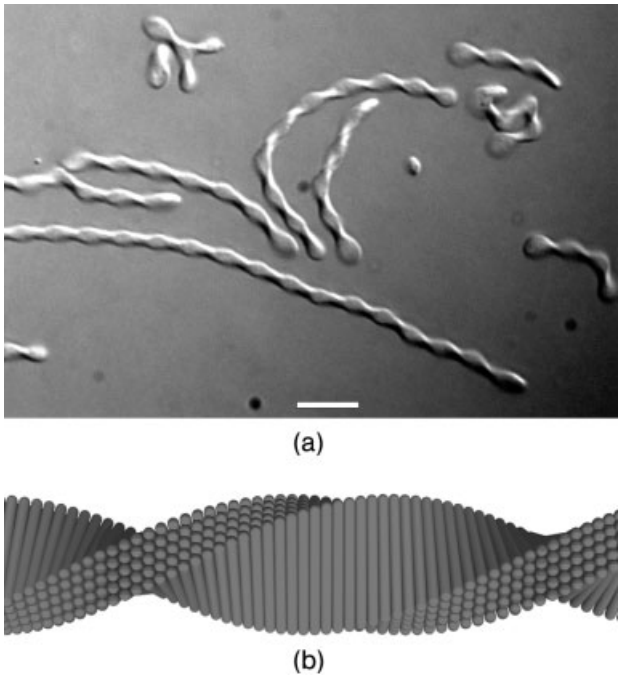

Fig. 1.33 (a) A DIC image of a suspension of self-assembled ribbons in a mixture of *fd* and dextran (M_w = 500 000) in 20 mM Tris and 100 mM NaCl buffer. Scale bar indicates 5 μm. (b) A schematic illustration of the configuration of the rods within a single ribbon.

ribbons to form branches, as shown in Fig. 1.33a. The difference in energy between twisted ribbons and flat membranes must be very low, as it is often possible to observe both planar membranes and twisted ribbons within the same sample.

A sequence of images showing the transformation of a twisted ribbon into a flat membrane is shown in Fig. 1.34. In this particular case we have applied a flow field, which can simultaneously untwist the ribbon and stretch it to many times its initial length. After the flow is stopped, some of the ribbons remain under tension because they are fixed at both of their ends. Subsequently, over a period of minutes these ribbons under tension will break and relax toward their equilibrium state. In the same sample some structures will relax back to a twisted ribbon and remain in that state for many hours. However, in this particular case, after an initial fast relaxation to the state shown in Fig. 1.34c, the twisted ribbon continued to slowly untwist until it became a flat two-dimensional membrane shown in Fig. 1.34e.

One possible reason for the stability of twisted ribbons is the chiral nature of *fd* itself. As discussed previously, a bulk solution of *fd* at intermediate con-

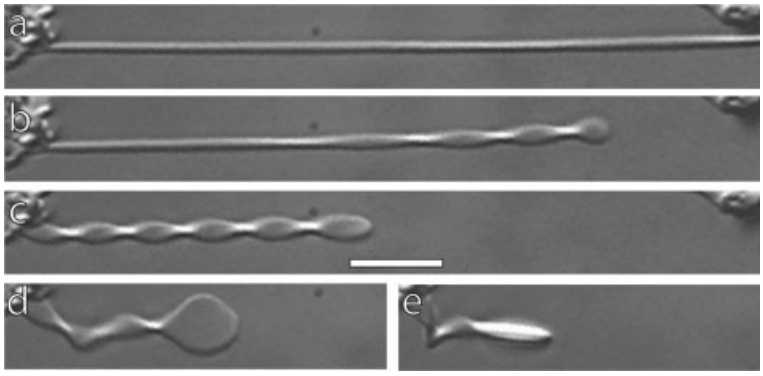

Fig. 1.34 A sequence of images illustrating the collapse of a stretched, untwisted ribbon into a two-dimensional membrane. The ribbons are stretched by applying a shear flow. In this process, by chance both of the ends of the ribbon are fixed. After a while the tension induces the fast collapse of a stretched ribbon into a twisted ribbon, which subsequently slowly untwists into a flat membrane. The images are taken roughly a few seconds apart. Scale bar indicates 5 μm.

centrations forms a twisted cholesteric structure instead of a nematic phase. This indicates that *fd* rods prefer to be slightly twisted with respect to each other. A flat membrane such as the one shown in Fig. 1.32 is geometrically incompatible with twist. However, when rods form an elongated strip, it is possible for them to twist with respect to each other. Therefore, we expect two contributions to the total energy, which determines the shape of a twisted ribbon or two-dimensional membrane. The formation of a flat membrane is favored by line tension, since this creates a structure with minimum area-to-circumference ratio, while the formation of twisted ribbon is favored by the chiral contribution to the free energy. It should be possible to measure the line tension experimentally by analyzing the fluctuations of the membrane. Preliminary experiments indicate that it is also possible to apply torque to birefringent ribbons and either overtwist or untwist ribbons using an optical tweezer. We hope that from these experiments the chiral contribution to the free energy can be determined. These measurements should shed more light on the stability of twisted ribbons and colloidal membranes.

It is important to determine whether colloidal membranes are a kinetically trapped metastable state, or if they represent a true equilibrium structure in region 3 of the phase diagram shown in Fig. 1.31. Their pronounced tendency to grow, albeit very slowly, indicates that they are indeed equilibrium structures. In some samples that are a few months old, we observed membranes that are millimeters in size. It is also possible to observe a process of coalescence of two membranes, as shown in a sequence of images in Fig. 1.32c. In order for coalescence to take place, the rods in both membranes have to be aligned along the same direction. We note that the membranes do not stack

up on top of each other unless the polymer concentration is significantly higher. There are additional observations with regards to the kinetics of the underlying isotropic–smectic phase transition that suggest that membranes are stable structures for a specific range of *fd* and polymer concentrations. These are discussed in more detail in Section 1.9.2.

The formation of colloidal membranes seems a poorly explored, yet very generic, phenomenon frequently observed in rod-like particles with attractive interactions. It is observed when *fd* is mixed with a wide variety of polymers, such as dextran, poly(ethylene oxide) (PEO) (Dogic and Fraden 2001), and poly(*N*-isopropylacrylamide) (NIPA) (Alsayed et al. 2004), and ferro-fluids (Lin 2004). In addition to the *fd* system, membranes are also observed in mixtures of tobacco mosaic virus (TMV) with bovine serum albumin (BSA) and PEO (Adams et al. 1998) and in pure suspensions of inorganic rod-like colloids made of β-FeOOH (Maeda and Maeda 2003). The latter particles have no polymer added, but it is very likely that they have direct attractive forces of van der Waals origin. Since the intermolecular interactions between these components are well known, it would be of great interest to measure the bending rigidity of the membrane and see how it depends on molecular parameters, such as rod length or polymer osmotic pressure.

One possible explanation for the stability of colloidal membranes are the entropic forces associated with confining the fluctuations of the membrane when a stack of membranes forms. If these fluctuations are associated with wavelengths much larger than the thickness of the membrane, they can be described within continuum theory. A stack of fluctuating membranes confined by two walls will show strong effective repulsive interactions, first described by Helfrich (1973) and then by Lipowsky (1995). The competition between Helfrich repulsion and long-range attractive van der Waals interactions can give rise to phase transitions from bound to unbound membranes (Lipowsky 1995). Because of the large thickness of the membrane, the bending rigidity is very large for colloidal membranes. Consequently, one does not expect strong repulsive interactions associated with long-wavelength fluctuations, which can lead to stability of the colloidal membranes. However, in addition to long-wavelength fluctuations, the surface of the membrane is roughened at length scales comparable to the thickness of the membrane by the relative displacement of molecules with respect to each other. These fluctuation modes are often called “protrusions” (Goetz et al. 1999). The origin of the short-range repulsion often observed between lipid membranes has been attributed to these protrusion fluctuations (Israelachvili 1991; Wennerstrom and Israelachvilli 1992). In lipid membranes these forces have a very short range of a few ångströms, but in colloidal membranes, due to the extreme anisotropy of the constituent rods, they could easily reach 100 nm. It seems

plausible that these protrusion fluctuations can lead to thermodynamic stability of colloidal membranes.

1.7.1 Monte Carlo Simulation of Colloidal Membranes

To examine this issue in more detail, we have preformed a Monte Carlo simulation on a simplified system. Instead of simulating the full rod–polymer mixture, we have focussed on a one-component system of perfectly parallel rods, which interact with each other via direct attractive interactions. The attraction potential is designed so that it mimics the depletion potential between two rods (Fig. 1.23). If spherocylinders are pointing along the z direction, in the xy direction the strength of the attractive potential is proportional to the overlap area between two disks whose diameter is equal to $D_{\mathrm{sc}} + D_{\mathrm{sp}}$. The strength of the potential also depends on the relative displacement of the center of mass of each spherocylinder along the z direction. The depletion potential is at a maximum value when the relative displacement along the z direction of two spherocylinders is zero. The overlap along the z direction is equal to $L + D_{\mathrm{sc}} - |z_1 - z_2|$ if this quantity is larger than zero. Subsequently, this dimension is multiplied with the overlap area in the xy direction and the whole value of the excluded volume is multiplied by an overall constant, which characterizes the strength of the potential.

Initially, we place the rods so that they form a single-crystalline membrane and find that at low temperatures the rods never escape the membrane and the membrane remains stable for the whole duration of the simulation. At high temperature, rods evaporate from the membrane and the membrane eventually disintegrates. For temperatures where the membrane remains stable, we measure the effective intermolecular potential between two membranes. The probability that the membranes are separated by distance h is determined. Once this probability is known, it is easy to extract the effective potential between two membranes, $U_{\mathrm{eff}} = -k_{\mathrm{B}}T \ln \rho(z)$. To sample all energetically unfavorable separations sufficiently, we use the technique of multiple histograms as described by Frenkel and Smith (1996).

Effective potentials obtained from this simulation are shown in Fig. 1.35. At high temperatures, the effective interaction between two membranes is completely repulsive. If mapped onto an athermal rod–polymer mixture, high temperature corresponds to low polymer concentration or equivalently low osmotic pressure. In this region we expect that isolated colloidal membranes will be the equilibrium structures. As the temperature is gradually reduced, the effective potential changes from repulsive to attractive. In a certain temperature range ($\beta = 2.50$) there is both a local minimum, which favors bound membranes, and a global minimum energy, which favors membranes that are

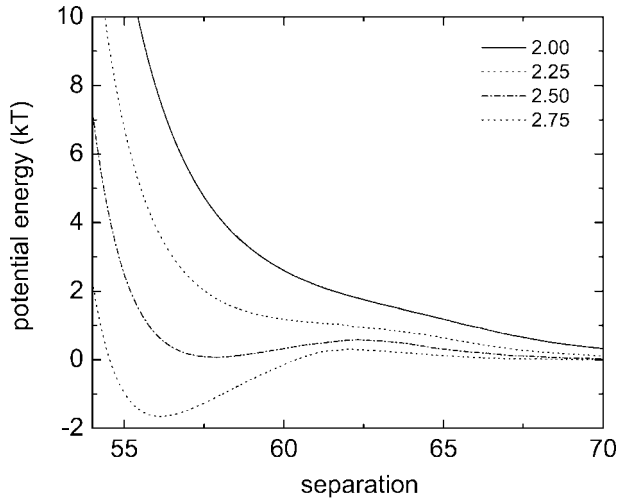

Fig. 1.35 Effective potential between two membranes obtained from Monte Carlo simulations. The aspect ratio of the rods is 25 ($L = 50$, $D_{sc} = 2$), while the range of interaction is $0.75\,D_{sc} = 1.5$. To obtain the strength of the intermolecular attraction, the overlap volume is multiplied by a constant Π, which in this particular case is –0.002. The potential was obtained for four different temperatures ($\beta = 1/k_B T$), which are indicated in the upper right corner. There were 144 rods within each membrane. The order within each membrane is that of a two-dimensional crystal. However, we expect that a similar intermembrane potential will be found for liquid-like membranes.

infinitely far apart. This would indicate that the swelling transition of a bound membrane pair is a first-order phase transition. At low temperatures there is a deep attractive minimum. We would therefore expect that under these conditions individual colloidal membranes would not be stable, but would stack up on top of each other, making smectic filaments. This structure is indeed observed in experiments in region 4 of the phase diagram shown in Fig. 1.31. These experiments are discussed in more detail in Section 1.9. Our simulations also suggest that a smectic phase composed of highly anisotropic attractive rods will swell with increasing temperature before they melt into the nematic phase. This is in fact observed in a novel thermotropic mixture of *fd* and NIPA polymer (Alsayed et al. 2004). The behavior of this particular system is discussed in more detail in Section 1.9.4.

It is perhaps not entirely surprising that for highly anisotropic rods the long-range order along the rod axis will melt at a different temperature when compared to the order within each layer (colloidal membrane). In our simple example of perfectly aligned rods, it is always possible to decrease the strength of attraction between layers (membranes) by increasing the length of the spherocylinder by a factor 2 and decreasing the strength of depletion interaction by a factor 2. While this decreases the strength of interaction be-

tween the layers, the interaction of rods within each layer remains unchanged. Therefore, we believe that the stability of colloidal membranes is the result of the high aspect ratio of our system. This argument is true as long as the average protrusion fluctuations are smaller than the range of the attractive potential. To establish a closer connection with experiments, our simulations will have to be repeated on a more realistic system where the rods are flexible and charged, and are allowed both translational and rotational degrees of freedom.

1.7.2 Crystalline Membranes

The two-dimensional membranes described in the previous subsection were formed in a mixture of *fd* and polymers with relatively high molecular weight. Their fluidity and the ease with which they are deformed by an external field, such as a shear flow, strongly suggest that the rods within each membrane have a liquid-like structure. By decreasing the polymer size, it is possible to obtain two-dimensional membranes with hexagonal shape (Fig. 1.36). The shape of these membranes indicates that the *fd* rods within each membrane assume a crystal-like configuration, but this would have to be confirmed by X-ray experiments. Changing polymer concentration modifies the appearance of the crystalline membranes dramatically. At high polymer concentration, the polymer membrane boundary is relatively sharp. The induction time for crystal nucleation as evidenced by the turbidity of the sample is relatively short. Consequently, many nuclei are formed relatively quickly. Each membrane has a specific nucleation site protruding into the third dimension. It seems plausible that multimeric *fd* always present at low volume fraction forms the initial nucleation site.

At lower polymer concentration, the induction time can be up to an hour and the polymer membrane boundary is more fluid-like. Since there are relatively few nuclei, crystals grow to a size of 30–40 μm over a period of a few days. Unlike crystals at higher polymer concentrations, when viewed from the side they exhibit fluctuations visible with an optical microscope. A large number of these membranes have screw-like dislocations, which can easily be identified when viewing a membrane side-on (Fig. 1.36b and c).

The concentration of rods within the membrane is so high ($\approx 250\,\mathrm{mg\,ml^{-1}}$) that the polymer is probably completely excluded. There is complete phase separation into immiscible phases, and the osmotic pressure of the isotropic polymer solution is identical to the pressure of the rods within the membrane. Polymers with a small radius of gyration, such as poly(ethylene glycol) (PEG, $M_\mathrm{w} = 8000$, $R_\mathrm{g} = 4$ nm), are able to induce a much higher osmotic pressure in the membrane when compared to larger polymers, such as dextran

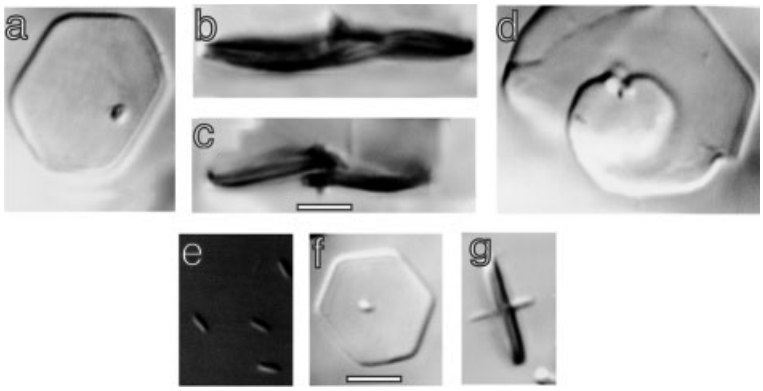

Fig. 1.36 Two-dimensional crystalline membranes observed in a mixture of *fd* and low-molecular-weight PEO (M_w = 8000). (a–d) Images taken at a relatively low polymer concentration. Under these conditions, it is possible to observe crystalline membranes that have screw-like dislocations. Images (b) and (c) are side-on images of the same membrane focussed at different z positions. (e–g) Images of nuclei (e) and membranes (f,g) taken at high polymer concentration. On average, the size of the membranes under these conditions is much smaller than for those shown in images (a–d). Scale bars indicate 5 μm. (After Dogic and Fraden, 2001).

($M_w = 150\,000$, $R_g = 11$ nm), for which liquid membranes are observed. It follows that, with increasing osmotic pressure, the rods within the membrane undergo a two-dimensional liquid to crystal phase transition analogous to crystallization observed in two-dimensional disks (Bates and Frenkel 2000). We have not yet obtained conditions for which it is possible to change experimental parameters continuously so that the liquid-like membranes transform into crystalline ones. However, this remains intriguing because of the possible existence of the hexatic phase at intermediate concentrations between the liquid and crystal phases (Halperin and Nelson 1978).

1.8
Surface-Induced Smectic Ordering in Rod–Polymer Mixtures

So far, we have only been concerned with the behavior of rod-like particles in bulk phases. However, we also observe unexpected phenomena at the interfaces between two phases, which will be summarized in this section. From studies of materials at the molecular scale, it is well known that surfaces play an important role in the kinetics of bulk phase transitions. Most materials, such as ice, exhibit surface pre-melting in which a thin layer of melted liquid forms at the gas–solid interface. This occurs at temperatures below the bulk liquid–solid phase transition (Dash et al. 1995; Lied et al. 1994). In contrast,

the phenomenon of surface freezing, where a thin layer of ordered phase spontaneously appears at the liquid–gas interface above the temperature of the bulk liquid to crystal phase transition, is observed in very few materials, most notably alkanes, thermotropic liquid crystals, and surfactant polymers (Wu et al. 1993; Ocko et al. 1986; Lang 1999). It has been noted that the nucleation of the bulk phase transition is closely related to the behavior of the sample at the interface. The observation that it is difficult to prepare superheated crystals is explained by the presence of the surface pre-melted layer, which acts as a heterogeneous nucleation site (van der Veen 1999; Cahn 1986). For materials that exhibit surface freezing, the opposite effect is true. Thus it is difficult to supercool the liquid phase below the equilibrium crystallization transition (Sloutskin et al. 2001; Sear 2002).

While most surface freezing transitions have been studied in molecular systems, we recently observed a similar phenomenon in a colloidal *fd*–dextran mixture. If the mixture described in Fig. 1.31 is prepared below the bulk isotropic–smectic coexistence (region 2 of the phase diagram shown in Fig. 1.31), surface-induced formation of the smectic phase is observed. An image of an isotropic–nematic surface completely covered with the surface smectic phase is shown in Fig. 1.37e. Below the image plane is a dense nematic suspension, while above the image plane is an isotropic dextran solution. The layered smectic-like structure is observed only within a thin layer confined to the isotropic–nematic interface. From optical images it is difficult to measure the exact thickness of this layer, but we can estimate that it is at most a few hundred nanometers thick. If a bulk phase-separated sample that exhibits surface freezing is mixed by vigorous shaking, small nematic tactoids will form. The interface of these tactoids will be covered with surface-induced smectic phase, as illustrated in Fig. 1.39b. As the tactoids coalesce, the smectic phase always remains confined to the narrow layer next to the interface. This provides strong support that the smectic structures in Fig. 1.37e are entirely induced by the isotropic–nematic surface.

In molecular systems that exhibit surface freezing, it is usually found that, with increasing temperature, the thickness of the surface frozen layer continuously decreases. Surprisingly, we find that, with decreasing osmotic pressure of the mixture, the surface-induced smectic phase swells to the point where isolated layers are observed. Therefore, the surface-induced smectic phase behaves very differently from the bulk phase. While the bulk smectic phase of pure rods melts into a nematic phase, the surface-induced smectic phase continuously swells. It is found that isolated layers exhibit large fluctuations and the rods within a layer are always aligned along the director of the background nematic field. Therefore, it is possible to think of the background nematic as a confining field. The tight coupling between the surface smectic layers and the fluctuating nematic background can lead to enhanced fluctua-

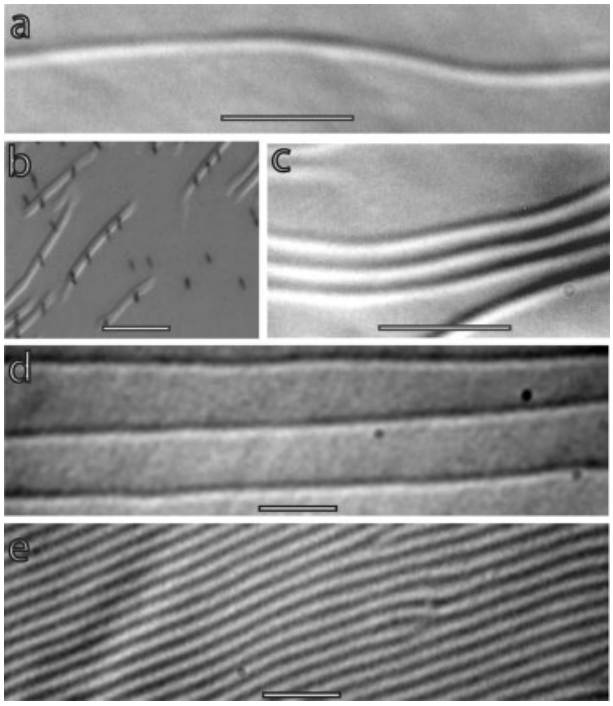

Fig. 1.37 DIC optical micrographs of the surface-induced smectic phase. The image lies in the plane of the isotropic–nematic interface, with the denser nematic phase being below the image plane and the lighter polymer-rich isotropic phase above the image plane. (a) With decreasing polymer concentration, the surface-induced smectic phase swells until individual layers are observed. In (b), a low volume fraction of rods are labeled with the fluorescent dye Alexa 488 and appear as black lines. Overlaying the fluorescent image with a DIC image indicates that the surface-induced phase has smectic C configuration. Scale bars indicate 5 μm.

tions similar to those encountered when a semi-flexible polymer is suspended in a fluctuating nematic background (Dogic et al. 2004b). Quantitative analysis of the fluctuations of the surface-induced smectic phase has not yet been performed.

On a surface partially covered with smectic layers, the layers can be either bundled together (Fig. 1.37c) or spaced far apart from each other (Fig. 1.37d). These configurations indicate the presence of both attractive interactions, which cause bundle formation, and repulsive interactions, which cause layer swelling. Because of their size, the smectic layers diffuse very slowly on the surface and it is very difficult to determine the equilibrium configuration. Often, even weeks after the samples are prepared, the structures continue to evolve. At present it is not yet clear what main physical forces are responsible for the effective potential between swollen surface smectic layers. Recently we

have been able to manipulate individual layers on the surface and are hoping to measure the forces between individual smectic layers experimentally.

The reason for the formation of the surface-induced smectic phase can perhaps be construed from theoretical studies of the isotropic–nematic interface in a hard-rod suspension. After some controversy, it is now well established that the density profile across the isotropic–nematic interface for Onsager rods is monotonically increasing (Chen and Noolandi 1992; Shundyak and van Roij 2001). However, if more complex mixtures of thin and thick rods are prepared in the neighborhood of the triple point, it is found that the interface profile can be highly non-monotonic (Shundyak and van Roij 2002). The presence of the surface induced smectic phase would be a natural consequence of a non-monotonic density across the isotropic–nematic interface. Since the only parameter that determines the phase behavior of hard rods is their concentration, and if their density is higher at the interface with the polymer-rich isotropic phase, it would follow that at the interface the smectic phase would form first. At present, little is known theoretically or experimentally about the quantitative aspects of the density profiles across interfaces in rod–polymer mixtures.

Besides *fd*–dextran mixtures, a surface-induced smectic phase has also been observed in mixtures of *fd* and PEO. Experimentally we find that the range of stability of the surface-induced smectic phase is very sensitive to the size of the polymer. For a mixture of *fd* and dextran ($M_{\mathrm{w}} = 150\,000$), it is possible to observe the surface-induced smectic phase at rod concentrations 3.5% below the bulk isotropic–smectic phase transition, while this decreases to 1.5% for a mixture of *fd* and larger dextran ($M_{\mathrm{w}} = 500\,000$). For mixtures of *fd* and even larger dextran ($M_{\mathrm{w}} = 2000\,000$), we have not observed any surface-induced freezing.

Much remains to be understood about the surface-induced smectic structures. For example, fluorescence images (Fig. 1.37b) and polarization microscopy indicate that the rods within each layer actually have a smectic-C-like configuration. This again is in stark contrast to the bulk phase behavior.

1.9
Kinetics of Liquid-Crystalline Phase Transitions

While the subject of how a crystal nucleus grows out of a dense liquid composed of spherical particles has been studied in great detail (Debenedetti 1996), less is known about how a smectic or nematic phase will nucleate from isotropic rods. What is the shape of the critical nucleus of nematic rods forming from a metastable isotropic solution? What determines the height of the nucleation barrier of the nematic droplet? These questions remain

mostly unanswered, and the kinetics of phase transitions in rod-like particles remains essentially unexplored. When the possibility of both positional and orientational order is taken into account, the complexity of kinetic pathways increases even further. Here we summarize our recent experimental work on the kinetics of the phase transitions in liquid crystals. We first briefly review the behavior of pure rods, and then focus in more detail on the behavior of rod–polymer mixtures.

It is important to mention that, because of the slow time scales and large length scales involved, colloids are in many ways an ideal system to study fundamental questions with regard to the kinetics of phase transitions. The time and length scales involved make the system amenable to determining the real spatial structure using optical microscopy. For example, in a recent study using optical microscopy, it was possible to directly visualize the critical nuclei of a colloidal crystal growing from a metastable liquid (Gasser et al. 2001). Experiments such as these make it possible to test the fundamental concepts of classical nucleation theory.

1.9.1 Kinetics of the Isotropic–Nematic and Nematic–Smectic Phase Transitions in Hard-Rod Suspensions

While the phases formed by colloidal liquid crystals are structurally identical to those found in low-molecular-weight, single-component, thermotropic liquid crystals, it seems that the kinetics of phase transitions in rod-like colloids can be very different from their thermotropic counterparts.

If a sample is prepared in the isotropic–cholesteric coexistence region, it will spontaneously form nematic droplets in the isotropic background (Fig. 1.38). The shape of the droplet is determined by three factors: (1) surface tension, which acts to minimize the surface area of the droplet; (2) boundary conditions for the orientation of the rods at the I–N interface; and (3) elastic energy, which is minimized when the rods are parallel. For the virus, the boundary conditions are that the rods align parallel to the I–N interface. Minimizing the surface tension creates a spherical droplet, but the high curvature leads to a large elastic energy. The equilibrium shape is an elongated droplet, which lowers the elastic energy at the cost of raising the surface energy. The shape of these droplets was analyzed in a recent theoretical work (Prinsen and van der Schoot 2003). Understanding the shape of nematic tactoids is the first step toward understanding the nucleation of the nematic phase out of a metastable isotropic solution. The actual shape of the critical tactoids and the height of the barrier for the nucleation of the nematic phase of hard rods from the isotropic phase remain open questions.

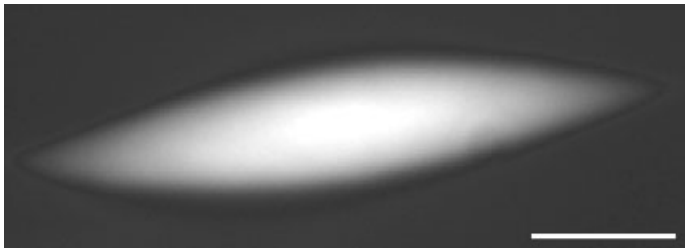

Fig. 1.38 An optical micrograph of an anisotropic nematic tactoid suspended in the background isotropic liquid. Scale bar indicates 5 μm.

Solutions of TMV, which closely approximate a suspension of hard rods with infinite rigidity, exhibit a nematic–smectic transition that is either a second-order or a very weakly first-order phase transition (Wang et al. 1994). In contrast to these experimental findings, the latest computer simulations of the nematic–smectic phase transition in hard rods indicates a first-order phase transition with about a 2% discontinuity between coexisting nematic and smectic concentrations (Polson 1997). On the other hand, the cholesteric–smectic phase transition in semi-flexible *fd* virus is found to be strongly first-order and no pre-transitional fluctuations have been observed (Dogic and Fraden 1997). It was speculated that the finite flexibility of *fd* virus changes the order of the nematic phase transition, which was confirmed theoretically (Tkachenko 1996).

1.9.2 Kinetics of the Isotropic–Smectic Phase Transition

By adding enough dextran to a solution of *fd*, it is possible to widen the isotropic–nematic coexistence to the point where direct isotropic–smectic coexistence is obtained. Taking advantage of the size of *fd* viruses, it is possible to visualize the formation of smectic layers directly using optical microscopy as they nucleate from the metastable isotropic phase. It is not at all obvious how the kinetics of this phase transition proceeds.

We have studied the kinetics of the isotropic–smectic phase transition in an immiscible *fd*–dextran mixture whose phase diagram is shown in Fig. 1.31. At low polymer concentrations, below 49 mg ml^{-1} in region 1, coexistence between an immiscible polymer-rich isotropic phase and a rod-rich nematic phase is observed. The shape of the nematic droplets formed in the background isotropic phase is very similar to anisotropic tactoids formed at isotropic–nematic coexistence in pure virus suspensions. In region 2 the smectic phase wets the isotropic–nematic interface as discussed in Section 1.8.

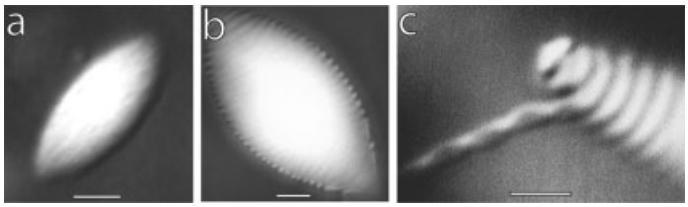

Fig. 1.39 Multiple steps by which colloidal membranes are created from a metastable isotropic suspension in an *fd*–dextran mixture. (a) In a first step, within minutes of preparing the homogeneous mixture, a metastable nematic tactoid forms from the isotropic suspension. (b) As a second step, the isotropic–nematic interface is almost immediately covered with the surface-induced smectic phase. (c) Finally, in a third step, after a period of days, colloidal ribbons such as those discussed in Section 1.7 are formed. This sample is prepared in region 2 of the phase diagram shown in Fig. 1.31. Scale bars indicate 3 μm.

In region 3 of the phase diagram there is evidence that the isolated colloidal membranes discussed in Section 1.7 form an equilibrium structure. Depending on the precise location within region 3, we have observed two different kinetic pathways by which these membranes form from a metastable isotropic suspension. At lower polymer concentration, the structures observed during the multiple-step kinetics for the formation of the membranes are shown in Fig. 1.39. In a first, fast step, we observe a very quick formation of a metastable nematic tactoid (Fig. 1.39a). Instantaneously, in the second step, the isotropic–nematic interface of the tactoids is covered with the surface-induced smectic phase (Fig. 1.39b). In the third, slow step, which takes a few days, the surface-induced smectic phase acts as a nucleation site for the formation of twisted ribbons (Fig. 1.39c). These ribbons grow from the interface and can reach many hundreds of micrometers in length. The fact that the *fd*–dextran mixture is essentially immiscible indicates that the ribbons grow due to the diffusion of rods from the metastable nematic phase through the surface-induced smectic phase into the more stable ribbon-like structures.

If the polymer concentration is increased within region 3 of Fig. 1.31, membranes directly nucleate from the isotropic solution as illustrated in Fig. 1.40a. The membranes remain stable in this region, as they laterally coalesce (Fig. 1.32) and can reach sizes of many tens of micrometers in diameter. These structures were discussed at length in Section 1.7. Finally, at higher polymer concentration, in region 4, the membranes stack up on top of each other and form elongated filaments, which internally have a smectic-like structure (Fig. 1.40b) (Frenkel and Schilling 2002). This transition from isolated membranes to smectic filaments is predicted by the simulations of parallel spherocylinders with direct attractive interactions described in more detail in Section 1.7. It is important to mention that the boundaries between

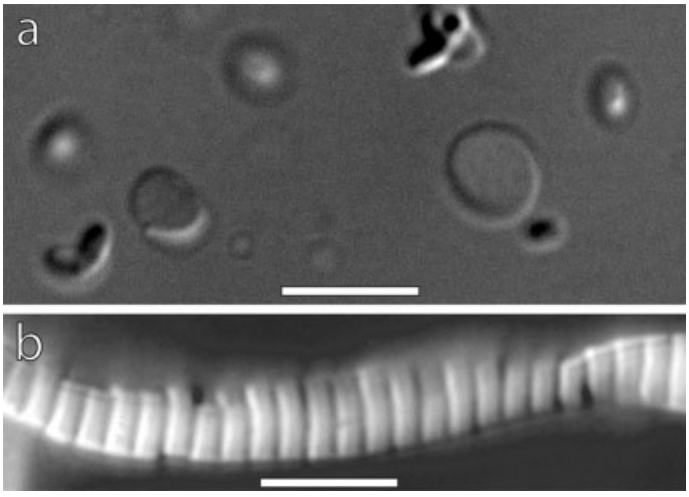

Fig. 1.40 (a) At higher concentrations of polymer in region 3 of the phase diagram shown in Fig. 1.31, we observe the nucleation of colloidal membranes directly out of metastable isotropic solution. (b) With further increasing polymer concentration in region 4, bulk smectic filaments are formed. Scale bars indicate 3 μm.

different structures are not very well defined and it is often possible to observe multiple structures within the same sample.

As discussed in Section 1.8, the bulk isotropic–smectic phase transition is superseded by the surface-induced formation of the smectic phase at the isotropic–nematic interface. For a long time it was thought that the state of order at the interface regulates the kinetics of the bulk phase transition. The kinetic pathway illustrated in Fig. 1.39 provides direct visual evidence for the importance of the surface smectic layer to the overall kinetic pathway of the formation of the smectic phase.

Another factor that can significantly affect the kinetics of the phase transition is the presence of a metastable phase boundary (Sirota and Herhold 1999; ten Wolde and Frenkel 1997; Olmsted et al. 1998). For example, colloids with short-range attractions have an equilibrium phase diagram as shown in Fig. 1.20b, where a gas–liquid phase transition is metastable with respect to the gas–crystal phase transition. Recent simulations suggest a remarkable enhancement of the nucleation rate of a crystal when the sample is prepared in the vicinity of the critical point associated with the metastable gas–liquid phase transition (ten Wolde and Frenkel 1997). The reason is because the crystal nucleus is formed in two steps for these particular conditions. In a first step, a dense liquid droplet associated with the metastable gas–liquid phase separation is formed; and in a subsequent step, a crystal nucleates within this dense droplet. This significantly reduces the nucleation barrier when compared to nucleation of a crystal directly from a dilute gas phase.

In a similar way, the presence of the metastable nematic phase is important for the nucleation of the smectic phase or colloidal membranes. Figure 1.39 shows that, for slightly supersaturated rod–polymer mixtures, a metastable nematic tactoid nucleates in a first, fast step. Subsequently, isolated colloidal membranes are formed after two additional intermediate stages – the surface smectic (Fig. 1.39b) and the twisted ribbon (Fig. 1.39c).

1.9.3
Filamentous Structures Associated With Nematic–Smectic Phase Transitions

In certain regions of the rod–sphere phase diagram, the whole sample forms a single lamellar phase (Fig. 1.28). However, upon changing the concentration of either component of the rod–sphere mixture, it is also possible to obtain coexistence between the lamellar phase and either a nematic or a smectic phase with a wavelength different from the lamellar phase. In contrast to nematic tactoids in the isotropic background, the droplets associated with lamellar–nematic or smectic–nematic coexistence assume the shape of elongated filaments with a cylindrical cross-section. Often these filaments can be many millimeters long (Fig. 1.41a). They are observed in both rod–sphere and rod–polymer mixtures when the total rod concentration is close to the nematic–smectic phase transition. In contrast, when polymers are added to a nematic phase of *fd* rods at low concentrations close to the I–N phase transition, they will phase-separate into isotropic, polymer-rich tactoids in the background nematic phase. These inverted tactoids (Fig. 1.39e) have the same shape as nematic tactoids in an isotropic background (Fig. 1.38).

It is of interest to examine how the cylindrical smectic filaments transform into polymer-rich tactoids with increasing dilution. If a sample containing smectic filaments, such as the one shown in Fig. 1.41a, is diluted with buffer solution, the layers within a filament will swell, as illustrated in Fig. 1.41b. Upon continued dilution, the layers swell further and filaments decrease in length, so it is possible to observe their ends (Fig. 1.41c). Finally, at the lowest concentration, individual polymer-rich tactoids are observed in the nematic background. These tactoids are often deformed by a few isolated monolayers. While filaments observed in Fig. 1.41 are obtained by adding a low volume fraction of polymer or spheres to a very dense nematic phase that is close to the nematic–smectic phase transition, it is also possible to obtain very similar filamentous structures by adding a high concentration of polymer to dilute isotropic rods. In this case, one obtains smectic filaments that coexist with an isotropic background suspension. The formation of such filaments was theoretically studied by Frenkel and Schilling (2002).

The observation of nematic–lamellar phase coexistence might seem contradictory to the generic phase diagram of the rod–polymer mixture shown

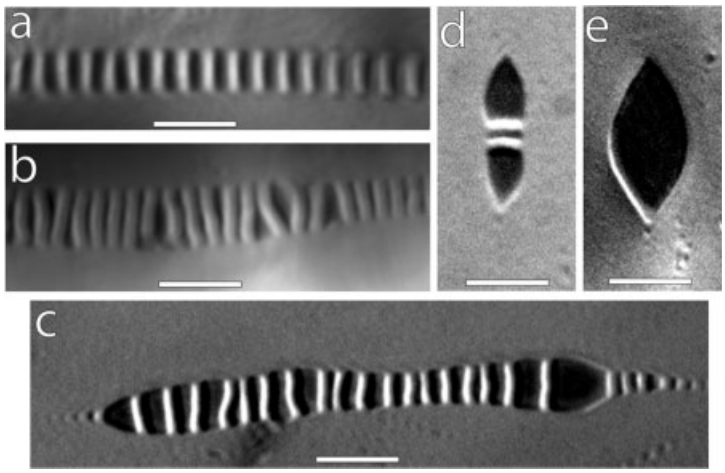

Fig. 1.41 Coexistence between the lamellar phase and the background nematic phase observed in a mixture of *fd* and dextran ($M_w = 500\,000$). The virus–polymer mixture is prepared in a Tris buffer at pH 8.0 and 100 mM ionic strength. The sequence of images illustrate the transformation of layered lamellar filaments into isotropic, polymer-rich tactoids that occurs when polymer is added to the mixture. Scale bars indicate 5 μm.

in Fig. 1.31. In this phase diagram, there are no indications of the lamellar phase or tie-lines between the nematic and lamellar phases. In order to obtain the bulk coexistence necessary to measure the phase diagram, we had to centrifuge the samples in regions 3 and 4. Due to the density difference between the lamellar layers and dextran solution, it seems plausible that the centrifugation procedure induces the lamellar to smectic phase transition. It seems likely that, as the volume fraction of rods within region 3 is increased, we actually go from isolated membranes to swollen lamellar phase to smectic phase. However, this is merely a speculation at this point. We do feel that the phase diagram presented in Fig. 1.31 is not final and that the location of the lamellar phase in the rod–polymer mixture should be carefully examined in future work.

While Fig. 1.41 illustrates the behavior observed in *fd*–polymer mixtures, identical filaments are also observed in mixtures of *fd* and polystyrene spheres with $D_{sp} = 0.1$ μm (Fig. 1.42). There are, however, two important differences between these two cases. First, in the polymer–*fd* mixture, it is possible to prepare samples with different layer spacings, and with decreasing osmotic pressure these layers continuously swell (see Fig. 1.44). In contrast, the *fd*–PS mixture exhibits only lamellar phases with constant 1.1 μm spacing. This might be because there is a direct phase transition from the isotropic phase to the lamellar phase in the rod–PS mixture. Therefore, the swelling transition might be preempted by the melting of rods into the isotropic phase. Second, in

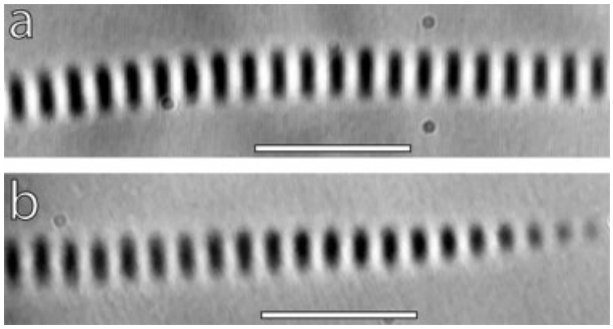

Fig. 1.42 Coexistence between the lamellar phase and the background nematic phase observed in a mixture of polystyrene spheres ($D_{\mathrm{sp}} = 0.1$ μm) and *fd* virus at 5 mM ionic strength (10 mM Tris, pH 8.15). Unlike the layered filaments formed in *fd*–dextran mixtures, the spacing of these filaments is always 1.1 μm. They can be many millimeters long, but occasionally it is possible to observe a tapered end of a filament, as illustrated in image (b). Scale bar is 5 μm.

the *fd*–PS mixture, it is also possible to obtain coexistence between a smectic phase with 0.9 μm spacing and a lamellar phase with 1.1 μm periodicity. This indicates a first-order phase transition between a smectic and lamellar phase. So far we have not observed a similar discontinuous transition between two layered structures with different periodicities in *fd*–polymer mixtures. In fact, the work summarized in the next section indicates that the swelling of the lamellar phase in *fd*–polymer mixtures is continuous.

1.9.4
Multiple Pathways Observed in Melting of the Lamellar Phase

Up to now we have only discussed the behavior of entropic suspensions of rods, or rod–polymer mixtures. Athermal, excluded-volume interactions govern the phase behavior of such systems, and the only parameters that determine the phase diagram are the concentrations of the constituent components. In athermal systems, it is possible to melt the structure using shear flow and subsequently study the process of nucleation and growth of ordered structures, such as the smectic phase or colloidal crystals (Dogic 2003; Gasser et al. 2001). However, to study the reverse process of melting would require changing the colloidal concentration *in situ*, which is a challenging experimental task.

To overcome this difficulty and have an easily tunable experimental parameter with which it is possible to control the phase behavior of colloidal systems, we have recently designed a novel thermotropic–lyotropic *fd*–polymer mixture (Alsayed et al. 2004). Instead of athermal polymers such as dextran or poly(ethylene oxide) (PEO), we used the thermo-sensitive polymer

poly(*N*-isopropylacrylamide) (NIPA). The solubility of NIPA in water is highly temperature-dependent, and below its Θ temperature of 31°C it assumes a swollen coil, while above this temperature it is water-insoluble and assumes a collapsed globule form (Wu and Wang 1998). A small increase in temperature results in increasing monomer–monomer attraction, which in turn decreases the osmotic pressure of the polymer solution. When this polymer solution is in coexistence with an immiscible suspension of hard rods, aqueous solvent flows from the low-osmotic-pressure polymer-rich phase into the higher-osmotic-pressure rod-rich phase. This subsequently dilutes the rods and leads to a temperature-induced phase transition in a suspension of hard rods.

At low temperatures, the *fd*–NIPA mixture forms a microscopically phase-separated lamellar phase similar to those discussed in Section 1.6.1. With increasing temperature, dislocations act as nucleation sites for the formation of the nematic tactoids (Fig. 1.43b). Interestingly, the nematic tactoids in the smectic background have a shape very similar to those encountered at isotropic–nematic coexistence. As discussed in Section 1.6.1 the nematic phase is highly immiscible with spherical particles, and therefore the formation of the nematic tactoids is accompanied by the expulsion of the polymer into lamellar layers, which results in the swelling of the layers (Fig. 1.43c). With further increase in temperature, most of the sample melts into the nematic phase, which coexists with highly swollen lamellar filaments (Fig. 1.43d). These lamellar filaments transform into isotropic droplets (Fig. 1.43e–g) in a similar way to filaments observed in *fd*–dextran mixtures and described in Section 1.9.3.

The process of lamellar melting can also be followed with light scattering to obtain the lamellar layer spacing averaged over a large sample volume

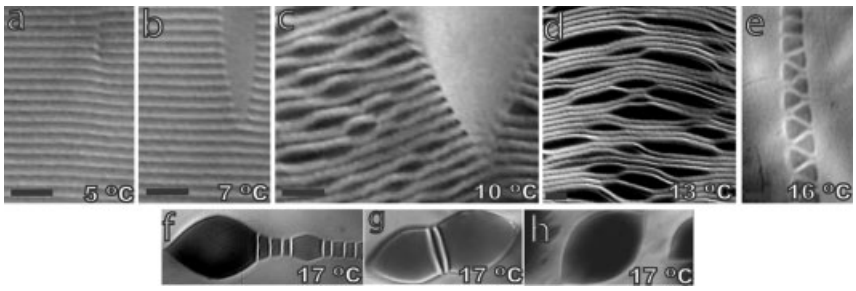

Fig. 1.43 Melting of the lamellar phase observed in an *fd*–NIPA mixtures (50 mg ml^{-1} *fd* and 7.5 mg ml^{-1} NIPA). At low temperatures, the mixture forms a uniform lamellar phase with periodicity of 1.3 μm. Images (a) to (f) indicate the process by which the microphase-separated lamellar phase melts into bulk isotropic–nematic coexistence. Scale bars indicate 5 μm. (After Alsayed et al., 2004).

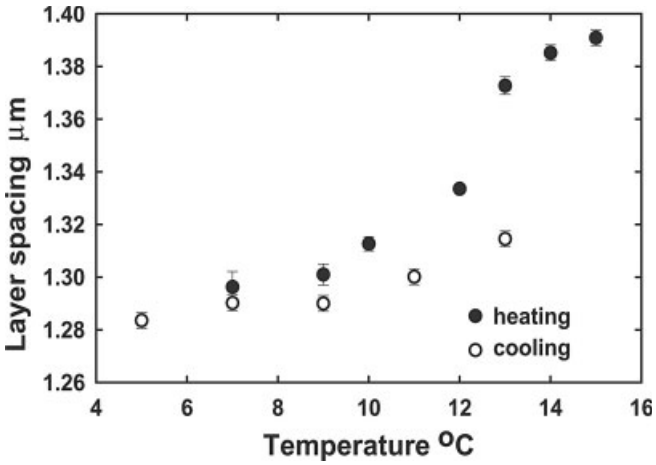

Fig. 1.44 Plot of the lamellar periodicity as a function of temperature obtained from a light-scattering experiment. Upon heating, it is possible to swell the sample to 1.40 μm; while upon cooling, we only observe the formation of a lamellar phase of 1.31 μm, indicating the presence of large hysteresis. Images illustrating the appearance of the lamellar phase at each temperature in the heating cycle are shown in Fig. 1.43. (After Alsayed et al., 2004).

(Fig. 1.44). The scattering pattern shows a single sharp ring, and with increasing temperature it simultaneously moves to lower angles and broadens significantly. This indicates that the lamellar phase continuously swells. Above a temperature of 15°C, only large forward scattering is observed. Interestingly, when cooling the sample down from high temperatures, lamellar spacing is only observed at temperatures below 13°C. This indicates that the lamellar melting is a strongly first-order phase transition with large hysteresis and a large nucleation barrier.

It is worth looking back at the results for the effective intermolecular potential between colloidal membranes obtained from computer simulations of perfectly aligned spherocylinders with a depletion attraction potential. These simulations indicate that the position of the minimum between two layers continuously increases with increasing temperature until the layers become unbound (Fig. 1.35). This is in qualitative agreement with the experiments shown in Fig. 1.44.

The behavior of the *fd*–NIPA mixture in a different region of the phase diagram, where a low volume fraction of *fd* is dissolved in the background polymer, exhibits a coexistence between multilayer lamellar droplets and isolated colloidal membranes, such as that shown in Fig. 1.45a. With increasing temperature, the multilayer droplets melt around 26°C. However, single isolated layers remain stable up to temperatures of 30°C. Once a nematic tactoid nucleates within the membrane, the rest of the membrane is quickly trans-

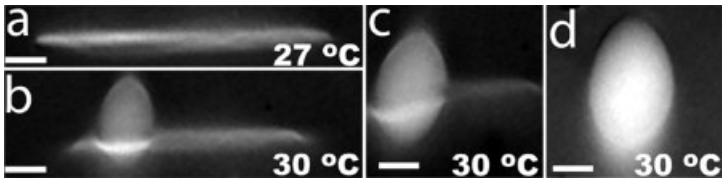

Fig. 1.45 Isolated colloidal membranes observed when a low volume fraction of *fd* rods are dissolved in the background NIPA polymer (7.5 mg ml^{-1} *fd* and 37 mg ml^{-1} NIPA). Below 25°C there is a coexistence between isolated membranes and multiple layers stacked up on top of each other. At 26°C multiple layers melt into nematic tactoids, while single-layer membranes remain stable up to 30°C. At this temperature, small three-dimensional tactoids nucleate within the two-dimensional membrane. Scale bars indicate 5 μm. (After Alsayed et al., 2004).

formed into the nematic phase. This observation suggests that there is a topological nucleation barrier for melting of the two-dimensional membrane into a three-dimensional nematic tactoid. In order for the tactoid to form, there has to be a collective protrusion of the rods into the third dimension. By examining the behavior of isolated membranes in Fig. 1.45 and stacks of membranes in Fig. 1.44, it is possible to conclude that there are nucleation barriers not only to freezing into the lamellar phase, but also for melting of the lamellar phase. This is in stark contrast to three-dimensional crystals, which are very difficult to superheat above their melting temperature (Dash 1999).

The structures observed during the process of lamellar melting are in many ways very similar to the structures observed in athermal *fd*–polymer mixtures described in the previous two subsections. The advantage of *fd*–NIPA mixtures is that it is possible to cycle continuously between these structures by simply changing the temperature. However, there are a few differences worth mentioning between this study and previous studies on the isotropic–smectic coexistence. The NIPA polymers used in these experiments have large radius of gyration ($R_g = 70$ nm) compared to the dextran ($M_w = 150\,000$, $R_g = 20$ nm) used for studies of the isotropic–smectic phase transition. For this large polymer we do not observe the phenomenon of surface freezing. In addition, *fd* mixtures with large polymers have a pronounced tendency to form a lamellar phase, while smaller polymers such as dextran 150000 phase-separate directly into isotropic–smectic coexistence (Fig. 1.39).

1.10 Conclusions and Open Questions

In this chapter we have summarized the phase behavior of colloidal rods and mixtures of rod-like and sphere-like colloids whose interactions are dominated by short-range repulsive interactions. We first reviewed the Onsager theory of the isotropic–nematic phase transition, which treats the excluded-volume interactions at a second virial level. The Onsager theory can be generalized to include positionally ordered smectic phases. The predictions of these very simple theories, which are confirmed by computer simulations, are that rods form isotropic, nematic, and smectic phases with increasing concentration. This agrees well with the experimentally measured phase diagram of monodisperse virus particles. The measurements of the order parameter represent the most stringent test of the Onsager theory extended to semi-flexible charged rods. For this particular experiment, the agreement with theory is quantitative at high ionic strength. These experiments firmly establish *fd* rods as ideal hard-rod systems.

While the phase behavior of hard rods is well understood, extending the theory to account for long-range repulsive interactions due to surface charge results in significant quantitative differences with experiment. These effects become significant at either low ionic strength or high rod concentration. Another extension of the Onsager theory has been to include attractive interactions. Introducing such interactions results in a rapid breakdown of the second virial approximation. So far there are no satisfactory theoretical solutions to these problems.

A major part of this chapter has been devoted to the description of numerous novel structures observed in rod–sphere mixtures. While the behavior of the bulk suspension of pure rods is at least qualitatively understood, the observation of lamellar phases, colloidal membranes, surface-induced smectic phases, and twisted ribbons are mostly lacking a theoretical description. We believe that these structures are generic to the phase behavior of rod–sphere mixtures and will be observed in other model rod-like systems as they are developed in the future.

In many ways the phase behavior of rod–sphere mixtures encompasses the behavior of both thermotropic liquid crystals and amphiphilic molecules. The classic model systems of soft condensed matter physics, such as thermotropic liquid crystals or amphiphilic molecules, are reasonably well understood. On the one hand, thermotropic liquid crystals with increasing temperature melt from layered smectic phases into nematics and finally into the orientationally disordered isotropic phase. There are only scattered reports of a smectic phase that can be successfully swollen by the addition of isotropic solvent (Rieker 1995). On the other hand, amphiphilic systems, such as lipid mem-

branes, form a layered smectic phase at high concentration. With dilution, these systems will swell to a large degree until they form isolated vesicles. The latter systems will almost never melt into the nematic phase. With increasing dilution of rod–sphere mixtures, we observe both swelling of the smectic layers to the point where isolated membranes are observed and their subsequent melting into a nematic phase. The competition between these two processes results in a myriad of novel colloidal structures, which are outlined in the present chapter. The relative stability of these structures will have to be carefully examined in future work.

Acknowledgments

This chapter summarizes recent experiments on the liquid-crystalline phase behavior of rod-like viruses and virus–sphere mixtures carried out in our laboratories. Important contributions to this research have been made by Kirstin Purdy, Marie Adams, Eric Grelet, and Phil Huang at Brandeis University, by Ahmed Alsayed and Arjun Yodh at the University of Pennsylvania, and by Edward Barry at the Rowland Institute at Harvard. Zvonimir Dogic is supported by a Junior Fellowship from the Rowland Institute at Harvard, while Seth Fraden is supported by an NSF-DMR grant. Additional information and movies are available at the following websites: http://www.elsie.brandeis.edu and http://www.rowland.harvard.edu/rjf/dogic/index.php.

References

Adams, M. and Fraden, S., 1998, *Biophys. J.* **74**, 669.
Adams, M., Dogic, Z., Keller, S. L., and Fraden, S., 1998, *Nature* **393**, 349.
Alsayed, A. M., Dogic, Z., and Yodh, A. G., 2004, *Phys. Rev. Lett.* **93**, 057801.
Anderson, V. J. and Lekkerkerker, H. N. W., 2002, *Nature* **416**, 811.
Ao, X. L. and Meyer, R. B., 1991, *Physica A* **176**, 63.
Asakura, S. and Oosawa, F., 1958, *J. Polym. Sci.* **33**, 183.
Bartlett, P., Ottewill, R. H., and Pusey, P. N., 1992, *Phys. Rev. Lett.* **68**, 3801.
Bates, M. A. and Frenkel, D., 2000, *Phys. Rev. E* **61**, 5223.
Bawden, C. F., Pirie, N. W., Bernal, J. D., and Fankuchen, I., 1936, *Nature* **138**, 1051.
Biben, T. and Hansen, J. P., 1991, *Phys. Rev. Lett.* **66**, 2215.
Bloomfield, V. A., 1991, *Biopolymers* **31**, 1471.
Bolhuis, P. G. and Frenkel, D., 1994a, *Phys. Rev. Lett.* **72**, 2211.
Bolhuis, P. G. and Frenkel, D., 1994b, *J. Chem. Phys.* **101**, 9869.
Bolhuis, P. G. and Frenkel, D., 1997, *J. Chem. Phys.* **106**, 668.

Bolhuis, P. G., Stroobants, A., Frenkel, D., and Lekkerkerker, H. N. W., 1997, *J. Chem. Phys.* **107**, 1551.
Booy, F. P. and Fowler, A. G., 1985, *Int. J. Biol. Macromol.* **7**, 327.
Borukhov, I. and Bruinsma, R. F., 2001, *Phys. Rev. Lett.* **87**, 158101.
Buitenhuis, J., Donselaar, L. N., Buining, P. A., Stroobants, A., and Lekkerkerker, H. N. W., 1995, *J. Colloid Interface Sci.* **175**, 46.
Cahn, R. W., 1986, *Nature* **323**, 668.
Chen, Z. Y., 1993, *Macromolecules* **26**, 3419.
Chen, Z. Y. and Noolandi, J., 1992, *Phys. Rev. E.* **45**, 2389.
Cotter, M. A., 1979, in: *The Molecular Physics of Liquid Crystals*, eds. G. R. Luckhurst and G. W. Gray, pp. 169–89. Academic Press, London.
Cotter, M. A. and Wacker, D. C., 1978, *Phys. Rev. A* **18**, 2669.
Crocker, J. C., Matteo, J. A., Dinsmore, A. D., and Yodh, A. G., 1999, *Phys. Rev. Lett.* **82**, 4352.
Cui, S. and Cheng, Z. Y., 1994, *Phys. Rev. E.* **50**, 3747.
Dash, J. G., 1999, *Rev. Mod. Phys.* **71**, 1737.
Dash, J. G., Fu, H. Y., and Wettlaufer, J. S., 1995, *Rep. Prog. Phys.* **58**, 115.
Debenedetti, P. G., 1996, *Metastable Liquids: Concepts and Principles.* Princeton University Press, Princeton, NJ.
Dijkstra, M., 2001, *Current Opinion in Coll. and Interface Science* **6**, 372.
Dijkstra, M. and van Roij, R., 1997, *Phys. Rev. E* **56**, 5594.
Dijkstra, M., van Roij, R., and Evans, R., 1998, *Phys. Rev. Lett.* **81**, 2268.
Dijkstra, M., Brader, J. M., and Evans, R., 1999, *J. of Phys.-Cond. Matt.* **11**, 10079.
Dinsmore, A. D., Yodh, A. G., and Pine, D. J., 1995, *Phys. Rev. E* **52**, 4045.
Dinsmore, A. D., Warren, P. B., Poon, W. C. K., and Yodh, A. G., 1997, *Europhys. Lett.* **40**, 337.
Dogic, Z., 2003, *Phys. Rev. Lett.* **91**, 165701.
Dogic, Z. and Fraden, S., 1997, *Phys. Rev. Lett.* **78**, 2417.
Dogic, Z. and Fraden, S., 2000, *Langmuir* **16**, 7820.
Dogic, Z. and Fraden, S., 2001, *Phil. Trans. R. Soc. Lond. A* **359**, 997.
Dogic, Z., Frenkel, D., and Fraden, S., 2000, *Phys. Rev. E* **62**, 3925.
Dogic, Z., Purdy, K. R., Grelet, E., Adams, M., and Fraden, S., 2004a, *Phys. Rev. E* **69**, 051702.
Dogic, Z., Zhang, J., Lau, A. W. C., Aranda-Espinoza, H., Dalhaimer, P., Disher, D. E., Janmey, P. A., Kamien, R. D., Lubensky, T. C., and Yodh, A. G., 2004b, *Phys. Rev. Lett.* **92**, 125503.
DuPre, D. B. and Duke, R. W., 1975, *J. Chem. Phys.* **63**, 143.
DuPre, D. P. and Yang, S., 1991, *J. Chem. Phys.* **94**, 7466.
Edgar, C. D. and Gray, D. G., 2002, *Macromolecules* **35**, 7400.
Forsyth, Jr., P. A., Marcelja, S., Mitchell, D. J., and Ninham, B. W., 1978, *Adv. Colloid Interface Sci.* **9**, 37.

Fraden, S., 1995, in: *Observation, Prediction, and Simulation of Phase Transitions in Complex Fluids*, eds. M. Baus, L. F. Rull, and J. P. Ryckaert, pp. 113–164. Kluwer Academic, Dordrecht.

Fraden, S., Hurd, A. J., Meyer, R. B., Cahoon, M., and Caspar, D. L. D., 1985, *J. Phys. (Paris)* **C3**, 85.

Fraden, S., Maret, G., Caspar, D. L. D., and Meyer, R. B., 1989, *Phys. Rev. Lett.* **63**, 2068.

Fraden, S., Maret, G., and Caspar, D. L. D., 1993, *Phys. Rev. E* **48**, 2816.

Frenkel, D., 1988, *J. Phys. Chem.* **92**, 3280.

Frenkel, D. and Schilling, T., 2002, *Phys. Rev. E* **66**, 041606.

Frenkel, D. and Smith, B., 1996, *Understanding Molecular Simulation*. Academic Press, New York.

Frenkel, D., Lekkerkerker, H., and Stroobants, A., 1988, *Nature* **332**, 822.

Gabriel, J. C. P. and Davidson, P., 2003, *Coll. Chem. I, Topics Curr. Chem.* **226**, 119.

Gasser, U., Weeks, E. R., Schofield, A., Pusey, P. N., and Weitz, D. A., 2001, *Science* **292**, 258.

Gast, A. P., Hall, C. K., and Russel, W. B., 1983a, *Faraday Discuss. Chem. Soc.* **76**, 189.

Gast, A. P., Hall, C. K., and Russel, W. B., 1983b, *J. Colloid Interface Sci.* **96**, 251.

Gast, A. P., Russel, W. B., and Hall, C. K., 1986, *J. Colloid Interface Sci.* **109**, 161.

Gelbart, W. M. and Barboy, B., 1980, *Acc. Chem. Res.* **13**, 290.

Gelbart, W. M., Ben-Shaul, A., and Roux, D. (eds.), 1994, *Micelles, Membranes, Microemulsions, and Monolayers*. Springer, New York.

Goetz, R., Gompper, G., and Lipowsky, R., 1999, *Phys. Rev. Lett.* **82**, 221.

Grelet, E. and Fraden, S., 2003, *Phys. Rev. Lett.* **90**, 198302.

Griess, G. A., Moreno, E. T., Herrmann, R., and Serwer, P., 1990, *Biopolymers* **29**, 1277.

Hagen, M. H. J. and Frenkel, D., 1994, *J. Chem. Phys.* **101**, 4093.

Halperin, B. I. and Nelson, D. R., 1978, *Phys. Rev. Lett.* **41**, 121.

Hanke, A., Eisenriegler, E., and Dietrich, S., 1999, *Phys. Rev. E* **59**, 6853.

Hansen, J. P. and McDonald, I. R., 1986, *Theory of Simple Liquids*, 2nd edn. Academic Press, London.

Harris, A. B., Kamien, R. D., and Lubensky, T. C., 1997, *Phys. Rev. Lett.* **78**, 1476.

Helfrich, W., 1973, *Z. Naturforsch.* **28c**, 693.

Hentschke, R., 1990, *Macromolecules* **23**, 1192.

Herrmann, R., Neugebauer, K., Pirkl, E., Zentgraf, H., and Schaller, H., 1980, *Mol. Gen. Genet.* **177**, 231.

Herzfeld, J., Berger, A. E., and Wingate, J. W., 1984, *Macromolecules* **17**, 1718.

Hosino, M., Nakano, H., and Kimura, H., 1979, *J. Phys. Soc. Jpn.* **46**, 1709.
Hurd, A. J., Fraden, S., Lonberg, F., and Meyer, R. B., 1985, *J. Phys. (Paris)* **46**, 905.
Imhof, A. and Dhont, J. K. G., 1995, *Phys. Rev. Lett.* **75**, 1662.
Israelachvili, J., 1991, *Intermolecular and Surface Forces*, 2nd edn. Academic Press, London.
Issaenko, S. A., Harris, A. B., and Lubensky, T. C., 1999, *Phys. Rev. E* **60**, 578.
Jizuka, E. and Yang, J. T., 1978, in: *Liquid Crystals and Ordered Fluids*, ed. J. Johnson. Plenum, New York.
Kamien, R. D., Doussal, P. L., and Nelson, D. R., 1992, *Phys. Rev. A* **45**, 8728.
Kayser, Jr., R. F. and Raveche, H. J., 1978, *Phys. Rev. A* **17**, 2067.
Khokhlov, A. R. and Semenov, A. N., 1981, *Physica* **108a**, 546.
Khokhlov, A. R. and Semenov, A. N., 1982, *Physica* **112a**, 605.
Kierfeld, J. and Lipowsky, R., 2003, *Europhys. Lett.* **62**, 285.
Koda, T. and Kimura, H., 1994, *J. Phys. Soc. Jpn.* **63**, 984.
Koda, T., Numajiri, M., and Ikeda, S., 1996, *J. Phys. Soc. Jpn.* **65**, 3551.
Koenderink, G. H., Vliegenthat, G. A., Kluijtmans, S. G. J., van Blaaderen, A., Philipse, A. P., and Lekkerkerker, H. N. W., 1999, *Langmuir* **15**, 4693.
Kramer, E. M. and Herzfeld, J., 1998, *Phys. Rev. E* **58**, 5934.
Kramer, E. M. and Herzfeld, J., 1999, *J. Chem. Phys.* **110**, 8825.
Kramer, E. M. and Herzfeld, J., 2000, *J. Chem. Phys.* **61**, 6872.
Kreibig, U. and Wetter, C., 1980, *Z. Naturforsch.* **35c**, 750.
Kuhl, T. L., Leckband, D. E., Lasic, D. D., and Israelachvili, J. N., 1994, *Biophys. J.* **66**, 1479.
Lago, S., Cuetos, A., Martinez, B., and Rull, L. F., 2004, *J. Mol. Recognition* **17**, 417.
Lang, P., 1999, *J. Phys. Chem. B* **103**, 5100.
Lapointe, J. and Marvin, D. A., 1973, *Mol. Cryst. Liq. Cryst.* **19**, 269.
Lau, A. W. C., Lin, K. H., and Yodh, A. G., 2003, *Phys. Rev. E* **66**, 020401.
Lebowitz, J. L. and Rowlison, J. S., 1964, *J. Chem. Phys.* **41**, 133.
LeDoussal, P. and Nelson, D. R., 1991, *Europhys. Lett.* **15**, 161.
Lee, K., Borukhov, I., Gelbart, W. M., Liu, A. J., and Stevens, M. J., 2004, *Phys. Rev. Lett.* **93**, 128101.
Lee, S. W., Mao, C. B., Flynn, C. E., and Belcher, A. M., 2002, *Science* **296**, 892.
Lee, S. W., Wood, B. M., and Belcher, A. M., 2003, *Langmuir* **19**, 1592.
Leforestier, A. and Livolant, F., 1993, *Biophys. J.* **65**, 56.
Lekkerkerker, H. N. W. and Stroobants, A., 1994, *Nuovo Cimento D* **16**, 949.
Lekkerkerker, H. N. W., Coulon, P., der Haegen, V., and Deblieck, R., 1984, *J. Chem. Phys.* **80**, 3427.
Lekkerkerker, H. N. W., Poon, W. C.-K., Pusey, P. N., Stroobants, A., and Warren, P. B., 1992, *Europhys. Lett.* **20**, 559.
Lied, A., Dosch, H., and Bilgram, J. H., 1994, *Phys. Rev. Lett.* **72**, 3554.

Lin, K. H., 2004, unpublished results.
Lin, K. H., Crocker, J. C., Zeri, A. C., and Yodh, A. G., 2001, *Phys. Rev. Lett.* **87**, 088301.
Lipowsky, R., 1995, in: *Generic Interactions of Flexible Membranes.*, eds. R. Lipowsky and E. Sackmann, pp. 521–602. Elsevier, Amsterdam.
Livolant, F., 1991, *Physica A* **176**, 117.
Maeda, H. and Maeda, Y., 2003, *Phys. Rev. Lett.* **90**, 018303.
Maguire, J. F., McTague, J. P., and Rondalez, F., 1980, *Phys. Rev. Lett.* **45**(23), 1891.
Mao, Y., Cates, M. E., and Lekkerkerker, H. N. W., 1995, *Physica A* **222**, 10.
Mao, Y., Cates, M. E., and Lekkerkerker, H. N. W., 1997, *J. Chem. Phys.* **106**, 3721.
Meijer, E. J. and Frenkel, D., 1991, *Phys. Rev. Lett.* **67**, 1110.
Meijer, E. J. and Frenkel, D., 1994, *J. Chem. Phys.* **100**, 6873.
Meyer, R. B., 1968, *Appl. Phys. Lett.* **12**, 281.
Meyer, R. B., 1969, *Appl. Phys. Lett.* **14**, 208.
Meyer, R. B., 1990, in: *Dynamics and Patterns in Complex Fluids*, eds. A. Onuki and K. Kawasaki, p. 62. Springer-Verlag, Berlin.
Model, P. and Russel, M., Filamentous Bacteriophage, in: *The Bacteriophages*, ed. R. Calender, pp. 375–456, Plenum, New York.
Mulder, B., 1987, *Phys. Rev. A* **35**, 3095.
Nordmeier, E., 1993, *J. Phys. Chem.* **97**, 5770.
Ocko, B. M., Braslau, A., Pershan, P. S., Als-Nielsen, J., and Deutch, M., 1986, *Phys. Rev. Lett.* **57**, 94.
Odijk, T., 1986, *Macromolecules* **19**, 2313.
Odijk, T., 1987, *J. Phys. Chem.* **91**, 6060.
Oldenbourg, R., 1981, PhD thesis, University Konstanz.
Oldenbourg, R., Wen, X., Meyer, R. B., and Caspar, D. L. D., 1988, *Phys. Rev. Lett.* **61**, 1851.
Olmsted, P. D., Poon, W. C. K., McLeish, T. C. B., Terrill, N. J., and Ryan, A. J., 1998, *Phys. Rev. Lett.* **81**, 373.
Onsager, L., 1949, *Ann. N. Y. Acad. Sci.* **51**, 627.
Pelcovits, R. A., 1996, *Liq. Cryst.* **21**, 361.
Pelta, J., Durand, D., Doucet, J., and Livolant, F., 1996, *Biophys. J.* **71**, 48.
Pindak, R. S., Huang, C. C., and Ho, J. T., 1974, *Phys. Rev. Lett* **32**(2), 43.
Polson, J. M., 1997, *Phys. Rev. E* **56**, R6260.
Poon, W. C. K. and Pusey, P. N., 1995, in: *Observation, Prediction, and Simulation of Phase Transitions in Complex Fluids*, eds. M. Baus, L. F. Rull, and J. P. Ryckaert, pp. 3–51. Kluwer Academic, Dordrecht.
Poulin, P., Stark, H., Lubensky, T. C., and Weitz, D. A., 1997, *Science* **275**, 1770.
Prinsen, P. and van der Schoot, P., 2003, *Phys. Rev. E* **68**, 021701.

Purdy, K. R. and Fraden, S., 2004a, *Phys. Rev. E* **70**, 061703.
Purdy, K. R. and Fraden, S., 2004b, The influence of charge and flexibility on smectic phase formation in filamentous virus suspensions, cond-mat/0406700.
Purdy, K. R., Dogic, Z., Fraden, S., Ruhm, A., Lurio, L., and Mochrie, S. G. J., 2003, *Phys. Rev. E* **67**, 031708.
Purdy, K. R., Varga, S., Galindo, A., Jackson, G., and Fraden., S., 2005, Nematic phase transitions in mixtures of thin and thick colloidal rods, *Phys. Rev. Lett.* **94**, 057801.
Rieker, T. P., 1995, *Liq. Cryst.* **19**, 497.
Sambrook, J., Fritsch, E. F., and Maniatis, T., 1989, in: *Molecular Cloning: A Laboratory Manual*, 2nd edn, chap. 4. Cold Spring Harbor Laboratory Press, Cold Spring Harbor, NY.
Sambrook, J. and Russell, D. W., 2000, *Molecular Cloning: A Laboratory Manual*, 3rd edn. Cold Spring Harbor Laboratory Press, Cold Spring Harbor, NY.
Sato, T. and Teramoto, A., 1994, *Acta Polym.* **45**, 399.
Savenko, S. V. and Dijkstra, M., 2004, *Phys. Rev. E* **70**, 011705.
Sear, R. P., 2002, *Langmuir* **18**, 7571.
Sear, R. P. and Jackson, G., 1995, *J. Chem. Phys.* **102**, 2622.
Sear, R. P. and Mulder, B. M., 1996, *J. Chem. Phys.* **105**, 7727.
Senechal, E., Maret, G., and Dransfeld, K., 1980, *Int. J. Biol. Macromol.* **2**, 256.
Shundyak, K. and van Roij, R., 2001, *J. Phys.: Condens. Matter* **13**, 4789.
Shundyak, K. and van Roij, R., 2002, *Phys. Rev. Lett.* **88**, 205501.
Sikorav, J. L., Pelta, J., and Livolant, F., 1994, *Biophys. J.* **67**, 1387.
Sirota, E. B. and Herhold, A. B., 1999, *Science* **283**, 529.
Sloutskin, E., Sirota, E. B., Kraack, H., Ocko, B. M., and Deutsch, M., 2001, *Phys. Rev. E* **64**, 031708.
Song, L., Kim, U., Wilcoxon, J., and Schurr, J. M., 1991, *Biopolymers* **31**, 547.
Stephen, M. J. and Straley, J. R., 1974, *Rev. Mod. Phys.* **46**, 617.
Straley, J. P., 1976, *Phys. Rev. A* **14**, 1835.
Stroobants, A., Lekkerkerker, H. N. W., and Odijk, T., 1986, *Macromolecules* **19**, 2232.
Tang, J. and Fraden, S., 1993, *Phys. Rev. Lett.* **71**, 3509.
Tang, J. and Fraden, S., 1995, *Liq. Cryst.* **19**, 459.
Tang, J. and Fraden, S., 1996, *Biopolymers* **39**, 13.
Tang, J. X., Wong, S., Tran, P. T., and Janmey, P. A., 1996, *Ber. Bunsenges. Phys. Chem.* **100**, 796.
Tang, J. X., Ito, T., Traub, P., and Janmey, P. A., 1997, *Biochemistry* **36**, 12600.
ten Wolde, P. R. and Frenkel, D., 1997, *Science* **277**, 1975.
Tkachenko, A. V., 1996, *Phys. Rev. Lett.* **77**, 4218.
Tracy, M. A., Garcia, J. L., and Pecora, R., 1993, *Macromolecules* **26**, 1862.

Tuinier, R., Vliegenthart, G. A., and Lekkerkerker, H. N. W., 2000, *J. Chem. Phys.* **113**, 10768.
Tuinier, R., Aart, D. G. A. L., Wensink, H. H., and Lekkerkerker, H. N. W., 2003, *Phys. Chem.* **5**, 3707.
van der Schoot, P., 1996, *J. Phys. II (France)* **6**, 1557.
van der Schoot, P., 2000, *J. Chem. Phys.* **112**, 9132.
van der Schoot, P., 2002, *J. Chem. Phys.* **117**, 3538.
van der Schoot, P. and Odijk, T., 1992, *J. Chem. Phys.* **97**, 515.
van der Veen, J. F., 1999, *Surf. Sci.* **433–435**, 1.
van Roij, R., 1994, *J. Phys. II (France)* **4**, 1763.
van Roij, R., 1996, *Simple Theories of Complex Fluids*. Universiteit Utrecht, Utrecht.
van Roij, R. and Mulder, B., 1996, *J. Chem. Phys.* **105**, 11237.
van Roij, R., Bolhuis, P., Mulder, B., and Frenkel, D., 1995, *Phys. Rev. E* **52**, R1277.
van Roij, R., Mulder, B., and Dijkstra, M., 1998, *Physica A* **261**, 374.
Van Winkle, D. H., Davidson, M. W., Chen, W. X., and Rill, R. L., 1990, *Macromolecules* **23**, 4140.
Verma, R., Crocker, J. C., Lubensky, T. C., and Yodh, A. G., 2000, *Macromolecules* **33**, 177.
Vliegenthart, G. A. and Lekkerkerker, H. N. W., 1999, *J. Chem. Phys.* **111**, 4154.
Vliegenthart, G. A., van Blaaderen, A., and Lekkerkerker, H. N. W., 1999, *Faraday Discuss.* **112**, 173.
Vrij, A., 1976, *Pure Appl. Chem.* **48**, 471.
Vroege, G. J. and Lekkerkerker, H. N. W., 1992, *Rep. Prog. Phys.* **8**, 1241.
Wang, J. H., Lonberg, F., Ao, X., and Meyer, R. B., 1994, in: *Ordering in Macromolecular Systems*, eds. A. Teramoto, M. Kobayashi, and T. Norisuje. Springer-Verlag, Berlin.
Warren, P. B., 1994, *J. Phys. I (France)* **4**, 237.
Welsh, L. C., Symmons, M. F., Perham, C. N. R. N., Marseglia, E. A., and Marvin, D. A., 1996, *Macromolecules* **29**, 7075.
Wen, X. and Meyer, R. B., 1987, *Phys. Rev. Lett.* **59**, 1325.
Wen, X., Meyer, R. B., and Caspar, D. L. D., 1989, *Phys. Rev. Lett.* **63**, 2760.
Wennerstrom, H. and Israelachvilli, J. N., 1992, *J. Phys. Chem.* **96**, 520.
Wetter, C., 1985, *Biol. unserer Z.* **3**, 81.
Widom, B., 1967, *Science* **157**, 375.
Wong, G. C. L., Lin, A., Tang, J. X., Li, Y., Janmey, P. A., and Safinya, C. R., 2003, *Phys. Rev. Lett.* **91**, 018103.
Wu, C. and Wang, X., 1998, *Phys. Rev. Lett.* **80**, 4092.
Wu, X. Z., Sirota, E. B., Sinha, S. K., Ocko, B. M., and Deutsch, M., 1993, *Phys. Rev. Lett.* **70**, 958.
Yaman, K., Jeppesen, C., and Marques, C. M., 1998, *Europhys. Lett.* **42**, 221.

Yu, S. M., Conticello, V., Zhang, G., Kayser, C., Fournier, M., Mason, T., and Tirrell, D., 1997, *Nature* **389**, 167.

Zimmermann, K., Hagedorn, J., Heuck, C. C., Hinrichsen, M., and Ludwig, J., 1986, *J. Biol. Chem.* **261**, 1653.

Zocher, H., 1925, *Z. Anorg. Allg. Chem.* **147**, 91.

2
Field Theory of Polymer–Colloid Interactions

Erich Eisenriegler

Abstract

Methods of field theory are used to investigate the universal interactions between long flexible polymers and mesoscopic colloidal particles. Polymer-induced immersion free energies of single particles, the pair and three-body interactions between particles, and the interactions between a particle and a wall are discussed for both spherical and anisotropic particles, such as ellipsoids or dumbbells. The induced interactions of anisotropic particles are orientation-dependent. For small particle size we use systematic "small-particle expansions", similar to short-distance expansions in field theory. We also consider polymer density profiles near walls and particles and the polymer pressure on their surfaces, and compare with other approaches, such as the Asakura–Oosawa and Derjaguin approximations and Monte Carlo simulations.

2.1
Introduction

In colloidal suspensions containing polymer chains, there are tunable effective interactions between the colloid particles. For entropic reasons, free non-adsorbing polymer chains avoid the space between two particles, leading to an unbalanced pressure, which pushes them toward each other. Figure 2.1 illustrates the corresponding mechanism leading to an attraction between a particle and a wall. Such depletion forces for an isolated pair of immersed particles or for a single immersed particle near a wall have been measured in recent experiments (Ohshima et al. 1997; Verma et al. 1998; Rudhardt et al. 1998).

Soft Matter, Vol. 2: Complex Colloidal Suspensions. Edited by G. Gompper and M. Schick

ISBN: 3-527-31369-9

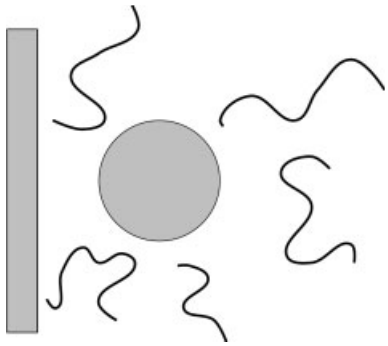

Fig. 2.1 Unbalanced pressure due to polymer depletion pushes the particle toward the wall.

Dilute systems of long flexible polymers show (de Gennes 1979; des Cloizeaux and Jannink 1990; Schäfer 1998) the characteristic features of *critical behavior* – a correlation length that is large on a microscopic scale, and mesoscopic properties that, to a large extent, are independent of the chemical microstructure, i.e. *universal* and obey power and *scaling* laws. For example, the mean square radius of gyration $\mathcal{R}_{\rm g}^2$ of a single isolated chain follows the power law[1)]

$$\mathcal{R}_{\rm g}^2 \propto N^{2\nu} \tag{2.1}$$

as the number N of monomers or repeat units becomes large. Although the chemical structure of the monomers may be quite different for different types of polymer chains, the exponent ν is the same. In $d = 3$ dimensions and in the case of a good solvent (effective repulsion between monomers),

$$\nu = 0.588 \tag{2.2}$$

Another example is the osmotic pressure Π of polymer chains. It obeys a scaling law (de Gennes 1979; des Cloizeaux and Jannink 1990; Schäfer 1998)

$$\Pi = k_{\rm B}TnX(n\mathcal{R}_{\rm g}^d) \tag{2.3}$$

where n is the number density of polymer chains, and $n\mathcal{R}_{\rm g}^d$ characterizes the degree of overlap between chains. Although it is assumed that N is large and that the monomer density nN is much smaller than in a dense polymer melt, the overlap may be either large (semidilute solution) or small (dilute

1) The same power-law exponent 2ν appears in the mean square end-to-end distance $\mathcal{R}_{\rm ee}^2$, and the ratio $\mathcal{R}_{\rm g}^2/\mathcal{R}_{\rm ee}^2$ tends to a universal number for $N \to \infty$.

solution). Equation (2.3) makes two non-trivial statements. First, for a given polymer–solvent system, $\Pi/(k_{\mathrm{B}}Tn)$ only depends upon the two variables n and $\mathcal{R}_{\mathrm{g}}$ via the product $n\mathcal{R}_{\mathrm{g}}^{d}$. Second, the scaling function X is universal, i.e. the same for different systems.

There is a well-known correspondence (de Gennes 1979) between the statistics of long flexible polymers and critical spin systems. Thus powerful methods of field theory for spin systems are at our disposal for investigating polymer problems.

In this chapter we consider the interaction of polymers with container walls or mesoscopic colloidal particles. The focus is on purely repulsive impenetrable boundaries, leading to polymer *depletion*. Polymer adsorption will not be considered. We shall see how the ideas and methods of field theories with boundaries (Binder 1986; Diehl 1986; Diehl 1997) lead to considerable progress in understanding the basic properties of polymer–colloid mixtures, such as the universal forms of the solvation free energies of single colloidal particles and of the polymer-induced interactions between two and more particles. We exploit various types of short-distance expansions in field theory. *Boundary operator expansions* (Diehl 1986; Diehl 1997) enable us to study, in a systematic way, the relation between the pressure exerted on a wall or colloidal particle and the local polymer density. The recently developed *small-particle operator expansion* (Burkhardt and Eisenriegler 1995; Eisenriegler and Ritschel 1995) allows us to obtain the quantitative distance and angle dependences of the effective interactions induced between two and more small mesoscopic particles of spherical or anisotropic shape. For spherical particles and *dumbbells* composed of two touching or overlapping spheres (van Blaaderen 2003; van Blaaderen 2004; Johnson et al. 2005), the *conformal invariance* (Cardy 1986) of the critical field theory can be used to determine the necessary expansion coefficients by conformally mapping the particle shapes onto simpler geometries.

Even in the case of *ideal* chains (de Gennes 1979), where the excluded-volume interaction between chain monomers is neglected, integrating out the polymer degrees of freedom is non-trivial due to the presence of the colloidal particles, and the above-mentioned methods of field theory are very useful.

In Section 2.2 we consider polymers in an infinite homogeneous space, without walls or particles, and their relation to field theory. The operator-product expansion is discussed. Boundaries are introduced in Section 2.3, and we consider the simplest case of ideal polymers and the corresponding Gaussian field theory. In Section 2.4 the effect of a planar wall is studied, in particular the polymer depletion and entropy reduction near the wall. We relate the density of polymer material near the boundary to the pressure on the boundary, discuss the spatial dependence of the density profile near the

boundary wall for a solution of free polymers, and derive the pressure distribution along the boundary for an end-grafted chain, pointing out the connection with boundary operator expansions in field theory. Polymers interacting with a single spherical particle of radius R are considered in Section 2.5. For a large sphere in a dilute solution with $R \gg \mathcal{R}_{\rm g}$, the rigid-polymer model of Asakura and Oosawa is a reasonable approximation. For polymers interacting with a small mesoscopic sphere, we use the systematic small-radius operator expansion, which is borrowed from field theory. We also present results of an approximate treatment for the dependence on size ratio $R/\mathcal{R}_{\rm g}$ of the solvation free energy of a sphere in a polymer solution with inter-chain overlap.

Sections 2.6 to 2.8 are devoted to the *polymer-induced interaction* between a spherical particle and a wall and between two and more particles. In addition to the Derjaguin and small-sphere expansions for large and small sphere radius, respectively, we discuss, in Section 2.7.3, the complete crossover in size ratio $R/\mathcal{R}_{\rm g}$ of the sphere–wall interaction mediated by ideal chains. Non-pairwise interactions between three particles are considered in Section 2.8.3. In Section 2.6.1 the predictions of the density–pressure relation and the value of its universal amplitude in the good solvent case are compared with high-precision simulations of a chain trapped between two parallel walls. Finally in Section 2.9 we consider colloidal particles of *anisotropic* shape and the orientation-dependent interactions with a wall that are induced by a polymer solution. Here the main focus is on colloidal ellipsoids and dumbbells.

2.2 Polymers and Field Theory

Since microscopic details are irrelevant, there is much freedom in choosing a model. One of the most convenient models for analytical calculations is the "bead–spring" model (de Gennes 1979; des Cloizeaux and Jannink 1990; Schäfer 1998), with the single-chain partition function

$$Z_N(\boldsymbol{r}_{\rm A},\boldsymbol{r}_{\rm B}) = \int {\rm d}\boldsymbol{r}_1 \cdots \int {\rm d}\boldsymbol{r}_{N-1}\, P(\boldsymbol{r}_{\rm A}-\boldsymbol{r}_1)\cdots P(\boldsymbol{r}_{N-1}-\boldsymbol{r}_{\rm B}) \times \widehat{\prod}_{(i,i')}[1-bl^d\delta(\boldsymbol{r}_i-\boldsymbol{r}_{i'})] \tag{2.4}$$

Here the product of N normalized Gaussians

$$P(\boldsymbol{x}) = (4\pi l^2)^{-d/2}\,{\rm e}^{-x^2/(4l^2)} \tag{2.5}$$

determines the structure of a chain with fixed end-points $\boldsymbol{r}_{\rm A}$ and $\boldsymbol{r}_{\rm B}$ and $N-1$ internal beads at $\boldsymbol{r}_1,\ldots,\boldsymbol{r}_{N-1}$, and it introduces a characteristic size l

per monomer. The product $\hat{\prod}$ is over the $\binom{N-1}{2}$ pairs (i, i') of internal beads. Since $b > 0$, configurations where the beads overlap are less probable. The hat on $\prod$ means that only products of δ functions are retained, where every bead position $\boldsymbol{r}_i$ occurs no more than once. This makes the model well-defined.

First consider an *ideal* polymer chain with $b = 0$. Then $Z_N = Z_N^0$ is a convolution of the P-functions, which is easily calculated. In terms of Fourier transforms,

$$\int \mathrm{d}(\boldsymbol{r}_\mathrm{A} - \boldsymbol{r}_\mathrm{B})\, \mathrm{e}^{\mathrm{i}\boldsymbol{p}(\boldsymbol{r}_\mathrm{A}-\boldsymbol{r}_\mathrm{B})} Z_N^0(\boldsymbol{r}_\mathrm{A}, \boldsymbol{r}_\mathrm{B}) = (\tilde{P}(p))^N \tag{2.6}$$

where

$$\tilde{P}(p) = \mathrm{e}^{-p^2 l^2} \tag{2.7}$$

is the Fourier transform of P, which implies

$$Z_N^0(\boldsymbol{r}_\mathrm{A}, \boldsymbol{r}_\mathrm{B}) = (4\pi N l^2)^{-d/2}\, \mathrm{e}^{-(\boldsymbol{r}_\mathrm{A}-\boldsymbol{r}_\mathrm{B})^2/(4Nl^2)} \tag{2.8}$$

This particularly simple coarse-graining behavior comes from choosing the macroscopic Gaussian shape of the ideal-chain end-to-end distance distribution at the microscopic level.

There is an important relation between the (discrete) Laplace transform

$$G_t(\boldsymbol{r}_\mathrm{A}, \boldsymbol{r}_\mathrm{B}) = \sum_{N=1}^{\infty} l^2\, \mathrm{e}^{-Nl^2 t} Z_N(\boldsymbol{r}_\mathrm{A}, \boldsymbol{r}_\mathrm{B}) \tag{2.9}$$

of the chain partition function Z and the order-parameter correlation function or propagator $\langle \Phi_\alpha(\boldsymbol{r}_\mathrm{A}) \Phi_\beta(\boldsymbol{r}_\mathrm{B}) \rangle$ in a Ginzburg–Landau field theory. For an ideal chain this follows from the Fourier transform

$$\begin{aligned} \int \mathrm{d}(\boldsymbol{r}_\mathrm{A} - \boldsymbol{r}_\mathrm{B})\, \mathrm{e}^{\mathrm{i}\boldsymbol{p}(\boldsymbol{r}_\mathrm{A}-\boldsymbol{r}_\mathrm{B})} G_t^{(0)}(\boldsymbol{r}_\mathrm{A}, \boldsymbol{r}_\mathrm{B}) &= \sum_{N=1}^{\infty} l^2\, \mathrm{e}^{-Nl^2 t}\, \mathrm{e}^{-p^2 N l^2} \\ &= \frac{l^2}{\mathrm{e}^{l^2(t+p^2)} - 1} \end{aligned} \tag{2.10}$$

For $t + p^2$ much smaller than the squared wavevector cutoff l^{-2}, this reproduces the usual form $1/(t + p^2)$ of the propagator in a Gaussian Ginzburg–Landau field theory and tends to zero for $t + p^2$ much larger than l^{-2}. Note that the Laplace variable t conjugate to the monomer number N in the chain plays the role of the temperature deviation from the critical point in the field theory.

To represent a polymer chain with an excluded-volume interaction of strength b, consider a Φ^4 theory for a k-component order-parameter field $\Phi = (\Phi_1, \Phi_2, \ldots, \Phi_k)$ with Gaussian propagators

$$\langle \Phi_\alpha(\boldsymbol{r}) \Phi_\beta(\boldsymbol{r}') \rangle_0 = \delta_{\alpha,\beta} G_t^0(\boldsymbol{r}, \boldsymbol{r}') \tag{2.11}$$

as in Eq. (2.10) and a Φ^4 interaction Hamiltonian

$$\mathcal{H}' = b l^{d-4} \int \mathrm{d}\boldsymbol{r} \, \frac{1}{2} \sum_{\alpha,\beta}^{k} \frac{1}{2} \Phi_\alpha^2(\boldsymbol{r}) \, \frac{1}{2} \Phi_\beta^2(\boldsymbol{r}) \tag{2.12}$$

with an amplitude proportional to the excluded-volume strength b in Eq. (2.4). With the notation

$$\varphi_{\mathrm{AB}}^{(1)} \equiv \Phi_1(\boldsymbol{r}_\mathrm{A}) \Phi_1(\boldsymbol{r}_\mathrm{B}) \tag{2.13}$$

the contribution $\langle \varphi_{\mathrm{AB}}^{(1)} (-\mathcal{H}')^{\mathcal{M}} / \mathcal{M}! \rangle_{0,\mathrm{conn}}$ of $\mathcal{M}$th order in b to the correlation function $\langle \varphi_{\mathrm{AB}}^{(1)} \rangle$ decomposes by Wick factorization into two classes of terms. Terms in the first class are independent of the component number k since all the summation indices of the $\mathcal{H}'$ interactions equal the external index 1, due to the Kronecker δ functions in the unperturbed propagators (2.11). Taking into account the combinatorial factors, one finds that these terms are equal to the Laplace transform of the corresponding contributions in a perturbation expansion of the chain partition function in (2.4). Terms in the second class involve sums over all the component indices and are proportional to non-vanishing integer powers of k. They vanish on formally setting k equal to zero in the perturbation expansion, so that (des Cloizeaux and Jannink 1990; Schäfer 1998)

$$\sum_N l^2 \, \mathrm{e}^{-N l^2 t} Z_N(\boldsymbol{r}_\mathrm{A}, \boldsymbol{r}_\mathrm{B}) = \langle \varphi_{\mathrm{AB}}^{(1)} \rangle \big|_{k=0} \tag{2.14}$$

Other quantities besides the partition function Z_N are of interest. One of these is the fraction

$$F_\mathrm{m}(\boldsymbol{r}) \, \mathrm{d}\boldsymbol{r} = \frac{1}{N-1} \sum_{j=1}^{N-1} \delta(\boldsymbol{r} - \boldsymbol{r}_j) \, \mathrm{d}\boldsymbol{r} \tag{2.15}$$

of beads (monomers) in a volume element $\mathrm{d}\boldsymbol{r}$ containing a given point $\boldsymbol{r}$ in space. Due to the simple normalization

$$\int \mathrm{d}\boldsymbol{r} \, F_\mathrm{m}(\boldsymbol{r}) = 1 \tag{2.16}$$

the fraction density F_{m} is less dependent on microscopic details and conventions[2] than the monomer density $(N-1)F_{\mathrm{m}}$. A further advantage is that, in the scaling limit of large N, the scaling dimension of F_{m} equals its naive inverse-length dimension d. For a long chain with ends fixed at $\boldsymbol{r}_{\mathrm{A}}$ and $\boldsymbol{r}_{\mathrm{B}}$, the configurational average $\{F_{\mathrm{m}}\}_{\mathrm{A,B}}$ of F_{m} is given by[3]

$$\{F_{\mathrm{m}}\}_{\mathrm{A,B}} = \frac{(Nl^2)^{-1}\mathcal{L}\langle \frac{1}{2}\boldsymbol{\Phi}^2(\boldsymbol{r})\cdot\varphi^{(1)}_{\mathrm{AB}}\rangle\big|_{k=0}}{\mathcal{L}\langle\varphi^{(1)}_{\mathrm{AB}}\rangle\big|_{k=0}} \tag{2.17}$$

Here the dot following the scalar product, $\boldsymbol{\Phi}^2(\boldsymbol{r}) = \sum_\alpha \Phi_\alpha^2(\boldsymbol{r})$, denotes a cumulant average, and $\mathcal{L} = \mathcal{L}_{t\to Nl^2}$ is the inverse of the Laplace transform on the left-hand side of Eq. (2.14). Thus the denominator on the right-hand side of (2.17) equals the partition function $Z_N(\boldsymbol{r}_{\mathrm{A}}, \boldsymbol{r}_{\mathrm{B}})$. Equation (2.17) follows from similar arguments as (2.14) (see, for example, des Cloizeaux and Jannink 1990; Schäfer 1998; Eisenriegler 1993; Eisenriegler 1998).

Relations such as Eqs. (2.14) and (2.17) can be used to derive universal critical properties of a polymer chain from Landau–Ginzburg–Wilson $(\Phi^2)^2$ field theory. For example, Eq. (2.14) gives an expansion of the field-theoretical correlation function on the right-hand side in a power series in $\mathrm{e}^{-l^2 t}$, which converges and is analytic for large enough t, i.e. in the "paramagnetic" region. Decreasing the temperature t toward its critical value t_{c}, where the correlation function is singular, is equivalent to approaching the radius of convergence of the series. Thus the singular behavior for $t \searrow t_{\mathrm{c}}$ is related to the behavior of the polymer partition function Z_N for $N \to \infty$.

First consider the polymer partition function

$$Z_N(\boldsymbol{r}_{\mathrm{A}}) = \int \mathrm{d}\boldsymbol{r}_{\mathrm{B}}\, Z_N(\boldsymbol{r}_{\mathrm{A}}, \boldsymbol{r}_{\mathrm{B}}) \tag{2.18}$$

with one end fixed. Equation (2.14) gives

$$\sum_N l^2\, \mathrm{e}^{-Nl^2 t} Z_N(\boldsymbol{r}_{\mathrm{A}}) \propto l^2[(t-t_{\mathrm{c}})l^2]^{-\gamma} \tag{2.19}$$

where γ is the susceptibility exponent, since the integral $\int \mathrm{d}\boldsymbol{r}_{\mathrm{B}}$ of the correlation function on the right-hand side of (2.14) is the susceptibility.

2) For a real polymer chain, the value of N depends on which chemical piece is regarded as a monomer. Note also that the dimensionless quantity N has, in accordance with Eq. (2.1), the non-vanishing inverse-length scaling dimension $-1/\nu$.

3) Since we are interested in the long-chain limit $N \gg 1$, we do not distinguish here between $N-1$ and N. Note that the Z-factors cancel on expressing the right-hand side of (2.17) in terms of renormalized quantities (des Cloizeaux and Jannink 1990; Schäfer 1998; Eisenriegler 1993; Eisenriegler 1998).

Equation (2.19) implies that

$$Z_N(\boldsymbol{r}_\mathrm{A}) \propto \mathrm{e}^{Nl^2 t_\mathrm{c}} N^{\gamma-1} \tag{2.20}$$

as $N \to \infty$. While t_c and thus the exponential N dependence are non-universal,[4] the values (Zinn-Justin 1989; Cardy and Hamber 1980; Nienhuis 1982)

$$\gamma - 1 = 0,\ 0.161,\ \tfrac{11}{32} \tag{2.21}$$

for the power-law exponent $\gamma - 1$ in spatial dimensions $d = 4$, 3, 2 are universal.

In a similar way from the scaling behavior

$$\langle \Phi_1(\boldsymbol{r})\Phi_1(\boldsymbol{0})\rangle\big|_{k=0} \propto \xi_\mathrm{FT}^{-2x}\mathcal{X}(r/\xi_\mathrm{FT}) \tag{2.22}$$

of the correlation function, which involves the correlation length $\xi_\mathrm{FT} \propto (t - t_\mathrm{c})^{-\nu}$ of the field theory (FT), one obtains the mean square end-to-end distance

$$\begin{aligned}\mathcal{R}_\mathrm{ee}^2 &= \int \mathrm{d}\boldsymbol{r}_\mathrm{B}\,(\boldsymbol{r}_\mathrm{A} - \boldsymbol{r}_\mathrm{B})^2 Z_N(\boldsymbol{r}_\mathrm{A}, \boldsymbol{r}_\mathrm{B}) \Big/ \int \mathrm{d}\boldsymbol{r}_\mathrm{B}\, Z_N(\boldsymbol{r}_\mathrm{A}, \boldsymbol{r}_\mathrm{B}) \\ &\propto (\mathcal{L}\xi_\mathrm{FT}^{d+2-2x})/(\mathcal{L}\xi_\mathrm{FT}^{d-2x}) \propto N^{2\nu}\end{aligned} \tag{2.23}$$

(cf. footnote 1). Here x is the scaling dimension of the order parameter, related to γ and ν via $d - 2x = \gamma/\nu$. Thus the polymer exponent ν in Eq. (2.1) coincides with the exponent of the correlation length of the field theory for the case $k = 0$, and[5]

$$\nu = \tfrac{1}{2},\ 0.588,\ \tfrac{3}{4},\ 1 \tag{2.24}$$

for $d = 4$, 3, 2, 1.

The polymer partition function for the two ends microscopically close is proportional to (de Gennes 1979)

$$Z_N(0,0) \propto \mathrm{e}^{Nl^2 t_\mathrm{c}} N^{-\nu d} \tag{2.25}$$

4) In our model (2.4) the partition function $Z_N^{(0)}(\boldsymbol{r}_\mathrm{A})$ without self-repulsion ($b = 0$) equals 1, consistent with $\gamma^{(0)} = 1$ and $t_\mathrm{c}^{(0)} = 0$ in (2.20). On turning on the repulsion ($b > 0$), the partition function $Z_N(\boldsymbol{r}_\mathrm{A})$ must *decrease*, and thus $t_\mathrm{c} < 0$.

5) For $d = 3$ see, for example, Zinn-Justin (1989); and for exponents of the $\mathcal{O}(k)$ model in two dimensions, see Cardy and Hamber (1980) and Nienhuis (1982).

Due to the *negative* exponent $-\nu d$, for large N it is much smaller than the partition function (2.20) with unrestricted end-to-end distance. Equation (2.25) is consistent with the m-fold derivative[6)]

$$\sum_N \mathrm{e}^{-Nl^2(t-t_\mathrm{c})} N^m \, \mathrm{e}^{-Nl^2 t_\mathrm{c}} Z_N(0,0) \propto \frac{\mathrm{d}^m}{\mathrm{d}t^m} \langle \Phi_1^2(0) \rangle \big|_{k=0} \tag{2.26}$$

of (2.14), since the right-hand side is $\propto (t - t_\mathrm{c})^{-(m+1-\nu d)}$.

Now we consider the normalized distribution of the end-to-end distance. For $|\boldsymbol{r}_\mathrm{A} - \boldsymbol{r}_\mathrm{B}|$ and $\mathcal{R}_\mathrm{ee}$ large on a microscopic scale,

$$Z_N(\boldsymbol{r}_\mathrm{A}, \boldsymbol{r}_\mathrm{B}) / Z_N(\boldsymbol{r}_\mathrm{A}) = \mathcal{R}_\mathrm{ee}^{-d} \mathcal{Y}(|\boldsymbol{r}_\mathrm{A} - \boldsymbol{r}_\mathrm{B}| / \mathcal{R}_\mathrm{ee}) \tag{2.27}$$

which is consistent with the scaling behavior (2.22) and with Eq. (2.14). It is interesting to consider the distribution for distances $|\boldsymbol{r}_\mathrm{A} - \boldsymbol{r}_\mathrm{B}|$ much smaller than $\mathcal{R}_\mathrm{ee}$. In this case (de Gennes 1979; des Cloizeaux and Jannink 1990)

$$\mathcal{Y}(y) \propto y^\theta, \quad y \ll 1 \tag{2.28}$$

with the short-distance exponent

$$\theta = \frac{\gamma - 1}{\nu} = d - 2x - \frac{1}{\nu} = x_{\Phi^2} - 2x \tag{2.29}$$

where

$$x_{\Phi^2} = d - \frac{1}{\nu} \tag{2.30}$$

is the critical exponent of the energy density (cf. footnote 6). The expression for θ follows from Eqs. (2.14), (2.23), and (2.27), and the plausible assumption that the $N \to \infty$ dependence of $Z_N(\boldsymbol{r}_\mathrm{A}, \boldsymbol{r}_\mathrm{B})$ with finite and fixed $|\boldsymbol{r}_\mathrm{A} - \boldsymbol{r}_\mathrm{B}|$ is the same as that of $Z_N(0,0)$ in (2.25). Using Eqs. (2.21) and (2.24), one finds

$$\theta = 0, \ 0.27, \ \tfrac{11}{24} \tag{2.31}$$

for $d = 4$, 3, 2.

The exponent θ vanishes at the upper critical dimension $d = 4$, where the excluded-volume interaction is only marginally relevant, and where the distribution is a Gaussian. For $d < 4$ the exponent θ is positive and leads to a

6) The differentiation in (2.26) with $m = 2, 3, \ldots$ eliminates non-asymptotic corrections to $Z_N(0,0)$ and analytic non-scaling corrections to the "energy density" $\langle \Phi_1^2(0) \rangle$, which would contribute to (2.26) for $m = 0$, 1.
The scaling contribution to $\langle \Phi_1^2(0) \rangle$ is $\propto (t - t_\mathrm{c})^{\nu d - 1} \propto \xi_\mathrm{FT}^{-(d-1/\nu)}$.

distribution that *increases* with increasing distance $|\boldsymbol{r}_{\mathrm{A}} - \boldsymbol{r}_{\mathrm{B}}|$ for $|\boldsymbol{r}_{\mathrm{A}} - \boldsymbol{r}_{\mathrm{B}}| \ll \mathcal{R}_{\mathrm{ee}}$. It decreases, of course, for $|\boldsymbol{r}_{\mathrm{A}} - \boldsymbol{r}_{\mathrm{B}}| \gg \mathcal{R}_{\mathrm{ee}}$. This is a consequence of the excluded-volume interaction , which suppresses configurations with close ends.

Equation (2.28) is a special case of a general short-distance relation, which can be written in the operator form (Zinn-Justin 1989)

$$\boldsymbol{\Phi}(\boldsymbol{r}_{\mathrm{B}})\boldsymbol{\Phi}(\boldsymbol{r}_{\mathrm{A}}) \propto |\boldsymbol{r}_{\mathrm{A}} - \boldsymbol{r}_{\mathrm{B}}|^{x_{\Phi^2}-2x}\ \boldsymbol{\Phi}^2\left(\frac{\boldsymbol{r}_{\mathrm{A}} + \boldsymbol{r}_{\mathrm{B}}}{2}\right) \tag{2.32}$$

for distances

$$l \ll |\boldsymbol{r}_{\mathrm{A}} - \boldsymbol{r}_{\mathrm{B}}| \ll \text{other lengths} \tag{2.33}$$

Equation (2.32) holds in correlation functions if $|\boldsymbol{r}_{\mathrm{A}} - \boldsymbol{r}_{\mathrm{B}}|$, while large on the microscopic scale l, is much smaller than the other lengths (such as the correlation length ξ_{FT} or the distances from $|\boldsymbol{r}_{\mathrm{A}} + \boldsymbol{r}_{\mathrm{B}}|/2$ to the positions of other operators) that appear in the correlation function. The same exponent (2.29) appears in all the correlation functions, and its form follows from the requirement that both sides of (2.32) have the same scaling dimension. The factor of proportionality in (2.32) is also independent of the particular correlation function.

Equation (2.32) can be generalized to higher order in the "small" distance $|\boldsymbol{r}_{\mathrm{A}} - \boldsymbol{r}_{\mathrm{B}}|$ by including contributions of higher-dimensional operators on its right-hand side. These *operator-product expansions* are a basic property of local field theories. The *small-particle operator expansions* that we use in Sections 2.5.2 and 2.9.1 below are other examples where a perturbation of "small" spatial extent is expanded in a series of point operators. The size of the small particle plays the role of the small distance.

2.3 Polymers Interacting with Boundaries

Consider the case where the polymer chain can only move in a part of the space due to an impenetrable boundary. One example is a half-space with a planar boundary. Another is the exterior of a mesoscopic (colloidal) particle, in which case the boundary is curved. In this chapter we assume inert impenetrable boundaries, which act on the monomers like a hard wall. Here, too, it is possible to map (Eisenriegler 1993) the problem onto a field theory, and relations of the form (2.14) and (2.17) also apply. In the field theory the Dirichlet condition

$$\boldsymbol{\Phi} = 0 \tag{2.34}$$

is satisfied at the boundary (Binder 1986; Diehl 1986; Diehl 1997).

The main effect of the boundary is to generate a boundary layer that is depleted of chain monomers, since the number of chain conformations, and thus the entropy, is strongly reduced near the boundary. The depletion shows up most clearly in the density profiles of chain monomers and chain ends.

Let us make this more explicit for random-walk-like "ideal" polymer chains with vanishing excluded-volume interaction strength b in (2.4). The partition function

$$Z_N^0(\boldsymbol{r}_\mathrm{A}, \boldsymbol{r}_\mathrm{B}) = Z(L; \boldsymbol{r}_\mathrm{A}, \boldsymbol{r}_\mathrm{B}), \quad L = Nl^2 \tag{2.35}$$

satisfies the diffusion equation

$$\left(\frac{\partial}{\partial L} - \Delta_{\boldsymbol{r}_\mathrm{A}}\right) Z(L; \boldsymbol{r}_\mathrm{A}, \boldsymbol{r}_\mathrm{B}) = 0, \quad Z(L{=}0; \boldsymbol{r}_\mathrm{A}, \boldsymbol{r}_\mathrm{B}) = \delta(\boldsymbol{r}_\mathrm{A} - \boldsymbol{r}_\mathrm{B}) \tag{2.36}$$

where L plays the role of time. In free space this is consistent with the form (2.8) of Eq. (2.35). The meaning of L follows from the expressions

$$\mathcal{R}_\mathrm{ee}^2 = 2dL, \quad \mathcal{R}_\mathrm{g}^2 = dL/3 \tag{2.37}$$

for the mean square end-to-end distance $\mathcal{R}_\mathrm{ee}^2$ and radius of gyration $\mathcal{R}_\mathrm{g}^2$ of an unconstrained ideal chain in d spatial dimensions with the ratio $\mathcal{R}_\mathrm{ee}^2/\mathcal{R}_\mathrm{g}^2 = 6$. The *boundary* corresponds to an external potential W acting on each monomer. This introduces (de Gennes 1979) a term $W(\boldsymbol{r}_\mathrm{A})Z(\boldsymbol{r}_\mathrm{A}, \boldsymbol{r}_\mathrm{B})$ in the diffusion equation, which then looks like the time-dependent Schrödinger equation. For a hard boundary with $W = 0$ in the space available to the polymer and $W = \infty$ in the forbidden space, Z satisfies Eq. (2.36) in the available space, and the Dirichlet boundary condition

$$Z(L; \boldsymbol{r}_\mathrm{A}, \boldsymbol{r}_\mathrm{B}) \to 0 \quad \text{for } \boldsymbol{r}_\mathrm{A} \text{ or } \boldsymbol{r}_\mathrm{B} \to \text{hard boundary} \tag{2.38}$$

Equation (2.38) corresponds to the Dirichlet condition (2.34) of the field theory, and the diffusion equation (Eq. 2.36) with "initial condition" to the "Ornstein–Zernicke equation"

$$(t - \Delta_{\boldsymbol{r}_\mathrm{A}}) G(t; \boldsymbol{r}_\mathrm{A}, \boldsymbol{r}_\mathrm{B}) = \delta(\boldsymbol{r}_\mathrm{A} - \boldsymbol{r}_\mathrm{B}) \tag{2.39}$$

for the propagator

$$G(t; \boldsymbol{r}_\mathrm{A}, \boldsymbol{r}_\mathrm{B}) = \langle \varphi_\mathrm{AB} \rangle, \quad \varphi_\mathrm{AB} \equiv \Phi(\boldsymbol{r}_\mathrm{A})\Phi(\boldsymbol{r}_\mathrm{B}) \tag{2.40}$$

in the one-component Gaussian field theory with quadratic Hamiltonian

$$H = \int \mathrm{d}\boldsymbol{r}\, \left[\tfrac{1}{2}(\nabla\Phi)^2 + \tfrac{1}{2}t\Phi^2\right] + \int \mathrm{d}\sigma\, \tfrac{1}{2}c\Phi^2 \tag{2.41}$$

which corresponds to ideal polymers. Here $\int \mathrm{d}\boldsymbol{r}$ is an integration over the accessible volume, and the integral $\int \mathrm{d}\sigma$ extends over the boundary. The boundary condition (2.34) is imposed by taking the limit $c \to \infty$. The relationship (2.14) between G and Z now reads

$$\int_0^\infty \mathrm{d}L\, \mathrm{e}^{-Lt} Z(L; \boldsymbol{r}_\mathrm{A}, \boldsymbol{r}_\mathrm{B}) = G(t; \boldsymbol{r}_\mathrm{A}, \boldsymbol{r}_\mathrm{B}) \tag{2.42}$$

and Eq. (2.39) follows from (2.36) on using the relation

$$\int_0^\infty \mathrm{d}L\, \mathrm{e}^{-Lt} \frac{\partial}{\partial L} Z = -\delta(\boldsymbol{r}_\mathrm{A} - \boldsymbol{r}_\mathrm{B}) + tG \tag{2.43}$$

implied by Eq. (2.42) and the "initial condition" in (2.36).

Besides $Z(L; \boldsymbol{r}, \boldsymbol{r}')$, we shall also consider the partition function[7)]

$$\mathcal{E}(\boldsymbol{r}) = \int \mathrm{d}\boldsymbol{r}'\, Z(L; \boldsymbol{r}, \boldsymbol{r}') \tag{2.44}$$

of the chain with one end fixed, while the free end $\boldsymbol{r}'$ is integrated over the available space. This quantity is proportional to the density profile of *endpoints* in a dilute solution of chains in the available space bounded by the surface. It also satisfies the diffusion equation in Eq. (2.36) and the Dirichlet boundary condition (2.38), but the "initial condition" in (2.36) is changed to

$$\mathcal{E}(\boldsymbol{r})\big|_{L=0} = 1 \tag{2.45}$$

For $\boldsymbol{r}$ far from any surface, one expects from Eq. (2.8) that

$$\mathcal{E}(\boldsymbol{r} \to \mathrm{bulk}) = 1, \quad L \text{ arbitrary} \tag{2.46}$$

For a solution of ideal chains, the *monomer* density profile is proportional to the quantity

$$\mathcal{M}(\boldsymbol{r}) = \frac{1}{L}\int_0^L \mathrm{d}L'\, \mathcal{E}(L', \boldsymbol{r})\mathcal{E}(L-L', \boldsymbol{r}) = \frac{1}{L}\, \mathcal{L}[\chi(\boldsymbol{r})]^2 \tag{2.47}$$

7) We shall frequently use the notation $\mathcal{E}(\boldsymbol{r})$, $\mathcal{M}(\boldsymbol{r})$, $\chi(\boldsymbol{r})$ for $\mathcal{E}(L, \boldsymbol{r})$, $\mathcal{M}(L, \boldsymbol{r})$, $\chi(t, \boldsymbol{r})$, suppressing the L or t dependence.

which also tends to unity in the bulk. The convolution $\int \mathrm{d}L'\, \mathcal{E}\mathcal{E}$ is proportional to the number of ideal-chain conformations (de Gennes 1979) with a monomer at $\boldsymbol{r}$, the propagator integral

$$\chi(\boldsymbol{r}) = \int \mathrm{d}\boldsymbol{r}'\, G(t, \boldsymbol{r}, \boldsymbol{r}') \tag{2.48}$$

is the susceptibility in the Ginzburg–Landau model of a magnet, and $\mathcal{L}$ is the inverse of the Laplace transform on the left-hand side of Eq. (2.42), so that $\mathcal{L}\chi$ equals $\mathcal{E}$. Note that

$$\int \mathrm{d}\boldsymbol{r}_\mathrm{A} \int \mathrm{d}\boldsymbol{r}_\mathrm{B}\, \langle \varphi_\mathrm{AB} \cdot \tfrac{1}{2}\Phi^2(\boldsymbol{r})\rangle = [\chi(\boldsymbol{r})]^2 \tag{2.49}$$

in the Gaussian model, due to Wick's theorem. As in Eq. (2.17), this shows that the operator Φ^2 corresponds to the monomer density.

In the presence of excluded-volume interactions between chain monomers, results in $d = 3$ spatial dimensions can only be obtained perturbatively. For a single chain, one may start with an ideal chain and expand with respect to the excluded-volume interaction strength b in Eq. (2.4). For polymer solutions with inter-chain overlap, one may start with mean-field theory, where an effective potential $W_\mathrm{eff} = bl^{d-2}nN\mathcal{M}(\boldsymbol{r})$ due to the monomer distribution is included inside the bracket in the diffusion equation (2.36) for the single-chain partition function, and expand with respect to fluctuations. However, these expansions fail[8] in the "critical region" of long flexible chains in high dilution, and it is necessary first to map the polymer system from the critical to a "non-critical" region by means of the renormalization group (des Cloizeaux and Jannink 1990; Schäfer 1998; Eisenriegler 1993). A reasonable first approximation is the "renormalized mean-field approximation", where the non-critical region is described by mean-field theory (Schäfer 1998). All this is in complete analogy to "ordinary" critical systems (Nelson 1976).

8) For example, one finds (de Gennes 1979; Eisenriegler 1993) from Eq. (2.4) that the amplitude of the first relative correction in the expansion of the mean square end-to-end distance $\mathcal{R}_\mathrm{ee}^2/(\mathcal{R}_\mathrm{ee}^2)_\mathrm{ideal} = 1 + b\sigma + \mathcal{O}(b^2)$ *grows* for $d < 4$ as $\sigma \propto N^{(4-d)/2}$, as the number N of monomers in the chain increases.

2.4 Polymers Interacting with a Planar Wall

2.4.1 Ideal Polymers

For a polymer in the half-space $z > 0$ bounded by a planar wall, one can use the method of images to satisfy the hard-wall boundary condition (2.38) at the boundary $z = 0$. Subtracting from the solution (2.8) in free space, which "starts" from $\boldsymbol{r}_{\mathrm{B}} = (\boldsymbol{r}_{\mathrm{B}\parallel}, z_{\mathrm{B}})$, the solution that starts from the image point $\boldsymbol{r}_{\mathrm{BI}} = (\boldsymbol{r}_{\mathrm{B}\parallel}, -z_{\mathrm{B}})$, one obtains

$$Z(L; \boldsymbol{r}_{\mathrm{A}}, \boldsymbol{r}_{\mathrm{B}}) = (4\pi L)^{-(d-1)/2}\, \mathrm{e}^{-|\boldsymbol{r}_{\mathrm{A}\parallel} - \boldsymbol{r}_{\mathrm{B}\parallel}|^2/(4L)} (4\pi L)^{-1/2} \times \left[\mathrm{e}^{-(z_{\mathrm{A}} - z_{\mathrm{B}})^2/(4L)} - \mathrm{e}^{-(z_{\mathrm{A}} + z_{\mathrm{B}})^2/(4L)}\right] \tag{2.50}$$

This satisfies the diffusion equation and initial condition (2.36) in the half-space and the boundary condition (2.38) at $z = 0$.

For the partition function

$$\mathcal{E}(\boldsymbol{r}) = \mathcal{E}_{\mathrm{h}}(z) \equiv \int_{(z'>0)} \mathrm{d}\boldsymbol{r}'\, Z(L; \boldsymbol{r}, \boldsymbol{r}') \tag{2.51}$$

with only one end fixed, Eq. (2.50) implies

$$\mathcal{E}(\boldsymbol{r}) = \mathrm{erf}(y/2) \tag{2.52}$$

where

$$y = \frac{z}{\sqrt{L}} \tag{2.53}$$

and

$$\mathrm{erf}(x) = \frac{2}{\sqrt{\pi}} \int_0^x \mathrm{d}\zeta\, \mathrm{e}^{-\zeta^2} \tag{2.54}$$

is the error function. The subscript "h" in Eq. (2.51) stands for "half-space". The width of the depletion zone of $\mathcal{E}_{\mathrm{h}}$ near the wall is $\propto \sqrt{L}$, i.e. of the order of the root mean square end-to-end distance or radius of gyration (see Eq. 2.37).

From Eq. (2.47) the bulk-normalized monomer density profile is given by

$$\mathcal{M} = 1 + 4[-2\,\mathrm{i}^2\mathrm{erfc}(y/2) + \mathrm{i}^2\mathrm{erfc}(y)] \tag{2.55}$$

where $\mathrm{i}^2\mathrm{erfc}$ is the two-fold iterated complementary error function (Abramowitz and Stegun 1972). The monomer density profile $\mathcal{M}$ has the parabolic form

$$\mathcal{M} \to z^2/L \tag{2.56}$$

for $z \ll \sqrt{L}$, has a point of inflection at $z = y_\mathrm{w}\sqrt{L} = 0.72\sqrt{L}$, and approaches the bulk value of unity from below for $z \gg \sqrt{L}$.

Expressions for the "magnetic analogs", i.e. the Laplace transforms

$$G(t;\boldsymbol{r},\boldsymbol{r}') = \int \frac{\mathrm{d}\boldsymbol{p}}{(2\pi)^{d-1}}\, \mathrm{e}^{\mathrm{i}\boldsymbol{p}(\boldsymbol{r}_\parallel - \boldsymbol{r}'_\parallel)} \frac{1}{2w}\left[\mathrm{e}^{-|z-z'|w} - \mathrm{e}^{-(z+z')w}\right]$$

$$w = \sqrt{t+p^2} \tag{2.57}$$

and

$$\chi(\boldsymbol{r}) = [1 - \exp(-z\sqrt{t})]/t \tag{2.58}$$

of Z and $\mathcal{E}$, are noted for later use.

2.4.2 Behavior Near the Wall: Density–Pressure Relation and Boundary Operator Expansion

Here we consider both ideal polymers and real polymers in a good solvent. For a dilute, monodisperse solution of free polymers in the half-space with a planar boundary wall, the bulk-normalized density profiles $\mathcal{E}$ for ends or $\mathcal{M}$ for monomers have the scaling form

$$\mathcal{P}(z) = Y(z/\mathcal{R}_\mathrm{g}) \tag{2.59}$$

with universal scaling functions $Y = Y_\mathrm{e}$ or Y_m for $\mathcal{P} = \mathcal{E}$ or $\mathcal{M}$. Here z, the distance from the wall, is large on the microscopic scale, and, for $z \gg \mathcal{R}_\mathrm{g}$, $Y \to 1$. For

$$\text{microscopic distances} \ll z \ll \mathcal{R}_\mathrm{g} \tag{2.60}$$

$\mathcal{E}$ and $\mathcal{M}$ have a power-law behavior in z. The power-law exponents are positive, in accordance with the depletion phenomenon, and are known as "surface exponents". In the case of $\mathcal{E}$, the exponent is new (Eisenriegler 1993) and not a simple combination of the bulk exponents ν and γ. In the case of $\mathcal{M}$, the exponent is $1/\nu$.

The reason for the second power law is that the monomer density near the wall is related (de Gennes 1979) to the *force* that the polymers exert on the wall. The force per unit area is given by

$$\frac{f}{\mathcal{A}} = k_{\mathrm{B}}Tn \equiv p_0 \tag{2.61}$$

with n the chain density in the bulk, since it equals the chain osmotic pressure in the bulk, which by the ideal-gas law is $k_{\mathrm{B}}Tn$. This suggests (de Gennes 1979) that the monomer density $Nn\mathcal{M}(z)$ in the region (2.60) must also be independent of N, implying via (2.1) that

$$\mathcal{M} \equiv Y_{\mathrm{m}}(z/\mathcal{R}_{\mathrm{g}}) \to B_{\mathrm{g}}(z/\mathcal{R}_{\mathrm{g}})^{1/\nu} \tag{2.62}$$

for $z \ll \mathcal{R}_{\mathrm{g}}$, with B_{g} a universal amplitude.

As in Eq. (2.15), it is advantageous to introduce a modified monomer density

$$m(\boldsymbol{r}) = \sum_{P=1}^{\mathcal{N}} (\mathcal{R}_{\mathrm{g}}^{1/\nu}/N) \sum_{j=1}^{N} \delta(\boldsymbol{r} - \boldsymbol{r}_{P,j}) \tag{2.63}$$

for a system of $\mathcal{N}$ chains. This quantity is less dependent on microscopic details than the ordinary monomer density $(N/\mathcal{R}_{\mathrm{g}}^{1/\nu})m$. For free chains in the half-space (denoted "(fc,h)")

$$\{m(\boldsymbol{r})\}_{(\mathrm{fc,h})} = \mathcal{R}_{\mathrm{g}}^{1/\nu} n\mathcal{M}(z) \to B_{\mathrm{g}} z^{1/\nu} p_{(\mathrm{fc,h})}/(k_{\mathrm{B}}T) \tag{2.64}$$

where the curly brackets denote a chain ensemble average, and $p_{(\mathrm{fc,h})} = p_0 \equiv k_{\mathrm{B}}Tn$ is the polymer pressure on the wall, according to Eq. (2.61).

The relation between density and pressure close to a planar boundary wall

$$\{m(\boldsymbol{r}_{\parallel}, z)\}_{(\mathrm{ensemble})} \to B_{\mathrm{g}} z^{1/\nu} p_{(\mathrm{ensemble})}(\boldsymbol{r}_{\parallel})/(k_{\mathrm{B}}T) \tag{2.65}$$

applies not only to dilute free chains in the half-space as given in (2.64), with the pressure independent of the position $\boldsymbol{r}_{\parallel}$ in the wall, but also in other situations. Of particular interest are (1) a single chain with one end (or the two ends) fixed in the half-space, (2) a single chain trapped between two parallel plates, (3) a dilute or semidilute polymer solution in the half-space, and (4) a dilute or semidilute polymer solution in the half-space containing a mesoscopic obstacle (particle). While the densities and pressures are quite different in these different cases, their ratio $B_{\mathrm{g}} z^{1/\nu}$ is the same. The density–pressure relation, with the same factor $B_{\mathrm{g}} z^{1/\nu}$, even applies if the

boundary is not planar but has a non-vanishing mesoscopic radius of curvature R. One example, the surface of a spherical particle of radius R in a polymer solution, is discussed in Section 2.5. The mesoscopic distance z of $\boldsymbol{r}$ from the point in the boundary has to be small not only compared to $\mathcal{R}_{\mathrm{g}}$ (or the Edwards' correlation length ξ), but also compared to R. The amplitude B_{g} is independent of microscopic details to the same extent as the exponent ν. In particular, it depends on the spatial dimension d and is different for ideal chains and chains with excluded-volume interaction. For ideal chains

$$B_{\mathrm{g}} = B_{\mathrm{g}}^{(\mathrm{ideal})} = d/3 \tag{2.66}$$

follows from Eqs. (2.37), (2.56), and (2.64).

The density–pressure relation (2.65) can be understood from a field-theoretical analysis, which also allows one to calculate the universal and situation-independent amplitude B_{g}. For example, consider the case (1) [denoted (A,B;h)] of a chain with ends fixed at $\boldsymbol{r}_{\mathrm{A}}$ and $\boldsymbol{r}_{\mathrm{B}}$. Since Eq. (2.17) also applies to a chain in the presence of a boundary (Eisenriegler 1993; Diehl 1986; Diehl 1997), one finds, on comparing Eq. (2.15) with Eq. (2.63), that

$$\{m(\boldsymbol{r}_{\parallel}, z)\}_{(\mathrm{A,B;h})} = \frac{\mathcal{L}\langle \Psi_{\mathrm{g}}(\boldsymbol{r}_{\parallel}, z) \cdot \varphi_{\mathrm{AB}}^{(1)} \rangle_{\mathrm{h}}\big|_{k=0}}{\mathcal{L}\langle \varphi_{\mathrm{AB}}^{(1)} \rangle_{\mathrm{h}}\big|_{k=0}} \tag{2.67}$$

where

$$\Psi_{\mathrm{g}}(r_{\parallel}, z) = \mathcal{R}_{\mathrm{g}}^{1/\nu} (Nl^2)^{-1} \, \tfrac{1}{2} \boldsymbol{\Phi}^2(r_{\parallel}, z) \tag{2.68}$$

Here $\langle \cdots \rangle_{\mathrm{h}}$ denotes the field-theoretical half-space average with the Dirichlet boundary condition (2.34). The behavior on approaching the wall follows from the boundary operator expansion (Dietrich and Diehl 1981; Eisenriegler 1997)

$$\boldsymbol{\Phi}^2(\boldsymbol{r}_{\parallel}, z) \propto z^{d - x_{\Phi^2}} T_{\perp,\perp}(\boldsymbol{r}_{\parallel}, 0) \tag{2.69}$$

which is a short-distance relation analogous to the bulk relation (2.32) in which one operator approaches another one. The operator

$$T_{\perp,\perp}(\boldsymbol{r}_{\parallel}, 0) = \tfrac{1}{2} [(\partial_z \boldsymbol{\Phi}(\boldsymbol{r}_{\parallel}, z))]_{z=0}^2 \equiv \tfrac{1}{2} \boldsymbol{\Phi}_{\perp}^2(\boldsymbol{r}_{\parallel}) \tag{2.70}$$

is the diagonal component, perpendicular to the wall, of the stress tensor at the Dirichlet surface. It is the boundary operator of lowest inverse length dimension that is even in $\boldsymbol{\Phi}$ and non-vanishing at the Dirichlet boundary, and it has scaling dimension d. Taking (2.30) into account, Eq. (2.69) provides the field-theoretical explanation of the $z^{1/\nu}$ behavior of m near the boundary.

The scaling dimension d of the surface operator (2.70) follows from the role of the stress tensor in generating coordinate transformations. For example, integrating $T_{\perp,\perp}$ over the planar boundary generates a shift away from the surface,[9] so that

$$\int \mathrm{d}^{d-1} r_{\parallel} \langle T_{\perp,\perp}(\boldsymbol{r}_{\parallel}, 0) \cdot \varphi_{\mathrm{AB}}^{(1)} \rangle_{\mathrm{h}} = (\partial_{z_{\mathrm{A}}} + \partial_{z_{\mathrm{B}}}) \langle \varphi_{\mathrm{AB}}^{(1)} \rangle_{\mathrm{h}} \tag{2.71}$$

if $z_{\mathrm{A}}, z_{\mathrm{B}} > 0$.

While the factor of proportionality in (2.69) is non-universal, the corresponding factor in

$$\Psi_{\mathrm{g}}(\boldsymbol{r}_{\parallel}, z) \to B_{\mathrm{g}} z^{1/\nu} T_{\perp,\perp}(\boldsymbol{r}_{\parallel}, 0) \tag{2.72}$$

is given by the universal number B_{g}. On using the shift identity, Eq. (2.72) implies (Eisenriegler 1997)

$$\int \mathrm{d}^{d-1} r_{\parallel} \left\{ m(\boldsymbol{r}_{\parallel}, z) \right\}_{(\mathrm{A,B;h})} \to B_{\mathrm{g}} z^{1/\nu} (\partial_{z_{\mathrm{B}}} + \partial_{z_{\mathrm{A}}}) \ln Z_N^{(\mathrm{h})}(\boldsymbol{r}_{\mathrm{A}}, \boldsymbol{r}_{\mathrm{B}}) \tag{2.73}$$

Since the right-hand side equals $B_{\mathrm{g}} z^{1/\nu}$ times the modulus of the force on the wall, (2.73) is consistent with the density–pressure relation (2.65). In cases (2) and (4), one may argue similarly (Eisenriegler 1997). The estimate

$$B_{\mathrm{g}} \approx 0.99, \quad d = 3 \tag{2.74}$$

for polymer chains in a good solvent in $d = 3$ follows from a first-order expansion (Eisenriegler 1997; Eisenriegler 1993) in $\varepsilon = 4 - d$ and is very close to the ideal-chain value $B_{\mathrm{g}}^{\mathrm{ideal}} = 1$.

For an *ideal* chain in $d = 3$ with two ends and one end fixed, respectively, the forces on the wall are given by

$$f/k_{\mathrm{B}}T = \mathcal{R}_{\mathrm{g}}^{-1}(y_{\mathrm{A}} + y_{\mathrm{B}})/[\exp(y_{\mathrm{A}} y_{\mathrm{B}}) - 1] \tag{2.75}$$

and

$$f/k_{\mathrm{B}}T = \partial_{z_{\mathrm{A}}} \ln \operatorname{erf}(y_{\mathrm{A}}/2) \tag{2.76}$$

where $y_{\mathrm{A}} = z_{\mathrm{A}}/\mathcal{R}_{\mathrm{g}}$ and $y_{\mathrm{B}} = z_{\mathrm{B}}/\mathcal{R}_{\mathrm{g}}$. They change from an $\mathcal{R}_{\mathrm{g}}$-independent power-law behavior for small distances z_{A} or z_{B} to an exponential dependence

9) For the Gaussian model, the shift identity (2.71) follows directly from (2.57) and (2.70), using Wick's theorem to show that both sides of (2.71) equal

$$\int \mathrm{d}\boldsymbol{p}\, (2\pi)^{1-d}\, \mathrm{e}^{\mathrm{i}\boldsymbol{p}(\boldsymbol{r}_{\mathrm{A}\parallel} - \boldsymbol{r}_{\mathrm{B}\parallel})} \mathrm{e}^{-(z_{\mathrm{A}} + z_{\mathrm{B}})w}$$

with w from Eq. (2.57). For non-Gaussian field theories of the Φ^4 type, see Diehl et al. (1983) and Appendix 5C in Eisenriegler (1993).

for large distances, e.g. for one end fixed from $\propto z_{\mathrm{A}}^{-1}$ at $z_{\mathrm{A}} \ll \mathcal{R}_{\mathrm{g}}$ to $\propto \mathcal{R}_{\mathrm{g}}^{-1} \exp(-z_{\mathrm{A}}^2/(4\mathcal{R}_{\mathrm{g}}^2))$ at $z_{\mathrm{A}} \gg \mathcal{R}_{\mathrm{g}}$.

2.4.3 Slightly Deformed Planar Wall

Consider again the case (1) [denoted (A,B;h)] of a chain with ends fixed at $\boldsymbol{r}_{\mathrm{A}}$ and $\boldsymbol{r}_{\mathrm{B}}$ in the half-space. In Eq. (2.73) the density–pressure relation (2.65) has been verified only in *integrated* form as a relation between the local density integrated along the wall and the total force on the wall. The latter is determined by the change in polymer free energy if the wall is shifted away from the polymer system, from $z = 0$ to $z = -\eta$, with η small and *independent* of the lateral position $\boldsymbol{r}_{\parallel}$ in the wall.

The *local* relation (2.65) predicts, via (2.67) and (2.72), the field-theoretical expression

$$\frac{p_{(\mathrm{A,B;h})}(\boldsymbol{r}_{\parallel})}{k_{\mathrm{B}}T} = \frac{\mathcal{L}\langle T_{\perp,\perp}(\boldsymbol{r}_{\parallel},0)\varphi_{\mathrm{AB}}^{(1)}\rangle_{\mathrm{h}}\big|_{k=0}}{\mathcal{L}\langle\varphi_{\mathrm{AB}}^{(1)}\rangle_{\mathrm{h}}\big|_{k=0}} \tag{2.77}$$

for the pressure distribution. In order to check it, one needs to relate the left-hand side of (2.77) to the free-energy change for a wall shift $\eta = \eta(\boldsymbol{r}_{\parallel})$ that *varies* with $\boldsymbol{r}_{\parallel}$, leading to a slightly deformed boundary wall. Denoting the half-space with deformed boundary by h′, the change is

$$\begin{aligned} -\int \mathrm{d}\boldsymbol{r}_{\parallel}\, \eta(\boldsymbol{r}_{\parallel}) p_{(\mathrm{A,B;h})}(\mathrm{r}_{\parallel})/k_{\mathrm{B}}T &= -\ln[Z_N^{(\mathrm{h}')}(\boldsymbol{r}_{\mathrm{A}},\boldsymbol{r}_{\mathrm{B}})/Z_N^{(\mathrm{h})}(\boldsymbol{r}_{\mathrm{A}},\boldsymbol{r}_{\mathrm{B}})] \\ &= -\frac{\mathcal{L}[\langle\varphi_{\mathrm{AB}}^{(1)}\rangle_{\mathrm{h}'} - \langle\varphi_{\mathrm{AB}}^{(1)}\rangle_{\mathrm{h}}]\big|_{k=0}}{\mathcal{L}\langle\varphi_{\mathrm{AB}}^{(1)}\rangle_{\mathrm{h}}]\big|_{k=0}} \end{aligned} \tag{2.78}$$

where we have used the half-space counterparts of (2.14) and expanded to first order in η. The relation

$$\langle\varphi_{\mathrm{AB}}^{(1)}\rangle_{\mathrm{h}'} - \langle\varphi_{\mathrm{AB}}^{(1)}\rangle_{\mathrm{h}} = \int \mathrm{d}\boldsymbol{r}_{\parallel}\, \eta(\boldsymbol{r}_{\parallel})\langle T_{\perp,\perp}(\boldsymbol{r}_{\parallel},0)\cdot\varphi_{\mathrm{AB}}^{(1)}\rangle_{\mathrm{h}} + \mathcal{O}(\eta^2) \tag{2.79}$$

remains to be checked.

Concentrating for simplicity on ideal chains, the corresponding relation

$$\langle\varphi_{\mathrm{AB}}\rangle_{\mathrm{h}'} - \langle\varphi_{\mathrm{AB}}\rangle_{\mathrm{h}} = \int \mathrm{d}\boldsymbol{r}_{\parallel}\, \eta(\boldsymbol{r}_{\parallel})\langle\Phi(\boldsymbol{r}_{\mathrm{A}})\Phi_{\perp}(\boldsymbol{r}_{\parallel})\rangle_{\mathrm{h}}\langle\Phi_{\perp}(\boldsymbol{r}_{\parallel})\Phi(\boldsymbol{r}_{\mathrm{B}})\rangle_{\mathrm{h}} \tag{2.80}$$

is easy to prove: (a) Applying $(t - \Delta_{\boldsymbol{r}_{\mathrm{A}}})$ to the right-hand side of (2.80) leads to a vanishing result. Thus $\langle\varphi_{\mathrm{AB}}\rangle_{\mathrm{h}'}$ does indeed satisfy

the Ornstein–Zernicke equation (2.39) for interior points $\boldsymbol{r}_{\mathrm{A}}, \boldsymbol{r}_{\mathrm{B}}$ of the half-space. (b) For $\boldsymbol{r}_{\mathrm{A}} \to (\boldsymbol{r}_{\parallel}, 0)$, the propagator $\langle\varphi_{\mathrm{AB}}\rangle_{\mathrm{h}'}$ tends to $[z_{\mathrm{A}} + \eta(\boldsymbol{r}_{\mathrm{A}\parallel})]\langle\Phi_{\perp}(\boldsymbol{r}_{\mathrm{A}\parallel})\Phi(\boldsymbol{r}_{\mathrm{B}})\rangle_{\mathrm{h}}$ and vanishes at the *deformed* boundary $z_{\mathrm{A}} = -\eta$. The reason is that

$$\langle\Phi(\boldsymbol{r}_{\mathrm{A}})\Phi_{\perp}(\boldsymbol{r}_{\parallel})\rangle_{\mathrm{h}} \to \delta(\boldsymbol{r}_{\parallel} - \boldsymbol{r}_{\mathrm{A}\parallel}), \quad z_{\mathrm{A}} \to 0 \tag{2.81}$$

as one may verify from the relation

$$\int \mathrm{d}\boldsymbol{r}_{\parallel}\, \mathrm{e}^{\mathrm{i}\boldsymbol{p}(\boldsymbol{r}_{\parallel} - \boldsymbol{r}_{\mathrm{A}\parallel})}\langle\Phi(\boldsymbol{r}_{\mathrm{A}})\Phi_{\perp}(\boldsymbol{r}_{\parallel})\rangle_{\mathrm{h}} = \mathrm{e}^{-z_{\mathrm{A}}w} \tag{2.82}$$

following from Eq. (2.57), which for arbitrary $\boldsymbol{p}$ in the test function $\exp[\mathrm{i}\boldsymbol{p}(\boldsymbol{r}_{\parallel} - \boldsymbol{r}_{\mathrm{A}\parallel})]$ tends to unity as $z_{\mathrm{A}} \to 0$.

For a chain in the half-space with only one end fixed, the pressure distribution $p_{\mathrm{A;h}}(\boldsymbol{r}_{\parallel})/k_{\mathrm{B}}T$ follows from the right-hand side of (2.77) on replacing $\varphi^{(1)}_{\mathrm{AB}}$ by $\int \mathrm{d}\boldsymbol{r}_{\mathrm{B}}\, \varphi^{(1)}_{\mathrm{AB}}$ in the numerator and denominator. For an ideal chain in $d = 3$ with the end $\boldsymbol{r}_{\mathrm{A}} = (\boldsymbol{r}_{\mathrm{A}\parallel}{=}0, z_{\mathrm{A}}{\to}0)$ fixed right at the wall, the pressure formula then yields the distribution

$$\frac{p_{\mathrm{A;h}}(\boldsymbol{r}_{\parallel})}{k_{\mathrm{B}}T} = \mathrm{e}^{-r_{\parallel}^2/(4\mathcal{R}_{\mathrm{g}}^2)}\frac{1}{2\pi r_{\parallel}^3}\left(1 + \frac{r_{\parallel}^2}{2\mathcal{R}_{\mathrm{g}}^2}\right) \tag{2.83}$$

a result obtained by Breidenich et al. (2000) by slightly different methods.

Note that both the force (2.76) and the pressure distribution (2.83) are independent of the chain length $\mathcal{R}_{\mathrm{g}}^2$ for $\mathcal{R}_{\mathrm{g}}$ large. The reason is that the number of contacts with the wall does not increase as the length increases, since in the half-space enough space is available for the chain to avoid the wall. For a chain trapped between two walls, the behavior is different, as we discuss below in Section 2.6.

2.4.4
Surface Tension

The polymer-induced surface tension σ is the surface free energy per unit area of the polymer system in the half-space. For a solution of ideal chains in $d = 3$

$$\sigma = k_{\mathrm{B}}Tn\mathcal{R}_{\mathrm{g}}2/\sqrt{\pi} \tag{2.84}$$

as shown below in Eq. (2.97).

In the dilute–semidilute scaling region, the surface tension for arbitrary inter-chain overlap $s = n\mathcal{R}_{\mathrm{g}}^d$ for chains in a good solvent is given by

(de Gennes 1979; des Cloizeaux and Jannink 1990; Schäfer 1998)

$$\sigma = k_{\mathrm{B}} T n \mathcal{R}_{\mathrm{g}} Y(s) \tag{2.85}$$

which is similar to the scaling law (2.3) for the osmotic pressure in the bulk solution.

While the universal scaling function Y for the dilute regime of small s can be expanded in a power series

$$Y \to Y_0 + sY_1 + \cdots \tag{2.86}$$

corresponding to a virial expansion, in the semidilute regime of large s the leading behavior is

$$Y \to Y_\infty s^{(1-\nu)/(d\nu-1)}, \quad s \to \infty \tag{2.87}$$

since, with this exponent,

$$\sigma \to k_{\mathrm{B}} T Y_\infty (n \mathcal{R}_{\mathrm{g}}^{1/\nu})^{(d-1)/(d-1/\nu)} \tag{2.88}$$

depends solely on the *monomer* density $\propto n\mathcal{R}_{\mathrm{g}}^{1/\nu}$ and not on the chain density n, as expected (de Gennes 1979) for strongly overlapping chains. In the semidilute limit $\sigma/k_{\mathrm{B}}T \propto \xi^{-(d-1)}$, where the screening length ξ is related to the monomer density by (de Gennes 1979; des Cloizeaux and Jannink 1990; Schäfer 1998)

$$n\mathcal{R}_{\mathrm{g}}^{1/\nu} \propto \xi^{-(d-1/\nu)} \tag{2.89}$$

This should be compared with the osmotic pressure behavior $X \propto s^{1/(d\nu-1)}$ and $\Pi/k_{\mathrm{B}}T \propto \xi^{-d}$ in the semidilute limit (de Gennes 1979; des Cloizeaux and Jannink 1990; Schäfer 1998).

A quantitative estimate of the scaling function Y in $d = 3$ spatial dimensions [where $\nu = 0.588$, see (2.24), and $(1-\nu)/(d\nu-1) = 0.539$] can be obtained (Maassen et al. 2001) from the "renormalized mean-field approximation", which is based on the field-theoretical renormalization group (Schäfer 1998). This leads to the approximate values

$$\begin{aligned} Y_0 &\approx 2/\sqrt{\pi} = 1.13 \\ Y_1 &\approx 3.29 \\ Y_\infty &\approx 3.38 \end{aligned} \tag{2.90}$$

and a complete scaling function that is in fair agreement with Monte Carlo simulations, as shown in Fig. 3 of Louis et al. (2002).

2.5 Spherical Particle in a Polymer Solution

2.5.1 Ideal Polymers

Here we consider a spherical particle in a solution of ideal polymers in $d = 3$.

2.5.1.1 End Density

For the bulk-normalized end density near a spherical particle of radius R and centered at the origin (Lipowsky 1995),

$$\mathcal{E}(\boldsymbol{r}) = \int_{(r'>R)} \mathrm{d}^3 r'\, Z(\boldsymbol{r}, \boldsymbol{r}') = 1 - \frac{R}{r}\,\mathrm{erfc}\left(\frac{r-R}{\sqrt{4L}}\right) \tag{2.91}$$

where

$$\mathrm{erfc}(x) = 1 - \mathrm{erf}(x) \tag{2.92}$$

is the complementary error function. This expression satisfies the diffusion equation in (2.36), the initial condition (2.45), and the Dirichlet boundary condition as in (2.38) at the particle surface $r = R$.

Let us compare two limits of this expression. For $R \to \infty$ with the distance from the surface $r - R \equiv z$ fixed, Eq. (2.91) reduces to the half-space result of Eq. (2.52). For R and r fixed and $L \equiv \mathcal{R}_{\mathrm{g}}^2 \to \infty$,

$$\mathcal{E}(\boldsymbol{r}) \to 1 - \frac{R}{r} \tag{2.93}$$

Note that the width of the depletion zone is of the order of R, while the width is of order $\mathcal{R}_{\mathrm{g}}$ for a large particle or a planar wall. This illustrates the crucial role of the particle-to-polymer size ratio $R/\mathcal{R}_{\mathrm{g}}$.

2.5.1.2 Free Energy of Immersion

On immersing a spherical particle in a dilute solution of $\mathcal{N}$ ideal or real polymer chains in a large volume V, the polymer free energy changes by

$$\frac{F}{k_{\mathrm{B}}T} = -\mathcal{N}\ln\frac{\int_{V\setminus S}\mathrm{d}^3 r\,\mathcal{E}(\boldsymbol{r})}{\int_V \mathrm{d}^3 r\,\mathcal{E}_{\mathrm{b}}(\boldsymbol{r})} = -\mathcal{N}\ln\left[1 - \frac{\int_V \mathrm{d}^3 r\,(\mathcal{E}_{\mathrm{b}}(\boldsymbol{r}) - \mathcal{E}(\boldsymbol{r}))}{\int_V \mathrm{d}^3 r\,\mathcal{E}_{\mathrm{b}}(\boldsymbol{r})}\right] \tag{2.94}$$

since the difference F of free energies with and without the particle and per $k_{\rm B}T$ equals minus the logarithm of the ratio of the partition functions. Here $V\backslash S$ denotes the outer space of the sphere, and $\mathcal{E}(\boldsymbol{r})$ is the bulk-normalized partition function of the chain with one end fixed in the presence of the sphere, while the corresponding partition function $\mathcal{E}_{\rm b}(\boldsymbol{r})$ in the bulk is equal to unity. Expanding the logarithm in Eq. (2.94) and using the vanishing of $\mathcal{E}(\boldsymbol{r})$ for $\boldsymbol{r}$ inside the sphere, we find

$$\frac{F}{k_{\rm B}T} = n\left\{\tfrac{4}{3}\pi R^3 + 4\pi\int_R^\infty {\rm d}r\, r^2[1-\mathcal{E}(\boldsymbol{r})]\right\}, \quad n = \frac{\mathcal{N}}{V} \tag{2.95}$$

On using the ideal-chain result (2.91) and introducing the integration variable $x = (r-R)/\sqrt{4L}$, the integral in (2.95) becomes

$$4\pi\int_R^\infty = 4\pi R\times 4L\int_0^\infty {\rm d}x\left(x+\frac{R}{\sqrt{4L}}\right){\rm erfc}(x) = 4\pi RL + 8\sqrt{\pi}R^2\sqrt{L} \tag{2.96}$$

and (Jansons and Phillips 1990; Eisenriegler et al. 1996)

$$F = p_0 4\pi R^3\left[\frac{1}{3}+\frac{2}{\sqrt{\pi}}\frac{\sqrt{L}}{R}+\frac{L}{R^2}\right] \tag{2.97}$$

where

$$p_0 = k_{\rm B}Tn \tag{2.98}$$

is the ideal-gas pressure of the polymer solution. Equation (2.97) applies for arbitrary particle-to-polymer size ratio $R/\sqrt{L} = R/\mathcal{R}_{\rm g}$.

Compare Eq. (2.97) with the corresponding free energy in the simple model of Asakura and Oosawa (Asakura and Oosawa 1954; Asakura and Oosawa 1958), in which polymer flexibility is neglected and a free polymer interacts with the colloid like a hard sphere of radius $\tilde{\mathcal{R}}$, which is of the order of $\mathcal{R}_{\rm g}$ (see Fig. 2.2). In this model (denoted by "phs"), instead of Eq. (2.91), the partition function $\mathcal{E}(\boldsymbol{r})$ equals unity for $r > R+\tilde{\mathcal{R}}$ and vanishes for $r < R+\tilde{\mathcal{R}}$, so that the fraction inside the square brackets in Eq. (2.94) becomes

$$\frac{\int_V {\rm d}^3r\,(\mathcal{E}_{\rm b}(\boldsymbol{r})-\mathcal{E}(\boldsymbol{r}))}{\int_V {\rm d}^3r\,\mathcal{E}_{\rm b}(\boldsymbol{r})} = \frac{\frac{4}{3}\pi(R+\tilde{\mathcal{R}})^3}{V} \tag{2.99}$$

and the free-energy cost is given by

$$F_{\rm phs} = p_0\,4\pi(\tfrac{1}{3}R^3 + R^2\tilde{\mathcal{R}} + R\tilde{\mathcal{R}}^2 + \tfrac{1}{3}\tilde{\mathcal{R}}^3) \tag{2.100}$$

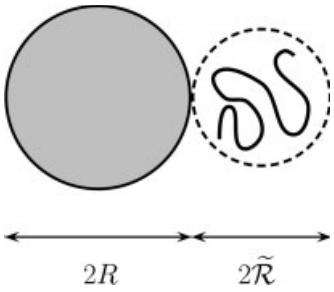

Fig. 2.2 Colloidal particle interacting with a rigid polymer sphere.

On comparing Eq. (2.100) with Eq. (2.97), one finds that the leading term is correctly reproduced for large particle-to-polymer size ratio $R/\mathcal{R}_{\rm g} \gg 1$. Even the leading correction, which corresponds to the surface tension (2.84), is reproduced if we choose an Asakura–Oosawa radius of

$$\tilde{\mathcal{R}} = 2\sqrt{L/\pi} \equiv 2\mathcal{R}_{\rm g}/\sqrt{\pi} \tag{2.101}$$

However, for small size ratio $R/\mathcal{R}_{\rm g} \ll 1$, the Asakura–Oosawa model leads to a free-energy cost $\propto \tilde{\mathcal{R}}^3 \propto \mathcal{R}_{\rm g}^3$, which is much larger than the free-energy cost $\propto R\mathcal{R}_{\rm g}^2$ for flexible chains. This is not surprising, since a flexible polymer chain can coil around the small particle, and the entropy loss vanishes for $R \to 0$, while in the case of a rigid polymer sphere there is a finite entropy loss even in the case of a point particle with $R = 0$ (see Fig. 2.3).

In the expression (2.95) for the immersion free energy, the end density $\mathcal{E}$ could be replaced[10] by the monomer density $\mathcal{M}$, both bulk-normalized. It is

Fig. 2.3 Small colloidal particle interacting with a rigid polymer (left) and with a flexible polymer (right).

10) Instead of integrating the chain partition function with one end fixed over the normalization volume, one could also integrate the partition function for a fixed position of the mid-monomer, or of any given monomer in the chain, in order to obtain the ratio of partition functions with and without the particle in Eq. (2.94). In the bulk, all these fixed monomer partition functions are equal, due to translational invariance. Thus, in (2.95) one may replace $\mathcal{E}$ by the average $\mathcal{M}$ of the bulk-normalized partition functions with one fixed monomer.

the (positive) mean number

$$[-\Delta\mathcal{N}]_n = n\int \mathrm{d}\boldsymbol{r}[\mathcal{E}_{\text{without particle}}(\boldsymbol{r}) - \mathcal{E}_{\text{with particle}}(\boldsymbol{r})]$$
$$= n\int \mathrm{d}\boldsymbol{r}[\mathcal{M}_{\text{without particle}}(\boldsymbol{r}) - \mathcal{M}_{\text{with particle}}(\boldsymbol{r})] \tag{2.102}$$

of chains removed on immersing the particle in the solution, for a given chain density n in the bulk, which determines

$$\frac{F}{k_{\mathrm{B}}T} = [-\Delta\mathcal{N}]_n \tag{2.103}$$

if the solution is dilute.[11)]

2.5.1.3 Monomer Density Profile and the Density–Pressure Relation

In order to calculate the monomer density $\mathcal{M}$ near the surface of the sphere, one may use the form

$$\chi(t;\boldsymbol{r}) = \frac{1}{t}\left[1 - \frac{R}{r}\,\mathrm{e}^{-(r-R)\sqrt{t}}\right] \tag{2.104}$$

of the "susceptibility" in (2.48) in the presence of the sphere, which corresponds to $\mathcal{E}$ in Eq. (2.91). Expanding about $r = R$ and using (2.47) leads to

$$\mathcal{M} \to \mathcal{M}^{(\mathrm{as})} = \frac{1}{L}(r-R)^2\mathcal{L}_{t\to L}\left[\frac{1}{\sqrt{t}} + \frac{1}{tR}\right]^2$$
$$= \frac{1}{L}(r-R)^2\left\{1 + \frac{4}{R}\sqrt{\frac{L}{\pi}} + \frac{L}{R^2}\right\} \tag{2.105}$$

in the asymptotic (as) scaling region $r \to R$. This is indeed proportional to the pressure

$$p \equiv \frac{1}{4\pi R^2}\frac{\mathrm{d}F}{\mathrm{d}R} = p_0\left[1 + \frac{4}{R}\sqrt{\frac{L}{\pi}} + \frac{L}{R^2}\right] \tag{2.106}$$

11) Equations (2.103) and (2.132) are consistent with the more general expression

$$F = \int_0^n \mathrm{d}n'\,(\mathrm{d}\Pi(n')/\mathrm{d}n')\,[-\Delta\mathcal{N}]_{n'}/n'$$

for the immersion free energy of the particle, which also applies to polymer solutions with *non-vanishing* inter-chain overlap and bulk pressure Π [see Louis et al. (2002) and references cited therein]. In the dilute region, $\mathrm{d}\Pi/\mathrm{d}n' = k_{\mathrm{B}}T$ and $[-\Delta\mathcal{N}]_{n'}/n'$ are independent of n', and Eqs. (2.103) and (2.132) are recovered.

that the polymer solution exerts on the sphere surface. Here F is the free energy in Eq. (2.97), and p_0 is the ideal-gas pressure in Eq. (2.98).

The factor of proportionality depends, of course, on the distance $r-R$ from the surface, but is independent of the surface curvature. It is consistent with the density–pressure relation, with the form

$$(\mathcal{R}_{\mathrm{g}})^{1/\nu} n\mathcal{M}^{(\mathrm{as})} = B_{\mathrm{g}} \frac{p_{(\mathrm{fc,S})}}{k_{\mathrm{B}}T} (r-R)^{1/\nu} \tag{2.107}$$

(Eisenriegler 1997) as in (2.64), if we use the ideal-chain expressions $\mathcal{R}_{\mathrm{g}}^2 = L$, $\nu = 1/2$, and $B_{\mathrm{g}} = 1$ in $d = 3$. Here the subscript (fc,S) stands for "free chains outside a sphere".

For *arbitrary* distance from the surface, the monomer density follows from Eqs. (2.47) and (2.104) as (Taniguchi et al. 1992)

$$\mathcal{M} = 1 + 4[-2(R/r)\,\mathrm{i}^2\mathrm{erfc}(y'/2) + (R/r)^2\,\mathrm{i}^2\mathrm{erfc}(y')] \tag{2.108}$$

with $y' = (r-R)/\sqrt{L}$. The planar wall expression (2.55) is contained in (2.108) as a special case.

2.5.2 Small-Sphere Expansion

Particles with large size ratio can be investigated by means of small-curvature expansions of the Helfrich or Derjaguin type [see e.g. Eisenriegler (1997), Hanke et al. (1999), Bringer et al. (1999)]. Here we concentrate on the opposite case of *small* spherical particles, which, while large on a microscopic scale, are much smaller than the polymer size $\mathcal{R}_{\mathrm{g}}$ and other characteristic mesoscopic lengths.

The effect of the particle on the chain can be described in terms of a δ-function potential, located at the center $\boldsymbol{r}_{\mathrm{S}}$ of the particle, which weakly repels the monomers. This implies that the Boltzmann weight W_{S} for the chain that arises from the presence of the sphere tends, for small R, to (Eisenriegler et al. 1996)

$$W_{\mathrm{S}}[\boldsymbol{r}_j] \to 1 - A_{\mathrm{g}} R^{d-1/\nu} m(\boldsymbol{r}_{\mathrm{S}}) \tag{2.109}$$

where the $[r_j]$-dependent modified monomer density $m(\boldsymbol{r})$, with a scaling dimension equal to its inverse length dimension $d-1/\nu$, is defined in Eq. (2.63). The exponent of R in (2.109) follows from comparing scaling dimensions, and the amplitude A_{g} is dimensionless and universal (Hanke et al. 1999; Eisenriegler 2000). The potential is "weak" for small R, since $d - 1/\nu > 0$.

For ideal chains (Eisenriegler et al. 1996; Hanke et al. 1999; Eisenriegler 2000)

$$A_{\mathrm{g}} = \frac{12\pi^{d/2}}{d\,\Gamma(\frac{1}{2}(d-2))} \tag{2.110}$$

i.e. $A_{\mathrm{g}} = 4\pi$ in $d = 3$, and for chains in a good solvent

$$A_{\mathrm{g}} \approx 18, \quad d = 3 \tag{2.111}$$

As an application of Eq. (2.109), consider the bulk-normalized end density in a dilute polymer solution with an embedded sphere

$$\mathcal{E}(\boldsymbol{r}) = \frac{\int \mathrm{d}\boldsymbol{r}'\, Z_{N,\mathrm{S}}(\boldsymbol{r},\boldsymbol{r}')}{\int \mathrm{d}\boldsymbol{r}'\, Z_{N,\mathrm{b}}(\boldsymbol{r},\boldsymbol{r}')} = \{W_{\mathrm{S}}\}_{(\boldsymbol{r},\mathrm{b})} \tag{2.112}$$

where the average $\{\cdots\}_{(\boldsymbol{r},\mathrm{b})}$ is over all configurations of a single chain with one end fixed at the point $\boldsymbol{r}$ in the bulk. Using (2.109),

$$\mathcal{E}(\boldsymbol{r}) \to 1 - A_{\mathrm{g}}\{m(\boldsymbol{r}_{\mathrm{S}})\}_{(\boldsymbol{r},\mathrm{b})} \tag{2.113}$$

For an ideal chain Eq. (2.63) leads to

$$\begin{aligned}\{m(\boldsymbol{r}_{\mathrm{S}})\}_{(\boldsymbol{r},\mathrm{b})} &= \frac{\mathcal{R}_{\mathrm{g}}^2}{N}\,\frac{\sum_{j=1}^{N} Z_{j,\mathrm{b}}(\boldsymbol{r},\boldsymbol{r}_{\mathrm{S}})\int \mathrm{d}\boldsymbol{r}'\, Z_{N-j,\mathrm{b}}(\boldsymbol{r}_{\mathrm{S}},\boldsymbol{r}')}{\int \mathrm{d}\boldsymbol{r}'\, Z_{N,\mathrm{b}}(\boldsymbol{r},\boldsymbol{r}')} \\ &= \frac{\mathcal{R}_{\mathrm{g}}^2}{L}\int_0^L \mathrm{d}L'\, Z_{\mathrm{b}}(L';\boldsymbol{r},\boldsymbol{r}_{\mathrm{S}})\end{aligned} \tag{2.114}$$

In the regime $\mathcal{R}_{\mathrm{g}}^2 \propto L \gg (\boldsymbol{r}-\boldsymbol{r}_{\mathrm{S}})^2$ considered in (2.93), we replace the upper limit of integration L by ∞, and (2.42) yields

$$\{m(\boldsymbol{r}_{\mathrm{S}})\}_{(\boldsymbol{r},\mathrm{b})} \to \frac{\mathcal{R}_{\mathrm{g}}^2}{L}\,\frac{\tilde{S}_d}{|\boldsymbol{r}-\boldsymbol{r}_{\mathrm{S}}|^{d-2}}, \quad \tilde{S}_d = \frac{\Gamma(\frac{1}{2}(d-2))}{4\pi^{d/2}} \tag{2.115}$$

Here the second factor is the Gaussian propagator at the critical point, i.e. the solution of (2.39) in the bulk for vanishing Laplace variable t. For $d = 3$, where $A_{\mathrm{g}} = 4\pi$, $\tilde{S}_d = 1/(4\pi)$, and $\mathcal{R}_{\mathrm{g}}^2/L = 1$, the prediction (2.113), (2.115) of the small-sphere expansion (2.109) is consistent with the result (2.93) of the direct calculation.

As a second application, consider the free-energy cost F of immersing a small spherical particle in a bulk solution. Since the change in free energy due to a weak perturbation with a Boltzmann factor W close to unity equals,

apart from a factor $-k_{\mathrm{B}}T$, the unperturbed average [over free chains in the bulk, denoted "(fc,b)"] of the perturbation $W-1$,

$$\frac{F}{k_{\mathrm{B}}T} \to -\{W-1\}_{(\mathrm{fc,b})} = A_{\mathrm{g}} R^{d-1/\nu} \mathcal{R}_{\mathrm{g}}^{1/\nu} n \tag{2.116}$$

This relation is quite general and also applies to dilute and semidilute solutions in a good solvent. For a solution of ideal chains in $d=3$, it reduces to the result $F \to k_{\mathrm{B}}Tn\,4\pi RL$ in (2.97) for a small sphere.

The full power of small-particle expansions such as (2.109) will become apparent in Sections 2.7 to 2.9, where we study the polymer-induced interaction of the small particle with a wall or another particle.

The replacement (2.109) has a field-theoretical counterpart. To see this, consider for a single chain the fraction

$$Z_{N,\mathrm{S}}(\boldsymbol{r}_{\mathrm{A}}, \boldsymbol{r}_{\mathrm{B}}) / Z_{N,\mathrm{b}}(\boldsymbol{r}_{\mathrm{A}}, \boldsymbol{r}_{\mathrm{B}}) = \{W_{\mathrm{S}}\}_{(\boldsymbol{r}_{\mathrm{A}}, \boldsymbol{r}_{\mathrm{B}};\mathrm{b})} \tag{2.117}$$

of chain configurations with fixed ends at $\boldsymbol{r}_{\mathrm{A}}$ and $\boldsymbol{r}_{\mathrm{B}}$ that survive on immersing a spherical particle, and assume that $R \ll \mathcal{R}_{\mathrm{g}},\ |\boldsymbol{r}_{\mathrm{A}} - \boldsymbol{r}_{\mathrm{S}}|,\ |\boldsymbol{r}_{\mathrm{B}} - \boldsymbol{r}_{\mathrm{S}}|$, so that (2.109) can be used. Rewriting $\{m\}_{(\boldsymbol{r}_{\mathrm{A}}, \boldsymbol{r}_{\mathrm{B}};\mathrm{b})} = \mathcal{R}_{\mathrm{g}}^{1/\nu} \{F_{\mathrm{m}}\}_{(\boldsymbol{r}_{\mathrm{A}}, \boldsymbol{r}_{\mathrm{B}};\mathrm{b})}$ by means of (2.17) and $Z_{N,\mathrm{b}}$ by (2.14) in terms of the field theory, one finds

$$Z_{N,\mathrm{S}}(\boldsymbol{r}_{\mathrm{A}}, \boldsymbol{r}_{\mathrm{B}}) \to \mathcal{L} \left\langle [1 - A_{\mathrm{g}} R^{d-1/\nu} \Psi_{\mathrm{g}}(\boldsymbol{r}_{\mathrm{S}})] \cdot \varphi_{\mathrm{AB}}^{(1)} \right\rangle_{\mathrm{b}} \tag{2.118}$$

with Ψ_{g} from (2.68). This shows that the Boltzmann factor $\exp(-\mathcal{H}_{\mathrm{S}})$ for the field $\boldsymbol{\Phi}$ that arises from the presence of the sphere tends for small R to

$$\exp(-\mathcal{H}_{\mathrm{S}}[\boldsymbol{\Phi}]) \propto 1 - A_{\mathrm{g}} R^{d-1/\nu} \Psi_{\mathrm{g}}(\boldsymbol{r}_{\mathrm{S}}) \tag{2.119}$$

Thus, as expected in the Landau–Ginzburg–Wilson field theory, a small mesoscopic sphere with Dirichlet condition (2.34) [corresponding to a "free spin" boundary condition in a model for magnetism (Binder 1986; Diehl 1986; Diehl 1997)] at its surface acts, at distant points, like a temperature that is enhanced in a microscopic region around $\boldsymbol{r}_{\mathrm{S}}$, as described by the point operator $\Psi_{\mathrm{g}} \propto \boldsymbol{\Phi}^2$ in Eq. (2.68).

2.5.3
Polymer Solution of Arbitrary Overlap

On immersing a sphere in a polymer solution in a good solvent in $d = 3$ spatial dimensions, the free-energy cost F depends, apart from the size ratio $R/\mathcal{R}_{\rm g}$, on the degree of overlap $s = n\mathcal{R}_{\rm g}^3$ between the chains (see Fig. 2.4). While for a large particle $F = \frac{4}{3}\pi R^3 \Pi$, with Π the bulk osmotic pressure (2.3), for a small particle the expression in (2.116) with $A_{\rm g}$ from (2.111) applies. Thus $F/k_{\rm B}T$ displays a crossover between the simple power laws $\propto R^3 n, \propto (R/\xi)^3$, and $\propto n\mathcal{R}_{\rm g}^{1/\nu} R^{3-1/\nu}$, which apply in the lower and upper left corners, and in the region of large $\mathcal{R}_{\rm g}/R$, respectively, of Fig. 2.4. The smooth crossovers between the three power laws occur where $\mathcal{R}_{\rm g}/\xi$, ξ/R, or $R/\mathcal{R}_{\rm g}$ are of order unity (see the dashed lines in Fig. 2.4).

Applying the "renormalized mean-field approximation" of Maassen et al. (2001) to a sphere in a polymer solution with an inter-chain overlap of $\frac{4}{3}\pi\mathcal{R}_{\rm g}^3 n = 1.16$, i.e. where the chains just begin to overlap, leads to the depen-

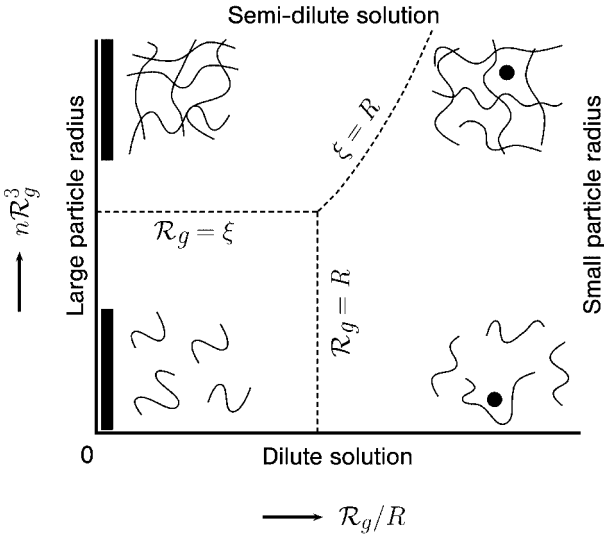

Fig. 2.4 Various limits of a single spherical particle in a solution of non-adsorbing polymers in a good solvent. The sphere becomes a *planar wall* for vanishing $\mathcal{R}_{\rm g}/R$ (i.e. for points on the vertical axis). It becomes a *"small" sphere*, with radius much smaller than the characteristic mesoscopic polymer lengths (such as the radius of gyration $\mathcal{R}_{\rm g}$ of a polymer chain in the dilute solution or the mesh size ξ in the semidilute solution), as $\mathcal{R}_{\rm g}/R$ becomes large with the inter-chain overlap $n\mathcal{R}_{\rm g}^3$ kept fixed. The following limits are shown: planar wall in a dilute solution (lower left corner); planar wall in a semidilute solution (upper left corner); small sphere in a dilute solution (lower right corner); and small sphere in a semidilute solution (upper right corner). The dashed lines are crossover regions.

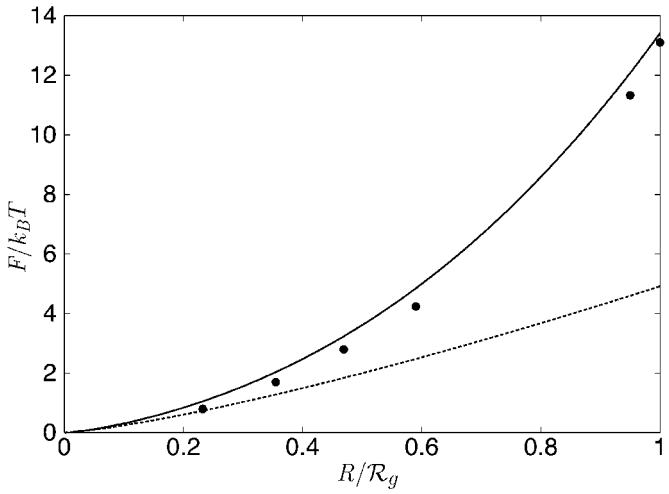

Fig. 2.5 Size-ratio dependence of the free-energy cost F for an inter-chain overlap of $\frac{4}{3}\pi\mathcal{R}_{\rm g}^3 n = 1.16$. The "renormalized mean-field approximation" (full line) is compared with Monte Carlo results (black dots). The dashed line shows the asymptotic behavior for small spheres.

dence[12] of $F/k_{\rm B}T$ on the size ratio $R/\mathcal{R}_{\rm g}$ shown by the full line in Fig. 2.5. This agrees quite well with the Monte Carlo results from Fig. 8 in Louis et al. (2002), shown as black dots. The dashed line in Fig. 2.5 shows the result of the small-sphere expansion (2.116).

12) R. Maassen, E. Eisenriegler, and A. Bringer, unpublished. Extending the discussion in Section III of Maassen et al. (2001) to a sphere of arbitrary mesoscopic radius R, Eqs. (3.2) to (3.5) there are supplemented by $R = \mu^{-1}R_r$ and $R_r \to \bar{R}_r(\lambda) = R_r\,{\rm e}^{-\lambda}$, and Eq. (3.10) is replaced by

$$\frac{\rho_0}{\bar{L}_r} + \zeta_0\bar{n}_r\bar{L}_r + \frac{R_0}{\bar{R}_r^2} = 1$$

The analogues of Eqs. (3.6) to (3.9) and (3.11) to (3.14) for the immersion free energy of the sphere are

$$F/k_{\rm B}T = \mathcal{F}(n_r, L_r, R_r, u_r) = \mathcal{F}(\bar{n}_r, \bar{L}_r, \bar{R}_r, u_{r,{\rm FP}})$$

and

$$\mathcal{F}(\bar{n}_r, \bar{L}_r, \bar{R}_r, u_{r,{\rm FP}}) \approx \mathcal{F}_{\rm tree}(\bar{n}_r, \bar{L}_r, \bar{R}_r, u_{r,{\rm FP}})$$

The value $R_0 = 0.18$ has been chosen so that, for $R \ll \mathcal{R}_{\rm g}, \xi$, the result

$$4\pi(\rho_0/R_0)^{1-1/\nu} n \mathcal{R}_{\rm g}^{1/\nu} R^{3-1/\nu}$$

for $\mathcal{F}_{\rm tree}$ is consistent with (2.116) and (2.111) from the small-sphere expansion.

2.6
Parallel Plates and Plate–Wall Interaction

2.6.1
Chain Trapped Between Two Parallel Plates

2.6.1.1 Force on the Plates

Consider a single chain confined between two parallel planar walls (plates) with separation D. On decreasing D, the partition function of the chain decreases, and its free energy increases. The chain exerts a disjoining force f on each of the two plates, with

$$f/k_{\mathrm{B}}T = D^{-1}Y(D/\mathcal{R}_{\mathrm{g}}) \tag{2.120}$$

in the scaling region. For a wide slit, $Y \to 1$, and

$$f/k_{\mathrm{B}}T \to D^{-1}, \quad \mathcal{R}_{\mathrm{g}} \ll D \tag{2.121}$$

since this limit corresponds to the half-space with a polymer density $n = 1/(DA)$, if we confine the chain to a large but finite lateral area $A \gg D^{d-1}$. For a narrow slit

$$Y(D/\mathcal{R}_{\mathrm{g}}) \propto (D/\mathcal{R}_{\mathrm{g}})^{-1/\nu}, \quad \mathcal{R}_{\mathrm{g}} \gg D \tag{2.122}$$

since $f/k_{\mathrm{B}}T \propto N$ (see de Gennes 1979).

Note the difference in the $N \to \infty$ behavior of $f/k_{\mathrm{B}}T$ for a chain trapped between parallel walls and a chain fixed at a distance z_{A} from the boundary wall of a half-space. While the force f is $\propto N$ in the first case, in the half-space the long chain can avoid the boundary wall, and f in Eq. (2.76) is *independent* of N.

In terms of the ratio

$$U(D/\mathcal{R}_{\mathrm{g}}) = D^{-1}\int_0^D \mathrm{d}z\, \mathcal{E}_{\mathrm{film}}(z) \tag{2.123}$$

of the partition function of a single chain between two plates, averaged over the distance z of its fixed end from one plate, to the partition function of the chain with fixed end in the bulk, the force reads

$$\frac{f}{k_{\mathrm{B}}T} = \frac{\partial}{\partial D}\ln(DU) \tag{2.124}$$

i.e. $Y(y)$ equals $1 + \partial \ln U/\partial \ln y$.

2.6.1.2 Ideal Chain

For an ideal chain, the function U can be calculated, e.g. via (2.44), from the Laplace transform

$$G_{\rm film}(\boldsymbol{r}_\parallel, z; \boldsymbol{r}'_\parallel, z') = \int \frac{{\rm d}^{d-1}p}{(2\pi)^{d-1}}\, {\rm e}^{{\rm i}\boldsymbol{p}(\boldsymbol{r}-\boldsymbol{r}')_\parallel}\, \frac{\sinh[wz_{\rm min}]\sinh[w(D-z_{\rm max})]}{w\sinh(wD)} \tag{2.125}$$

of the partition function $Z_{\rm film}(\boldsymbol{r}, \boldsymbol{r}')$ of a chain confined between two parallel repulsive plates with the ends fixed at $\boldsymbol{r}$ and $\boldsymbol{r}'$. Here w is from Eq. (2.57), and $z_{\rm min} = \min(z, z')$, $z_{\rm max} = \max(z, z')$. This leads to

$$\begin{aligned} DU &= \mathcal{L}\int {\rm d}(\boldsymbol{r}-\boldsymbol{r}')_\parallel \int_0^D {\rm d}z \int_0^D {\rm d}z'\, G_{\rm film} \\ &= \mathcal{L}\left(\frac{D}{t} - \frac{2}{t^{3/2}} + \frac{4}{t^{3/2}}\frac{1}{1+{\rm e}^{Dt^{1/2}}}\right) \\ &= D\sum_{j=1,3,5,\ldots} \frac{8}{(\pi j)^2}\, {\rm e}^{-(\pi j)^2 L/D^2} \end{aligned} \tag{2.126}$$

with the limits

$$U \to \left(1,\ \frac{8}{\pi^2}\, {\rm e}^{-\pi^2 L/D^2}\right) \tag{2.127}$$

for ($\mathcal{R}_{\rm g} \ll D,\ \mathcal{R}_{\rm g} \gg D$), which are consistent with (2.121) and (2.122).

2.6.1.3 Monomer Density Profile and Density–Force Relation

The modified density profile for the number of monomers of the trapped chain has the scaling form

$$\begin{aligned} &\int {\rm d}^{d-1}r_\parallel \, \{m(\boldsymbol{r}_\parallel, z)\}_{\rm (one\ chain\ in\ film)} \\ &\qquad = (\mathcal{R}_{\rm g}^{1/\nu}/D) X_{\rm g}(z/\mathcal{R}_{\rm g}, D/\mathcal{R}_{\rm g}) \end{aligned} \tag{2.128}$$

valid if D, $\mathcal{R}_{\rm g}$, and the distance z from one of the two walls are large compared with the microscopic lengths.

For a wide slit with $\mathcal{R}_{\rm g} \ll D$,

$$X_{\rm g} \to \mathcal{M}_{\rm h}(z/\mathcal{R}_{\rm g}), \quad z \le D/2 \tag{2.129}$$

is determined by the bulk-normalized half-space profile $\mathcal{M} = \mathcal{M}_{\rm h}$ introduced in Eq. (2.59). The density–force relation (2.65) is fulfilled, since, due to Eq. (2.62), the left-hand side of (2.128) for $z \ll \mathcal{R}_{\rm g}$ tends to $B_{\rm g} z^{1/\nu}/D$, which equals $B_{\rm g} z^{1/\nu} f/k_{\rm B}T$ [see (2.121)].

For a narrow slit with $\mathcal{R}_{\rm g} \gg D$, consider for simplicity an ideal polymer chain, where

$$X_{\rm g} \to 2\sin^2(z\pi/D), \quad \mathcal{R}_{\rm g} \gg D \tag{2.130}$$

As expected, the result is independent of $\mathcal{R}_{\rm g}$ and readily follows via Eqs. (2.47) and (2.48) from a representation of the propagator or Green's function $G_{\rm film}$ in (2.125) in terms of eigenfunctions, in which the ground state dominates (de Gennes 1979). Thus the near-wall behavior of the left-hand side of (2.128) is given by $(\mathcal{R}_{\rm g}^{1/\nu}/D)2(z\pi)^2/D^2$ and again equals $B_{\rm g} z^{1/\nu} f/k_{\rm B}T$, since $f/k_{\rm B}T \to \partial_D(-\pi^2 L/D^2)$ in this limit due to (2.124) and (2.127), and since $B_{\rm g} = 1$, $\nu = 1/2$, and $\mathcal{R}_{\rm g}^{1/\nu} = L$ for ideal chains in $d = 3$.

For excluded-volume interactions between chain monomers, the density profile in a narrow slit in $d = 2$ (strip) and $d = 3$ (two parallel walls) has been obtained and the density–force relation tested by means of Monte Carlo simulations on hypercubic lattices [see Hsu and Grassberger (2003) and Hsu and Grassberger (2004)]. Coping with rather large corrections to scaling by choosing an appropriate ("Domb–Joyce") value for the excluded-volume strength, and allowing (de Gennes 1979) for a small non-vanishing extrapolation length, Hsu and Grassberger (2003) and Hsu and Grassberger (2004) find the values

$$B = (2.04 \pm 0.04,\ 1.70 \pm 0.08), \quad d = (2,\ 3) \tag{2.131}$$

in two and three spatial dimensions for the quantity
$B = [\mathcal{R}_{\rm ee}^2/(d\mathcal{R}_{\rm g}^2)]^{1/(2\nu)} B_{\rm g}$, which determines the universal amplitude $B_{\rm g}$ in the density–pressure relation (2.65). The value for $d = 2$ is consistent with the field-theoretical prediction $B = 2.01$ and for $d = 3$ not far from the estimate $B = 1.85$ based on a first-order expansion in $\varepsilon = 4 - d$ [see Eisenriegler (1997) and Eisenriegler (1998)]. The estimate (2.74) of $B_{\rm g}$ follows from $B = 1.85$ and the universal amplitude $6\mathcal{R}_{\rm g}^2/\mathcal{R}_{\rm ee}^2 = 0.959$ in $d = 3$ given by Schäfer (1998).

2.6.2
Plate–Wall Interaction

Inserting a particle in a dilute solution of polymers (with or without excluded-volume interaction) in the half-space bounded by a planar wall increases the

polymer free energy by

$$F = p_0 \int \mathrm{d}\boldsymbol{r}\, [\mathcal{E}_{\text{without particle}}(\boldsymbol{r}) - \mathcal{E}_{\text{with particle}}(\boldsymbol{r})] \tag{2.132}$$

where the $\mathcal{E}$ are the bulk-normalized end densities, the integral is over the half-space (with $\mathcal{E}_{\text{with particle}}$ vanishing inside the particle), and p_0 is the ideal-gas pressure in Eq. (2.98). The right-hand side of Eq. (2.132) equals, apart from a factor $k_\mathrm{B}T$, the number $[-\Delta\mathcal{N}]_n$ of chains removed on inserting the particle (cf. footnotes 10 and 11), and the derivation is similar to that of Eqs. (2.94), (2.102), and (2.103).

The free energy of interaction

$$\delta F = F - \lim_{D\to\infty} F \tag{2.133}$$

between the particle and the wall follows from F on subtracting its value for infinite distance, i.e. the free energy it costs to immerse the particle in bulk solution.

We now immerse a particle with the shape of an (infinitely thin) plate that is oriented parallel to the wall, with area $\mathcal{A}$ and a linear dimension $\mathcal{A}^{1/(d-1)}$ that is much larger than $\mathcal{R}_\mathrm{g}$ and the distance D between wall and plate. Then one may disregard edge effects, $\mathcal{E}_{\text{with particle}}(\boldsymbol{r}_\parallel, z)$ between the wall and the plate is independent of $\boldsymbol{r}_\parallel$ and equal to $\mathcal{E}_{\text{film}}$ of the previous subsection, and the free-energy cost per unit area is

$$F/\mathcal{A} = p_0 \left[D - \int_0^D \mathrm{d}z\, \mathcal{E}_{\text{film}}(z) \right] = p_0 D(1-U) \tag{2.134}$$

The free-energy difference in this equation *increases* for increasing D, and the force per unit area $\partial_D F/\mathcal{A} = \partial_D \delta F/\mathcal{A}$ pushing the plate toward the wall is given by (Asakura and Oosawa 1954)

$$p_0\{1 - U - D\,\partial U/\partial D\} = p_0 - nDUf \tag{2.135}$$

where the force f of a single chain between plates is given by (2.124). The number of chains per unit area between the large plate and the wall equals $n\int_0^\infty \mathrm{d}z\, \mathcal{E}_{\text{film}} = nDU$, since it can be expressed by the number of chain ends via the bulk-normalized end density $\mathcal{E}$ and the number density n of chains in the bulk. Thus the force per unit area in the last expression of Eq. (2.135) is the difference of the ideal-gas pressure p_0 of the chains outside and the disjoining force per unit area $nDUf$ of the chains in between the wall and the plate.

For *ideal* chains, substituting Eq. (2.126) into (2.134) leads to the expression

$$\delta F/\mathcal{A} = -p\mathcal{L}\frac{4}{t^{3/2}}\frac{1}{1+\mathrm{e}^{Dt^{1/2}}} = -4pL^{1/2}\int\frac{\mathrm{d}\tau}{2\pi\mathrm{i}}\,\mathrm{e}^{\tau}\frac{1}{\tau^{3/2}}\frac{1}{1+\mathrm{e}^{\theta\tau^{1/2}}} \quad (2.136)$$

for the free energy of interaction between plate and wall per unit area. Here the integration path in the complex τ plane encircles the cut that extends from $\tau = -\infty$ to $\tau = 0$ counterclockwise, and the scaling variable $\theta = D/L^{1/2}$ equals $D/\mathcal{R}_{\mathrm{g}}$ in $d = 3$. Equation (2.136) implies the limiting behavior

$$\delta F/\mathcal{A} = -p_0\{2[2(L/\pi)^{1/2}] - D + \cdots,\ 16(L/\pi)^{1/2}\theta^{-2}\,\mathrm{e}^{-(\theta/2)^2}\} \quad (2.137)$$

for $\{D \ll L^{1/2},\ D \gg L^{1/2}\}$. This is consistent with the general results that for $D/\mathcal{R}_{\mathrm{g}} \to 0$ the force per unit area on the plate equals the bulk pressure p_0 and that $\delta F/\mathcal{A}$ equals minus twice the free energy per unit area due to a single boundary wall. For an ideal chain, this is $2p_0(L/\pi)^{1/2}$ (see (2.84) or the second term on the right-hand side of (2.97)).

2.7 Sphere–Wall Interaction

Here we consider a spherical particle (S) in a polymer solution in the half-space (h) bounded by a planar wall (w), as shown in Fig. 2.6.

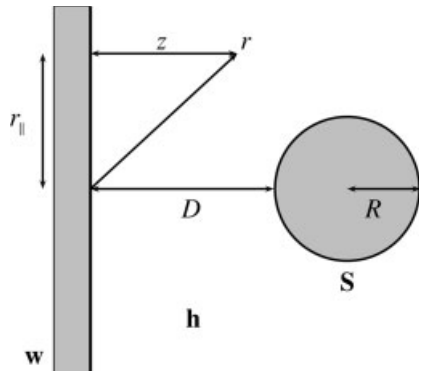

Fig. 2.6 A spherical particle (S) immersed in a polymer solution near a planar wall (w). The monomer and end densities of polymer chains (not shown) depend on the position $\boldsymbol{r} = (\boldsymbol{r}_\parallel, z)$ in the half-space (h).

2.7.1 Derjaguin Approximation for a Large Sphere

For a *large* spherical particle with $R \gg \mathcal{R}_{\rm g}, D$, one may apply the Derjaguin approximation, which replaces the sphere by a local superposition of immersed plates with local distance

$$\tilde{D} = D + \frac{r_{\parallel}^2}{2R} \tag{2.138}$$

from the wall and leads to the form

$$\delta F = \int \mathrm{d}^{d-1} r_{\parallel} \, [\delta F_{\rm p\|w}/\mathcal{A}]_{D\to\tilde{D}} \tag{2.139}$$

of the free energy of interaction between the sphere and the wall. Here $\delta F_{\rm p\|w}/\mathcal{A}$ is the free energy of interaction per unit area between the wall and a plate considered in Section 2.6.2. For ideal chains with $\delta F_{\rm p\|w}/\mathcal{A}$ given by Eq. (2.136), one finds

$$\delta F = -2p_0 R \mathcal{R}_{\rm g}^2 \mathcal{V}(D/\mathcal{R}_{\rm g}) \tag{2.140}$$

in $d = 3$, where

$$\mathcal{V}(\theta) = 4\pi \int \frac{\mathrm{d}\tau}{2\pi \mathrm{i}} \, \mathrm{e}^{\tau} \tau^{-2} \ln[1 + \exp(-\theta \tau^{1/2})] \tag{2.141}$$

implying that

$$\mathcal{V} \to \{4\pi \ln 2 - 4\sqrt{\pi}\,\theta + (\pi/2)\theta^2 + \cdots, \; 32\sqrt{\pi}\,\theta^{-3} \exp[-(\theta/2)^2]\} \tag{2.142}$$

for $\{D \ll \mathcal{R}_{\rm g}, \; D \gg \mathcal{R}_{\rm g}\}$.

The supposedly exact Derjaguin expressions (2.140) to (2.142) should be compared with the Asakura–Oosawa type (Asakura and Oosawa 1954; Asakura and Oosawa 1958) prediction $\delta F_{\rm phs} = -p_0 v$, where v is the volume of the overlap between a layer of width $\tilde{\mathcal{R}}$ around the sphere and a layer of width $2\tilde{\mathcal{R}}$ with center on the wall. Choosing the effective sphere radius $\tilde{\mathcal{R}}$ of the polymer as in Eq. (2.101) and defining $\mathcal{V}_{\rm phs}$ as in Eq. (2.140), one finds, for $R \gg \mathcal{R}_{\rm g}, D$, that

$$\mathcal{V}_{\rm phs} = [2\sqrt{2} - \sqrt{(\pi/2)}\,\theta]^2 \tag{2.143}$$

provided $D < 2\tilde{\mathcal{R}} \equiv 4\mathcal{R}_{\rm g}/\sqrt{\pi}$, and $\mathcal{V}_{\rm phs} = 0$ for $D \geq 2\tilde{\mathcal{R}}$. While the linear and quadratic terms in θ are *identical* to those in (2.142), $\mathcal{V}_{\rm phs}(0) = 8$ is about 10% smaller than $\mathcal{V}(0) = 8.71$. A comparison for arbitrary $D/\mathcal{R}_{\rm g}$ is shown in Fig. 2.7.

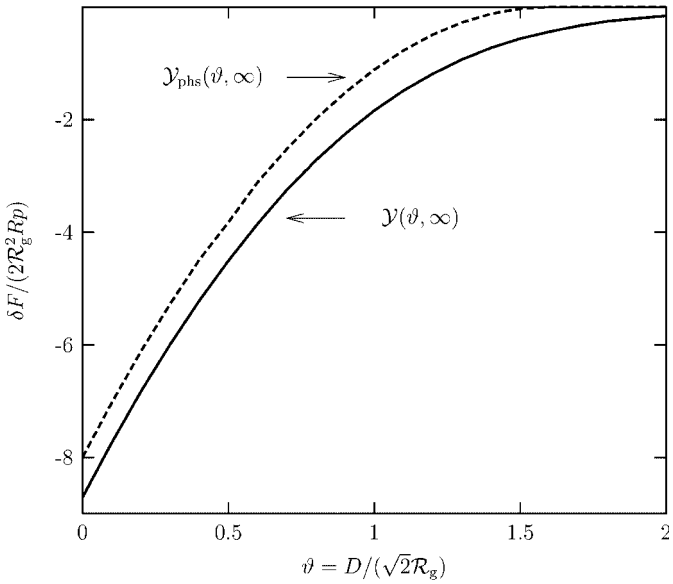

Fig. 2.7 Scaled interaction free energy $\delta F/(2\mathcal{R}_{\rm g}^2 Rp_0) = \mathcal{Y}(D/(\sqrt{2}\mathcal{R}_{\rm g}), R/(\sqrt{2}\mathcal{R}_{\rm g}))$ of a sphere and a wall for large particle-to-polymer size ratio $R/\mathcal{R}_{\rm g}$. The lower curve $\mathcal{Y}(\vartheta,\infty) = -\mathcal{V}(D/\mathcal{R}_{\rm g})$ is the exact Derjaguin result (2.141), and the upper curve $\mathcal{Y}_{\rm phs}(\vartheta,\infty) = -\mathcal{V}_{\rm phs}$ is the Asakura–Oosawa approximation (2.143).

2.7.2
Small-Particle Expansion for a Small Sphere

Immersing a small spherical particle with $R \ll D, \mathcal{R}_{\rm g}$ in a polymer solution in the half-space changes the polymer free energy per $k_{\rm B}T$ by

$$\frac{F}{k_{\rm B}T} = -\{W-1\}_{\rm (fc,hs)} = A_{\rm g} R^{d-1/\nu} \mathcal{R}_{\rm g}^{1/\nu} n \mathcal{M}_{\rm h}(z_{\rm S}) \tag{2.144}$$

where $\mathcal{M}_{\rm h}$ is the bulk-normalized monomer density in the half-space without the sphere, and $z_{\rm S} = D + (R/2)$ is the distance of the center of the sphere from the boundary wall. As in the derivation of (2.116), we have used here the small-sphere expansion (2.109) and the form on the left-hand side of (2.64) of the modified monomer density $\{m\}_{\rm (fc,hs)}$ in the half-space. Subtracting the free-energy change at $z_{\rm S} = \infty$, i.e. in the bulk, where $\mathcal{M}_{\rm h} = 1$, one finds

$$\delta F = -k_{\rm B}T n A_{\rm g} R^{d-1/\nu} \mathcal{R}_{\rm g}^{1/\nu} [1 - \mathcal{M}_{\rm h}(z_{\rm S})] \tag{2.145}$$

for the free energy of interaction (2.133) between sphere and wall. Equation (2.145) applies not only to a solution of ideal chains where $\mathcal{M}_{\rm h}$ is given by

(2.55) but also, with the appropriate form of $\mathcal{M}_{\rm h}$, to dilute or semidilute polymer solutions in a good solvent.

For illustration and later use we confirm Eq. (2.144) by a field-theoretical calculation in the case of a dilute polymer solution, where Eq. (2.132) applies. Substituting the form

$$\mathcal{E}(\boldsymbol{r}_{\rm A}) = \int \mathrm{d}\boldsymbol{r}_{\rm B}\, \langle \varphi^{(1)}_{\rm AB} \rangle \Big/ \int \mathrm{d}\boldsymbol{r}_{\rm B}\, \langle \varphi^{(1)}_{\rm AB} \rangle_{\rm b}$$

of the bulk-normalized end-density in (2.132) and using (2.119) to expand

$$\langle \varphi^{(1)}_{\rm AB} \rangle_{\rm h} - \langle \varphi^{(1)}_{\rm AB} \rangle_{\rm S,h} \to \langle \varphi^{(1)}_{\rm AB} \cdot \Psi_{\rm g}(\boldsymbol{r}_{\rm S}) \rangle_{\rm h} A_{\rm g} R^{d-1/\nu} \tag{2.146}$$

for a small sphere radius R, one finds

$$F = p_0 A_{\rm g} R^{d-1/\nu} \{m(\boldsymbol{r}_{\rm S})\}_{\rm (fc,h)}/n \tag{2.147}$$

since the half-space profile is given by (Eisenriegler 1997)

$$\{m(\boldsymbol{r})\}_{\rm (fc,h)} = n\, \frac{\int \mathrm{d}\boldsymbol{r}_{\rm A} \int \mathrm{d}\boldsymbol{r}_{\rm B}\, \mathcal{L} \langle \varphi^{(1)}_{\rm AB} \cdot \Psi_{\rm g}(\boldsymbol{r}) \rangle_{\rm h}}{\int \mathrm{d}\boldsymbol{r}_{\rm B}\, \mathcal{L} \langle \varphi^{(1)}_{\rm AB} \rangle_{\rm b}} \tag{2.148}$$

where the limit $k = 0$ is understood. Equation (2.147) is in agreement with (2.144) if the form of $\{m\}_{\rm (fc,h)}$ on the left-hand side of (2.64) is taken into account.

For *ideal* chains in $d = 3$, the above result simplifies, since $\int \mathrm{d}\boldsymbol{r}_{\rm B}\, \mathcal{L} \langle \varphi^{(1)}_{\rm AB} \rangle_{\rm b} = 1$ and $\Psi_{\rm g} = \Phi^2/2$. One can use Eqs. (2.49) and (2.47) to obtain $F = p_0 A_{\rm g} R L \mathcal{M}_{\rm h}(z_{\rm S})$, which is consistent with Eq. (2.144).

2.7.3 Arbitrary Size Ratios

Here we consider the sphere–wall interaction mediated by a solution of ideal chains for *arbitrary* size ratio $R/\mathcal{R}_{\rm g}$. The half-space profile $\mathcal{M}_{\rm h}$ in Eq. (2.145) and the function $-\mathcal{V}$ in Eq. (2.140) increase monotonically with increasing distance from the surface so that the interaction is *attractive* for both small and large spheres. However, the behaviors for small and large spheres are quite different. For a small sphere, δF has a point of inflection where the mean force $\partial_D \delta F/\partial D$ pushing the particle toward the wall has a maximum. For a large sphere, the force decreases monotonically with increasing distance.

Figure 2.8 shows numerical results (Bringer et al. 1999) for the end density $\mathcal{E}(\boldsymbol{r})$ obtained by solving the diffusion equation (2.36), and from which

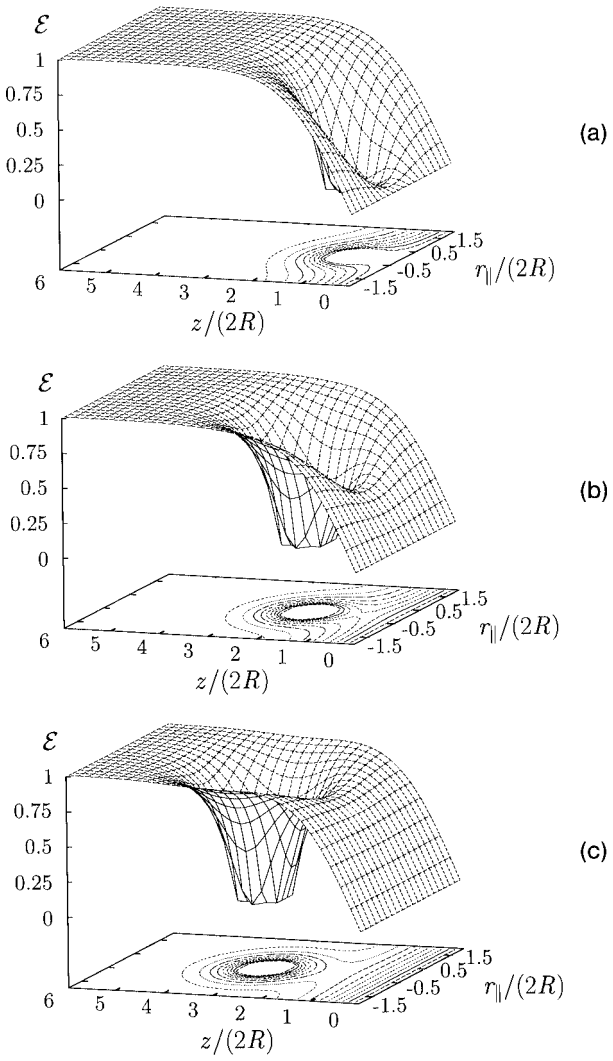

Fig. 2.8 Bulk-normalized density of chain ends $\mathcal{E}(r_\parallel, z)$ for $R/(\sqrt{2}\mathcal{R}_\mathrm{g}) = 1/4$ and (a) $D/R = 1$, (b) $D/R = 3$, and (c) $D/R = 5$. The deviation $\mathcal{E}_\mathrm{h} - \mathcal{E}$ from the density without the sphere, and thus the number $-\Delta\mathcal{N}$ of chains removed on inserting the sphere, decreases as the sphere approaches the wall.

the immersion free energy for a sphere near a wall can be calculated via Eq. (2.132). The resulting dependence of $\delta F/(2\mathcal{R}_\mathrm{g}^2 R p_0) \equiv \mathcal{Y}(\vartheta, \rho)$ on the scaled sphere–wall distance $\vartheta = D/(\sqrt{2}\mathcal{R}_\mathrm{g}) \equiv \theta/\sqrt{2}$ is shown for various size ratios $\rho = R/(\sqrt{2}\mathcal{R}_\mathrm{g})$ in Fig. 2.9. Also shown is the scaling function

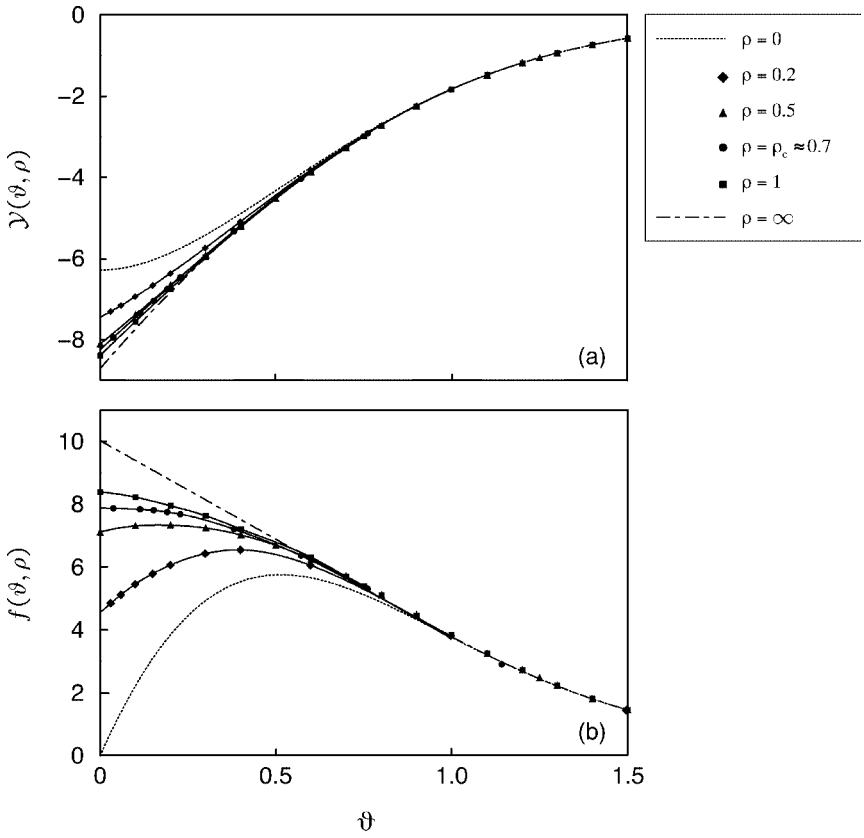

Fig. 2.9 (a) Scaling function $\mathcal{Y}(\vartheta,\rho)$ for the interaction free energy versus $\vartheta = D/(\sqrt{2}\mathcal{R}_{\rm g})$ for various fixed values of $\rho = R/(\sqrt{2}\mathcal{R}_{\rm g})$, ranging from $\rho = \infty$ (lowest curve, Derjaguin approximation (2.140) and (2.141)) to $\rho = 0$ (uppermost curve, small radius expansion (2.145)). The squares, circles, triangles, and diamonds show numerical data. For $\rho < \rho_{\rm c} \approx 0.7$ there is an inflection point in the ϑ dependence of $\mathcal{Y}$, which is absent for $\rho > \rho_{\rm c}$.
(b) Scaling function $f(\vartheta,\rho)$ of the polymer-induced force. The points of inflection of $\mathcal{Y}$ in (a) correspond to *maxima* of f. For $\rho > \rho_{\rm c}$, the function $f(\vartheta,\rho)$ has a maximum at $\vartheta = 0$, corresponding to a sphere that touches the wall.

$f(\vartheta,\rho) = \partial_\vartheta \mathcal{Y}(\vartheta,\rho) \equiv \partial_D \delta F/(\sqrt{2}\mathcal{R}_{\rm g} R p_0)$ of the mean force $\partial_D \delta F$ pushing the *particle* toward the wall.

Besides expressing F via Eq. (2.132) in terms of the number $-\Delta\mathcal{N}$ of removed chains, which is a global quantity, one may study the polymer-induced interaction between sphere and wall by means of the local density–pressure relation (2.65). Since $\partial_D \delta F$ equals the reduction of the force on the *wall* due to insertion of the sphere and must be related to the near-wall behavior of the monomer densities $\mathcal{M}$ and $\mathcal{M}_{\rm h}$ in the presence and absence of the sphere

(Eisenriegler 1997; Bringer et al. 1999), then

$$\partial_D \delta F = p_0 \int \mathrm{d}\boldsymbol{r}_\parallel \, [1 - (\mathcal{M}(\boldsymbol{r})/\mathcal{M}_\mathrm{h}(z))_{z\to 0}] \tag{2.149}$$

This result shows that the depletion $\mathcal{M}(\boldsymbol{r}) < \mathcal{M}_\mathrm{h}(z)$ of the monomer density due to the sphere leads to a positive $\partial_D \delta F$, i.e. to an attractive sphere–wall interaction. Some results for the monomer depletion are shown in Fig. 2.10.

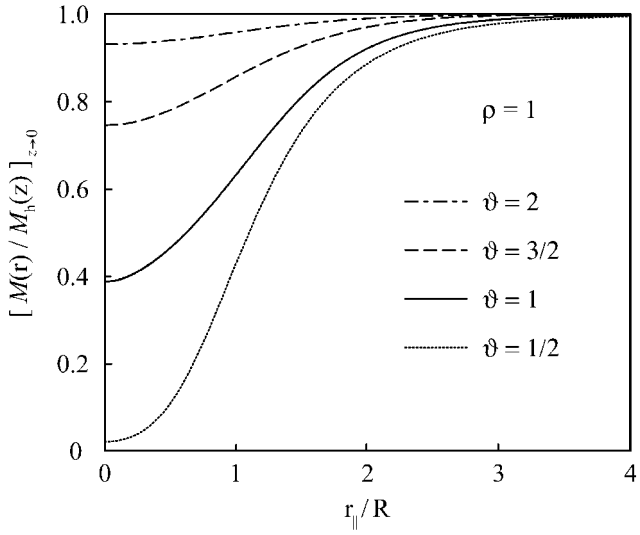

Fig. 2.10 Depletion of the normalized monomer density $[\mathcal{M}(\boldsymbol{r})/\mathcal{M}_\mathrm{h}(z)]_{z\to 0}$ near the wall due to the sphere as a function of $r_\parallel/R$ for $\rho = R/(\sqrt{2}\mathcal{R}_\mathrm{g}) = 1$ and various values of $\vartheta = D/(\sqrt{2}\mathcal{R}_\mathrm{g})$ (see Fig. 2.6). For $\rho = 1 > \rho_\mathrm{c}$, the depletion is more pronounced, and hence the force increases, as the sphere moves toward the wall, i.e. as ϑ is decreased (see Fig. 2.9).

2.8
Interaction Between Two or More Spheres

2.8.1
Derjaguin Approximation for Large Spheres

For two spheres "a" and "b" with radii R_a and R_b much larger than mesoscopic polymer lengths, such as $\mathcal{R}_\mathrm{g}$ or the screening length ξ, and the smallest surface-to-surface distance D between the spheres, one may proceed as in Section 2.7.1. The local distance between the two spheres is

$$\tilde{D} = D + \frac{r_\parallel^2}{2R_\mathrm{a}} + \frac{r_\parallel^2}{2R_\mathrm{b}} \tag{2.150}$$

Comparing with Eq. (2.138), one sees that the Derjaguin expression for the free energy of interaction δF between the two spheres is given by Eqs. (2.139) to (2.141) except that R is now replaced by $(1/R_\mathrm{a} + 1/R_\mathrm{b})^{-1}$. In particular, for ideal chains in $d = 3$,

$$\delta F = -2p_0 \frac{R_\mathrm{a} R_\mathrm{b}}{R_\mathrm{a} + R_\mathrm{b}} \mathcal{R}_\mathrm{g}^2 \mathcal{V}(D/\mathcal{R}_\mathrm{g}) \tag{2.151}$$

where $\mathcal{V}$ is given in Eqs. (2.141) and (2.142).

2.8.2 Two Small Spheres

For polymer configurations with two particles "a" and "b" present, the Boltzmann factor contains the product $W_\mathrm{a} W_\mathrm{b}$ of the single-particle contributions. Each factor has the form (2.109), if the particles are spheres with radii R_a and R_b much smaller than the center-to-center distance $r_\mathrm{ab} = |\boldsymbol{r}_\mathrm{a} - \boldsymbol{r}_\mathrm{b}|$ and the mesoscopic polymer lengths. The difference F in polymer free energy in the presence and absence of the particles is $F = -k_\mathrm{B}T \ln\{W_\mathrm{a} W_\mathrm{b}\}$, where the curly brackets denote an average over all chain configurations in the bulk solution without particles. The free energy of interaction or potential of mean force between the two particles,

$$\delta F = -k_\mathrm{B}T \ln\left(\frac{\{W_\mathrm{a} W_\mathrm{b}\}}{\{W_\mathrm{a}\}\{W_\mathrm{b}\}}\right) \tag{2.152}$$

is the difference between F and the sum $F_\mathrm{a} + F_\mathrm{b}$ of the free energies $-k_\mathrm{B}T \ln\{W_\mathrm{a}\}$ and $-k_\mathrm{B}T \ln\{W_\mathrm{b}\}$ for immersing "a" without "b" and "b" without "a". Clearly δF depends on r_ab and tends to zero for $r_\mathrm{ab} \to \infty$. On expanding δF in terms of $W_\mathrm{a} - 1$ and $W_\mathrm{b} - 1$ for small particles, the self-terms of first and second order drop out, and

$$\begin{aligned} \frac{\delta F}{k_\mathrm{B}T} &= -[\{(W_\mathrm{a} - 1)(W_\mathrm{b} - 1)\} - \{W_\mathrm{a} - 1\}\{W_\mathrm{b} - 1\}] \\ &= -A_\mathrm{g}^2 (R_\mathrm{a} R_\mathrm{b})^{d-1/\nu} \mathcal{K}(r_\mathrm{ab}) \,, \quad R \ll r_\mathrm{ab}, \mathcal{R}_\mathrm{g}, \xi \,, \end{aligned} \tag{2.153}$$

where

$$\mathcal{K}(r_\mathrm{ab}) = \{m(\boldsymbol{r}_\mathrm{a}) m(\boldsymbol{r}_\mathrm{b})\} - (n\mathcal{R}_\mathrm{g}^{1/\nu})^2 \tag{2.154}$$

is the correlation function of modified monomer densities (2.63) in the solution without particles.

Equations (2.153) and (2.154) allow us to relate (Eisenriegler 2000) the non-monotonic dependence (Chatterjee and Schweizer 1998) of the second virial coefficient of a dilute solution of small spherical colloids on the degree of inter-chain overlap in the embedding polymer solution to the overlap dependence of the compressibility of the polymer solution without colloids.

For a *semidilute* solution, it has been conjectured (Obukhov and Semenov 2005) that the correlation function $\mathcal{K}$ becomes negative as $r_{\rm ab}$ increases beyond a certain distance of the order of the screening length ξ, passes through a minimum, and then *increases* toward zero. This conjecture implies via Eq. (2.153) a free energy δF of interaction between the two particles that *decreases* toward zero, i.e. a depletion *repulsion*, at large distances.

If the polymer solution is *dilute*, the average $\{\cdots\}$ in Eq. (2.154) factors into averages over configurations of a *single* chain. Contributions to $m(\boldsymbol{r}_{\rm a})m(\boldsymbol{r}_{\rm b})$ from different chains ($P \neq P'$ in the product $\sum_P \sum_{P'}$ of two modified monomer densities m in Eq. (2.63)) cancel the last term in (2.154), and contributions from the same chain $P = P'$ lead to

$$\mathcal{K}(r_{\rm ab}) \to n \int {\rm d}\boldsymbol{y}\, \{m(\boldsymbol{r}_{\rm a})m(\boldsymbol{r}_{\rm b})\}_{\boldsymbol{y}}, \quad \text{dilute solution} \tag{2.155}$$

In Eq. (2.154) and above (2.155), m denotes the density of *all* chains in the solution. However, in (2.155), m is the density of a *single* chain, and $\{m\,m\}_{\boldsymbol{y}}$ is the average over configurations of the single chain in the bulk with one end fixed at the position $\boldsymbol{y}$. In terms of the "magnetic analog" or field theory, (2.155) reads

$$\mathcal{K}(r_{\rm ab}) \to n\, \frac{\mathcal{L} \int {\rm d}\boldsymbol{r}_{\rm A} \int {\rm d}\boldsymbol{r}_{\rm B}\, \langle \varphi^{(1)}_{\rm AB} \cdot \Psi(\boldsymbol{r}_{\rm a}) \cdot \Psi(\boldsymbol{r}_{\rm b})\rangle\big|_{k=0}}{\mathcal{L} \int {\rm d}\boldsymbol{r}_{\rm B}\, \langle \varphi^{(1)}_{\rm AB}\rangle\big|_{k=0}} \tag{2.156}$$

where $\langle\cdots\rangle$ is the k-component average in the bulk without particles. For *ideal* chains, the denominator on the right-hand side of (2.156) equals unity, $\Psi \to \Phi^2/2$, and the average in the numerator can be evaluated by Wick's theorem, leading to

$$\mathcal{K}(r_{\rm ab}) \to n\, 2\mathcal{L}\, \frac{1}{t^2}\, \frac{{\rm e}^{-\sqrt{t}\, r_{\rm ab}}}{4\pi r_{\rm ab}} = \frac{2n}{\pi r_{\rm ab}}\, \mathcal{R}_{\rm g}^2\, {\rm i}^2{\rm erfc}\left(\frac{r_{\rm ab}}{2\mathcal{R}_{\rm g}}\right) \tag{2.157}$$

which is essentially the Fourier transform of the Debye scattering function (de Gennes 1979; des Cloizeaux and Jannink 1990; Schäfer 1998). Here ${\rm i}^2{\rm erfc}$ is the two-fold iterated complementary error function (Abramowitz and Stegun 1972). This is monotonically decreasing and leads to an interaction (2.153) between the two spheres that is *attractive* at all distances.

2.8.3 Three Small Spheres

A polymer solution induces not only pairwise-additive but also many-body interactions. For example, the immersion free energy

$$F_{\rm abc} = F_{\rm a} + F_{\rm b} + F_{\rm c} + \delta F_{\rm ab} + \delta F_{\rm bc} + \delta F_{\rm ac} + \delta F_{\rm abc} \tag{2.158}$$

of three spherical particles "a", "b", and "c" contains a three-body term $\delta F_{\rm abc}$. Here $F_{\rm a}$ is the single-particle contribution of particle "a", and $\delta F_{\rm ab}$ is the interaction free energy of the two particles "a" and "b", as defined in the previous subsection.

The leading contributions for small spherical particles in a solution of ideal chains in $d = 3$ are given by (Hanke et al. 1999)

$$\begin{aligned} F_{\rm a}/p_0 &= 4\pi R_{\rm a}\mathcal{R}_{\rm g}^2 \\ \delta F_{\rm ab}/p_0 &= -32\pi R_{\rm a}R_{\rm b}\frac{\mathcal{R}_{\rm g}^2}{r_{\rm ab}}\epsilon_2\left(\frac{r_{\rm ab}}{2\mathcal{R}_{\rm g}}\right) \\ \delta F_{\rm abc}/p_0 &= 32\pi R_{\rm a}R_{\rm b}R_{\rm c}\mathcal{R}_{\rm g}^2\left[\frac{1}{r_{\rm ba}r_{\rm ac}}\,\epsilon_2\left(\frac{r_{\rm ba}+r_{\rm ac}}{2\mathcal{R}_{\rm g}}\right)\right. \\ &\quad \left. + \frac{1}{r_{\rm ab}r_{\rm bc}}\,\epsilon_2\left(\frac{r_{\rm ab}+r_{\rm bc}}{2\mathcal{R}_{\rm g}}\right) + \frac{1}{r_{\rm ac}r_{\rm cb}}\,\epsilon_2\left(\frac{r_{\rm ac}+r_{\rm cb}}{2\mathcal{R}_{\rm g}}\right)\right] \end{aligned} \tag{2.159}$$

where

$$\epsilon_2(\varrho) = {\rm i}^2{\rm erfc}(\varrho) \tag{2.160}$$

While the one- and two-body terms in Eqs. (2.159) are from (2.116), (2.153), and (2.157), the three-body term comes from

$$\delta F_{\rm abc}/p_0 = A_{\rm g}^3(R_{\rm a}R_{\rm b}R_{\rm c})^{d-1/\nu}\int {\rm d}\boldsymbol{y}\,\{m(\boldsymbol{r}_{\rm a})m(\boldsymbol{r}_{\rm b})m(\boldsymbol{r}_{\rm c})\}_{\boldsymbol{y}} \tag{2.161}$$

for a dilute polymer solution. Its evaluation for ideal chains is similar to that of (2.157).

Note that $\delta F_{\rm abc}$ in Eqs. (2.159) is negligible if one of the inter-particle distances significantly exceeds $\mathcal{R}_{\rm g}$.

2.8.4 Arbitrary Size Ratios

For *ideal* chains, the dependence of the two-sphere interaction on the colloid-to-polymer size ratio could be investigated via the diffusion equation, as

described in Section 2.7.3 and Bringer et al. (1999). In Tuinier et al. (2000) explicit estimates were obtained by approximating the density profile $\mathcal{M}$ of chain monomers in the presence of two spheres by the *product* of the profiles of the two single spheres.

2.9 Small Anisotropic Particles

Here we consider anisotropic particles that are large on a microscopic scale but much *smaller* than characteristic mesoscopic polymer lengths such as $\mathcal{R}_g$, and we concentrate on the case of *ideal* polymers.

For simplicity, the discussion is confined to particle shapes with a symmetry axis of revolution and reflection symmetry about the center. This encompasses prolate or oblate ellipsoids and the dumbbells composed of two touching or overlapping spheres, shown in Fig. 2.11. Both types of particle shapes can be synthesized (Snoeks et al. 2000; van Blaaderen 2003; van Blaaderen 2004; Johnson et al. 2005).

For the dumbbell shapes, detailed predictions can easily be made (Eisenriegler 2004). The reason is that on large length scales a system at the critical point is not only scale-invariant but also *conformally* invariant (Cardy 1986).

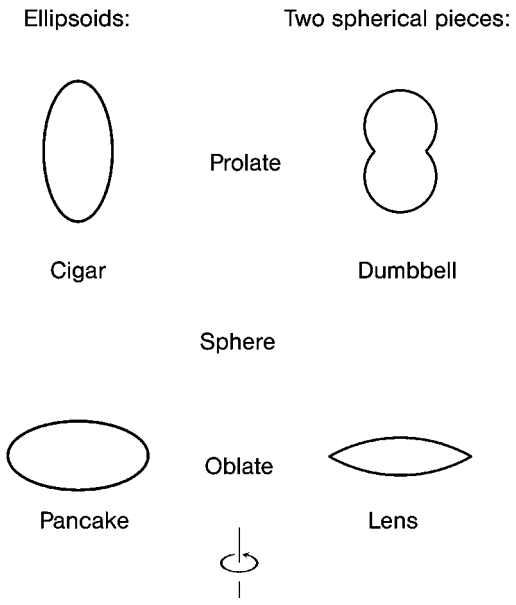

Fig. 2.11 Simple shapes of anisotropic colloidal particles with a symmetry axis of revolution and reflection symmetry about the center.

The space outside a dumbbell of two touching spheres, for example, can be obtained from the space inside two parallel plates by means of an inversion about the point midway between the plates, which is a conformal, angle-preserving, transformation. Due to the high symmetry, much is known about a critical system between parallel plates and can be taken over to the dumbbell geometry. It is instructive to compare dumbbells with ellipsoids, which are studied by Eisenriegler et al. (2003).

2.9.1 Operator Expansions for Small Anisotropic Particles

Here we generalize the operator approach for small *spherical* particles in Section 2.5.2 to the case of *anisotropic* particles. In addition to isotropic operators such as $\Psi \propto \Phi^2$ in (2.119), we must now include *anisotropic* operators (Eisenriegler et al. 2003; Eisenriegler 2004; Eisenriegler and Bringer 2005).

For a particle P with a symmetry axis of revolution and reflection symmetry about the center, the Boltzmann factor in the corresponding one-component Gaussian field theory has the expansion

$$\exp(-\mathcal{H}_{\rm P}[\Phi]) \propto 1 - w_{\rm I} - w_{\rm A} \tag{2.162}$$

with

$$w_{\rm I} = \beta_{\rm I} O_{\rm I} + \cdots \tag{2.163}$$

the isotropic contribution and

$$w_{\rm A} = \beta_{\rm VI} O_{\rm VI} + \beta_{\rm VII} O_{\rm VII} + \cdots \tag{2.164}$$

the anisotropic contribution. Here we explicitly display only the *leading* terms, with the operators[13)]

13) In the Gaussian model, the operators $O_{\rm VI}$ and $O_{\rm VII}$ are related to the second derivative along the particle axis $\partial_\parallel^2 \epsilon$ of the energy density $\epsilon \propto -\Phi^2$ and to the diagonal component $T_{\parallel,\parallel} = \sum_{\mu,\nu} \rho_\mu \rho_\nu T_{\mu\nu}$ of the stress tensor parallel to the particle axis, at the critical point of the Gaussian field theory, and to isotropic operators via

$$O_{\rm VI} = \tfrac{1}{2} T_{\parallel,\parallel} + \frac{d-2}{8(d-1)} \partial_\parallel^2 \Phi^2 + \frac{1}{8(d-1)} \Delta \Phi^2 - \tfrac{1}{4} \Phi \Delta \Phi$$

and

$$O_{\rm VII} = -\tfrac{1}{2} T_{\parallel,\parallel} + \frac{d}{8(d-1)} \partial_\parallel^2 \Phi^2 - \frac{1}{8(d-1)} \Delta \Phi^2 + \tfrac{1}{4} \Phi \Delta \Phi \,, .$$

This leads to a parameterization of the small-particle expansion as in Eisenriegler (2004). For *non*-Gaussian field theories, $\partial_\parallel^2 \epsilon$ and the appropriate stress component $T_{\parallel,\parallel}$ remain operators with a definite scaling dimension [see e.g. Brown and Collins (1980)]. Note that the weight $(\beta_{\rm VI} - \beta_{\rm VII})/2$ of $T_{\parallel,\parallel}$ *vanishes* for the needle with $\beta_{\rm VI}, \beta_{\rm VII}$ in (2.195).

$$O_{\rm I} = \Phi^2/2, \quad O_{\rm VI} = (\partial_\parallel \Phi)^2/2, \quad O_{\rm VII} = \Phi(\partial_\parallel^2 \Phi)/2 \tag{2.165}$$

where

$$\partial_\parallel = \sum_{\alpha=1}^{3} \rho_\alpha \partial_\alpha \tag{2.166}$$

is a derivative along the axis of revolution characterized by the unit vector $\boldsymbol{\rho}$. The scaling dimensions $d-2$, d, and d of $O_{\rm I}$, $O_{\rm VI}$, and $O_{\rm VII}$ determine the orders $\beta_{\rm I} \propto (\text{size})^{d-2}$, $\beta_{\rm VI} \propto \beta_{\rm VII} \propto (\text{size})^d$ in the particle *size* (typical particle diameter) of the three amplitudes shown in Eqs. (2.163) and (2.164).

The small-particle operator expansion can be used at and near the critical point of the field theory as long as the particle size is much smaller than the correlation length $\xi_{\rm FT} \propto \sqrt{t}$. Since the amplitudes $\beta_{\rm I}$, $\beta_{\rm VI}$, and $\beta_{\rm VII}$ of the leading isotropic and anisotropic operators are independent of t, a simple way to determine their dependence on the particle *shape* is to calculate the propagator $\langle \Phi(\boldsymbol{r}_1)\Phi(\boldsymbol{r}_2)\rangle_{\rm P}^{\rm (c)} \equiv \langle \varphi_{12}\rangle_{\rm P}^{\rm (c)}$ in the Gaussian model, right at the critical (c) point $t=0$ and in the presence of the particle, and compare orders $(\text{size})^{d-2}$ and $(\text{size})^d$ with the small-particle expansion

$$\langle \varphi_{12}\rangle_{\rm P}^{\rm (c)} = \langle [1 - w_{\rm I} - w_{\rm A}] \cdot \varphi_{12}\rangle_{\rm b}^{\rm (c)} \tag{2.167}$$

which follows from (2.162). Here $\varphi_{12} \equiv \Phi(\boldsymbol{r}_1)\Phi(\boldsymbol{r}_2)$ is defined as in (2.40), and the quantities $\langle O_j \cdot \varphi_{12}\rangle_{\rm b}$ on the right-hand side of (2.167) denote Wick decompositions into factors $\langle \Phi\Phi\rangle_{\rm b}$, which correspond to connected diagrams.

2.9.1.1 Dumbbells

The exterior of two *tangentially touching* spheres (see the dumbbell in Fig. 2.12) is mapped onto the space (film) between two parallel planes by means of the inversion

$$\hat{\boldsymbol{r}} \equiv (\hat{\boldsymbol{r}}_\parallel, \hat{z}) = \frac{\boldsymbol{r}}{r^2}(2R)^2, \quad \boldsymbol{r} \equiv (\boldsymbol{r}_\perp, r_\parallel) \tag{2.168}$$

about the dumbbell center $\boldsymbol{r} = 0$. This is a conformal, angle-preserving transformation that maps the surfaces of the two spheres of radius R with centers on the negative and positive $r_\parallel$ axis onto the planar boundaries $\hat{z} = -2R$ and $+2R$ of the film. Here $\boldsymbol{r}_\perp$ and $r_\parallel$ are the components of $\boldsymbol{r}$ perpendicular and parallel to the dumbbell axis of revolution, and $\hat{\boldsymbol{r}}_\parallel$ and $\hat{z}$ are the components of $\hat{\boldsymbol{r}}$ parallel and perpendicular to the boundary planes of the film. Once the propagator in the film geometry is known, the propagator outside the dumbbell follows from the transformation (Cardy 1986)

$$\langle \Phi(\boldsymbol{r}_1)\Phi(\boldsymbol{r}_2)\rangle_{\rm DB}^{\rm (c)} = b(\hat{\boldsymbol{r}}_1)^{x_\Phi} b(\hat{\boldsymbol{r}}_2)^{x_\Phi} \langle \Phi(\hat{\boldsymbol{r}}_1)\Phi(\hat{\boldsymbol{r}}_2)\rangle_{\rm film}^{\rm (c)} \tag{2.169}$$

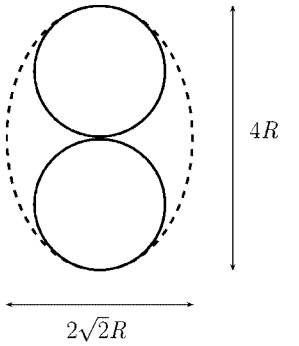

Fig. 2.12 Dumbbell of two tangentially touching spheres of radius R (full lines) and its circumscribing ellipsoid (dashed lines).

under a conformal mapping, where

$$b(\hat{\boldsymbol{r}}) = |\det(\partial\hat{\boldsymbol{r}}/\partial\boldsymbol{r})|^{1/d} = (2R)^2/r^2 \tag{2.170}$$

is the local dilatation factor of the mapping (2.168).

For two *overlapping* spheres or a lens, the exterior can be conformally mapped onto the interior of a *wedge* (see Fig. 2.13). The mapping is an inversion about the point denoted by the heavy dot on the left-hand side of the two parts of Fig. 2.13. The two boundary half-planes of the wedge and the edge where they meet are mapped onto the two spherical boundary surfaces of the particle and the circle of diameter $\mathcal{D}$ where they intersect. Since the mapping preserves angles, the opening angle α of the wedge equals the angle of intersection of the two spheres.

The angle $\alpha = \pi/2$ is an interesting and simple special case. The Gaussian wedge propagator follows from the propagator in the bulk on adding three mirror images about the boundary planes. Adapting the transformation laws (2.169) and (2.170) to this case yields

$$\begin{aligned}\langle\varphi_{12}\rangle^{(\mathrm{c})}_{\mathrm{DB}(\pi/2)}/\tilde{S}_d = r_{12}^{-(d-2)} + R^{d-2}\big[&- (q_1^+ q_2^+ + R^2 r_{12}^2)^{-(d-2)/2} \\ &+ (q_1^+ q_2^+ + q_1^- q_2^- + R^2 r_{12}^2)^{-(d-2)/2} \\ &- (q_1^- q_2^- + R^2 r_{12}^2)^{-(d-2)/2}\big]\end{aligned} \tag{2.171}$$

for the dumbbell propagator, with

$$q_i^{\pm} = (r_i^{\pm})^2 - R^2, \quad (r_i^{\pm})^2 = r_i^2 \pm r_{i\parallel}\sqrt{2}R + R^2/2 \tag{2.172}$$

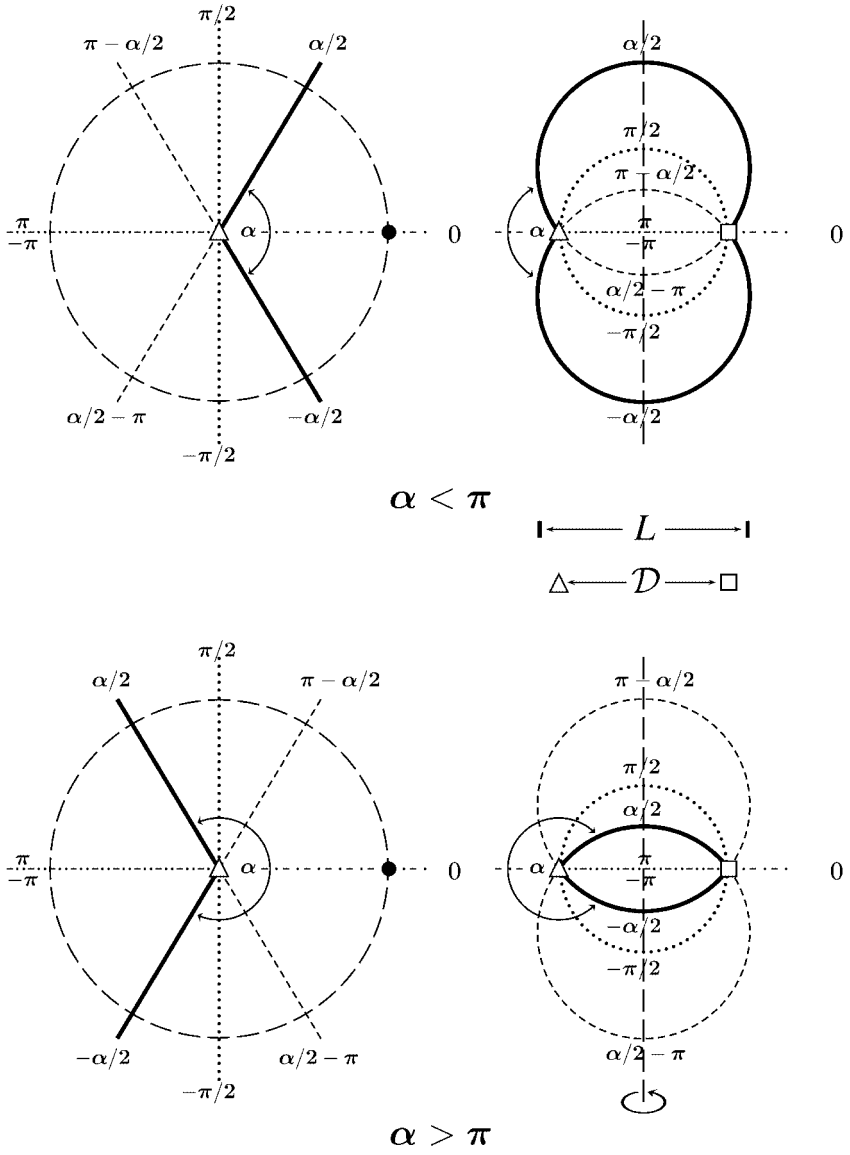

Fig. 2.13 Conformal mapping of a dumbbell or lens onto a wedge.

for $i = 1, 2$, and with $\tilde{S}_d$ from (2.115). Here r_i^+ and r_i^- are the distances of the point $\boldsymbol{r}_i$ from the centers of the two spheres of radius R that form the dumbbell. One can easily check that the right-hand side of (2.171) vanishes if, for example, $\boldsymbol{r}_1$ approaches the surface of the sphere with center on the positive $r_\parallel$ axis so that q_1^+ vanishes. Each of the four contributions in (2.171) satisfies the Laplace equation.

Expanding for $r_i \gg R$ up to order R^d, one finds

$$\begin{aligned}\langle\varphi_{12}\rangle^{(\mathrm{c})}_{\mathrm{DB}(\pi/2)} \to \tilde{S}_d\, r_{12}^{-(d-2)} - R^{d-2}(2-2^{-(d-2)/2})\tau_{\mathrm{I}}/\tilde{S}_d \\ - R^d\{\tau_{\mathrm{IV}}(2-2^{-d/2})/(d-2) \\ + \tau_{\mathrm{VI}}[1+(2^{-(d-2)/2}/(d-2))] + \tau_{\mathrm{VII}}\}/\tilde{S}_d \end{aligned} \tag{2.173}$$

where the

$$\tau_i = \langle\varphi_{12}\cdot O_i\rangle^{(\mathrm{c})}_{\mathrm{b}} \tag{2.174}$$

are Gaussian bulk averages at the critical point involving the operators (2.165), and

$$O_{\mathrm{IV}} = (\nabla\Phi)^2/2 \tag{2.175}$$

is a non-leading isotropic operator. Explicit expressions for τ_i follow from Wick's theorem and the form of the propagator in the bulk [the second factor in (2.115)]. For $d = 3$ they can be obtained from Eqs. (3.38) to (3.44) in Eisenriegler et al. (2003).

Dumbbells with an angle $\alpha = \pi/g$ with $g = 3, 4, \ldots$ can be treated in a similar fashion,[14] with an increasing number of images for increasing g. For tangentially touching spheres, DB = DB(0), the $r_i \gg R$ expansion of the propagator $\langle\varphi_{12}\rangle^{(\mathrm{c})}_{\mathrm{DB}(0)}$ can be explicitly evaluated via Eq. (2.169), since the corresponding film propagator has a simple expansion for the two points $\hat{\boldsymbol{r}}_i$ near $\hat{\boldsymbol{r}} = 0$ in the midplane of the film [see e.g. Section 3B and Appendix C of Eisenriegler (2004)]. This result for $\langle\varphi_{12}\rangle^{(\mathrm{c})}_{\mathrm{DB}(0)}$ and the result (2.173) for $\langle\varphi_{12}\rangle^{(\mathrm{c})}_{\mathrm{DB}(\pi/2)}$ imply, in $d = 3$, the weights

$$[\beta_{\mathrm{I}}(0);\beta_{\mathrm{I}}(\pi/2)] = 4\pi R[2\ln 2; 2-2^{-1/2}] = 4\pi R[1.386; 1.293] \tag{2.176}$$

for the leading isotropic operator O_{I} and

$$\begin{aligned}[\beta_{\mathrm{VI}}(0);\beta_{\mathrm{VI}}(\pi/2)]O_{\mathrm{VI}} + [\beta_{\mathrm{VII}}(0);\beta_{\mathrm{VII}}(\pi/2)]O_{\mathrm{VII}} \\ = 2\pi R^3\{[6.010; 3.414]O_{\mathrm{VI}} + [3.606; 2]O_{\mathrm{VII}}\}\end{aligned} \tag{2.177}$$

for the leading anisotropic operators. The numbers in (2.177) follow from the analytic expressions $5\zeta(3) = 6.010$ and $3\zeta(3) = 3.606$, where ζ is the Riemann zeta function, and $2(1+2^{-1/2}) = 3.414$.

14) For a wedge of arbitrary angle, see Cardy (1983), and for dumbbells and lenses with arbitrary α, see Eisenriegler and Bringer (2005).

As expected intuitively, the dumbbell of two overlapping spheres with angle $\pi/2$ has a smaller isotropic weight and considerably smaller anisotropic weights than the dumbbell of touching spheres of the same radius.

2.9.1.2 Ellipsoids

Consider a particle with the shape of a prolate or oblate ellipsoid of revolution in $d = 3$ dimensions as shown in Fig. 2.11. We introduce the interfocal distance $2f$, which is related to the long and short axes l and s of the ellipsoid by

$$l^2 - s^2 = (2f)^2 \tag{2.178}$$

and the dimensionless parameter

$$\xi_{\mathrm{E}} = (l, s)/(2f) \quad \text{for } (\text{prolate}, \text{oblate}) \tag{2.179}$$

characterizing the degree of shape anisotropy of the particle. For $\xi_{\mathrm{E}} \to \infty$, the prolate or oblate ellipsoid becomes a sphere of radius $l/2 = s/2$; for $\xi_{\mathrm{E}} \to 1$, the prolate ellipsoid becomes an infinitely thin needle of length $l = 2f$; and for $\xi_{\mathrm{E}} \to 0$, the oblate ellipsoid becomes an infinitely thin circular disk of radius $l/2 = f$. The parameter ξ_{E} also appears on introducing spheroidal coordinate systems (Flammer 1957).

The leading isotropic and anisotropic contributions in the expansion (2.162) to (2.164) for the ellipsoid are determined by

$$\beta_{\mathrm{I}} = f B_{\mathrm{I}}(\xi_{\mathrm{E}}) \tag{2.180}$$

and

$$\beta_{\mathrm{VI}} O_{\mathrm{VI}} + \beta_{\mathrm{VII}} O_{\mathrm{VII}} = f^3 [B_{\mathrm{VI}}(\xi_{\mathrm{E}}) O_{\mathrm{VI}} + B_{\mathrm{VII}}(\xi_{\mathrm{E}}) O_{\mathrm{VII}}] \tag{2.181}$$

where (Eisenriegler et al. 2003)

$$B_{\mathrm{I}} = 4\pi \left(\frac{1}{a_{\mathrm{p}}}, \frac{1}{a_{\mathrm{o}}} \right) \tag{2.182}$$

is positive and

$$B_{\mathrm{VI}} = \frac{4\pi}{3} \left(\left[a_{\mathrm{p}} - \frac{1}{\xi_{\mathrm{E}}} \right]^{-1} + 2 \left[a_{\mathrm{p}} - \frac{\xi_{\mathrm{E}}}{\xi_{\mathrm{E}}^2 - 1} \right]^{-1}, \left[\frac{1}{\xi_{\mathrm{E}}} - a_{\mathrm{o}} \right]^{-1} + 2 \left[\frac{\xi_{\mathrm{E}}}{1 + \xi_{\mathrm{E}}^2} - a_{\mathrm{o}} \right]^{-1} \right) \tag{2.183}$$

$$B_{\mathrm{VII}} = \tfrac{1}{3} (B_{\mathrm{I}}, -B_{\mathrm{I}}) \tag{2.184}$$

for the (prolate, oblate) cases, respectively. Here

$$(a_{\rm p}, a_{\rm o}) = \left(\frac{1}{2}\ln\left[\frac{\xi_{\rm E}+1}{\xi_{\rm E}-1}\right],\ \arctan\frac{1}{\xi_{\rm E}}\right) = \left(\operatorname{arcosh}\frac{l}{s},\ \arccos\frac{s}{l}\right) \tag{2.185}$$

A small prolate ellipsoid was considered before by Odijk (2000), where $\beta_{\rm I}$ was determined and denoted by $8\pi E$.

The special cases of a weakly deformed sphere, a thin needle, and a circular disk are discussed by Eisenriegler et al. (2003). Here we consider, for both the dumbbells with $\alpha = 0$ and $\alpha = \pi/2$, the prolate circumscribing ellipsoid (CE) that circumscribes the dumbbell, touches it at the highest and lowest points, and has the same curvature at these points (see Figs. 2.12 and 2.14). For the CE of the dumbbell with $\alpha = 0$,

$$l = 4R, \quad s = 2\sqrt{2}R, \quad f = \sqrt{2}R, \quad \xi_{\rm E} = \sqrt{2} \tag{2.186}$$

and for $\alpha = \pi/2$

$$\begin{aligned} &l = (2+\sqrt{2})R,\ \ s = 2\sqrt{1+\tfrac{1}{2}\sqrt{2}}\,R, \\ &f = \sqrt{\tfrac{1}{2}(\sqrt{2}+1)}\,R,\ \ \xi_{\rm E} = \sqrt{\sqrt{2}+1} \end{aligned} \tag{2.187}$$

On using (2.180) to (2.184), this yields the weights

$$[\beta_{\rm I}(0); \beta_{\rm I}(\pi/2)]_{\rm CE} = 4\pi R[1.609; 1.437] \tag{2.188}$$

of the leading isotropic operator $O_{\rm I}$, and the leading anisotropic contributions

$$\begin{aligned} &[\beta_{\rm VI}(0); \beta_{\rm VI}(\pi/2)]_{\rm CE} O_{\rm VI} + [\beta_{\rm VII}(0); \beta_{\rm VII}(\pi/2)]_{\rm CE} O_{\rm VII} \\ &\quad = 2\pi R^3 \{[3.743; 2.038] O_{\rm VI} + [2.139; 1.156] O_{\rm VII}\} \end{aligned} \tag{2.189}$$

in the operator expansions for the circumscribing ellipsoids.

Table 2.1 collects the amplitudes for the particles in Figs. 2.12 and 2.14. The leading isotropic and anisotropic perturbations of the polymer system for the dumbbells are weaker and stronger, respectively, than for their circumscribing ellipsoids. The dumbbells are indeed smaller and more anisotropic than the ellipsoids. The amplitudes of $O_{\rm VI}$ and $O_{\rm VII}$ reflect the greater anisotropy of the dumbbell of tangentially touching spheres ($\alpha = 0$) and its circumscribed ellipsoid than of the corresponding particles for $\alpha = \pi/2$. This will show up in the polymer-induced torque on the particle due to a planar wall. The isotropic weights that determine the immersion free energies in a bulk solution of the

Tab. 2.1 Small mesoscopic particles interacting with ideal chains in $d = 3$. The quantities $\beta_{\rm I}$ and $\beta_{\rm VI}, \beta_{\rm VII}$ are the amplitudes of the leading isotropic and anisotropic contributions to the Boltzmann weight reductions $w_{\rm I}$ and $w_{\rm A}$ in (2.162). The dumbbells DB(0) and DB($\pi/2$) are composed of two spheres with radius R that touch tangentially and intersect at an angle $\pi/2$, respectively, and CE(0) and CE($\pi/2$) are their circumscribing ellipsoids, shown in Figs. 2.12 and 2.14. The isotropic weights are compared with the weight for a sphere of radius R.

	DB(0)	CE(0)	DB($\pi/2$)	CE($\pi/2$)	Sphere
$\beta_{\rm I}/(4\pi R)$	1.386	1.609	1.293	1.437	1
$\beta_{\rm VI}/(2\pi R^3)$	6.010	3.743	3.414	2.038	0
$\beta_{\rm VII}/(2\pi R^3)$	3.606	2.139	2	1.156	0

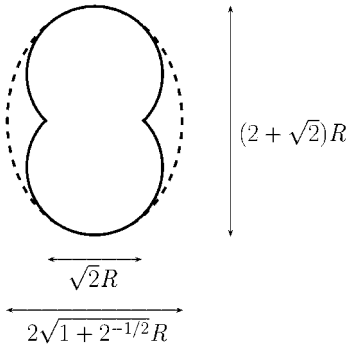

Fig. 2.14 Dumbbell of two spheres of radius R intersecting at an angle $\alpha = \pi/2$ (full lines) and the circumscribing ellipsoid (dashed lines).

dumbbell and the ellipsoid differ less for $\alpha = \pi/2$ (about 10%) than for $\alpha = 0$ (about 15%).

2.9.2 Interaction Between an Anisotropic Particle and a Wall

The evaluation of the free energy $(F_{\rm P})_{\rm W}$ required to immerse a small anisotropic particle P with its center at a distance $z_{\rm P}$ from a planar wall proceeds as in Section 2.7.2. First consider the leading contribution

$$[(F_{\rm P})_{\rm W}]_{\rm leading}/p_0 = \beta_{\rm I}\mathcal{L}[\chi_{\rm h}(z_{\rm P})]^2 = \beta_{\rm I}\mathcal{R}_{\rm g}^2\mathcal{M}_{\rm h}(z_{\rm P}/\mathcal{R}_{\rm g}) \tag{2.190}$$

which is of first order in the particle size and comes from the isotropic operator $O_{\rm I}$. Here $\mathcal{M}_{\rm h}$ is the bulk-normalized monomer density in the half-space, denoted by $\mathcal{M}$ in Eq. (2.55).

The free-energy cost $[(F_{\rm P})_{\rm W}]_{\rm leading}$ of immersing a small anisotropic particle in the unbounded bulk is given by Eq. (2.190) with $\mathcal{M}_{\rm h} = 1$. Explicit

results for the two dumbbells and ellipsoids from Figs. 2.12 and 2.14 follow on substituting the expressions for $\beta_{\rm I}$ from Table 2.1.

The leading anisotropic contribution to $(F_{\rm P})_{\rm W}$ comes from the two anisotropic operators $O_{\rm VI}$ and $O_{\rm VII}$. Proceeding as in (2.146) with (2.119) and (2.147), and using Wick's theorem, one finds

$$[(F_{\rm P})_{\rm W}]_{\text{leading anisotropic}}/p_0 = \mathcal{L}\{\beta_{\rm VI}[\partial_\parallel \chi_{\rm h}(z)]^2 + \beta_{\rm VII}\chi_{\rm h}(z)[\partial_\parallel^2 \chi_{\rm h}(z)]\}_{z=z_{\rm P}}$$
$$= (\cos^2\vartheta)\mathcal{B} \tag{2.191}$$

where

$$\mathcal{B} = (\beta_{\rm VI} + \beta_{\rm VII})\,\mathrm{erfc}\left(\frac{z_{\rm P}}{\mathcal{R}_{\rm g}}\right) - \beta_{\rm VII}\,\mathrm{erfc}\left(\frac{z_{\rm P}}{2\mathcal{R}_{\rm g}}\right) \tag{2.192}$$

Here ϑ is the angle between the axis of revolution of the particle and the surface normal of the wall at $z = 0$, as shown for ellipsoids in Fig. 2.15. The factor $\cos\vartheta$ in the orientation-dependent interaction (2.191) comes from the derivative $\partial_\parallel$, defined in (2.166) via $\partial_\parallel \psi(z) = \rho_z \psi'(z)$, where $\rho_z = \cos\vartheta$ is the component of $\boldsymbol{\rho}$ perpendicular to the wall.

The quantity $\mathcal{B}$ is proportional to the third power of the particle size (see Table 2.1) and has the limits

$$\mathcal{B} \to \left\{\beta_{\rm VI}\left[1 - \left(2 + \frac{\beta_{\rm VII}}{\beta_{\rm VI}}\right)\frac{z_{\rm P}}{\sqrt{\pi}\mathcal{R}_{\rm g}}\right],\ -\beta_{\rm VII}\frac{2\mathcal{R}_{\rm g}}{\sqrt{\pi}z_{\rm P}}\,\mathrm{e}^{-\frac{1}{4}(z_{\rm P}/\mathcal{R}_{\rm g})^2}\right\} \tag{2.193}$$

for $\{z_{\rm P}/\mathcal{R}_{\rm g} \ll 1,\ z_{\rm P}/\mathcal{R}_{\rm g} \gg 1\}$. In the intermediate regime, $\mathcal{B}$ changes sign at a scaled distance $z_{\rm P}/\mathcal{R}_{\rm g} = y_0(l/s)$, which depends on the shape of the

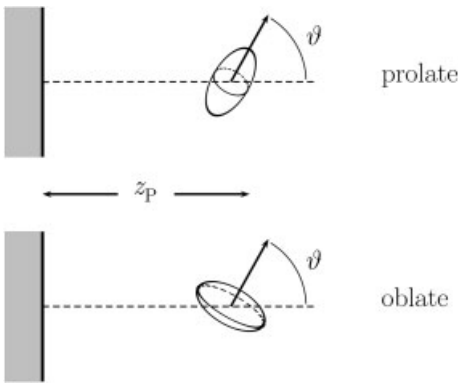

Fig. 2.15 Particles of prolate and oblate ellipsoidal shape near a planar wall. The ellipsoid is oriented parallel to the wall for $\vartheta = \pi/2$ in the prolate case and for $\vartheta = 0$ in the oblate case.

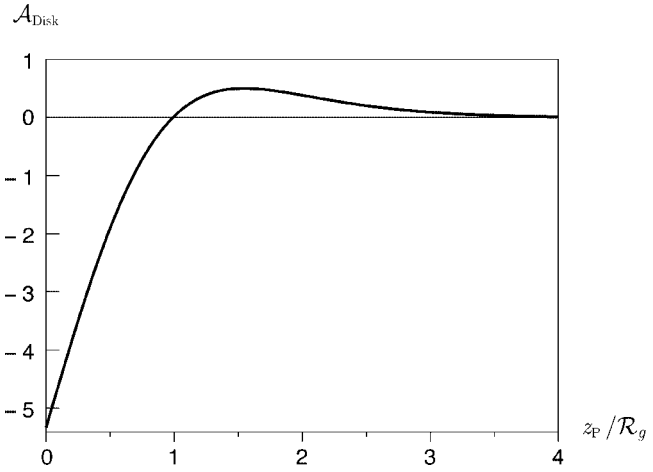

Fig. 2.16 The amplitude $\mathcal{A} \propto \mathcal{B}/$ (particle size)^3, which specifies the dependence (2.191) of the free energy of immersion $(\delta_{\mathrm{P}}F)_{\mathrm{W}}$ on the orientation of the small anisotropic particle with respect to the planar wall. The case $\mathcal{A}_{\mathrm{Disk}} = \mathcal{B}/R^3_{\mathrm{Disk}}$ of a circular disk of radius R_{Disk} given in Eq. (2.194) is shown. On decreasing the distance z_{P} between the center of the disk and the wall, $\mathcal{A}_{\mathrm{Disk}}$ passes through a maximum value of 0.501 at $z_{\mathrm{P}}/\mathcal{R}_{\mathrm{g}} = 1.55$, changes sign at $z_{\mathrm{P}}/\mathcal{R}_{\mathrm{g}} = y_{0,\mathrm{Disk}} = 0.99$, and drops to the value $-16/3$ for $z_{\mathrm{P}}/\mathcal{R}_{\mathrm{g}} \ll 1$. For $z_{\mathrm{P}}/\mathcal{R}_{\mathrm{g}} > y_{0,\mathrm{Disk}}$ and $< y_{0,\mathrm{Disk}}$, respectively, the most favorable orientation of the disk is perpendicular and parallel to the wall with $\cos\vartheta = 0$ and 1, respectively (see Eq. (2.191) and Fig. 2.15). For a general prolate or oblate small ellipsoid, the qualitative form of $\mathcal{B}/(\mathrm{particle\ size})^3$ is that of $-\mathcal{A}_{\mathrm{Disk}}$ or $\mathcal{A}_{\mathrm{Disk}}$, respectively.

particle. For the special case of a circular disk with a radius $R_{\mathrm{Disk}} = f$, one finds $\beta_j = f^3 B_j(0) = -R^3_{\mathrm{Disk}}(16/3, 8/3)$ for $j = (\mathrm{VI}, \mathrm{VII})$ and

$$\mathcal{B}/R^3_{\mathrm{Disk}} \equiv \mathcal{A}_{\mathrm{Disk}} \equiv 8\left[-\mathrm{erfc}\left(\frac{z_{\mathrm{P}}}{\mathcal{R}_{\mathrm{g}}}\right) + \frac{1}{3}\,\mathrm{erfc}\left(\frac{z_{\mathrm{P}}}{2\mathcal{R}_{\mathrm{g}}}\right)\right] \tag{2.194}$$

which is shown in Fig. 2.16.

Since β_{VI} and β_{VII} are both (positive, negative) for (prolate, oblate) particles, the free energy $(F_{\mathrm{P}})_{\mathrm{W}}$ for larger particle–wall separations $z_{\mathrm{P}}/\mathcal{R}_{\mathrm{g}} > y_0$ is lowest if the particle is aligned perpendicular to the wall with $\vartheta = (0, \pi/2)$, and for the smaller separations $z_{\mathrm{P}}/\mathcal{R}_{\mathrm{g}} < y_0$, if it is aligned parallel to the wall with $\vartheta = (\pi/2, 0)$.

This interesting behavior of $(F_{\mathrm{P}})_{\mathrm{W}}$ and the torque can be most easily understood *intuitively* for an ellipsoid with the shape of a thin needle of length l and maximum width s, which for $s \to 0$ in $d = 3$ is an infinitesimally small perturbation of the polymer system with (Eisenriegler et al. 2003)

$$\beta_{\mathrm{I}} \to \frac{2\pi l}{\lambda}, \quad \beta_{\mathrm{VII}} \to \frac{\pi l^3}{6\lambda}, \quad \frac{\beta_{\mathrm{VI}}}{\beta_{\mathrm{VII}}} \to 1 + \frac{1}{\lambda}\,. \tag{2.195}$$

Here $\lambda = \ln(2l/s)$ tends logarithmically to infinity as the width of the needle becomes much smaller than its length. In this limit $\beta_{\rm VI}/\beta_{\rm VII} \to 1$, $\beta_{\rm VI}O_{\rm VI} + \beta_{\rm VII}O_{\rm VII} \to \beta_{\rm VII}\,\partial_{\parallel}^2\Phi^2/4$, and

$$\mathcal{B} \to \beta_{\rm VII}[2\,{\rm erfc}(y_{\rm P}) - {\rm erfc}(y_{\rm P}/2)] = \beta_{\rm VII}\,\frac{1}{2}\left[\frac{{\rm d}^2}{{\rm d}y^2}\mathcal{M}_{\rm h}\right]_{y=y_{\rm P}} \tag{2.196}$$

where $y_{\rm P} = z_{\rm P}/\mathcal{R}_{\rm g}$, is proportional to the *curvature* of the monomer density $\mathcal{M}_{\rm h}$ in the half-space without the particle. For the needle y_0 equals the point of inflection $y_{\rm w} = 0.72$ of $\mathcal{M}_{\rm h}$.

This is plausible, since turning the needle around its center from a parallel to a perpendicular orientation with respect to the wall lowers the polymer free energy if the needle is inserted at a distance from the wall where $\mathcal{M}_{\rm h}''$ is negative. The reason is that the needle prefers polymer-depleted regions, and on turning it, the half of the needle closer to the wall gains more depletion than the farther half of the needle loses. If $\mathcal{M}_{\rm h}''$ is positive, the situation is reversed.

For the other shapes, the particle is not an infinitesimal perturbation, $\beta_{\rm VI}/\beta_{\rm VII} > 1$, and the $y_{\rm P}$ dependence of $\mathcal{B}$ differs from the y dependence of $\mathcal{M}_{\rm h}''$. For example an expansion for particles with $\beta_{\rm VI}/\beta_{\rm VII}$ slightly larger than unity shows that y_0 is *larger* than $y_{\rm w}$.

For the interaction with chains in a good solvent, one can expect interesting modifications of the ideal-chain results, since the degeneracy of scaling dimensions of the two anisotropic operators in Eqs. (2.162) to (2.166) is lifted and the stress-tensor component $T_{\parallel,\parallel}$ mentioned in footenote 13 (see page 132) becomes the leading anisotropic particle–operator.

2.10 Summary and Concluding Remarks

The methods of field theory are useful not only for pure polymer systems (de Gennes 1979; des Cloizeaux and Jannink 1990; Schäfer 1998) but also for polymers interacting with boundaries and colloidal particles.

For example, the density–pressure relation (2.65), which is based on the field-theoretical boundary operator expansion (2.72), predicts both the power-law exponent $1/\nu$ for the spatial variation of the density profile of chain monomers near a boundary (de Gennes 1979) and the amplitude $B_{\rm g}$ relating the density to the pressure that the polymers exert on the boundary. The two universal numbers $1/\nu$ and $B_{\rm g}$ have been estimated with both field theory and Monte Carlo simulations (Hsu and Grassberger 2003; Hsu and Grassberger

2004), and there is satisfactory agreement, as we discuss in Section 2.6.1 for a polymer chain trapped between parallel walls.

Other examples are the small-sphere expansion (2.109), based on the expansion (2.119) for a spherical inclusion in the field theory, and the corresponding expansions (2.162) to (2.166) for small anisotropic particles. These expansions represent the particle in terms of local polymer or field-theoretical operators, multiplied by amplitudes that depend on the size and shape of the particle. If there are additional perturbations, such as a wall or other particles, their distances, orientations, and shapes only affect the averages of the particle operators, and not the amplitudes. Thus the complicated problem of determining the induced interaction between the particle and the perturbations reduces, for small particle size, to two much simpler problems: (1) calculating the necessary correlation functions in the presence of the perturbations, with the particle, including its shape and boundary condition, *replaced* by a point operator, and (2) evaluating the corresponding amplitude by considering the particle in the *absence* of the perturbations. For the leading isotropic and anisotropic amplitudes, it is sufficient to consider the corresponding field theory right at the critical point.

At the critical point, the theory is not only scale-invariant but also conformally invariant (Cardy 1986). In addition to translations, rotations, and dilatations, conformal transformations include the *inversion about a sphere*. These transformations map spheres onto spheres and allow us to derive the critical point behavior in the presence of a colloidal particle with the shape of a sphere, a dumbbell composed of two touching spheres, and a dumbbell of two overlapping spheres or a lens from the simpler geometries of the half-space, the space between parallel plates, and in a wedge, respectively (see Fig. 2.13). This considerably simplifies the calculation of small particle amplitudes.

We have applied these and other field-theoretical tools (such as the diffusion equation for ideal polymers or the "renormalized mean-field approximation" for polymers with inter-chain interactions) to polymer–colloid interactions involving one or more colloidal particles.

In Sections 2.4 and 2.5, we discuss polymers interacting with a *single* wall and sphere, respectively. For a solution of ideal polymer chains, the induced density profiles are given in Eqs. (2.52), (2.55), (2.91), (2.105), and (2.108), and the free energy F it costs to immerse the spherical particle in Eq. (2.97). The form of the free energy F is compared with the Asakura–Oosawa expression (2.100), which neglects chain flexibility. The result (2.116) for F for a small sphere applies in the good solvent regime and for arbitrary inter-chain overlap. Results for the overlap dependence of the surface tension of a large sphere and the colloid-to-polymer size dependence of F for finite overlap are shown in Eqs. (2.85)–(2.90) and in Fig. 2.5, respectively. The pressure distribution

and force on a wall from an end-grafted ideal chain are given in Eqs. (2.83), (2.75), and (2.76).

Induced interactions between a plate and a wall, between a sphere and a wall, and between two and three spheres are discussed in Sections 2.6, 2.7, and 2.8, respectively. The ideal-chain results for the plate–wall interaction and the related Derjaguin expression for the interaction of a large sphere with a wall are given in Eqs. (2.136), (2.137), and (2.140) to (2.142), respectively. Figure 2.7 compares the Derjaguin expression with the Asakura–Oosawa approximation (2.143). The result (2.144) for a small sphere applies in both dilute and semidilute solutions, and Fig. 2.9 shows the sphere–wall interaction and force for arbitrary particle-to-polymer size ratio. The latter can be obtained either from the number of chains removed on inserting the particle, following from Eq. (2.132) and the end density in Fig. 2.8, or from the force on the wall, following from the density–force relation (2.149) and the local monomer density. Figure 2.10 shows the corresponding depletion profiles near the wall. Results for the interaction of two large spheres are given in Eq. (2.151). For small spheres, the small-particle expansion allows us to evaluate the polymer-induced many-body interactions systematically, and we give the results for two and three spheres in Eqs. (2.153), (2.154), (2.157), and (2.159), respectively.

In Section 2.9 we consider small *anisotropic* colloidal particles, such as prolate or oblate ellipsoids of revolution and dumbbells, composed of two spheres that touch or intersect at an angle α (see Fig. 2.11). For the interaction with ideal chains, the small-particle amplitudes of ellipsoids are given in Eqs. (2.180) to (2.184), and of dumbbells with $\alpha = 0$ (touching spheres) and $\alpha = \pi/2$ in (2.176) and (2.177), respectively. In Table 2.1 we compare the two dumbbells with the smallest circumscribing ellipsoids, as shown in Figs. 2.12 and 2.14. The preferred orientation of the anisotropic particle interacting with a planar wall (see Fig. 2.15) changes from perpendicular to parallel to the wall as the particle–wall distance decreases (see Eqs. (2.191) to (2.194) and Fig. 2.16). The change in preferred orientation is understood most easily for a needle-shaped particle – see the paragraph containing Eq. (2.195).

We have only considered situations with a *few* colloidal particles, obtaining the polymer-induced immersion free energies of single particles, the pair (and three-body) interaction free energies between colloid particles, and that between a single particle and a wall. These results are interesting in their own right and should be experimentally observable (Verma et al. 1998; Ohshima et al. 1997; Rudhardt et al. 1998). They are also a necessary prerequisite for calculating the phase diagrams of polymer–colloid mixtures for finite colloid concentrations.

Acknowledgment

It is a pleasure to thank T.W. Burkhardt for useful discussions.

References

Abramowitz, M. and Stegun, I., 1972, *Handbook of Mathematical Functions*. Dover Publications, New York.
Asakura, S. and Oosawa, F., 1954, *J. Chem. Phys.* **22**, 1255.
Asakura, S. and Oosawa, F., 1958, *J. Polym. Sci.* **33**, 183.
Binder, K., 1986, in: *Phase Transitions and Critical Phenomena*, eds. C. Domb and J. Lebowitz, Vol. 8, pp. 1–144. Academic Press, London.
Breidenich, M., Netz, R., and Lipowsky, R., 2000, *Europhys. Lett.* **49**, 431.
Bringer, A., Eisenriegler, E., Schlesener, F., and Hanke, A., 1999, *Eur. Phys. J. B* **11**, 101.
Brown, L. and Collins, J., 1980, *Ann. Phys.* **130**, 215.
Burkhardt, T. and Eisenriegler, E., 1995, *Phys. Rev. Lett.* **74**, 3189.
Cardy, J., 1983, *J. Phys. A* **16**, 3617.
Cardy, J., 1986, in: *Phase Transitions and Critical Phenomena*, eds. C. Domb and J. Lebowitz, Vol. 11, pp. 55–126. Academic Press, London.
Cardy, J. and Hamber, H., 1980, *Phys. Rev. Lett.* **45**, 499.
Chatterjee, A. and Schweizer, K., 1998, *J. Chem. Phys.* **109**, 10464.
de Gennes, P.-G., 1979, *Scaling Concepts in Polymer Physics*. Cornell University Press, Ithaca, NY.
des Cloizeaux, J. and Jannink, G., 1990, *Polymers in Solution*. Clarendon, Oxford.
Diehl, H. W., 1986, in: *Phase Transitions and Critical Phenomena*, eds. C. Domb and J. Lebowitz, Vol. 10, pp. 75–267. Academic Press, London.
Diehl, H. W., 1997, *Int. J. Mod. Phys. B* **11**, 3503.
Diehl, H., Dietrich, S., and Eisenriegler, E., 1983, *Phys. Rev. B* **27**, 2937.
Dietrich, S. and Diehl, H., 1981, *Z. Phys. B* **43**, 315.
Eisenriegler, E., 1993, *Polymers Near Surfaces*. World Scientific, Singapore.
Eisenriegler, E., 1997, *Phys. Rev. E* **55**, 3116.
Eisenriegler, E., 1998, in: *Lecture Notes in Physics*, eds. H. Meyer-Ortmanns and A. Kluemper, Vol. 508, pp. 1–24. Springer, Berlin.
Eisenriegler, E., 2000, *J. Chem. Phys.* **113**, 5091.
Eisenriegler, E., 2004, *J. Chem. Phys.* **121**, 3299.
Eisenriegler, E. and Bringer, A., 2005, *J. Phys. Condens. Matter* **17**, S1711.
Eisenriegler, E. and Ritschel, U., 1995, *Phys. Rev. B* **51**, 13717.
Eisenriegler, E., Hanke, A., and Dietrich, S., 1996, *Phys. Rev. E* **54**, 1134.
Eisenriegler, E., Bringer, A., and Maassen, R., 2003, *J. Chem. Phys.* **118**, 8093.

Flammer, C., 1957, *Spheroidal Wave Functions*. Stanford University Press, Stanford, CA.
Hanke, A., Eisenriegler, E., and Dietrich, S., 1999, *Phys. Rev. E* **59**, 6853.
Hsu, H.-P. and Grassberger, P., 2003, *Eur. Phys. J. B* **36**, 209.
Hsu, H.-P. and Grassberger, P., 2004, *J. Chem. Phys.* **120**, 2034.
Jansons, K. and Phillips, C., 1990, *J. Colloid Interface Sci*. **137**, 75.
Johnson, P. M., van Kats, C. M., and van Blaaderen, A., 2005, *Langmuir* (to be published).
Lipowsky, R., 1995, *Europhys. Lett*. **30**, 197.
Louis, A., Bolhuis, P., Meijer, E., and Hansen, J.-P., 2002, *J. Chem. Phys.* **116**, 10 547.
Maassen, R., Eisenriegler, E., and Bringer, A., 2001, *J. Chem. Phys*. **115**, 5292.
Nelson, D., 1976, *Phys. Rev. B* **14**, 1123.
Nienhuis, B., 1982, *Phys. Rev. Lett*. **49**, 1062.
Obukhov, S. P. and Semenov, A. N., 2005, *J. Phys. Condens. Matter* **17**, S1747.
Odijk, T., 2000, *Physica A* **278**, 347.
Ohshima, Y. N., Sakagami, H., Okumoto, K., Tokoyoda, A., Igarishi, T., Shintaku, K. B., Toride, S., Sekino, H., Kabuto, K., and Nishio, I., 1997, *Phys. Rev. Lett*. **78**, 3963.
Rudhardt, D., Bechinger, C., and Leiderer, P., 1998, *Phys. Rev. Lett*. **81**, 1330.
Schäfer, L., 1998, *Excluded Volume Effects in Polymer Solutions*. Springer, Heidelberg.
Snoeks, E., van Blaaderen, A., van Dillen, T., van Kats, C. M., Brongersma, M. L., and Polman, A., 2000, *Adv. Mater.* **12**, 1511.
Taniguchi, T., Kawakatsu, T., and Kawasaki, K., 1992, *Slow Dyn. Condens. Matter* **256**, 503.
Tuinier, R., Vliegenthart, G., and Lekkerkerker, H., 2000, *J. Chem. Phys*. **113**, 10768.
van Blaaderen, A., 2003, *Science* **301**, 470.
van Blaaderen, A., 2004, *Materials Research Society Bulletin*, Vol. 29, No. 2.
Verma, R., Crocker, J. C., Lubensky, T. C., and Yodh, A. G., 1998, *Phys. Rev. Lett*. **81**, 4004.
Zinn-Justin, J., 1989, *Quantum Field Theory and Critical Phenomena*. Clarendon, Oxford.

3
Rod-Like Brownian Particles in Shear Flow

Jan K. G. Dhont and Wim J. Briels

Abstract

This chapter is a self-contained treatment of various aspects concerning suspensions of uniaxial rod-like colloidal particles in flow. First of all, the friction coefficients of rods in an otherwise unbounded fluid will be calculated and the motion of a single rod in flow will be discussed, for both a non-Brownian and a Brownian rod. The generalized diffusion equation for interacting rods, the so-called N-particle Smoluchowski equation, is then discussed, on the basis of which the Doi–Edwards equation of motion for the orientational order-parameter tensor is derived. This microscopic derivation reveals the approximations that are involved in the Doi–Edwards theory. One of the approximations involves the neglect of dynamical correlations. Computer simulations indicate that such correlations might be important. On the basis of the Doi–Edwards equation (supplemented with an appropriate closure relation) together with experimental results, the phase behavior of rods in simple shear flow is addressed. A microscopic expression for the stress tensor for suspensions of rigid colloidal particles is then derived, and subsequently expressed in terms of the orientational order-parameter tensor. The viscoelastic response of suspensions of stiff rods is discussed, and theory is compared with experiments and simulations. In the last section, current research interests will be briefly discussed, including banding transitions, the non-equilibrium phase diagram under flow conditions, and phase separation kinetics.

Soft Matter, Vol. 2: Complex Colloidal Suspensions. Edited by G. Gompper and M. Schick

ISBN: 3-527-31369-9

3.1 Introduction

Flow affects the microstructural order of colloidal systems in two respects: center-to-center correlations are affected by flow, and flow can induce changes in orientational order. For spherical colloids, flow-induced changes of macroscopic properties find their origin entirely in shear-induced changes of center-to-center correlations. For non-spherical colloidal particles, there is the additional effect that flow tends to align single colloidal particles due to the torques that the flowing solvent exerts on their cores. For very elongated colloidal cores, single-particle alignment is dominant over shear-induced changes of center-to-center correlations. For such systems, equations for one-particle orientational distribution functions, with the neglect of flow-induced distortions of center-to-center correlations, are sufficient to predict their macroscopic behavior under flow. For spherical colloidal particles, however, one-particle distribution functions are not affected by flow, so that theory for spheres should be based on equations for correlation functions.

This chapter deals with stiff, uniaxial colloidal rods with a very large aspect ratio in shear flow. It will be assumed throughout the chapter that the center-to-center correlation function is not affected by flow, and is thus equal to the corresponding correlation function in equilibrium, in the absence of flow. In addition, the singlet function of rods surrounding a given rod is taken equal to the singlet function of that given rod at the same instant of time. As will be discussed, these two simplifications are equivalent to the neglect of dynamical correlations. There are indications from computer simulations, however, that dynamical correlations might play a role.

Examples of flow-affected macroscopic phenomena that will be discussed in the present chapter are the shear-induced shift of the isotropic–nematic phase transition and the shear-rate-dependent viscoelastic response. The effect of shear flow on microstructural order, which is at the origin of shear-induced macroscopic phenomena, will be considered in detail. In addition, shear flow induces phenomena that do not occur in the absence of flow, such as pattern formation (or, more specifically, shear banding) and dynamical states under stationary applied flow. These will be addressed only briefly at the end of this chapter.

The aim of this chapter is to set up, in a self-contained fashion, a microscopic theory of the behavior of rods in flow. Some of the results presented here are on a textbook level, some are re-derivations of well-known equations, and some are at the edge of current research interests. Much of the introductory material on colloids is also discussed by Doi and Edwards (1986), Russel et al. (1991) and Dhont (1996).

First of all, the so-called *velocity-gradient tensor* will be defined in Section 3.2. This tensor describes the type of flow that is applied. Two types of flow are of particular importance: simple shear flow and elongational (or extensional) flow. Simple shear flow is a velocity profile where the gradient in the fluid flow velocity is constant, whereas for elongational flow the sample is compressed in one direction and elongated in the other direction. Such flows can be either stationary or oscillatory.

Colloidal rods tend to align in a flow field due to the interaction of the solvent with the surface of the core of the rods. As a first step to understand how orientational order is affected by flow, the force and torque of the solvent on a single rod in an otherwise unbounded fluid must be calculated. Since the linear dimensions of the rods are much larger than the size of solvent molecules, the solvent can be described on the basis of hydrodynamics. The rod is treated as a macroscopic object as far as its interactions with solvent molecules is concerned. The basic knowledge of hydrodynamics relevant for colloids is developed in Section 3.3. The main result here is that inertial effects can be neglected on a time scale that is relevant for colloids, leading to the so-called *creeping flow equations* for the solvent flow velocity. These are linear equations of motion, for which the Green's function, known as the *Oseen tensor*, is derived in Section 3.3. Friction of rods in a flowing solvent is then treated on the basis of these basic hydrodynamic equations in Section 3.4. Friction coefficients can be calculated exactly for ellipsoidal rods of arbitrary aspect ratio, which involves an exact solution of the creeping flow equations (Happel and Brenner 1983). Alternatively, friction coefficients are derived in Section 3.4 on the basis of the bead model for a rod, by analyzing the forces that act on beads.

Once the hydrodynamic friction coefficients are known, the orbits of the orientation of a non-Brownian rod in a flow field can be analyzed. These so-called *Jeffery orbits* are discussed in Section 3.5. Here, interactions between rods are not incorporated, i.e. the orbits of a single rod in an otherwise unbounded fluid are considered.

Brownian motion in the absence of flow is then analyzed in Section 3.6 on the basis of Newton's equation of motion. This equation of motion includes a random force that describes forces originating from collisions of solvent molecules with the surface of the colloidal particle. Such equations of motion containing a fluctuating term are referred to as *Langevin equations*. Specifying certain statistical properties of the random force allows one to distinguish between several important time scales and the calculation of the *mean square displacement*. Again, this analysis is performed for a single rod in an otherwise unbounded solvent.

For the description of Brownian motion and diffusion of rods at higher rod concentration, where interactions between rods are important, it is more

convenient to employ equations of motion for probability density functions. The fundamental equation of motion of this sort, the so-called *Smoluchowski equation*, is derived in Section 3.7. In the same section it is shown that the diffusive properties as obtained in Section 3.6 on the basis of the Langevin equation are reproduced by the Smoluchowski equation.

At higher concentrations and when a flow field is applied, the orientational order can be quantified by means of the *orientational order-parameter tensor* $\boldsymbol{S}$. This tensor is introduced in Section 3.8. It is shown that the largest eigenvalue of this tensor is a measure for the degree of orientational order and that the corresponding eigenvector defines the preferred orientation of the rods.

Orientational order for very dilute rod suspensions under flow are discussed in Section 3.9. Interactions between rods are neglected here. Solutions of the Smoluchowski equation are shown to be in accordance with computer simulations.

Orientational order and phase behavior of concentrated suspensions in flow are analyzed by means of an equation of motion for the order-parameter tensor $\boldsymbol{S}$, which is known as the *Doi–Edwards equation*. In Section 3.10 this equation of motion is derived from the Smoluchowski equation. This derivation is a microscopic basis of the Doi–Edwards equation, which reveals the approximations that are implicit in the Doi–Edwards equation. To obtain a closed equation of motion for the second-order tensor $\boldsymbol{S}$, a closure relation must be used for a fourth-order tensor. There are a number of propositions for such a closure relation. A simple closure relation will be discussed in Section 3.10, which is shown to be accurate to within about 10%. This particular closure relation, however, cannot describe non-stationary states under stationary flow conditions like tumbling and wagging. To describe such states, the Smoluchowski equation itself should be solved numerically. This will not be discussed in the present chapter.

The isotropic–nematic phase transition is discussed in Section 3.11, both without and with simple shear flow. The bifurcation diagram is introduced and the paranematic-to-nematic and nematic-to-paranematic spinodals in the shear-rate versus concentration plane are calculated. The prediction of the shear-rate-dependent location of binodals is much more complicated, and requires equations of motion for the orientational order-parameter tensor *and* the flow field velocity, which should accurately account for strong inhomogeneities in concentration, orientational order parameter, and shear rate. Such equations of motion will not be derived in this chapter, but only briefly discussed in the last section on current research.

In the derivation of the Doi–Edwards equation of motion from the Smoluchowski equation, dynamical correlations are neglected. Computer simulations indicate, however, that such correlations are important for the description of diffusion. The discrepancy between the analytically obtained effective

collective diffusion coefficients within the Doi–Edwards theory and that found in computer simulations is discussed in Section 3.12.

A microscopic derivation of the stress tensor in terms of the concentration and the orientational order-parameter tensor is given in Section 3.13. Within certain approximations, a very similar expression as in the Doi–Edwards–Kuzuu theory is obtained. On the basis of this expression for the stress tensor, the (nonlinear) viscoelastic response of rod suspensions is discussed in Section 3.14. Analytical and numerical predictions are compared to experiments and computer simulations. A surprising finding is that the zero-shear, zero-frequency shear viscosity is a linear function of the concentration up to very high concentrations, in accordance with computer simulations. Comparison with experiments indicates a sensitive dependence of the viscoelastic behavior on the flexibility of the core of the rods. So far, no theory on the dynamics and viscoelastic response is available that incorporates flexibility.

Section 3.15 is a (certainly biased) overview of the current research interests in the field of rod suspensions under shear flow. The possible non-equilibrium phase diagram is addressed, together with banding transitions, non-stationary states, and the kinetics of phase separation and band formation.

3.2
The Velocity-Gradient Tensor

A linear flow profile is characterized by means of the so-called velocity-gradient tensor $\boldsymbol{G}$, where the flow velocity $\boldsymbol{u}$ at position $\boldsymbol{r}$ is written as $\boldsymbol{u} = \boldsymbol{G} \cdot \boldsymbol{r}$. For spatially varying flow profiles, velocities can be described locally by such a linear flow profile, provided that gradients are small on the length scale set by the size of the colloidal particles. The velocity-gradient tensor can have several different forms. In the case of so-called *simple shear flow*, the velocity-gradient tensor is usually denoted as $\boldsymbol{\Gamma}$, and is equal to

$$\boldsymbol{\Gamma} = \dot{\gamma} \begin{pmatrix} 0 & 1 & 0 \\ 0 & 0 & 0 \\ 0 & 0 & 0 \end{pmatrix}, \quad \text{simple shear flow} \tag{3.1}$$

The corresponding flow profile is a flow in the x direction, with its gradient in the y direction, as sketched in Fig. 3.1(a). The z direction is commonly referred to as the vorticity direction. The strength of the flow is characterized by the *shear rate* $\dot{\gamma}$, which equals the spatial gradient $\partial u_x / \partial y$ of the flow velocity u_x in the x direction. For so-called *elongational* or *extensional flow*, where the velocity-gradient tensor is denoted as $\boldsymbol{E}$, we have

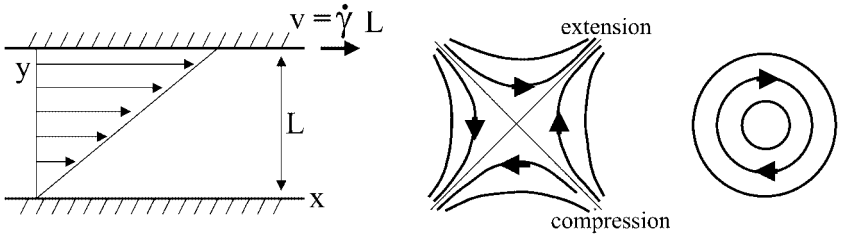

Fig. 3.1 (a) Simple shear flow, where L is the gap width; (b) elongational flow, sometimes also referred to as extensional flow, where the extensional and compressional axes are indicated; (c) rotational flow, with arrows indicating the flow direction.

$$\boldsymbol{E} = \dot{\gamma} \begin{pmatrix} 0 & 1 & 0 \\ 1 & 0 & 0 \\ 0 & 0 & 0 \end{pmatrix}, \quad \text{elongational flow} \tag{3.2}$$

the flow of which is sketched in Fig. 3.1(b). In such an elongational flow, deformable objects tend to elongate along the so-called extensional axis, and suppressed along the compressional axis. These two directions are indicated in Fig. 3.1(b). Whenever it is not specified whether simple shear flow or elongational flow is considered, the velocity-gradient tensor will be denoted as $\boldsymbol{G}$.

We will encounter the symmetric part $\boldsymbol{E} = \frac{1}{2}[\boldsymbol{G} + \boldsymbol{G}^{\mathrm{T}}]$ of the velocity-gradient tensor, where the superscript "T" stands for the transpose of the corresponding tensor. For elongational flow, the velocity-gradient tensor is already symmetric: this is why we denoted the velocity-gradient tensor for elongational flow by $\boldsymbol{E}$ in Eq. (3.2). For simple shear flow we have

$$\boldsymbol{E} = \tfrac{1}{2}\dot{\gamma} \begin{pmatrix} 0 & 1 & 0 \\ 1 & 0 & 0 \\ 0 & 0 & 0 \end{pmatrix}, \quad \text{simple shear flow} \tag{3.3}$$

We will sometimes also encounter the antisymmetric part $\boldsymbol{\Omega} = \frac{1}{2}[\boldsymbol{G} - \boldsymbol{G}^{\mathrm{T}}]$ of the velocity-gradient tensor. For elongational flow the antisymmetric part is zero, while for simple shear flow we have

$$\boldsymbol{\Omega} = \tfrac{1}{2}\dot{\gamma} \begin{pmatrix} 0 & 1 & 0 \\ -1 & 0 & 0 \\ 0 & 0 & 0 \end{pmatrix}, \quad \text{simple shear flow} \tag{3.4}$$

The flow velocities corresponding to flow with a velocity-gradient tensor equal to $\boldsymbol{E}$ in Eq. (3.3) or $\boldsymbol{\Omega}$ in Eq. (3.4) are sketched in Fig. 3.1(b) and (c), respectively. The former case is an elongational flow, also referred to as extensional flow; while the second is pure rotational flow. Note that

$$\boldsymbol{\Gamma} = \boldsymbol{E} + \boldsymbol{\Omega} \tag{3.5}$$

so that simple shear flow can be decomposed into a linear combination of elongational and rotational flow.

In laboratory experiments, the shear rate is either independent of time, or the shear rate can be sinusoidally oscillating:

$$\begin{aligned} \dot{\gamma} &= \text{time independent}, && \text{stationary flow} \\ \dot{\gamma}(t) &= \dot{\gamma}_0 \cos(\omega t), && \text{oscillatory flow} \end{aligned} \tag{3.6}$$

where ω is the frequency of oscillation and $\dot{\gamma}_0$ is referred to as the *shear-rate amplitude*. Oscillatory experiments can be employed to probe the dynamics of a system of Brownian particles.

3.3 Hydrodynamics

Consider a system containing large rod-like particles immersed in a fluid. There are three types of interactions to be distinguished in such a system: interactions of rods with rods, solvent molecules with solvent molecules, and rods with solvent molecules. The latter two types of interactions can be described on the basis of phenomenological equations for fluid flow, provided that the linear dimensions of the rods are much larger than the size of the solvent molecules. Such solutions of large molecules are referred to as *Brownian* or *colloidal systems*. The large difference in relevant length scales between the solvent and the assembly of Brownian rods allows one to describe the solvent on a phenomenological level, without losing the microscopic basis for the assembly of Brownian particles. In such a phenomenological treatment, only the macroscopic quantities of the fluid, such as its viscosity and mass density, enter the equations of interest. In the present section, the friction coefficients of rods are calculated, which will be used later in this chapter in the microscopic equations of motion for rod-like Brownian particles.

The mechanical state of the solvent is characterized by the local velocity $\boldsymbol{u}(\boldsymbol{r}, t)$ at position $\boldsymbol{r}$ at time t, the pressure $p(\boldsymbol{r}, t)$, and the mass density $\rho(\boldsymbol{r}, t)$. All these fields are averages over small volume elements that are located at the various positions $\boldsymbol{r}$. These volume elements must be so small that

the state of the fluid hardly changes within the volume elements. At the same time, the volume elements should contain many fluid molecules, to be able to define such averages properly. In particular we wish to define the thermodynamic state of volume elements, which is possible when they contain a large number of solvent molecules, and when they are in internal equilibrium, i.e. when there is *local equilibrium*. In this way the temperature field $T(\boldsymbol{r}, t)$ may be defined. The temperature dependence of, for example, the mass density is then described by thermodynamic relations. These thermodynamic relations are an important ingredient in a general theory of hydrodynamics. For our purposes, however, the temperature and mass density may be considered constant. Temperature variations due to viscous dissipation in the solvent are assumed to be negligible. At constant temperature, the only mechanism to change the mass density of the solvent is to vary the pressure. For fluids, however, exceedingly large pressures are needed to change the density significantly; that is, fluids are quite *incompressible*. Brownian motion is not vigorous enough to induce such extreme pressure differences, so that the density will also be assumed constant. The assumption of constant temperature and density is also a matter of time scales. The relaxation times for local temperature and pressure differences in the solvent are much faster than typical time scales relevant for Brownian motion.

Assuming constant temperature and mass density leaves just two variables that describe the state of the fluid: the fluid flow velocity $\boldsymbol{u}(\boldsymbol{r}, t)$ and the pressure $p(\boldsymbol{r}, t)$. Thermodynamic relations need not be considered in this case, simplifying the phenomenological analysis considerably.

3.3.1 The Continuity Equation

The rate of change of the mass of fluid contained in some arbitrary volume $\mathcal{W}$ is equal to the mass of fluid flowing through its boundary $\partial\mathcal{W}$. The local velocity at surface elements on $\partial\mathcal{W}$ can be written as the sum of its components parallel and perpendicular to the surface. The parallel component does not contribute to the inward and outward fluxes of mass through the boundary $\partial\mathcal{W}$. Only the component $\boldsymbol{u} \cdot \hat{\boldsymbol{n}}$ of the flow perpendicular to the surface gives rise to the inward and outward fluxes of mass, where $\hat{\boldsymbol{n}}$ is the unit normal of the corresponding surface element. Hence,

$$\frac{\mathrm{d}}{\mathrm{d}t} \int_{\mathcal{W}} \mathrm{d}\boldsymbol{r}\, \rho(\boldsymbol{r}, t) = - \oint_{\partial\mathcal{W}} \mathrm{d}\boldsymbol{S} \cdot [\rho(\boldsymbol{r}, t)\boldsymbol{u}(\boldsymbol{r}, t)]$$

where $\mathrm{d}\boldsymbol{S} = \hat{\boldsymbol{n}}\, \mathrm{d}S$, with $\mathrm{d}S$ an infinitesimal surface area. The minus sign on the right-hand side is added because the mass in $\mathcal{W}$ decreases when $\boldsymbol{u}$ is along the outward normal. The time derivative on the left-hand side can

be taken inside the integral, while the integral on the right-hand side can be written as an integral over the volume $\mathcal{W}$, using Gauss's integral theorem. This leads to

$$\int_{\mathcal{W}} \mathrm{d}\boldsymbol{r} \left(\frac{\partial}{\partial t} \rho(\boldsymbol{r}, t) + \nabla \cdot [\rho(\boldsymbol{r}, t) \boldsymbol{u}(\boldsymbol{r}, t)] \right) = 0$$

where ∇ is the gradient operator with respect to $\boldsymbol{r}$. Since the volume $\mathcal{W}$ is an arbitrary volume, the integrand must be equal to zero. This can be seen by choosing $\mathcal{W}$ as a sphere centered at some position $\boldsymbol{r}$, with an (infinitesimally) small radius. Within that small sphere, the integrand in the above integral is constant, so that the integral reduces to the product of the volume of $\mathcal{W}$ and the value of the integrand at the point $\boldsymbol{r}$. Hence,

$$\frac{\partial}{\partial t} \rho(\boldsymbol{r}, t) + \nabla \cdot [\rho(\boldsymbol{r}, t) \boldsymbol{u}(\boldsymbol{r}, t)] = 0$$

This equation expresses conservation of mass, and is referred to as the *continuity equation*.

For a fluid with a constant mass density, the continuity equation reduces to

$$\nabla \cdot \boldsymbol{u}(\boldsymbol{r}, t) = 0 \tag{3.7}$$

Fluids with an essentially constant mass density are referred to as *incompressible fluids*, and Eq. (3.7) is therefore sometimes referred to as the *incompressibility equation*. Being nothing more than the condition to ensure conservation of mass, this single equation is not sufficient to calculate the fluid flow velocity. It must be supplemented by Newton's equation of motion to obtain a closed set of equations.

3.3.2 The Navier–Stokes Equation

The Navier–Stokes equation is Newton's equation of motion for a small amount of mass contained in a volume element within a fluid. Consider such an infinitesimally small volume element, the volume of which is denoted as $\delta\boldsymbol{r}$. The position $\boldsymbol{r}$ of that volume element as a function of time is set by Newton's equation of motion. The momentum that is carried by the mass element is equal to $\rho(\boldsymbol{r}, t)(\delta\boldsymbol{r})\boldsymbol{u}(\boldsymbol{r}, t)$, so that Newton's equation of motion reads

$$\rho(\boldsymbol{r}, t) \delta\boldsymbol{r} \frac{\mathrm{d}\boldsymbol{u}(\boldsymbol{r}, t)}{\mathrm{d}t} = \boldsymbol{f}$$

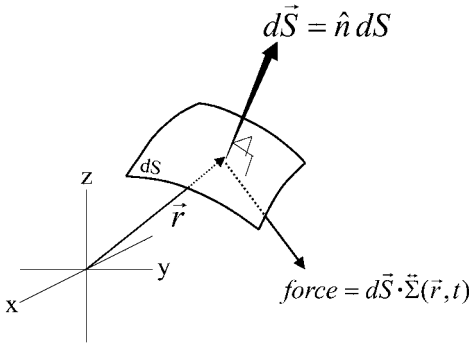

Fig. 3.2 Definition of the stress tensor $\boldsymbol{\Sigma}$.

where $\boldsymbol{f}$ is the total force that is exerted on the mass element. Since in Newton's equations of motion $\boldsymbol{r}$ is the time-dependent position coordinate of the volume element, and $\mathrm{d}\boldsymbol{r}/\mathrm{d}t = \boldsymbol{u}$ is the velocity of the volume element, the above equation can be written as

$$\rho(\boldsymbol{r}, t)\delta\boldsymbol{r}\left[\frac{\partial \boldsymbol{u}(\boldsymbol{r}, t)}{\partial t} + \boldsymbol{u}(\boldsymbol{r}, t) \cdot \nabla \boldsymbol{u}(\boldsymbol{r}, t)\right] = \boldsymbol{f}$$

Here, $\nabla \boldsymbol{u}$ is a dyadic product, i.e. a tensor whose ijth component is equal to $\nabla_i \boldsymbol{u}_j$, with ∇_i the differentiation with respect to r_i, the ith component of $\boldsymbol{r}$.

The total force $\boldsymbol{f}$ on the volume element consists of two parts. First of all, there may be external fields that exert forces on the fluid. These forces are denoted by $(\delta\boldsymbol{r})\boldsymbol{f}^{\mathrm{ext}}(\boldsymbol{r})$, that is, $\boldsymbol{f}^{\mathrm{ext}}$ is the external force on the fluid per unit volume. The second part arises from interactions of the volume element with the surrounding fluid.

The forces due to interactions with the surrounding fluid are formally expressed in terms of the *stress tensor* $\boldsymbol{\Sigma}(\boldsymbol{r}, t)$, which is defined as follows. Consider an infinitesimally small surface area in the fluid, with surface area $\mathrm{d}S$ and normal unit vector $\hat{\boldsymbol{n}}$. The force per unit area exerted by the fluid located on the side of the surface area to which the unit normal is directed, onto the fluid on the opposite side of the surface area, is by definition equal to $\mathrm{d}\boldsymbol{S} \cdot \boldsymbol{\Sigma}$, with $\mathrm{d}\boldsymbol{S} = \hat{\boldsymbol{n}}\,\mathrm{d}S$ (see Fig. 3.2).

Hence, by definition, the force of the surrounding fluid on the volume element $\delta\boldsymbol{r}$ is equal to

$$\oint_{\partial\delta\boldsymbol{r}} \mathrm{d}\boldsymbol{S}' \cdot \boldsymbol{\Sigma}(\boldsymbol{r}', t) = \int_{\delta\boldsymbol{r}} \mathrm{d}\boldsymbol{r}'\, \nabla' \cdot \boldsymbol{\Sigma}(\boldsymbol{r}', t) = \delta\boldsymbol{r}\, \nabla \cdot \boldsymbol{\Sigma}(\boldsymbol{r}, t)$$

where $\partial\delta\boldsymbol{r}$ is the boundary of the volume element. We have used Gauss's integral theorem to rewrite the surface integral as a volume integral. The last

equation is valid due to the infinitesimal size $\delta \boldsymbol{r}$ of the volume element at position $\boldsymbol{r}$. The force $\boldsymbol{f}^{\mathrm{h}}$ on the volume element due to the interaction with the surrounding fluid is thus given by

$$\boldsymbol{f}^{\mathrm{h}}(\boldsymbol{r},t) = (\delta \boldsymbol{r})\, \nabla \cdot \boldsymbol{\Sigma}(\boldsymbol{r},t) \tag{3.8}$$

There are two contributions to the stress tensor: a contribution resulting from gradients in the fluid flow velocity, and a contribution due to pressure gradients.

Consider first the forces due to pressure gradients. Let us take the volume element $\delta \boldsymbol{r}$ to be a cube, with side of length δl. The pressure p is the force per unit area, so that the force on the volume element in the x direction is equal to

$$(\delta l)^2[p(x-\tfrac{1}{2}\delta l, y, z, t) - p(x+\tfrac{1}{2}\delta l, y, z, t)] = -(\delta l)^3 \frac{\partial}{\partial x} p(x, y, z, t)$$

where $(\delta l)^2$ is the area of the faces of the cube. The force on the volume element is thus $-(\delta \boldsymbol{r})\nabla p(\boldsymbol{r},t)$. We therefore arrive at $\nabla \cdot \boldsymbol{\Sigma} = -\nabla p$. The contribution of pressure gradients to the stress tensor is thus easily seen to be equal to

$$\boldsymbol{\Sigma}(\boldsymbol{r},t) = -p(\boldsymbol{r},t)\, \hat{\boldsymbol{I}}$$

with $\hat{\boldsymbol{I}}$ the (3×3)-dimensional unit tensor. This contribution to the stress tensor is referred to as the *isotropic part of the stress tensor*, since it is proportional to the unit tensor and therefore does not have a preferred spatial direction.

Next, consider the forces on the volume element due to gradients in the fluid flow velocity. When the fluid flow velocity is uniform, i.e. when there are no gradients in the fluid flow velocity, the only forces on the volume element are due to the pressure and possibly external forces. In addition, there are friction forces only when the volume element has a velocity that differs from that of the surrounding fluid. The contribution to the stress tensor due to friction forces is therefore a function of the spatial derivatives of the flow velocity, not of the velocity itself. This contribution to the stress tensor can be formally expanded in a power series with respect to the gradients in the fluid flow velocity. For not too large gradients (such that the fluid velocity is approximately constant over distances of many times the molecular dimension), the leading term in such an expansion suffices to describe friction forces. The contribution of gradients in the fluid flow velocity to the stress tensor is thus a linear combination of the derivatives $\nabla_i u_j(\boldsymbol{r},t)$, where ∇_i is the derivative with respect to the ith component of $\boldsymbol{r}$, and $u_j(\boldsymbol{r},t)$ is the jth component of $\boldsymbol{u}(\boldsymbol{r},t)$.

There are also no friction forces when the fluid is in uniform rotation, in which case the flow velocity is equal to $\boldsymbol{u} = \boldsymbol{\Omega} \times \boldsymbol{r}$, with $\boldsymbol{\Omega}$ the angular velocity. Such a fluid flow corresponds to rotation of the vessel containing the fluid, relative to the observer. Linear combinations of the form

$$\nabla_i u_j(\boldsymbol{r}, t) + \nabla_j u_i(\boldsymbol{r}, t) \tag{3.9}$$

are easily verified to vanish in the case $\boldsymbol{u} = \boldsymbol{\Omega} \times \boldsymbol{r}$. The stress tensor is thus proportional to such linear combinations of gradients in the fluid velocity field.

For isotropic fluids, with no preferred spatial direction, the most general expression for the components Σ_{ij} of the stress tensor as a result of friction is therefore

$$\Sigma_{\mathrm{D},ij} = \eta_0[\nabla_i u_j + \nabla_j u_i - \tfrac{2}{3}\delta_{ij}\nabla \cdot \boldsymbol{u}(\boldsymbol{r}, t)] + \zeta_0 \delta_{ij}\, \nabla \cdot \boldsymbol{u} \tag{3.10}$$

where the subscript "D" stands for the *deviatoric part of the stress tensor*. The terms $\sim \nabla \cdot \boldsymbol{u}(\boldsymbol{r}, t)$ on the right-hand side are due to the linear combinations (3.9) with $i = j$. The term $-\frac{2}{3}\nabla \cdot \boldsymbol{u}(\boldsymbol{r}, t)$ is introduced to make the expression between the square brackets traceless (meaning that the sum of the diagonal elements of that contribution is zero). It could also have been absorbed into the last term on the right-hand side. The constants η_0 and ζ_0, which are scalar quantities for isotropic fluids, are the *shear viscosity* and the *bulk viscosity* of the fluid, respectively. Notice that all terms proportional to $\nabla \cdot \boldsymbol{u}(\boldsymbol{r}, t)$ are zero for incompressible fluids.

We thus find the following expression for the total stress tensor for an isotropic fluid:

$$\begin{aligned} \boldsymbol{\Sigma}(\boldsymbol{r}, t) = \eta_0\{\nabla \boldsymbol{u}(\boldsymbol{r}, t) + [\nabla \boldsymbol{u}(\boldsymbol{r}, t)]^{\mathrm{T}} - \tfrac{2}{3}\,\hat{\boldsymbol{I}}\,\nabla \cdot \boldsymbol{u}(\boldsymbol{r}, t)\} \\ + \{\zeta_0\,\nabla \cdot \boldsymbol{u}(\boldsymbol{r}, t) - p(\boldsymbol{r}, t)\}\,\hat{\boldsymbol{I}} \end{aligned} \tag{3.11}$$

where the superscript "T" stands for transposition. This expression for the stress tensor leads to the *Navier–Stokes equation*:

$$\begin{aligned} &\rho \frac{\partial \boldsymbol{u}(\boldsymbol{r}, t)}{\partial t} + \rho\, \boldsymbol{u}(\boldsymbol{r}, t) \cdot \nabla \boldsymbol{u}(\boldsymbol{r}, t) \\ &= \eta_0\, \nabla^2 \boldsymbol{u}(\boldsymbol{r}, t) - \nabla p(\boldsymbol{r}, t) + (\zeta_0 + \tfrac{1}{3}\eta_0)\nabla(\nabla \cdot \boldsymbol{u}(\boldsymbol{r}, t)) + \boldsymbol{f}^{\mathrm{ext}}(\boldsymbol{r}) \end{aligned} \tag{3.12}$$

where the mass density and the shear and bulk viscosities are now taken to be independent of position. For incompressible fluids, for which $\nabla \cdot \boldsymbol{u}(\boldsymbol{r}, t) = 0$ (see Eq. 3.7), the Navier–Stokes equation reduces to

$$\rho\frac{\partial \boldsymbol{u}(\boldsymbol{r},t)}{\partial t} + \rho\,\boldsymbol{u}(\boldsymbol{r},t)\cdot\nabla\boldsymbol{u}(\boldsymbol{r},t) = \nabla\cdot\boldsymbol{\Sigma}(\boldsymbol{r},t) + \boldsymbol{f}^{\mathrm{ext}}(\boldsymbol{r},t)$$
$$= \eta_0\nabla^2\boldsymbol{u}(\boldsymbol{r},t) - \nabla p(\boldsymbol{r},t) + \boldsymbol{f}^{\mathrm{ext}}(\boldsymbol{r}) \quad (3.13)$$

Together with the continuity equation (Eq. 3.7) for incompressible fluids, this equation fully determines the fluid flow and pressure once the external force and boundary conditions are specified.

3.3.3 The Creeping Flow Equations

The different terms in the Navier–Stokes equation (Eq. 3.13) can be very different in magnitude, depending on the problem at hand. In the present case we are interested in fluid flow around small-sized objects (colloidal particles). Let us estimate the magnitude of the various terms in the Navier–Stokes equation for this case. A typical value for the fluid flow velocity is the velocity v of the colloidal objects. The fluid flow velocity decreases from a value v, close to a Brownian particle, to a much smaller value, over a distance of the order of a typical linear dimension a of the particles (for spherical particles, a is the radius; for rotating rods, a is the length of the rod). Hence, typically, $|\nabla^2\boldsymbol{u}| \approx v/a^2$. Similarly, $|\boldsymbol{u}\cdot\nabla\boldsymbol{u}| \approx v^2/a$. The rate of change of $\boldsymbol{u}$ is v divided by the time it takes the colloidal particle to lose its velocity due to friction with the fluid. This time interval is equal to a few times M/γ, with M the mass of the colloidal particle and γ its friction coefficient (this will be discussed in more detail later in this chapter). Introducing the rescaled variables,

$$\boldsymbol{u}' = \boldsymbol{u}/v, \quad \boldsymbol{r}' = \boldsymbol{r}/a, \quad t' = t/(M/\gamma)$$

transforms the Navier–Stokes equation (Eq. 3.13) to

$$\frac{\rho\gamma v}{M}\frac{\partial \boldsymbol{u}'}{\partial t'} + \frac{\rho v^2}{a}\boldsymbol{u}'\cdot\nabla'\boldsymbol{u}' = \frac{\eta_0 v}{a^2}\nabla'^2\boldsymbol{u}' - \frac{1}{a}\nabla' p + \boldsymbol{f}^{\mathrm{ext}}$$

where ∇' is the gradient operator with respect to $\boldsymbol{r}'$. Introducing further the dimensionless pressure and external force,

$$p' = \frac{a}{\eta_0 v}p, \quad \boldsymbol{f}'^{\,\mathrm{ext}} = \frac{a^2}{\eta_0 v}\boldsymbol{f}^{\mathrm{ext}}$$

transforms the Navier–Stokes equation further to

$$\rho\frac{a^2\gamma}{M\eta_0}\frac{\partial \boldsymbol{u}'}{\partial t'} + Re\,\boldsymbol{u}'\cdot\nabla'\boldsymbol{u}' = \nabla'^2\boldsymbol{u}' - \nabla' p' + \boldsymbol{f}'^{\,\mathrm{ext}} \quad (3.14)$$

The dimensionless number Re is the so-called *Reynolds number*, which is equal to

$$Re = \frac{\rho a v}{\eta_0} \tag{3.15}$$

By construction we have

$$|\boldsymbol{u}' \cdot \nabla' \boldsymbol{u}'| \approx |{\nabla'}^2 \boldsymbol{u}'| \approx 1$$

Hence, for very small values of the Reynolds number, the term proportional to $\boldsymbol{u} \cdot \nabla \boldsymbol{u}$ on the left-hand side of Eq. (3.14) may be neglected. Furthermore, for spherical particles we have $\gamma = 6\pi\eta_0 a$, so that $\rho a^2 \gamma / M\eta_0 = 9\rho/2\rho_\mathrm{p} \approx 9/2$, with ρ_p the mass density of the Brownian particle. The prefactor of $\partial \boldsymbol{u}'/\partial t'$ is thus approximately equal to $9/2$. The time derivative should generally be kept as it stands, also for small Reynolds numbers. Now suppose, however, that one is interested in a description on the diffusive time scale $\tau_\mathrm{D} \gg M/\gamma$ (the significance of the diffusive time scale will be discussed later in this chapter). For such times, the time derivative $\partial \boldsymbol{u}'/\partial t'$ is long relaned to zero, since $\boldsymbol{u}$ goes to zero as a result of friction during the time interval M/γ. One may then neglect the contribution to the time derivative that is due to relaxation of momentum of the Brownian particle as a result of friction with the solvent. The remaining time dependence of $\boldsymbol{u}$ on the diffusive time scale is due to the possible time dependence of the external force and to interactions with other Brownian rods, which vary significantly only over time intervals larger than the diffusive time scale. The value of the corresponding derivative $\partial \boldsymbol{u}/\partial t$ can now be estimated as above: the only difference is that the time should be rescaled not with respect to the time M/γ, but with respect to the diffusive time scale τ_D. We now have $t' = t/\tau_\mathrm{D}$, $\boldsymbol{u}' = \boldsymbol{u}/v$, and $|\partial \boldsymbol{u}'/\partial t'| \approx 1$. The transformed Navier–Stokes equation in this case reads

$$\frac{9}{2}\frac{\rho}{\rho_\mathrm{p}}\frac{M/\gamma}{\tau_\mathrm{D}}\frac{\partial \boldsymbol{u}'}{\partial t'} + Re\, \boldsymbol{u}' \cdot \nabla' \boldsymbol{u}' = {\nabla'}^2 \boldsymbol{u}' - \nabla' p' + \boldsymbol{f}'^{\,\mathrm{ext}}$$

where all derivatives of the fluid flow velocity $\boldsymbol{u}'$ are of the order 1. Since $\tau_\mathrm{D} \gg M/\gamma$, the time derivative due to changes of the fluid flow velocity as a result of the time-varying external force and interactions with other Brownian particles may now be neglected in addition.

For small Reynolds numbers and on the diffusive time scale, the Navier–Stokes equation (3.16), written in terms of the original unprimed quantities, therefore simplifies to

$$\nabla p(\boldsymbol{r}, t) - \eta_0 \nabla^2 \boldsymbol{u}(\boldsymbol{r}, t) = \boldsymbol{f}^{\mathrm{ext}}(\boldsymbol{r}) \tag{3.16}$$

This equation together with the incompressibility equation (Eq. 3.7) are the *creeping flow equations*. "Creeping" refers to the fact that the Reynolds number is small, which is the case when the typical fluid flow velocity v is small.

A typical value for the velocity of a Brownian particle can be estimated from the equipartition theorem, $\frac{1}{2}M\langle v^2\rangle = \frac{3}{2}k_\mathrm{B}T$ (k_B is Boltzmann's constant and T is temperature). Estimating $v \approx \sqrt{\langle v^2\rangle}$, using a typical mass of 10^{-17} kg for a spherical particle with a radius of 100 nm and the density and viscosity of water, the Reynolds number is found to be equal to 10^{-2}. The hydrodynamics of a fluid in which colloidal particles are embedded can thus be described on the basis of the creeping flow equations.

For small Reynolds numbers and on the Brownian time scale, inertial forces on fluid elements are thus small in comparison to pressure and friction forces. The neglect of inertial contributions in the Navier–Stokes equation leads to the linear equation (Eq. 3.16), which can be solved analytically in some cases.

3.3.4 The Oseen Tensor

An external force acting only at a single point $\boldsymbol{r}'$ in the fluid is mathematically described by a delta distribution:

$$\boldsymbol{f}^\mathrm{ext}(\boldsymbol{r}) = \boldsymbol{f}_0\delta(\boldsymbol{r}-\boldsymbol{r}') \tag{3.17}$$

The prefactor $\boldsymbol{f}_0$ is the total force $\int \mathrm{d}\boldsymbol{r}'\, \boldsymbol{f}^\mathrm{ext}(\boldsymbol{r}')$ acting on the fluid. Since the creeping flow equations are linear, the fluid flow velocity at some point $\boldsymbol{r}$ in the fluid, due to the point force at $\boldsymbol{r}'$, is directly proportional to that point force. Hence,

$$\boldsymbol{u}(\boldsymbol{r}) = \boldsymbol{T}(\boldsymbol{r}-\boldsymbol{r}')\cdot\boldsymbol{f}_0$$

The tensor $\boldsymbol{T}$ is commonly referred to as the *Oseen tensor*, named after the scientist who first derived an explicit expression for this tensor (Oseen 1927). The Oseen tensor connects the point force at a point $\boldsymbol{r}'$ to the resulting fluid flow velocity at a point $\boldsymbol{r}$. Note that $\boldsymbol{T}$ is a function of only the difference coordinate $\boldsymbol{r}-\boldsymbol{r}'$ due to the translational invariance of a homogeneous fluid. Similarly, the pressure at a point $\boldsymbol{r}$ is linearly related to the point force,

$$p(\boldsymbol{r}) = \boldsymbol{g}(\boldsymbol{r}-\boldsymbol{r}')\cdot\boldsymbol{f}_0$$

The vector $\boldsymbol{g}$ is referred to here as the *pressure vector*.

Consider an external force that is continuously distributed over the entire fluid. Due to the linearity of the creeping flow equations, the fluid flow velocity

at some point $\boldsymbol{r}$ is simply the superposition of the fluid flow velocities resulting from the forces acting at each point in the fluid. Hence,

$$\boldsymbol{u}(\boldsymbol{r}) = \int \mathrm{d}\boldsymbol{r}'\, \boldsymbol{T}(\boldsymbol{r}-\boldsymbol{r}') \cdot \boldsymbol{f}^{\mathrm{ext}}(\boldsymbol{r}') \tag{3.18}$$

The same holds for the pressure,

$$p(\boldsymbol{r}) = \int \mathrm{d}\boldsymbol{r}'\, \boldsymbol{g}(\boldsymbol{r}-\boldsymbol{r}') \cdot \boldsymbol{f}^{\mathrm{ext}}(\boldsymbol{r}') \tag{3.19}$$

In mathematical language, the Oseen tensor and the pressure vector are Green's functions of the creeping flow equations for the fluid flow velocity and pressure, respectively. Once these Green's functions are known and the external force is specified, the resulting fluid velocity and pressure can be calculated through the evaluation of the above integrals. The calculation of the Green's functions is thus equivalent to solving the creeping flow equations, provided that the external forces are known.

Let us calculate the Oseen tensor and pressure vector. To this end, substitute Eqs. (3.18) and (3.19) into the creeping flow equations (Eqs. 3.7 and 3.16). This leads to

$$\int \mathrm{d}\boldsymbol{r}'\, [\nabla \cdot \boldsymbol{T}(\boldsymbol{r}-\boldsymbol{r}')] \cdot \boldsymbol{f}^{\mathrm{ext}}(\boldsymbol{r}') = 0$$

$$\int \mathrm{d}\boldsymbol{r}'\, [\nabla \boldsymbol{g}(\boldsymbol{r}-\boldsymbol{r}') - \eta_0 \nabla^2 \boldsymbol{T}(\boldsymbol{r}-\boldsymbol{r}') - \hat{\boldsymbol{I}}\delta(\boldsymbol{r}-\boldsymbol{r}')] \cdot \boldsymbol{f}^{\mathrm{ext}}(\boldsymbol{r}') = \boldsymbol{0}$$

where, as before, $\hat{\boldsymbol{I}}$ is the (3×3)-dimensional unit tensor. Since the external force is arbitrary, the expressions in the square brackets must be equal to zero, so that the Green's functions satisfy the following differential equations:

$$\nabla \cdot \boldsymbol{T}(\boldsymbol{r}) = \boldsymbol{0}$$

$$\nabla \boldsymbol{g}(\boldsymbol{r}) - \eta_0 \nabla^2 \boldsymbol{T}(\boldsymbol{r}) = \hat{\boldsymbol{I}}\delta(\boldsymbol{r}) \tag{3.20}$$

A single equation for the pressure vector is obtained by taking the divergence of the second equation, with the use of the first equation:

$$\nabla^2 \boldsymbol{g}(\boldsymbol{r}) = \nabla \cdot \hat{\boldsymbol{I}}\delta(\boldsymbol{r}) = \nabla\delta(\boldsymbol{r})$$

Using

$$\frac{1}{4\pi}\nabla^2 \frac{1}{r} = -\delta(\boldsymbol{r}) \tag{3.21}$$

it follows that

$$\boldsymbol{g}(\boldsymbol{r}) = -\frac{1}{4\pi}\nabla\frac{1}{r} + \boldsymbol{G}(\boldsymbol{r})$$

Here, $\boldsymbol{G}$ is a vector for which $\nabla^2\boldsymbol{G} = \boldsymbol{0}$, while $\boldsymbol{G} \to \boldsymbol{0}$ as $r \to \infty$. It can be shown that such a vector is $\boldsymbol{0}$. Hence,

$$\boldsymbol{g}(\boldsymbol{r}) = -\frac{1}{4\pi}\nabla\frac{1}{r} = \frac{1}{4\pi}\frac{\boldsymbol{r}}{r^3} \tag{3.22}$$

The differential equation to be satisfied by the Green's function for the fluid flow velocity (the Oseen tensor) is found by substitution of Eq. (3.22) into Eq. (3.20):

$$\nabla^2\left[\frac{1}{4\pi}\frac{1}{r}\hat{\boldsymbol{I}} - \eta_0\boldsymbol{T}(\boldsymbol{r})\right] = \frac{1}{4\pi}\left[3\frac{\boldsymbol{r}\boldsymbol{r}}{r^5} - \frac{1}{r^3}\hat{\boldsymbol{I}}\right]$$

An obvious choice for the term in the square brackets on the left-hand side of the above expression is of the form

$$\frac{1}{4\pi}\frac{1}{r}\hat{\boldsymbol{I}} - \eta_0\boldsymbol{T}(\boldsymbol{r}) = \alpha_0\frac{1}{r^n}\hat{\boldsymbol{I}} + \alpha_1\frac{1}{r^m}\frac{\boldsymbol{r}\boldsymbol{r}}{r^2}$$

with $\alpha_{0,1}$, n, and m constants. These constants can indeed be chosen such that this ansatz is the solution of the differential equation [with the boundary condition that $\boldsymbol{T}(\boldsymbol{r}) \to \boldsymbol{0}$ as $r \to \infty$]. A somewhat lengthy, but straightforward, calculation yields

$$\boldsymbol{T}(\boldsymbol{r}) = \frac{1}{8\pi\eta_0}\frac{1}{r}\left[\hat{\boldsymbol{I}} + \frac{\boldsymbol{r}\boldsymbol{r}}{r^2}\right] \tag{3.23}$$

This concludes the determination of the Green's functions for the creeping flow equations.

3.4 Hydrodynamic Friction of a Single Rod

The behavior of rod-like colloids in shear flow is strongly coupled to the friction between the solvent and the surface of the rods. In the present section, friction coefficients for very long and thin rods will be calculated on the basis of the creeping flow equations. This is most easily done by considering a rod to be made up of spherical beads with diameter D (as depicted in Fig. 3.3). For very long and thin rods, the friction coefficients for such "necklaces" are

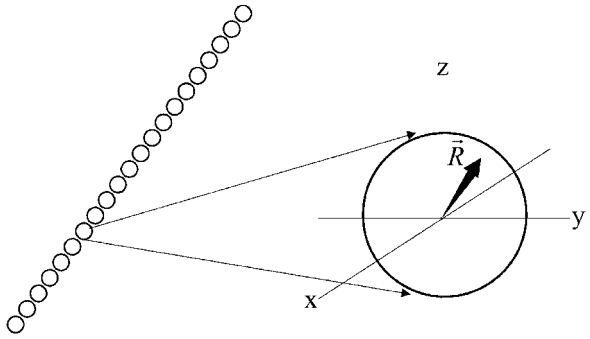

Fig. 3.3 The "necklace" representation of a very long and thin rod, and the definition of the vector $\boldsymbol{R}$ on the surface of a bead, relative to the position of that bead.

the same as for cylindrical rods with thickness D. The number of spherical beads is equal to $n+1 = L/D$ (with L the length of the rod), where the bead index number ranges from $-\frac{1}{2}n$ to $+\frac{1}{2}n$. The position of the central bead (for which $n = 0$) defines the position coordinate of the rod.

The flow velocity around a moving rod in shear flow is given, according to Eq. (3.18), by

$$\boldsymbol{u}(\boldsymbol{r}) = \boldsymbol{G}\cdot\boldsymbol{r} + \oint_{\partial V} \mathrm{d}S'\, \boldsymbol{T}(\boldsymbol{r}-\boldsymbol{r}')\cdot\boldsymbol{f}(\boldsymbol{r}') \tag{3.24}$$

where the integral ranges over the surface ∂V of the rod. Here, the force $\boldsymbol{f}(\boldsymbol{r}')$ is the force per unit area that a surface element at $\boldsymbol{r}'$ exerts on the fluid. The first term on the right-hand side in Eq. (3.24) is the flow that would have existed in the absence of the rod; the second term is the contribution due to the presence of the rod. For stick boundary conditions we have that

$$\boldsymbol{u}(\boldsymbol{r}) = \boldsymbol{v}_{\mathrm{c}} + \boldsymbol{\Omega}\times(\boldsymbol{r}-\boldsymbol{r}_{\mathrm{c}}), \quad \text{for } \boldsymbol{r}\in\partial V \tag{3.25}$$

where $\boldsymbol{v}_{\mathrm{c}}$ is the translational velocity of the center of the rod, $\boldsymbol{r}_{\mathrm{c}}$ is the position of the center of the rod, and $\boldsymbol{\Omega}$ is the rod's angular velocity relative to its center.

Within the bead model discussed above, ∂V is the sum of the surfaces ∂V_j of the beads, with j ranging from $-\frac{1}{2}n$ to $+\frac{1}{2}n$. The center position of the jth bead will be denoted as $\boldsymbol{r}_j = \boldsymbol{r}_{\mathrm{c}} + jD\hat{\boldsymbol{u}}$, where $\hat{\boldsymbol{u}}$ is the unit vector along the long axis of the rod, which specifies its orientation. Within the bead model, Eq. (3.24) reads

$$\begin{aligned}\boldsymbol{u}(\boldsymbol{R}+\boldsymbol{r}_j) = {} & \boldsymbol{G}\cdot(\boldsymbol{R}+\boldsymbol{r}_j) \\ & + \sum_{i=-\frac{1}{2}n}^{\frac{1}{2}n} \oint_{\partial V^0} \mathrm{d}S'\, \boldsymbol{T}(\boldsymbol{R}-\boldsymbol{R}'+\boldsymbol{r}_{ji})\cdot\boldsymbol{f}_i(\boldsymbol{R}')\end{aligned} \tag{3.26}$$

with $\boldsymbol{R} = \boldsymbol{r} - \boldsymbol{r}_j$ and $\boldsymbol{R}' = \boldsymbol{r}' - \boldsymbol{r}_i$ the position vectors with length $D/2$ on the surface ∂V^0 of a bead with its center at $\boldsymbol{r}_i$ (see Fig. 3.3). The stick boundary condition (3.25) now becomes

$$\begin{aligned}\boldsymbol{u}(\boldsymbol{R}+\boldsymbol{r}_j) &= \boldsymbol{v}_\mathrm{c} + \boldsymbol{\Omega}\times(\boldsymbol{R}+\boldsymbol{r}_j-\boldsymbol{r}_\mathrm{c}) \\ &= \boldsymbol{v}_\mathrm{c} + \boldsymbol{\Omega}\times(\boldsymbol{R}+jD\boldsymbol{u}), \quad \text{for } R = D/2 \text{ and all } j \end{aligned} \tag{3.27}$$

In the next two subsections we consider translation (without rotation) and rotation (without translation). The motion of a translating *and* rotating rod is a linear superposition of the results for these two special cases, due to the linearity of the creeping flow equations and their boundary conditions.

3.4.1 Translational Friction

Let us first consider a translating rod in an otherwise quiescent fluid, without shear flow. The boundary condition (3.27) reduces simply to $\boldsymbol{u}(\boldsymbol{R}+\boldsymbol{r}_j) = \boldsymbol{v}_\mathrm{c}$. The representation (3.26) for $\boldsymbol{u}$ thus yields

$$\begin{aligned}\boldsymbol{v}_\mathrm{c} = \sum_{i=-\frac{1}{2}n}^{\frac{1}{2}n} \oint_{\partial V^0} \mathrm{d}S'\, \boldsymbol{T}(\boldsymbol{R}-\boldsymbol{R}'+\boldsymbol{r}_{ji})\cdot\boldsymbol{f}_i(\boldsymbol{R}'), \\ \text{for } R = D/2 \text{ and all } j \end{aligned} \tag{3.28}$$

Integration of both sides over the surface of the entire rod, i.e. operating on both sides with $\sum_{j=-\frac{1}{2}n}^{\frac{1}{2}n} \oint_{\partial V^0} \mathrm{d}S$, yields

$$\begin{aligned}\boldsymbol{v}_\mathrm{c} = \frac{1}{\pi L D} \sum_{j=-\frac{1}{2}n}^{\frac{1}{2}n} \sum_{i=-\frac{1}{2}n}^{\frac{1}{2}n} \\ \times \oint_{\partial V^0} \mathrm{d}S \oint_{\partial V^0} \mathrm{d}S'\, \boldsymbol{T}(\boldsymbol{R}-\boldsymbol{R}'+\boldsymbol{r}_{ji})\cdot\boldsymbol{f}_i(\boldsymbol{R}') \end{aligned} \tag{3.29}$$

Using the fact that

$$\begin{aligned}&\oint_{\partial V^0} \mathrm{d}S'\, \boldsymbol{T}(\boldsymbol{r}-\boldsymbol{R}') \\ &= \frac{D}{4\eta_0}\left\{\left[\frac{D}{2r}+\frac{1}{3}\left(\frac{D}{2r}\right)^3\right]\hat{\boldsymbol{I}} + \left[\frac{D}{2r}-\left(\frac{D}{2r}\right)^3\right]\frac{\boldsymbol{r}\boldsymbol{r}}{r^2}\right\}\end{aligned} \tag{3.30}$$

it is found that, for $i = j$, the surface integrals in Eq. (3.29) are equal to

$$\oint_{\partial V^0} \mathrm{d}S\, \boldsymbol{T}(\boldsymbol{R} - \boldsymbol{R}' + \boldsymbol{r}_{ji}) = \frac{D}{3\eta_0}\hat{\boldsymbol{I}}, \quad \text{for } i = j \tag{3.31}$$

For $i \neq j$, the Oseen tensor may be Taylor-expanded as

$$\boldsymbol{T}(\boldsymbol{R} - \boldsymbol{R}' + \boldsymbol{r}_{ji}) = \boldsymbol{T}(\boldsymbol{r}_{ij}) + (\boldsymbol{R} - \boldsymbol{R}') \cdot \nabla_i \boldsymbol{T}(\boldsymbol{r}_{ij}) + \cdots \tag{3.32}$$

with ∇_i the gradient operator with respect to $\boldsymbol{r}_i$. Only the leading-order term in this Taylor expansion must be retained to obtain expressions for friction coefficients that are valid to leading order in L/D (if you wish you may include the next higher-order Taylor terms and convince yourself that these terms do not contribute in leading order). Using Eqs. (3.31) and (3.32) to leading order in Eq. (3.29) gives

$$\boldsymbol{v}_\mathrm{c} \approx -\frac{1}{3\pi\eta_0 L} \sum_{i=-\frac{1}{2}n}^{\frac{1}{2}n} \boldsymbol{F}_i^\mathrm{h} - \frac{D}{L} \left[\sum_{j=-\frac{1}{2}n}^{\frac{1}{2}n} \sum_{i=-\frac{1}{2}n,\, i\neq j}^{\frac{1}{2}n} \boldsymbol{T}(\boldsymbol{r}_{ij}) \right] \cdot \boldsymbol{F}_i^\mathrm{h} \tag{3.33}$$

where

$$\oint_{\partial V^0} \mathrm{d}S'\, \boldsymbol{f}_i(\boldsymbol{R}') = -\boldsymbol{F}_i^\mathrm{h} \tag{3.34}$$

is the total force of the fluid on bead i. The first term on the right-hand side is simply the sum of the Stokes friction forces on the beads, while the second term represents the contribution due to hydrodynamic interaction between the beads. For very long rods, all forces $\boldsymbol{F}_i^\mathrm{h}$ may be taken equal, i.e. end-effects may be neglected, since the majority of beads (away from the ends of the rod) experience approximately the same force. Substituting $\boldsymbol{F}_i^\mathrm{h} = (D/L)\boldsymbol{F}^\mathrm{h}$, with $\boldsymbol{F}^\mathrm{h}$ the total force on the rod, yields

$$\boldsymbol{v}_\mathrm{c} = -\frac{1}{3\pi\eta_0 L}\boldsymbol{F}^\mathrm{h} - \left(\frac{D}{L}\right)^2 \left[\sum_{j=-\frac{1}{2}n}^{\frac{1}{2}n} \sum_{i=-\frac{1}{2}n,\, i\neq j}^{\frac{1}{2}n} \boldsymbol{T}(\boldsymbol{r}_{ij}) \right] \cdot \boldsymbol{F}^\mathrm{h} \tag{3.35}$$

The double bead index summation can be calculated up to leading order by replacing sums by integrals (for details, see the Appendix, Section 3.16.1). It is thus found that

$$\begin{aligned} \sum_{j=-\frac{1}{2}n}^{\frac{1}{2}n} \sum_{i=-\frac{1}{2}n,\, i\neq j}^{\frac{1}{2}n} \boldsymbol{T}(\boldsymbol{r}_{ij}) &= \frac{1}{8\pi\eta_0 D}[\hat{\boldsymbol{I}} + \hat{\boldsymbol{u}}\hat{\boldsymbol{u}}] \sum_{j=-\frac{1}{2}n}^{\frac{1}{2}n} \sum_{i=-\frac{1}{2}n,\, i\neq j}^{\frac{1}{2}n} \frac{1}{|i-j|} \\ &\approx \frac{1}{4\pi\eta_0 D}[\hat{\boldsymbol{I}} + \hat{\boldsymbol{u}}\hat{\boldsymbol{u}}] \frac{L}{D} \ln\left(\frac{L}{D}\right) \end{aligned} \tag{3.36}$$

We finally obtain, to leading order

$$\boldsymbol{v}_{\mathrm{c}} = -\frac{1}{3\pi\eta_0 L}\boldsymbol{F}^{\mathrm{h}} - \frac{1}{4\pi\eta_0 L}\ln\left(\frac{L}{D}\right)[\hat{\boldsymbol{I}} + \hat{\boldsymbol{u}}\hat{\boldsymbol{u}}]\cdot\boldsymbol{F}^{\mathrm{h}}$$

$$\approx -\frac{1}{4\pi\eta_0 L}\ln\left(\frac{L}{D}\right)[\hat{\boldsymbol{I}} + \hat{\boldsymbol{u}}\hat{\boldsymbol{u}}]\cdot\boldsymbol{F}^{\mathrm{h}} \tag{3.37}$$

Notice that the Stokes friction of each bead does not contribute in leading order: the major contribution comes from hydrodynamic fields near each bead generated by the remaining beads. Hydrodynamic interaction between the beads is thus essential for the friction of a translating rod.

Inversion of Eq. (3.37) yields

$$\boldsymbol{F}^{\mathrm{h}} = -\boldsymbol{\Gamma}_{\mathrm{f}}\cdot\boldsymbol{v}_{\mathrm{c}}, \quad \text{with } \boldsymbol{\Gamma}_{\mathrm{f}} = \frac{4\pi\eta_0 L}{\ln(L/D)}[\hat{\boldsymbol{I}} - \tfrac{1}{2}\hat{\boldsymbol{u}}\hat{\boldsymbol{u}}] \tag{3.38}$$

where the tensor $\boldsymbol{\Gamma}_{\mathrm{f}}$ is referred to as the *friction tensor*. In contrast to a spherical particle, the friction force is generally not collinear with its velocity. When the motion of the rod is parallel to its orientation, the friction force of the rod with the fluid is found from Eq. (3.38) to be equal to

$$\boldsymbol{F}^{\mathrm{h}} = -\gamma_{\parallel}\boldsymbol{v}_{\mathrm{c}} \tag{3.39}$$

with $\gamma_{\parallel}$ the *friction coefficient for parallel motion*,

$$\gamma_{\parallel} = \frac{2\pi\eta_0 L}{\ln(L/D)} \tag{3.40}$$

For motion perpendicular to the centerline it is likewise found that

$$\boldsymbol{F}^{\mathrm{h}} = -\gamma_{\perp}\boldsymbol{v}_{\mathrm{c}} \tag{3.41}$$

with $\gamma_{\perp}$ the *friction coefficient for perpendicular motion*,

$$\gamma_{\perp} = \frac{4\pi\eta_0 L}{\ln(L/D)} \tag{3.42}$$

Notice that this friction constant is twice as large as for parallel motion. This is only true for very long and thin rods. For rods with smaller aspect ratios, corrections to the limiting expressions (3.40) and (3.42) were considered by de la Torre and Bloomfield (1981). Also note that the friction tensor can be written as

$$\boldsymbol{\Gamma}_{\mathrm{f}} = \gamma_{\parallel}\hat{\boldsymbol{u}}\hat{\boldsymbol{u}} + \gamma_{\perp}[\hat{\boldsymbol{I}} - \hat{\boldsymbol{u}}\hat{\boldsymbol{u}}] \tag{3.43}$$

where the dyadic product $\hat{\boldsymbol{u}}\hat{\boldsymbol{u}}$ is the projection operator parallel to the orientation direction of the rod and $\hat{\boldsymbol{I}} - \hat{\boldsymbol{u}}\hat{\boldsymbol{u}}$ is the projection operator in the direction perpendicular to $\hat{\boldsymbol{u}}$. This expression for the friction tensor is generally also valid for shorter rods, in which case, however, correction terms should be added to the limiting expressions (3.40) and (3.42), as discussed by de la Torre and Bloomfield (1981).

Consider now the additional contribution of shear flow. The forces $\boldsymbol{F}_i^{\mathrm{h}}$ as a function of the bead index i may be obtained directly from the above considerations as follows. Each bead i has a velocity, relative to the externally imposed fluid flow velocity, equal to

$$\boldsymbol{v}_{\mathrm{c}} - \boldsymbol{G}\cdot\boldsymbol{r}_i = \boldsymbol{v}_{\mathrm{c}} - \boldsymbol{G}\cdot\boldsymbol{r}_{\mathrm{c}} - iD\boldsymbol{G}\cdot\hat{\boldsymbol{u}}$$

The *relative* change of this velocity between neighboring beads is thus $\sim 1/i$, and is small for beads away from the center. Large groups of beads therefore experience a friction force as in the case of a uniformly translating rod in an otherwise quiescent fluid. Beads away from the center therefore experience a friction force parallel to the centerline equal to

$$\boldsymbol{F}_{i,\parallel}^{\mathrm{h}} = -\frac{D}{L}\gamma_{\parallel}\hat{\boldsymbol{u}}\hat{\boldsymbol{u}}\cdot(\boldsymbol{v}_{\mathrm{c}} - \boldsymbol{G}\cdot\boldsymbol{r}_{\mathrm{c}} - iD\boldsymbol{G}\cdot\hat{\boldsymbol{u}})$$

and a friction force perpendicular to the centerline equal to

$$\boldsymbol{F}_{i,\perp}^{\mathrm{h}} = -\frac{D}{L}\gamma_{\perp}[\hat{\boldsymbol{I}} - \hat{\boldsymbol{u}}\hat{\boldsymbol{u}}]\cdot(\boldsymbol{v}_{\mathrm{c}} - \boldsymbol{G}\cdot\boldsymbol{r}_{\mathrm{c}} - iD\boldsymbol{G}\cdot\hat{\boldsymbol{u}})$$

Here, the apparent local velocity of the fluid is decomposed into its components parallel and perpendicular to the rod's centerline, and the friction coefficient on the bead is equal to that of an entire rod divided by the number $n+1 = L/D$ of beads. The total force that the fluid exerts on the rod is now simply found by summation over all beads:

$$\begin{aligned}\boldsymbol{F}^{\mathrm{h}} &= \sum_{i=-\frac{1}{2}n}^{\frac{1}{2}n}[\boldsymbol{F}_{i,\parallel}^{\mathrm{h}} + \boldsymbol{F}_{i,\perp}^{\mathrm{h}}] \\ &= -(\gamma_{\parallel}\hat{\boldsymbol{u}}\hat{\boldsymbol{u}} + \gamma_{\perp}[\hat{\boldsymbol{I}} - \hat{\boldsymbol{u}}\hat{\boldsymbol{u}}])\cdot(\boldsymbol{v}_{\mathrm{c}} - \boldsymbol{G}\cdot\boldsymbol{r}_{\mathrm{c}}) \\ &= -\frac{4\pi\eta_0 L}{\ln(L/D)}[\hat{\boldsymbol{I}} - \tfrac{1}{2}\hat{\boldsymbol{u}}\hat{\boldsymbol{u}}]\cdot(\boldsymbol{v}_{\mathrm{c}} - \boldsymbol{G}\cdot\boldsymbol{r}_{\mathrm{c}})\end{aligned} \tag{3.44}$$

The last equation is only valid for very long and thin rods. The first equation is also valid for shorter rods, where the expressions for the two friction co-

efficients were calculated by de la Torre and Bloomfield (1981). This result is precisely Eq. (3.38) for translational motion in an otherwise quiescent fluid, where the velocity of the rod's center is taken relative to the local shear flow velocity. Such a result is intuitively clear, as additional friction forces due to the shear flow on the beads with a positive bead index simply cancel with the same forces on beads with a negative index.

3.4.2 Rotational Friction

Consider a rod in shear flow with its center at the origin (so that $\boldsymbol{v}_{\mathrm{c}} = \boldsymbol{0} = \boldsymbol{r}_{\mathrm{c}}$) and with a prescribed angular velocity $\boldsymbol{\Omega}$ perpendicular to its centerline. The rotational friction coefficient may be obtained directly from the above results on translational friction, with arguments similar to those given at the end of the previous subsection where the effect of shearing motion of the fluid on translational friction is considered. The velocity of bead i relative to the local fluid flow velocity is equal to

$$\boldsymbol{\Omega} \times \boldsymbol{r}_i - \boldsymbol{G} \cdot \boldsymbol{r}_i = iD\boldsymbol{\Omega} \times \hat{\boldsymbol{u}} - iD\boldsymbol{G} \cdot \hat{\boldsymbol{u}}$$

The *relative* change of this velocity between neighboring beads is thus $\sim 1/i$, and is small for beads away from the origin. Large groups of beads therefore experience a friction force as in the case of a uniformly translating rod in an otherwise quiescent fluid. Beads away from the origin therefore experience a friction force parallel to the centerline equal to

$$\boldsymbol{F}^{\mathrm{h}}_{i,\parallel} = -\frac{D}{L}\gamma_{\parallel}\hat{\boldsymbol{u}}\hat{\boldsymbol{u}} \cdot (iD\boldsymbol{\Omega} \times \hat{\boldsymbol{u}} - iD\boldsymbol{G} \cdot \hat{\boldsymbol{u}}) \tag{3.45}$$

and a friction force perpendicular to the centerline equal to

$$\boldsymbol{F}^{\mathrm{h}}_{i,\perp} = -\frac{D}{L}\gamma_{\perp}[\hat{\boldsymbol{I}} - \hat{\boldsymbol{u}}\hat{\boldsymbol{u}}] \cdot (iD\boldsymbol{\Omega} \times \hat{\boldsymbol{u}} - iD\boldsymbol{G} \cdot \hat{\boldsymbol{u}}) \tag{3.46}$$

The torque on the rod is thus equal to

$$\begin{aligned}\boldsymbol{\mathcal{T}}^{\mathrm{h}} &= \sum_{i=-\frac{1}{2}n}^{\frac{1}{2}n} \boldsymbol{r}_i \times [\boldsymbol{F}^{\mathrm{h}}_{i,\parallel} + \boldsymbol{F}^{\mathrm{h}}_{i,\perp}] \\ &= -\frac{D^3}{L}\gamma_{\perp}[\hat{\boldsymbol{u}} \times (\boldsymbol{\Omega} \times \hat{\boldsymbol{u}}) - \hat{\boldsymbol{u}} \times (\boldsymbol{G} \cdot \hat{\boldsymbol{u}})] \sum_{i=-\frac{1}{2}n}^{\frac{1}{2}n} i^2 \end{aligned} \tag{3.47}$$

where we have used $\gamma_\perp = 2\gamma_\parallel$ (see Eqs. 3.40 and 3.42). Since $\hat{\boldsymbol{u}} \perp \boldsymbol{\Omega}$, and using the fact that

$$\sum_{i=1}^{k} i^2 = \tfrac{1}{6}k(k+1)(2k+1) \approx \tfrac{1}{3}k^3 \quad \text{for large } k$$

it is thus found that,

$$\boldsymbol{\mathcal{T}}^{\mathrm{h}} = -\gamma_{\mathrm{r}}[\boldsymbol{\Omega} - \hat{\boldsymbol{u}} \times (\boldsymbol{G} \cdot \hat{\boldsymbol{u}})] \tag{3.48}$$

where

$$\gamma_{\mathrm{r}} = \frac{1}{12}L^2\gamma_\perp = \frac{\pi\eta_0 L^3}{3\ln(L/D)} \tag{3.49}$$

is the *rotational friction coefficient*. Notice that a torque-free rod in shear flow thus attains an angular velocity equal to $\hat{\boldsymbol{u}} \times (\boldsymbol{G} \cdot \hat{\boldsymbol{u}})$. For rods with smaller aspect ratios, corrections to the limiting expression (3.49) are given by de la Torre and Bloomfield (1981).

For the special case of simple shear flow, where $\boldsymbol{G} = \boldsymbol{\Gamma}$ as given in Eq. (3.1), the above result predicts a zero torque on the rod when it is oriented along the flow direction, since then $\hat{\boldsymbol{u}} \times (\boldsymbol{\Gamma} \cdot \hat{\boldsymbol{u}}) = \boldsymbol{0}$. From symmetry, it follows that for such orientations the total force $\boldsymbol{F}_i^{\mathrm{h}}$ of the fluid on each bead is zero, so that the torque is indeed $\boldsymbol{0}$. What is neglected in Eq. (3.47) is the variation of the fluid flow velocity over the surface of each bead, which is a good approximation for orientations away from alignment along the flow direction. When the rod is oriented along the flow direction, however, the fluid flow variation over the surfaces of the beads gives rise to a small but non-zero torque (see Fig. 3.4). The torque is only non-zero when the finite thickness of the rod is taken into account, and its magnitude is at least an order D/L smaller than the torque $\gamma_{\mathrm{r}}\hat{\boldsymbol{u}} \times (\boldsymbol{\Gamma} \cdot \hat{\boldsymbol{u}})$ for orientations not parallel to the flow direction.

As will be seen in Section 3.5 on Jeffery orbits, which are the orbits described by $\hat{\boldsymbol{u}}$ of a non-Brownian rod in shear flow, the small torque on a rod that is oriented along the flow direction is essential to obtain the realistic periodic motion for $\hat{\boldsymbol{u}}$: without this small contribution, $\hat{\boldsymbol{u}}$ would simply end up in the direction parallel to the flow. Let us therefore consider this small, but essential, contribution to the torque for non-Brownian rods.

The additional contribution to the torque is due to variations of the fluid forces over the bead surfaces. Taking these variations into account, the torque is by definition equal to (∂V is again the surface of the rod)

$$\boldsymbol{\mathcal{T}}^{\mathrm{h}} = -\oint_{\partial V} \mathrm{d}S'\, \boldsymbol{r}' \times \boldsymbol{f}(\boldsymbol{r}')$$

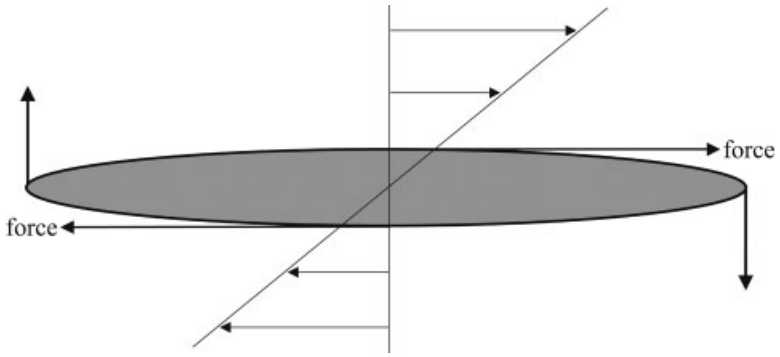

Fig. 3.4 A rod in simple shear flow with its centerline parallel to the flow direction experiences a non-zero torque entirely due to its non-zero thickness.

$$= -\sum_{i=-\frac{1}{2}n}^{\frac{1}{2}n} \oint_{\partial V^0} \mathrm{d}S' \, (\boldsymbol{R}' + \boldsymbol{r}_i) \times \boldsymbol{f}_i(\boldsymbol{R}')$$

$$= \sum_{i=-\frac{1}{2}n}^{\frac{1}{2}n} \boldsymbol{r}_i \times \boldsymbol{F}_i^{\mathrm{h}} - \sum_{i=-\frac{1}{2}n}^{\frac{1}{2}n} \oint_{\partial V^0} \mathrm{d}S' \, \boldsymbol{R}' \times \boldsymbol{f}_i(\boldsymbol{R}') \qquad (3.50)$$

The last term on the right-hand side is now extra as compared to the case where the additional torque due to variations of the hydrodynamic forces over the rod's surface is neglected. This is the term that is responsible for a finite torque when the rod is oriented along the flow direction. The first term on the right-hand side has already been considered before with the neglect of end-effects. In calculating the additional contribution $\Delta\boldsymbol{\mathcal{T}}^{\mathrm{h}}$ (the last term on the right-hand side) end-effects will also be neglected, meaning that the variation of the hydrodynamic forces over the bead surface is taken to be the same for all beads. The variation of the fluid flow in which a bead is embedded is given by $\boldsymbol{\Gamma} \cdot \boldsymbol{R}'$. We are only interested in the component of this flow in the direction along $\hat{\boldsymbol{u}}$, since the complementary perpendicular component gives rise to rotation about the centerline, which does not affect $\hat{\boldsymbol{u}}$. This parallel component of the flow along the surface of the rod is equal to $\hat{\boldsymbol{u}}\hat{\boldsymbol{u}} \cdot \boldsymbol{\Gamma} \cdot \boldsymbol{R}'$, and the corresponding parallel force is proportional to this flow velocity. Hence,

$$\boldsymbol{f}_i(\boldsymbol{R}') = C \, \hat{\boldsymbol{u}}\hat{\boldsymbol{u}} \cdot \boldsymbol{\Gamma} \cdot \boldsymbol{R}' \qquad (3.51)$$

where C is an as yet unknown constant. It now follows that

$$\Delta\boldsymbol{\mathcal{T}}^{\mathrm{h}} = -C \sum_{i=-\frac{1}{2}n}^{\frac{1}{2}n} \oint_{\partial V^0} \mathrm{d}S' \, \boldsymbol{R}' \times (\boldsymbol{\Gamma} \cdot \boldsymbol{R}')$$

$$= C \frac{L}{D} \frac{\pi D^4}{12} \hat{\boldsymbol{u}} \times (\boldsymbol{\Gamma}^{\mathrm{T}} \cdot \hat{\boldsymbol{u}}) \tag{3.52}$$

where the superscript "T" stands for transposition. The constant C can now be determined by comparing this result to solutions of the creeping flow equations for the simple case that the rod is oriented along the flow direction. For the cases of a cylinder without end-effects and for a long and thin ellipsoidal particle, it can be shown that

$$C = -\frac{6\eta_0}{D} \qquad \text{for cylinders without end-effects} \tag{3.53}$$

$$= -\frac{4\eta_0}{D \ln(L/D)} \qquad \text{for long and thin ellipsoids} \tag{3.54}$$

The different results are not just the result of neglect of end-effects in the case of the cylindrical particle. The precise value of C is sensitive to the precise shape of the surface of the rod: the torque on a rod aligned along the flow direction depends on how the fluid is "pushed away" or "sucked in" as it flows along its surface.

We thus finally find the following expression for the torque:

$$\boldsymbol{\mathcal{T}}^{\mathrm{h}} = -\gamma_{\mathrm{r}} [\boldsymbol{\Omega} - \hat{\boldsymbol{u}} \times (\boldsymbol{\Gamma} \cdot \hat{\boldsymbol{u}}) + \kappa^2 \hat{\boldsymbol{u}} \times (\boldsymbol{\Gamma}^{\mathrm{T}} \cdot \hat{\boldsymbol{u}})] \tag{3.55}$$

where the dimensionless constant κ^2 is equal to

$$\kappa^2 = \frac{3}{2} \left(\frac{D}{L} \right)^2 \ln \left(\frac{L}{D} \right) \qquad \text{for cylinders without end-effects} \tag{3.56}$$

$$= \left(\frac{D}{L} \right)^2 \qquad \text{for long and thin ellipsoids} \tag{3.57}$$

Since for colloidal rods the precise geometry of their surface is usually not known, and κ^2 is sensitive to that geometry, the constant κ^2 should be considered as a fitting parameter when performing experiments. This parameter tends to zero with decreasing values of D/L.

3.5
Motion of Non-Brownian Rods in Shear Flow: Jeffery Orbits

The first thing that comes to mind when beginning to study the effect of shear flow on dilute suspensions of rods is to ask about their motion without considering Brownian motion. The trajectory of motion of a Brownian rod will be the smooth trajectory of a non-Brownian rod that is randomly "corrugated" due to Brownian motion. In this section we ask for the orientational orbits that a non-Brownian rod (a "fiber") traverses when subjected to shear flow. These orbits are commonly the referred to as *Jeffery orbits*, named after G. B. Jeffery, who first considered this problem [a more compact formulation as compared to the original work of Jeffery (1922) has been formulated by Hinch and Leal (1972) and Leal and Hinch (1972)]. We shall consider Jeffery orbits of rods in elongational flow and simple shear flow, respectively.

The expressions derived in the previous section for very long and thin rods will be used to calculate such Jeffery orbits. Jeffery (1922) derived exact expressions for ellipsoidal rods, while Bretherton (1962) showed that the same equations of motion can be applied to arbitrarily shaped, cylindrically symmetric, slender bodies, provided that the body is modelled as an equivalent ellipsoid. The expressions obtained in the following are the asymptotic limits for large aspect ratios of those derived by Jeffery and Bretherton. It turns out, however, that for aspect ratios L/D larger than about 3–4, the errors that are made in using these asymptotic expressions (but employing the correct value for the rotational friction coefficient) are typically less than about 5% [asymptotic limits are obtained when, typically, $1/(1+r^2)$ is approximated by $1/r^2$, where $r = L/D$]. This is confirmed by simulations (see, for example, Ingber and Mondy 1994).

Interactions between fibers at high fiber concentration and the intrinsic flexibility of fibers do of course have an effect on the orbits described by a rod. Simulations on Jeffery orbits where interactions and flexibility are considered have been performed by Yamamoto and Matsuoka (1995). The theory described here assumes rigid rods. A discussion and references on the effect of interactions between fibers, wall effects, and rheology of fiber suspensions can be found in the book by Papathanasiou and Guell (1997). The treatment here describes the motion of a single fiber, which is not affected by interactions with other fibers or a wall.

Jeffery orbits are most conveniently described in terms of the spherical coordinates φ and Θ of the unit vector $\hat{\boldsymbol{u}}$ that specifies the orientation of the rod. These coordinates, relative to the flow and gradient direction in the case of simple shear flow, are sketched in Fig. 3.5. In the case of elongational flow, the elongation axis is oriented along $\{\varphi, \Theta\} = \{\pi/4, \pi/2\}$ (compare Fig. 3.1a and b). In Fig. 3.5, φ for the corresponding rod is negative.

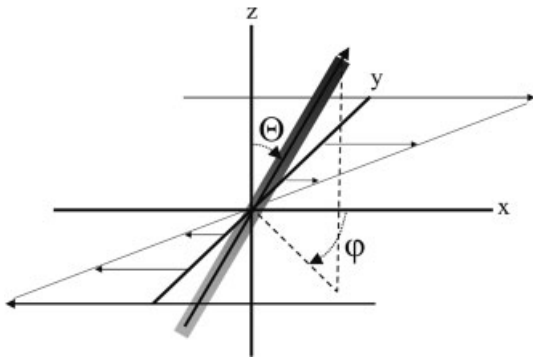

Fig. 3.5 Definition of the spherical coordinates φ and Θ, relative to the flow and gradient direction, in the case of simple shear flow. The flow is in the x direction while the gradient is in the y direction. In this example, $\varphi < 0$.

3.5.1 Jeffery Orbits in Elongational Flow

According to Eq. (3.48), the torque $\boldsymbol{\mathcal{T}}^{\mathrm{h}}$ that the fluid exerts on a very long and thin rod with an angular velocity $\boldsymbol{\Omega}$ in a shear field with velocity-gradient tensor $\boldsymbol{G} = \boldsymbol{E}$ (see Eq. 3.2) is equal to

$$\boldsymbol{\mathcal{T}}^{\mathrm{h}} = -\gamma_{\mathrm{r}}[\boldsymbol{\Omega} - \hat{\boldsymbol{u}} \times (\boldsymbol{E} \cdot \hat{\boldsymbol{u}})] \tag{3.58}$$

where γ_{r} is the rotational friction coefficient. It will turn out that, for elongational flow, the torque exerted on the rod when it is oriented parallel to the flow direction [the last term in Eq. (3.55)] is of no relevance, contrary to simple shear flow. When no external torque acts on the rod, the hydrodynamic torque in Eq. (3.58) is $\mathbf{0}$, so that

$$\boldsymbol{\Omega} = \hat{\boldsymbol{u}} \times (\boldsymbol{E} \cdot \hat{\boldsymbol{u}}) \tag{3.59}$$

On the other hand, by definition,

$$\frac{\mathrm{d}\hat{\boldsymbol{u}}}{\mathrm{d}t} = \boldsymbol{\Omega} \times \hat{\boldsymbol{u}} \tag{3.60}$$

Substitution of Eq. (3.59) into Eq. (3.60), using the fact that $\hat{\boldsymbol{u}} \times (\hat{\boldsymbol{u}} \times \boldsymbol{a}) = (\hat{\boldsymbol{u}} \cdot \boldsymbol{a})\hat{\boldsymbol{u}} - \boldsymbol{a}$ for arbitrary vectors $\boldsymbol{a}$, yields

$$\frac{\mathrm{d}\hat{\boldsymbol{u}}}{\mathrm{d}t} = \boldsymbol{E} \cdot \hat{\boldsymbol{u}} - (\hat{\boldsymbol{u}} \cdot \boldsymbol{E} \cdot \hat{\boldsymbol{u}})\hat{\boldsymbol{u}} \tag{3.61}$$

This equation of motion for the orientation $\hat{\boldsymbol{u}}$ describes the rotational orbits of a long and thin rod, without Brownian motion, in elongational flow. Expressing the orientation in terms of spherical angular coordinates, and substitution of the explicit form of $\boldsymbol{E}$ in Eq. (3.2), the following equations of motion for these coordinates are obtained:

$$\begin{aligned}
\frac{\mathrm{d}\Theta}{\mathrm{d}t}\cos\Theta\cos\varphi - \frac{\mathrm{d}\varphi}{\mathrm{d}t}\sin\Theta\sin\varphi &= -\dot{\gamma}\sin^3\Theta\sin\varphi\cos^2\varphi + \frac{\dot{\gamma}}{2}\sin\Theta\sin\varphi \\
\frac{\mathrm{d}\Theta}{\mathrm{d}t}\cos\Theta\sin\varphi + \frac{\mathrm{d}\varphi}{\mathrm{d}t}\sin\Theta\cos\varphi &= -\dot{\gamma}\sin^3\Theta\sin^2\varphi\cos\varphi \\
&\quad + \frac{\dot{\gamma}}{2}\sin\Theta\cos\varphi \qquad (3.62) \\
\frac{\mathrm{d}\Theta}{\mathrm{d}t} &= \dot{\gamma}\sin\Theta\cos\Theta\sin\varphi\cos\varphi
\end{aligned}$$

It may seem that we have here three equations for two unknowns (Θ and φ): however, each one of these equations may be derived from the remaining two. Elimination of $\mathrm{d}\Theta/\mathrm{d}t$ from one of the first two equations, using the third equation, yields the following seemingly simple set of two equations of motion for the spherical angular coordinates:

$$\begin{aligned}
\frac{\mathrm{d}\varphi}{\mathrm{d}t} &= -\dot{\gamma}[\sin^2\varphi - \tfrac{1}{2}] \\
\frac{\mathrm{d}\Theta}{\mathrm{d}t} &= \dot{\gamma}\sin\Theta\cos\Theta\sin\varphi\cos\varphi \qquad (3.63)
\end{aligned}$$

The first of these equations is easily integrated, to yield

$$\begin{aligned}
\int_{\varphi(t=0)}^{\varphi(t)} \frac{\mathrm{d}\varphi'}{\sin^2\varphi' - \frac{1}{2}} &= \ln\left\{\frac{[\tan(\varphi(t)) - 1][\tan(\varphi(t{=}0)) + 1]}{[\tan(\varphi(t)) + 1][\tan(\varphi(t{=}0)) - 1]}\right\} \\
&= -\dot{\gamma}t \qquad (3.64)
\end{aligned}$$

Solving for $\tan(\varphi(t))$ leads to

$$\tan(\varphi(t)) = \frac{1 + C(t)}{1 - C(t)}, \quad \text{with } C(t) = \frac{\tan(\varphi(t{=}0)) - 1}{\tan(\varphi(t{=}0)) + 1}\exp(-\dot{\gamma}t) \qquad (3.65)$$

At infinite time, the spherical coordinate φ of $\hat{\boldsymbol{u}}$ thus becomes equal to $\pi/4$ (or equivalently $5\pi/4$). Hence, the projection of $\hat{\boldsymbol{u}}$ onto the xy plane (the flow-gradient plane) is along the direction of the extensional axis of the elongational flow. The reason for this is easily inferred from Fig. 3.1b.

Dividing the two equations of motion in Eq. (3.63) yields

$$\frac{\mathrm{d}\Theta}{\sin\Theta\cos\Theta} = -\frac{\mathrm{d}\varphi\,\sin\varphi\cos\varphi}{\sin^2\varphi - \frac{1}{2}}$$

Integration of both sides now leads to

$$\tan(\Theta(t)) = \tan(\Theta(t{=}0))\sqrt{\frac{\sin^2(\varphi(t{=}0)) - \frac{1}{2}}{\sin^2(\varphi(t)) - \frac{1}{2}}} \tag{3.66}$$

where $\varphi(t)$ can be obtained from Eq. (3.65). Since $\varphi(t)$ tends to $\pi/4$ (or $5\pi/4$), the above solution predicts that $\tan\Theta$ tends to infinity, and hence $\Theta(t) \to \pi/2$. Hence, independent of the initial condition, a rod will end up in the velocity-gradient plane along the extensional axis. This is verified in Fig. 3.6a, which shows numerical results for the spherical coordinates. Here, the distance between each data point is $1/(10\dot{\gamma})$. Data are shown for small values of $\varphi(t{=}0)$. For larger initial values for φ, the orbit just starts on one of the curves shown and then traces the same orbit. As can be seen from the uppermost left curve in Fig. 3.6a, when the initial value of Θ is small, the rod spends a relatively long time around the unstable stationary solution $\{\Theta, \varphi\} = \{0, \pi/4\}$ of the equations of motion, before reaching the final stable state $\{\Theta, \varphi\} = \{\pi/2, \pi/4\}$. That is, $\hat{\boldsymbol{u}}$ first rotates to the extensional direction where $\varphi = \pi/4$, keeping its angle Θ with the vorticity direction relatively small. This angle then slowly increases, after which there is an acceleration towards the final orientation.

3.5.2 Jeffery Orbits in Simple Shear Flow

As we have seen in Section 3.3 on hydrodynamics, the torque $\boldsymbol{\mathcal{T}}^{\mathrm{h}}$ that the fluid exerts on a very long and thin rod with an angular velocity $\boldsymbol{\Omega}$ in a shear field with velocity-gradient tensor $\boldsymbol{G} = \boldsymbol{\Gamma}$ (see Eq. 3.1) is equal to

$$\boldsymbol{\mathcal{T}}^{\mathrm{h}} = -\gamma_{\mathrm{r}}[\boldsymbol{\Omega} - \hat{\boldsymbol{u}} \times (\boldsymbol{\Gamma}\cdot\hat{\boldsymbol{u}}) + \kappa^2\,\hat{\boldsymbol{u}} \times (\boldsymbol{\Gamma}^{\mathrm{T}}\cdot\hat{\boldsymbol{u}})] \tag{3.67}$$

where γ_{r} is the rotational friction coefficient. The parameter κ^2 tends to zero for decreasing values of D/L, and measures the torque of the rod when aligned such that $\varphi = 0$, for which case $\hat{\boldsymbol{u}} \times (\boldsymbol{\Gamma}\cdot\hat{\boldsymbol{u}}) = \boldsymbol{0}$. Neglecting this small contribution results in an orientation of the rod in the flow direction for long times, while for a rod of finite thickness, where κ^2 is small but non-zero, a periodic motion results. Contrary to the case of elongational flow, considered in the previous subsection, the small but finite contribution $\sim \kappa^2$ is essential for a correct description in the case of simple shear flow.

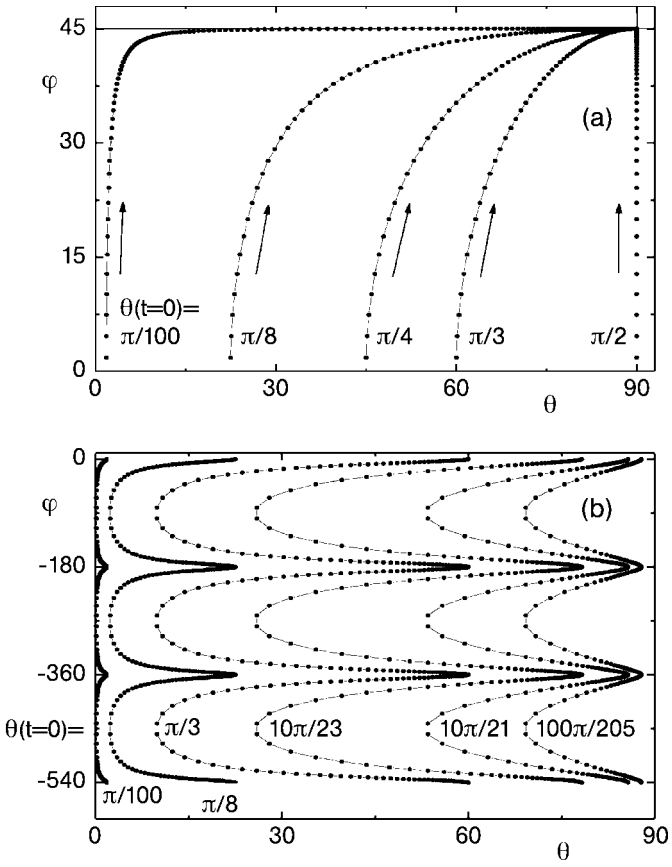

Fig. 3.6 (a) Jeffery orbits for elongational flow for initial values $\varphi(t{=}0) = \pi/100$ and various values for $\Theta(t{=}0)$, as indicated in the figure. Data points (dots) correspond to time steps equal to $1/(10\dot{\gamma})$. The arrows indicate the direction of the temporal evolution of the spherical coordinates. (b) Jeffery orbits for simple shear flow with $\kappa = 0.1$, for various values of $\Theta(t{=}0)$, as indicated in the figure. The points on the orbits mark time intervals of $T/200$; $\varphi(t)$ decreases with time.

When no other torque is acting on the rod, the hydrodynamic torque is $\mathbf{0}$, so that

$$\boldsymbol{\Omega} = \hat{\boldsymbol{u}} \times (\boldsymbol{\Gamma} \cdot \hat{\boldsymbol{u}}) - \kappa^2\, \hat{\boldsymbol{u}} \times (\boldsymbol{\Gamma}^{\mathrm{T}} \cdot \hat{\boldsymbol{u}}) \tag{3.68}$$

Precisely as for elongational flow, this implies that

$$\frac{\mathrm{d}\hat{\boldsymbol{u}}}{\mathrm{d}t} = \boldsymbol{\Gamma} \cdot \hat{\boldsymbol{u}} - \kappa^2\, \boldsymbol{\Gamma}^{\mathrm{T}} \cdot \hat{\boldsymbol{u}} - (\hat{\boldsymbol{u}} \cdot \boldsymbol{\Gamma} \cdot \hat{\boldsymbol{u}})\hat{\boldsymbol{u}} \tag{3.69}$$

In terms of spherical coordinates, this is equivalent to

$$\begin{aligned}
\frac{\mathrm{d}\Theta}{\mathrm{d}t}\cos\Theta\cos\varphi - \frac{\mathrm{d}\varphi}{\mathrm{d}t}\sin\Theta\sin\varphi &= -\dot\gamma(1-\kappa^2)\sin^3\Theta\sin\varphi\cos^2\varphi \\
&\quad +\dot\gamma\sin\Theta\sin\varphi \\
\frac{\mathrm{d}\Theta}{\mathrm{d}t}\cos\Theta\sin\varphi + \frac{\mathrm{d}\varphi}{\mathrm{d}t}\sin\Theta\cos\varphi &= -\dot\gamma(1-\kappa^2)\sin^3\Theta\sin^2\varphi\cos\varphi \\
&\quad -\dot\gamma\kappa^2\sin\Theta\cos\varphi \\
\frac{\mathrm{d}\Theta}{\mathrm{d}t} &= \dot\gamma(1-\kappa^2)\sin\Theta\cos\Theta\sin\varphi\cos\varphi
\end{aligned} \tag{3.70}$$

Precisely as in the previous case of elongational flow, we thus arrive at the following equations of motion for the spherical angular coordinates:

$$\begin{aligned}
\frac{\mathrm{d}\varphi}{\mathrm{d}t} &= -\dot\gamma[\sin^2\varphi + \kappa^2\cos^2\varphi] \\
\frac{\mathrm{d}\Theta}{\mathrm{d}t} &= \dot\gamma(1-\kappa^2)\sin\Theta\cos\Theta\sin\varphi\cos\varphi
\end{aligned} \tag{3.71}$$

The first of these equations is easily integrated to yield

$$\begin{aligned}
\int_{\varphi(t=0)}^{\varphi(t)} \frac{\mathrm{d}\varphi'}{\sin^2\varphi' + \kappa^2\cos^2\varphi'} &= \frac{1}{\kappa}\left\{\arctan\left[\frac{1}{\kappa}\tan(\varphi(t))\right] - C'\right\} \\
&= -\dot\gamma t
\end{aligned} \tag{3.72}$$

where C' is an integration constant, equal to

$$C' = \arctan\left[\frac{1}{\kappa}\tan(\varphi(t{=}0))\right] \tag{3.73}$$

Hence,

$$\tan(\varphi(t)) = \kappa\tan(C' - \dot\gamma\kappa t) \tag{3.74}$$

Since $\varphi(t)$ is periodic, trajectories of $\hat{\boldsymbol{u}}$ do not depend on $\varphi(t{=}0)$, so that, without loss of generality, we may take $\varphi(t{=}0) = 0$. For this choice, according to Eq. (3.73), $C' = 0$. The solution (3.74) thus simplifies to

$$\tan(\varphi(t)) = -\kappa\tan(\dot\gamma\kappa t) \tag{3.75}$$

It follows that $\varphi(t)$ is a periodic function of time, with period T that is independent of the initial value of $\hat{\boldsymbol{u}}$, and is equal to

$$T = \frac{2\pi}{\dot{\gamma}\kappa} \tag{3.76}$$

It should be noted that terms of order $(D/L)^2$ are neglected in the equation of motion (3.69) for the orientation (except for the important contribution $\sim \kappa^2$ to the torque), so that the expression for the period T here is valid to within terms of that order.

Division of the two equations of motion in Eq. (3.71) yields

$$\frac{\mathrm{d}\Theta}{\sin\Theta\cos\Theta} = (\kappa^2 - 1)\frac{\mathrm{d}\varphi\,\sin\varphi\cos\varphi}{\sin^2\varphi + \kappa^2\cos^2\varphi}$$

Integration of both sides leads to

$$\tan(\Theta(t)) = \tan(\Theta(t{=}0))\sqrt{\frac{1 + (\kappa^2 - 1)\cos^2(\varphi(t{=}0))}{1 + (\kappa^2 - 1)\cos^2(\varphi(t))}} \tag{3.77}$$

where $\varphi(t)$ follows from Eq. (3.75). Jeffery orbits are plotted in Fig. 3.6b for various values of $\Theta(t{=}0)$ and for $\kappa = 0.1$. As already mentioned above, the parameter κ is a measure of the torque on the rod when aligned in the velocity-gradient plane, and tends to 0 for $D/L \to 0$. For long and thin rods, for which κ is small, this torque is small, and the rod spends a relatively long time around this particular orientation. For $\kappa = 0$, that is, in the unrealistic case of zero thickness of the rod, the above result predicts that the rod ends up at an orientation where $\varphi = 0$ (or a multiple of π). The small, but finite, value of κ, however, results in periodic motion of the rod. In the present case of simple shear flow, the small torque as a result of the finite thickness of the rod in the equation of motion (3.69) is thus essential, since this small contribution will lead to a continuing motion of the rod, not ending in an orientation in the flow direction at infinite time. As can be seen from Fig. 3.6, the rod spends a relatively long time at orientations where φ is a multiple of π. For smaller values of κ, this would be even more pronounced.

3.5.3 An Experiment

Experimental results for the angle χ between the director in the velocity-gradient plane and the flow direction as obtained from dichroism measurements on hematite suspensions are shown in Fig. 3.7 (data are taken from

Vermant et al., 2001). The laser beam is along the vorticity direction, so that dichroism in the velocity-gradient plane is probed. The flow is imposed at time $t = 0$, from an initially isotropic dispersion. The geometrical aspect ratio of the hematite rods is 2.5 with a polydispersity of about 25%. For small times, rods are preferentially oriented with an angle of $45°$ with the flow direction, due to the orientational effect of the elongational part of the simple shear flow. For a single rod, the angle χ is equal to φ in Eq. (3.75). Hence, according to Eq. (3.75), χ should scale with the strain $\dot{\gamma}t$, which is indeed confirmed by these experiments. The temporal oscillations of χ are damped because of the polydispersity in aspect ratio. The shear rates are chosen large enough so that, during the time interval where damping occurs, orientational Brownian motion of the rods does not play a role. According to Eqs. (3.76) and (3.56), each different aspect ratio leads to a different period T of oscillation of $\varphi(t)$, so that after some time different rods are "out of phase", which gives rise to damping of the oscillations of the measured angle χ. Since the dispersions are very dilute, so that the rods do not interact with each other, the angle χ can be calculated taking polydispersity into account [details can be found in Vermant et al. (2001)]. Using the equations derived in the present section and properly averaging with respect to polydispersity in aspect ratio fits the experimental master curve in Fig. 3.7. The effective aspect ratio as obtained from this fit is 1.75 (instead of the geometrical aspect ratio of 2.5)

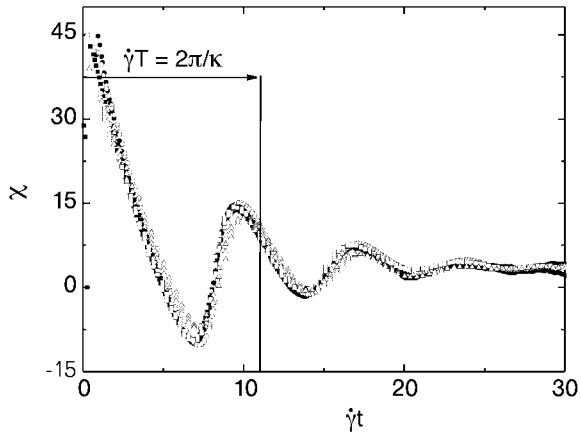

Fig. 3.7 The angle χ between the projection of the director onto the velocity-gradient plane and the flow direction as a function of strain $\dot{\gamma}t$, for five different shear rates, $\dot{\gamma} = 1$ (filled circles), 1.7 (filled squares), 3 (open circles), 5 (open squares) and $7\ \mathrm{s}^{-1}$ (open triangles), as obtained from dichroism measurements by Vermant et al. (2001). The sample consists of ellipsoidal hematite rods with an aspect ratio of 2.5 with a polydispersity of about 25%, dissolved in a slightly acidic water/glycerin 5/95 mixture. The average length of the rods is 430 nm and their thickness is 170 nm. The vertical line indicates the period of time T as obtained from Eq. (3.76).

and a polydispersity of 65% (instead of 25%). These differences between the effective and geometrical values are due to the deviation of the rods from an ideal ellipsoidal shape. The period of oscillation as given by Eq. (3.76) is seen to be of the right magnitude (despite the fact that Eq. (3.76) is only valid for long and thin rods, while the present hematite rods are quite short and thick).

3.6 Brownian Motion of a Free Rod (Without Shear Flow)

Before going to Brownian rods in shear flow, we shall consider translational and rotational Brownian motion of a long and thin rod in the absence of flow. Brownian motion can be studied on the basis of Newton's equation of motion, supplemented with fluctuating forces and torques resulting from collisions of solvent molecules with the rod. Such equations of motion with a fluctuating component are referred to as *Langevin equations*. We shall first review Newton's equations of motion before formulating the Langevin equations for a long and thin rod. On the basis of these equations, important time scales can be defined. Due to the very large size and mass of the rod in comparison to the solvent molecules, the rod moves on a time scale that is much larger than the typical relaxation times of solvent molecules. In addition, it will turn out that velocities relax quite fast due to friction with the solvent. This enables us to coarse-grain equations of motion to the so-called Brownian time scale, on which velocities and angular momenta have long relaxed to equilibrium with the heat bath of solvent molecules.

In an experiment, the time scale is set by the time interval over which observables are averaged during a measurement. For example, taking photographs of a Brownian particle is an experiment on a time scale that is set by the shutter time of the camera. Subsequent photographs reveal the motion of the Brownian particle averaged over a time interval equal to the shutter time. Any theory considering the motion of the Brownian particle obtained in such a way should of course be aimed at the calculation of observables, averaged over that time interval. A time scale is thus the minimum time resolution of an experiment or theory.

3.6.1 Newton's Equations of Motion for a Rigid Body

Let us first recall Newton's equations of motion for non-spherical rigid particles. The rigid body contains a large number of molecules, with positions $\boldsymbol{r}_n$, momenta $\boldsymbol{p}_n$, and masses m_n, where $n = 1, 2, 3, \ldots$. The positions of the molecules are fixed relative to each other; that is, the body is rigid as a result

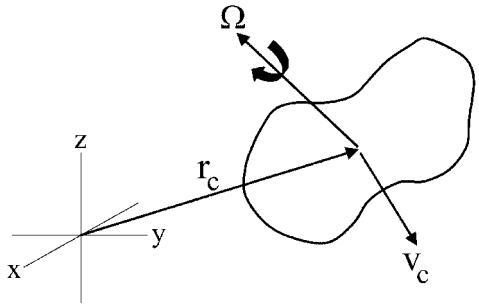

Fig. 3.8 Motion of a rigid body: $\boldsymbol{\Omega}$ is the angular velocity and $\boldsymbol{v}_\mathrm{c}$ is the translational velocity of the reference point $\boldsymbol{r}_\mathrm{c}$.

of intermolecular interactions. The velocity $\boldsymbol{v}_n$ of molecule n is composed of two parts: the rigid body can rotate and translate. To make the distinction between the two contributions, the velocities are written as

$$\boldsymbol{v}_n = \boldsymbol{\Omega} \times (\boldsymbol{r}_n - \boldsymbol{r}_\mathrm{c}) + \boldsymbol{v}_\mathrm{c} \tag{3.78}$$

where $\boldsymbol{r}_\mathrm{c}$ is an arbitrary point inside the rigid body with a translational velocity $\boldsymbol{v}_\mathrm{c}$, and $\boldsymbol{\Omega}$ is the angular velocity with respect to the point $\boldsymbol{r}_\mathrm{c}$ (see Fig. 3.8).

Newton's equation of motion for the total momentum $\boldsymbol{p}$ reads

$$\frac{\mathrm{d}\boldsymbol{p}}{\mathrm{d}t} \equiv \frac{\mathrm{d}}{\mathrm{d}t}\sum_n \boldsymbol{p}_n = \boldsymbol{\Omega} \times \sum_n m_n[\boldsymbol{v}_n - \boldsymbol{v}_\mathrm{c}] + \frac{\mathrm{d}\boldsymbol{\Omega}}{\mathrm{d}t}$$

$$\times \sum_n m_n[\boldsymbol{r}_n - \boldsymbol{r}_\mathrm{c}] + M\frac{\mathrm{d}\boldsymbol{v}_\mathrm{c}}{\mathrm{d}t} = \boldsymbol{F} \tag{3.79}$$

where $\boldsymbol{F}$ is the total *external force* on the particle, and $M = \sum_n m_n$ is the total mass of the particle. With the following choice for the point $\boldsymbol{r}_\mathrm{c}$,

$$\boldsymbol{r}_\mathrm{c} = \sum_n m_n \boldsymbol{r}_n \Big/ \sum_n m_n \tag{3.80}$$

which is the *center of mass* of the rigid body, Eq. (3.79) becomes similar to Newton's equation of motion for a spherical particle:

$$\frac{\mathrm{d}\boldsymbol{p}_\mathrm{c}}{\mathrm{d}t} = \boldsymbol{F} \tag{3.81}$$

where $\boldsymbol{p}_\mathrm{c} = M\boldsymbol{v}_\mathrm{c}$. The rotational motion of the particle is characterized by the angular momentum $\boldsymbol{J}$,

$$\boldsymbol{J} \equiv \sum_n \boldsymbol{r}_n^\mathrm{c} \times \boldsymbol{p}_n^\mathrm{c} \tag{3.82}$$

where the superscript "c" refers to coordinates relative to the center-of-mass coordinate ($\boldsymbol{r}_n^{\mathrm{c}} = \boldsymbol{r}_n - \boldsymbol{r}_{\mathrm{c}}$ and $\boldsymbol{p}_n^{\mathrm{c}} = \boldsymbol{p}_n - \boldsymbol{p}_{\mathrm{c}}$). The equation of motion of the angular momentum $\boldsymbol{J}$ follows simply by differentiating the defining equation (3.82), and using Newton's equation of motion for each molecule separately:

$$\frac{\mathrm{d}\boldsymbol{J}}{\mathrm{d}t} = \sum_n \boldsymbol{r}_n^{\mathrm{c}} \times \boldsymbol{F}_n \equiv \boldsymbol{\mathcal{T}} \tag{3.83}$$

with $\boldsymbol{F}_n$ the force on the nth molecule. The last equality in this equation defines the *torque* $\boldsymbol{\mathcal{T}}$ on the particle. Equations (3.81) and (3.83) are Newton's equations of motion for translational and rotational motion, respectively.

Note that the angular momentum is a linear function of the angular velocity $\boldsymbol{\Omega}$, since, according to Eqs. (3.78), (3.80), and (3.82),

$$\boldsymbol{J} = \sum_n m_n \boldsymbol{r}_n^{\mathrm{c}} \times (\boldsymbol{\Omega} \times \boldsymbol{r}_n^{\mathrm{c}}) \tag{3.84}$$

The right-hand side can be written as a tensor multiplication of $\boldsymbol{\Omega}$,

$$\boldsymbol{J} = \boldsymbol{I}^{\mathrm{c}} \cdot \boldsymbol{\Omega} \tag{3.85}$$

with $\boldsymbol{I}^{\mathrm{c}}$ the *inertia tensor*, the ijth component of which is

$$I_{ij}^{\mathrm{c}} \equiv \sum_n m_n [(r_n^{\mathrm{c}})^2 \delta_{ij} - (r_n^{\mathrm{c}})_i (r_n^{\mathrm{c}})_j] \tag{3.86}$$

with δ_{ij} the Kronecker delta ($\delta_{ij} = 0$ for $i \neq j$, and $\delta_{ij} = 1$ for $i = j$). The torque, angular momentum, angular velocity, and inertia tensor may be considered as the rotational counterparts of force, momentum, translational velocity, and mass, respectively.

For the analysis of time scales, we shall need the expression for the kinetic energy E_{kin} of a rotating rod. Using Eqs. (3.78), (3.80), and (3.86), one finds

$$\begin{aligned}
E_{\mathrm{kin}} &= \sum_n \tfrac{1}{2} m_n \boldsymbol{v}_n \cdot \boldsymbol{v}_n \\
&= \sum_n \tfrac{1}{2} m_n [\boldsymbol{\Omega} \times \boldsymbol{r}_n^{\mathrm{c}} + \boldsymbol{v}_{\mathrm{c}}] \cdot [\boldsymbol{\Omega} \times \boldsymbol{r}_n^{\mathrm{c}} + \boldsymbol{v}_{\mathrm{c}}] \\
&= \sum_n \tfrac{1}{2} m_n v_{\mathrm{c}}^2 + \sum_n \tfrac{1}{2} m_n (\boldsymbol{\Omega} \times \boldsymbol{r}_n^{\mathrm{c}}) \cdot (\boldsymbol{\Omega} \times \boldsymbol{r}_n^{\mathrm{c}}) \\
&= \tfrac{1}{2} M v_{\mathrm{c}}^2 + \sum_n \frac{1}{2} m_n [\Omega^2 (r_n^{\mathrm{c}})^2 - (\boldsymbol{\Omega} \cdot \boldsymbol{r}_n^{\mathrm{c}})^2] \\
&\equiv \tfrac{1}{2} M v_{\mathrm{c}}^2 + \tfrac{1}{2} \boldsymbol{\Omega} \cdot \boldsymbol{I}^{\mathrm{c}} \cdot \boldsymbol{\Omega}
\end{aligned} \tag{3.87}$$

The first term on the right-hand side in the last line is the translational kinetic energy, and the second term is the kinetic energy associated with rotation about the center of mass.

3.6.2
The Langevin Equation for a Long and Thin Rod

Clearly, thermal collisions of solvent molecules with the Brownian particle result in stochastic motion of both the position of its center of mass as well as its orientation. The Langevin equations are Newton's equations of motion (3.81) for translational motion and (3.83) for rotational motion supplemented with a fluctuating force and torque, respectively, which account for collisions of the rod with solvent molecules.

In the following, we specialize to a long and thin cylindrically symmetric rod. For such a long and thin rod, the rotational motion around the cylinder axis of symmetry need not be considered. The components of the inertia tensor related to rotational motion around the long cylinder axis are very small in comparison to its remaining components, and may be disregarded. The angular velocity $\boldsymbol{\Omega}$ is therefore understood to denote the component of the angular velocity perpendicular to the cylinder axis of symmetry (see Fig. 3.9).

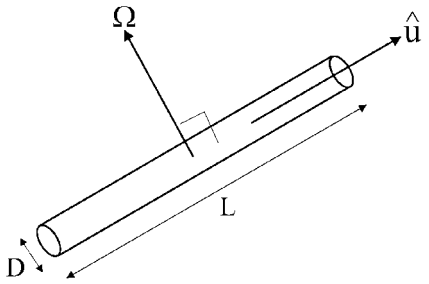

Fig. 3.9 For a long and thin rod, the angular velocity may be thought of as being perpendicular to its orientation.

The component $\boldsymbol{\Omega}$ of the angular velocity that changes the orientation of the rod is equal to

$$\boldsymbol{\Omega} = \hat{\boldsymbol{u}} \times \frac{\mathrm{d}\hat{\boldsymbol{u}}}{\mathrm{d}t} \tag{3.88}$$

This can be seen as follows. By definition we have

$$\frac{\mathrm{d}\hat{\boldsymbol{u}}}{\mathrm{d}t} = \boldsymbol{\Omega} \times \hat{\boldsymbol{u}} \tag{3.89}$$

Operating on both sides with $\hat{\boldsymbol{u}}\times$, using the fact that $\hat{\boldsymbol{u}}\times(\boldsymbol{\Omega}\times\hat{\boldsymbol{u}}) = (\hat{\boldsymbol{u}}\cdot\hat{\boldsymbol{u}})\boldsymbol{\Omega} - (\hat{\boldsymbol{u}}\cdot\boldsymbol{\Omega})\hat{\boldsymbol{u}}$, and noting that $\hat{\boldsymbol{u}}\cdot\hat{\boldsymbol{u}} = 1$ and $\hat{\boldsymbol{u}}\cdot\boldsymbol{\Omega} = 0$, Eq. (3.88) is recovered.

The force and torque of the solvent on the rod consists of two parts. Once the rods have attained a finite translational and rotational velocity, there is a systematic force equal to $-\boldsymbol{\Gamma}_{\mathrm{f}}\cdot\boldsymbol{p}/M$ (see Eq. 3.38) and a systematic torque equal to $-\gamma_{\mathrm{r}}\boldsymbol{\Omega}$ (see Eq. 3.48) on the rod due to friction. The second part is the fluctuating force and torque discussed before. Denoting the fluctuating force by $\boldsymbol{f}$ and the fluctuating torque by $\boldsymbol{T}$, the complete set of Langevin equations reads (we omit the superscripts "c" in the following):

$$\begin{aligned}
\mathrm{d}\boldsymbol{p}/\mathrm{d}t &= -(\boldsymbol{\Gamma}_{\mathrm{f}}/M)\cdot\boldsymbol{p} + \boldsymbol{f}(t)\\
\mathrm{d}\boldsymbol{r}/\mathrm{d}t &= \boldsymbol{p}/M\\
\mathrm{d}\boldsymbol{J}/\mathrm{d}t &= -\gamma_{\mathrm{r}}\boldsymbol{\Omega} + \boldsymbol{T}(t)\\
\boldsymbol{I}\cdot\boldsymbol{\Omega} &= \boldsymbol{J}
\end{aligned} \tag{3.90}$$

Since systematic interactions with the solvent molecules are made explicit through friction contributions, the ensemble average of the fluctuating force and torque are zero:

$$\begin{aligned}
\langle\boldsymbol{f}(t)\rangle &= \boldsymbol{0}\\
\langle\boldsymbol{T}(t)\rangle &= \boldsymbol{0}
\end{aligned} \tag{3.91}$$

Due to the aforementioned large separation in time scales on which the solvent molecules relax and the rod moves, it is sufficient for the calculation of the thermal movement of the Brownian particle to use a delta correlated fluctuating force and torque in time, that is

$$\begin{aligned}
\langle\boldsymbol{f}(t)\boldsymbol{f}(t')\rangle &= \boldsymbol{G}_{\mathrm{trans}}\delta(t-t')\\
\langle\boldsymbol{T}(t)\boldsymbol{T}(t')\rangle &= \boldsymbol{G}_{\mathrm{rot}}\delta(t-t')
\end{aligned} \tag{3.92}$$

where δ is the delta distribution and $\boldsymbol{G}_{\mathrm{trans}}$ and $\boldsymbol{G}_{\mathrm{rot}}$ are constant (3×3)-dimensional tensors (where the subscripts stand for "translation" and "rotation"), which may be regarded as a measure for the strength of the fluctuating force and torque. They are referred to as the *translational* and *rotational fluctuation strength*, respectively. Such delta correlations limit the description to a time resolution that is large with respect to the solvent time scale of 10^{-13} s.

Note that for the rods with a large aspect ratio L/D considered here, the inertia tensor in Eq. (3.86) is easily calculated, replacing the sum over molecules by an integral. For a constant local mass density ρ of the rod material, the inertia tensor becomes

$$\boldsymbol{I} = \int \mathrm{d}\boldsymbol{r}'\, \rho[r'^{\,2}\,\hat{\boldsymbol{I}} - \boldsymbol{r}'\boldsymbol{r}'] \approx \pi \left(\frac{D}{2}\right)^2 \rho \int_{-\frac{1}{2}L}^{\frac{1}{2}L} \mathrm{d}l\, l^2 [\hat{\boldsymbol{I}} - \hat{\boldsymbol{u}}\hat{\boldsymbol{u}}]$$

$$= \tfrac{1}{12} M L^2 [\hat{\boldsymbol{I}} - \hat{\boldsymbol{u}}\hat{\boldsymbol{u}}] \tag{3.93}$$

The typical magnitude for the inertia tensor is thus $\frac{1}{12}ML^2$. Note that, since $\boldsymbol{\Omega}$ is perpendicular to $\hat{\boldsymbol{u}}$ (see Eq. 3.88), it follows from Eq. (3.93) that

$$\boldsymbol{I} \cdot \boldsymbol{\Omega} = \tfrac{1}{12} M L^2 \boldsymbol{\Omega} \tag{3.94}$$

This result will be convenient in our further analysis of the Langevin equation.

3.6.3
Brownian Time Scale: Relaxation Rates of Translational and Rotational Velocity

The Langevin equation (3.90) can be used to estimate the time scale on which the translational and rotational velocity decay to equilibrium with the heat bath of solvent molecules. First consider the translational velocity. Ensemble averaging the first equation in (3.90), using Eq. (3.92), gives

$$\frac{\mathrm{d}\langle \boldsymbol{p} \rangle}{\mathrm{d}t} = -\left\langle \frac{\boldsymbol{\Gamma}_{\mathrm{f}}}{M} \cdot \boldsymbol{p} \right\rangle \tag{3.95}$$

Remember that the friction tensor $\boldsymbol{\Gamma}_{\mathrm{f}}$ depends on the orientation of the rod, and therefore cannot be taken outside the ensemble averaging brackets $\langle \ldots \rangle$. However, the interest here is in an *estimate* of the relaxation time of the translational velocity. Since the magnitude of the friction coefficient of a rod varies only by a factor of 2 depending on its orientation, one can use the typical magnitude of the elements of $\boldsymbol{\Gamma}_{\mathrm{f}}$ in Eq. (3.95). This typical magnitude follows from the expression in Eq. (3.38) as $2\pi\eta_0 L/\ln(L/D)$. The time scale on which the translational velocity relaxes can thus be estimated from

$$\frac{\mathrm{d}\langle \boldsymbol{p} \rangle}{\mathrm{d}t} \approx -\frac{2\pi\eta_0 L}{M \ln(L/D)} \langle \boldsymbol{p} \rangle \tag{3.96}$$

It follows that (with $\boldsymbol{p}(0)$ the initial translational momentum)

$$\langle \boldsymbol{p} \rangle(t) \approx \boldsymbol{p}(0) \exp(-t/\tau_{\mathrm{trans}}), \text{ with } \tau_{\mathrm{trans}} = \frac{M \ln(L/D)}{2\pi\eta_0 L} \approx 1 \text{ ns} \tag{3.97}$$

Thus a typical value for the relaxation time τ_{trans} of the translational velocity of a rod is found to be of the order of a nanosecond.

The time scale on which rotational velocities relax can be estimated from the last two of the equations in (3.90). Ensemble averaging gives, using Eq. (3.91),

$$\frac{\mathrm{d}\langle \boldsymbol{J} \rangle}{\mathrm{d}t} = -\gamma_{\mathrm{r}} \langle \boldsymbol{\Omega} \rangle$$

$$\langle \boldsymbol{I} \cdot \boldsymbol{\Omega} \rangle = \langle \boldsymbol{J} \rangle \tag{3.98}$$

Using Eq. (3.94) in the second equation, and substitution of the result into the first equation, leads to

$$\frac{\mathrm{d}\langle \boldsymbol{\Omega} \rangle}{\mathrm{d}t} = -\frac{12\gamma_{\mathrm{r}}}{ML^2} \langle \boldsymbol{\Omega} \rangle \tag{3.99}$$

and hence [with $\boldsymbol{\Omega}(0)$ the initial angular velocity]

$$\langle \boldsymbol{\Omega} \rangle(t) = \boldsymbol{\Omega}(0) \exp(-t/\tau_{\mathrm{rot}})$$

$$\text{with } \tau_{\mathrm{rot}} = \frac{12ML^2}{\gamma_{\mathrm{r}}} = \frac{M \ln(L/D)}{4\pi\eta_0 L} \approx 1 \text{ ns} \tag{3.100}$$

where the expression (3.49) for the rotational friction coefficient has been used. Thus the relaxation times for translational and rotational velocities are both of the order of a nanosecond.

Within a description where time is coarse-grained to a time much larger than τ_{trans} and τ_{rot}, *inertial forces and torques on the rod can be neglected*. This will turn out to be an important fact in further theoretical developments discussed later in this chapter. The corresponding coarsening in length scale and orientational angle will be discussed in the following section. The time scale that is much larger than τ_{trans} and τ_{rot}, but still small enough to resolve position and orientation in sufficient detail, is referred to as the *Brownian or diffusive time scale*.

3.6.4
Brownian Length Scale and Brownian Angle

As discussed at the beginning of this section, a coarsening in time implies a coarsening of position and angular orientation. On the Brownian time scale, the spatial and angular resolution is no better than the distance over which the Brownian particle moves and the angle over which a rod typically rotates, respectively, during a time interval equal to the Brownian time scale.

Consider first the length Δl that the rod traverses during a time $\tau \gg \tau_{\mathrm{trans}}$. This so-called *Brownian length scale* is easily obtained by integration of Eq. (3.97):

$$\Delta l = \int_0^\tau \mathrm{d}t \, \frac{|\langle \boldsymbol{p}(t) \rangle|}{M} = \frac{|\boldsymbol{p}(0)|}{M} \, \tau_{\mathrm{trans}} \left[1 - \exp\left(-\frac{\tau}{\tau_{\mathrm{trans}}} \right) \right]$$

$$\approx \frac{|\boldsymbol{p}(0)|}{M} \, \tau_{\mathrm{trans}} \tag{3.101}$$

A typical value for $|\boldsymbol{p}(0)|$ is obtained from the equipartition theorem:

$$|\boldsymbol{p}(0)| \approx \sqrt{\langle |\boldsymbol{p}|^2 \rangle} = \sqrt{3 M k_{\mathrm{B}} T} \tag{3.102}$$

The Brownian length scale is thus estimated as

$$\Delta l \approx \sqrt{3 M k_{\mathrm{B}} T} \, \frac{\ln(L/D)}{2\pi \eta_0 L} \tag{3.103}$$

Using typical numerical values for the quantities involved gives

$$\frac{\Delta l}{L} \approx 10^{-4}\text{–}10^{-3} \tag{3.104}$$

The conclusion is that displacements that are very small in comparison to the length of the rod are still resolved on the Brownian time scale. If $\Delta L/L$ had been a large number, it would have made no sense to coarsen to the Brownian time scale, since then it would not have been possible to describe the motion of the rod accurately.

Next consider the typical angle $\Delta\Theta$ over which a rod rotates during a time $\tau \gg \tau_{\mathrm{rot}}$. This is the so-called *Brownian angle*. Integration of Eq. (3.100) gives

$$\Delta\Theta = \int_0^\tau \mathrm{d}t \, |\langle \boldsymbol{\Omega}(t) \rangle| = |\boldsymbol{\Omega}(0)| \, \tau_{\mathrm{rot}} [1 - \exp(-\tau/\tau_{\mathrm{rot}})]$$

$$\approx |\boldsymbol{\Omega}(0)| \, \tau_{\mathrm{rot}} \tag{3.105}$$

According to Eq. (3.94), the rotational contribution to the kinetic energy in Eq. (3.87) is equal to $\frac{1}{24} M L^2 |\boldsymbol{\Omega}|^2$. Hence, according to the equipartition theorem, a typical value for $|\boldsymbol{\Omega}_0|$ can be estimated as

$$|\boldsymbol{\Omega}(0)| \approx \sqrt{\langle |\boldsymbol{\Omega}|^2 \rangle} = 6 \sqrt{\frac{k_{\mathrm{B}} T}{M L^2}} \tag{3.106}$$

The Brownian angle is thus of the order

$$\Delta\Theta \approx 6\sqrt{Mk_{\mathrm{B}}T}\,\frac{\ln(L/D)}{4\pi\eta_0 L^2} \tag{3.107}$$

For typical numerical values we have [note that, according to Eq. (3.103), the right-hand side is equal to $\sqrt{3}\,\Delta L/L$]

$$\frac{\Delta\Theta}{\pi} \approx 10^{-4}\text{–}10^{-3} \tag{3.108}$$

Thus very small angular displacements can still be resolved on the Brownian time scale.

For the study of processes where significant translational and rotational displacements of the Brownian particle are essential, a statistical description on the Brownian time scale is therefore sufficient.

3.6.5 Calculation of Fluctuation Strengths

Analyzing the Langevin equation requires the determination of the fluctuation strengths in Eq. (3.92). This can be done using the equipartition theorem for translational and rotational motion, after having solved the Langevin equation for $\boldsymbol{p}(t)$ and $\boldsymbol{\Omega}(t)$.

First consider the translational velocity. Integration of the first equation of motion in (3.90) yields

$$\boldsymbol{p}(t) = \exp\left(-\frac{\boldsymbol{\Gamma}_{\mathrm{f}}}{M}t\right)\cdot\boldsymbol{p}(0) + \int_0^t \mathrm{d}t'\,\exp\left[-\frac{\boldsymbol{\Gamma}_{\mathrm{f}}}{M}(t-t')\right]\cdot\boldsymbol{f}(t') \tag{3.109}$$

The exponent of a tensor, $\boldsymbol{A}$ say, is defined through the Taylor expansion

$$\exp(\boldsymbol{A}) \equiv \sum_{n=0}^{\infty}\frac{1}{n!}\boldsymbol{A}^n \tag{3.110}$$

where $\boldsymbol{A}^n$ is $\boldsymbol{A}\cdot\boldsymbol{A}\cdots\boldsymbol{A}$ (n times), and $\boldsymbol{A}^0 \equiv \hat{\boldsymbol{I}}$, the identity tensor. Now, from Eq. (3.43) it is easily shown by induction that

$$\boldsymbol{\Gamma}_{\mathrm{f}}^n = \gamma_{\parallel}^n\,\hat{\boldsymbol{u}}\hat{\boldsymbol{u}} + \gamma_{\perp}^n[\hat{\boldsymbol{I}} - \hat{\boldsymbol{u}}\hat{\boldsymbol{u}}] \tag{3.111}$$

and hence, from the defining expression (3.110) for the tensor exponential,

$$\exp\left[-\frac{\boldsymbol{\Gamma}_{\mathrm{f}}}{M}(t-t')\right] = \exp\left[-\frac{\gamma_{\parallel}}{M}(t-t')\right]\hat{\boldsymbol{u}}\hat{\boldsymbol{u}} + \exp\left[-\frac{\gamma_{\perp}}{M}(t-t')\right][\hat{\boldsymbol{I}}-\hat{\boldsymbol{u}}\hat{\boldsymbol{u}}] \qquad (3.112)$$

Equation (3.109) can thus be written as

$$\boldsymbol{p}(t) = \boldsymbol{p}_{\parallel}(t) + \boldsymbol{p}_{\perp}(t), \quad \text{with } \boldsymbol{p}_{\parallel} \equiv \hat{\boldsymbol{u}}\hat{\boldsymbol{u}}\cdot\boldsymbol{p} \text{ and } \boldsymbol{p}_{\perp} \equiv [\hat{\boldsymbol{I}}-\hat{\boldsymbol{u}}\hat{\boldsymbol{u}}]\cdot\boldsymbol{p} \quad (3.113)$$

with

$$\boldsymbol{p}_{\parallel}(t) \equiv \exp\left(-\frac{\gamma_{\parallel}}{M}t\right)\boldsymbol{p}_{\parallel}(0) + \int_0^t \mathrm{d}t' \, \exp\left[-\frac{\gamma_{\parallel}}{M}(t-t')\right]\boldsymbol{f}_{\parallel}(t')$$

$$\boldsymbol{p}_{\perp}(t) \equiv \exp\left(-\frac{\gamma_{\perp}}{M}t\right)\boldsymbol{p}_{\perp}(0) + \int_0^t \mathrm{d}t' \, \exp\left[-\frac{\gamma_{\perp}}{M}(t-t')\right]\boldsymbol{f}_{\perp}(t') \qquad (3.114)$$

where the components of the random force parallel and perpendicular to the orientation of the rods are respectively defined as

$$\boldsymbol{f}_{\parallel}(t) \equiv \hat{\boldsymbol{u}}(t)\hat{\boldsymbol{u}}(t)\cdot\boldsymbol{f}(t) \quad \text{and} \quad \boldsymbol{f}_{\perp}(t) \equiv [\hat{\boldsymbol{I}}-\hat{\boldsymbol{u}}(t)\hat{\boldsymbol{u}}(t)]\cdot\boldsymbol{f}(t) \quad (3.115)$$

Instead of using the full tensor form in Eq. (3.95) for the fluctuating force, we shall only need correlation functions of inner products of its two components $\boldsymbol{f}_{\parallel}$ and $\boldsymbol{f}_{\perp}$. Since $\boldsymbol{f}(t)$ varies with time much faster than $\hat{\boldsymbol{u}}(t)$, the latter is virtually constant over time intervals equal to many times the correlation time of the former. The conditional ensemble averages of $\boldsymbol{f}_{\parallel}$ and $\boldsymbol{f}_{\perp}$, with a prescribed $\hat{\boldsymbol{u}}$, are therefore still $\mathbf{0}$, and their correlation functions are still delta-correlated on a time scale much larger than the solvent time scale. For the same reason,

$$\langle \boldsymbol{f}_{\parallel}(t)\cdot\boldsymbol{f}_{\perp}(t')\rangle = 0 \qquad (3.116)$$

We shall therefore define two independent fluctuation strengths for the fluctuating force parallel and perpendicular to the orientation of the rods:

$$\langle \boldsymbol{f}_{\parallel}(t) \cdot \boldsymbol{f}_{\parallel}(t') \rangle = G_{\parallel} \delta(t - t')$$

$$\langle \boldsymbol{f}_{\perp}(t) \cdot \boldsymbol{f}_{\perp}(t') \rangle = G_{\perp} \delta(t - t') \tag{3.117}$$

Notice that we are working here with inner products instead of dyadic products as for the spherical particle, so that both $G_{\parallel}$ and $G_{\perp}$ are scalars. Since $\langle \boldsymbol{p}_{\parallel}(t) \cdot \boldsymbol{p}_{\perp}(t) \rangle = 0$, the kinetic energy corresponding to translational motion of the Brownian rod is the sum of two quadratic terms related to the perpendicular velocity and a single quadratic term related to the parallel velocity. From the equipartition theorem it is thus found that

$$\lim_{t \to \infty} \langle \boldsymbol{p}_{\parallel}(t) \cdot \boldsymbol{p}_{\parallel}(t) \rangle = M/\beta$$

$$\lim_{t \to \infty} \langle \boldsymbol{p}_{\perp}(t) \cdot \boldsymbol{p}_{\perp}(t) \rangle = 2M/\beta \tag{3.118}$$

On substitution of Eq. (3.114) into the above expressions, using Eqs. (3.116) and (3.117), it is readily found that

$$G_{\parallel} = 2\gamma_{\parallel}/\beta$$

$$G_{\perp} = 4\gamma_{\perp}/\beta \tag{3.119}$$

This concludes the determination of the translational fluctuation strengths, which will be used to investigate the translational Brownian motion of the rod in the following section.

Next consider the fluctuation strength for the correlation function in Eq. (3.92) of the torque. Using Eq. (3.94) in the last equation in (3.90), substituting the result into the third equation and integrating yields

$$\boldsymbol{\Omega}(t) = \boldsymbol{\Omega}(0) \exp\left(-\frac{12\gamma_{\mathrm{r}}}{ML^2} t\right) + \frac{12}{ML^2} \int_0^t \mathrm{d}t' \, \boldsymbol{T}(t') \, \exp\left[-\frac{12\gamma_{\mathrm{r}}}{ML^2}(t - t')\right] \tag{3.120}$$

Using the second equation in (3.92) thus leads to

$$\lim_{t \to \infty} \langle \boldsymbol{\Omega}(t) \boldsymbol{\Omega}(t) \rangle = \frac{6}{\gamma_{\mathrm{r}} ML^2} \boldsymbol{G}_{\mathrm{r}} \tag{3.121}$$

From Eq. (3.87) for the kinetic energy together with Eq. (3.94), one finds that the kinetic energy due to rotational motion is equal to $\frac{1}{24} ML^2 \Omega^2(t)$.

The equipartition theorem implies that $\frac{1}{24}ML^2\Omega^2(t) = \frac{3}{2}k_\mathrm{B}T$. Hence,

$$\lim_{t\to\infty}\langle\boldsymbol{\Omega}(t)\boldsymbol{\Omega}(t)\rangle = 12\,\hat{\boldsymbol{I}}\,\frac{k_\mathrm{B}T}{ML^2} \tag{3.122}$$

Combining this with Eq. (3.121) identifies the rotational fluctuation strength

$$\boldsymbol{G}_\mathrm{r} = \hat{\boldsymbol{I}}\,\frac{2\gamma_\mathrm{r}}{\beta} \tag{3.123}$$

This expression allows for the analysis of the rotational part of the Langevin equation.

3.6.6
Translational Brownian Motion of a Rod

The simplest quantity that characterizes translational Brownian motion is the *mean square displacement*, defined as

$$W(t) \equiv \langle|\boldsymbol{r}(t) - \boldsymbol{r}(t{=}0)|^2\rangle \tag{3.124}$$

where the angle brackets denote ensemble averaging. This quantity can be calculated from the Langevin equation as follows.

We shall calculate the mean square displacement on the Brownian time scale. As mentioned before, inertial forces can be neglected on the Brownian time scale. Neglecting the inertial force $\mathrm{d}\boldsymbol{p}/\mathrm{d}t$ on the left-hand side of the first equation in (3.90) gives

$$\mathrm{d}\boldsymbol{r}/\mathrm{d}t = \boldsymbol{\Gamma}_\mathrm{f}^{-1}\cdot\boldsymbol{f}(t) \tag{3.125}$$

where $\boldsymbol{\Gamma}_\mathrm{f}^{-1}$ is the inverse of $\boldsymbol{\Gamma}_\mathrm{f}$. The reason for neglecting the inertial force can be made more explicit as follows. Let $t' = t/\tau$ be the dimensionless time in units of the Brownian time scale τ. Rescaling the first equation in Eq. (3.90) gives

$$\frac{\tau_\mathrm{trans}}{\tau}\,\frac{\mathrm{d}\boldsymbol{p}}{\mathrm{d}t'} = -\tau_\mathrm{trans}\,\frac{\boldsymbol{\Gamma}_\mathrm{f}}{M}\cdot\boldsymbol{p} + \tau_\mathrm{trans}\boldsymbol{f}(\tau\,t') \tag{3.126}$$

Since the typical magnitude of the elements of the tensor $\boldsymbol{\Gamma}_\mathrm{f}/M$ is $1/\tau_\mathrm{trans}$ (see Eqs. 3.38 and 3.97), so that $\tau_\mathrm{trans}\boldsymbol{\Gamma}_\mathrm{f}/M$ is of order unity, and $\tau \gg \tau_\mathrm{trans}$ on the Brownian time scale, this is a singularly perturbed differential equation. That is, the inertial term is important only over a very small time interval in t', which is the mathematical boundary layer connected to the singular perturbation.

During this time interval, the momentum coordinate relaxes to equilibrium with the solvent. Beyond this small time interval, where $\mathrm{d}\boldsymbol{p}/\mathrm{d}t'$ is no longer very large, the inertial contribution can be neglected. This immediately leads to Eq. (3.125).

The inverse of the friction tensor appearing in Eq. (3.125) is easily calculated:

$$\boldsymbol{\Gamma}_{\mathrm{f}}^{-1} = \frac{1}{\gamma_{\parallel}}\hat{\boldsymbol{u}}\hat{\boldsymbol{u}} + \frac{1}{\gamma_{\perp}}[\hat{\boldsymbol{I}} - \hat{\boldsymbol{u}}\hat{\boldsymbol{u}}] \tag{3.127}$$

The Langevin equation can thus be written in terms of the parallel and perpendicular components of the random force (see Eq. 3.115)

$$\frac{\mathrm{d}\boldsymbol{r}}{\mathrm{d}t} = \frac{1}{\gamma_{\parallel}}\boldsymbol{f}_{\parallel}(t) + \frac{1}{\gamma_{\perp}}\boldsymbol{f}_{\perp}(t) \tag{3.128}$$

hence

$$\boldsymbol{r}(t) = \boldsymbol{r}(t{=}0) + \int_0^t \mathrm{d}t' \left[\frac{1}{\gamma_{\parallel}}\boldsymbol{f}_{\parallel}(t') + \frac{1}{\gamma_{\perp}}\boldsymbol{f}_{\perp}(t')\right] \tag{3.129}$$

Using the fact that the fluctuating forces are delta-correlated with fluctuation strengths given in Eq. (3.119), one readily finds that

$$W(t) = 6\bar{D}t \tag{3.130}$$

where

$$\bar{D} = \tfrac{1}{3}(D_{\parallel} + 2D_{\perp}) \tag{3.131}$$

Here we have introduced the Einstein translational diffusion coefficients for parallel and perpendicular motion:

$$\begin{aligned} D_{\parallel} &= k_{\mathrm{B}}T/\gamma_{\parallel} \\ D_{\perp} &= k_{\mathrm{B}}T/\gamma_{\perp} \end{aligned} \tag{3.132}$$

For times $t \ll \tau_{\mathrm{trans}}$, where friction with the solvent is not effective, the velocity of the center of mass of a rod is constant. The mean square displacement then varies like $\sim t^2$. On the Brownian time scale, that is for times $t \gg \tau_{\mathrm{trans}}$, many independent collisions of the rod with solvent molecules have occurred. This apparently leads to a linear variation of $W(t)$ with time. Such dynamic behavior is called *diffusive*.

3.6.7 Orientational Correlations

The simplest quantity that characterizes rotational Brownian motion is the *rotational mean square displacement*

$$W_{\mathrm{rot}}(t) \equiv \langle |\hat{\boldsymbol{u}}(t) - \hat{\boldsymbol{u}}(t{=}0)|^2 \rangle = 2[1 - \langle \hat{\boldsymbol{u}}(t) \rangle \cdot \hat{\boldsymbol{u}}(t{=}0)] \qquad (3.133)$$

This rotational displacement is calculated on the Brownian time scale. For the same reason as for translational motion, the inertial term for the rotational Langevin equation of motion can be neglected on the Brownian time scale. The third of the equations of motion in (3.90) thus reduces to

$$\boldsymbol{\Omega} = \hat{\boldsymbol{u}} \times \frac{\mathrm{d}\hat{\boldsymbol{u}}}{\mathrm{d}t} = \frac{1}{\gamma_{\mathrm{r}}} \boldsymbol{T}(t) \qquad (3.134)$$

where Eqs. (3.88) and (3.94) have been used. As a first step to obtain an expression for the rotational mean square displacement (3.133), the differential equation (Eq. 3.134) should be solved for $\hat{\boldsymbol{u}}(t)$ in terms of the fluctuating torque $\boldsymbol{T}$. To this end, Eq. (3.134) is rewritten as

$$\frac{\mathrm{d}\hat{\boldsymbol{u}}}{\mathrm{d}t} = \frac{1}{\gamma_{\mathrm{r}}} \boldsymbol{T}(t) \times \hat{\boldsymbol{u}} \qquad (3.135)$$

To integrate this equation, the right-hand side is written as a tensor multiplication

$$\mathrm{d}\hat{\boldsymbol{u}}/\mathrm{d}t = \boldsymbol{A}(t) \cdot \hat{\boldsymbol{u}} \qquad (3.136)$$

with

$$\boldsymbol{A}(t) \equiv \frac{1}{\gamma_{\mathrm{r}}} \begin{pmatrix} 0 & -T_3(t) & T_2(t) \\ T_3(t) & 0 & -T_1(t) \\ -T_2(t) & T_1(t) & 0 \end{pmatrix} \qquad (3.137)$$

where T_j is the jth component of $\boldsymbol{T}$. The differential equation (Eq. 3.136) is equivalent to the integral equation

$$\hat{\boldsymbol{u}}(t) = \hat{\boldsymbol{u}}(0) + \int_0^t \mathrm{d}t' \, \boldsymbol{A}(t') \cdot \hat{\boldsymbol{u}}(t') \qquad (3.138)$$

which is solved by iteration:

$$\hat{\boldsymbol{u}}(t) = \hat{\boldsymbol{u}}(0) + \sum_{n=1}^{\infty} \int_0^t \mathrm{d}t_1 \int_0^{t_1} \mathrm{d}t_2 \int_0^{t_2} \mathrm{d}t_3 \cdots \int_0^{t_{n-2}} \mathrm{d}t_{n-1} \int_0^{t_{n-1}} \mathrm{d}t_n \times \boldsymbol{A}(t_1) \cdot \boldsymbol{A}(t_2) \cdots \boldsymbol{A}(t_n) \cdot \hat{\boldsymbol{u}}(0) \tag{3.139}$$

For the calculation of the ensemble average of $\hat{\boldsymbol{u}}(t)$, the ensemble averages of the multiple integrals over products of the $\boldsymbol{A}$ tensors must be evaluated explicitly. From the definition of the tensor $\boldsymbol{A}$, it follows immediately that

$$\boldsymbol{A}(t) \cdot \hat{\boldsymbol{u}}(0) = \frac{1}{\gamma_\mathrm{r}} \boldsymbol{T}(t) \times \hat{\boldsymbol{u}}(0) \tag{3.140}$$

$$\begin{aligned} \boldsymbol{A}^2(t) \cdot \hat{\boldsymbol{u}}(0) &= \frac{1}{\gamma_\mathrm{r}^2} \boldsymbol{T}(t) \times [\boldsymbol{T}(t) \times \hat{\boldsymbol{u}}(0)] \\ &= \frac{1}{\gamma_\mathrm{r}^2} [-T^2(t)\, \hat{\boldsymbol{I}} + \boldsymbol{T}(t)\boldsymbol{T}(t)] \cdot \hat{\boldsymbol{u}}(0) \end{aligned} \tag{3.141}$$

Since the ensemble average of the random torque, and hence of $\boldsymbol{A}$, is zero, and its correlation function is delta-correlated in time, the first two terms in the ensemble-averaged iterated solution are found from Eqs. (3.123) and (3.137),

$$\int_0^t \mathrm{d}t_1 \, \langle \boldsymbol{A}(t_1) \rangle \cdot \hat{\boldsymbol{u}}(0) = \boldsymbol{0} \tag{3.142}$$

$$\int_0^t \mathrm{d}t_1 \int_0^{t_1} \mathrm{d}t_2 \, \langle \boldsymbol{A}(t_1) \cdot \boldsymbol{A}(t_2) \rangle \cdot \hat{\boldsymbol{u}}(0) = -2 \frac{k_\mathrm{B} T}{\gamma_\mathrm{r}} t \hat{\boldsymbol{u}}(0) \tag{3.143}$$

Here we have used the fact that

$$\int_0^{t_1} \mathrm{d}t_2 \, \delta(t_1 - t_2) = \tfrac{1}{2}$$

Since t_1 is not in the interior of the integration range here, this integral is *not* equal to 1. That its value is equal to $\frac{1}{2}$ can be seen as follows.

On the smallest time scale, the correlation function $\langle \boldsymbol{T}(t_1)\boldsymbol{T}(t_2) \rangle$ of the random torque, and hence of $\boldsymbol{A}$, is a symmetric function of the difference $t_1 - t_2$. The integral with respect to t_2 in Eq. (3.139) ranges over half of the symmetric correlation function (see Fig. 3.10), and is thus equal to $\frac{1}{2} \times$ the integral ranging over the entire range of the argument. To evaluate the ensemble averages over higher-order products of $\boldsymbol{A}$ in the iterated solution (3.139), we use the fact that, on the Brownian time scale, $\boldsymbol{T}$ and hence also $\boldsymbol{A}$ are Gaussian variables. On the Brownian time scale, $\boldsymbol{T}$ is an average over many

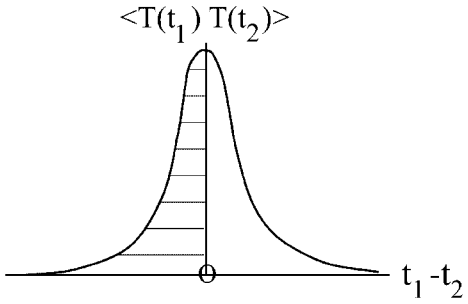

Fig. 3.10 Integration of the correlation function of the torque over half the domain of its argument.

independent realizations, so that, according to the central limit theorem, it is a Gaussian variable. All the ensemble averages of products of an odd number of $\boldsymbol{A}$ tensors are thus zero. The ensemble averages of products of an even number of $\boldsymbol{A}$ tensors can be written as a sum of products of averages of only two $\boldsymbol{A}$ tensors. Consider, for example, the ensemble average of the $n = 4$ term in the iterated solution [summation over the repeated indices p, q, r, s is understood here, A_{ij} is the ijth component of $\boldsymbol{A}$, and $\hat{u}_s(0)$ is the sth component of $\hat{\boldsymbol{u}}(0)$],

$$\begin{aligned}
&\int_0^t \mathrm{d}t_1 \int_0^{t_1} \mathrm{d}t_2 \int_0^{t_2} \mathrm{d}t_3 \int_0^{t_3} \mathrm{d}t_4 \, \langle A_{ip}(t_1) A_{pq}(t_2) A_{qr}(t_3) A_{rs}(t_4) \rangle \hat{u}_s(0) \\
&= \int_0^t \mathrm{d}t_1 \int_0^{t_1} \mathrm{d}t_2 \int_0^{t_2} \mathrm{d}t_3 \int_0^{t_3} \mathrm{d}t_4 \, [\langle A_{ip}(t_1) A_{pq}(t_2) \rangle \langle A_{qr}(t_3) A_{rs}(t_4) \rangle \hat{u}_s(0) \\
&\quad + \langle A_{ip}(t_1) A_{qr}(t_3) \rangle \langle A_{pq}(t_2) A_{rs}(t_4) \rangle \hat{u}_s(0) \\
&\quad + \langle A_{ip}(t_1) A_{rs}(t_4) \rangle \langle A_{pq}(t_2) A_{qr}(t_3) \rangle \hat{u}_s(0)]
\end{aligned}$$

For the respective products of ensemble averages in the above equation, we need to evaluate the following three integrations over delta distributions:

$$\int_0^t \mathrm{d}t_1 \int_0^{t_1} \mathrm{d}t_2 \int_0^{t_2} \mathrm{d}t_3 \int_0^{t_3} \mathrm{d}t_4 \, \delta(t_1 - t_2) \delta(t_3 - t_4)$$

$$\int_0^t \mathrm{d}t_1 \int_0^{t_1} \mathrm{d}t_2 \int_0^{t_2} \mathrm{d}t_3 \int_0^{t_3} \mathrm{d}t_4 \, \delta(t_1 - t_3) \delta(t_2 - t_4)$$

$$\int_0^t \mathrm{d}t_1 \int_0^{t_1} \mathrm{d}t_2 \int_0^{t_2} \mathrm{d}t_3 \int_0^{t_3} \mathrm{d}t_4 \, \delta(t_1 - t_4) \delta(t_2 - t_3)$$

The first of these four-fold integrals is equal to

$$\int_0^t \mathrm{d}t_1 \int_0^{t_1} \mathrm{d}t_2 \int_0^{t_2} \mathrm{d}t_3 \int_0^{t_3} \mathrm{d}t_4 \, \delta(t_1 - t_2)\delta(t_3 - t_4) = \left(\frac{1}{2}\right)^2 \frac{1}{2}\, t^2$$

where the factor $(1/2)^2$ originates from integration of delta functions ranging over half the domain of their arguments, as explained above. By inspection, the other two four-fold integrals turn out to be zero, because the arguments of the delta functions are non-zero in the entire integration range. Only products with the consecutive time ordering $t_1 \to t_2 \to t_3 \to \cdots \to t_n$ contribute. Using the expression (3.123) for the rotational fluctuation strength, we thus arrive at the following result:

$$\int_0^t \mathrm{d}t_1 \int_0^{t_1} \mathrm{d}t_2 \int_0^{t_2} \mathrm{d}t_3 \int_0^{t_3} \mathrm{d}t_4 \, \langle \boldsymbol{A}(t_1) \cdot \boldsymbol{A}(t_2) \cdot \boldsymbol{A}(t_3) \cdot \boldsymbol{A}(t_4) \rangle \cdot \hat{\boldsymbol{u}}(0)$$

$$= \left(-\frac{4}{\beta\gamma_\mathrm{r}}\right)^2 \left(\frac{1}{2}\right)^2 \frac{1}{2}\, t^2 \hat{\boldsymbol{u}}(0)$$

In the next higher-order terms in the ensemble average of the iterative solution (3.139), the product with the consecutive time ordering is likewise the only surviving one. Along similar lines, one shows that, for even n,

$$\int_0^t \mathrm{d}t_1 \cdots \int_0^{t_{n-1}} \mathrm{d}t_n \langle \boldsymbol{A}(t_1) \cdots \boldsymbol{A}(t_n) \rangle = \left(-\frac{4}{\beta\gamma_\mathrm{r}}\right)^{n/2} \left(\frac{1}{2}\right)^{n/2} \frac{1}{(n/2)!}\, t^{n/2}\, \hat{\boldsymbol{I}}$$

The iterative solution is thus

$$\langle \hat{\boldsymbol{u}}(t) \rangle = \left[\sum_{n=0}^{\infty} \frac{1}{n!} (-2D_\mathrm{r})^n t^n \right] \hat{\boldsymbol{u}}(0) = \exp(-2D_\mathrm{r} t)\hat{\boldsymbol{u}}(0) \qquad (3.144)$$

where the *rotational diffusion coefficient* D_r is defined by the Einstein relation

$$D_\mathrm{r} = k_\mathrm{B}T/\gamma_\mathrm{r} \qquad (3.145)$$

The *rotational mean square displacement* is thus equal to

$$W_\mathrm{rot}(t) = 2[1 - \exp(-2D_\mathrm{r} t)] \qquad (3.146)$$

For small times, this result is quite similar to Eq. (3.130) for the mean square displacement of the center of mass of a rod,

$$W_\mathrm{rot}(t) = \langle |\hat{\boldsymbol{u}}(t) - \hat{\boldsymbol{u}}(t{=}0)|^2 \rangle = 4D_\mathrm{r} t, \quad D_\mathrm{r} t \ll 1 \qquad (3.147)$$

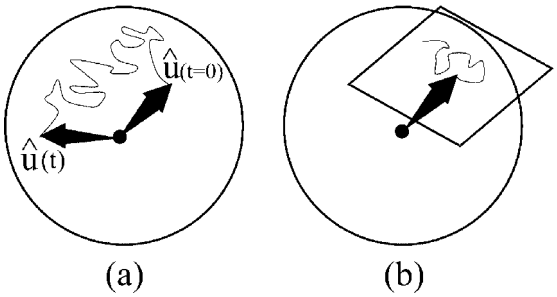

Fig. 3.11 (a) Rotational diffusion visualized as diffusion of a point on the unit sphere. (b) For small times, this is equivalent to diffusion of a point on a two-dimensional surface.

This corresponds to diffusion of a point in two dimensions. Rotational Brownian motion may be visualized as a point on the unit spherical surface, representing the tip of the unit vector $\hat{\boldsymbol{u}}$, which exerts Brownian motion (see Fig. 3.11a). For small times, this is Brownian motion on a two-dimensional flat surface (see Fig. 3.11b). For larger times, the tip experiences the curvature of the unit spherical surface, leading to more complex behavior as described by Eq. (3.146).

3.7 Equations of Motion for Interacting Rods

So far, we have considered rods that do not interact with other rods. For systems of interacting rods, properties are most easily studied by means of probability density functions (PDFs) of positions and orientations. In this section we shall derive the fundamental equation of motion for the probability density function of the positions and orientations of an assembly of N interacting rods. This equation of motion is commonly referred to as the *Smoluchowski equation*. An essential ingredient in the derivation of this equation of motion is the neglect of inertia on the Brownian time scale, as discussed before. The Smoluchowski equation also describes the dynamics of non-interacting rods, and is shown to reproduce the results obtained in previous sections. In addition, the behavior of non-interacting rods in shear flow is discussed at the end of this section.

3.7.1
The N-Particle Smoluchowski Equation

Consider a single cylindrically symmetric, rigid rod embedded in solvent. The position coordinate of the rod will be denoted by $\boldsymbol{r}$, while its orientation is characterized by the unit vector $\hat{\boldsymbol{u}}$, which is directed along the long axis of the rod. The "micro-state" of the rod is thus set by a point in $\Re^3$ (the position vector $\boldsymbol{r}$) and a point on the unit spherical surface (the tip of the vector $\hat{\boldsymbol{u}}$), as depicted in Fig. 3.12.

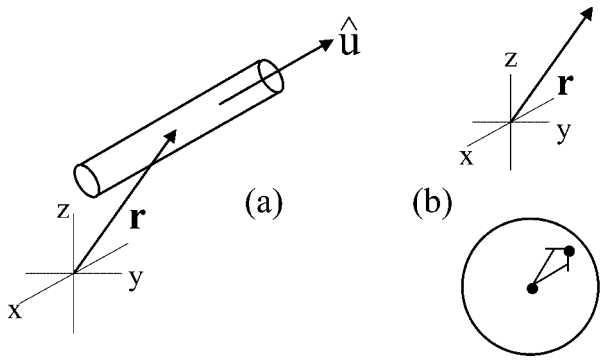

Fig. 3.12 (a) Definition of the position coordinate $\boldsymbol{r}$ and the orientation $\hat{\boldsymbol{u}}$ of a rod. (b) The micro-state of a single rod is set by a point in $\Re^3$ (the position coordinate) and a point on the unit spherical surface (the orientation).

The points in $\Re^3$ and on the unit spherical surface exhibit chaotic motion due to translational and rotational Brownian motion, respectively. Consider now an ensemble of $\mathcal{N}$ containers, where each container is filled with solvent and contains just a single Brownian rod. The micro-state of this ensemble (as far as the colloidal rod is concerned) is set by $\mathcal{N}$ points in $\Re^3$ (for the positions) and $\mathcal{N}$ points on the unit spherical surface (for the orientations). Let $\mathcal{W}$ denote an arbitrary volume in $\Re^3$, and $\mathcal{A}$ an arbitrary surface area on the unit spherical surface (see Fig. 3.13). The density of points at a certain position and orientation is proportional to the probability of finding a rod in that micro-state. To find an equation of motion for that probability, we shall require the time rate of change of the number of points inside $\mathcal{W}$ and $\mathcal{A}$. The time-dependent "number of points" $N(t)$ is related to the probability density function $P(\boldsymbol{r}, \hat{\boldsymbol{u}}, t)$ for the position $\boldsymbol{r}$ and orientation $\hat{\boldsymbol{u}}$, as

$$N(t) = \int_{\mathcal{W}} \mathrm{d}\boldsymbol{r} \int_{\mathcal{A}} \mathrm{d}\hat{\boldsymbol{u}}\, P(\boldsymbol{r}, \hat{\boldsymbol{u}}, t) \tag{3.148}$$

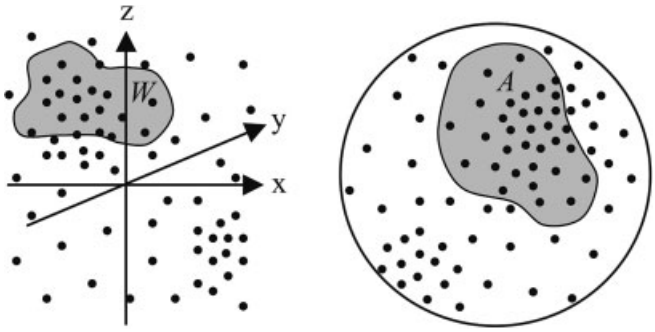

Fig. 3.13 The micro-state of the ensemble is given by a point distribution in $\Re^3$ and on the unit spherical surface. $\mathcal{W}$ and $\mathcal{A}$ are arbitrary subspaces in $\Re^3$ and on the unit spherical surface, respectively.

where $\mathrm{d}\hat{\boldsymbol{u}}$ denotes an infinitesimally small surface element on the unit spherical surface (in spherical coordinates, this surface element is equal to $\sin\Theta\,\mathrm{d}\Theta\,\mathrm{d}\varphi$). The time rate of change of the number of points in $\mathcal{W}$ and $\mathcal{A}$ is thus given by

$$\frac{\mathrm{d}N(t)}{\mathrm{d}t} = \int_{\mathcal{W}} \mathrm{d}\boldsymbol{r} \int_{\mathcal{A}} \mathrm{d}\hat{\boldsymbol{u}}\, \frac{\partial}{\partial t} P(\boldsymbol{r}, \hat{\boldsymbol{u}}, t) \tag{3.149}$$

The rate of change of the number of points is related to the inward and outward fluxes of points through the boundaries $\partial\mathcal{W}$ and $\partial\mathcal{A}$ of $\mathcal{W}$ and $\mathcal{A}$, respectively.

Consider first the flux through $\partial\mathcal{W}$. Let $\boldsymbol{v}$ denote the translational velocity of the center of mass of the rod. The only component of $\boldsymbol{v}$ that contributes to inward or outward flux through $\partial\mathcal{W}$ is the component that is perpendicular to $\mathcal{W}$: when $\boldsymbol{v}$ is locally parallel to $\partial\mathcal{W}$, there is no local inward or outward flux contribution. The component of $\boldsymbol{v}$ that is perpendicular to $\partial\mathcal{W}$ is equal to $\hat{\boldsymbol{n}}\cdot\boldsymbol{v}$, where $\hat{\boldsymbol{n}}$ is the unit normal (which is chosen to be directed outward of $\mathcal{W}$). The local contribution to the rate of change of the number of points in $\mathcal{W}$ is equal to the local density of points $P(\boldsymbol{r}, \hat{\boldsymbol{u}}, t)$, multiplied by the perpendicular component $\hat{\boldsymbol{n}} \cdot \boldsymbol{v}$ of $\boldsymbol{v}$. The total rate of change $\mathrm{d}N_{\mathcal{W}}(t)/\mathrm{d}t$ of the number of points due to the inward and outward fluxes through $\partial\mathcal{W}$ is thus equal to (with $\mathrm{d}\boldsymbol{S} = \hat{\boldsymbol{n}}\,\mathrm{d}S$, where $\mathrm{d}S$ is an infinitesimally small surface element on $\partial\mathcal{W}$; see Fig. 3.14a)

$$\frac{\mathrm{d}N_{\mathcal{W}}(t)}{\mathrm{d}t} = -\oint_{\partial\mathcal{W}} \mathrm{d}\boldsymbol{S} \cdot \int_{\mathcal{A}} \mathrm{d}\hat{\boldsymbol{u}}\, [\boldsymbol{v} P(\boldsymbol{r}, \hat{\boldsymbol{u}}, t)] \tag{3.150}$$

The minus sign here is due to the fact that the direction of $\hat{\boldsymbol{n}}$ is pointing outward of $\mathcal{W}$: when $\boldsymbol{v} \sim \hat{\boldsymbol{n}}$, so that $\hat{\boldsymbol{n}} \cdot \boldsymbol{v} > 0$, the number of points in $\mathcal{W}$

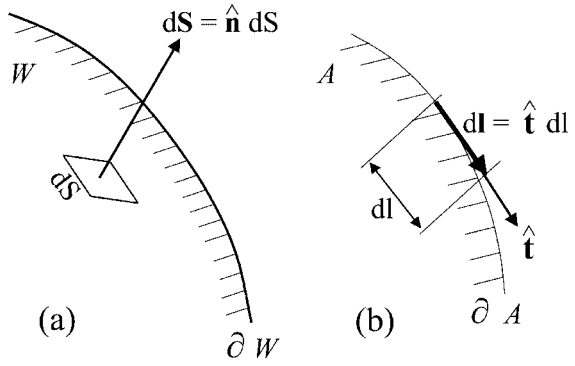

Fig. 3.14 (a) Part of the boundary $\partial\mathcal{W}$ and (b) part of the boundary $\partial\mathcal{A}$. For an explanation of the symbols in this figure, see the main text.

decreases in time. Applying *Gauss's integral theorem* it is found that

$$\frac{\mathrm{d}N_{\mathcal{W}}(t)}{\mathrm{d}t} = -\int_{\mathcal{W}} \mathrm{d}\boldsymbol{r} \int_{\mathcal{A}} \mathrm{d}\hat{\boldsymbol{u}}\, \nabla \cdot [\boldsymbol{v} P(\boldsymbol{r}, \hat{\boldsymbol{u}}, t)] \tag{3.151}$$

Next consider the contribution $\mathrm{d}N_{\mathcal{A}}(t)/\mathrm{d}t$ of the rate of change due to inward and outward fluxes through the boundary $\partial\mathcal{A}$ of $\mathcal{A}$. This boundary is a closed curve on the unit spherical surface. Since $\hat{\boldsymbol{u}}$ is always perpendicular to the unit spherical surface, the vector that is locally perpendicular to $\partial\mathcal{A}$ is equal to $\mathrm{d}\boldsymbol{l} \times \hat{\boldsymbol{u}}$, where $\mathrm{d}\boldsymbol{l}$ is the infinitesimally small vector that is locally tangential to the curve $\partial\mathcal{A}$ (see Fig. 3.14b). The component of the velocity $\mathrm{d}\hat{\boldsymbol{u}}/\mathrm{d}t$ that is perpendicular to $\partial\mathcal{A}$ is thus equal to $(\mathrm{d}\boldsymbol{l} \times \hat{\boldsymbol{u}}) \cdot \mathrm{d}\hat{\boldsymbol{u}}/\mathrm{d}t$, which is the component that determines the inward and outward fluxes. Since this is equal to $\mathrm{d}\boldsymbol{l} \cdot (\hat{\boldsymbol{u}} \times \mathrm{d}\hat{\boldsymbol{u}}/\mathrm{d}t)$, the total rate of change $\mathrm{d}N_{\mathcal{A}}(t)/\mathrm{d}t$ of the number of points in $\mathcal{A}$ is thus equal to

$$\frac{\mathrm{d}N_{\mathcal{A}}(t)}{\mathrm{d}t} = -\int_{\mathcal{W}} \mathrm{d}\boldsymbol{r} \oint_{\partial\mathcal{A}} \mathrm{d}\boldsymbol{l} \cdot \left(\hat{\boldsymbol{u}} \times \frac{\mathrm{d}\hat{\boldsymbol{u}}}{\mathrm{d}t}\right) P(\boldsymbol{r}, \hat{\boldsymbol{u}}, t) \tag{3.152}$$

Applying *Stokes's integral theorem*, it is found that

$$\frac{\mathrm{d}N_{\mathcal{A}}(t)}{\mathrm{d}t} = -\int_{\mathcal{W}} \mathrm{d}\boldsymbol{r} \int_{\mathcal{A}} \mathrm{d}\hat{\boldsymbol{u}}\, \hat{\boldsymbol{u}} \cdot \left[\nabla_{\hat{\boldsymbol{u}}} \times \left(\hat{\boldsymbol{u}} \times \frac{\mathrm{d}\hat{\boldsymbol{u}}}{\mathrm{d}t}\right) P(\boldsymbol{r}, \hat{\boldsymbol{u}}, t)\right] \tag{3.153}$$

where $\nabla_{\hat{\boldsymbol{u}}}$ is the gradient operator with respect to the Cartesian components of $\hat{\boldsymbol{u}}$. Using Eq. (3.88) for the angular velocity, and using the fact that $\hat{\boldsymbol{u}} \cdot \nabla_{\hat{\boldsymbol{u}}} \times (\cdots) = (\hat{\boldsymbol{u}} \times \nabla_{\hat{\boldsymbol{u}}}) \cdot (\cdots)$, Eq. (3.153) can be rewritten as

$$\frac{\mathrm{d}N_{\mathcal{A}}(t)}{\mathrm{d}t} = -\int_{\mathcal{W}} \int_{\mathcal{A}} \mathrm{d}\hat{\boldsymbol{u}}\, (\hat{\boldsymbol{u}} \times \nabla_{\hat{\boldsymbol{u}}}) \cdot [\boldsymbol{\Omega} P(\boldsymbol{r}, \hat{\boldsymbol{u}}, t)] \tag{3.154}$$

Combining Eqs. (3.151) and (3.154) we thus find that

$$\begin{aligned}\frac{\mathrm{d}N(t)}{\mathrm{d}t} &= \frac{\mathrm{d}N_{\mathcal{A}}(t)}{\mathrm{d}t} + \frac{\mathrm{d}N_{\mathcal{W}}(t)}{\mathrm{d}t} \\ &= -\int_{\mathcal{W}} \mathrm{d}\boldsymbol{r} \int_{\mathcal{A}} \mathrm{d}\hat{\boldsymbol{u}} \left\{ \nabla \cdot [\boldsymbol{v} P(\boldsymbol{r}, \hat{\boldsymbol{u}}, t)] + \hat{\mathcal{R}} \cdot [\boldsymbol{\Omega} P(\boldsymbol{r}, \hat{\boldsymbol{u}}, t)] \right\} \end{aligned} \tag{3.155}$$

where the *rotation operator* $\hat{\mathcal{R}}$ is introduced for convenience as

$$\hat{\mathcal{R}}(\cdots) = \hat{\boldsymbol{u}} \times \nabla_{\hat{\boldsymbol{u}}}(\cdots) \tag{3.156}$$

The differentiation with respect to $\hat{\boldsymbol{u}}$ should be taken at constant length of $\hat{\boldsymbol{u}}$. Fortunately, the outer product with $\hat{\boldsymbol{u}}$ eliminates the component along $\hat{\boldsymbol{u}}$ of $\nabla_{\hat{\boldsymbol{u}}}$. Hence, the differentiation in Eq. (3.156) can be done with respect to the unconstrained Cartesian coordinates of $\hat{\boldsymbol{u}}$. Note the similarity between the translational and rotational contributions to the rate of change: instead of the translational velocity $\boldsymbol{v}$, the angular velocity $\boldsymbol{\Omega}$ appears in the rotational contribution; and instead of the gradient operator ∇, the rotation operator $\hat{\mathcal{R}}$ appears. From Eqs. (3.149) and (3.155) it is now found that

$$\int_{\mathcal{W}} \mathrm{d}\boldsymbol{r} \int_{\mathcal{A}} \mathrm{d}\hat{\boldsymbol{u}} \left\{ \frac{\partial}{\partial t} P(\boldsymbol{r}, \hat{\boldsymbol{u}}, t) + \nabla \cdot [\boldsymbol{v} P(\boldsymbol{r}, \hat{\boldsymbol{u}}, t)] + \hat{\mathcal{R}} \cdot [\boldsymbol{\Omega} P(\boldsymbol{r}, \hat{\boldsymbol{u}}, t)] \right\} = 0 \tag{3.157}$$

Since this holds for arbitrary volumes $\mathcal{W}$ and surface areas $\mathcal{A}$, the integrand must be equal to 0. Hence,

$$\frac{\partial}{\partial t} P(\boldsymbol{r}, \hat{\boldsymbol{u}}, t) = -\nabla \cdot [\boldsymbol{v} P(\boldsymbol{r}, \hat{\boldsymbol{u}}, t)] - \hat{\mathcal{R}} \cdot [\boldsymbol{\Omega} P(\boldsymbol{r}, \hat{\boldsymbol{u}}, t)] \tag{3.158}$$

Here, we have considered a system that contained just a single rod. For a suspension that contains N rods, instead of just $\{\boldsymbol{r}, \hat{\boldsymbol{u}}\}$, the relevant phase-space coordinates are

$$\{\boldsymbol{r}_1, \boldsymbol{r}_2, \ldots, \boldsymbol{r}_N, \hat{\boldsymbol{u}}_1, \hat{\boldsymbol{u}}_2, \ldots, \hat{\boldsymbol{u}}_N\}$$

where $\boldsymbol{r}_j$ is the position of the jth rod, and $\hat{\boldsymbol{u}}_j$ its orientation. The equation of motion for the probability density function P of these phase-space coordinates is found from Eq. (3.158) by simply adding the inward and outward fluxes over all rods:

$$\frac{\partial}{\partial t} P(\boldsymbol{r}_1, \ldots, \boldsymbol{r}_N, \hat{\boldsymbol{u}}_1, \ldots, \hat{\boldsymbol{u}}_N, t) = -\sum_{j=1}^{N} \{ \nabla_j \cdot [\boldsymbol{v}_j P] + \hat{\mathcal{R}}_j \cdot [\boldsymbol{\Omega}_j P] \} \tag{3.159}$$

The full phase-space coordinate dependence of P is not denoted here on the right-hand side for brevity. Here, $\hat{\mathcal{R}}_j$ is defined as in Eq. (3.156), with $\hat{\boldsymbol{u}}$ replaced by $\hat{\boldsymbol{u}}_j$. This is an exact result, since it merely expresses the conservation of the number of rods.

As a last step, the translational and rotational velocities have to be expressed in terms of functions of the phase-space coordinates. In doing so, we shall neglect hydrodynamic interactions between the rods. The reason for this neglect is two-fold. First of all, as will be seen later, the volume fractions of interest scale as D/L (with D the thickness and L the length of the rods). That is, the volume fraction where the isotropic–nematic phase transition occurs scales as D/L. For the study of dynamics in the isotropic phase and the isotropic–nematic phase transition, the volume fractions are thus very low. This implies that on average two arbitrary surface elements of distinct rods are very far apart. Therefore, hydrodynamic interactions are probably much less important than for suspensions of spherical particles. Secondly, the precise form of the hydrodynamic interaction functions for rods is unknown, even on the two-body level.

The key relation to express the velocities in terms of phase functions is the force balance equation. As seen above, the translational and angular momentum coordinates are relaxed to equilibrium with the heat bath of solvent molecules on the Brownian time scale, so that the total force (and torque) on each Brownian particle is zero. There are three non-inertial forces (and torques) working on each rod: the hydrodynamic force $\boldsymbol{F}_j^{\mathrm{h}}$ (torque $\boldsymbol{T}_j^{\mathrm{h}}$) that the solvent exerts on the rod, the direct interaction force $\boldsymbol{F}_j^{\mathrm{I}}$ (torque $\boldsymbol{T}_j^{\mathrm{I}}$), and the Brownian force $\boldsymbol{F}_j^{\mathrm{Br}}$ (torque $\boldsymbol{T}_j^{\mathrm{Br}}$), which will be discussed and specified later. Hence,

$$\begin{aligned} \text{total force} = \boldsymbol{0} &= \boldsymbol{F}_j^{\mathrm{h}} + \boldsymbol{F}_j^{\mathrm{I}} + \boldsymbol{F}_j^{\mathrm{Br}} \\ \text{total torque} = \boldsymbol{0} &= \boldsymbol{T}_j^{\mathrm{h}} + \boldsymbol{T}_j^{\mathrm{I}} + \boldsymbol{T}_j^{\mathrm{Br}} \end{aligned} \tag{3.160}$$

The direct force is minus the gradient of the total potential energy Φ of the assembly of Brownian particles,

$$\boldsymbol{F}_j^{\mathrm{I}} = -\nabla_j \Phi(\boldsymbol{r}_1, \ldots, \boldsymbol{r}_N, \hat{\boldsymbol{u}}_1, \ldots, \hat{\boldsymbol{u}}_N) \tag{3.161}$$

while the direct torque is related to Φ as

$$\boldsymbol{T}_j^{\mathrm{I}} = -\hat{\mathcal{R}}_j \Phi \tag{3.162}$$

With the neglect of hydrodynamic interactions, the hydrodynamic torque and force are just the friction forces of a single rod with the solvent. This friction force is equal to (see Eq. 3.44)

$$\boldsymbol{F}_j^{\mathrm{h}} = (\gamma_{\parallel}\hat{\boldsymbol{u}}\hat{\boldsymbol{u}} + \gamma_{\perp}[\hat{\boldsymbol{I}} - \hat{\boldsymbol{u}}\hat{\boldsymbol{u}}]) \cdot (\boldsymbol{v}_{\mathrm{c}} - \boldsymbol{G} \cdot \boldsymbol{r}_{\mathrm{c}}) \tag{3.163}$$

The torque due to friction with the solvent is equal to (see Eq. 3.48)

$$\boldsymbol{\mathcal{T}}_j^{\mathrm{h}} = -\gamma_{\mathrm{r}}[\boldsymbol{\Omega}_j - \hat{\boldsymbol{u}}_j \times \boldsymbol{G} \cdot \hat{\boldsymbol{u}}_j] \tag{3.164}$$

As discussed before, in the case of simple shear flow, the second term in the square brackets is **0** when the rod's orientation is along the flow direction. To describe the Jeffery orbits of non-Brownian rods correctly, we therefore had to add the small torque that acts on rods with such an orientation (see Eq. 3.55). For Brownian rods this small torque is irrelevant, since rods oriented parallel to the flow direction will attain other orientations due to Brownian motion before the mentioned small torque becomes active.

The translational velocity can be found from Eqs. (3.160) and (3.163) as

$$\boldsymbol{v}_j = (D_{\parallel}\hat{\boldsymbol{u}}_j\hat{\boldsymbol{u}}_j + D_{\perp}[\hat{\boldsymbol{I}} - \hat{\boldsymbol{u}}_j\hat{\boldsymbol{u}}_j]) \cdot (-\beta\nabla_j\Phi + \beta\boldsymbol{F}_j^{\mathrm{Br}}) + \dot{\gamma}\hat{\boldsymbol{G}} \cdot \boldsymbol{r}_j \tag{3.165}$$

while the rotational velocity is found from Eqs. (3.160) and (3.164) as

$$\boldsymbol{\Omega}_j = D_{\mathrm{r}}(-\beta\hat{\mathcal{R}}_j\Phi + \beta\boldsymbol{T}_j^{\mathrm{Br}}) + \dot{\gamma}\hat{\boldsymbol{u}}_j \times (\hat{\boldsymbol{G}} \cdot \hat{\boldsymbol{u}}_j) \tag{3.166}$$

Here, $\hat{\boldsymbol{G}} = \boldsymbol{G}/\dot{\gamma}$ is the "normalized" velocity-gradient tensor,

$$D_{\parallel} = k_{\mathrm{B}}T/\gamma_{\parallel} \quad \text{and} \quad D_{\perp} = k_{\mathrm{B}}T/\gamma_{\perp} \tag{3.167}$$

are the translational diffusion coefficients for motion parallel and perpendicular to the long axis of the rods, respectively, and

$$D_{\mathrm{r}} = k_{\mathrm{B}}T/\gamma_{\mathrm{r}} \tag{3.168}$$

is the *rotational diffusion coefficient*. These diffusion coefficients depend on the length L and thickness D of the rod, and the shear viscosity η_0 of the solvent (see Eqs. 3.40, 3.42, and 3.49):

$$\begin{aligned} D_{\mathrm{r}} &= \frac{3k_{\mathrm{B}}T\ln(L/D)}{\pi\eta_0 L^3} \\ D_{\parallel} &= \frac{k_{\mathrm{B}}T\ln(L/D)}{2\pi\eta_0 L} \\ D_{\perp} &= \tfrac{1}{2}D_{\parallel} \end{aligned} \tag{3.169}$$

Note that, due to the last two equations here, Eq. (3.165) can be rewritten as

$$\boldsymbol{v}_j = \tfrac{3}{4}\bar{D}[\hat{\boldsymbol{I}} + \hat{\boldsymbol{u}}_j\hat{\boldsymbol{u}}_j] \cdot \{-\beta\nabla_j\Phi + \beta\boldsymbol{F}_j^{\mathrm{Br}}\} + \dot{\gamma}\hat{\boldsymbol{G}} \cdot \boldsymbol{r}_j \tag{3.170}$$

where the *translational diffusion coefficient* $\bar{D}$ is equal to

$$\bar{D} = \tfrac{1}{3}[D_\parallel + 2D_\perp] = \tfrac{4}{3}D_\perp = \tfrac{2}{3}D_\parallel = \frac{k_{\mathrm{B}}T\ln(L/D)}{3\pi\eta_0 L} \tag{3.171}$$

The reason for referring to D_{r} and $\bar{D}$ as "diffusion coefficients" will become clear in the following section, where diffusion of non-interacting rods is considered. The above expressions for diffusion coefficients are valid for very long and thin rods. For shorter rods, corrections to these limiting expressions are given by de la Torre and Bloomfield (1981).

We still have to express the Brownian contributions to the total force and torque in terms of phase functions. This is achieved as follows. In the absence of flow, for infinite time $t \to \infty$, when the suspension attains equilibrium, the probability density function P is proportional to the Boltzmann exponential $\exp(-\beta\Phi)$, and $\partial P/\partial t = 0$. From the long-time limit of Eq. (3.159), together with Eqs. (3.166) and (3.170) in the absence of shear flow, it follows that

$$\begin{aligned} \boldsymbol{F}_j^{\mathrm{Br}} &= -k_{\mathrm{B}}T\nabla_j \ln(P) \\ \boldsymbol{T}_j^{\mathrm{Br}} &= -k_{\mathrm{B}}T\hat{\mathcal{R}}_j \ln(P) \end{aligned} \tag{3.172}$$

These Brownian contributions to the total force and torque are the result of the fact that the force balance equations (3.160) are only valid on the diffusive time scale. On such a coarsened time scale, not only the purely microscopic forces $\boldsymbol{F}_j^{\mathrm{h}}$ and $\boldsymbol{F}_j^{\mathrm{I}}$ (and the corresponding torques) act on the colloidal particles. The additional Brownian force (and torque) arises from interactions of the colloidal particle with the solvent molecules, averaged with respect to the equilibrium probability density function for the phase-space coordinates of the fluid molecules in the external field imposed by the colloidal particles with prescribed positions and orientations. Even in a very dilute system of colloidal particles (an "ideal gas"), where interactions between the colloidal particles can be neglected, the equilibrium state is one where the macroscopic density is constant, independent of position. The forces that drive such an ideal gas to the homogeneous state are the Brownian forces.

In this way the following equation of motion for the probability density function P of the phase-space coordinates $\{\boldsymbol{r}_1, \ldots, \boldsymbol{r}_N, \hat{\boldsymbol{u}}_1, \ldots, \hat{\boldsymbol{u}}_N\}$ is obtained:

$$\frac{\partial P}{\partial t} = \sum_{j=1}^{N} \left\{ \tfrac{3}{4}\bar{D}\nabla_j \cdot (\hat{\boldsymbol{I}} + \hat{\boldsymbol{u}}_j\hat{\boldsymbol{u}}_j) \cdot [\nabla_j P + \beta P \nabla_j \Phi] - \dot{\gamma}\nabla_j \cdot [P\hat{\boldsymbol{G}} \cdot \boldsymbol{r}_j] \right.$$

$$\left. + D_{\mathrm{r}}\hat{\mathcal{R}}_j \cdot [\hat{\mathcal{R}}_j P + \beta P \hat{\mathcal{R}}_j \Phi] - \dot{\gamma}\hat{\mathcal{R}}_j \cdot [P\hat{\boldsymbol{u}}_j \times (\hat{\boldsymbol{G}} \cdot \hat{\boldsymbol{u}}_j)] \right\} \qquad (3.173)$$

This is the *Smoluchowski equation* for very long and thin, rigid rods, where hydrodynamic interactions are neglected.

An alternative, perhaps more satisfying, derivation of the Smoluchowski equation is to start from the Liouville equation for a binary mixture: solvent molecules and colloidal particles. The Smoluchowski equation is then found after integrating over the fast phase-space variables (the phase-space coordinates of the solvent molecules and the momentum coordinates of the colloidal particles). Such an approach has been taken, for spherical colloids, by Deutch and Oppenheim (1971) and Murphy and Aquirre (1972). The Smoluchowski equation for spherical particles has been used as a starting point to derive the Smoluchowski equation for rods by Erpenbeck and Kirkwood (1963).

3.7.2
Translational and Rotational Diffusion of Non-Interacting Rods Without Shear Flow

Consider the mean square center-of-mass displacement of a freely diffusing rod. Its position at time $t = 0$ will be chosen at the origin: $\boldsymbol{r}(t{=}0) = \boldsymbol{0}$. Free diffusion occurs in suspensions where the concentration of colloidal particles is so small that, on average, rods do not notice each other. In that case, the interaction potential in the Smoluchowski equation (3.173) may be neglected ($\Phi = 0$), and N can be taken equal to 1, resulting in

$$\frac{\partial}{\partial t}P(\boldsymbol{r}, \hat{\boldsymbol{u}}, t) = \tfrac{3}{4}\bar{D}\nabla \cdot [\hat{\boldsymbol{I}} + \hat{\boldsymbol{u}}\hat{\boldsymbol{u}}] \cdot \nabla P + D_{\mathrm{r}}\hat{\mathcal{R}}^2 P \qquad (3.174)$$

where $\hat{\mathcal{R}}^2 = \hat{\mathcal{R}} \cdot \hat{\mathcal{R}}$. For the highly dilute systems under consideration, each orientation has equal probability, $P(\boldsymbol{r}, \hat{\boldsymbol{u}}, t)$ is independent of $\hat{\boldsymbol{u}}$, and is simply proportional to $P(\boldsymbol{r}, t)$. Equation (3.174) thus reduces to

$$\frac{\partial}{\partial t}P(\boldsymbol{r}, t) = \tfrac{3}{4}\bar{D}\nabla \cdot [\hat{\boldsymbol{I}} + \hat{\boldsymbol{u}}\hat{\boldsymbol{u}}] \cdot \nabla P(\boldsymbol{r}, t) \qquad (3.175)$$

Integration of both sides with respect to $\hat{\boldsymbol{u}}$, using the fact that[1)]

$$\oint \mathrm{d}\hat{\boldsymbol{u}}\, [\hat{\boldsymbol{I}} + \hat{\boldsymbol{u}}\hat{\boldsymbol{u}}] = \tfrac{4}{3}\hat{\boldsymbol{I}}$$

1) The integral $\oint \mathrm{d}\hat{\boldsymbol{u}}\, (\cdots)$ stands for integration over the unit spherical surface. In terms of the angular spherical coordinates Θ and φ of $\hat{\boldsymbol{u}}$, this integral is $\int_0^{\pi} \mathrm{d}\Theta \int_0^{2\pi} \mathrm{d}\varphi\, \sin\Theta\, (\cdots)$.

thus leads to

$$\frac{\partial}{\partial t}P(\boldsymbol{r},t) = \bar{D}\nabla^2 P(\boldsymbol{r},t) \tag{3.176}$$

The equation of motion for the dyadic product $\langle \boldsymbol{r}(t)\boldsymbol{r}(t)\rangle$ is obtained by multiplying both sides with $\boldsymbol{r}\,\boldsymbol{r}$ and integrating:

$$\frac{\mathrm{d}}{\mathrm{d}t}\int \mathrm{d}\boldsymbol{r}\,\boldsymbol{r}\boldsymbol{r}\,P(\boldsymbol{r},t) \equiv \frac{\mathrm{d}}{\mathrm{d}t}\langle \boldsymbol{r}(t)\boldsymbol{r}(t)\rangle = \bar{D}\int \mathrm{d}\boldsymbol{r}\,\boldsymbol{r}\boldsymbol{r}\,\nabla^2 P(\boldsymbol{r},t)$$

$$= \bar{D}\int \mathrm{d}\boldsymbol{r}\,P(\boldsymbol{r},t)\nabla^2\boldsymbol{r}\boldsymbol{r} = 2\bar{D}\,\hat{\boldsymbol{I}}$$

where Gauss's integral theorem has been used twice in the second line. Since $\langle \boldsymbol{r}(t{=}0)\boldsymbol{r}(t{=}0)\rangle = \boldsymbol{0}$, time integration immediately leads to

$$\langle \boldsymbol{r}(t)\boldsymbol{r}(t)\rangle = 2\bar{D}t\,\hat{\boldsymbol{I}}$$

and hence

$$W(t) \equiv \langle r^2(t)\rangle = 6\bar{D}t \tag{3.177}$$

in accordance with the result (3.130) as obtained from the Langevin equation. Note that, on taking the trace of the dyadic product, each spatial dimension (three in this case) gives rise to a factor 2 on the right-hand side in the mean square displacement in Eq. (3.177). Diffusion in two dimensions gives a prefactor of 4 instead of 6, in accordance with the result in Eq. (3.147) for short-time rotational diffusion.

Let us now consider the time dependence of the orientation $\langle \hat{\boldsymbol{u}}(t)\rangle$, given that $\hat{\boldsymbol{u}}(t{=}0) = \hat{\boldsymbol{u}}(0)$. For a homogeneous system, $P(\boldsymbol{r},\hat{\boldsymbol{u}},t)$ is independent of $\boldsymbol{r}$, so that Eq. (3.174) reduces to

$$\frac{\partial}{\partial t}P(\hat{\boldsymbol{u}},t) = D_\mathrm{r}\hat{\mathcal{R}}^2 P(\hat{\boldsymbol{u}},t) \tag{3.178}$$

Multiplying both sides with $\hat{\boldsymbol{u}}$ and integrating over the unit spherical surface gives

$$\frac{\mathrm{d}}{\mathrm{d}t}\langle \hat{\boldsymbol{u}}(t)\rangle = D_\mathrm{r}\oint \mathrm{d}\hat{\boldsymbol{u}}\,\hat{\boldsymbol{u}}\hat{\mathcal{R}}^2 P(\hat{\boldsymbol{u}},t)$$

From Stokes's integral theorem it follows that, for any two (well-behaved) functions f and g of $\hat{\boldsymbol{u}}$,

$$\oint \mathrm{d}\hat{\boldsymbol{u}}\,f(\hat{\boldsymbol{u}})\hat{\mathcal{R}}g(\hat{\boldsymbol{u}}) = -\oint \mathrm{d}\hat{\boldsymbol{u}}\,g(\hat{\boldsymbol{u}})\hat{\mathcal{R}}f(\hat{\boldsymbol{u}}) \tag{3.179}$$

Applying this result twice leads to

$$\oint \mathrm{d}\hat{\boldsymbol{u}}\, \hat{\boldsymbol{u}}\hat{\mathcal{R}}^2 P(\hat{\boldsymbol{u}},t) = \oint \mathrm{d}\hat{\boldsymbol{u}}\, P(\hat{\boldsymbol{u}},t)\hat{\mathcal{R}}^2\hat{\boldsymbol{u}} = -2\langle\hat{\boldsymbol{u}}(t)\rangle$$

where it is used that $\hat{\mathcal{R}}^2\hat{\boldsymbol{u}} = -2\hat{\boldsymbol{u}}$. The equation of motion we were after thus reads

$$\frac{\mathrm{d}}{\mathrm{d}t}\langle\hat{\boldsymbol{u}}(t)\rangle = -2D_\mathrm{r}\langle\hat{\boldsymbol{u}}(t)\rangle$$

the solution of which is

$$\langle\hat{\boldsymbol{u}}(t)\rangle = \exp(-2D_\mathrm{r}t)\hat{\boldsymbol{u}}(0) \tag{3.180}$$

in accordance with Eqs. (3.133) and (3.146) as obtained from the Langevin equation. As discussed in Section 3.6.2 on the Langevin-equation approach, for small times where $D_\mathrm{r}t \ll 1$, this result can be interpreted as translational diffusion of the tip of $\hat{\boldsymbol{u}}$ on a two-dimensional surface.

3.8 The Orientational Order Parameter

At higher concentrations, where interactions between rods are important, a transition from an isotropic distribution of orientations to an orientationally ordered nematic state can occur (as will be discussed in more detail later). Orientational order is also induced by shear flow in otherwise isotropic suspensions. For such ordered states the degree of orientational order varies, depending on the concentration of rods and the shear rate. In the present section the so-called *orientational order parameter* will be defined, which measures the degree of orientational order.

The preferred orientation $\hat{\boldsymbol{n}}$ of the rods is referred to as the *director*. The simplest measure for the degree of orientation that comes to mind is $\langle\cos\Theta\rangle = \langle\hat{\boldsymbol{u}}\rangle\cdot\hat{\boldsymbol{n}}$, where Θ is the angle between the orientation $\hat{\boldsymbol{u}}$ of a given rod and the director $\hat{\boldsymbol{n}}$ (see Fig. 3.15). However, due to symmetry, orientation $+\hat{\boldsymbol{u}}$ is as equally likely to occur as orientation $-\hat{\boldsymbol{u}}$, so that $\langle\hat{\boldsymbol{u}}\rangle = \boldsymbol{0}$. The next simplest measure[2)] would then be $\langle\cos^2\Theta\rangle = \langle\hat{\boldsymbol{u}}\hat{\boldsymbol{u}}\rangle : \hat{\boldsymbol{n}}\hat{\boldsymbol{n}}$. Hence, the simplest quantity that characterizes the orientational state is the so-called *orientational order-parameter tensor*,

2) Here the contraction symbol ":" stands for summation over two adjacent indices; that is, for two tensors $\boldsymbol{A}$ and $\boldsymbol{B}$, by definition, $\boldsymbol{A} : \boldsymbol{B} = \sum_{n,m} A_{nm}B_{mn}$.

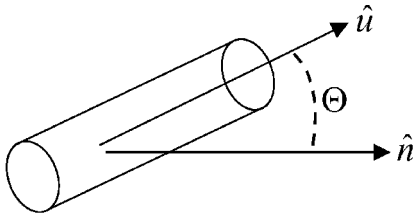

Fig. 3.15 Definition of the angle Θ between the orientation $\hat{\boldsymbol{u}}$ of a rod and the director $\hat{\boldsymbol{n}}$.

$$\boldsymbol{S} \equiv \langle \hat{\boldsymbol{u}}\hat{\boldsymbol{u}} \rangle \equiv \oint \mathrm{d}\hat{\boldsymbol{u}}\, \hat{\boldsymbol{u}}\hat{\boldsymbol{u}}\, P(\hat{\boldsymbol{u}}) \tag{3.181}$$

where the integration ranges over the unit spherical surface (see footnote 1). Furthermore, $P(\hat{\boldsymbol{u}})$ is the probability density function (PDF) for the orientation $\hat{\boldsymbol{u}}$ of a rod, which can in principle be obtained from the solution of the N-particle Smoluchowski equation (Eq. 3.173), noting that

$$P(\hat{\boldsymbol{u}}) = \int \mathrm{d}\boldsymbol{r}_1 \cdots \int \mathrm{d}\boldsymbol{r}_N \oint \mathrm{d}\hat{\boldsymbol{u}}_2 \cdots \oint \mathrm{d}\hat{\boldsymbol{u}}_N\, P(\boldsymbol{r}_1, \ldots, \boldsymbol{r}_N, \hat{\boldsymbol{u}}, \hat{\boldsymbol{u}}_2, \ldots, \hat{\boldsymbol{u}}_N) \tag{3.182}$$

The PDF of $\hat{\boldsymbol{u}}$ can be time-dependent, in which case orientational dynamics can be studied.

What information can be distilled from a specified $\boldsymbol{S}$? To answer this question, let $\hat{\boldsymbol{e}}$ be a unit vector, and let φ denote the angle between the orientation $\hat{\boldsymbol{u}}$ of a given rod and $\hat{\boldsymbol{e}}$. Consider the function

$$f \equiv \langle \cos^2 \varphi \rangle = \boldsymbol{S} : \hat{\boldsymbol{e}}\hat{\boldsymbol{e}} = \sum_{m,n} S_{mn}\hat{e}_m\hat{e}_n \tag{3.183}$$

where S_{nm} is the nmth component of $\boldsymbol{S}$, and $\hat{e}_n$ is the nth component of $\hat{\boldsymbol{e}}$. Since the maximum value of $\cos^2 \varphi$ is attained when $\varphi = 0$, and the most likely direction of $\hat{\boldsymbol{u}}$ is along the director, it is evident that the unit vector $\hat{\boldsymbol{e}}$ that maximizes f is the director. Maximization of f has to be performed under the constraint that $\hat{\boldsymbol{e}}$ is a unit vector, i.e. $\hat{\boldsymbol{e}} \cdot \hat{\boldsymbol{e}} = 1$. According to Lagrange's principle, we therefore have to maximize the function

$$f^* = f - \lambda \hat{\boldsymbol{e}} \cdot \hat{\boldsymbol{e}} = \sum_{mn} (S_{mn} - \lambda \delta_{mn})\hat{e}_m\hat{e}_n \tag{3.184}$$

where λ is the Lagrange multiplier, and δ_{nm} is the Kronecker delta ($\delta_{mn} = 0$ when $m \neq n$, and $\delta_{mn} = 1$ when $m = n$). From $\partial f / \partial \hat{e}_m = 0$ it is easily

found that

$$\boldsymbol{S} \cdot \hat{\boldsymbol{e}} = \lambda \hat{\boldsymbol{e}} \text{ maximizes or minimizes } f^* \tag{3.185}$$

By taking the inner product on both sides it follows that

$$\lambda = \boldsymbol{S} : \hat{\boldsymbol{e}}\hat{\boldsymbol{e}} \text{ when } \hat{\boldsymbol{e}} \text{ maximizes or minimizes } f^* \tag{3.186}$$

We thus find that *the eigenvector of $\boldsymbol{S}$ with the largest eigenvalue is the director $\hat{\boldsymbol{n}}$ and the largest eigenvalue is equal to* $\langle \cos^2 \Theta \rangle = \boldsymbol{S} : \hat{\boldsymbol{n}}\hat{\boldsymbol{n}}$.

According to Eqs. (3.183) and (3.186), the largest eigenvalue of $\boldsymbol{S}$ characterizes the degree of alignment, and is referred to as the *scalar orientational order parameter*. Note that the largest eigenvalue of $\boldsymbol{S}$ is equal to $\frac{1}{3}$ in the isotropic state (since then $\boldsymbol{S} = \frac{1}{3}\hat{\boldsymbol{I}}$), and is equal to 1 for a perfectly aligned state (since then $\boldsymbol{S} = \hat{\boldsymbol{n}}\hat{\boldsymbol{n}}$). A commonly used equivalent measure is the so-called P_2 order parameter, which is defined as

$$P_2 \equiv \langle P_2(\cos\Theta) \rangle = \tfrac{1}{2}[3\langle \cos^2 \Theta \rangle - 1] = \tfrac{1}{2}[3\lambda - 1] \tag{3.187}$$

where $P_2(x)$ is the second-order Legendre polynomial. The reason for introducing this "rescaled" scalar order parameter P_2 is that it is equal to 0 for an isotropic state and equal to 1 for a perfectly aligned state.

When, for a particular nematic suspension, the remaining two smaller eigenvalues are equal, the nematic is referred to as "uniaxial". When they are unequal, the nematic is referred to as "biaxial". For a uniaxial nematic, the projections of the rods onto the plane perpendicular to the director are isotropically distributed, while for a biaxial nematic the orientations of the rods in this projection have a second preferred direction, $\hat{\boldsymbol{n}}'$ (see Fig. 3.16).

Biaxiality of nematic ordering is found, for example, when a suspension of rigid rods is subjected to simple shear flow. A nematic state of cylindrically shaped rods, in the absence of an external field, is expected to be uniaxial.

The procedure to find the order parameter is to calculate the tensor $\boldsymbol{S}$ and determine its eigenvalues. The largest eigenvalue measures the degree of orientational order and the corresponding eigenvector gives the preferred direction of alignment. We shall derive an equation of motion for $\boldsymbol{S}$ from the Smoluchowski equation later in this chapter.

3.9 Non-Interacting Brownian Rods in Shear Flow

In the present section we shall discuss probability density functions (PDFs) and orientational order-parameter matrices for a single Brownian rod sub-

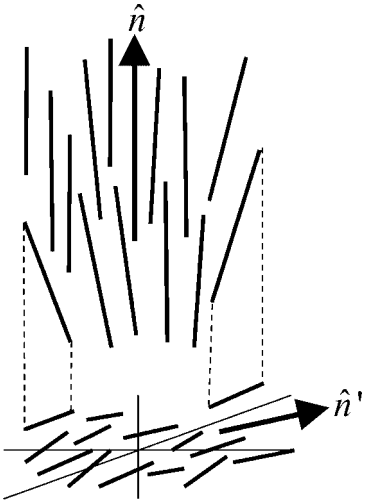

Fig. 3.16 For a biaxial nematic, the projections of the rods onto the plane perpendicular to the director $\hat{\boldsymbol{n}}$ have a preferred orientation $\hat{\boldsymbol{n}}'$ as well. For a uniaxial nematic, the order in this plane is isotropic.

jected to flow. On applying a stationary flow, the orientational PDF of a single rod attains a stationary form. This stationary, time-independent PDF is determined by the interplay of the aligning effect of the flow and isotropy-restoring rotational diffusion.

The stationary form of the Smoluchowski equation (Eq. 3.173) for a single rod reads

$$0 = \hat{\mathcal{R}}^2 P(\hat{\boldsymbol{u}}) - Pe_{\mathrm{r}}\, \hat{\mathcal{R}} \cdot [P(\hat{\boldsymbol{u}})\hat{\boldsymbol{u}} \times (\hat{\boldsymbol{G}} \cdot \hat{\boldsymbol{u}})] \tag{3.188}$$

where the dimensionless parameter Pe_{r} is commonly referred to as the *rotational Peclet number*, which is defined as

$$Pe_{\mathrm{r}} = \dot{\gamma}/D_{\mathrm{r}} \tag{3.189}$$

This Peclet number is a measure of the effect of the shear flow relative to isotropy-restoring rotational diffusion. For small Peclet numbers, rotational diffusion is relatively fast, so that the PDF is only slightly anisotropic.

As explained below Eq. (3.156), the differentiation in $\hat{\mathcal{R}}$ is with respect to the Cartesian coordinates of $\hat{\boldsymbol{u}}$, without the constraint that $\hat{\boldsymbol{u}}$ is a unit vector.

The stationary equation of motion can be solved in closed analytical form when the velocity-gradient tensor $\boldsymbol{G}$ is symmetric (as for elongational flow). This solution is discussed in the next subsection. When the velocity-gradient tensor is not symmetric (as for simple shear flow), the solution cannot be

obtained in a simple closed analytical form, but must be obtained by numerical methods. However, expansion of the orientational PDF for small Peclet numbers is feasible.

3.9.1 Elongational Flow

For pure straining motion, the velocity-gradient tensor $\hat{\boldsymbol{G}}$ is equal to the symmetric tensor $\hat{\boldsymbol{E}}$ in Eq. (3.2). A symmetric velocity-gradient tensor admits a solution of the simpler equation

$$\mathbf{0} = \hat{\mathcal{R}} P(\hat{\boldsymbol{u}}) - Pe_{\mathrm{r}}[P(\hat{\boldsymbol{u}})\hat{\boldsymbol{u}} \times (\hat{\boldsymbol{E}} \cdot \hat{\boldsymbol{u}})] \tag{3.190}$$

where one of the $\hat{\mathcal{R}}$ operators in Eq. (3.188) is removed. Division by $P(\hat{\boldsymbol{u}})$ thus yields

$$\mathbf{0} = \hat{\mathcal{R}} \ln[P(\hat{\boldsymbol{u}})] - Pe_{\mathrm{r}}\hat{\boldsymbol{u}} \times (\hat{\boldsymbol{E}} \cdot \hat{\boldsymbol{u}}) \tag{3.191}$$

From one of the relations in the Appendix (Section 3.16.2), it follows immediately that the solution is given by

$$P(\hat{\boldsymbol{u}}) = \frac{1}{C(Pe_{\mathrm{r}})} \exp[\tfrac{1}{2} Pe_{\mathrm{r}}(\hat{\boldsymbol{u}} \cdot \hat{\boldsymbol{E}} \cdot \hat{\boldsymbol{u}})] \tag{3.192}$$

where C is the Pe_{r}-dependent normalization constant,

$$\begin{aligned} C(Pe_{\mathrm{r}}) &= \oint \mathrm{d}\hat{\boldsymbol{u}} \, \exp[\tfrac{1}{2} Pe_{\mathrm{r}}(\hat{\boldsymbol{u}} \cdot \hat{\boldsymbol{E}} \cdot \hat{\boldsymbol{u}})] \\ &= \int_0^{2\pi} \mathrm{d}\varphi \int_0^{\pi} \mathrm{d}\Theta \, \sin\Theta \, \exp[Pe_{\mathrm{r}} \sin^2\Theta \sin\varphi \cos\varphi] \end{aligned} \tag{3.193}$$

This normalization constant may be determined as a function of Pe_{r} by numerical integration. Alternatively, $C(Pe_{\mathrm{r}})$ may be expanded for small Pe_{r} in a power series in Pe_{r}, or its asymptotic form for large Pe_{r} may be calculated. Taylor expansion of the exponential in Eq. (3.193) with respect to Pe_{r} readily gives

$$C(Pe_{\mathrm{r}}) = 4\pi + \frac{2\pi}{15} Pe_{\mathrm{r}}^2 + \frac{\pi}{630} Pe_{\mathrm{r}}^4 + \mathcal{O}(Pe_{\mathrm{r}}^6) \tag{3.194}$$

For large (positive) Peclet numbers, asymptotic forms for $C(Pe_{\mathrm{r}})$ can be obtained by a saddle-point analysis, which we shall not discuss here. For

intermediate values of Pe_r, the integral in Eq. (3.193) for $C(Pe_r)$ must be evaluated numerically.

The orientational order-parameter tensor can be calculated from the above given forms for the PDF $P(\hat{\boldsymbol{u}})$ and Eq. (3.181), and from that the scalar orientational order parameter P_2 as defined in Eq. (3.187) and the angle χ between the director and the flow direction may be obtained. These are plotted as functions of Pe_r in Fig. 3.17. The solid lines are obtained from numerical integration of Eq. (3.193), while the dotted lines correspond to the limiting analytical results in Eq. (3.194) for small Peclet numbers [including the corresponding expansion of the exponential in Eq. (3.192) for the PDF]. For elongational flow, χ is always equal to $45°$, which is obvious from the flow field as sketched in Fig. 3.1: rods will orient along the extensional axis.

3.9.2 Simple Shear Flow

In the case of pure shearing motion, the velocity-gradient tensor $\hat{\boldsymbol{G}}$ is equal to the tensor $\hat{\boldsymbol{\Gamma}}$ in Eq. (3.1). For such a non-symmetric velocity-gradient tensor, the above method of solution cannot be copied, since the corresponding Eq. (3.190) has no solutions for a non-symmetric tensor $\boldsymbol{G}$.

For small rotational Peclet numbers, the deviation of the PDF from isotropy is small, so that the solution of the stationary equation of motion (3.188) can be expanded as

$$P(\hat{\boldsymbol{u}}) = \frac{1}{4\pi} + Pe_r P_1(\hat{\boldsymbol{u}}) + Pe_r^2 P_2(\hat{\boldsymbol{u}}) + \cdots \tag{3.195}$$

Substitution of this expansion into Eq. (3.188) and equating coefficients of equal powers of Pe_r, one readily finds the following recursive set of differential equations for the as yet unknown functions P_j:

$$\hat{\mathcal{R}}^2 P_j(\hat{\boldsymbol{u}}) = \hat{\mathcal{R}} \cdot [P_{j-1}(\hat{\boldsymbol{u}})\hat{\boldsymbol{u}} \times (\hat{\boldsymbol{\Gamma}} \cdot \hat{\boldsymbol{u}})], \quad j \geq 1 \tag{3.196}$$

where $P_0(\hat{\boldsymbol{u}}) = 1/4\pi$ is the isotropic PDF without shear flow. Normalization requires that

$$\oint \mathrm{d}\hat{\boldsymbol{u}}\, P_j(\hat{\boldsymbol{u}}) = 0, \quad j \geq 1 \tag{3.197}$$

Let us consider the first two corrections from isotropy in the expansion (3.195).

For $j = 1$, using the fact that $P_0(\hat{\boldsymbol{u}}) = 1/4\pi$, Eq. (3.196) reads

$$\hat{\mathcal{R}}^2 P_1(\hat{\boldsymbol{u}}) = \frac{1}{4\pi}\hat{\mathcal{R}} \cdot [\hat{\boldsymbol{u}} \times (\hat{\boldsymbol{\Gamma}} \cdot \hat{\boldsymbol{u}})] = -\frac{3}{4\pi}(\hat{\boldsymbol{u}} \cdot \hat{\boldsymbol{E}} \cdot \hat{\boldsymbol{u}}) \tag{3.198}$$

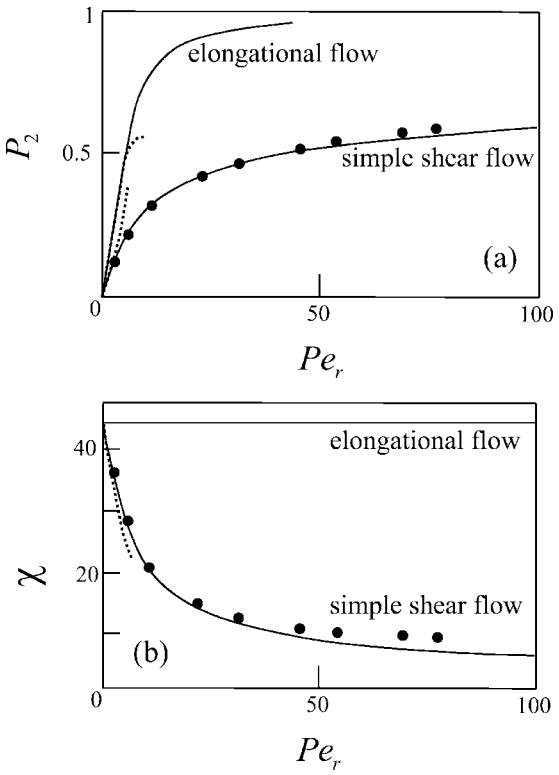

Fig. 3.17 (a) The scalar orientational order parameter $P_2 = \frac{1}{2}[3\lambda - 1]$, with λ the largest eigenvalue of $\boldsymbol{S}$ (see Eq. 3.187) as a function of the rotational Peclet number $Pe_{\mathrm{r}} = \dot{\gamma}/D_{\mathrm{r}}$ for elongational flow and simple shear flow. The solid lines are numerical results, the dotted lines correspond to the limiting analytical solutions (3.194) and (3.202) for elongational and simple shear, respectively, and the data points are computer simulation results by Winkler et al. (2004) and Winkler and Gompper (2004).
(b) The angle χ between the director and the flow direction. The dotted line is the angle that follows from the limiting form (3.202) of the PDF for simple shear flow.

where $\hat{\boldsymbol{E}}$ is the symmetric part of the velocity-gradient tensor $\hat{\boldsymbol{\Gamma}}$, that is, $\hat{\boldsymbol{E}} = \frac{1}{2}(\hat{\boldsymbol{\Gamma}} + \hat{\boldsymbol{\Gamma}}^{\mathrm{T}})$. The above equation follows from the relations given in the Appendix (Section 3.16.2).[3] Using these relations once more immediately leads to

$$P_1(\hat{\boldsymbol{u}}) = \frac{1}{8\pi}(\hat{\boldsymbol{u}} \cdot \hat{\boldsymbol{E}} \cdot \hat{\boldsymbol{u}}) = \frac{1}{8\pi} \sin^2\Theta \sin\varphi \cos\varphi \tag{3.199}$$

3) Note that in the combination $\hat{\boldsymbol{u}} \cdot \boldsymbol{M} \cdot \hat{\boldsymbol{u}}$, one can replace the tensor $\boldsymbol{M}$ by its symmetric part $\frac{1}{2}(\boldsymbol{M} + \boldsymbol{M}^{\mathrm{T}})$, since $\hat{\boldsymbol{u}} \cdot (\boldsymbol{M} - \boldsymbol{M}^{\mathrm{T}}) \cdot \hat{\boldsymbol{u}} = 0$.

Substitution of this solution for P_1 into Eq. (3.196) for $j = 2$ yields

$$\hat{\mathcal{R}}^2 P_2(\hat{\boldsymbol{u}}) = \frac{1}{8\pi}\hat{\mathcal{R}} \cdot [(\hat{\boldsymbol{u}} \cdot \hat{\boldsymbol{E}} \cdot \hat{\boldsymbol{u}})(\hat{\boldsymbol{u}} \times \hat{\boldsymbol{\Gamma}} \cdot \hat{\boldsymbol{u}})]$$

$$= \frac{1}{8\pi}[\hat{u}_2^2 - 5(\hat{\boldsymbol{u}} \cdot \hat{\boldsymbol{E}} \cdot \hat{\boldsymbol{u}})^2] \tag{3.200}$$

From the relations in Section 3.16.2, one readily verifies that

$$\hat{\mathcal{R}}^2(\hat{\boldsymbol{u}} \cdot \hat{\boldsymbol{E}} \cdot \hat{\boldsymbol{u}})^2 = 2\hat{u}_1^2 + 2\hat{u}_2^2 - 20(\hat{\boldsymbol{u}} \cdot \hat{\boldsymbol{E}} \cdot \hat{\boldsymbol{u}})^2$$

The third equation in Section 3.16.2 now shows that the solution to Eq. (3.200) is given by

$$P_2(\hat{\boldsymbol{u}}) = \frac{1}{32\pi}[(\hat{\boldsymbol{u}} \cdot \hat{\boldsymbol{E}} \cdot \hat{\boldsymbol{u}})^2 + \tfrac{1}{3}(\hat{u}_1^2 - \hat{u}_2^2) - \tfrac{1}{15}] \tag{3.201}$$

$$= \frac{1}{32\pi}[\sin^4\Theta \sin^2\varphi \cos^2\varphi + \tfrac{1}{3}\sin^2\Theta(\cos^2\varphi - \sin^2\varphi) - \tfrac{1}{15}]$$

The constant $\frac{1}{15}$ in the square brackets has been subtracted in order that P_2 satisfies the normalization constraint (3.197).

Collecting results, we thus obtain the following small Peclet number expansion (valid up to $\mathcal{O}(Pe_r^3)$):

$$P(\hat{\boldsymbol{u}}) = \frac{1}{4\pi} + Pe_r\frac{1}{8\pi}(\hat{\boldsymbol{u}} \cdot \hat{\boldsymbol{E}} \cdot \hat{\boldsymbol{u}})$$

$$+Pe_r^2\frac{1}{32\pi}[(\hat{\boldsymbol{u}} \cdot \hat{\boldsymbol{E}} \cdot \hat{\boldsymbol{u}})^2 + \tfrac{1}{3}(\hat{u}_1^2 - \hat{u}_2^2) - \tfrac{1}{15}] \tag{3.202}$$

The corresponding scalar orientational order parameter P_2 and the angle χ between the director and the flow direction are plotted in Fig. 3.17, together with the numerical solution of Eq. (3.188). The dotted lines in Fig. 3.17 correspond to asymptotic solutions for small Peclet numbers. The solid lines correspond to numerical solutions of Eqs. (3.188), while the data points are simulation results by Winkler et al. (2004) and Winkler and Gompper (2004). In these simulations, the aspect ratio of the rods is $L/D = 15$, and there is a finite flexibility (the average end-to-end distance is 98% of the contour length). This may be the reason for the small deviations at higher Peclet numbers. For short rods the order parameter is expected to be smaller than for long rods. In Fig. 3.17a, however, the simulation results for the order parameter are slightly above those corresponding to the numerical solution of the Smoluchowski equation. This is an indication of a sensitive dependence of orientational order induced by shear flow on the flexibility of rods.

In contrast to elongational flow, rods subjected to simple shear flow will rotate in the velocity-gradient plane. The orientational order parameter for elongational flow is therefore large compared to that for simple shear flow. For small Peclet numbers, rods in simple shear flow spend most of their time during rotation in a direction where $\chi = 45°$. This is the result of an interplay between the Brownian torque on the rod and the torque that the fluid exerts on the rod. A preferred alignment along the flow direction implies a strongly peaked orientational PDF. In that case the Brownian torque, being equal to $-k_{\mathrm{B}}T\hat{\mathcal{R}}\ln[P(\hat{\boldsymbol{u}})]$, would be very large. The Brownian torque thus tends to diminish the strongly peaked PDF in the flow direction. This competition leads, according to the above analysis, to a preferred alignment along the extensional axis of the shear flow at very small shear rates. For larger Peclet numbers, where the torque that the fluid exerts on the rod is dominant, the angle χ tends to 0, that is, rods are on average aligned along the flow direction.

3.10 The Doi–Edwards Equation of Motion and the Maier–Saupe Potential

In this section we shall derive an equation of motion for the orientational order-parameter tensor $\boldsymbol{S}$ for homogeneous systems of long and thin rods with short-range repulsive interactions subjected to shear flow. This equation of motion is known as the Doi–Edwards equation (Doi and Edwards 1986), and is derived here from the Smoluchowski equation (Eq. 3.173). In such a microscopic derivation, the assumptions under which the Doi–Edwards equation holds will become clear. For the very long and thin rods under consideration here, the stationary equation of motion for the PDF $P(\hat{\boldsymbol{u}})$ for the orientation $\hat{\boldsymbol{u}}$ of a rod, as obtained from the Smoluchowski equation, complies with Onsager's free-energy functional (Onsager 1933; Onsager 1942; Onsager 1949). Expanding the interaction term in the equation of motion with respect to the orientational order parameter leads in a natural way to the Maier–Saupe potential (Maier and Saupe 1958; Maier and Saupe 1959; Maier and Saupe 1960).

3.10.1 Equation of Motion for $\boldsymbol{P(\hat{u}, t)}$

Let us first derive the equation of motion for $P(\hat{\boldsymbol{u}}, t)$. According to Eqs. (3.182) (where P is now time-dependent), such an equation of motion can be obtained from the Smoluchowski equation (Eq. 3.173) by integration with respect to $\boldsymbol{r}_1, \ldots, \boldsymbol{r}_N, \hat{\boldsymbol{u}}_2, \ldots, \hat{\boldsymbol{u}}_N$.

In contrast to elongational flow, rods subjected to simple shear flow will rotate in the velocity-gradient plane. The orientational order parameter for elongational flow is therefore large compared to that for simple shear flow. For small Peclet numbers, rods in simple shear flow spend most of their time during rotation in a direction where $\chi = 45°$. This is the result of an interplay between the Brownian torque on the rod and the torque that the fluid exerts on the rod. A preferred alignment along the flow direction implies a strongly peaked orientational PDF. In that case the Brownian torque, being equal to $-k_{\mathrm{B}}T\hat{\mathcal{R}}\ln[P(\hat{\boldsymbol{u}})]$, would be very large. The Brownian torque thus tends to diminish the strongly peaked PDF in the flow direction. This competition leads, according to the above analysis, to a preferred alignment along the extensional axis of the shear flow at very small shear rates. For larger Peclet numbers, where the torque that the fluid exerts on the rod is dominant, the angle χ tends to 0, that is, rods are on average aligned along the flow direction.

3.10 The Doi–Edwards Equation of Motion and the Maier–Saupe Potential

In this section we shall derive an equation of motion for the orientational order-parameter tensor $\boldsymbol{S}$ for homogeneous systems of long and thin rods with short-range repulsive interactions subjected to shear flow. This equation of motion is known as the Doi–Edwards equation (Doi and Edwards 1986), and is derived here from the Smoluchowski equation (Eq. 3.173). In such a microscopic derivation, the assumptions under which the Doi–Edwards equation holds will become clear. For the very long and thin rods under consideration here, the stationary equation of motion for the PDF $P(\hat{\boldsymbol{u}})$ for the orientation $\hat{\boldsymbol{u}}$ of a rod, as obtained from the Smoluchowski equation, complies with Onsager's free-energy functional (Onsager 1933; Onsager 1942; Onsager 1949). Expanding the interaction term in the equation of motion with respect to the orientational order parameter leads in a natural way to the Maier–Saupe potential (Maier and Saupe 1958; Maier and Saupe 1959; Maier and Saupe 1960).

3.10.1 Equation of Motion for $\boldsymbol{P(\hat{u}, t)}$

Let us first derive the equation of motion for $P(\hat{\boldsymbol{u}}, t)$. According to Eqs. (3.182) (where P is now time-dependent), such an equation of motion can be obtained from the Smoluchowski equation (Eq. 3.173) by integration with respect to $\boldsymbol{r}_1, \ldots, \boldsymbol{r}_N, \hat{\boldsymbol{u}}_2, \ldots, \hat{\boldsymbol{u}}_N$.

Analytical progress can be made by assuming a pairwise additive total potential, that is

$$\Phi(\boldsymbol{r}_1,\ldots,\boldsymbol{r}_N,\hat{\boldsymbol{u}}_1,\ldots,\hat{\boldsymbol{u}}_N)=\sum_{i<j}V(\boldsymbol{r}_i-\boldsymbol{r}_j,\hat{\boldsymbol{u}}_i,\hat{\boldsymbol{u}}_j) \tag{3.203}$$

with V the pair-interaction potential. This is exact for the rods with hard-core interactions (or rods with very short-range repulsive interactions) that we shall consider. According to the integral theorems of Gauss and Stokes, we have, respectively,

$$\int \mathrm{d}\boldsymbol{r}_j\,\nabla_j\cdot(\cdots)=0 \quad \text{and} \quad \oint \mathrm{d}\hat{\boldsymbol{u}}_j\,\hat{\mathcal{R}}_j\cdot(\cdots)=0 \tag{3.204}$$

Using the above relations, integration of both sides of the Smoluchowski equation (Eq. 3.173) with respect to $\boldsymbol{r}_1,\ldots,\boldsymbol{r}_N$ and $\hat{\boldsymbol{u}}_2,\ldots,\hat{\boldsymbol{u}}_N$ leads to (with $\hat{\boldsymbol{u}}=\hat{\boldsymbol{u}}_1$)

$$\begin{aligned}\frac{\partial}{\partial t}P(\hat{\boldsymbol{u}},t)=D_{\mathrm{r}}\hat{\mathcal{R}}\cdot[\hat{\mathcal{R}}P(\hat{\boldsymbol{u}},t)-\beta P(\hat{\boldsymbol{u}},t)\bar{\boldsymbol{T}}(\hat{\boldsymbol{u}},t)]\\ -\hat{\mathcal{R}}\cdot[P(\hat{\boldsymbol{u}},t)\hat{\boldsymbol{u}}\times(\boldsymbol{\Gamma}\cdot\hat{\boldsymbol{u}})]\end{aligned} \tag{3.205}$$

The torque $\bar{\boldsymbol{T}}$ is defined as (with $\boldsymbol{R}=\boldsymbol{r}_1-\boldsymbol{r}_2$ and $\hat{\boldsymbol{u}}'=\hat{\boldsymbol{u}}_2$)

$$\bar{\boldsymbol{T}}(\hat{\boldsymbol{u}},t)=-\bar{\rho}\int \mathrm{d}\boldsymbol{R}\oint \mathrm{d}\hat{\boldsymbol{u}}'\,P(\hat{\boldsymbol{u}}',t)g(\boldsymbol{R},\hat{\boldsymbol{u}},\hat{\boldsymbol{u}}',t)\hat{\mathcal{R}}V(\boldsymbol{R},\hat{\boldsymbol{u}},\hat{\boldsymbol{u}}') \tag{3.206}$$

where $\bar{\rho}=N/V$ is the number density of rods, and where the pair correlation function g is defined as (with $\boldsymbol{r}=\boldsymbol{r}_1$ and $\boldsymbol{r}'=\boldsymbol{r}_2$)

$$\begin{aligned}&P(\boldsymbol{r},\boldsymbol{r}',\hat{\boldsymbol{u}},\hat{\boldsymbol{u}}',t)\\ &\equiv\int \mathrm{d}\boldsymbol{r}_3\cdots\int \mathrm{d}\boldsymbol{r}_N\oint \mathrm{d}\hat{\boldsymbol{u}}_3\cdots\oint \mathrm{d}\hat{\boldsymbol{u}}_N\,P(\boldsymbol{r},\boldsymbol{r}',\boldsymbol{r}_3,\ldots,\boldsymbol{r}_N,\hat{\boldsymbol{u}},\hat{\boldsymbol{u}}',\hat{\boldsymbol{u}}_3,\ldots,\hat{\boldsymbol{u}}_N,t)\\ &\equiv\frac{1}{V^2}P(\hat{\boldsymbol{u}},t)P(\hat{\boldsymbol{u}}',t)g(\boldsymbol{r},\boldsymbol{r}',\hat{\boldsymbol{u}},\hat{\boldsymbol{u}}',t)\end{aligned} \tag{3.207}$$

with $P(\boldsymbol{r},\boldsymbol{r}',\hat{\boldsymbol{u}},\hat{\boldsymbol{u}}',t)$ the PDF for the positions and orientations of two rods. Since the product $(1/V)P(\hat{\boldsymbol{u}}',t)g(\boldsymbol{r},\boldsymbol{r}',\hat{\boldsymbol{u}},\hat{\boldsymbol{u}}')$ is the conditional PDF for the position $\boldsymbol{r}'$ and orientation $\hat{\boldsymbol{u}}'$ of a rod, given the orientation $\hat{\boldsymbol{u}}$ and position $\boldsymbol{r}$ of the other rod, the torque in Eq. (3.206) is the torque on a rod, with prescribed orientation $\hat{\boldsymbol{u}}$ and position $\boldsymbol{r}$, averaged over the orientations and positions

of the other rods. In fact, Eq. (3.205) is nothing other than the one-particle Smoluchowski equation with the addition of an "external torque" $\bar{\boldsymbol{T}}$.

A closed equation of motion for $P(\hat{\boldsymbol{u}}, t)$ is obtained when g is known. For equilibrium suspensions of very long and thin, rigid and repulsive rods, similar arguments as used by Onsager (1933) lead to (see Section 3.10.3 for details)

$$g(\boldsymbol{r}-\boldsymbol{r}', \hat{\boldsymbol{u}}, \hat{\boldsymbol{u}}', t) = \exp[-\beta V(\boldsymbol{r}-\boldsymbol{r}', \hat{\boldsymbol{u}}, \hat{\boldsymbol{u}}')] \tag{3.208}$$

where V is the pair-interaction potential. This expression is valid in the isotropic and nematic states (provided the degree of alignment is not too high). That Eq. (3.208) is a good approximation for suspensions of very long and thin rods in equilibrium even at high concentrations is shown in Section 3.10.3. What is neglected in using Eq. (3.208) are dynamic contributions to correlations and the influence of shear flow. So far, nothing is known about dynamic correlations, and we shall assume here that these contributions can be neglected. Furthermore, the effect of shear flow is to align rods, that is, shear flow strongly affects the singlet PDF $P(\hat{\boldsymbol{u}}, t)$. Correlations between the centers of mass of the very long and thin rods, measured by the pair correlation function g, are much less affected by flow.

In the case of hard-core interactions, we have the identity

$$\begin{aligned}
&\exp[-\beta V(\boldsymbol{r}-\boldsymbol{r}', \hat{\boldsymbol{u}}, \hat{\boldsymbol{u}}')]\hat{\mathcal{R}}V(\boldsymbol{r}-\boldsymbol{r}', \hat{\boldsymbol{u}}, \hat{\boldsymbol{u}}') \\
&\quad = -\beta^{-1}\hat{\mathcal{R}}\{\exp[-\beta V(\boldsymbol{r}-\boldsymbol{r}', \hat{\boldsymbol{u}}, \hat{\boldsymbol{u}}')] - 1\} \\
&\quad = \beta^{-1}\hat{\mathcal{R}}\mathcal{X}(\boldsymbol{r}-\boldsymbol{r}', \hat{\boldsymbol{u}}, \hat{\boldsymbol{u}}')
\end{aligned} \tag{3.209}$$

with $\mathcal{X}$ the characteristic function of the excluded volume for two rods: $\mathcal{X} = 1$ when the cores of the two rods overlap and $\mathcal{X} = 0$ otherwise. The torque (3.206) can now be written as

$$\bar{\boldsymbol{T}}(\hat{\boldsymbol{u}}, t) = -\hat{\mathcal{R}}V^{\mathrm{eff}}(\hat{\boldsymbol{u}}, t) \tag{3.210}$$

where the *effective potential* V^{eff} is equal to (with $\boldsymbol{R} = \boldsymbol{r}' - \boldsymbol{r}$)

$$\begin{aligned}
V^{\mathrm{eff}}(\hat{\boldsymbol{u}}, t) &= \beta^{-1}\bar{\rho}\int \mathrm{d}\boldsymbol{R} \oint \mathrm{d}\hat{\boldsymbol{u}}'\, P(\hat{\boldsymbol{u}}', t)\mathcal{X}(\boldsymbol{R}, \hat{\boldsymbol{u}}, \hat{\boldsymbol{u}}') \\
&= 2DL^2\beta^{-1}\bar{\rho}\oint \mathrm{d}\hat{\boldsymbol{u}}'\, P(\hat{\boldsymbol{u}}', t)|\hat{\boldsymbol{u}} \times \hat{\boldsymbol{u}}'|
\end{aligned} \tag{3.211}$$

where in the last equation we have used the fact that

$$\int \mathrm{d}\boldsymbol{R}\,\mathcal{X}(\boldsymbol{R},\hat{\boldsymbol{u}},\hat{\boldsymbol{u}}') = 2DL^2|\hat{\boldsymbol{u}}\times\hat{\boldsymbol{u}}'| \tag{3.212}$$

for very long and thin rods. The effective potential V^{eff} is commonly referred to as the *Doi–Edwards potential*. We thus find the following closed equation of motion for $P(\hat{\boldsymbol{u}},t)$:

$$\frac{\partial}{\partial t}P(\hat{\boldsymbol{u}},t) = D_{\mathrm{r}}\hat{\mathcal{R}}\cdot\left[\hat{\mathcal{R}}P(\hat{\boldsymbol{u}},t) + 2DL^2\bar{\rho}P(\hat{\boldsymbol{u}},t)\hat{\mathcal{R}}\oint \mathrm{d}\hat{\boldsymbol{u}}'\,P(\hat{\boldsymbol{u}}',t)|\hat{\boldsymbol{u}}\times\hat{\boldsymbol{u}}'|\right]$$
$$-\dot{\gamma}\hat{\mathcal{R}}\cdot[P(\hat{\boldsymbol{u}},t)\hat{\boldsymbol{u}}\times(\hat{\boldsymbol{\Gamma}}\cdot\hat{\boldsymbol{u}})] \tag{3.213}$$

Note that this equation is nonlinear in $P(\hat{\boldsymbol{u}},t)$.

We note here, for those who are familiar with Onsager's work (Onsager 1933; Onsager 1942; Onsager 1949), that the stationary solution $P(\hat{\boldsymbol{u}})$ of the equation of motion (3.213) without shear flow satisfies

$$\ln[P(\hat{\boldsymbol{u}})] + 2DL^2\bar{\rho}\oint \mathrm{d}\hat{\boldsymbol{u}}'\,P(\hat{\boldsymbol{u}}',t)|\hat{\boldsymbol{u}}\times\hat{\boldsymbol{u}}'| = C \tag{3.214}$$

where C is an integration constant. This is precisely the Euler–Lagrange equation that complies with the Onsager free-energy functional for very long and thin rods with excluded-volume interactions.

An important thing to notice is that the outer product $\hat{\boldsymbol{u}}\times(\boldsymbol{\Gamma}\cdot\hat{\boldsymbol{u}})$ in Eq. (3.213) cannot be written in the form $\hat{\mathcal{R}}f$, with f a scalar field. Therefore, the simple shear contribution to the equation of motion (3.213) for $P(\hat{\boldsymbol{u}},t)$ cannot be incorporated as a potential. Simple shear flow is thus a non-conservative external field. Since no potential for shear flow can be defined, one cannot define a free energy. Thermodynamic considerations for systems under shear flow are therefore questionable. It has yet to be seen how accurate thermodynamic approaches for systems under shear flow are. To describe coexistence under shear flow conditions, one must in principle resort to equations of motion, and time-integrate these up to the stationary state. Since sharp interfaces may exist in such stationary states, the equations of motion should accurately describe situations where strong gradients in concentration and orientational order parameter are present.

3.10.2
Equation of Motion for $\boldsymbol{S}(t)$

Following Doi and Edwards (1986), an equation of motion for $\boldsymbol{S}$ can be obtained by operating on both sides of Eq. (3.213) with $\oint \mathrm{d}\hat{\boldsymbol{u}}\,(\hat{\boldsymbol{u}}\hat{\boldsymbol{u}})(\cdots)$ (see Eq. (3.181), where P is now time-dependent). The first term on the right-hand side of Eq. (3.213) is easily found to render

$$\oint \mathrm{d}\hat{\boldsymbol{u}}\,(\hat{\boldsymbol{u}}\hat{\boldsymbol{u}})\hat{\mathcal{R}}^2 P(\hat{\boldsymbol{u}},t) = \oint \mathrm{d}\hat{\boldsymbol{u}}\,P(\hat{\boldsymbol{u}},t)\hat{\mathcal{R}}^2(\hat{\boldsymbol{u}}\hat{\boldsymbol{u}}) = 2\,\hat{\boldsymbol{I}} - 6\boldsymbol{S} \quad (3.215)$$

where in the first equation two partial integrations have been done, and in the second equation the fact that $\hat{\mathcal{R}}^2(\hat{\boldsymbol{u}}\hat{\boldsymbol{u}}) = 2\,\hat{\boldsymbol{I}} - 6\hat{\boldsymbol{u}}\hat{\boldsymbol{u}}$ has been used. To make further analytical progress, we shall expand the second term in the equation of motion (3.213) up to third order in the orientational order parameter. That is, we shall expand with respect to the eigenvalues of matrices like $\boldsymbol{q} = \hat{\boldsymbol{u}}\hat{\boldsymbol{u}} - \frac{1}{3}\,\hat{\boldsymbol{I}}$, whose eigenvalues are in between $-\frac{1}{3}$ and $\frac{2}{3}$. Such a third-order Ginzburg–Landau expansion complies with a fourth-order expansion of the free energy in the absence of flow. Since the outer product in Eq. (3.213) for the effective potential can be written as (with $\boldsymbol{q}' = \hat{\boldsymbol{u}}'\hat{\boldsymbol{u}}' - \frac{1}{3}\,\hat{\boldsymbol{I}}$)

$$|\hat{\boldsymbol{u}} \times \hat{\boldsymbol{u}}'| = \sqrt{1 - \hat{\boldsymbol{u}}\hat{\boldsymbol{u}} : \hat{\boldsymbol{u}}'\hat{\boldsymbol{u}}'} = \sqrt{\tfrac{2}{3} - \boldsymbol{q} : \boldsymbol{q}'}$$

we can Taylor-expand up to leading order with respect to $\boldsymbol{q}$ and $\boldsymbol{q}'$,

$$|\hat{\boldsymbol{u}} \times \hat{\boldsymbol{u}}'| \approx \sqrt{\tfrac{2}{3}}\,[1 - \tfrac{3}{4}\boldsymbol{q} : \boldsymbol{q}'] \quad (3.216)$$

Since the next higher-order term in this Taylor expansion is of fourth order, this truncation leads to a Ginzburg–Landau expansion up to third order of the equation of motion for $\boldsymbol{S}$. Since $\sqrt{\frac{2}{3}}$ differs by only 3.8% from the exact value $\pi/4$ for the isotropic average value of $|\hat{\boldsymbol{u}} \times \hat{\boldsymbol{u}}'|$, we shall replace $\sqrt{\frac{2}{3}}$ in Eq. (3.216) by $\pi/4$. Errors due to the truncation of the Taylor expansion in Eq. (3.216) are probably larger. Resubstitution of the definition of the $\boldsymbol{q}$ in terms of bilinear products of the $\hat{\boldsymbol{u}}$ then leads to

$$|\hat{\boldsymbol{u}} \times \hat{\boldsymbol{u}}'| \approx \tfrac{5}{16}\pi[1 - \tfrac{3}{5}\hat{\boldsymbol{u}}\hat{\boldsymbol{u}} : \hat{\boldsymbol{u}}'\hat{\boldsymbol{u}}'] \quad (3.217)$$

The effective potential (3.211) within this Ginzburg–Landau expansion can be written as

$$V^{\mathrm{eff}}(\hat{\boldsymbol{u}},t) = \tfrac{5}{8}\pi\beta^{-1}DL^2\bar{\rho}[1 - \tfrac{3}{5}\boldsymbol{S} : \hat{\boldsymbol{u}}\hat{\boldsymbol{u}}] \quad (3.218)$$

which is known as the *Maier–Saupe potential* (Maier and Saupe 1958; Maier and Saupe 1959; Maier and Saupe 1960). Using the Ginzburg–Landau expansion (3.218) in the Smoluchowksi equation (Eq. 3.213), and operating on both sides with $\oint \mathrm{d}\hat{\boldsymbol{u}}\,(\hat{\boldsymbol{u}}\hat{\boldsymbol{u}})(\cdots)$, leads to the Doi–Edwards equation of motion,

$$\begin{aligned}\frac{\mathrm{d}}{\mathrm{d}t}\boldsymbol{S} = &-6D_{\mathrm{r}}[\boldsymbol{S} - \tfrac{1}{3}\,\hat{\boldsymbol{I}} - (L/D)\varphi(\boldsymbol{S}\cdot\boldsymbol{S} - \boldsymbol{S}^{(4)} : \boldsymbol{S})] \\ &+ \dot{\gamma}[\hat{\boldsymbol{\Gamma}}\cdot\boldsymbol{S} + \boldsymbol{S}\cdot\hat{\boldsymbol{\Gamma}}^{\mathrm{T}} - 2\boldsymbol{S}^{(4)} : \hat{\boldsymbol{E}}]\end{aligned} \quad (3.219)$$

where the concentration is now expressed in terms of the volume fraction $\varphi = \frac{1}{4}\pi D^2 L\bar{\rho}$, and, as before, $\hat{\boldsymbol{\Gamma}} = \boldsymbol{\Gamma}/\dot{\gamma}$ is the normalized velocity-gradient tensor, which is introduced to make the shear-rate dependence more explicit. Furthermore, $\boldsymbol{S}^{(4)}$ is a fourth-order polyadic tensor, defined as

$$\boldsymbol{S}^{(4)} \equiv \langle \hat{\boldsymbol{u}}\hat{\boldsymbol{u}}\hat{\boldsymbol{u}}\hat{\boldsymbol{u}}\rangle \tag{3.220}$$

In order to obtain a closed equation of motion for $\boldsymbol{S}$, the fourth-order tensor $\boldsymbol{S}^{(4)}$ should be expressed in terms of $\boldsymbol{S}$. Such a closure relation is discussed below.

3.10.3
Density Expansion of the Pair Correlation Function

Before deriving an orientational closure relation, we will discuss the reason why Eq. (3.208) is a good approximation in equilibrium for very long and thin rods with short-range repulsive interactions, even for high concentrations.

The first two terms in the density expansion of the equilibrium pair correlation function are

$$g(\boldsymbol{r}_1{-}\boldsymbol{r}_2, \hat{\boldsymbol{u}}_1, \hat{\boldsymbol{u}}_2) = \exp[-\beta V(\boldsymbol{r}_1{-}\boldsymbol{r}_2, \hat{\boldsymbol{u}}_1, \hat{\boldsymbol{u}}_2)] \tag{3.221}$$
$$\times \left[1 + \bar{\rho}\int \mathrm{d}\boldsymbol{r}_3 \oint \mathrm{d}\hat{\boldsymbol{u}}_3\, \mathcal{X}(\boldsymbol{r}_1{-}\boldsymbol{r}_3, \hat{\boldsymbol{u}}_1, \hat{\boldsymbol{u}}_3)\mathcal{X}(\boldsymbol{r}_3{-}\boldsymbol{r}_2, \hat{\boldsymbol{u}}_3, \hat{\boldsymbol{u}}_3) + \cdots\right]$$

Since the characteristic functions in the integrand are only non-zero when the core of rod 3 overlaps with both the cores of rods 1 and 2, the integration with respect to $\hat{\boldsymbol{u}}_3$ effectively extends over an angular range of the order D/L (see Fig. 3.18). The integration with respect to $\boldsymbol{r}_3$ contributes at most $\sim DL^2$. Hence, the second term in the above expression is at most of order $(D/L)DL^2\bar{\rho} \sim \varphi$. Since the volume fractions of interest scale like D/L (see Onsager 1933, 1942, 1949, and later in this chapter), the first order in density contribution to the pair correlation function is negligibly small for very long and thin rods. Higher-order terms are similarly very small.

The above arguments as far as the $\hat{\boldsymbol{u}}_3$ integration is concerned only hold when the angle between $\hat{\boldsymbol{u}}_1$ and $\hat{\boldsymbol{u}}_2$ is much larger than $\sim D/L$, as is clear from Fig. 3.18. Otherwise, the $\hat{\boldsymbol{u}}_3$ integration extends over a much larger angular range than just $\sim D/L$. Hence, the expression (3.208) for the pair correlation function is valid for high concentrations, provided that the degree of alignment is not very high. Scaling of the angular integration range with D/L does not hold for all configurations of the three rods. A more careful

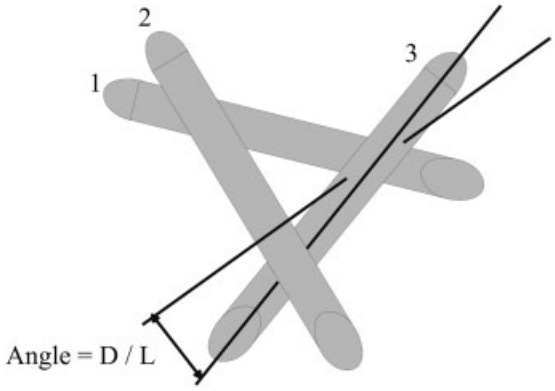

Fig. 3.18 The effective angular integration range corresponding to the orientation of rod 3.

analysis shows that the second term in Eq. (3.221) is of order $(D/L)\ln(L/D)$ instead of D/L.

3.10.4 Orientational Closure Relation

There are a number of orientational closure relations for the contraction in Eq. (3.220) that can be used in Eq. (3.219) to obtain a closed equation of motion for $\boldsymbol{S}(t)$ [for an overview, see Forest and Wang (2003)]. Here we will derive a simple closure relation that is shown to be reasonably accurate. It turns out that the various tumbling and wagging phenomena where rods coherently rotate under stationary shear flow (not to be confused with the Jeffery orbits discussed before) cannot be accurately described by most of the existing closure relations. Such periodic solutions for the orientational order should be analyzed on the basis of Eq. (3.213) without using a Ginzburg–Landau expansion for $|\hat{\boldsymbol{u}} \times \hat{\boldsymbol{u}}'|$.

The fourth-order average in Eq. (3.220) occurs in the form of a double contraction,

$$\boldsymbol{A} \equiv \boldsymbol{S}^{(4)} : \boldsymbol{M} \tag{3.222}$$

where $\boldsymbol{M}$ is equal to $\boldsymbol{S}$. As pointed out by Hinch and Leal (1976), orientational order increases monotonically with increasing shear rate, so that interpolation between the known forms for $\boldsymbol{S}^{(4)}$ in the isotropic state and in the perfectly aligned state will probably lead to quite accurate closures. The four-point average $\boldsymbol{S}^{(4)}$ is known exactly for the two extreme cases of perfect alignment (along the director $\hat{\boldsymbol{n}}$) and the isotropic state,

$$\langle \hat{\boldsymbol{u}}\hat{\boldsymbol{u}}\hat{\boldsymbol{u}}\hat{\boldsymbol{u}}\rangle_{ijkl} = \begin{cases} \hat{\boldsymbol{n}}_i\hat{\boldsymbol{n}}_j\hat{\boldsymbol{n}}_k\hat{\boldsymbol{n}}_l, & \text{perfect alignment} \\ \frac{1}{15}[\delta_{ij}\delta_{kl} + \delta_{ik}\delta_{jl} + \delta_{ik}\delta_{jl}], & \text{isotropic} \end{cases} \tag{3.223}$$

with δ_{ij} the Kronecker delta ($\delta_{ij} = 1$ when $i = j$, and $\delta_{ij} = 0$ when $i \neq j$). Furthermore, we have the following trivial identities:

$$A_{ij} \equiv \sum_{n,m} \langle \hat{\boldsymbol{u}}_i\hat{\boldsymbol{u}}_j\hat{\boldsymbol{u}}_n\hat{\boldsymbol{u}}_m\rangle \boldsymbol{M}_{mn} = A_{ji}$$

$$\sum_i A_{ii} = \sum_i \sum_{n,m} \langle \hat{\boldsymbol{u}}_i\hat{\boldsymbol{u}}_i\hat{\boldsymbol{u}}_n\hat{\boldsymbol{u}}_m\rangle \boldsymbol{M}_{mn} = \sum_{n,m} \boldsymbol{S}_{nm}\boldsymbol{M}_{mn} \equiv \boldsymbol{S} : \boldsymbol{M} \tag{3.224}$$

The last identity is especially important in order to ensure that the trace of $\boldsymbol{S}$ remains equal to 1 on time integration of the equation of motion (3.219). Using closures that do not satisfy (3.224) violates the time invariance of the trace of the order parameter. Furthermore,

$$\boldsymbol{A} = \langle \hat{\boldsymbol{u}}\hat{\boldsymbol{u}}\hat{\boldsymbol{u}}\hat{\boldsymbol{u}}\rangle : \overline{\boldsymbol{M}} \tag{3.225}$$

with

$$\overline{\boldsymbol{M}} \equiv \tfrac{1}{2}[\boldsymbol{M} + \boldsymbol{M}^{\mathrm{T}}] \tag{3.226}$$

the symmetric part of $\boldsymbol{M}$, where the superscript "T" stands for "transposition". This equation implies that the closure relation must be a function of $\overline{\boldsymbol{M}}$.

Since order parameters tend to increase monotonically with shear rate, an accurate closure relation can be found by constructing an interpolation form between the exact results (3.223) such that the conditions (3.224) and (3.225) are satisfied. Substitution of the most general form of linear combinations of first- and second-order terms in $\boldsymbol{S}$ (insisting that no isotropic terms $\sim \hat{\boldsymbol{I}}$ contribute), i.e.

$$\begin{aligned} \boldsymbol{A} = {} & c_1\boldsymbol{S}\cdot\overline{\boldsymbol{M}} + c_2\overline{\boldsymbol{M}}\cdot\boldsymbol{S} + c_3\boldsymbol{S}\,\hat{\boldsymbol{I}} : \overline{\boldsymbol{M}} + c_4\boldsymbol{S}\cdot\boldsymbol{S}\cdot\overline{\boldsymbol{M}} + c_5\boldsymbol{S}\cdot\overline{\boldsymbol{M}}\cdot\boldsymbol{S} \\ & + c_6\overline{\boldsymbol{M}}\cdot\boldsymbol{S}\cdot\boldsymbol{S} + c_7\boldsymbol{S}\,\boldsymbol{S} : \overline{\boldsymbol{M}} + c_8\overline{\boldsymbol{M}}\,\boldsymbol{S} : \boldsymbol{S} \end{aligned}$$

into Eqs. (3.223) to (3.226) renders algebraic equations for the coefficients c_j, leading to

$$\begin{aligned} \langle \hat{\boldsymbol{u}}\hat{\boldsymbol{u}}\hat{\boldsymbol{u}}\hat{\boldsymbol{u}}\rangle : \boldsymbol{M} = {} & \tfrac{1}{5}[\boldsymbol{S}\cdot\overline{\boldsymbol{M}} + \overline{\boldsymbol{M}}\cdot\boldsymbol{S} - \boldsymbol{S}\cdot\boldsymbol{S}\cdot\overline{\boldsymbol{M}} - \overline{\boldsymbol{M}}\cdot\boldsymbol{S}\cdot\boldsymbol{S} \\ & + 2\boldsymbol{S}\cdot\overline{\boldsymbol{M}}\cdot\boldsymbol{S} + 3\boldsymbol{S}\,\boldsymbol{S} : \overline{\boldsymbol{M}}] \end{aligned} \tag{3.227}$$

Substitution of the closure relation (3.227) into the equation of motion (3.219) finally leads to a closed equation of motion for the orientational order-parameter tensor.

The accuracy of the closure relation (3.227) is discussed in the Appendix (Section 3.16.3). Comparison with exact numerical solutions of the Smoluchowski equation (3.205) for non-interacting rods shows that the closure approximation (3.227) with $\boldsymbol{M} = \boldsymbol{S}$ and with $\boldsymbol{M} = \boldsymbol{E}$ are accurate to within 1% and 10%, respectively. Computer simulations show that this accuracy extends to interacting rods.

3.11
Paranematic–Nematic Spinodals and the Binodal Under Shear Flow

Since shear flow tends to align rods, it will affect the location of isotropic–nematic phase transition lines. The shear-induced shift of spinodals is theoretically more easily calculated than the shift of binodals. For the prediction of the location of binodals as a function of shear rate, the equations of motion must be time-integrated up to the stationary state where two bulk phases coexist. These equations of motion must account accurately for the usually sharp interface between the two bulk phases. Equations of this sort have been derived in Dhont and Briels (2002) and Dhont and Briels (2003) (see also Section 3.12 as far as the stress tensor is concerned), but remain to be analyzed. On the basis of approaches that partly rely on thermodynamic arguments, similar equations of motion can be derived to predict the phase behavior of rods under shear flow (Olmsted and Lu 1999; Olmsted 1999; Olmsted et al. 2000; Lu et al. 2000; Fielding and Olmsted 2003). These equations of motion are in principle valid for small gradients in concentration and orientational order parameter, and are therefore probably not able to predict the location of the binodal accurately. Nevertheless, the analysis of such equations of motion reveals interesting behavior, such as gradient banding, which will be discussed later in this chapter.

In the absence of flow, computer simulations where free energies are calculated can be used to obtain binodal concentrations for arbitrary aspect ratios (Bolhuis and Frenkel 1997).

The experimental situation is different. Here it is much more difficult to measure the location of spinodals as compared to binodals. In the following we shall first discuss how the shear-rate dependence of spinodals can be calculated, and an experiment is discussed where a line in between the paranematic–nematic and nematic–paranematic spinodals is probed. As far as the binodal is concerned, there are no theoretical (or simulation) results

available yet. We shall discuss an experiment where the location of the binodal is measured by means of time-resolved rheology experiments.

3.11.1 Spinodals

A spinodal point is defined as a point in the shear rate versus concentration diagram (the so-called *non-equilibrium phase diagram*), where a stable stationary solution of the equation of motion (3.219) for the orientational order parameter turns into an unstable solution. In the absence of shear flow, such spinodal points can also be found by means of thermodynamics. Once a solution becomes unstable, the system will start to phase-separate without any time delay. In order to describe such spinodal decomposition kinetics, one needs to consider the extension of the equation of motion (3.213) or (3.219) to inhomogeneous systems, where gradient contributions stabilize the system against the formation of very large gradients. In the absence of shear flow, such equations of motion are analyzed by Doi et al. (1988), Shimada et al. (1988) and Winters et al. (2000). For spinodal decomposition kinetics under shear flow, these equations of motion must be supplemented by an effective Navier–Stokes equation beyond the initial stage of demixing. Spinodal decomposition of rod-like systems will be strongly affected by flow, since flow affects orientational order. Analyzing such coupled equations of motion as derived by Dhont and Briels (2002) and Dhont and Briels (2003) is in progress. In the present section we shall limit the discussion to the shear-induced shift of spinodals.

As far as the location of spinodals is concerned, the non-equilibrium phase diagram can most conveniently be understood on the basis of so-called *bifurcation diagrams*. A bifurcation diagram is a plot in the orientational order parameter versus concentration plane, where, for a given shear rate, the order parameter for the stationary solutions of the equation of motion (3.219) is indicated. There are two possible stationary solutions: stable and unstable ones. Let $\boldsymbol{S}_0$ denote a stationary solution of Eq. (3.219), that is, the right-hand side of Eq. (3.219) vanishes for $\boldsymbol{S} = \boldsymbol{S}_0$. Let $\delta\boldsymbol{S}$ be a small perturbation. The stationary solution $\boldsymbol{S}_0$ is referred to as *stable* when an initial state $\boldsymbol{S}_0 + \delta\boldsymbol{S}$ relaxes back to $\boldsymbol{S}_0$ in time, provided $\delta\boldsymbol{S}$ is small enough. The state $\boldsymbol{S}_0$ is referred to as *unstable* when $\delta\boldsymbol{S}$ does not relax to $\boldsymbol{0}$, no matter how small this perturbation is chosen. A linear stability analysis is required to decide whether a stationary solution is either stable or unstable. Such a stability analysis for the stationary isotropic state $\boldsymbol{S}_0 = \frac{1}{3}\hat{\boldsymbol{I}}$ in the absence of shear flow can be performed analytically. Using the closure relation (3.227) in Eq. (3.219) with

$\dot{\gamma} = 0$, substitution of

$$\boldsymbol{S}(t) = \tfrac{1}{3}\,\hat{\boldsymbol{I}} + \delta\boldsymbol{S}(t) \tag{3.228}$$

and linearization with respect to $\delta\boldsymbol{S}(t)$ readily leads to

$$\frac{\mathrm{d}}{\mathrm{d}t}\delta\boldsymbol{S} = -6D_{\mathrm{r}}^{\mathrm{eff}}\delta\boldsymbol{S} \tag{3.229}$$

where

$$D_{\mathrm{r}}^{\mathrm{eff}} = D_{\mathrm{r}}[1 - \tfrac{1}{5}(L/D)\varphi] \tag{3.230}$$

is an effective rotational diffusion coefficient. The solution of Eq. (3.229) reads

$$\delta\boldsymbol{S}(t) = \exp[-6D_{\mathrm{r}}^{\mathrm{eff}}t]\delta\boldsymbol{S}(t{=}0) \tag{3.231}$$

The perturbation $\delta\boldsymbol{S}$ thus grows exponentially in time when $D_{\mathrm{r}}^{\mathrm{eff}} < 0$, i.e. when $(L/D)\varphi > 5$. For $(L/D)\varphi > 5$, the isotropic phase becomes unstable, and the new stable state is the nematic state with a relatively large value for λ. On subsequently lowering the concentration, the nematic state becomes unstable at $(L/D)\varphi < 40/9 = 4.44\ldots$, and the system returns to the isotropic state.

A stability analysis can in principle be done once S_0 is known, and hence an effective rotational diffusion coefficient can be defined also for non-zero shear rates. For non-zero shear rates this effective diffusion coefficient is generally a tensor rather than a scalar. An important thing to note is that the largest eigenvalue of this diffusion tensor becomes 0 at a spinodal point. Rotational diffusion therefore becomes very slow in the neighborhood of a spinodal point, which is reminiscent of critical slowing down.

The isotropic-to-nematic spinodal concentration $(L/D)\varphi = 5$ should be compared to the exact value 4 found by Onsager (1933), or, equivalently, from a linear stability analysis of Eq. (3.213), without performing a Ginzburg–Landau expansion on $|\hat{\boldsymbol{u}} \times \hat{\boldsymbol{u}}'|$. The difference between our result and the exact result for the location of the isotropic-to-nematic spinodal point in the absence of shear flow is mainly due to the Ginzburg–Landau expansion (3.217), and to a lesser extent to the closure relation (3.227) (which is accurate to within 1% for $\boldsymbol{M} = \boldsymbol{S}$).

Note that $D_{\mathrm{r}}^{\mathrm{eff}}$ is a collective diffusion coefficient since it describes the collective relaxation (or growth) of an initially misaligned state, where each rod contributes to the misalignment relative to the isotropic state. This diffusion coefficient is only weakly concentration-dependent because such a relaxation

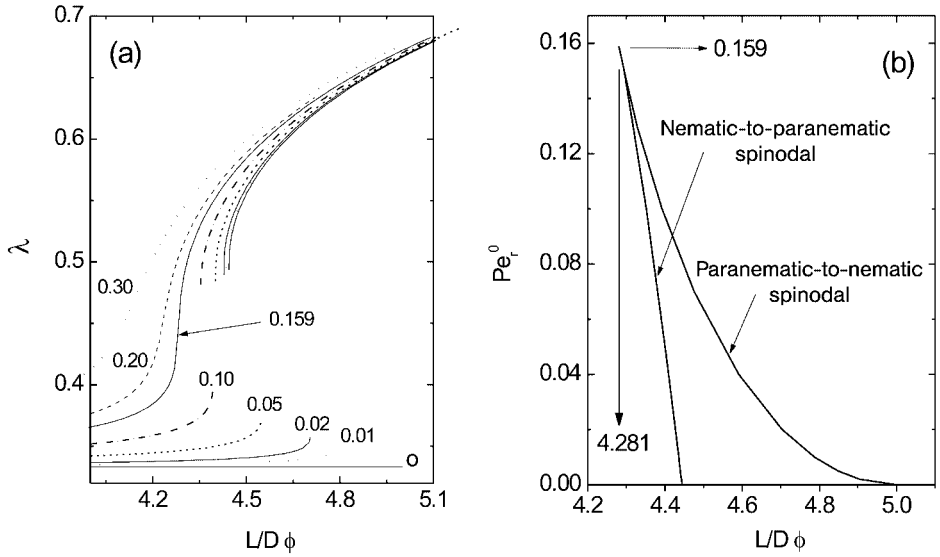

Fig. 3.19 (a) Bifurcation diagrams, where only stable stationary solutions $\boldsymbol{S}_0$ of Eq. (3.219) [together with the closure relation (3.227)] are shown. Here, λ is the largest eigenvalue of $\boldsymbol{S}_0$ and φ is the volume fraction of rods. The numbers in the plot refer to $Pe_{\mathrm{r}}^0 \equiv \dot{\gamma}/D_{\mathrm{r}}$.
(b) Spinodal points as found from the bifurcation diagrams.

(or initial growth) requires very small, collective reorientations of the rods. The concentration dependence of the tracer rotational diffusion coefficient considered by Doi and Edwards (1986), on the contrary, is much more pronounced due to "entanglements", since now large reorientations of the rods are important. As will be shown in Section 3.12, the effective rotational diffusion coefficient does not depend in a linear fashion on concentration. This is due to the neglect of dynamic correlations.

Spinodals will be shifted to lower concentrations on applying simple shear flow, since shear flow tends to align the rods, and therefore stabilizes the nematic state over the paranematic state. These spinodal points must be obtained numerically from Eqs. (3.219) and (3.227), since generally the stationary solution $\boldsymbol{S}_0$ is not known analytically. In Fig. 3.19a, bifurcation diagrams are given for various values of the bare Peclet number $Pe_{\mathrm{r}}^0 \equiv \dot{\gamma}/D_{\mathrm{r}}$.

We note here that an otherwise isotropic stable state is aligned by shear flow. Such an aligned state is referred to as a *paranematic state*. Similarly, an otherwise stable nematic state is more strongly aligned by shear flow.

The shear-rate-dependent paranematic-to-nematic spinodal (where the paranematic phase becomes unstable on increasing the concentration) and nematic-to-paranematic spinodal (where the nematic phase becomes unstable on lowering the concentration), as obtained from the bifurcation diagram

in Fig. 3.19a, are plotted in Fig. 3.19b. In the absence of shear flow, as discussed above, the isotropic-to-nematic spinodal concentration is located at $(L/D)\varphi = 5$, while the nematic-to-isotropic spinodal concentration is found to be equal to $(L/D)\varphi = 40/9 = 4.44\ldots$.

For a critical rotational Peclet number $Pe_r^0 = 0.159\ldots$, the two spinodals meet in a non-equilibrium critical point. For larger shear rates, where $Pe_r^0 > 0.159\ldots$, there is a continuous and reversible transition between the paranematic and nematic states: here, shear forces are so large that rod–rod interactions are no longer able to induce a discontinuous transition.

An important thing to note is that the concentration always enters through the combination $(L/D)\varphi$. For long and thin rods, the volume fractions of interest thus scale as $\sim L/D \ll 1$. This is the reason why hydrodynamic interactions become less important for very long and thin rods, as mentioned before. The strength of direct interactions, on the contrary, is not small, since, at $(L/D)\varphi = \mathcal{O}(1)$, these interactions are sufficiently strong to induce a phase transition.

Recent time-resolved birefringence experiments by Lenstra et al. (2001) confirm a shear-induced shift of paranematic–nematic phase boundary lines (see Fig. 3.20). Here, the shear rate is gradually changed from a high shear

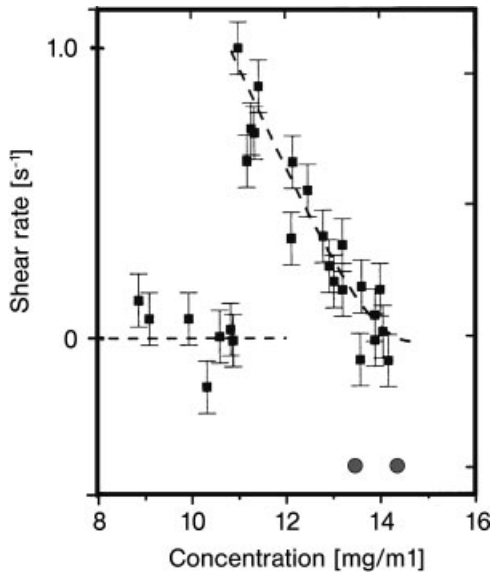

Fig. 3.20 The shear-induced shift of spinodal concentrations as probed with time-resolved birefringence measurements by Lenstra et al. (2001). The sloping line is located in between the two spinodal concentrations. The circles below indicate the binodal concentrations in the absence of shear flow.

rate (where the one-phase state is stable) to a lower shear rate (possibly in the two-phase region), followed by the reverse. During such a shear-rate sweep, the birefringence is probed. Due to the slowing down of the orientational dynamics close to a spinodal line, the birefringence will exhibit hysteresis, the magnitude of which depends on the sweep rate. Such time-resolved birefringence measurements probe a line in the non-equilibrium phase diagram that is in between the two spinodal concentrations (Lenstra et al. 2001). The system that is used here consists of dispersions of the *fd* virus, which was used for the first time for systematic studies on phase behavior and phase separation kinetics by Fraden et al. (1989), Tang and Fraden (1993), Tang and Fraden (1995) and Grelet and Fraden (2003), including suspensions of tobacco mosaic virus (see also Chapter 5 by Dogic and Fraden in this book). Paranematic–nematic phase separation for this system is slow enough to perform a shear-rate sweep during a time interval where phase separation does not play a role for the measured birefringence. The *fd* virus is a semi-flexible rod rather than a perfectly rigid rod, and the potential between the rods is not a perfect hard-core potential. The contour length of an *fd* virus particle is 880 nm, while its persistence length is 2200 nm. This is the reason why, in the absence of shear flow, the experimental binodal concentrations (indicated by the two dots in Fig. 3.20) are found not to agree quantitatively with those predicted by Onsager. As can be seen in Fig. 3.20, the shear-induced shift of spinodals is much more pronounced as compared to the prediction in Fig. 3.19b. The origin of this discrepancy is most probably the flexibility of the *fd* virus. The critical shear rate, however, is in reasonable agreement with the predicted critical shear rate $Pe_{\mathrm{r}}^{0} \approx 0.159$ (the bare rotational diffusion coefficient of the *fd* virus is known to be 10–20 s^{-1}). So far, there is no theory dealing with the dynamics of semi-flexible Brownian particles on the same level as the Smoluchowski approach for stiff rods outlined above.

3.11.2 The Binodal

An experimental binodal of an *fd* virus suspension is given in Fig. 3.21. Binodal points are determined from time-dependent viscosity measurements after a shear-rate quench from a high shear rate, where the one-phase state is stable, to a lower shear rate, $\dot{\gamma}_{-}$ say. Whenever $\dot{\gamma}_{-}$ is within the paranematic–nematic two-phase region, demixing will occur after the quench into a paranematic and a nematic phase. Developing inhomogeneities give rise to a temporal change of the viscosity, the amplitude of which increases with the depth of the quench. The amplitude of the time-dependent response of the viscosity vanishes on the binodal. A point on the binodal can thus be obtained by interpolation of the amplitude as a function of $\dot{\gamma}_{-}$ to zero. For

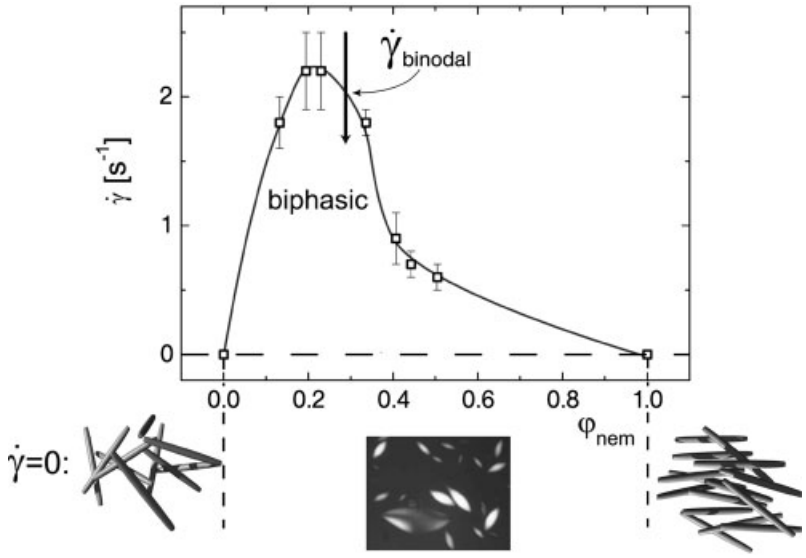

Fig. 3.21 The paranematic–nematic binodal of an *fd* virus suspension, where dextran is added to induce attractions between the rods, leading to faster phase separation. Here, $\varphi_{\rm nem}$ is the fraction of coexisting nematic that is mixed with the corresponding isotropic bulk phase (at zero shear rate). The lower figures show (from left to right) the isotropic state, a polarization microscopy image of tactoids that form during phase separation (courtesy of Kyongok Kang), and the nematic state. The vertical line indicates a possible shear-rate quench.

more details, see Lettinga and Dhont (2004). Contrary to the experiments on the location of the spinodal as described in the previous subsection, here dextran is added to the *fd* virus suspension in order to enhance phase separation, which renders these experiments feasible.

3.11.3
A Remark on Pattern Formation and Time-Periodic States

There are two regions in the non-equilibrium phase diagram to be distinguished that are related to pattern formation and time-periodic states. As will be seen later, shear flow can induce pattern formation within the two-phase region, i.e. the region bounded by the paranematic–nematic binodal. Here "bands" are alternately stacked in the vorticity direction, where the average orientational order within the bands differs. This type of shear-induced pattern formation is referred to as *vorticity banding*. In addition, coherent rotation of rods in the otherwise nematic state leads to oscillations of the director under stationary shear flow. Such *tumbling and wagging states* have been analyzed in great detail by Marrucci and Maffettone (1990a), Marrucci and Maffettone (1990b), Rienäcker and Hess (1999), Forest and Wang (2003) and Hess and

Kröger (2004). As stated before, the closure relation that is employed for the fourth-order tensor in Eq. (3.220) in terms of $\boldsymbol{S}$ sensitively determines whether these periodic states are correctly described. Our closure relation (3.227), although accurate to within about 10%, does not give rise to tumbling and wagging at all, like many other closures. Instead, it is more appropriate to analyze Eq. (3.213) as such. A numerical analysis of this equation of motion indeed predicts tumbling and wagging regimes in the non-equilibrium phase diagram, although the time-periodic states as predicted by Eq. (3.213) are not yet fully explored. In all of these equations of motion, however, dynamic correlations are neglected. As will be discussed in Section 3.12, such correlations might play some role of importance.

3.12
How Important Are Dynamic Correlations?

Dynamic correlations find their origin in the finite time that it takes for the surroundings of a given particle to adjust to the changing position and orientation of that particle. Consider, for example, an assembly of rods as depicted in Fig. 3.22(a). For convenience, the orientations of all the rods in this figure are taken to be the same in the initial state. Suppose that one is interested in the orientational dynamics of the shaded rod in Fig. 3.22. During a small time interval, the shaded rod moves to a new orientation due to rotational Brownian motion, as depicted in Fig. 3.22(b). If one then freezes the orientation of the shaded rod, the surrounding rods will change their average orientation to adjust to the field imposed by the frozen shaded rod, as depicted in Fig. 3.22(c). This adjustment takes a finite time. The shaded rod thus experiences a surrounding configuration of other rods that is always "lagging behind" the configuration that would have existed in the case of "coexistence" with the shaded rod. The surrounding rods therefore act with a finite torque on the shaded rod, even in an isotropic suspension, due to such dynamic correlations. This is not what is found from Eq. (3.206), when the PDF $P(\hat{\boldsymbol{u}}', t)$ of the surrounding rods is taken equal to its isotropic form $1/4\pi$, *and* g is approximated by the Boltzmann exponential (3.208). In order to describe *self-rotational diffusion* of a rod on the basis of Eq. (3.206), dynamic correlations are essential.

The neglect of dynamic correlations in the derivation of the Doi–Edwards equation (3.219) becomes clearer on calculating the correlation function $\langle \hat{\boldsymbol{u}}(t) \cdot \hat{\boldsymbol{u}}(0) \rangle$ for an isotropic dispersion. Thus, consider a rod (the dashed rod in Fig. 3.22) with a specified orientation $\hat{\boldsymbol{u}}(0)$ at time $t = 0$. Noting that

$$\frac{\mathrm{d}}{\mathrm{d}t} \langle \hat{\boldsymbol{u}}(t) \cdot \hat{\boldsymbol{u}}(0) \rangle = \hat{\boldsymbol{u}}(0) \cdot \oint \mathrm{d}\hat{\boldsymbol{u}}\, \hat{\boldsymbol{u}} \frac{\partial P(\hat{\boldsymbol{u}}, t)}{\partial t}$$

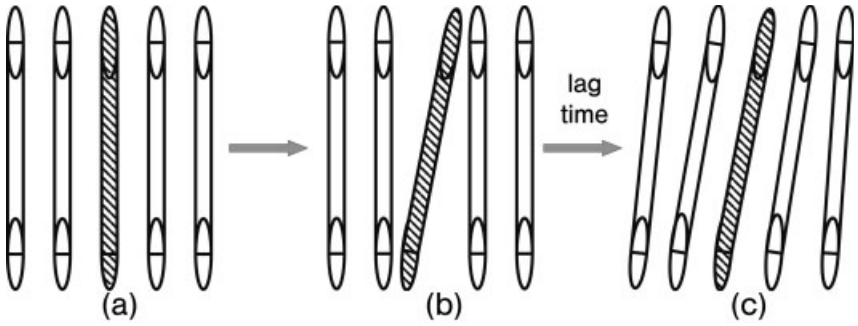

Fig. 3.22 A sketch to explain the origin of "dynamic correlations".
(a) An initial configuration of rods, which for simplicity is taken to be the perfectly aligned state. The orientational dynamics of the shaded rod is considered in the main text.
(b) After a small time, the shaded rod has moved to a different orientation due to Brownian motion. For clarity, the corresponding movements of the other rods is not depicted here.
(c) The surrounding rods need a finite time to adjust to the new orientation of the shaded rod.

multiplying both sides of the Smoluchowski equation (3.206) with $\hat{\boldsymbol{u}} \cdot \hat{\boldsymbol{u}}(0)$, and integrating with respect to $\hat{\boldsymbol{u}}$ readily leads to

$$\frac{\mathrm{d}}{\mathrm{d}t}\langle \hat{\boldsymbol{u}}(t) \cdot \hat{\boldsymbol{u}}(0)\rangle = -2D_{\mathrm{s}}^{\mathrm{eff}}(t)\langle \hat{\boldsymbol{u}}(t) \cdot \hat{\boldsymbol{u}}(0)\rangle \tag{3.232}$$

where the effective self-rotational diffusion coefficient is equal to

$$D_{\mathrm{s}}^{\mathrm{eff}}(t) \equiv D_{\mathrm{r}}\left[1 - \tfrac{1}{2}\beta \frac{\langle \bar{\boldsymbol{T}}(\hat{\boldsymbol{u}}(t)) \cdot [\hat{\boldsymbol{u}}(t) \times \hat{\boldsymbol{u}}(0)]\rangle}{\langle \hat{\boldsymbol{u}}(t) \cdot \hat{\boldsymbol{u}}(0)\rangle}\right] \tag{3.233}$$

where the torque $\bar{\boldsymbol{T}}(\hat{\boldsymbol{u}}(t))$ is given by Eq. (3.206) with an obvious change of notation. The PDF $P(\hat{\boldsymbol{u}}', t)$ in expression (3.206) for the torque is that of the other rods (the non-shaded rods in Fig. 3.22). When the PDF $P(\hat{\boldsymbol{u}}', t)$ of the other rods is taken to be equal to $1/4\pi$, and approximating the pair correlation function with the Boltzmann exponential (3.208), one finds that $\bar{\boldsymbol{T}}(\hat{\boldsymbol{u}}(t)) = \boldsymbol{0}$. Hence, $D_{\mathrm{s}}^{\mathrm{eff}}(t) = D_{\mathrm{r}}$, which is obviously wrong, since rotational motion of the shaded rod is certainly hindered by the presence of other rods. A non-zero torque results from dynamic correlations: $P(\hat{\boldsymbol{u}}', t)$ of rods in the neighborhood of the shaded rod differs from $1/4\pi$ due to the presence of the moving shaded rod, and the pair correlation function is not equal to the equilibrium Boltzmann exponential for the same reason.

The linear concentration dependence of the effective diffusion coefficient (3.230), which is a *collective diffusion coefficient*, is entirely due to the neglect of dynamic correlations. Molecular dynamics computer simulations, where the tail of the orientational correlation function is fitted to obtain the effective

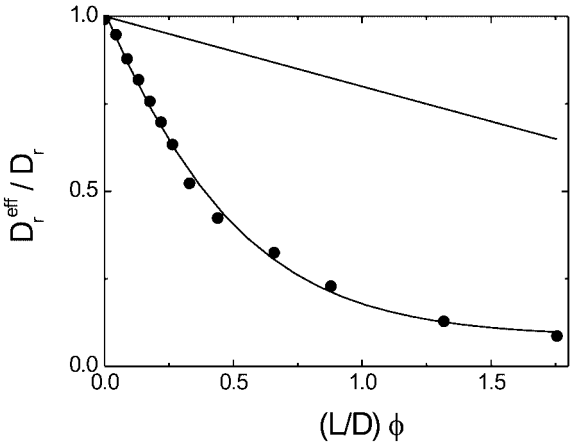

Fig. 3.23 The effective diffusion coefficient as defined in the previous section from the theory (Eq. 3.230), where dynamic correlations are neglected and from simulations by Tao et al. (2005) (the solid line through the simulation data points are merely a guide to the eye).

diffusion coefficient, show a strong nonlinear concentration dependence (Tao et al. 2005), as shown in Fig. 3.23. This indicates that dynamic correlations are important. As yet, no attempt has been made to incorporate dynamic correlations in the analysis of the Smoluchowski equation (3.206). As will be seen later, computer simulations do predict a linear concentration dependence of the shear viscosity. It thus seems that dynamic correlations are of minor importance for the viscoelastic response of suspensions of rods, contrary to diffusive behavior.

3.13 The Stress Tensor for Rod Suspensions

In addition to the orientational order of rods in shear flow, the viscous behavior of these systems is of interest. In this section we shall derive a microscopic expression for the stress tensor and express it in terms of the orientational order-parameter tensor (see also Dhont and Briels (2002) and Dhont and Briels (2003)). Viscoelastic response functions can then be calculated once the equation of motion (3.219) for $\boldsymbol{S}(t)$ is solved.

3.13.1 The Basic Idea

Let $\boldsymbol{U}(\boldsymbol{r},t)$ and $\rho_{\mathrm{m}}(\boldsymbol{r},t)$ denote the suspension velocity and mass density, respectively. The velocity satisfies the Navier–Stokes equation (Eq. 3.13), where

the divergence of the stress tensor is averaged over the phase-space coordinates $\mathbf{\Gamma}$ of the colloidal rods,

$$\rho_{\mathrm{m}}(\boldsymbol{r},t)\left[\frac{\partial \boldsymbol{U}(\boldsymbol{r},t)}{\partial t}+\boldsymbol{U}(\boldsymbol{r},t)\cdot\nabla\boldsymbol{U}(\boldsymbol{r},t)\right]=\langle\nabla\cdot\boldsymbol{\sigma}(\boldsymbol{r}|\mathbf{\Gamma}(t))\rangle \quad (3.234)$$

Here, $\boldsymbol{\sigma}$ is the stress tensor of the solvent in which the rods are embedded, or of the core material of the rods, depending on whether $\boldsymbol{r}$ is within the solvent or inside the core of a rod. Clearly, $\boldsymbol{\sigma}$ depends on the phase-space coordinates $\mathbf{\Gamma}$ of all the rods.

The fundamental quantity in hydrodynamics is the momentum density $\rho\boldsymbol{v}$, with ρ and $\boldsymbol{v}$ the microscopic density and velocity, respectively. Therefore, the appropriate definition of the macroscopic velocity $\boldsymbol{U}$ is

$$\rho_{\mathrm{m}}(\boldsymbol{r},t)\boldsymbol{U}=\langle\rho\boldsymbol{v}\rangle \quad (3.235)$$

It can be shown (Dhont and Briels 2002) that, if the mass density difference between the fluid and the core material of which the rods consist is small and/or if the volume fraction of colloidal material is very small, the definition in Eq. (3.235) reduces simply to

$$\boldsymbol{U}(\boldsymbol{r},t)=\langle\boldsymbol{v}(\boldsymbol{r}|\mathbf{\Gamma}(t))\rangle \quad (3.236)$$

where $\boldsymbol{u}$ is equal to the fluid velocity or the velocity of a piece of colloidal material, depending on whether $\boldsymbol{r}$ is within the solvent or inside the core of a colloidal rod.

Let $P(\mathbf{\Gamma},t)$ denote the probability density function of $\mathbf{\Gamma}$, which is the solution of the Smoluchowski equation (3.173). By definition we then have

$$\boldsymbol{U}(\boldsymbol{r},t)=\int \mathrm{d}\mathbf{\Gamma}\, P(\mathbf{\Gamma},t)\boldsymbol{v}(\boldsymbol{r}|\mathbf{\Gamma}) \quad (3.237)$$

In the derivation of the general expression for the divergence of the stress tensor, we shall encounter the ensemble average

$$\langle\nabla^2\boldsymbol{v}(\boldsymbol{r})\rangle=\int \mathrm{d}\mathbf{\Gamma}\, P(\mathbf{\Gamma},t)\nabla^2\boldsymbol{v}(\boldsymbol{r}|\mathbf{\Gamma})$$

Since the Laplace operator can be taken in front of the phase-space integral, and the suspension flow velocity is given by Eq. (3.236), it trivially follows that

$$\langle\nabla^2\boldsymbol{v}(\boldsymbol{r})\rangle=\nabla^2\boldsymbol{U}(\boldsymbol{r},t) \quad (3.238)$$

This result will be of importance later in this section.

In order to obtain an explicit Navier–Stokes equation, the ensemble average of the body force $\nabla \cdot \boldsymbol{\sigma}(\boldsymbol{r}|\boldsymbol{\Gamma})$ should be expressed in terms of suspension properties. To this end, consider a rectangular volume element δV located at $\boldsymbol{r}$, with linear dimensions δ_x, δ_y, and δ_z in the x, y, and z directions, respectively. In the formal limit that the size of the volume element vanishes, the ensemble-averaged total force per unit volume of the surrounding material on the volume element is nothing other than the divergence of the stress tensor that should be used in the Navier–Stokes equation (3.234). This force consists of three parts: forces that arise (1) from interactions between colloidal particles outside on those within the rectangular volume element, (2) from interactions between solvent molecules and colloidal particles, and (3) from interactions between solvent molecules on either side of the boundary of the volume element. The corresponding stress tensors will be referred to as the "particle–particle stress tensor" $\boldsymbol{\Sigma}^{\mathrm{pp}}$, the "particle–solvent stress tensor" $\boldsymbol{\Sigma}^{\mathrm{ps}}$, and the "solvent–solvent stress tensor" $\boldsymbol{\Sigma}^{\mathrm{ss}}$, respectively. The divergence of the suspension stress tensor $\boldsymbol{\Sigma}$ is the sum of these three body forces:

$$\nabla \cdot \boldsymbol{\Sigma} \equiv \langle \nabla \cdot \boldsymbol{\sigma}(\boldsymbol{r}|\boldsymbol{\Gamma}(t)) \rangle = \nabla \cdot \boldsymbol{\Sigma}^{\mathrm{pp}} + \nabla \cdot \boldsymbol{\Sigma}^{\mathrm{ps}} + \nabla \cdot \boldsymbol{\Sigma}^{\mathrm{ss}} \qquad (3.239)$$

These three contributions will be calculated explicitly in the next subsections. First of all, a general expression for the ensemble-averaged body force $\nabla \cdot \boldsymbol{\Sigma}$ will be derived, after which this expression will be expressed in terms of a probability density function. Finally, this expression will be simplified by means of the same Ginzburg–Landau expansion used to derive the Doi–Edwards equation (Eq. 3.219), which leads to an expression for the stress tensor involving the concentration and the orientational order-parameter tensor $\boldsymbol{S}$.

3.13.1.1 Particle–Particle Stress Tensor $\boldsymbol{\Sigma}^{\mathrm{pp}}$

The force that colloidal particles outside the volume element exert on those within the volume element is equal to

$$\sum_j{}^{*} \boldsymbol{F}_j$$

where $\boldsymbol{F}_j$ is the force that all colloidal particles exert on colloidal particle j, and the asterisk on the summation is used to indicate that the summation ranges only over those colloidal particles that are inside the volume element, i.e. those for which $\boldsymbol{r}_j \in \delta V$. Note that mutual interactions between colloidal particles within the volume element cannot give rise to a net force on that volume element. The force per unit volume, for formally vanishing size of the volume element, is thus equal to

$$\nabla \cdot \boldsymbol{\Sigma}^{\mathrm{pp}} = \lim_{\delta_x,\delta_y,\delta_z \to 0} \frac{1}{\delta_x \delta_y \delta_z} \sum_{j=1}^{N} \langle \mathcal{X}_{\boldsymbol{r}}(\boldsymbol{r}_j) \boldsymbol{F}_j \rangle \tag{3.240}$$

where N is the total number of colloidal particles in the system under consideration, $\boldsymbol{r}_j$ is the position coordinate of a colloidal particle, and $\mathcal{X}_{\boldsymbol{r}}$ is the characteristic function of the rectangular volume element, which was introduced in the previous section. The characteristic function is defined as

$$\mathcal{X}_{\boldsymbol{r}}(\boldsymbol{R}) = \begin{cases} 1, & \text{when } \boldsymbol{R} \in \delta V \\ 0, & \text{otherwise} \end{cases} \tag{3.241}$$

The subscript "$\boldsymbol{r}$" on the characteristic function is used to indicate that the volume element δV is located at position $\boldsymbol{r}$. The characteristic function effectively limits the summation to colloidal particles that are inside δV, i.e. those for which $\boldsymbol{r}_j \in \delta V$. Furthermore, as discussed before, the total force $\boldsymbol{F}_j$ on the jth colloidal particle due to interactions with all other colloidal particles is equal to

$$\boldsymbol{F}_j = -\nabla_j \Phi - k_{\mathrm{B}} T \nabla_j \ln P \tag{3.242}$$

where Ψ is the total potential energy of the assembly of N rods in the suspension, and P is the probability density function of the phase-space coordinates of all the colloidal rods: $-\nabla_j \Phi$ is the force due to potential interactions, and $-k_{\mathrm{B}} T \nabla_j \ln P$ is the Brownian force, where ∇_j is the gradient operator with respect to $\boldsymbol{r}_j$. Since [with $\delta(\boldsymbol{r} - \boldsymbol{r}_j)$ the three-dimensional delta distribution]

$$\lim_{\delta_x,\delta_y,\delta_z \to 0} \mathcal{X}_{\boldsymbol{r}}(\boldsymbol{r}_j)/\delta_x \delta_y \delta_z = \delta(\boldsymbol{r} - \boldsymbol{r}_j) \tag{3.243}$$

as is easily verified by integration of both sides with respect to $\boldsymbol{r}_j$, this immediately leads to

$$\nabla \cdot \boldsymbol{\Sigma}^{\mathrm{pp}} = \sum_{j=1}^{N} \langle \delta(\boldsymbol{r} - \boldsymbol{r}_j) \boldsymbol{F}_j \rangle \tag{3.244}$$

Together with Eq. (3.242) for the forces, this is the microscopic expression for the contribution to the divergence of the stress tensor which is due to inter-colloidal particle forces.

3.13.1.2 Particle–Solvent Stress Tensor $\boldsymbol{\Sigma}^{\mathrm{ps}}$

The particle–solvent stress arises from forces on the volume element due to interactions between colloidal particles and solvent molecules. These forces

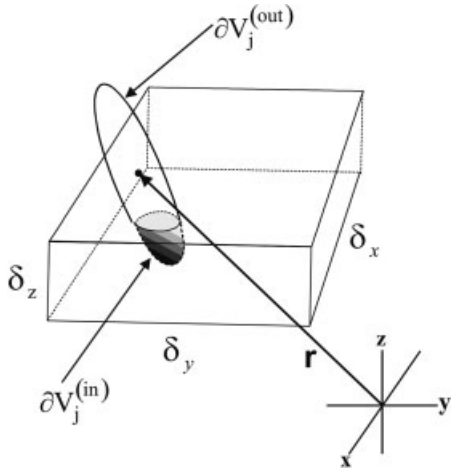

Fig. 3.24 The rectangular volume element δV at position $\boldsymbol{r}$ intersects with the core of colloidal rod j with its position coordinate $\boldsymbol{r}_j$ outside the volume element. Thus $\partial V^{(\mathrm{out})}$ is that part of the surface area ∂V_j of the rod that is outside the volume element, and $\partial V_j^{(\mathrm{in})}$ is that part inside.

are mediated to the volume element by colloidal particles that intersect with the surface enclosing the rectangular volume element. Consider first the force that is mediated to the solvent within the volume element by a colloidal particle with its position coordinate outside the volume element (see Fig. 3.24). The instantaneous force that the colloidal particle exerts on the solvent inside the volume element is equal to

$$-\int_{\partial V_j^{(\mathrm{in})}(\boldsymbol{r}_j,\hat{\boldsymbol{u}}_j)} \mathrm{d}\boldsymbol{S}' \cdot \boldsymbol{\sigma}(\boldsymbol{r}')$$

Here, the surface area $\partial V_j^{(\mathrm{in})}$ is that part of the surface area of the colloidal particle that is inside the volume element (see Fig. 3.24). This range of integration depends on both the position $\boldsymbol{r}_j$ of the colloidal particle j and its orientation $\hat{\boldsymbol{u}}_j$. Furthermore, $\mathrm{d}\boldsymbol{S}'$ is the normal surface element on the surface area of the colloidal particle, and $\boldsymbol{\sigma}$ is the stress tensor of the solvent. The minus sign in Eq. (3.245) arises from the fact that $\mathrm{d}\boldsymbol{S}' \cdot \boldsymbol{\sigma}(\boldsymbol{r}')$ is equal to $\mathrm{d}S'\, \boldsymbol{f}^{\mathrm{h}}(\boldsymbol{r}')$, with $\boldsymbol{f}^{\mathrm{h}}(\boldsymbol{r}')$ the force per unit area that the fluid exerts on the surface element $\mathrm{d}\boldsymbol{S}'$, which is minus the force that this surface element exerts on the fluid. In terms of this hydrodynamic force, Eq. (3.245) is more conveniently written as

$$-\int_{\partial V_j^{(\mathrm{in})}(\boldsymbol{r}_j,\hat{\boldsymbol{u}}_j)} \mathrm{d}S'\, \boldsymbol{f}^{\mathrm{h}}(\boldsymbol{r}')$$

The ensemble-averaged force $\boldsymbol{F}^{\mathrm{out}}$ of all the colloidal particles outside the volume element on the solvent inside the element is thus equal to

$$\boldsymbol{F}^{\mathrm{out}} = -\left\langle \sum_{j=1}^{N} [1 - \mathcal{X}_{\boldsymbol{r}}(\boldsymbol{r}_j)] \oint_{\partial V_j(\boldsymbol{r}_j, \hat{\boldsymbol{u}}_j)} \mathrm{d}S' \, \boldsymbol{f}^{\mathrm{h}}(\boldsymbol{r}') \mathcal{X}_{\boldsymbol{r}}(\boldsymbol{r}') \right\rangle \quad (3.245)$$

where, as before, $\mathcal{X}_{\boldsymbol{r}}$ is the characteristic function of the volume element. The characteristic function $1 - \mathcal{X}_{\boldsymbol{r}}(\boldsymbol{r}_j)$ for the volume outside the volume element assures that, in the summation over all colloidal particles, only those which are outside the volume element are counted. Furthermore, the characteristic function $\mathcal{X}_{\boldsymbol{r}}(\boldsymbol{r}')$ assures that only points $\boldsymbol{r}'$ on the surface of the colloidal particle inside the volume element are taken into account. Including the characteristic function in the integrand in Eq. (3.245) allows for the extension of the integration range to the entire surface area $\partial V_j(\boldsymbol{r}_j, \hat{\boldsymbol{u}}_j)$ of the jth colloidal particle.

Similarly, in the case of a colloidal particle located inside the volume element, i.e. when $\boldsymbol{r}_j \in \delta V$, the instantaneous force that the colloidal particle exerts on the solvent outside the volume element is equal to

$$-\int_{\partial V_j^{(\mathrm{out})}(\boldsymbol{r}_j, \hat{\boldsymbol{u}}_j)} \mathrm{d}S' \, \boldsymbol{f}^{\mathrm{h}}(\boldsymbol{r}')$$

with $\partial V_j^{(\mathrm{out})}$ the part of the surface area of the colloidal particle located outside the volume element (see Fig. 3.24). This is minus the force that is exerted on the colloidal particle by the solvent outside the volume element. Hence, similarly as before, the ensemble-averaged force $\boldsymbol{F}^{\mathrm{in}}$ on the volume element due to interactions between solvent molecules outside and colloidal particles inside the volume element is found to be equal to

$$\boldsymbol{F}^{\mathrm{in}} = \left\langle \sum_{j=1}^{N} \mathcal{X}_{\boldsymbol{r}}(\boldsymbol{r}_j) \oint_{\partial V_j(\boldsymbol{r}_j, \hat{\boldsymbol{u}}_j)} \mathrm{d}S' \, \boldsymbol{f}^{\mathrm{h}}(\boldsymbol{r}') [1 - \mathcal{X}_{\boldsymbol{r}}(\boldsymbol{r}')] \right\rangle \quad (3.246)$$

where again we have used the fact that $1 - \mathcal{X}_{\boldsymbol{r}}(\boldsymbol{r}')$ is the characteristic function for the volume outside the volume element. From the representation (3.243) of the delta distribution, it is thus found that

$$\begin{aligned} \nabla \cdot \boldsymbol{\Sigma}^{\mathrm{ps}} &= \lim_{\delta_x, \delta_y, \delta_z \to 0} [\boldsymbol{F}^{\mathrm{out}} + \boldsymbol{F}^{\mathrm{in}}] / \delta_x \delta_y \delta_z \quad (3.247) \\ &= \left\langle \sum_{j=1}^{N} \delta(\boldsymbol{r} - \boldsymbol{r}_j) \boldsymbol{F}_j^{\mathrm{h}} \right\rangle - \left\langle \sum_{j=1}^{N} \oint_{\partial V_j(\boldsymbol{r}_j, \hat{\boldsymbol{u}}_j)} \mathrm{d}S' \, \delta(\boldsymbol{r} - \boldsymbol{r}') \boldsymbol{f}^{\mathrm{h}}(\boldsymbol{r}') \right\rangle \end{aligned}$$

where

$$\boldsymbol{F}_j^{\mathrm{h}} = \oint_{\partial V_j(\boldsymbol{r}_j,\hat{\boldsymbol{u}}_j)} \mathrm{d}S'\, \boldsymbol{f}^{\mathrm{h}}(\boldsymbol{r}') \tag{3.248}$$

is the total force that the solvent exerts on the jth colloidal particle.

3.13.1.3 Solvent–Solvent Stress Tensor $\boldsymbol{\Sigma}^{\mathrm{ss}}$

The force per unit volume that the solvent outside the volume element δV exerts on the solvent inside, for formally vanishing size of the volume element, is equal to

$$\nabla\cdot\boldsymbol{\Sigma}^{\mathrm{ss}} = \lim_{\delta_x,\delta_y,\delta_z\to 0} \frac{1}{\delta_x\delta_y\delta_z}\left\langle \int_{A_{\mathrm{s}}} \mathrm{d}\boldsymbol{S}'\cdot\boldsymbol{\sigma}(\boldsymbol{r}')\right\rangle \tag{3.249}$$

where A_{s} is the part of the surface area of the volume element that is occupied by solvent, which is the surface area of the volume element minus the part that is cut by cores of colloidal particles (see Fig. 3.25). Here, $\mathrm{d}\boldsymbol{S}'$ points outward of δV. The subscript "s" on the integration A_{s} refers to "solvent". For an incompressible solvent, we have

$$\boldsymbol{\sigma}(\boldsymbol{r}') = \eta_0\{\nabla'\boldsymbol{v}(\boldsymbol{r}') + [\nabla'\boldsymbol{v}(\boldsymbol{r}')]^{\mathrm{T}}\} - p(\boldsymbol{r}')\,\hat{\boldsymbol{I}} \tag{3.250}$$

with η_0 the solvent shear viscosity and $\boldsymbol{v}$ the solvent flow velocity. Furthermore, p is the mechanical pressure in the solvent, and $\hat{\boldsymbol{I}}$ is the identity tensor. The superscript "T" stands for transposition. Note that, since $\nabla^2 p(\boldsymbol{r}) = 0$ within the incompressible solvent, p is entirely determined by the boundary conditions for the solvent flow imposed by the surfaces of the colloidal particles and the container walls. Hence, $p(\boldsymbol{r}')$ depends implicitly on the positions and orientations of all the rods. Substitution of Eq. (3.250) into Eq. (3.249) leads to

$$\nabla\cdot\boldsymbol{\Sigma}^{\mathrm{ss}} = \boldsymbol{M}^{(1)} + \boldsymbol{M}^{(2)} \tag{3.251}$$

where

$$\boldsymbol{M}^{(1)} \equiv \lim_{\delta_x,\delta_y,\delta_z\to 0} \frac{\eta_0}{\delta_x\delta_y\delta_z}\left\langle \int_{A_{\mathrm{s}}} \mathrm{d}\boldsymbol{S}'\cdot\{\nabla'\boldsymbol{v}(\boldsymbol{r}') + [\nabla'\boldsymbol{v}(\boldsymbol{r}')]^{\mathrm{T}}\}\right\rangle \tag{3.252}$$

and

$$\boldsymbol{M}^{(2)} \equiv -\lim_{\delta_x,\delta_y,\delta_z\to 0} \frac{1}{\delta_x\delta_y\delta_z}\left\langle \int_{A_{\mathrm{s}}} \mathrm{d}\boldsymbol{S}'\, p(\boldsymbol{r}')\right\rangle \tag{3.253}$$

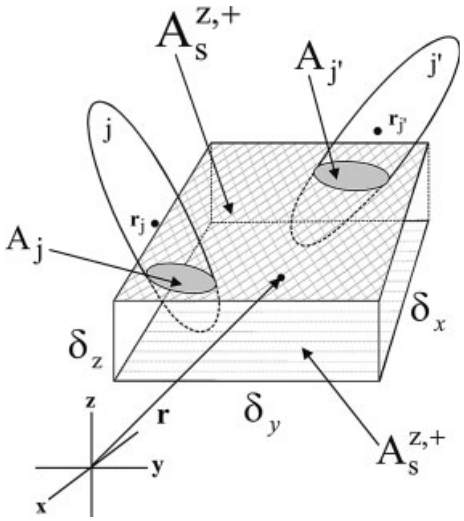

Fig. 3.25 The part of the surface area $\partial\delta V$ of the volume element that is occupied by solvent is denoted as A_s. This is $\partial\delta V$ minus the areas A_j of intersection of $\partial\delta V$ with the core of colloidal rod j. The part of A_s on the upper z side of the volume is denoted as $A_\mathrm{s}^{z,+}$, and on the lower side as $A_\mathrm{s}^{z,-}$.

Consider first the contribution $\boldsymbol{M}^{(1)}$. We can rewrite the integral as

$$\left\langle \int_{A_\mathrm{s}} \mathrm{d}\boldsymbol{S}' \cdot \{\nabla' \boldsymbol{v}(\boldsymbol{r}') + [\nabla' \boldsymbol{v}(\boldsymbol{r}')]^\mathrm{T}\} \right\rangle$$

$$= \left\langle \left[\oint_{\partial\delta V} - \sum_{j=1}^{N} \int_{A_j} \right] \mathrm{d}\boldsymbol{S}' \cdot \{\nabla' \boldsymbol{v}(\boldsymbol{r}') + [\nabla' \boldsymbol{v}(\boldsymbol{r}')]^\mathrm{T}\} \right\rangle \qquad (3.254)$$

where A_j is the area of intersection of the surface area $\partial\delta V$ of the volume element and the core of the colloidal particle j (see Fig. 3.25). For a rigid colloidal particle, the velocity inside the core is given by

$$\boldsymbol{v}(\boldsymbol{r}') = \boldsymbol{v}_j + \boldsymbol{\Omega}_j \times (\boldsymbol{r}' - \boldsymbol{r}_j), \quad \boldsymbol{r}' \in \text{core of particle } j \qquad (3.255)$$

where $\boldsymbol{v}_j$ is the translational velocity and $\boldsymbol{\Omega}_j$ is the rotational velocity of colloidal particle j. Hence (with $\boldsymbol{\epsilon}$ the Levi-Civita tensor, and $\Omega_{j,p}$ the pth component of $\boldsymbol{\Omega}_j$)

$$\nabla'_m v_n = \nabla_m [\boldsymbol{\Omega}_j \times (\boldsymbol{r}' - \boldsymbol{r}_j)]_n = \nabla'_m \epsilon_{npq} \Omega_{j,p} r'_q = \epsilon_{npm} \Omega_{j,p}$$

where summation over repeated indices is assumed. From the antisymmetry of the Levi-Civita tensor, it is thus found that

$$\int_{A_j} \mathrm{d}\boldsymbol{S}' \cdot \{\nabla' \boldsymbol{v}(\boldsymbol{r}') + [\nabla' \boldsymbol{v}(\boldsymbol{r}')]^{\mathrm{T}}\} = \boldsymbol{0} \tag{3.256}$$

Using Gauss's integral theorem, we thus find from Eqs. (3.254) and (3.256), for incompressible solvents,

$$\left\langle \int_{A_\mathrm{s}} \mathrm{d}\boldsymbol{S}' \cdot \{\nabla' \boldsymbol{v}(\boldsymbol{r}') + [\nabla' \boldsymbol{v}(\boldsymbol{r}')]^{\mathrm{T}}\} \right\rangle = \left\langle \int_{\delta V} \mathrm{d}\boldsymbol{r}' \, \nabla'^{\,2} \boldsymbol{v}(\boldsymbol{r}') \right\rangle$$

Hence, Eq. (3.252) reduces to

$$\boldsymbol{M}^{(1)} = \lim_{\delta_x, \delta_y, \delta_z \to 0} \frac{\eta_0}{\delta_x \delta_y \delta_z} \left\langle \int_{\delta V} \mathrm{d}\boldsymbol{r}' \, \nabla'^{\,2} \boldsymbol{v}(\boldsymbol{r}') \right\rangle = \eta_0 \langle \nabla^2 \boldsymbol{v}(\boldsymbol{r}) \rangle$$

From Eq. (3.238), it is thus finally found that

$$\boldsymbol{M}^{(1)} = \eta_0 \nabla^2 \boldsymbol{U}(\boldsymbol{r}, t) \tag{3.257}$$

The contribution $\boldsymbol{M}^{(2)}$ can be expressed in terms of suspension properties as follows. Let $A_\mathrm{s}^{z,+}$ denote the upper side of A_s, and similarly $A_\mathrm{s}^{z,-}$ the lower side, as indicated in Fig. 3.25. Furthermore, let $\hat{\boldsymbol{e}}_z$ denote the unit vector along the positive z axis. Since the unit normal on $A_\mathrm{s}^{z,+}$ is $\hat{\boldsymbol{e}}_z$ while the unit normal on $A_\mathrm{s}^{z,-}$ is $-\hat{\boldsymbol{e}}_z$, the contribution $\boldsymbol{M}_z^{(2)}$ from the upper and lower sides of A_s to $\boldsymbol{M}^{(2)}$ is equal to

$$\boldsymbol{M}_z^{(2)} = -\hat{\boldsymbol{e}}_z \lim_{\delta_x, \delta_y, \delta_z \to 0} \frac{1}{\delta_x \delta_y \delta_z} \left\langle \left[\int_{A_\mathrm{s}^{z,+}} - \int_{A_\mathrm{s}^{z,-}} \right] \mathrm{d}S' \, p(\boldsymbol{r}') \right\rangle$$

For small sizes of the volume element, the scalar

$$P^{\mathrm{ss}}(\boldsymbol{r} + \tfrac{1}{2}\delta_z \hat{\boldsymbol{e}}_z, t) \equiv \frac{1}{\delta_x \delta_y} \left\langle \int_{A_\mathrm{s}^{z,+}} \mathrm{d}S' \, p(\boldsymbol{r}') \right\rangle \tag{3.258}$$

defines the contribution to the suspension pressure due to solvent–solvent interactions at the position of the upper side of the volume element. A similar expression can be written down for P^{ss} at the lower side. It thus follows that

$$\begin{aligned} \boldsymbol{M}_z^{(2)} &= -\hat{\boldsymbol{e}}_z \lim_{\delta_z \to 0} \frac{1}{\delta_z} \left[P^{\mathrm{ss}}(\boldsymbol{r} + \tfrac{1}{2}\delta_z \hat{\boldsymbol{e}}_z, t) - P^{\mathrm{ss}}(\boldsymbol{r} - \tfrac{1}{2}\delta_z \hat{\boldsymbol{e}}_z, t) \right] \\ &= -\hat{\boldsymbol{e}}_z \frac{\partial P^{\mathrm{ss}}(\boldsymbol{r}, t)}{\partial z} \end{aligned}$$

In the same way, the contributions to $\boldsymbol{M}^{(2)}$ from the left and right sides, and from the front and back sides, of the volume element are obtained. Adding these contributions leads to

$$\boldsymbol{M}^{(2)} = -\nabla P^{\mathrm{ss}}(\boldsymbol{r}, t) \tag{3.259}$$

Thus from Eqs. (3.251), (3.257), and (3.259) we find the following expression for the divergence of the stress tensor that arises from solvent–solvent interactions:

$$\nabla \cdot \boldsymbol{\Sigma}^{\mathrm{ss}} = \eta_0 \nabla^2 \boldsymbol{U}(\boldsymbol{r}, t) - \nabla P^{\mathrm{ss}}(\boldsymbol{r}, t) \tag{3.260}$$

Note that P^{ss} is not just determined by boundary conditions when the suspension is inhomogeneous.

3.13.2 Total Stress Tensor

On the Smoluchowski time scale, as discussed before, the interaction force $\boldsymbol{F}_j$ in Eq. (3.242) balances with the hydrodynamic force in Eq. (3.248), i.e.

$$\boldsymbol{F}_j + \boldsymbol{F}_j^{\mathrm{h}} = \boldsymbol{0} \tag{3.261}$$

The first term in Eq. (3.247) for the particle–solvent stress thus cancels with the particle–particle stress in Eq. (3.244). Adding Eqs. (3.244), (3.247), and (3.260) therefore leads to the following expression for the divergence of the total stress tensor:

$$\begin{aligned} \nabla \cdot \boldsymbol{\Sigma} = {} & \eta_0 \nabla^2 \boldsymbol{U}(\boldsymbol{r}, t) - \nabla P^{\mathrm{ss}}(\boldsymbol{r}, t) \\ & - \sum_{j=1}^{N} \left\langle \oint_{\partial V_j(\boldsymbol{r}_j, \hat{\boldsymbol{u}}_j)} \mathrm{d}S' \, \delta(\boldsymbol{r} - \boldsymbol{r}') \boldsymbol{f}^{\mathrm{h}}(\boldsymbol{r}') \right\rangle \end{aligned} \tag{3.262}$$

This seemingly simple expression is valid for homogeneous suspensions as well as systems with large gradients in shear rate, concentration, and orientational order parameter. Suspension properties should not vary significantly over distances equal to the thickness of the rods, but may vary significantly over distances equal to the length of the rods.

3.13.3
Stress Tensor for Homogeneous Suspensions

Since $\boldsymbol{r}' \in \partial V_j$ in the integrand in Eq. (3.262), the magnitude of $\boldsymbol{r}' - \boldsymbol{r}_j$ is never larger than the linear dimension of the rigid colloidal particles. Hence, for not too large gradients of suspension properties, the delta distribution $\delta(\boldsymbol{r} - \boldsymbol{r}')$ can be Taylor-expanded around $\boldsymbol{r}' = \boldsymbol{r}_j$,

$$\delta(\boldsymbol{r} - \boldsymbol{r}') = \delta(\boldsymbol{r} - \boldsymbol{r}_j) + \sum_{n=1}^{\infty} \frac{1}{n!} (\boldsymbol{r}_j - \boldsymbol{r}')^n \odot \nabla^n \delta(\boldsymbol{r} - \boldsymbol{r}_j)$$

where $(\boldsymbol{r}_j - \boldsymbol{r}')^n$ and ∇^n are polyadic products, and $\odot$ is the n-fold contraction of these two products. Substitution of this expansion into Eq. (3.262) gives

$$\nabla \cdot \boldsymbol{\Sigma} = \eta_0 \nabla^2 \boldsymbol{U}(\boldsymbol{r}, t) - \nabla P^{\mathrm{ss}}(\boldsymbol{r}, t) - \sum_{j=1}^{N} \langle \delta(\boldsymbol{r} - \boldsymbol{r}_j) \boldsymbol{F}_j^{\mathrm{h}} \rangle \tag{3.263}$$

$$- \sum_{n=1}^{\infty} \frac{1}{n!} \nabla^n \sum_{j=1}^{N} \left\langle \delta(\boldsymbol{r} - \boldsymbol{r}_j) \odot \oint_{\partial V_j(\boldsymbol{r}_j, \hat{\boldsymbol{u}}_j)} \mathrm{d}S' \, (\boldsymbol{r}_j - \boldsymbol{r}')^n \boldsymbol{f}^{\mathrm{h}}(\boldsymbol{r}') \right\rangle$$

Consider a flow in the x direction with its gradient in the y direction. Since all suspension properties do not vary on the xz plane, the stress tensor is a function of y only. Hence,

$$\nabla \cdot \Delta\boldsymbol{\Sigma}(\boldsymbol{r}) = \hat{\boldsymbol{e}}_2 \cdot \frac{d\Delta\boldsymbol{\Sigma}(y)}{dy}$$

$$= -\frac{\partial}{\partial y} \sum_{j=1}^{N} \langle H(y - y_j) \, \delta(x - x_j) \, \delta(z - z_j) \, \boldsymbol{F}_j^h \rangle$$

where $\hat{\boldsymbol{e}}_2$ is the unit vector in the y-direction and where H is the Heaviside unit step function. Here it is used that $\delta(y - y_j) = \partial H(y - y_j)/\partial y$. For a homogeneous system, volume averaging thus leads to,

$$\hat{\boldsymbol{e}}_2 \cdot \Delta\boldsymbol{\Sigma}(y) = -\frac{1}{V} \int d\boldsymbol{r} \sum_{j=1}^{N} \langle H(y - y_j) \, \delta(x - x_j) \, \delta(z - z_j) \, \boldsymbol{F}_j^h \rangle$$

$$= -\frac{1}{V} \sum_{j=1}^{N} \langle (h - y_j) \, \boldsymbol{F}_j^h \rangle \;=\; \hat{\boldsymbol{e}}_2 \cdot \frac{1}{V} \sum_{j=1}^{N} \langle \boldsymbol{r}_j \, \boldsymbol{F}_j^h \rangle,$$

where h is the height of the box in the gradient direction. For the other components the same analysis can be repeated, thus leading to,

$$\Delta\boldsymbol{\Sigma} \;=\; \frac{1}{V}\sum_{j=1}^{N}\left\langle \boldsymbol{r}_j\,\boldsymbol{F}_j^h\right\rangle \tag{3.264}$$

In the last term in Eq. (3.263), only the leading order gradient contribution is non-zero for homogeneous suspensions, so that,

$$\begin{aligned}\sum_{n=1}^{\infty}\frac{1}{n!}\nabla^n\sum_{j=1}^{N}\left\langle \delta(\boldsymbol{r}-\boldsymbol{r}_j)\;\odot\oint_{\partial V_j(\boldsymbol{r}_j,\hat{\boldsymbol{u}}_j)} dS'\,(\boldsymbol{r}_j-\boldsymbol{r}')^n\,\boldsymbol{f}^h(\boldsymbol{r}')\right\rangle\\ =-\nabla\cdot\sum_{j=1}^{N}\left\langle \delta(\boldsymbol{r}-\boldsymbol{r}_j)\oint_{\partial V_j(\boldsymbol{r}_j,\hat{\boldsymbol{u}}_j)} dS'\,(\boldsymbol{r}'-\boldsymbol{r}_j)\,\boldsymbol{f}^h(\boldsymbol{r}')\right\rangle\end{aligned} \tag{3.265}$$

From Eqs. (3.263), (3.264), and (3.265), the volume averaged stress tensor for a homogeneous system is found to be equal to

$$\begin{aligned}\boldsymbol{\Sigma}=\eta_0\left[\nabla\boldsymbol{U}+(\nabla\boldsymbol{U})^T\right]-P^{ss}\,\hat{\boldsymbol{I}}\\ +\frac{1}{V}\sum_{j=1}^{N}\left\langle \boldsymbol{r}_j\,\boldsymbol{F}_j^h\right\rangle+\frac{1}{V}\sum_{j=1}^{N}\left\langle\oint_{\partial V_j(\boldsymbol{r}_j,\hat{\boldsymbol{u}}_j)} dS'\,(\boldsymbol{r}'-\boldsymbol{r}_j)\,\boldsymbol{f}^h(\boldsymbol{r}')\right\rangle\end{aligned} \tag{3.266}$$

which reproduces the expression for the stress tensor as derived by Batchelor (1970) and later by Strating (1995) in different ways.

3.13.4
Explicit Evaluation of Stress Tensor for Very Long and Thin Rods

Within the bead model for the rods (see Fig. 3.3), the surface integral that appears in Eq. (3.262) for the stress tensor can be written as a sum over beads as (with ∂V_α the surface area of bead α)

$$\oint_{\partial V_j(\boldsymbol{r}_j,\hat{\boldsymbol{u}}_j)}\mathrm{d}S'\,\delta(\boldsymbol{r}-\boldsymbol{r}')\boldsymbol{f}^{\mathrm{h}}(\boldsymbol{r}')=\sum_{\alpha}\delta(\boldsymbol{r}-\boldsymbol{r}_j-\alpha D\hat{\boldsymbol{u}}_j)\boldsymbol{F}^{\mathrm{h}}_{j,\alpha}$$

where $\boldsymbol{F}^{\mathrm{h}}_{j,\alpha}$ is the force that the fluid exerts on the αth bead of rod j. Hence,

$$\begin{aligned}\nabla\cdot\boldsymbol{\Sigma}=\eta_0\nabla^2\boldsymbol{U}(\boldsymbol{r},t)-\nabla P^{\mathrm{ss}}(\boldsymbol{r},t)\\ -\sum_{j=1}^{N}\sum_{\alpha}\langle\delta(\boldsymbol{r}-\boldsymbol{r}_j-\alpha D\hat{\boldsymbol{u}}_j)\boldsymbol{F}^{\mathrm{h}}_{j,\alpha}\rangle\end{aligned} \tag{3.267}$$

In order to evaluate the summation over beads, an explicit expression for $\boldsymbol{F}^{\mathrm{h}}_{j,\alpha}$ must be found. Consider the flow velocity $\boldsymbol{u}_{0,\alpha}$ of the fluid that would have existed in the absence of bead α. According to Eq. (3.18), this velocity is equal to

$$\boldsymbol{u}_{0,\alpha} = \boldsymbol{U}^{\star}_{\alpha} - \sum_{\beta\neq\alpha} \int_{\partial V_\beta} \mathrm{d}S' \, \boldsymbol{T}(\boldsymbol{r}_\alpha - \boldsymbol{r}') \cdot \boldsymbol{f}^{\mathrm{h},\star}_{\beta}(\boldsymbol{r}') \tag{3.268}$$

where the star is used to indicate the absence of bead α. Here, $\boldsymbol{U}^{\star}$ is the fluid flow velocity at the position of bead α that is due to the presence of the remaining rods and the externally imposed flow field, in the absence of bead α. The force $\boldsymbol{f}^{\mathrm{h},\star}_{\beta}(\boldsymbol{r}')$ is the force per unit area that the fluid exerts on the surface element at $\boldsymbol{r}'$ on the surface ∂V_β of bead β, again in the absence of bead α. For very long and thin rods, the majority of beads β experience a flow and force that are only a little different from those in the absence of bead α. We shall therefore set $\boldsymbol{f}^{\mathrm{h},\star}_{\beta}$ equal to the actual force $\boldsymbol{f}^{\mathrm{h}}_{\beta}$ in the presence of bead α. Within the bead model for the rod, Eq. (3.268) then reads

$$\boldsymbol{u}_{0,\alpha} = \boldsymbol{U}^{\star}_{\alpha} - \sum_{\beta\neq\alpha} \boldsymbol{T}(\boldsymbol{r}_\alpha - \boldsymbol{r}_\beta) \cdot \boldsymbol{F}^{\mathrm{h}}_{\beta} \tag{3.269}$$

where, as before, $\boldsymbol{F}^{\mathrm{h}}_{\beta}$ is the total force that the fluid exerts on bead β. When the gradients in the fluid flow velocity $\boldsymbol{U}^{\star}_{\alpha}$, stemming from other rods and an externally imposed field, are negligible on the length scale equal to the thickness D of the rod, the force on bead α is simply equal to $\boldsymbol{F}^{\mathrm{h}}_{\alpha} = -\gamma[\boldsymbol{v}_\alpha - \boldsymbol{u}_{0,\alpha}]$, where $\gamma = 3\pi\eta_0 D$ is the Stokes friction coefficient of a single bead and $\boldsymbol{v}_\alpha$ is the translational velocity of bead α. Hence, from Eqs. (3.269) and (3.23) for the Oseen tensor,

$$\boldsymbol{F}^{\mathrm{h}}_{j,\alpha} = -\gamma[\boldsymbol{v}_{j,\alpha} - \boldsymbol{U}^{\star}_{j,\alpha}] - \tfrac{3}{8}[\hat{\boldsymbol{I}} + \hat{\boldsymbol{u}}_j\hat{\boldsymbol{u}}_j] \cdot \sum_{\beta\neq\alpha} \frac{1}{|\alpha-\beta|} \boldsymbol{F}^{\mathrm{h}}_{j,\beta} \tag{3.270}$$

Now consider summations of the form

$$\sum_{\alpha} G(\alpha) \boldsymbol{F}^{\mathrm{h}}_{j,\alpha} \tag{3.271}$$

Multiplying both sides of Eq. (3.270) by $G(\alpha)$ and summing over α leads to

$$\begin{aligned}\sum_{\alpha} G(\alpha) \boldsymbol{F}^{\mathrm{h}}_{j,\alpha} = {} & -\gamma \sum_{\alpha} G(\alpha)[\boldsymbol{v}_{j,\alpha} - \boldsymbol{U}^{\star}_{j,\alpha}] \\ & -\tfrac{3}{8}[\hat{\boldsymbol{I}} + \hat{\boldsymbol{u}}_j\hat{\boldsymbol{u}}_j] \cdot \sum_{\alpha} \sum_{\beta\neq\alpha} \frac{G(\alpha)}{|\alpha-\beta|} \boldsymbol{F}^{\mathrm{h}}_{j,\beta}\end{aligned} \tag{3.272}$$

In the Appendix (see Section 3.16.4) it is shown that for specific functions $G(\alpha)$ it follows from the above relation that

$$\sum_{\alpha} G(\alpha)\boldsymbol{F}^{\mathrm{h}}_{j,\alpha} = -\frac{4}{3}\frac{\gamma}{\ln(L/D)}[\hat{\boldsymbol{I}} - \tfrac{1}{2}\hat{\boldsymbol{u}}_j\hat{\boldsymbol{u}}_j]\cdot\sum_{\alpha} G(\alpha)[\boldsymbol{v}_{j,\alpha} - \boldsymbol{U}^{\star}_{j,\alpha}] \tag{3.273}$$

For the sum in Eq. (3.267), the function $G(\alpha)$ is identified in Section 3.16.4, and the validity of Eq. (3.272) for that particular $G(\alpha)$ is proven. Using this result in Eq. (3.267) immediately leads to

$$\begin{aligned}\nabla\cdot\boldsymbol{\Sigma} &= \eta_0\nabla^2\boldsymbol{U}(\boldsymbol{r},t) - \nabla P^{\mathrm{ss}}(\boldsymbol{r},t) \\ &+ \frac{4}{3}\frac{\gamma}{\ln(L/D)}\left\langle\sum_{j=1}^{N}[\hat{\boldsymbol{I}} - \tfrac{1}{2}\hat{\boldsymbol{u}}_j\hat{\boldsymbol{u}}_j]\cdot\sum_{\alpha}\delta(\boldsymbol{r}-\boldsymbol{r}_j-\alpha D\hat{\boldsymbol{u}}_j)[\boldsymbol{v}_{j,\alpha} - \boldsymbol{U}^{\star}_{j,\alpha}]\right\rangle\end{aligned} \tag{3.274}$$

For each j, the ensemble average that involves the solvent velocity $\boldsymbol{U}^{\star}$ can be written as

$$\begin{aligned}&\left\langle[\hat{\boldsymbol{I}} - \tfrac{1}{2}\hat{\boldsymbol{u}}_j\hat{\boldsymbol{u}}_j]\cdot\sum_{\alpha}\delta(\boldsymbol{r}-\boldsymbol{r}_j-\alpha D\hat{\boldsymbol{u}}_j)\boldsymbol{U}^{\star}_{j,\alpha}\right\rangle \\ &= \int \mathrm{d}\boldsymbol{r}_j \oint \mathrm{d}\hat{\boldsymbol{u}}_j\, P(\boldsymbol{r}_j,\hat{\boldsymbol{u}}_j,t)[\hat{\boldsymbol{I}} - \tfrac{1}{2}\hat{\boldsymbol{u}}_j\hat{\boldsymbol{u}}_j]\cdot\sum_{\alpha}\delta(\boldsymbol{r}-\boldsymbol{r}_j-\alpha D\hat{\boldsymbol{u}}_j)\langle\boldsymbol{U}^{\star}_{j,\alpha}\rangle^{(\mathrm{c})}\end{aligned}$$

where $\langle\cdots\rangle^{(\mathrm{c})}$ denotes ensemble averaging with respect to the conditional PDF $P^{(\mathrm{c})}$ of $\{\boldsymbol{r}_1,\ldots,\boldsymbol{r}_{j-1},\boldsymbol{r}_{j+1},\ldots,\boldsymbol{r}_N,\hat{\boldsymbol{u}}_2,\ldots,\hat{\boldsymbol{u}}_{j-1},\hat{\boldsymbol{u}}_{j+1},\ldots,\hat{\boldsymbol{u}}_N\}$ for prescribed $\boldsymbol{r}_j$ and $\hat{\boldsymbol{u}}_j$, which is equal to

$$\begin{aligned}&P^{(\mathrm{c})}(\boldsymbol{r}_1,\ldots,\boldsymbol{r}_{j-1},\boldsymbol{r}_{j+1},\ldots,\boldsymbol{r}_N,\hat{\boldsymbol{u}}_1,\ldots,\hat{\boldsymbol{u}}_{j-1},\hat{\boldsymbol{u}}_{j+1},\ldots,\hat{\boldsymbol{u}}_N \mid \boldsymbol{r}_j,\hat{\boldsymbol{u}}_j,t) \\ &\quad\equiv P(\boldsymbol{r}_1,\ldots,\boldsymbol{r}_N,\hat{\boldsymbol{u}}_1,\ldots,\hat{\boldsymbol{u}}_N,t)/P(\boldsymbol{r}_1,\hat{\boldsymbol{u}}_1,t)\end{aligned}$$

We can thus rewrite Eq. (3.267) for the divergence of the stress tensor as

$$\begin{aligned}\nabla\cdot\boldsymbol{\Sigma} &= \eta_0\nabla^2\boldsymbol{U}(\boldsymbol{r},t) - \nabla P^{\mathrm{ss}}(\boldsymbol{r},t) \\ &+\frac{4}{3}\frac{\gamma}{\ln(L/D)}\frac{1}{N}\sum_{j=1}^{N}\int \mathrm{d}\boldsymbol{r}_j \oint \mathrm{d}\hat{\boldsymbol{u}}_j\,\rho(\boldsymbol{r}_j,\hat{\boldsymbol{u}}_j,t) \\ &\times[\hat{\boldsymbol{I}} - \tfrac{1}{2}\hat{\boldsymbol{u}}_j\hat{\boldsymbol{u}}_j]\cdot\sum_{\alpha}\delta(\boldsymbol{r}-\boldsymbol{r}_j-\alpha D\hat{\boldsymbol{u}}_j)[\boldsymbol{v}_{j,\alpha} - \langle\boldsymbol{U}^{\star}_{j,\alpha}\rangle^{(\mathrm{c})}]\end{aligned} \tag{3.275}$$

where $\rho(\boldsymbol{r}, \hat{\boldsymbol{u}}, t)$ is the density of rods with orientation $\hat{\boldsymbol{u}}$ at position $\boldsymbol{r}$,

$$\rho(\boldsymbol{r}, \hat{\boldsymbol{u}}, t) = NP(\boldsymbol{r}, \hat{\boldsymbol{u}}, t) \tag{3.276}$$

The conditional ensemble average $\langle \boldsymbol{U}^{\star}_{j,\alpha} \rangle^{(\mathrm{c})}$ is the contribution to the solvent flow velocity at the position of bead α of rod j, in the absence of that bead, which originates from the presence of other rods and the externally imposed flow, averaged over the positions and orientations of all other rods with a prescribed position and orientation of rod j. This average is to a good approximation equal to the suspension flow velocity $\boldsymbol{U}_{j,\alpha}$ at the position of bead α of rod j, i.e.

$$\langle \boldsymbol{U}^{\star}_{j,\alpha} \rangle^{(\mathrm{c})} = \boldsymbol{U}_{j,\alpha} \tag{3.277}$$

Using the fact that the bead velocity is given by

$$\boldsymbol{v}_{j,\alpha} = \boldsymbol{v}_j + \alpha D \boldsymbol{\Omega}_j \times \hat{\boldsymbol{u}}_j \tag{3.278}$$

together with Eqs. (3.170) and (3.166) for the translational and rotational velocity of a rod, Eq. (3.275) for the divergence of the stress tensor thus leads to (mathematical details are given in the Appendix, Section 3.16.5)

$$\begin{aligned}
&\nabla \cdot \boldsymbol{\Sigma}(\boldsymbol{r}, t) \\
&= \eta_0 \nabla^2 \boldsymbol{U}(\boldsymbol{r}, t) - \nabla P^{\mathrm{ss}}(\boldsymbol{r}, t) + \frac{k_{\mathrm{B}} T}{L^2} \oint \mathrm{d}\hat{\boldsymbol{u}} \\
&\quad \times \int_{-L/2}^{L/2} \mathrm{d}x \left\{ 12 \frac{x}{L} \hat{\boldsymbol{u}} \times \left[\hat{\mathcal{R}} \rho(\boldsymbol{r} - x\hat{\boldsymbol{u}}_0, \hat{\boldsymbol{u}}, t) \right]_{\hat{\boldsymbol{u}}_0 = \hat{\boldsymbol{u}}} - L \nabla \rho(\boldsymbol{r} - x\hat{\boldsymbol{u}}, \hat{\boldsymbol{u}}, t) \right\} \\
&\quad + \frac{2 D k_{\mathrm{B}} T}{L^2} \oint \mathrm{d}\hat{\boldsymbol{u}} \oint \mathrm{d}\hat{\boldsymbol{u}}' \int_{-L/2}^{L/2} \mathrm{d}x \int_{-L/2}^{L/2} \mathrm{d}l \int_{-L/2}^{L/2} \mathrm{d}l' \, \rho(\boldsymbol{r} - x\hat{\boldsymbol{u}}, \hat{\boldsymbol{u}}, t) \\
&\quad \times \left\{ 12 \frac{x}{L} \hat{\boldsymbol{u}} \times \left[\hat{\mathcal{R}} |\hat{\boldsymbol{u}} \times \hat{\boldsymbol{u}}'| \, \rho(\boldsymbol{r} - x\hat{\boldsymbol{u}}_0 - l\hat{\boldsymbol{u}} - l'\hat{\boldsymbol{u}}', \hat{\boldsymbol{u}}', t) \right]_{\hat{\boldsymbol{u}}_0 = \hat{\boldsymbol{u}}} \right. \\
&\qquad \left. - |\hat{\boldsymbol{u}} \times \hat{\boldsymbol{u}}'| \, L \nabla \rho(\boldsymbol{r} - (x+l)\hat{\boldsymbol{u}} - l'\hat{\boldsymbol{u}}', \hat{\boldsymbol{u}}', t) \right\} \\
&\quad + \frac{4\pi\eta_0}{L \ln(L/D)} \oint \mathrm{d}\hat{\boldsymbol{u}} \int_{-L/2}^{L/2} \mathrm{d}x \int_{-L/2}^{L/2} \mathrm{d}x' \, \rho(\boldsymbol{r} - x\hat{\boldsymbol{u}}, \hat{\boldsymbol{u}}, t)
\end{aligned}$$

$$\times [\hat{\boldsymbol{I}} - \tfrac{1}{2}\hat{\boldsymbol{u}}\hat{\boldsymbol{u}}] \cdot \Big\{ \boldsymbol{U}(\boldsymbol{r}+(x'-x)\hat{\boldsymbol{u}},t) - \boldsymbol{U}(\boldsymbol{r},t)$$

$$- 12\frac{xx'}{L^2}\hat{\boldsymbol{u}} \times [\hat{\boldsymbol{u}} \times \boldsymbol{U}(\boldsymbol{r}+(x'-x)\hat{\boldsymbol{u}},t)] \Big\} \tag{3.279}$$

Here, summations over bead indices α and β are replaced by integrals with respect to x and x', respectively (see Eqs. (3.321) and (3.324) in Section 3.16.5). The notation $[\hat{\mathcal{R}}(\cdots)]_{\hat{\boldsymbol{u}}_0=\hat{\boldsymbol{u}}}$ is used to indicate that the differentiation with respect to $\hat{\boldsymbol{u}}$ should be performed first, after which $\hat{\boldsymbol{u}}_0$ should be taken equal to $\hat{\boldsymbol{u}}$.

The first two contributions to the stress tensor are solvent contributions, the third term stems from Brownian forces, the fourth term from direct interactions, while the last term accounts for the suspension flow.

Contrary to commonly used expressions for the stress tensor for inhomogeneous suspensions, Eq. (3.279) contains convolution-type integrals. An expression that is similar to commonly used expressions for the stress tensor is obtained by gradient-expanding the convolution-type integrals and truncating this expansion after the fourth order in ∇ contributions. Such a truncation is expected to work only when the gradients are not very large. Our expression (3.279) for the divergence of the stress tensor, however, is valid even in the presence of large gradients.

3.13.5
Stress Tensor for a Homogeneous System Expressed in Terms of Order Parameter

For a homogeneous system, where the concentration, orientational order parameter and shear rate are independent of position, the probability density function ρ in the integrals in Eq. (3.279) can be gradient-expanded up to leading order in gradients that survives the convolution type of integrals. For example,

$$\rho(\boldsymbol{r}-x\hat{\boldsymbol{u}},\hat{\boldsymbol{u}},t) = \rho(\boldsymbol{r},\hat{\boldsymbol{u}},t) - x\hat{\boldsymbol{u}}\cdot\nabla\rho(\boldsymbol{r},\hat{\boldsymbol{u}},t)$$

$$+\tfrac{1}{2}x^2\hat{\boldsymbol{u}}\hat{\boldsymbol{u}} : \nabla\nabla\,\rho(\boldsymbol{r},\hat{\boldsymbol{u}},t) + \mathcal{O}(\nabla^3) \tag{3.280}$$

Using the same Ginzburg–Landau expansion (3.217) as before, a lengthy but straightforward calculation leads to the following expression for the stress tensor [where the fourth-order tensor $\boldsymbol{S}^{(4)}$ is defined in Eq. (3.220)]

$$\boldsymbol{\Sigma} = -P\,\hat{\boldsymbol{I}} + \boldsymbol{\Sigma}_{\mathrm{D}} \tag{3.281}$$

with $\boldsymbol{\Sigma}_{\mathrm{D}}$ the deviatoric part of the stress tensor,

$$\boldsymbol{\Sigma}_{\mathrm{D}} = 2\eta_0\dot{\gamma}\,\hat{\boldsymbol{E}} + 3\bar{\rho}k_{\mathrm{B}}T\big[\boldsymbol{S} - \tfrac{1}{3}\,\hat{\boldsymbol{I}} + (L/D)\varphi(\boldsymbol{S}^{(4)} : \boldsymbol{S} - \boldsymbol{S}\cdot\boldsymbol{S}) + \tfrac{1}{6}Pe_{\mathrm{r}}(\boldsymbol{S}^{(4)} : \hat{\boldsymbol{E}} - \tfrac{1}{3}\,\hat{\boldsymbol{I}}\,\boldsymbol{S} : \hat{\boldsymbol{E}})\big] \tag{3.282}$$

where Eq. (3.169) for D_{r} has been used. Here, $\bar{\rho} = N/V$ is the number density of the homogeneous system, $\varphi = \frac{1}{4}\pi D^2 L\bar{\rho}$ is the volume fraction of rods, and $Pe_{\mathrm{r}} = \dot{\gamma}/D_{\mathrm{r}}$ is the same *bare rotational Peclet number* that we encountered before. The tensor $\hat{\boldsymbol{E}}$ is, as before, equal to $\boldsymbol{E}/\dot{\gamma}$. Furthermore,

$$P = P^{\mathrm{ss}} + \bar{\rho}k_{\mathrm{B}}T[1 + \tfrac{5}{4}(L/D)\varphi(1 - \tfrac{3}{5}\boldsymbol{S} : \boldsymbol{S}) - \tfrac{1}{6}Pe_{\mathrm{r}}\boldsymbol{S} : \hat{\boldsymbol{E}}] \tag{3.283}$$

is the pressure.

The first term $\boldsymbol{S} - \frac{1}{3}\,\hat{\boldsymbol{I}}$ stems from the Brownian contribution in Eq. (3.279), the second term $\sim L/D$ from the direct interaction terms, and the term $\sim Pe_{\mathrm{r}}$ from the suspension flow terms.

Note that from Eq. (3.219), using the expression (3.169) for D_{r}, the deviatoric stress tensor can be rewritten more elegantly as

$$\boldsymbol{\Sigma}_{\mathrm{D}} = 2\eta_0\dot{\gamma}\left[\hat{\boldsymbol{E}} + \frac{(L/D)^2}{3\ln(L/D)}\varphi\left(\hat{\boldsymbol{\Gamma}}\cdot\boldsymbol{S} + \boldsymbol{S}\cdot\hat{\boldsymbol{\Gamma}}^{\mathrm{T}} - \boldsymbol{S}^{(4)} : \hat{\boldsymbol{E}} - \tfrac{1}{3}\,\hat{\boldsymbol{I}}\,\boldsymbol{S} : \hat{\boldsymbol{E}} - \frac{1}{\dot{\gamma}}\frac{\mathrm{d}\boldsymbol{S}}{\mathrm{d}t}\right)\right] \tag{3.284}$$

This form makes the proportionality of the stress tensor with the shear rate more explicit.

A similar expression for the stress tensor has been derived by Doi and Edwards (1978a), Doi and Edwards (1978b), Doi (1981), Kuzuu and Doi (1983) and Marrucci and Maffettone (1989). For non-interacting rods, i.e. for $(L/D)\varphi = 0$, Hinch and Leal (1976) found a constitutive relation similar to Eq. (3.284) by interpolating between known expressions for low and high shear rates.

3.14 Viscoelastic Response Functions

In the present section we shall analyze the viscous behavior of rod suspensions on the basis of the equation of motion (3.219) for $\boldsymbol{S}(t)$ and the Navier–Stokes equation with Eq. (3.284) for the stress tensor [together with the closure relation (3.227)]. Equations (3.219) and (3.284) are quite similar to those derived

on the basis of phenomenological arguments by Doi and Edwards (1978a), Doi and Edwards (1978b), Doi (1981), Kuzuu and Doi (1983), and Doi and Edwards (1986). We shall refer to this latter theory as the DEK theory, where DEK stands for "Doi–Edwards–Kuzuu". Our predictions will be compared to those of the DEK theory.

The DEK theory appears in the literature in various forms. Sometimes an effective rotational diffusion coefficient is used in the Smoluchowski equation and the equation of motion (3.219) instead of the bare diffusion coefficient D_{r}. This effective diffusion coefficient is calculated independently as a function of the order parameter and concentration. The present approach shows that this is not correct: the bare diffusion coefficient should be used in the equation of motion (3.219) and expressions (3.282) and (3.284) for the stress tensor. Interactions between rods are explicitly accounted for in these expressions. Sometimes the interaction contributions are omitted, and the above-mentioned effective diffusion coefficient is used. The effective diffusion coefficient is then assumed to account for interactions between rods. Either the interaction contributions are kept as they stand and the bare diffusion coefficient is used, or the interaction contributions are omitted and an effective diffusion coefficient should be used.

Viscoelastic response functions will be discussed for both low shear rates, where analytic expressions can be derived, and high shear rates, where numerical results will be given. For higher shear rates, shear thinning curves and nonlinear oscillatory response functions will be discussed. These results will be compared to other theories, computer simulations, and experiments. A remarkable feature is that the shear viscosity is predicted to vary linearly with concentration up to the isotropic–nematic phase transition, which is confirmed by computer simulations. Comparing theory with experimental data on *fd* virus suspensions, it turns out that a slight degree of flexibility has a large effect on the viscoelastic response functions.

3.14.1 Shear Viscosity and Normal Stresses for Low Shear Rates

In order to obtain analytic results for the leading-order shear-rate dependence of the zero-frequency shear viscosity and normal stress differences, the orientational order-parameter tensor is expanded up to third power in the shear rate,

$$\boldsymbol{S} = \tfrac{1}{3}\hat{\boldsymbol{I}} + \dot{\gamma}\Delta\boldsymbol{S}_1 + \dot{\gamma}^2\Delta\boldsymbol{S}_2 + \dot{\gamma}^3\Delta\boldsymbol{S}_3 + \cdots \tag{3.285}$$

Substitution of this expansion into the stationary form of the equation of motion (3.219) and noting that $\hat{\boldsymbol{I}} : \Delta\boldsymbol{S}_j = 0$, a straightforward but somewhat

lengthy calculation leads to the following expressions for the $\Delta \boldsymbol{S}_j$:

$$\dot{\gamma}\,\Delta \boldsymbol{S}_1 = \frac{1}{15}\frac{\dot{\gamma}}{D_{\mathrm{r}}^{\mathrm{eff}}}\,\hat{\boldsymbol{E}}$$

$$\dot{\gamma}^2 \Delta \boldsymbol{S}_2 = \frac{1}{450}\left(\frac{\dot{\gamma}}{D_{\mathrm{r}}^{\mathrm{eff}}}\right)^2 \left[\begin{pmatrix} 3 & 0 & 0 \\ 0 & -2 & 0 \\ 0 & 0 & -1 \end{pmatrix} + \frac{1}{10}\frac{D_{\mathrm{r}}}{D_{\mathrm{r}}^{\mathrm{eff}}}\frac{L}{D}\varphi \begin{pmatrix} 1 & 0 & 0 \\ 0 & 1 & 0 \\ 0 & 0 & -2 \end{pmatrix}\right]$$

$$\dot{\gamma}^3 \Delta \boldsymbol{S}_3 = \frac{1}{1125}\left(\frac{\dot{\gamma}}{D_{\mathrm{r}}^{\mathrm{eff}}}\right)^3 \left[-\frac{7}{3} + \frac{3}{10}\frac{D_{\mathrm{r}}}{D_{\mathrm{r}}^{\mathrm{eff}}}\frac{L}{D}\varphi + \frac{1}{50}\left(\frac{D_{\mathrm{r}}}{D_{\mathrm{r}}^{\mathrm{eff}}}\frac{L}{D}\varphi\right)^2\right] \hat{\boldsymbol{E}} \tag{3.286}$$

The concentration-dependent, effective rotational diffusion coefficient $D_{\mathrm{r}}^{\mathrm{eff}}$ is given in Eq. (3.230).

As can be seen from the above expressions, the actual expansion parameter is the *dressed rotational Peclet number*,

$$Pe_{\mathrm{r}}^{\mathrm{eff}} = \dot{\gamma}/D_{\mathrm{r}}^{\mathrm{eff}} \tag{3.287}$$

The expansion (3.285) is therefore valid only when $\dot{\gamma}/D_{\mathrm{r}}^{\mathrm{eff}}$ is small. For concentrations close to the spinodal line, where $D_{\mathrm{r}}^{\mathrm{eff}}$ is much smaller than the free rotational diffusion coefficient D_{r}, the shear rate should be equally smaller in order for the expansion (3.285) to be valid. Substitution of Eqs. (3.286) into Eq. (3.284) for the deviatoric part of the stress tensor leads to

$$\boldsymbol{\Sigma}_{\mathrm{D}} = 2\eta^{\mathrm{eff}}\dot{\gamma}\,\hat{\boldsymbol{E}} + \eta_0 \frac{1}{120}\frac{\dot{\gamma}^2}{D_{\mathrm{r}}^{\mathrm{eff}}}\alpha\varphi \begin{pmatrix} 19 & 0 & 0 \\ 0 & -11 & 0 \\ 0 & 0 & -8 \end{pmatrix} \tag{3.288}$$

where the coefficient α is equal to

$$\alpha = \frac{8}{45}\frac{(L/D)^2}{\ln(L/D)} \tag{3.289}$$

and the suspension shear viscosity η^{eff} is found to be equal to

$$\eta^{\mathrm{eff}} = \eta_0 \left\{1 + \left[1 - \frac{1}{50}\left(\frac{\dot{\gamma}}{D_{\mathrm{r}}^{\mathrm{eff}}}\right)^2\right]\alpha\varphi + \frac{1}{1500}\frac{\dot{\gamma}^2 D_{\mathrm{r}}}{(D_{\mathrm{r}}^{\mathrm{eff}})^3}\alpha\frac{L}{D}\varphi^2\right\} \tag{3.290}$$

up to second order in the shear rate. Expanding the dressed Peclet number with respect to the concentration yields, up to second order in concentration,

$$\eta^{\text{eff}} = \eta_0 \left\{ 1 + \left[1 - \frac{1}{50} \left(\frac{\dot{\gamma}}{D_{\text{r}}} \right)^2 \right] \alpha\varphi - \frac{11}{1500} \left(\frac{\dot{\gamma}}{D_{\text{r}}} \right)^2 \alpha \frac{L}{D} \varphi^2 \right\} \tag{3.291}$$

Note that the Huggins coefficient (the coefficient for the φ^2-contribution) vanishes at zero shear rate. There is a non-zero Huggins coefficient at zero shear rate when hydrodynamic interactions would have been taken into account. As discussed before, hydrodynamic interactions are not so important for the very long and thin rods under consideration here.

For zero shear rate, Eq. (3.291) for the effective viscosity is the rigid-rod analog of Einstein's equation $\eta^{\text{eff}} = \eta_0(1 + \frac{5}{2}\varphi)$ for the viscosity of very dilute suspensions of spheres. Note, however, that Eq. (3.291) is valid also for larger concentrations. That is, higher-order concentration contributions to the zero-shear viscosity are absent. This linear concentration dependence of the zero-shear suspension viscosity is the result of the use of the form (3.208) for the pair correlation function and the neglect of hydrodynamic interactions. As will be seen later in this section, such a linear concentration dependence is also seen in computer simulations for very long and thin rods.

Normal stress differences due to a weak shear flow follow immediately from Eq. (3.288) as

$$\begin{aligned} N_1 &\equiv \Sigma_{11} - \Sigma_{22} = \eta_0 \frac{1}{4} \frac{\dot{\gamma}^2}{D_{\text{r}}^{\text{eff}}} \alpha\varphi \\ N_2 &\equiv \Sigma_{22} - \Sigma_{33} = -\eta_0 \frac{1}{40} \frac{\dot{\gamma}^2}{D_{\text{r}}^{\text{eff}}} \alpha\varphi \end{aligned} \tag{3.292}$$

Note that α and φ can be large for very long and thin rods, even at low volume fractions φ, so that normal stress differences are predicted to be quite significant.

Expressions for linear response functions to oscillatory shear flow can be obtained by substitution of

$$\boldsymbol{S}(t) = \tfrac{1}{3}\hat{\boldsymbol{I}} + \dot{\gamma}_0[\Delta\boldsymbol{S}_{\text{c}} \cos(\omega t) + \Delta\boldsymbol{S}_{\text{s}} \sin(\omega t)] \tag{3.293}$$

into the equation of motion (3.219). Linearization with respect to the in- and out-of-phase response functions $\Delta\boldsymbol{S}_{\text{c}}$ and $\Delta\boldsymbol{S}_{\text{s}}$, respectively, keeping only linear terms in $\dot{\gamma}_0$, and using Eq. (3.6) for the shear rate $\dot{\gamma}$, one readily finds, in dimensionless form,

$$\boldsymbol{S}(t) = \tfrac{1}{3}\hat{\boldsymbol{I}} + \tfrac{2}{5}(\dot{\gamma}_0/\omega) F(\Omega^{\text{eff}}/6)[\cos(\omega t) + \tfrac{1}{6}\Omega^{\text{eff}} \sin(\omega t)]\, \hat{\boldsymbol{E}} \tag{3.294}$$

where

$$F(x) \equiv \frac{x}{1+x^2} \quad \text{and} \quad \Omega^{\text{eff}} = \omega / D_{\text{r}}^{\text{eff}} \tag{3.295}$$

The dimensionless frequency Ω^{eff} is a dressed, concentration-dependent *rotational Deborah number*. Substitution of Eqs. (3.294) and (3.295) into Eq. (3.284) for the stress tensor gives

$$\boldsymbol{\Sigma}_{\text{D}} = 2\dot{\gamma}_0 \hat{\boldsymbol{E}}[\eta' \cos(\omega t) + \eta'' \sin(\omega t)] \tag{3.296}$$

where the dissipative and storage shear viscosity, respectively, are equal to

$$\begin{aligned} \eta' &= \eta_0 \left[1 + \left(\frac{1}{4} + \frac{9}{2} \frac{F(\Omega^{\text{eff}}/6)}{\Omega^{\text{eff}}} \right) \alpha\varphi \right] \\ \eta'' &= \eta_0 \, \tfrac{3}{4} \, F(\Omega^{\text{eff}}/6) \alpha\varphi \end{aligned} \tag{3.297}$$

To leading order in shear rate, we thus find a Maxwellian behavior of the viscoelastic response function, with a concentration-dependent relaxation time that is set by the effective rotational diffusion coefficient. Note that

$$\frac{\eta^{\text{eff}} - \eta_\infty^{\text{eff}}}{\eta_0} = \tfrac{3}{4}\alpha\varphi = 6 \lim_{\Omega \to \infty} \frac{\eta''}{\Omega^{\text{eff}}} \tag{3.298}$$

where $\eta^{\text{eff}} = \eta_0(1 + \alpha\varphi)$ is the shear viscosity (3.291) at zero shear rate, and $\eta_\infty^{\text{eff}} \equiv \eta'(\Omega^{\text{eff}} \to \infty)$ is the high-frequency, zero-shear-rate viscosity. These are relationships that could be tested experimentally. As before, the predicted linear concentration dependence in Eq. (3.297) should hold over the entire concentration regime (up to the isotropic–nematic phase transition concentration), and could serve as an experimental test for the validity of the approximation (3.208) for the pair correlation function.

3.14.2
Viscoelastic Response at High Shear Rates

For larger shear rates, no analytical results can be obtained in view of the complexity of the equation of motion (3.219). Instead, Eq. (3.219) must be time-integrated numerically, with either a stationary or an oscillating shear rate, until transients have relaxed. The resulting solution is substituted into Eq. (3.284) for the stress tensor, from which viscoelastic response functions can be deduced.

The dimensionless numbers on which the stress response functions under stationary shear flow conditions depend are L/D, $(L/D)\varphi$, and the bare rotational Peclet number (3.189) for dilute systems or the dressed Peclet number

(3.287) for strongly interacting systems. As will be seen, the same Peclet numbers are of interest under oscillatory shear flow, except that the shear rate is replaced by the shear amplitude $\dot{\gamma}_0$ in Eq. (3.6). The frequency dependence is expressed in terms of the dressed Deborah number in Eq. (3.295) or the bare Deborah number

$$\Omega = \omega / D_{\mathrm{r}} \tag{3.299}$$

Numerical results are shown here for $L/D = 50$ as functions of the other dimensionless numbers: the essential features of the viscoelastic response functions do not depend on the aspect ratio for aspect ratios larger than about 10.

In Fig. 3.26 the suspension viscosity is plotted as a function of the squared rotational Peclet number for various concentrations, in both the otherwise isotropic phase (Fig. 3.26a) and the nematic state (Fig. 3.26b). The dashed lines in Fig. 3.26(a) correspond to the small Peclet number expansion (3.290). The range of validity of this expansion is seen to decrease for larger concentrations. The reason for this is that Eq. (3.290) is actually an expansion with respect to the dressed rotational Peclet number (3.287), while the effective rotational diffusion coefficient (3.230) becomes smaller on approaching the isotropic-to-

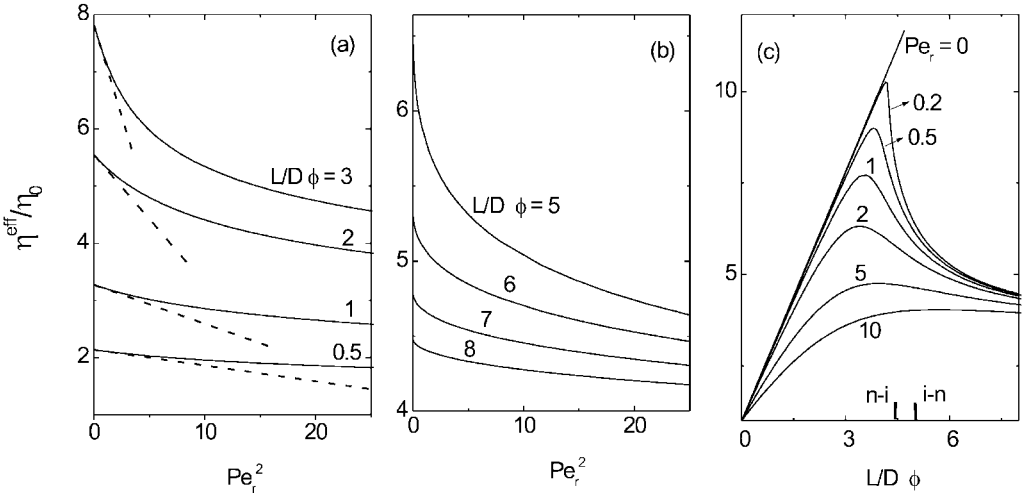

Fig. 3.26 (a) The suspension viscosity η^{eff} for the otherwise isotropic state, normalized by the solvent shear viscosity η_0, as a function of the squared Peclet number for several concentrations, as indicated in the figure. The dashed lines correspond to the low-shear-rate expansion (3.290). Here, and in the other two parts, $L/D = 50$. (b) The same as (a) for the nematic state. (c) The shear viscosity as a function of concentration for various shear rates, as indicated in the figure. The isotropic-to-nematic and nematic-to-isotropic spinodal concentrations are also indicated.

nematic spinodal point. Note that for a nematic there seems to be no regime at small shear rates where the viscosity varies linearly with $\dot{\gamma}^2$, contrary to a paranematic. Furthermore, the suspension viscosity of a nematic decreases with increasing concentration: the rise in stress on adding rods is smaller than its decrease due to the increase of the degree of orientational order. In Fig. 3.26(c), the dependence of the viscosity on concentration is shown for various shear rates. For shear rates close to the critical shear rate $Pe_{\mathrm{r}} = 0.159\ldots$, the viscosity decreases sharply with increasing concentration due to the sharp increase of the degree of alignment as the corresponding branch in the bifurcation diagram (Fig. 3.19a) is traced. For shear rates below the critical shear rate, the curves in Fig. 3.26(c) develop discontinuous jumps. Such jumps are probably of no experimental relevance, since phase separation will occur during an experiment. In the limit of zero shear rate, the viscosity depends linearly on concentration (see Eq. 3.290 with $\dot{\gamma} = 0$).

The normal stress differences N_1 and N_2 (normalized by $\eta_0\dot{\gamma}$) are plotted as functions of the shear rate for various concentrations in Fig. 3.27(a) and (b), respectively, for the paranematic state and in Fig. 3.27(c) and (d) for the nematic state. The dashed lines in Fig. 3.27(a) and (b) correspond to the low-shear-rate expansions (3.292). Note the strong shear-rate dependences in the otherwise isotropic state. As for the suspension viscosity, the absolute values of the normal stress differences for the nematic decrease on increasing the concentration. In Fig. 3.27(e) and (f), the normal stress differences are given as functions of the concentrations for various shear rates. The dashed lines correspond, as before, to the low-shear-rate expansions (3.292). For the same reason as with the suspension viscosity discussed above, there is a very strong concentration dependence for shear rates close to the critical shear rate.

3.14.3
Nonlinear Viscoelastic Response

Dynamic response functions can be obtained from a Fourier analysis of the time dependence of Eq. (3.284) for the stress tensor after substitution of the solutions of Eq. (3.219) under oscillatory shear flow, when transients have relaxed. The frequency dependence of η' and η'' for the otherwise isotropic state are given in Fig. 3.28(a) and (b), respectively, for various values of the Peclet number

$$Pe_{\mathrm{r},0} = \dot{\gamma}_0/D_{\mathrm{r}} \tag{3.300}$$

where $\dot{\gamma}_0$ is the shear amplitude as defined in Eq. (3.6). Response functions are plotted as functions of the dimensionless bare Deborah number (3.299). The dashed curves correspond to the leading Peclet number expansions (3.297). As soon as $Pe_{\mathrm{r},0} > 1$ (or, rather, $Pe_{\mathrm{r},0}^{\mathrm{eff}} = \dot{\gamma}_0/D_{\mathrm{r}}^{\mathrm{eff}} > 1$), there are deviations

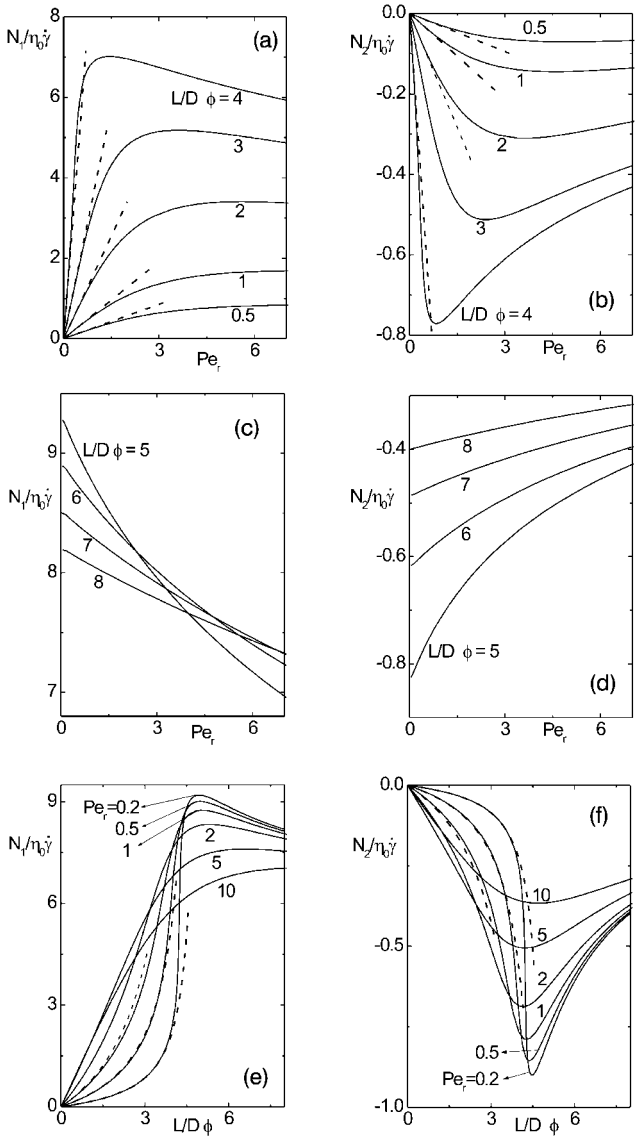

Fig. 3.27 (a) The normal stress difference N_1 for the otherwise isotropic state, normalized by $\eta_0\dot{\gamma}$ as a function of shear rate for various concentrations, as indicated in the figure. The dashed lines correspond to the low-shear-rate expansion (3.292). Here, and in the other five parts, $L/D = 50$. (b) The same as (a) for the normal stress difference N_2. The dashed lines correspond to the expansion (3.292). (c) The same as (a) for the nematic state. (d) The same as (b) for the nematic state. (e) The normal stress difference N_1 as a function of concentration for various shear rates, as indicated in the figure. The dashed lines correspond to the low-shear-rate expansion (3.292). (f) The same as (e) for the normal stress difference N_2. The dashed lines correspond to the low-shear-rate expansion (3.292).

from the leading-order expansions (3.297). Higher-order, nonlinear response functions now come into play as well. For these higher shear amplitudes, the time-dependent stress tensor can be Fourier-expanded as

$$\boldsymbol{\Sigma}_{\mathrm{D}} = 2\dot{\gamma}_0 \hat{\boldsymbol{E}} \sum_{n=0}^{\infty} [\eta'_{\mathrm{n}} \cos(n\omega t) + \eta''_{\mathrm{n}} \sin(n\omega t)] \tag{3.301}$$

where η'_0 and η''_0 are henceforth simply denoted as η' and η'', respectively. The nonlinear dissipative and elasticity response functions η'_{n} and η''_{n} are plotted for $n = 3$ and 5 in Fig. 3.28(c–f), for the paranematic state. The response functions for even n are zero. The nonlinear response functions exhibit oscillatory behavior as functions of the frequency. Note the very different frequency dependences of the third- and fifth-order functions. Except for the maximum in η''_3, the third-order response functions behave qualitatively similarly to those for near-critical systems of spherical colloids (Dhont and Nägele 1998). The corresponding response functions for the nematic state are given in Fig. 3.29(a–f). There are pronounced differences between the viscoelastic responses of the paranematic and nematic states. First of all, the response functions for the nematic state are only non-zero in a much smaller frequency range. The response functions for the nematic state are strongly varying functions of frequency in this small frequency range. Furthermore, the frequency dependence of, for example, η'' changes with $Pe_{\mathrm{r},0}$ in a quite different fashion as compared to the paranematic state. In a paranematic, η'' decreases on increasing $Pe_{\mathrm{r},0}$ without changing the location of its maximum too much, contrary to the nematic state, where the predominant effect of increasing $Pe_{\mathrm{r},0}$ is to shift the location of the maximum value of η'', while the maximum value itself does not change that drastically.

The present approach allows for the straightforward (numerical) calculation of response functions for superimposed oscillatory shear flow as well. We shall not discuss such response functions here.

3.14.4
Comparison with Other Theories, Simulations, and Experiments

An expression for the effective viscosity $\eta^{\mathrm{eff}}_{\mathrm{ellips}}$ at zero shear rate for non-interacting ellipsoidally shaped rods is due to Kuhn and Kuhn (1945) and Simha (1940) [see Larson (1999) for an extensive overview]. They found

$$\eta^{\mathrm{eff}}_{\mathrm{ellips}} = \eta_0 \left\{ 1 + \left[\frac{8}{5} + \frac{p_{\mathrm{e}}^2}{5} \left(\frac{1}{3[\ln(2p_{\mathrm{e}}) - 3/2]} + \frac{1}{\ln(2p_{\mathrm{e}}) - 1/2} \right) \right] \varphi \right\} \tag{3.302}$$

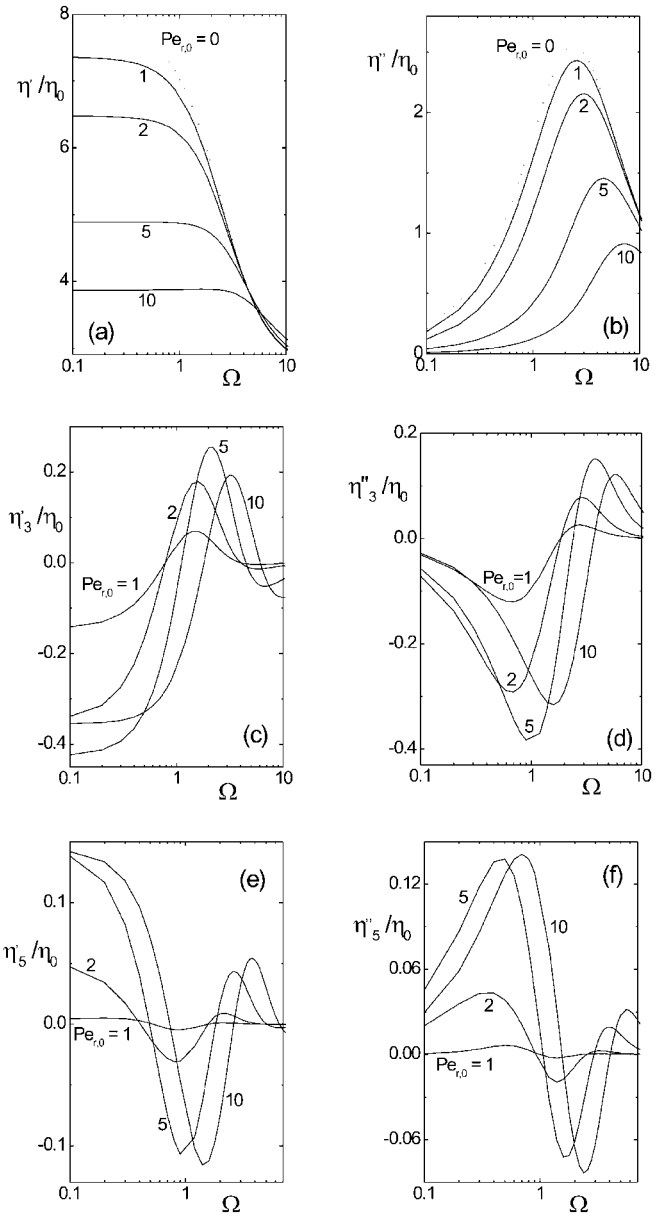

Fig. 3.28 Nonlinear response functions for the otherwise isotropic state.
(a) The dissipative response function η' as a function of the Deborah number (3.299) for various values of the Peclet number (3.300), as indicated in the figure. The dashed line corresponds to the leading-order expansion (3.297). Here, and in the other five parts, $L/D = 50$.
(b) The same as (a) for the elasticity response function η'', where the dashed line corresponds to Eq. (3.297).
(c) The same for the leading-order nonlinear dissipative response function η'_3.
(d) The leading-order nonlinear elasticity response function η''_3.
(e, f) The same as (c) and (d) for the response functions η'_5 and η''_5, respectively.

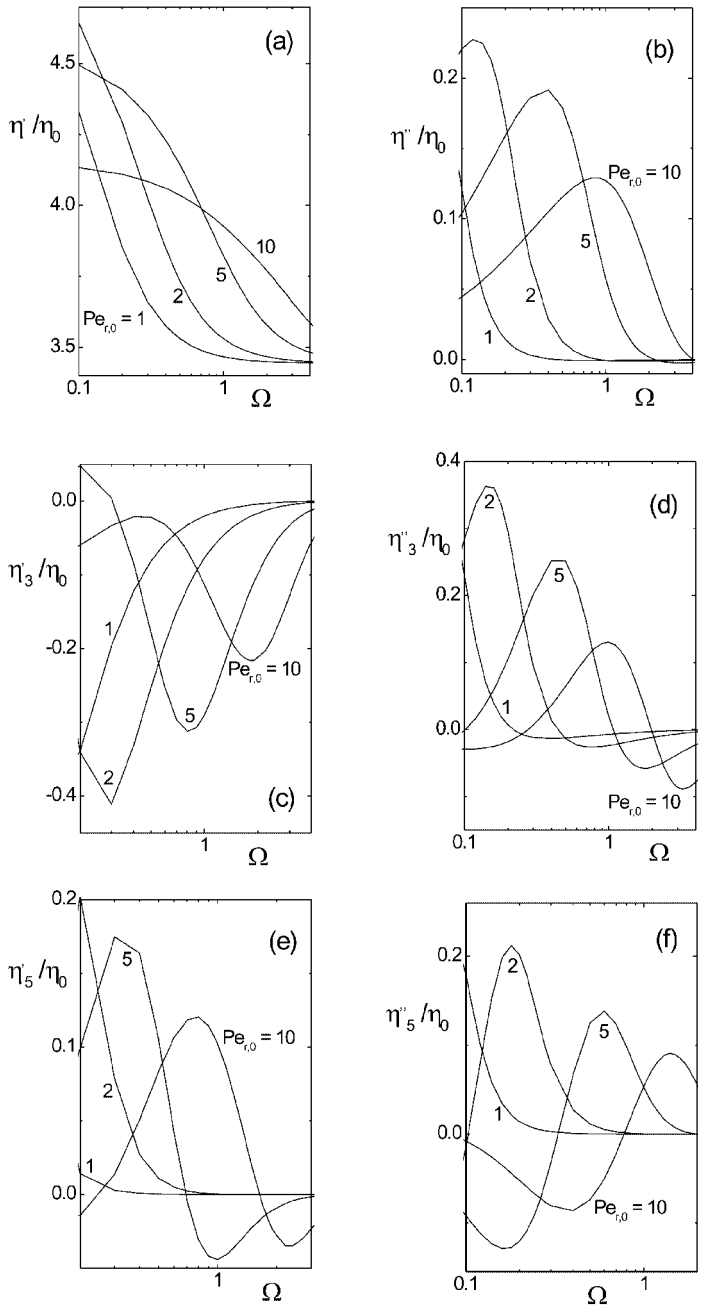

Fig. 3.29 The same as Fig. 3.28, but for the nematic state.

where $p_\mathrm{e} = L_\mathrm{e}/D_\mathrm{e}$ is the total length (L_e) over total thickness (D_e) ratio of the ellipsoidal rod. Expanding to leading order in p_e gives

$$\eta^{\mathrm{eff}}_{\mathrm{ellips}} = \eta_0 \left[1 + \frac{3}{2} \frac{8}{45} \frac{p_\mathrm{e}^2}{\ln p_\mathrm{e}} \varphi \right] \tag{3.303}$$

In order to compare this result with Eq. (3.291) for $\dot\gamma = 0$, note that for cylindrical rods (with $\bar\rho = N/V$ the number density of rods)

$$\left(\frac{L}{D}\right)^2 \varphi = \left(\frac{L}{D}\right)^2 \frac{\pi}{4} D^2 L \bar\rho = \frac{\pi}{4} L^3 \bar\rho$$

while for ellipsoidal rods

$$\left(\frac{L_\mathrm{e}}{D_\mathrm{e}}\right)^2 \varphi = \left(\frac{L_\mathrm{e}}{D_\mathrm{e}}\right)^2 \frac{\pi}{6} D_\mathrm{e}^2 L_\mathrm{e} \bar\rho = \frac{\pi}{6} L_\mathrm{e}^3 \bar\rho$$

When we choose the lengths of the cylindrical and ellipsoidal rods to be equal, i.e.

$$L = L_\mathrm{e} \tag{3.304}$$

it follows, for equal volume fractions, that our result (3.291) is identical to Eq. (3.303) [note that $\ln p_\mathrm{e} = \ln(L/D) + \mathcal{O}(1)$]. This identification also applies to the rotational and translational diffusion coefficients of free, non-interacting cylinders and ellipsoids: the leading-order expressions for these diffusion coefficients are identical for very long and thin cylinders and ellipsoids, when their lengths are taken equal. In the above we have chosen equal volume fractions and number densities of the cylindrical and ellipsoidal rods. This implies equal volumes of rods, from which a relation between the thickness of the rods follows as

$$D_\mathrm{e}/D = \sqrt{3/2} \tag{3.305}$$

Other choices for mapping results for ellipsoidal rods onto those for cylindrical rods can be used. The above mapping is simple, and correctly compares not only viscosity coefficients but also diffusion coefficients.

The leading shear-thinning behavior of the zero-frequency shear viscosity as found in Eq. (3.291) may be compared to the result obtained by Berry and Russel (1987), which reads, in our notation,

$$\eta^{\mathrm{eff}} = \eta_0 \left\{ 1 + \left[1 - \frac{1}{50} \left(\frac{\dot\gamma}{D_\mathrm{r}} \right)^2 \right] \alpha\varphi + \frac{2}{5} \left[1 - 0.0342 \left(\frac{\dot\gamma}{D_\mathrm{r}} \right)^2 \right] \alpha^2 \varphi^2 \right\} \tag{3.306}$$

up to second order in concentration and shear rate. This result is valid in the dilute regime, where $(L/D)^2\varphi \ll 1$. To first order in volume fraction, this agrees with our result (3.291). There are serious differences, however, for the φ^2 contribution. First of all, as discussed in the previous section, we predict a linear volume fraction dependence of the shear viscosity at zero shear rate. From Eq. (3.290), and from Eq. (3.297) at infinite frequency, we obtain

$$\eta^{\text{eff}} = \eta_0[1 + \alpha\varphi] \quad \text{and} \quad \eta_\infty^{\text{eff}} = \eta_0[1 + \tfrac{1}{4}\alpha\varphi] \tag{3.307}$$

where, as before, η^{eff} is the zero-frequency and η_∞^{eff} the high-frequency viscosity.

On the other hand, Berry and Russel's above result (3.306) for zero frequency predicts that at zero shear rate and up to second order in concentration

$$\eta^{\text{eff}} = \eta_0[1 + \alpha\varphi + \tfrac{2}{5}\alpha^2\varphi^2] \tag{3.308}$$

On the basis of this latter prediction, a pronounced φ^2 dependence for long and thin rods is expected, since $\alpha\varphi \sim (L/D)/\ln(L/D) \to \infty$ as $L/D \to \infty$, for a given value of $(L/D)\varphi$. For zero shear rate, we may compare the above predictions with computer simulations by Claeys and Brady (1993) on ellipsoidal rods. In Fig. 3.30a, simulation data from Claeys and Brady for effective zero-shear-rate viscosities at infinite frequencies are plotted for three aspect ratios p_e of the ellipsoidal rods: $p_e = 50$, 20 and 10. There is a remarkable linear concentration dependence over a large concentration range, especially for the longer rods. In fact, Claeys and Brady (1993) remark that: "Somewhat surprisingly, the dispersion containing 1% rods of aspect ratio 50 still responds hydrodynamically as if it were dilute, even though $n_\phi \frac{4}{3}\pi a^3 = 25$" (in their notation, n_ϕ is the number density of rods and $a = L/2$). Such a linear concentration dependence is also found in computer simulations on non-Brownian rods by Yamane et al. (1994) (see Fig. 3.30b). They state that: "... the excess viscosity is proportional to the number density n even in the region $nL^3 \approx 40, \ldots$". The magnitude of the second-order volume fraction contribution in the Berry–Russel equation (3.306) relative to the first-order contribution is $\frac{2}{5}\alpha\varphi \approx 50\%$ for the highest concentration shown in Fig. 3.30 for both $p_e = 20$ and 50. The large second-order concentration contributions predicted by Berry and Russel (1987) are thus in disagreement with the linear relationship found in Fig. 3.30. A decrease of the Huggins coefficient with increasing aspect ratio is confirmed in experiments on spindle-type colloidal hematite rods by Solomon and boger (1998; see Fig. 2 and Table III therein).

The slope of the simulation results for the high-frequency viscosity η_∞^{eff} versus the volume fraction in Fig. 3.30, taken from Claeys and Brady (1993),

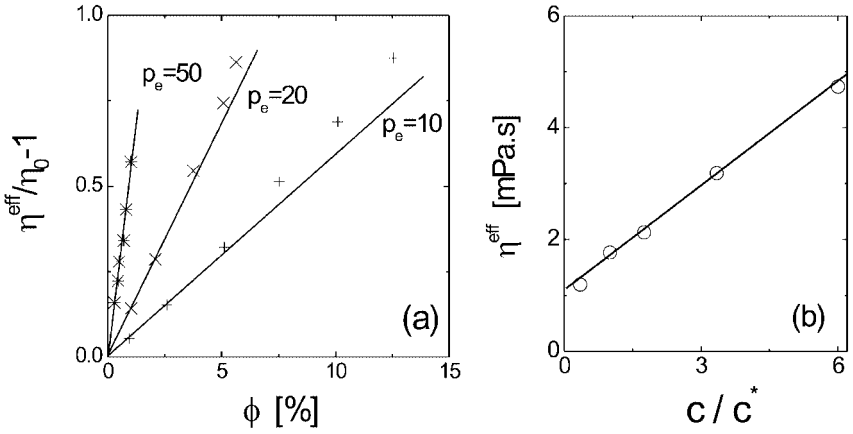

Fig. 3.30 (a) Brownian dynamics simulation data from Claeys and Brady (1993) for the suspension shear viscosity (at zero shear rate and infinite frequency) of ellipsoidal rods as a function of their volume fraction for various aspect ratios p_e, as indicated in the figure. (b) Linear concentration dependence of the shear viscosity as found in simulations by Yamane et al. (1994).

may be compared to the slope $\alpha/4$ as predicted in Eq. (3.307). Noting that the volume fraction of ellipsoids in Fig. 3.30(a) is equal to $(\pi/6)DL^2\bar{\rho}$, while for the cylindrical particles under consideration here the volume fraction is equal to $(\pi/4)DL^2\bar{\rho}$, a slope of 36 is found from the simulation data for $L/D = 50$, whereas from Eq. (3.289) we find a slope of 29. For $L/D = 20$ one finds a slope of 9 from Fig. 3.30, while $\alpha/4 = 6$, and for $L/D = 10$ one finds 3.8 and $\alpha/4 = 1.9$. The slope found from simulations thus seems to converge to the asymptotic result in Eq. (3.307) when the aspect ratio is large enough.

The linear concentration dependence of the zero-shear viscosity is not found within the DEK theory (Doi and Edwards 1986), where the concentration dependence originates from the assumed state dependence of the rotational tracer diffusion coefficient.

The experiments by Graf et al. (1993) and Schmidt et al. (2000) on *fd* virus suspensions do not show a linear concentration dependence of the zero-shear and zero-frequency viscosity (except maybe for the salt-free case in Fig. 3 of Graf et al., which should not be taken as proof of the present theory in view of the not well understood behavior of the *fd* virus at very low ionic strength). The higher-order concentration dependence as found for the *fd* virus, however, is much weaker than for hard spheres, indicating that, in accordance with our findings, elongated objects tend to diminish nonlinear concentration dependence. Similarly, a considerable second-order concentration dependence of the shear viscosity is found experimentally for xanthan gum by Chauveteau (1982). It is known that the *fd* virus is relatively stiff (contour length is 880 nm,

intrinsic persistence length is 2200 nm), but nevertheless behaves quite non-Onsager-like, in the sense that the relative isotropic–nematic biphasic gap width in the absence of shear flow is much narrower than the width for very long and thin, truly rigid rods (Tang and Fraden 1995). Hence, even for relatively stiff rod-like particles, the approximation (3.208) for the pair correlation function is not very good. Xanthan and "stiff" polymers like PBLG (Yang 1987; Mead and Larson 1990) are even more flexible than the *fd* virus. The non-zero Huggins coefficients at zero shear rate found experimentally for the *fd* virus by Graf et al. (1993), for xanthan gum by Chauveteau (1982), and for PBLG by Yang (1987) and Mead and Larson (1990) are probably due to flexibility. In view of this sensitivity to flexibility, it would be very interesting to include flexibility (even up to leading order in the inverse persistence length) in stress calculations. The sensitivity to slight flexibility obscures the comparison of theories with experiments for truly stiff rods.

The difference between the experimental rods mentioned above and the model rods in computer simulations is their degree of stiffness. The advantage of computer simulations is that the persistence length of rods can be made infinite. In the computer simulations mentioned above, hydrodynamics are taken into account. The different concentration dependences of the zero-shear viscosity (at least for long and thin rods) found in experiments as compared to simulations, as far as the Huggins coefficient is concerned, is therefore most likely due to flexibility.

Despite the sensitivity of viscoelastic response functions to flexibility, we shall nevertheless compare experimental data with our theoretical predictions. This comparison should be taken seriously only on a qualitative level. Figure 3.31 shows experimental data for the shear-rate dependence of the shear viscosity of xanthan with two different molecular weights (Chauveteau 1982), PBLG (Yang 1987), and a salt-free *fd* virus suspension (Graf et al. 1993). The intrinsic viscosity $[\eta] = \eta/\eta_0 - 1$, with η_0 the solvent shear viscosity, is plotted relative to its value $[\eta]_0$ at zero shear rate. For xanthan we took D_r =133 and 103 s^{-1} for low and high molecular weights, respectively, as reported by Berry and Russel (1987); for PBLG we took $D_r = 167\ s^{-1}$, as reported by Larson (1999); and for the salt-free *fd* virus we took $D_r = 11\ s^{-1}$ from Graf et al. (1993). The solid lines refer to the present theory with $L/D = 50$ (the precise form of these curves is insensitive to the aspect ratio). The xanthan and PBLG suspensions are dilute, and are seen to be in reasonable agreement with theory. The concentration of the salt-free *fd* virus suspension is equal to $6c^*$, where c^* is the overlap concentration. There is some deviation from the *fd* virus data in comparison to theory, which may be due to either flexibility or aggregation at low ionic strength.

The linear concentration dependence in Eq. (3.307) holds up to the isotropic–nematic phase transition. Within the nematic state, this result is no

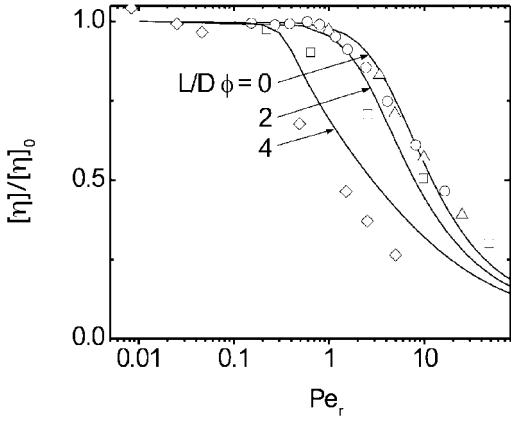

Fig. 3.31 The intrinsic viscosity $[\eta] = \eta/\eta_0 - 1$, relative to its value $[\eta]_0$ at zero shear rate, as a function of the bare rotational Peclet number. The solid lines are theoretical predictions for various values of $(L/D)\varphi$, as indicated in the figure, for $L/D = 50$ (the theoretical curves are insensitive to the precise value of the aspect ratio). The symbols relate to experimental data for xanthan by Chauveteau (1982) at low (circles) and high (triangles) molecular weight, for PBLG by Yang (1987) (squares), and for salt-free *fd* virus by Graf et al. (1993) (diamonds).

longer valid, since in deriving Eq. (3.307) we linearized around the isotropic state (see Eq. 3.285). As can be seen from Fig. 3.26(b), the viscosity decreases with increasing concentration for a nematic. As was mentioned before, this is the result of an increase in alignment on increasing the concentration. Such a decrease of the shear viscosity with increasing concentration is indeed observed experimentally (see for example Fig. 10.5 in Doi and Edwards, 1986 and Fig. 1 in Kiss and Porter, 1978). Furthermore, the type of concentration dependence of the shear viscosity at higher shear rates as found in Fig. 3.26(c) is also seen in experiments (see for example Fig. 10.9 in Doi and Edwards, 1986).

To leading order in concentration, the low-shear limiting expressions (3.292) for normal stress differences are also found by Hinch and Leal (1972), except that instead of the prefactor $-1/40$ they find $-1/28$. Within the DEK theory, it is found that, to leading order in shear rate,

$$N_1 = \eta_0 \frac{1}{30} \bar{\rho} k_{\mathrm{B}} T \frac{\dot{\gamma}^2}{\tilde{D}_{\mathrm{r}}^2}$$

$$N_2 = -\eta_0 \frac{1}{105} \bar{\rho} k_{\mathrm{B}} T \frac{\dot{\gamma}^2}{\tilde{D}_{\mathrm{r}}^2}$$

where $\bar{\rho}$ is the number concentration of rods and $\tilde{D}_{\mathrm{r}}$ is their state-dependent rotational tracer diffusion coefficient. Using the fact that $D_{\mathrm{r}} = 3k_{\mathrm{B}}T \ln(L/D)/\pi\eta_0 L^3$ in expression (3.289) for α, we find from Eq. (3.292)

that

$$N_1 = \eta_0 \frac{1}{30} \bar{\rho} k_\mathrm{B} T \frac{\dot{\gamma}^2}{D_\mathrm{r} D_\mathrm{r}^\mathrm{eff}}$$

$$N_2 = -\eta_0 \frac{1}{300} \bar{\rho} k_\mathrm{B} T \frac{\dot{\gamma}^2}{D_\mathrm{r} D_\mathrm{r}^\mathrm{eff}}$$

where the effective rotational, collective diffusion coefficient D^eff is given in Eq. (3.230). The prefactor for N_2 is almost a factor of 3 smaller than in the DEK theory, and in both expressions we find the combination $D_\mathrm{r} D_\mathrm{r}^\mathrm{eff}$ instead of $\tilde{D}_\mathrm{r}^2$. Experimental results for normal stress differences on fibers are reported by Zirnsak et al. (1994). Here, Brownian motion is very weak compared to shear forces, so that one should compare with the high-shear-rate results as plotted in Fig. 3.27. One should be careful in the comparison, since inertial effects in fiber suspensions may play a role. As can be seen from Fig. 3.27(a) and (b), both normal stress differences become linear functions of the shear rate for high shear rates (since $N_1/\dot{\gamma}$ and $N_2/\dot{\gamma}$ tend to constant, shear-rate-independent values). This remarkable linear shear-rate dependence is indeed typically found in experiments on fibers [see, for example, Fig. 11 in Zirnsak et al. (1994)]. In addition, in Figs. 16 and 17 of Zirnsak et al., it is found that the first normal stress difference varies linearly with concentration. This is also found in our Fig. 3.27(e) for high shear rates, for concentrations where $(L/D)\varphi$ is less than about 3. The concentrations in the experiments on fibers are indeed well within this range.

Normal stress differences that change from being positive to negative on increasing the shear rate, and for larger shear rates from negative to positive again, were reported by Iizuka (1978),[4] Kiss and Porter (1978), Kiss (1996) and Larson (1996) for PBLG solutions in *m*-cresol, and later for the same polymer by Magda et al. (1991). On the basis of a two-dimensional DEK-like approach for a homogeneous nematic, Marrucci and Maffettone (1989) predict that the normal stress difference N_1 is negative at low shear rates and becomes positive at higher shear rates (see their Fig. 10). This behavior is found for shear rates that are large enough to assure that stationary solutions of equations of motion exist, i.e. where tumbling or wagging are absent. Larson (1990) analyzed the full three-dimensional DEK theory (using closures as obtained by Hinch and Leal (1976)), and suggests that the experimentally observed sign changes of normal stress differences are due to the existence of tumbling or wagging nematic domains. By time averaging of stresses generated by tumbling domains over a number of oscillations, he indeed finds the kind of sign changes for normal stress differences that are observed experimentally.

4) Kiss and Porter (1978) refer to a personal communication with Iizuka, who apparently found negative normal stress differences before or at the same time as Kiss and Porter, but never published these data.

This kind of behavior is essentially also found within the two-dimensional DEK-like approach by Marrucci and Maffettone (1990a) and Marrucci and Maffettone (1990b). Magda et al. (1991) suggested that polydomain nematics may exhibit apparent steady flow behavior, even though each individual domain exhibits tumbling or wagging, since in a rheometer averages over many independent tumbling domains are probed. Tumbling and wagging can be observed in experiments by flow reversal, which renders the various domains coherently tumbling/wagging for some time. As mentioned before, whether a theory predicts tumbling and wagging is very sensitive to the closure relation that is used. Our closure relation (3.227) is not suited to describe tumbling and wagging. Other closure relations can be used to study these time-periodic states (Marrucci and Maffettone 1989; Larson 1990; Marrucci and Maffettone 1990a; Marrucci and Maffettone 1990b; Forest and Wang 2003). Due to the sensitivity for the prediction of time-periodic states on the closure relation, the most sensible thing to do seems to be to employ the original equation of motion (3.213), before introducing a Ginzburg–Landau expansion.

3.15 Current Research Topics

Some of the current research interests related to what has been discussed in the present chapter will be briefly described in this last section. Current research interests include:

1. shear-banding transitions,
2. non-equilibrium phase behavior under shear flow,
3. phase separation kinetics under flow conditions.

3.15.1 Shear-Banding Transitions

There are essentially two types of banding transitions observed experimentally in various types of systems containing mesoscopic entities: vorticity banding and gradient banding. Here, "bands" refer to coexisting regions under stationary flow which have different microstructural order and can sustain different shear rates and/or stresses. In the case of vorticity banding, regularly stacked bands in the vorticity direction are observed, which differ in their average orientational order. For gradient banding, two regions coexist, extending along the gradient direction, each with a different shear rate.

Fig. 3.32 A photograph from the side of an optical couette cell between two crossed polarizers. The couette cell contains an *fd* virus suspension in a vorticity-banded state. The width of the shear cell is about 5 cm, while the height of the bands is about 1 mm.

3.15.1.1 **Vorticity Banding**

Within part of the two-phase region (the region enclosed by the binodal), *fd* virus suspensions exhibit vorticity banding, where regularly stacked bands are formed along the vorticity direction. The height of these bands can be up to millimeters. A photograph of such a banded state in an optical couette cell between two crossed polarizers is given in Fig. 3.32. The difference in contrast of the two types of bands between crossed polarizers is due to the different orientational order in the bands. The director has different orientations in the two bands. The concentration difference in the two bands has been shown to be zero to within experimental error. The region in the phase diagram where vorticity banding is found is indicated in Fig. 3.33. At lower

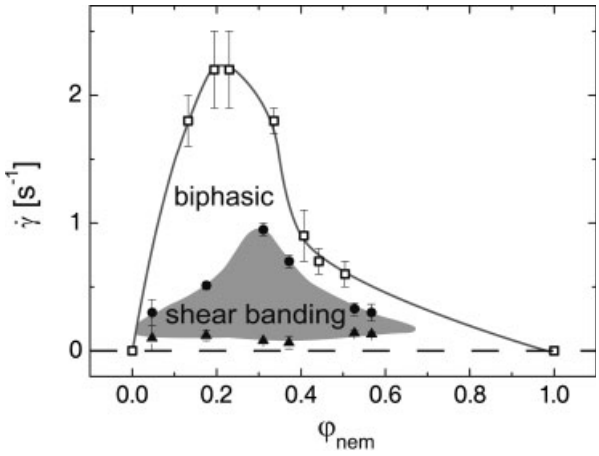

Fig. 3.33 Experimental phase diagram of the *fd* virus (with added dextran) including the vorticity-banding region.

concentrations, the boundary of the region where vorticity banding occurs coincides exactly with the binodal. It thus seems that inhomogeneities that are formed right after a shear-rate quench into the two-phase region (the region bounded by the paranematic–nematic binodal) are necessary to render normal stresses such that they induce an instability along the vorticity direction leading to banding. If this is indeed the case, equations of motion need to be analyzed that account for large gradients in concentration, orientational order parameter, and/or shear rate. For stiff colloidal rods, such equations of motion have been derived by Dhont and Briels (2002) and Dhont and Briels (2003). The particular normal stress behavior that leads to vorticity banding and the role of inhomogeneities leading to that behavior is not yet understood [however, see Olmsted and Lu (1999), where vorticity banding is assumed to occur whenever the velocity-gradient stress versus the shear rate relation is multi-valued]. At higher concentrations, there are indications that banding ceases to occur when tumbling/wagging sets in.

3.15.1.2 **Gradient Banding**

On the basis of the stationary forms of the equation of motion (3.219) and the expression (3.284) for the deviatoric stress tensor (where D_{r} is the bare, state-independent rotational diffusion coefficient), a non-monotonic behavior of the shear stress as a function of shear rate is found. Such a "van der Waals loop-like" behavior is only found for concentrations very close to the critical concentration $(L/D)\varphi = 4.281\ldots$, as can be seen in Fig. 3.34, where the dimensionless flow-gradient component $\sigma_{12} = \Sigma_{12}/\eta_0 D_{\mathrm{r}}$ of the stress tensor is plotted as a function of shear rate. Such a decrease of the stress in a certain shear-rate interval implies that the usual linear flow profile as depicted in Fig. 3.1(a) is unstable. The stable flow profile is now a banded flow, where two regions with different shear rates are in coexistence. Within these two regions (the "bands"), the shear rate is constant, independent of position. The shear rates within the two bands can be found from a modified equal-area construction on the van der Waals loop in Fig. 3.34 (Olmsted and Lu 1999; Olmsted 1999; Olmsted et al. 2000; Lu et al. 2000; Fielding and Olmsted 2003; Dhont 1999). As can be seen, the difference between these shear rates is very small. Since the concentration range where gradient banding is expected to occur and the difference in shear rates as sustained in the two bands are very small, gradient banding in suspensions of stiff rods will be difficult to detect experimentally. In addition, passing the critical point at a fixed concentration by increasing the shear rate, the two-phase region is also probed (see Figs. 3.19b and 3.21), as a result of which phase separation will occur during a rheological experiment. It is possible, however, that gradient banding also occurs within the two-phase region (the region bounded by the paranematic–nematic binodal), which has not yet been studied experimen-

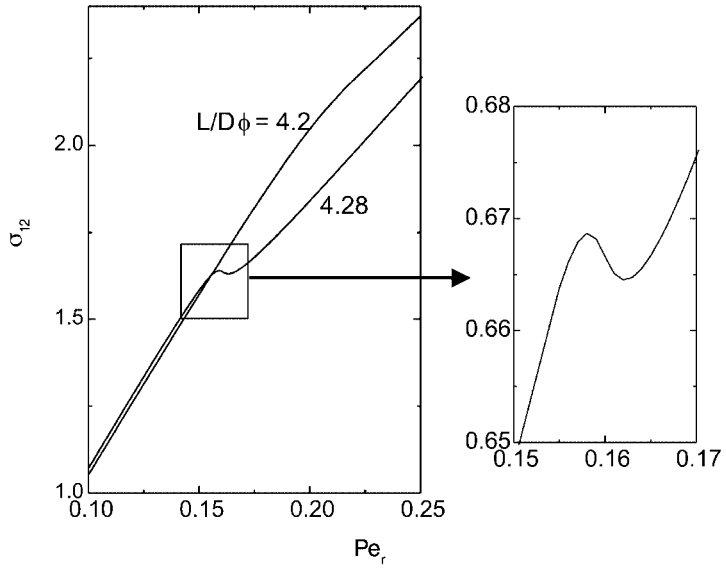

Fig. 3.34 The dimensionless flow-gradient component $\sigma_{12} \equiv \Sigma_{12}/\eta_0 D_{\rm r}$ of the stress tensor as a function of the shear rate for concentrations close to the critical concentration $(L/D)\varphi = 4.281\ldots$ (see Fig. 3.19b). The smaller figure on the right-hand side is a blow-up of the van der Waals loop.

tally. The situation for worm-like micellar systems is different. Here strong gradient banding has been observed outside the two-phase region. The reason for such pronounced gradient banding is probably that shear flow enhances alignment, which enhances head-to-tail collisions, leading to longer worms, leading in turn to a higher degree of alignment. This mechanism probably renders worm-like micellar systems much more strongly shear thinning as compared to, for example, *fd* virus suspensions, giving rise to a more pronounced van der Waals loop-like behavior of the stress versus shear rate.

Although gradient banding of suspensions of stiff rods is experimentally possibly less relevant, these systems do allow one to gain an understanding of the microscopic origin of the van der Waals loop-like behavior of the stress tensor. The reason for the strong shear-thinning behavior on passing the critical point is that rotational motion is very slow at the critical point (since there $D_{\rm r}^{\rm eff} = 0$, as discussed in Section 3.11.1), so that shear-aligning forces are no longer counterbalanced by rotational diffusion. A small increase in shear rate near the critical point therefore results in an appreciable increase of the degree of alignment, leading to strong shear thinning, giving rise to the van der Waals loop-like behavior of the stress tensor. It may be a general feature for the origin of gradient banding that the dynamics of a variable, that strongly couples to the stress, becomes very slow on increasing the shear rate.

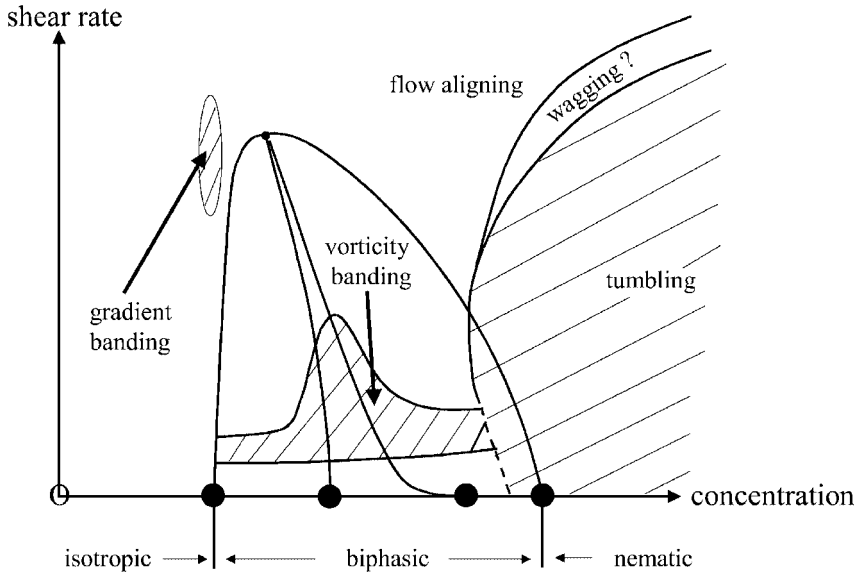

Fig. 3.35 A sketch of the possible non-equilibrium phase diagram of stiff rods.

3.15.2
Non-Equilibrium Phase Diagram Under Shear Flow

A sketch of a possible complete phase diagram of rods subjected to simple shear flow, for concentrations below the nematic-to-smectic transition, is given in Fig. 3.35. As discussed before, the location of the binodal and the region within the two-phase region (as enclosed by the binodal) where vorticity banding occurs have been obtained experimentally for an *fd* virus suspension with added dextran that induced slight attractions between the rods. At lower concentrations, the region where vorticity banding ceases to occur coincides with the binodal. There are indications that the vorticity banding ceases to occur at higher concentrations where non-stationary, time-periodic states become stable. Gradient banding is expected to occur in a very small concentration interval close to the critical point (as discussed above), but has so far not been observed experimentally.

The characteristic features of vorticity bands have not been investigated yet. It is not known how the band height varies with shear rate and concentration, the internal orientational order within the bands has not been investigated, and it is not known whether or not there is a dependence on the gap width of the shear cell.

The various types of non-stationary states as described in detail by Rienäcker and Hess (1999) and Hess and Kröger (2004). These various types

of time-periodic states are difficult to distinguish experimentally. So far, only tumbling and wagging states have been seen in *fd* virus suspensions by Lettinga and Dhont (2004). The phase diagram in Fig. 3.35 may, however, be more complicated as far as these time-periodic states are concerned.

3.15.3
Phase Separation Kinetics Under Flow Conditions

No experimental results for demixing kinetics of colloidal systems consisting of either spherical or rod-like colloids under shear flow have been published so far. An analysis of a simplified Smoluchowski equation in the initial stage of spinodal demixing of suspensions of rods in the *absence of flow* has been discussed by Winters et al. (2000). Initial spinodal decomposition of suspensions of spheres in the *presence of shear flow* has been analyzed by Dhont (1996), which reproduces features that were seen experimentally for fluid mixtures by Baumberger et al. (1991). There are as yet no theories on spinodal decomposition of suspensions of rod-like colloids *under shear flow*, although much work has been done on polymer blend demixing under flow conditions.

There are regions in the phase diagram where decomposition proceeds through spinodal demixing or by nucleation and growth, depending on the degree of orientational order of the initial state. These regions are most conveniently identified by means of the bifurcation diagrams as discussed in Section 3.11.

The kinetics of vorticity-band formation has not been studied so far. Experiments indicate that these bands are formed from an unstable state, i.e. by means of a spinodal type of demixing, with a time constant that varies with shear rate and concentration. The same experiments show a remarkably strong dependence of the height of the bands and the rate with which bands are formed on the gap width of the shear cell (Kang et al. 2004).

3.16
Appendix

3.16.1
Bead Index Summations

This appendix deals with the mathematical details of how bead index summations can be calculated by means of integration.

Consider the function appearing in Eq. (3.35):

$$f(L/D) = \sum_{j=-\frac{1}{2}n}^{\frac{1}{2}n} \sum_{i=-\frac{1}{2}n, i\neq j}^{\frac{1}{2}n} \frac{1}{|i-j|}$$

Let us first evaluate the sum

$$\sum_{i=-\frac{1}{2}n, i\neq j}^{\frac{1}{2}n} \frac{1}{|i-j|}$$

This sum equals the surface area of all the rectangles in Fig. 3.36. It can be replaced by an integral, when the summation range $(-\frac{1}{2}n, \frac{1}{2}n)$ is large,

$$\sum_{i=-\frac{1}{2}n, i\neq j}^{\frac{1}{2}n} \frac{1}{|i-j|} \approx \left[\int_{-\frac{1}{2}(n+1)}^{j-\frac{1}{2}} + \int_{j+\frac{1}{2}}^{\frac{1}{2}(n+1)} \right] \mathrm{d}i \, \frac{1}{|i-j|} \qquad (3.309)$$

The difference between the sum and the integral is the sum of the hatched surface areas in Fig. 3.36 (with their proper signs). For increasing L/D ratios, this difference tends to a constant, while the sum itself goes to infinity. The relative error that is made by replacing the sum by an integral thus tends to zero as L/D tends to infinity. The leading terms in the above integral are

$$\ln[j + \tfrac{1}{2}(n+1)] + \ln[\tfrac{1}{2}(n+1) - j]$$

This expression is substituted into Eq. (3.309), where the sum over j is again replaced by an integral. Using the standard integral

$$\int \mathrm{d}z \, z^m \ln z = z^{m+1} \left[\frac{\ln z}{m+1} - \frac{1}{(m+1)^2} \right]$$

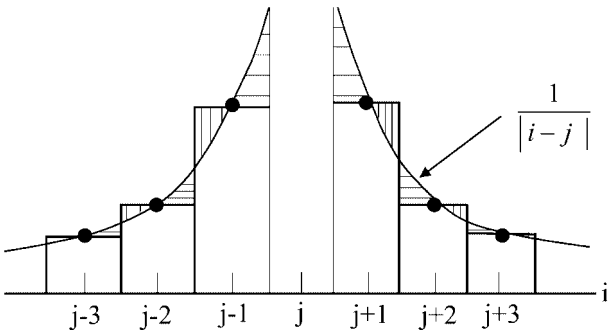

Fig. 3.36 The sum in Eq. (3.309) equals the surface area of all rectangles, and the integral is the surface area under the solid curve.

one ends up, to leading order in D/L, with the result given in Eq. (3.36). The two values of $j = \pm n/2$ do not contribute to leading order, so that, in the evaluation of summations, j may always be assumed in the interior of the summation range.

3.16.2 Useful Mathematical Identities

Useful mathematical identities that are frequently used in the present chapter are:

$$\hat{\mathcal{R}}^2(\cdots) = -2\hat{\boldsymbol{u}} \cdot \nabla_u(\cdots) - \hat{\boldsymbol{u}}\hat{\boldsymbol{u}} : \nabla_u\nabla_u(\cdots) + \nabla_u^2(\cdots)$$

$$\hat{\mathcal{R}}^2(\boldsymbol{a} \cdot \hat{\boldsymbol{u}})^2 = 2[a^2 - 3(\boldsymbol{a} \cdot \hat{\boldsymbol{u}})^2]$$

$$\hat{\mathcal{R}}^2(\hat{\boldsymbol{u}} \cdot \boldsymbol{M} \cdot \hat{\boldsymbol{u}}) = -6(\hat{\boldsymbol{u}} \cdot \boldsymbol{M} \cdot \hat{\boldsymbol{u}}) + 2\,\mathrm{Tr}\{\boldsymbol{M}\}$$

$$\hat{\mathcal{R}}^2(\hat{\boldsymbol{u}}\hat{\boldsymbol{u}}) = -6\hat{\boldsymbol{u}}\hat{\boldsymbol{u}} + 2\,\hat{\boldsymbol{I}}$$

$$(\hat{\boldsymbol{u}} \times \boldsymbol{M} \cdot \hat{\boldsymbol{u}}) \cdot \hat{\mathcal{R}}(\cdots) = [\nabla_u(\cdots)] \cdot (\boldsymbol{M} \cdot \hat{\boldsymbol{u}}) - \{\hat{\boldsymbol{u}} \cdot [\nabla_u(\cdots)]\}(\hat{\boldsymbol{u}} \cdot \boldsymbol{M} \cdot \hat{\boldsymbol{u}})$$

$$\hat{\mathcal{R}} \cdot [\hat{\boldsymbol{u}} \times (\boldsymbol{M} \cdot \hat{\boldsymbol{u}})] = -3(\hat{\boldsymbol{u}} \cdot \boldsymbol{M} \cdot \hat{\boldsymbol{u}}) + \mathrm{Tr}\{\boldsymbol{M}\}$$

$$\hat{\mathcal{R}} \cdot [(\cdots)(\hat{\boldsymbol{u}} \cdot \boldsymbol{M} \cdot \hat{\boldsymbol{u}})] = [\mathrm{Tr}\{\boldsymbol{M}\} - 3(\hat{\boldsymbol{u}} \cdot \boldsymbol{M} \cdot \hat{\boldsymbol{u}})](\cdots)$$
$$+(\boldsymbol{M} \cdot \hat{\boldsymbol{u}}) \cdot [\hat{\boldsymbol{I}} - \hat{\boldsymbol{u}}\hat{\boldsymbol{u}}] \cdot \nabla_u(\cdots)$$

$$\hat{\mathcal{R}} \cdot (\hat{\boldsymbol{u}} \times \boldsymbol{a}) = -2(\hat{\boldsymbol{u}} \cdot \boldsymbol{a})$$

$$\hat{\mathcal{R}}(\hat{\boldsymbol{u}} \cdot \boldsymbol{M} \cdot \hat{\boldsymbol{u}}) = \hat{\boldsymbol{u}} \times [\boldsymbol{M} \cdot \hat{\boldsymbol{u}} + \boldsymbol{M}^{\mathrm{T}} \cdot \hat{\boldsymbol{u}}]$$

$$\boldsymbol{a} \cdot \hat{\mathcal{R}}\hat{\boldsymbol{u}} = \boldsymbol{a} \times \hat{\boldsymbol{u}}$$

Here, $\boldsymbol{M}$ and $\boldsymbol{a}$ denote $\hat{\boldsymbol{u}}$-independent tensor and vector, respectively, and $(\cdots)$ denotes an arbitrary, but differentiable, scalar or vector field. The above identities are easily verified by explicit differentiation.

3.16.3 On the Accuracy of the Closure Relation (3.227)

In order to assess the accuracy of the closure relation (Eq. 3.227), we numerically solve the Smoluchowski equation (Eq. 3.213) for a single rod in shear flow, i.e. without the interaction term. From the stationary numerical solution $P(\hat{\boldsymbol{u}}, t\to\infty)$, both $\boldsymbol{S}$ and $\boldsymbol{S}^{(4)}$ can be obtained by numerical integration. This allows one to compare the approximation (3.227) with the exact form of $\boldsymbol{S}^{(4)}$.

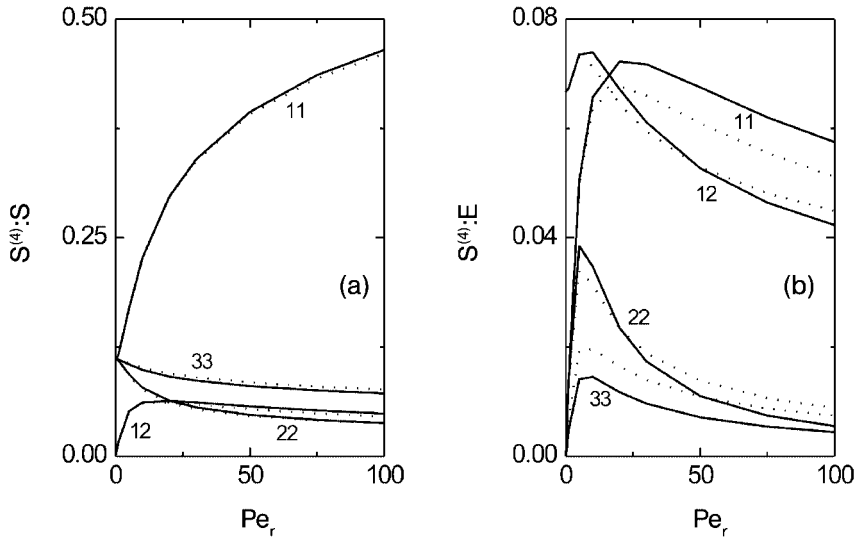

Fig. 3.37 A test of the accuracy of the closure relation (3.227) for (a) $\boldsymbol{M} = \hat{\boldsymbol{S}}$ and (b) $\boldsymbol{M} = \hat{\boldsymbol{E}}$. Solid lines are obtained from numerical solution of the Smoluchowski equation (3.213), and dotted lines are obtained from $\boldsymbol{S}$ using the closure relation (3.227). The numbers indicate the tensor elements. Tensor elements that are not shown are 0.

Note that the stationary solution of Eq. (3.213) is a function of the shear rate through the dimensionless rotational Peclet number $Pe_{\mathrm{r}} = \dot{\gamma}/D_{\mathrm{r}}$.

A comparison between the exact values (solid lines) and values obtained from the closure relation (3.227) (dotted lines) for the non-zero components of the tensors $\boldsymbol{S}^{(4)} : \boldsymbol{S}$ and $\boldsymbol{S}^{(4)} : \hat{\boldsymbol{E}}$ are given in Fig. 3.37(a) and (b), respectively. As can be seen, the shear-rate dependence of the various components is well reproduced by the closure relation. Moreover, the accuracy of the closure relation (3.227) is seen to be accurate to within 1% for $\boldsymbol{M} = \boldsymbol{S}$, and about 10% in the case $\boldsymbol{M} = \hat{\boldsymbol{E}}$. Computer simulations indicate the same accuracy for larger concentrations.

3.16.4
Evaluation of Sums Over Bead Index Numbers

Consider the evaluation of Eq. (3.272) to obtain an explicit expression for the sum in Eq. (3.271). As a first step, the double summation in Eq. (3.272) is rewritten as

$$\sum_{\alpha}\sum_{\beta\neq\alpha}\frac{G(\alpha)}{|\alpha-\beta|}\boldsymbol{F}^{\mathrm{h}}_{j,\beta} = \sum_{\alpha}\sum_{\beta\neq\alpha}\frac{G(\beta)}{|\alpha-\beta|}\boldsymbol{F}^{\mathrm{h}}_{j,\beta} + \sum_{\alpha}\sum_{\beta\neq\alpha}\frac{G(\alpha)-G(\beta)}{|\alpha-\beta|}\boldsymbol{F}^{\mathrm{h}}_{j,\beta} \tag{3.310}$$

The last term in this equation can be rewritten, by first interchanging the summation indices α and β, and subsequently interchanging the order of summations, as

$$\sum_{\alpha}\sum_{\beta\neq\alpha}\frac{G(\alpha)-G(\beta)}{|\alpha-\beta|}\boldsymbol{F}^{\mathrm{h}}_{j,\beta}=\sum_{\beta}\sum_{\alpha\neq\beta}\frac{G(\beta)-G(\alpha)}{|\alpha-\beta|}\boldsymbol{F}^{\mathrm{h}}_{j,\alpha}$$

$$=\sum_{\alpha}\boldsymbol{F}^{\mathrm{h}}_{j,\alpha}\sum_{\beta\neq\alpha}\frac{G(\beta)-G(\alpha)}{|\beta-\alpha|} \tag{3.311}$$

After a similar interchange of the order of summation in the first term on the right-hand side of Eq. (3.310), substitution of Eqs. (3.310) and (3.311) into Eq. (3.272) gives

$$\sum_{\alpha}G(\alpha)\boldsymbol{F}^{\mathrm{h}}_{j,\alpha}=-\gamma\sum_{\alpha}G(\alpha)[\boldsymbol{v}_{j,\alpha}-\boldsymbol{U}_{j,\alpha}] \tag{3.312}$$

$$-\tfrac{3}{8}[\hat{\boldsymbol{I}}+\hat{\boldsymbol{u}}_j\hat{\boldsymbol{u}}_j]\cdot\left[\sum_{\alpha}G(\alpha)\boldsymbol{F}^{\mathrm{h}}_{j,\alpha}\sum_{\beta\neq\alpha}\frac{1}{|\alpha-\beta|}+\Delta\right]$$

where

$$\Delta=\sum_{\alpha}\boldsymbol{F}^{\mathrm{h}}_{j,\alpha}\sum_{\beta\neq\alpha}\frac{G(\beta)-G(\alpha)}{|\beta-\alpha|} \tag{3.313}$$

Consider the first contribution in the square brackets in Eq. (3.312):

$$\sum_{\alpha}G(\alpha)\boldsymbol{F}^{\mathrm{h}}_{\alpha}\sum_{\beta\neq\alpha}\frac{1}{|\alpha-\beta|} \tag{3.314}$$

The sum $S(\alpha)\equiv\sum_{\beta\neq\alpha}1/|\alpha-\beta|$ can be approximated by an integral. To leading order one finds

$$S(\alpha)\equiv\sum_{\beta\neq\alpha}\frac{1}{|\alpha-\beta|}=\left[\int_{-\frac{1}{2}(L/D-1)}^{\alpha-\frac{1}{2}}+\int_{\alpha+\frac{1}{2}}^{\frac{1}{2}(L/D-1)}\right]\mathrm{d}x\,\frac{1}{|x-\beta|}$$

The integrals are easily evaluated to yield

$$S(\alpha)=2\ln 2+\ln[\tfrac{1}{2}(L/D-1)+\alpha]+\ln[\tfrac{1}{2}(L/D-1)-\alpha]$$

Except for α values close to the ends of the rod, this gives, to leading order,

$$S(\alpha)\approx 2\ln(L/D) \tag{3.315}$$

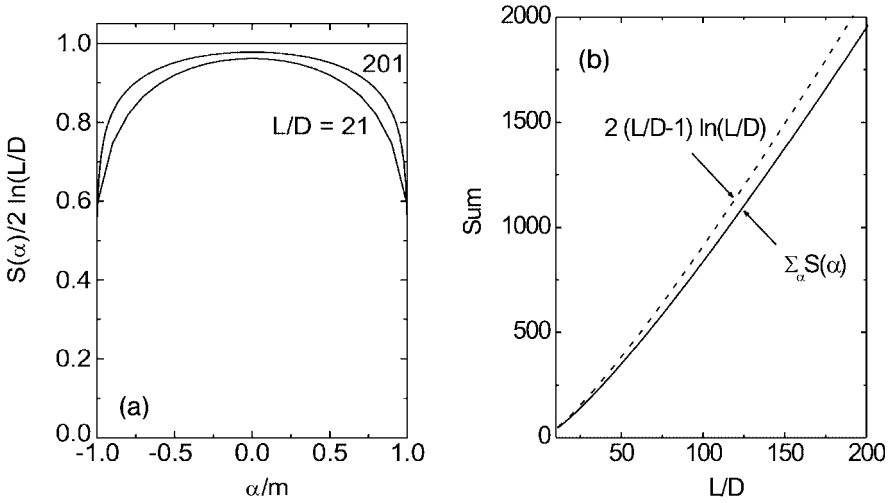

Fig. 3.38 (a) Plot of $S(\alpha)/2\ln(L/D)$ as a function of α/m with $2m+1$ the total number of beads [where $S(\alpha) \equiv \sum_{\beta\neq\alpha} 1/|\alpha-\beta|$]. The lower curve is for $L/D = 20$, the upper curve for $L/D = 201$. (b) The sums $\sum_\alpha S(\alpha)$ and $\sum_\alpha 2\ln(L/D) = 2(L/D-1)\ln(L/D)$ as functions of L/D. The relative error between the two sums never exceeds 8%, and very slowly converges to 0 with increasing L/D.

In Fig. 3.38(a), $S(\alpha)/2\ln(L/D)$ is plotted as a function of α/m, with $2m+1$ the number of beads (so that α/m ranges from -1 to $+1$). As can be seen, the approximation (3.315) is good to within about 10%, except at the very ends of the rod. In fact, the width of the region at the tips of the rod where Eq. (3.315) is not a good approximation asymptotically vanishes in the limit where $L/D \to \infty$. Hence, except when $G(\alpha)\boldsymbol{F}^{\rm h}_{j,\alpha}$ in Eq. (3.314) peaks at the ends of rod j, Eq. (3.315) can be used as a good approximation. For our purpose, there is no reason for the function $G(\alpha)\boldsymbol{F}^{\rm h}_{j,\alpha}$ to peak at the very ends of the rod. A quantitative estimate for the error made in using Eq. (3.315) is the difference between the sums $\sum_\alpha S(\alpha)$ and $\sum_\alpha 2\ln(L/D) = 2(L/D-1)\ln(L/D)$. These sums are plotted as functions of L/D in Fig. 3.38b. The relative error does not exceed 8% (for $L/D \leq 5$), and very slowly converges to 0 with increasing aspect ratio. Hence, to within about 10% error, we can approximate the expression in Eq. (3.314) by

$$\sum_\alpha G(\alpha)\boldsymbol{F}^{\rm h}_\alpha \sum_{\beta\neq\alpha} \frac{1}{|\alpha-\beta|} = 2\ln(L/D)\sum_\alpha G(\alpha)\boldsymbol{F}^{\rm h}_{j,\alpha} \qquad (3.316)$$

The term on the left-hand side in Eq. (3.312) can be neglected compared with this contribution, which is logarithmically larger.

For the divergence of the stress tensor in Eq. (3.267), we need to evaluate the sum

$$S \equiv \sum_{\alpha} \langle \delta(\boldsymbol{r} - \boldsymbol{r}_1 - \alpha D \hat{\boldsymbol{u}}_1) \boldsymbol{F}^{\mathrm{h}}_{1,\alpha} \rangle$$

where j is taken equal to 1 for convenience. Writing the ensemble average in terms of an integral with respect to the probability density function (PDF), P, of all phase-space coordinates of the colloidal rods, the integration with respect to $\boldsymbol{r}_1$ can be done immediately due to the delta distribution, leading to

$$S = \oint \mathrm{d}\hat{\boldsymbol{u}}_1 \int \mathrm{d}\boldsymbol{\Gamma} \sum_{\alpha} P(\boldsymbol{r}_1{=}\boldsymbol{r}{-}\alpha D \hat{\boldsymbol{u}}_1, \hat{\boldsymbol{u}}_1, \boldsymbol{\Gamma}, t)\, \boldsymbol{F}^{\mathrm{h}}_{1,\alpha}(\boldsymbol{r}_1{=}\boldsymbol{r}{-}\alpha\, D \hat{\boldsymbol{u}}_1, \hat{\boldsymbol{u}}_1, \boldsymbol{\Gamma})$$

where $\boldsymbol{\Gamma}$ stands for the phase-space coordinates $\boldsymbol{r}_2, \ldots, \boldsymbol{r}_N, \hat{\boldsymbol{u}}_2, \ldots, \hat{\boldsymbol{u}}_N$. The integrand is of the form of the left-hand side of Eq. (3.272), except that in $\boldsymbol{F}^{\mathrm{h}}_{1,\alpha}$ the position $\boldsymbol{r}_1$ is taken equal to $\boldsymbol{r} - \alpha D \hat{\boldsymbol{u}}_1$, which does not affect the present analysis leading to Eq. (3.273). The function $G(\alpha)$ is now equal to

$$G(\alpha) = P(\boldsymbol{r}_1{=}\boldsymbol{r}{-}\alpha D \hat{\boldsymbol{u}}_1, \hat{\boldsymbol{u}}_1, \boldsymbol{\Gamma}, t)$$

Since the PDF is a continuous differentiable function of $\boldsymbol{r}_1$, there is a scalar z between α and β, such that

$$\frac{G(\beta) - G(\alpha)}{\beta - \alpha} = \frac{\mathrm{d}G(z)}{\mathrm{d}z} \equiv \frac{\mathrm{d}P(\boldsymbol{r}_1{=}\boldsymbol{r}{-}z D \hat{\boldsymbol{u}}_1, \hat{\boldsymbol{u}}_1, \boldsymbol{\Gamma}, t)}{\mathrm{d}z}$$

The latter derivative is just the change of P on changing the position of rod number 1 by $D\hat{\boldsymbol{u}}_1$, i.e. its center is shifted over a distance D in the direction of its orientation. Since, for the very large aspect ratios under consideration, suspension properties are essentially constant over distances of the order D, this is a very small number. The number $R = (L/D)\, \mathrm{d} \ln[G(z)]/\mathrm{d}z$ measures the change of the "entropy" $\ln P$ over distances of the order of the length of the rods. In terms of this number, we have the order-of-magnitude estimate

$$\Delta \sim R \sum_{\alpha} G(\alpha) \boldsymbol{F}^{\mathrm{h}}_{1,\alpha}$$

Hence, according to Eq. (3.316), as long as the relative changes of suspension properties over the contour of the rods are much smaller than $\ln(L/D)$, Δ can be neglected compared with the first term in the square brackets in Eq. (3.312). This justifies the step from Eqs. (3.267) to Eqs. (3.273) and (3.274).

3.16.5
Derivation of Eq. (3.279)

After substitution of Eqs. (3.278), (3.170), (3.166), (3.172), and (3.277) into Eq. (3.275), it is immediately found that

$$\nabla\cdot\boldsymbol{\Sigma}=\eta_0\nabla^2\boldsymbol{U}(\boldsymbol{r},t)-\nabla P^{\rm ss}(\boldsymbol{r},t)+\boldsymbol{I}_{\rm r}+\boldsymbol{I}_{\rm t}+\boldsymbol{I}_{\rm u} \tag{3.317}$$

where

$$\boldsymbol{I}_{\rm r}=-\frac{\gamma\bar{D}D_{\rm r}}{\ln(L/D)}\left\langle\sum_{j=1}^{N}\sum_{\alpha}\alpha\delta(\boldsymbol{r}-\boldsymbol{r}_j-\alpha D\hat{\boldsymbol{u}}_j)[\beta\hat{\mathcal{R}}_j\Psi+\hat{\mathcal{R}}_j\ln P]\times\hat{\boldsymbol{u}}_j\right\rangle \tag{3.318}$$

$$\boldsymbol{I}_{\rm t}=-\frac{\gamma\bar{D}}{\ln(L/D)}\left\langle\sum_{j=1}^{N}\sum_{\alpha}\delta(\boldsymbol{r}-\boldsymbol{r}_j-\alpha D\hat{\boldsymbol{u}}_j)[\beta\nabla_j\Psi+\nabla_j\ln P]\right\rangle \tag{3.319}$$

and

$$\boldsymbol{I}_{\rm u}=\frac{4}{3}\frac{\gamma}{\ln(L/D)}\left\langle\sum_{j=1}^{N}[\hat{\boldsymbol{I}}-\tfrac{1}{2}\hat{\boldsymbol{u}}_j\hat{\boldsymbol{u}}_j]\cdot\sum_{\alpha}\delta(\boldsymbol{r}-\boldsymbol{r}_j-\alpha D\hat{\boldsymbol{u}}_j)\right.$$
$$\left.\times\left[\frac{D}{L}\sum_{\beta}\boldsymbol{U}_{j,\beta}-\boldsymbol{U}_{j,\alpha}-12\alpha\left(\frac{D}{L}\right)^3\hat{\boldsymbol{u}}_j\times\left(\hat{\boldsymbol{u}}_j\times\sum_{\beta}\beta\boldsymbol{U}_{j,\beta}\right)\right]\right\rangle \tag{3.320}$$

First, consider the relatively simple contribution

$$\boldsymbol{I}\equiv\left\langle\sum_{j=1}^{N}\sum_{\alpha}\alpha\delta(\boldsymbol{r}-\boldsymbol{r}_j-\alpha D\hat{\boldsymbol{u}}_j)\hat{\boldsymbol{u}}_j\times\hat{\mathcal{R}}_j\ln P\right\rangle$$
$$=\sum_{j=1}^{N}\sum_{\alpha}\alpha\int{\rm d}\boldsymbol{r}_1\cdots\int{\rm d}\boldsymbol{r}_N\oint{\rm d}\hat{\boldsymbol{u}}_1\cdots\oint{\rm d}\hat{\boldsymbol{u}}_N\,\delta(\boldsymbol{r}-\boldsymbol{r}_j-\alpha D\hat{\boldsymbol{u}}_j)\hat{\boldsymbol{u}}_j\times\hat{\mathcal{R}}_jP$$

that appears in Eq. (3.318) for $\boldsymbol{I}_{\rm r}$. In the second line the fact that $P\hat{\mathcal{R}}_j\ln P=\hat{\mathcal{R}}_jP$ is used, where, $P\equiv P(\boldsymbol{r}_1,\ldots,\hat{\boldsymbol{u}}_N,t)$ is the N-particle PDF. For each j, the integrations with respect to $\boldsymbol{r}_m$ and $\hat{\boldsymbol{u}}_m$ with $m\neq j$ can be done immediately. Assuming identical rods gives

$$\boldsymbol{I}=N\sum_{\alpha}\alpha\int{\rm d}\boldsymbol{r}_1\oint{\rm d}\hat{\boldsymbol{u}}_1\,\delta(\boldsymbol{r}-\boldsymbol{r}_1-\alpha D\hat{\boldsymbol{u}}_1)\hat{\boldsymbol{u}}_1\times\hat{\mathcal{R}}_1P(\boldsymbol{r}_1,\hat{\boldsymbol{u}}_1,t)$$

It is to be noted that the differentiation with respect to $\hat{\boldsymbol{u}}_1$ must be performed, after which $\boldsymbol{r}_1$ can be replaced by $\boldsymbol{r} - \alpha D\hat{\boldsymbol{u}}_1$ upon integration with respect to $\boldsymbol{r}_1$. Hence,

$$\boldsymbol{I} = N \sum_{\alpha} \alpha \oint \mathrm{d}\hat{\boldsymbol{u}}_1 \, \hat{\boldsymbol{u}}_1 \times \left[\hat{\mathcal{R}}_1 P(\boldsymbol{r} - \alpha D\hat{\boldsymbol{u}}_0, \hat{\boldsymbol{u}}_1, t)\right]_{\hat{\boldsymbol{u}}_0 = \hat{\boldsymbol{u}}_1}$$

The corresponding contribution to the divergence of the stress tensor in Eq. (3.279) follows by replacing the summation over the bead index number α by an integral as

$$\sum_{\alpha} f(\cdots - \alpha D\hat{\boldsymbol{u}}_1) = D^{-1} \int_{-L/2}^{L/2} \mathrm{d}x \, f(\cdots - x\hat{\boldsymbol{u}}_1) \tag{3.321}$$

Next consider the somewhat more complicated contribution:

$$\boldsymbol{I} \equiv \beta \left\langle \sum_{j=1}^{N} \sum_{\alpha} \alpha \delta(\boldsymbol{r} - \boldsymbol{r}_j - \alpha D\hat{\boldsymbol{u}}_j) \hat{\boldsymbol{u}}_j \times \hat{\mathcal{R}}_j \Psi \right\rangle$$

$$= \beta \sum_{j=1}^{N} \sum_{\alpha} \alpha \int \mathrm{d}\boldsymbol{r}_1 \cdots \int \mathrm{d}\boldsymbol{r}_N \oint \mathrm{d}\hat{\boldsymbol{u}}_1$$

$$\ldots \oint \mathrm{d}\hat{\boldsymbol{u}}_N \, \delta(\boldsymbol{r} - \boldsymbol{r}_j - \alpha D\hat{\boldsymbol{u}}_j) P \hat{\boldsymbol{u}}_j \times \hat{\mathcal{R}}_j \Psi$$

which appears in Eq. (3.318) for $\boldsymbol{I}_{\mathrm{r}}$. Using pairwise additivity (see Eq. 3.203), substitution of Eq. (3.207) together with Eq. (3.209), and assuming identical rods, it is readily found that

$$\boldsymbol{I} = \sum_{\alpha} \alpha \int \mathrm{d}\boldsymbol{r}_1 \oint \mathrm{d}\hat{\boldsymbol{u}}_1 \oint \mathrm{d}\hat{\boldsymbol{u}}_2 \, \delta(\boldsymbol{r} - \boldsymbol{r}_1 - \alpha D\hat{\boldsymbol{u}}_1) \rho(\boldsymbol{r}_1, \hat{\boldsymbol{u}}_1, t) \hat{\boldsymbol{u}}_1 \times \hat{\mathcal{R}}_1$$

$$\times \int \mathrm{d}\boldsymbol{r}_2 \, \rho(\boldsymbol{r}_2, \hat{\boldsymbol{u}}_2, t) \mathcal{X}(\boldsymbol{r}_1 - \boldsymbol{r}_2, \hat{\boldsymbol{u}}_1, \hat{\boldsymbol{u}}_2) \tag{3.322}$$

The integration with respect to $\boldsymbol{r}_2$ can be performed after transforming to the integration variable $\boldsymbol{R} = \boldsymbol{r}_1 - \boldsymbol{r}_2$:

$$\int \mathrm{d}\boldsymbol{r}_2 \, \rho(\boldsymbol{r}_2, \hat{\boldsymbol{u}}_2, t) \mathcal{X}(\boldsymbol{r}_1 - \boldsymbol{r}_2, \hat{\boldsymbol{u}}_1, \hat{\boldsymbol{u}}_2)$$

$$= \int \mathrm{d}\boldsymbol{R} \, \rho(\boldsymbol{r}_1 - \boldsymbol{R}, \hat{\boldsymbol{u}}_2, t) \mathcal{X}(\boldsymbol{R}, \hat{\boldsymbol{u}}_1, \hat{\boldsymbol{u}}_2)$$

$$= 2D|\hat{\boldsymbol{u}}_1 \times \hat{\boldsymbol{u}}_2| \int_{-L/2}^{L/2} \mathrm{d}l \int_{-L/2}^{L/2} \mathrm{d}l'\, \rho(\boldsymbol{r}_1 - l\hat{\boldsymbol{u}}_1 - l'\hat{\boldsymbol{u}}_2, \hat{\boldsymbol{u}}_2, t)$$

In the second equation, the integration with respect to $\boldsymbol{R}$ is transformed to integration with respect to $\{l, l', l''\}$, which are defined as

$$\boldsymbol{R} = l\hat{\boldsymbol{u}}_1 + l'\hat{\boldsymbol{u}}_2 + l'' \frac{\hat{\boldsymbol{u}}_1 \times \hat{\boldsymbol{u}}_2}{|\hat{\boldsymbol{u}}_1 \times \hat{\boldsymbol{u}}_2|} \quad \text{with} \quad -\tfrac{1}{2}L \le l, l' \le \tfrac{1}{2}L$$

$$\text{and} \quad -D \le l'' \le D \qquad (3.323)$$

The Jacobian of this transformation is equal to $|\hat{\boldsymbol{u}}_1 \times \hat{\boldsymbol{u}}_2|$. Since the suspension properties do not change significantly over distances of the order of the thickness D of the rods, the integration with respect to l'' gives rise to a prefactor $2D$. Hence,

$$\boldsymbol{I} = 2D \sum_\alpha \alpha \int \mathrm{d}\boldsymbol{r}_1 \oint \mathrm{d}\hat{\boldsymbol{u}}_1 \oint \mathrm{d}\hat{\boldsymbol{u}}_2 \int_{-L/2}^{L/2} \mathrm{d}l \int_{-L/2}^{L/2} \mathrm{d}l'\, \delta(\boldsymbol{r} - \boldsymbol{r}_1 - \alpha D\hat{\boldsymbol{u}}_1)$$

$$\times\, \rho(\boldsymbol{r}_1, \hat{\boldsymbol{u}}_1, t)\hat{\boldsymbol{u}}_1 \times \hat{\mathcal{R}}_1 |\hat{\boldsymbol{u}}_1 \times \hat{\boldsymbol{u}}_2| \rho(\boldsymbol{r}_1 - l\hat{\boldsymbol{u}}_1 - l'\hat{\boldsymbol{u}}_2, \hat{\boldsymbol{u}}_2, t)$$

As before, it should be noted that, upon integration with respect to $\boldsymbol{r}_1$, the delta distribution renders $\boldsymbol{r}_1 = \boldsymbol{r} - \alpha D\hat{\boldsymbol{u}}_1$ after the differentiation with respect to $\hat{\boldsymbol{u}}_1$ has been performed. Hence,

$$\boldsymbol{I} = 2D \sum_\alpha \alpha \oint \mathrm{d}\hat{\boldsymbol{u}}_1 \oint \mathrm{d}\hat{\boldsymbol{u}}_2 \int_{-L/2}^{L/2} \mathrm{d}l \int_{-L/2}^{L/2} \mathrm{d}l'$$

$$\times\, \rho(\boldsymbol{r} - \alpha D\hat{\boldsymbol{u}}_1, \hat{\boldsymbol{u}}_1, t)\hat{\boldsymbol{u}}_1 \times \left[\hat{\mathcal{R}}_1 |\hat{\boldsymbol{u}}_1\right.$$

$$\left.\times\, \hat{\boldsymbol{u}}_2 |\rho(\boldsymbol{r} - \alpha D\hat{\boldsymbol{u}}_0 - l\hat{\boldsymbol{u}}_1 - l'\hat{\boldsymbol{u}}_2, \hat{\boldsymbol{u}}_2, t)\right]_{\hat{\boldsymbol{u}}_0 = \hat{\boldsymbol{u}}}$$

The bead index summation is replaced by an integral similarly as in Eq. (3.321), leading to (with $\hat{\boldsymbol{u}} = \hat{\boldsymbol{u}}_1$ and $\hat{\boldsymbol{u}}' = \hat{\boldsymbol{u}}_2$)

$$\boldsymbol{I} = \frac{2}{D} \oint \mathrm{d}\hat{\boldsymbol{u}} \oint \mathrm{d}\hat{\boldsymbol{u}}' \int_{-L/2}^{L/2} \mathrm{d}x \int_{-L/2}^{L/2} \mathrm{d}l \int_{-L/2}^{l/2} \mathrm{d}l'\, x$$

$$\times\, \rho(\boldsymbol{r} - x, \hat{\boldsymbol{u}}, t)\hat{\boldsymbol{u}} \times \left[\hat{\mathcal{R}} |\hat{\boldsymbol{u}} \times \hat{\boldsymbol{u}}'| \rho(\boldsymbol{r} - x\hat{\boldsymbol{u}}_0 - l\hat{\boldsymbol{u}} - l'\hat{\boldsymbol{u}}', \hat{\boldsymbol{u}}, t)\right]_{\hat{\boldsymbol{u}}_0 = \hat{\boldsymbol{u}}}$$

This expression can be found in Eq. (3.279).
The contribution $\boldsymbol{I}_t$ to the stress tensor in Eq. (3.319) is evaluated similarly.

The β summations in the contribution $\boldsymbol{I}_{\mathrm{u}}$ in Eq. (3.320) are replaced by integrals, similar to Eq. (3.321), as

$$\sum_{\beta} \beta \boldsymbol{U}_{j,\beta} = D^{-2} \int \mathrm{d}x'\, x' \boldsymbol{U}(\boldsymbol{r}_j + x' \hat{\boldsymbol{u}}_j) \tag{3.324}$$

The prefactors in Eqs. (3.318) to (3.320) are found from Eqs. (3.169) and (3.171) to be equal to

$$\frac{\gamma \bar{D}}{\ln(L/D)} = \frac{D}{L} k_{\mathrm{B}} T \quad \text{and} \quad \frac{4}{3} \frac{\gamma D D_{\mathrm{r}}}{\ln(L/D)} = 12 \frac{D^2}{L^3} k_{\mathrm{B}} T$$

This concludes the mathematical details leading to Eq. (3.279).

References

Batchelor, G. K., 1970, *J. Fluid Mech.* **41**, 545.
Baumberger, T., Perrot, F., and Beysens, D., 1991, *Physica A* **174**, 31.
Berry, D. H. and Russel, W. B., 1987, *Fluid Mech.* **180**, 475.
Bolhuis, P. and Frenkel, D., 1997, *J. Chem. Phys.* **106**, 666.
Bretherton, F. P., 1962, *J. Fluid Mech.* **14**, 284.
Chauveteau, G., 1982, *J. Rheol.* **26**, 111.
Claeys, I. L. and Brady, J. F., 1993, *Fluid Mech.* **251**, 442.
de la Torre, J. G. and Bloomfield, V. A., 1981, *Q. Rev. Biophys.* **14**, 81.
Deutch, J. M. and Oppenheim, I. J., 1971, *J. Chem. Phys.* **54**, 3547.
Dhont, J. K. G., 1996, *An Introduction to Dynamics of Colloids.* Elsevier, Amsterdam.
Dhont, J. K. G., 1999, *Phys. Rev. E* **60**, 4534.
Dhont, J. K. G. and Briels, W. J., 2002, *J. Chem. Phys.* **117**, 3992.
Dhont, J. K. G. and Briels, W. J., 2003, *J. Chem. Phys.* **118**, 1466.
Dhont, J. K. G. and Nägele, G., 1998, *Phys. Rev. E* **58**, 7710.
Doi, M., 1981, *J. Polym. Sci.: Polym. Phys. Edn.* **19**, 229.
Doi, M. and Edwards, S. F., 1978a, *J. Chem. Soc., Faraday Trans. 2* **74**, 560.
Doi, M. and Edwards, S. F., 1978b, *J. Chem. Soc., Faraday Trans. 2* **74**, 918.
Doi, M. and Edwards, S. M., 1986, *The Theory of Polymer Dynamics.* Oxford University Press, Oxford.
Doi, M., Shimada, T., and Okano, K., 1988, *J. Chem. Phys.* **88**, 4070.
Erpenbeck, J. J. and Kirkwood, J. G., 1963, *J. Chem. Phys.* **38**, 1023.
Fielding, S. M. and Olmsted, P. D., 2003, *Eur. Phys. J. E* **11**, 65.
Forest, M. G. and Wang, Q., 2003, *Rheol. Acta* **42**, 20.
Fraden, S., Maret, G., Caspar, D. L. D., and Meyer, R. B., 1989, *Phys. Rev. Lett.* **63**, 2068.

Graf, C., Kramer, H., Deggelmann, M., Hagenbüchle, M., Johner, C., Martin, C., and Weber, R., 1993, *J. Chem. Phys.* **98**, 4920.
Grelet, E. and Fraden, S., 2003, *Phys. Rev. Lett.* **90**, 198302.
Happel, J. and Brenner, H., 1983, *Low Reynolds Number Hydrodynamics.* Martinus Nijhoff, The Hague.
Hess, S. and Kröger, M., 2004, *J. Phys.: Condens. Matter* **38**, 3835.
Hinch, E. J. and Leal, L. G., 1972, *J. Fluid Mech.* **52**, 683.
Hinch, E. J. and Leal, L. G., 1976, *J. Fluid Mech.* **76**, 187.
Iizuka, E., 1978, Personal communication with Kiss and Porter (1978)
Ingber, M. S. and Mondy, L. A., 1994, *J. Rheol.* **38**, 1829.
Jeffery, G. B., 1922, *Proc. R. Soc. London, Ser. A* **102**, 161.
Kang, K., Lettinga, M. P., and Dhont, J. K. G., 2004, unpublished.
Kiss, G., 1996, *J. Polym. Sci.: Part B: Polym. Phys.* **34**, 2263.
Kiss, G. and Porter, R. S., 1978, *J. Polym. Sci.: Polym. Symp.* **65**, 193.
Kuhn, W. and Kuhn, H., 1945, *Helv. Chim. Acta* **28**, 97 (in German).
Kuzuu, N. and Doi, M., 1983, *J. Phys. Soc. Japan* **52**, 3486.
Larson, R. G., 1990, *Macromolecules* **23**, 3983.
Larson, R. G., 1996, *J. Polym. Sci.: Part B: Polym. Phys.* **34**, 2267.
Larson, R. G., 1999, *The Structure and Rheology of Complex Fluids*. Oxford University Press, Oxford.
Leal, L. G. and Hinch, E. J., 1972, *J. Fluid Mech* **55**, 161.
Lenstra, T. A. J., Dogic, Z., and Dhont, J. K. G., 2001, *J. Chem. Phys.* **114**, 10151.
Lettinga, M. P. and Dhont, J. K. G., 2004, *J. Phys.: Condens. Matter* **16**, 3929.
Lu, C.-Y., Olmsted, P. D., and Ball, R. C., 2000, *Phys. Rev. Lett.* **84**, 642.
Magda, J. J., Baek, B. S.-G., de Vries, K. L., and Larson, R. G., 1991, *Macromolecules* **24**, 4460.
Maier, W. and Saupe, A., 1958, *Z. Naturforsch.* **13A**, 564.
Maier, W. and Saupe, A., 1959, *Z. Naturforsch.* **14A**, 882.
Maier, W. and Saupe, A., 1960, *Z. Naturforsch.* **15A**, 287.
Marrucci, G. and Maffettone, P. L., 1989, *Macromolecules* **22**, 4076.
Marrucci, G. and Maffettone, P. L., 1990a, *J. Rheol.* **34**, 1217.
Marrucci, G. and Maffettone, P. L., 1990b, *J. Rheol.* **34**, 1231.
Mead, D. W. and Larson, R. G., 1990, *Macromolecules* **23**, 2524.
Murphy, T. J. and Aquirre, J. L., 1972, *J. Chem. Phys.* **57**, 2098.
Olmsted, P. D., 1999, *Europhys. Lett.* **48**, 339.
Olmsted, P. D. and Lu, C.-Y. D., 1999, *Phys. Rev. E* **60**, 4397.
Olmsted, P. D., Radulescu, O., and Lu, C.-Y. D., 2000, *J. Rheol.* **44**, 257.
Onsager, L., 1933, *Chem. Rev.* **13**, 73.
Onsager, L., 1942, *Phys. Rev.* **62**, 558.
Onsager, L., 1949, *Ann. N. Y. Acad. Sci.* **51**, 627.

Oseen, C. W., 1927, *Neuere Methoden und Ergebnisse in der Hydrodynamik*. Akademische Verlagsgesellschaft, Leipzig.
Papathanasiou, T. D. and Guell, D. C., 1997, *Flow-Induced Alignment in Composite Materials*. Woodhead, Cambridge.
Rienäcker, G. and Hess, S., 1999, *Physica A* **267**, 294.
Russel, W. B., Saville, D. A., and Schowalter, W. R., 1991, *Colloidal Dispersions*. Cambridge University Press, Cambridge.
Schmidt, F. G., Hinner, B., Sackmann, E., and Tang, J. X., 2000, *Phys. Rev. E* **62**, 5509.
Shimada, T., Doi, M., and Okano, K., 1988, *J. Chem. Phys.* **88**, 7181.
Simha, R., 1940, *J. Phys. Chem.* **44**, 25.
Solomon, M. J. and Boger, D. V., 1998, *J. Rheol.* **42**, 929.
Strating, P., 1995, *J. Chem. Phys.* **103**, 10226.
Tang, J. and Fraden, S., 1993, *Phys. Rev. Lett.* **71**, 3509.
Tang, J. and Fraden, S., 1995, *Liq. Cryst.* **19**, 459.
Tao, Y., den Otter, W. K., Padding, J. P., and Briels, W. J., 2005, *J. Chem. Phys.* **122**, 244903.
Vermant, J., Yang, H., and Fuller, G. G., 2001, *AIChE J.* **47**, 790.
Winkler, R. G. and Gompper, G., 2004, unpublished.
Winkler, R. G., Mussawisade, K., Ripoll, M., and Gompper, G., 2004, *J. Phys.: Condens. Matter* **16**, S3941.
Winters, J. W., Odijk, T., and van der Schoot, P., 2000, *Phys. Rev. E* **63**, 011501.
Yamamoto, S. and Matsuoka, T., 1995, *J. Chem. Phys.* **102**, 2254.
Yamane, Y., Kaneda, Y., and Doi, M., 1994, *J. Non-Newtonian Fluid Mech.* **54**, 405.
Yang, J. T., 1987, *Dynamics of Polymeric Liquids*, vol. 2. John Wiley and Sons, New York.
Zirnsak, M. A., Hur, D. U., and Boger, D. V., 1994, *J. Non-Newtonian Fluid Mech.* **54**, 153.

Index

Soft Matter, Vol. 2: Complex Colloidal Suspensions. Edited by G. Gompper and M. Schick

ISBN: 3-527-31369-9